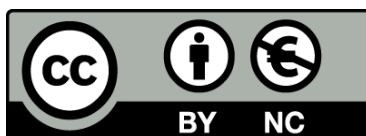




UNIVERSITAT DE
BARCELONA

**Diverse origin and processes
in the formation of diamond and other exotic minerals
in ophiolitic chromitites**

Núria Pujol Solà



Aquesta tesi doctoral està subjecta a la llicència **Reconeixement- NoComercial 4.0. Espanya de Creative Commons**.

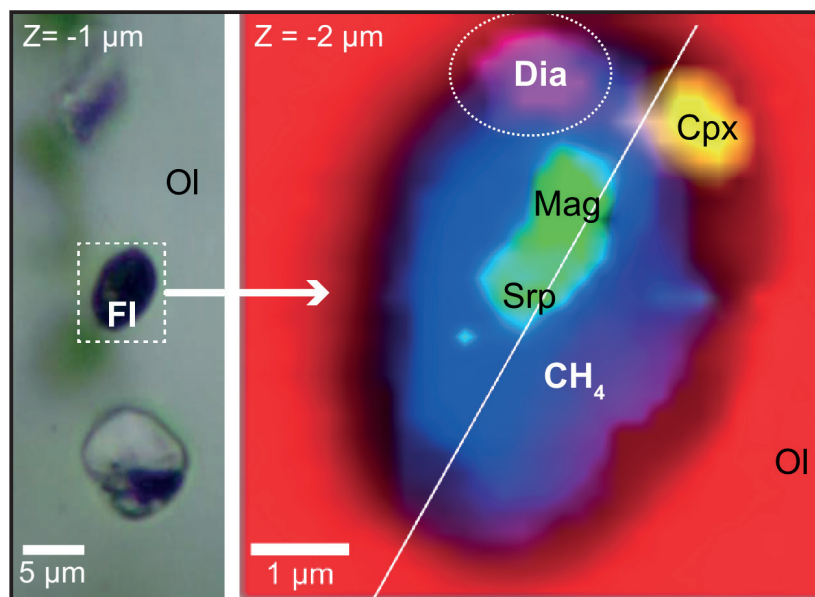
Esta tesis doctoral está sujeta a la licencia **Reconocimiento - NoComercial 4.0. España de Creative Commons**.

This doctoral thesis is licensed under the **Creative Commons Attribution-NonCommercial 4.0. Spain License**.



UNIVERSITAT DE
BARCELONA

Diverse origin and processes in the formation of diamond and other exotic minerals in ophiolitic chromitites



Ph.D. Thesis
Núria Pujol Solà
2021



UNIVERSITAT DE
BARCELONA

Facultat de Ciències
de la Terra

Diverse origin and processes in the formation of diamond and other exotic minerals in ophiolitic chromitites

Tesi doctoral presentada per

Núria Pujol Solà

Memòria de tesi doctoral presentada com a compendi d'articles per optar al títol de doctora per la Universitat de Barcelona amb Menció Internacional

Tesi realitzada dins el Programa de Doctorat de Ciències de la Terra per la Universitat de Barcelona, sota la direcció del Dr. Joaquín A. Proenza de la Universitat de Barcelona i el Dr. Antonio García Casco de la Universidad de Granada

La Doctoranda

Els Directors

PROENZA
FERNANDEZ
Z JOAQUIN
ANTONIO -
47913772B

Firmado digitalmente por
PROENZA
FERNANDEZ
JOAQUIN
ANTONIO -
47913772B
Fecha: 2021.05.03
14:28:19 +02'00'

Núria Pujol Solà

**Joaquín Antonio
Proenza Fernández**

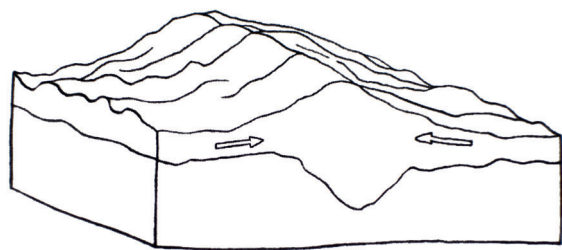
**Antonio Garcia
Casco**

Barcelona, maig de 2021

This work has been carried out in the Department de Mineralogia, Petrologia i Geologia Aplicada from the Facultat de Ciències de la Terra, Universitat de Barcelona.

Núria Pujol Solà benefited from the “Formación del Profesorado Universitario (FPU)” predoctoral grant by the Spanish “Ministerio de Educación y formación profesional”. The PhD thesis is framed within the project CGL2015-65824 “Diamante, circón y otros minerales “exóticos” en cromititas ofiolíticas y rocas asociadas, implicaciones para la geodinámica mantélica (DIACRO)” developed by the international research group “Caribbean lithosphere” (CALOR; <http://caribbeanlithos.ub.edu/>). The two short stays at the Universidad de Granada and Luleå University of Technology were funded by the “Ayudas complementarias de movilidad destinadas a beneficiarios del programa de Formación del Profesorado Universitario (FPU)” grants.

A la Glòria, en Josep, la Montse i en Pol.



“Si fes l’esforç d’evocar el cruixit eixordador. La fondària incandescent, roja i incontrolable. Si rememorés el xoc lent i terrible, les sacsejades i els terratrèmols, les columnes de fum i de pols, els esvorancs que es precipitaven fins al fons de roca líquida i calenta.”

“Veniu aquí, veniu, que us deixaré un tros d’esquena per fer-vos-hi una casa.”

Irene Solà
“Canto jo i la muntanya balla”

Acknowledgments / Agraïments / Agradecimientos

Over the past 4 (almost 5) years, I have met many people that made possible the development of this Ph.D. thesis. In the following (multilingual) lines, I would like to express my gratitude to everyone who has accompanied me along the way.

First and foremost, I would like to thank my co-advisors, Joaquín A. Proenza and Antonio García Casco, for this opportunity and all the dedication and guidance during this journey. *Moltes gràcies Joa per ser-hi sempre, per posar les coses tan fàcils i encarar sempre la feina "sin presión". Gràcies a tu he pogut aprendre molt tan a nivell científic com a nivell personal durant aquests anys. Muchas gracias, Antonio, por aceptarme como estudiante de doctorado sin conocerme, por tu entusiasmo y por abrirme las puertas a la Universidad de Granada. También quiero agradecer a José María González Jiménez su participación en la tesis y su motivación.*

Vull agrair de manera especial a en Joan Carles Melgarejo haver-me introduït al món de la recerca durant el grau i haver estat sempre inspiració i un suport a la universitat.

A la Júlia Farré, que ha estat la companya de viatge durant tants anys, moltes gràcies per totes les xerrades, experiències, aventures, viatges, congressos i pel suport que ha estat tan bàsic per tirar endavant. També a les amigues i companyes de doctorat, la Núria Bach i la Nia Schamuells.

El suport del Departament de Mineralogia Petrologia i Geologia Aplicada de la Facultat de Ciències de la Terra ha estat indispensable i vull agrair especialment a les persones que m'han ajudat des del principi i amb qui he col·laborat d'alguna manera durant la tesi. Moltes gràcies Lisard Torró, Cristina Villanova, Thomas Aiglsperger, Lidia Butjosa, Cristina Domènech, Josep Roqué, Marc Campeny, Sandra Amores, Salvador Galí, Àngels Canals, Maite Garcia i Esperança Tauler. També vull agrair el suport del personal administratiu, Elisenda Farré i Sandra Cegarra. Moltes gràcies als companys doctorands i amics, Jingyao Xu, Nils Reinhart, Ariana Carrazana, Jorge Macridachis, Diego Domínguez, Rosanna Margalef, als estudiants que han passat pel despatx, Sebastián Betancur, Helena Escalona, Carlos Ramírez, i als membres del Barcelona SGA-SEG Student Chapter per tots els moments compartits. También quiero agradecer el soporte del resto de miembros del grupo Geo-Caribe, Vanessa Colás, Carl Nelson, Carmen, Yamirka Rojas, Idael Blanco i Faouziya Haissen.

The investigation was conducted thanks to many people from different laboratories. From the *Centres Científics i Tecnològics de la Universitat de Barcelona (CCiTUB)*, I am particularly indebted to Xavier Llovet for his help and dedication during the EMPA sessions, to Tariq Jawhari for all the patience in the long analytical sessions, and to Javier García and David Artiaga for the SEM sessions. I also want to acknowledge the help by Dolors Barsó, Montse Sibila, Fadoua Zoura Oumada, and Vicenç Planella from the thin section lab at the *Universitat de Barcelona*. From the *Universidad de Granada*, I want to thank Jesús Montes from the thin section lab, Bendición Funes for her patience during the microRaman sessions, José Romero and Aleu Andreazini for the XRD measurements and for the coffees, Miguel Ángel Hidalgo for the assistance during the

EMPA sessions, and María del Mar Abad and María José Martínez for the support during the TEM sessions. I deeply thank Manuel Jesus Román Alpiste from the *Instituto Andaluz de Ciencias de la Tierra (IACT)* for the trace elements and dating analyses and the long analytical sessions, and Carlos J. Garrido and Károly Hidas for their hospitality in the IACT. Adolfo del Campo, from the *Instituto de Cerámica y Vidrio (CSIC)*, is profoundly acknowledged for his work with the confocal Raman maps to help characterize the nanodiamond grains or the “needles in the haystack”. Isabel Rivas and Laura Casado from the *Instituto de nanociencias de Aragón, Universidad de Zaragoza*, and Trifon Trifonov from the *Centre de Recerca en Ciència i Enginyeria Multiescala de Barcelona, Universitat Politècnica de Catalunya (UPC)* are thanked for their assistance during the FIB sessions. I also thank Ricardo Arenas and Sonia Sánchez Martínez from the *Universidad Complutense de Madrid* for the rewarding discussions and for their collaboration.

This project would not have been possible without the fieldwork organized by Faouziya Haissen to the Bou Azzer area, which was followed by the celebration of New Year’s Eve in the middle of the desert. I am really grateful to Faouziya, as well as to the MANAGEM mining company for their logistical support, to Moha Ikenne to share his knowledge on the area, and to all the participants to the field trip, who made of this trip a memorable experience. I also want to thank Marion Weber and Idael Blanco Quintero for the organization of the field trip to Medellín and all the participants.

I want to thank the hospitality received during my stay at the *Universidad de Granada*, especially to Antonio García Casco, José María González Jiménez, Fernando Gervilla, Antonio Sánchez Navas, and to the office colleagues Fabián Villares, Irene Morales, and Paola de Melo. I appreciate the opportunity to use different analytical techniques from the *Centro de Instrumentación Científica* during my stay. I also want to thank the warm welcome at the Luleå University of Technology from Thomas Aiglsperger, Bernhard Dold, Lena Alankagas, and specially from Carmen Zwhalen.

I would also like to thank the coauthors that participated in the four papers included in the Ph.D. thesis, who made accurate scientific revisions of the texts, and the reviewers, whose constructive comments and observations helped to improve the articles.

Finalment vull agrair el suport incondicional de la meua família, sobretot als meus pares per alimentar la meua curiositat des de ben petita, per animar-me sempre a saber més coses i per fer-me sentir capaç de tot, també a la meua germana, Montse, a la meua iaia i a en Xevi. Moltes gràcies als amics i amigues que m’han acompanyat durant aquesta etapa. I Pol, moltíssimes gràcies per formar part d’aquesta aventura, primer et vas animar a venir a viure al pol nord durant tres mesos i després la covid ha fet que passéssim mesos i mesos treballant de costat; has patit el final de la tesi, però has estat el millor suport que podia tenir.

Moltes gràcies! Muchas gracias! Thank you very much! Merci beaucoup! Tack så mycket!

Table of Contents

ABSTRACT	13
RESUM	15
1. GENERAL OVERVIEW	17
1.1 Ophiolites.	17
1.2 Ophiolitic chromitites	20
1.3 Exotic minerals in ophiolitic chromitites.	22
1.4 Hypothesis and objectives	26
1.5 Areas of study	26
1.5.1 <i>Eastern Cuba</i>	26
1.5.2 <i>Bou Azzer</i>	27
1.6 Published articles.	27
1.6.1 <i>Article 1</i>	27
1.6.2 <i>Article 2</i>	29
1.6.3 <i>Article 3</i>	30
1.6.4 <i>Article 4</i>	30
2. GENERAL RESULTS	31
2.1 Interaction zone between chromitite and gabbroic intrusions	31
2.2 Exotic minerals in high-Al chromitites	32
2.3 Diamond-bearing fluid inclusions in olivine from gabbro and chromitite ..	33
2.4 Neoproterozoic chromitites from Bou Azzer.	33
3. SUMMARY OF THE OVERALL DISCUSSIONS	35
3.1 Fe-Ti-Zr metasomatism in the oceanic lithosphere	35
3.2 Exotic minerals in high-Al chromitites from eastern Cuba ophiolites	37
3.2.1 <i>Nominally UHP mineral phases</i>	37
3.2.2 <i>Super-reduced (SuR) conditions and serpentinization</i>	38
3.2.3 <i>Metastable formation of diamond during serpentinization</i>	39

3.2.4 Continental crust-derived minerals.	41
3.3 Comparison of the Bou Azzer Neoproterozoic and the eastern Cuba Cretaceous chromitites	41
4. CONCLUDING REMARKS	45
REFERENCES	47
APPENDICES	59
A1. Article 1	59
<i>Pujol-Solà, N., Proenza, J.A., Garcia-Casco, A., González-Jiménez, J.M., Román-Alpiste, M.J., Garrido, C.J., Melgarejo, J.C., Gervilla, F., Llovet, X., 2020. Fe-Ti-Zr metasomatism in the oceanic mantle due to extreme differentiation of tholeiitic melts (Moa-Baracoa ophiolite, Cuba). Lithos 358–359, 105420. https://doi.org/10.1016/j.lithos.2020.105420</i>	
A2. Article 2	111
<i>Pujol-Solà, N., Proenza, J., Garcia-Casco, A., González-Jiménez, J., Andreazini, A., Melgarejo, J., Gervilla, F., 2018. An Alternative Scenario on the Origin of Ultra-High Pressure (UHP) and Super-Reduced (SuR) Minerals in Ophiolitic Chromitites: A Case Study from the Mercedita Deposit (Eastern Cuba). Minerals 8, 433. https://doi.org/10.3390/min8100433</i>	
A3. Article 3	137
<i>Pujol-Solà, N., Garcia-Casco, A., Proenza, J.A., González-Jiménez, J.M., del Campo, A., Colás, V., Canals, A., Sánchez-Navas, A., Roqué-Rosell, J., 2020. Diamond forms during low pressure serpentinisation of oceanic lithosphere. Geochemical Perspectives Letters 15, 19–24. https://doi.org/10.7185/geochemlet.2029</i>	
A4. Article 4	161
<i>Pujol-Solà, N., Domínguez-Carretero, D., Proenza, J.A., Haissen, F., Ikenne, M., González-Jiménez, J.M., Colás, V., Maacha, L., Garcia-Casco, A., 2021. The chromitites of the Neoproterozoic Bou Azzer ophiolite (Central Anti-Atlas, Morocco) revisited. Ore Geology Reviews 134, 104166. https://doi.org/10.1016/j.oregeorev.2021.104166</i>	

Abstract

The recent discovery of ultra-high pressure (UHP), super-reduced (SuR), and continental crust-derived minerals in ophiolitic chromitites worldwide has challenged the previous hypotheses for chromitite formation and has motivated the proposal of complex geodynamic models involving ultra-high pressure conditions of formation for the chromite or recycling of the ophiolitic rocks down to the Mantle Transition Zone (410 – 660 km depth). This thesis investigates in detail the chromitites and the associated ophiolitic rocks from the Moa-Baracoa massif in eastern Cuba and Bou Azzer in Morocco with emphasis on identifying the presence of exotic minerals, interpreting their formation, and understanding the related geodynamic processes.

The interaction of preexisting chromitites with evolved tholeiitic melts that triggered Fe-Ti-Zr metasomatism in the Potosí chromitites (eastern Cuba) is carefully investigated here. There is evidence of coarse granular textures and strongly variable mineralogy composed of recrystallized/neoformed Fe³⁺-Ti-rich chromite, Ti-rich amphibole, clinopyroxene, orthopyroxene, olivine, Mg-rich ilmenite, Zr-bearing oxides and silicates, and Fe-Cu-Ni sulfides in the interaction area. Thorough petrographic analysis coupled with the chemical composition of the mineral phases allowed to determine the sequence of mineral formation and to propose a two-stage genetic model: 1) the crystallization of an evolved MORB liquid, via fractional crystallization, produced water-rich residual melts strongly enriched in incompatible elements, and 2) batches of this evolved melt escaped and extensively reacted and metasomatized the surrounding chromitites. U/Pb dating of baddeleyite indicates that the age of the metasomatic event (134.4 ± 14 Ma) matches the age of magmatism related to ophiolite construction in eastern Cuba.

The high-Al chromitites of eastern Cuba (Mercedita and Potosí deposits) contain exotic minerals of the three categories: diamond, oriented clinopyroxene and rutile lamellae, graphite-like amorphous carbon, moissanite, native Cu and Si, Fe-Mn alloys, zircon, corundum, and

quartz. The studied diamond grains are nanometric in size, located in CH₄-bearing fluid inclusions within olivine, and systematically associated with a typical serpentinization mineral assemblage composed of serpentine-group minerals and magnetite. Textural-mineralogical evidences indicate that nanodiamond formed during low pressure and low temperature serpentinization in super-reduced microenvironments ($\log [fO_2; \text{MPa}] = -45.3$; $\Delta \log fO_2 [\text{Iron-Magnetite}] = -6.5$). The other SuR minerals (moissanite, graphite-like amorphous carbon, native elements, and alloys) also formed in super-reduced CH₄-rich microenvironments. On the other hand, nominally UHP phases such as the oriented clinopyroxene lamellae formed as exsolutions after the crystallization of chromite or can represent silicate melt inclusions attached to the growing chromite grains. Oriented rutile lamellae formed after the interaction of chromitites with mafic magma (gabbro sills). Finally, continental crust-derived minerals, such as zircon, likely represent xenocrystic material derived from the subducting slab that was entrapped by the chromitite parental melts.

The investigation of the Neoproterozoic Bou Azzer chromitites (Anti-Atlas, Morocco) allowed the comparison with the younger Cretaceous eastern Cuba chromitites and other Phanerozoic and Precambrian chromitites. It was possible to determine that the Bou Azzer chromitites formed in the fore-arc setting during subduction-initiation with two stages of evolution: 1) formation of intermediate-Cr chromitites from fore-arc basalts (FAB), and 2) formation of high-Cr chromitites after boninitic melts. These chromitites host inclusions of platinum group minerals and exotic minerals. The unusual mineralogy includes oriented clinopyroxene lamellae, moissanite, native Cu, diaspore, and zircon formed after chromite crystallization and post-magmatic serpentinization processes, thus completely ruling out ultra-high pressure conditions.

Altogether, the results of these investigations represent the first descriptions of exotic minerals in the Cuban and Moroccan ophiolites. The corresponding discussions allowed to reject hypotheses of ultra-high pressure formation or recycling for the studied chromitites and the associated ophiolitic sequences and to ultimately provide simpler formation models for the exotic minerals. Additionally, the investigation provided definitive evidence for the formation of metastable nanodiamond and other SuR phases during serpentinization of the oceanic lithosphere at low pressure and low temperature conditions. Therefore, the presence of diamond in oceanic rocks, in particular chromitites, cannot be taken as a general indication of deep mantle recycling at ultra-high pressure conditions.

Resum

Arran del descobriment de minerals exòtics d'ultra alta pressió, de condicions superreduïdes i derivats de l'escorça continental en cromitites ofiolítiques d'arreu del món, s'han proposat models geodinàmics molt complexos per explicar-ne la presència i la formació. Aquests models interpreten que les cromitites s'han format, o bé s'han reciclat, en condicions d'ultra alta pressió a la zona de transició del mantell (410 – 660 km de profunditat). En aquesta tesi doctoral s'han investigat en detall les cromitites ofiolítiques i les roques associades del massís de Moa-Baracoa a Cuba Oriental i de Bou Azzer al Marroc per tal d'identificar la presència de minerals exòtics i interpretar-ne la formació, així com entendre els processos geodinàmics relacionats.

A la zona de Potosí, Cuba Oriental, s'ha investigat la interacció de líquids toleítics evolucionats amb cromitites preexistents, que ha donat lloc a metasomatisme modal de tipus Fe-Ti-Zr. A la zona d'interacció s'observen textures granulars de gra groller i una mineralogia molt variable que inclou cromita recristal·litzada rica en Fe³⁺ i en Ti, amfibol ric en Ti, clinopiroxè, ortopiroxè, olivina, ilmenita rica en Mg, òxids i silicats de Zr i sulfurs de Fe, Cu i Ni. La petrografia en detall i l'estudi de la composició de les fases minerals ha permès determinar la seqüència de formació mineral i proposar un model de formació en dues etapes: 1) la cristal·lització d'un magma de tipus MORB (basalts de dorsal centro-oceànica) genera, mitjançant cristal·lització fraccionada, magmes residuals enriquits en aigua i en elements incompatibles, i 2) alguns d'aquests magmes residuals escapen de la cristal·lització i reaccionen amb les cromitites, produint així el metasomatisme observat. La datació U/Pb de cristalls de baddeleyita ha permès obtenir l'edat del metasomatisme (134.4 ± 14 Ma), que coincideix amb el rang d'edat determinat per a la formació de les ofiolites de Cuba Oriental.

A les cromitites ofiolítiques de Cuba Oriental (cromitites riques en alumini dels dipòsits de Mercedita i de Potosí) s'han pogut identificar minerals exòtics dels tres grups, que són: diamant,

lamel·les orientades de clinopiroxè i de rútil en cromita, carboni amorf, moissanita, Si i Cu natiu, aliatges de Fe-Mn, zircó, corindó i quars. Els grans de diamant estudiats són de mida nanomètrica, es troben en inclusions fluides juntament amb metà i estan sistemàticament associats amb fases típiques de la serpentinització, com són minerals del grup de la serpentina i magnetita. Totes les evidències texturals i mineraològiques indiquen que els nanodiamants es van formar durant la serpentinització en ambients superreduïts ($\log [fO_2; \text{MPa}] = -45.3; \Delta \log fO_2 [\text{Ferro-Magnetita}] = -6.5$) en condicions de baixa pressió i temperatura. Els altres minerals superreduïts, la moissanita, el carboni amorf, els elements nadius i els aliatges, també es van formar en microambients superreduïts produïts pels fluids rics en CH_4 relacionats amb la serpentinització. En canvi, les fases nominalment d'alta pressió, les lamel·les orientades de clinopiroxè, es van formar com a exsolucions degut a la cristal·lització de la cromita i podrien representar inclusions de fosos silicatats. Les lamel·les orientades de rútil es van formar per la interacció de les cromitites amb magmes màfics (gabres). Finalment, els minerals derivats de l'escorça continental, com el zircó, podrien representar material derivat de la placa subduït que va ser atrapat pels magmes dels quals va cristal·litzar posteriorment la cromita.

La investigació dels minerals exòtics a les cromitites neoproterozoïques de Bou Azzer (Anti-Atlas, Marroc) ha permès comparar-les amb les cromitites més recents de Cuba, d'edat cretàica, i també amb altres cromitites fanerozoïques i precambrianes. S'ha pogut determinar que les cromitites de Bou Azzer es van formar en una zona d'avant-arc, en un context d'inici de subducció on es poden diferenciar dos estadis de formació: 1) formació de les cromitites de composició intermèdia a partir de basalts d'avant-arc (FAB), i 2) formació de les cromitites riques en Cr a partir de boninites. Aquestes cromitites contenen inclusions de minerals del grup del platí i de minerals exòtics com són lamel·les orientades de clinopiroxè, moissanite, Cu natiu, diàspora i zircó. La formació dels minerals exòtics es relaciona amb la cristal·lització de la cromita i amb els processos posteriors de serpentinització, descartant també les condicions d'ultra alta pressió.

De manera global, els resultats d'aquestes investigacions representen la primera descripció de minerals exòtics a les ofiolites de Cuba i del Marroc. Les respectives discussions han permès descartar la formació o el reciclatge en condicions d'ultra alta pressió de les cromitites i de les roques ofiolítiques associades i, finalment, proposar models de formació més simples pels minerals exòtics. A més a més, s'ha pogut determinar que el diamant de mida nanomètrica i les altres fases superreduïdes es poden formar durant la serpentinització de la litosfera oceànica en condicions de baixa pressió i baixa temperatura. Per tant, no sempre es pot utilitzar la presència de diamant en roques oceàniques com a indicador inequívoc de condicions d'ultra alta pressió o de profunditat elevada.

1. General overview

1.1 Ophiolites

Since the onset of plate tectonics, it was made clear that oceanic lithosphere forms at spreading ridges and is consumed at subduction zones. For this reason, there is no oceanic lithosphere older than 200 Ma remaining in place nowadays (Müller *et al.*, 2008; Williams *et al.*, 2021). However, tectonic slices and fragments of ancient oceanic lithosphere, known as ophiolites, may be preserved accreted to continental margins as a result of collision events. The term “ophiolite” was first defined in 1972 by the participants in the *Penrose Conference* referring to a distinctive assemblage of mafic to ultramafic rocks representatives of oceanic lithosphere (Anonymous, 1972) formed at mid-ocean ridge settings, and it was refined in the following years to include the different types of ophiolites not formed at mid-ocean ridges (Miyashiro, 1973, 1975; Coleman, 1977; Pearce *et al.*, 1984; Nicolas, 1989; Dilek, 2003; Dilek and Furnes, 2011, 2014; Pearce, 2014).

A typical ophiolitic sequence includes from bottom to top (**Fig. 1**): (1) upper mantle peridotites, commonly harzburgites with layers of lherzolites, dunites, and pyroxenites, and eventually hosting chromitite bodies; (2) layered ultramafic-mafic rocks that form a transitional mantle-crust section corresponding to the petrological Moho; (3) layered to isotropic

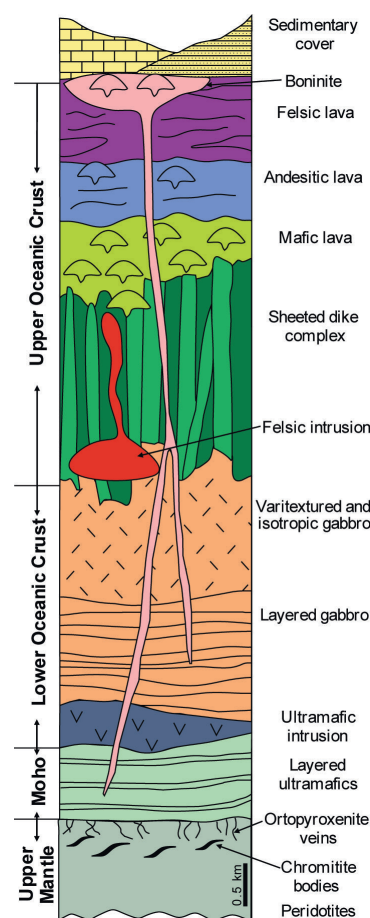


Figure 1. Schematic general sequence of a suprasubduction zone ophiolite. Modified from Dilek and Furnes (2014).

(massive) gabbros, consisting mainly of olivine gabbro and gabbro and subordinate troctolite, gabbronorite, norite, and anorthosite layers, with crosscutting pegmatitic gabbro and plagiogranite dikes near the top; (4) a sheeted dike complex; (5) extrusive rocks including pillow lavas, pillow breccias, and massive lava flows, with predominant basaltic composition but ranging from basalt to andesite, dacite and rhyolite at the top; and (6) an overlying sedimentary cover (**Fig. 1**; *e.g.*, Dilek and Furnes, 2014 and references therein).

Taking into account the geochemical characteristics, internal structure, thickness, proximity to plume or trenches, the mantle temperature and fertility, and the availability of fluids, Dilek and Furnes (2014) classified the ophiolitic sequences into two main categories: subduction-unrelated and subduction-related ophiolites. Subduction-unrelated ophiolites include continental margin, mid-ocean ridge, and plume-type ophiolites, whereas subduction-related ophiolites include suprasubduction zone ophiolites (fore-arc and back-arc) and volcanic arc type ophiolites (**Fig. 2**). Pearce (2014) divided the suprasubduction zone ophiolites according to their geochemical and petrological differences into subduction-initiation and back-arc basin ophiolites.

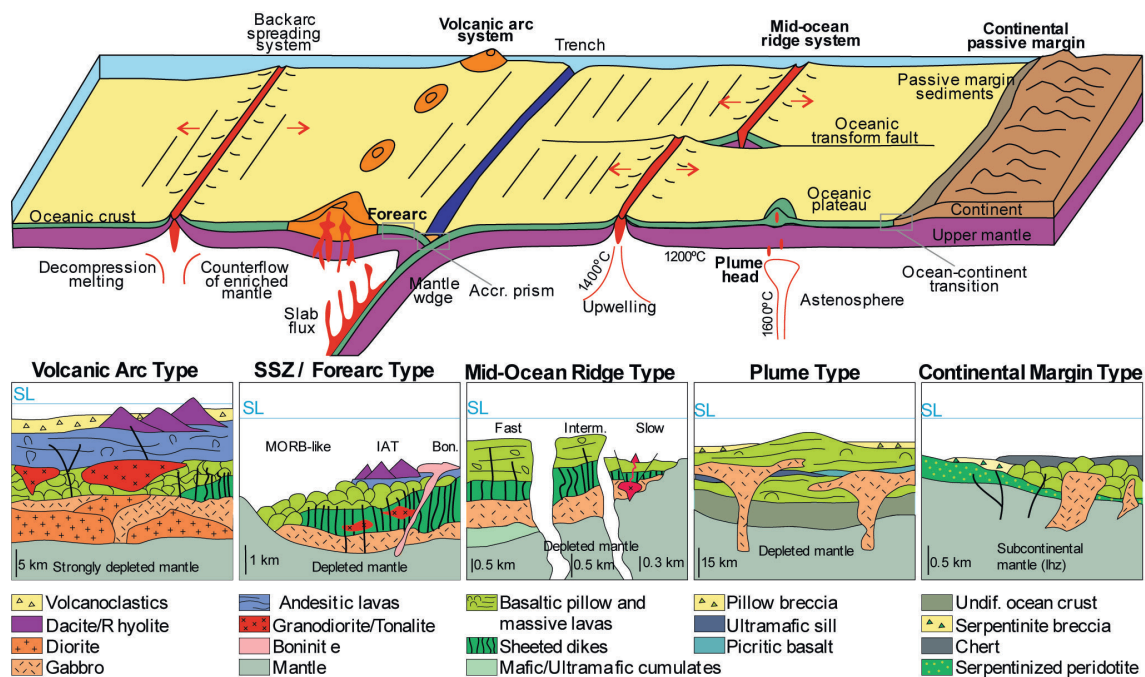


Figure 2. Top: Schematic geodynamic setting (not to scale) of magmatic construction of oceanic lithosphere. Bottom: Structural sequence of main ophiolites types; SL: sea level. Composed and modified from Dilek and Furnes (2011, 2014) and Furnes and Dilek (2017).

The study of ophiolites is fundamental to understand the processes of formation, deformation, and preservation of oceanic lithosphere and, because of their complexity and variety of rocks, it involves diverse geological disciplines including geochemistry, igneous and metamorphic petrology, and structural geology. Studies on ophiolites have shed light in many areas of Earth sciences, especially in the onset and reconstruction of plate tectonics (*e.g.*, Stern, 2005). For instance, the oldest suprasubduction zone ophiolites, the 3.8 Ga Nuvvuagittuq ophiolite in Canada and Isua ophiolite in SW Greenland (Furnes *et al.*, 2015 and references therein), suggest that

subduction processes might have been already active in the early Archean, much earlier than what was interpreted before (*e.g.*, Stern, 2005), although possibly not in the same style and rates as today (see Furnes *et al.*, 2015).

Ophiolites are also important from an economic point of view, since they may contain resources of Cr, Cu, Au, Zn, Ni, Co, Sc, and platinum group elements (PGE), as well as other minor but remarkable elements such as Bi, In, Se, Te, Cd, Ga, and Sb (*e.g.*, Leblanc, 1991; Hannington *et al.*, 1997; Proenza *et al.*, 2004; González-Jiménez *et al.*, 2014a, 2014b; Hannington, 2014; Monecke *et al.*, 2016; Aiglsperger *et al.*, 2016; Maurizot *et al.*, 2019; Pirajno *et al.*, 2020). Examples of these ore deposits are the chromitite bodies hosted within mantle peridotites that may host economical PGE concentrations (*e.g.*, Leblanc and Nicolas, 1992; Melcher *et al.*, 1997; Proenza *et al.*, 1999; González-Jiménez *et al.*, 2014a, 2014b); volcanogenic massive sulfides (VMS) related to hydrothermal processes during the structuration of the oceanic crust (*e.g.*, Galley and Koski, 1999; Piercey, 2011; Torró *et al.*, 2017); nickeliferous laterites formed after weathering of exhumed peridotites in tropical regions (*e.g.*, Lewis *et al.*, 2006; Butt and Cluxel, 2013; Villanova-de-Benavent *et al.*, 2014; Proenza, 2015; Maurizot *et al.*, 2019; Tobón *et al.*, 2020); and gold deposits hosted by listwaenites (*e.g.*, Buisson and Leblanc, 1986; Azer, 2013; Rajendran *et al.*, 2013). Non-metallic minerals such as chrysotile asbestos and jade have also been largely exploited from serpentinized peridotites (*e.g.*, Harlow and Sorensen, 2005; Cárdenas-Párraga *et al.*, 2012).

Suprasubduction zone (SSZ) ophiolites (Pearce *et al.*, 1984) are the most typical and abundant type of ophiolite (*e.g.*, Wakabayashi and Dilek, 2004; Metcalf and Shervais, 2008; Wakabayashi *et al.*, 2010; Stern *et al.*, 2012; Dilek and Furnes, 2014; Furnes *et al.*, 2015). These are structured in a fore-arc – arc – back-arc geodynamic setting (**Fig. 3**) during the evolution of subduction, from subduction-initiation to steady-state subduction and mature volcanic arc formation. In this geodynamic setting, melting of mantle peridotites occurs at relatively shallow depths (<100 km; **Figs. 3 and 4**; Niu, 1997; Walter, 2003; Marchesi *et al.*, 2016; Butjosa, 2018) at pressures <40 kbar, generally in the spinel harzburgite stability field (**Fig. 4**). Boninite magmas are generated via high degrees of partial melting (>20%) of refractory mantle (~1130 – 1275 °C) at low-pressure (0.3 – 1.7 kbar; see reviews by Kushiro, 2007; Pearce and Reagan, 2019), whereas the average

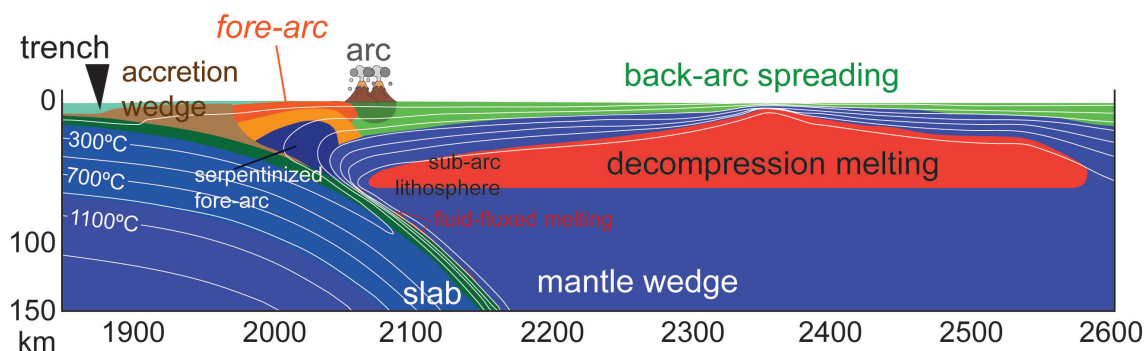


Figure 3. Schematic cross-section of an intra-oceanic arc associated with retreating subduction. Modified from Gerya (2011).

mantle separation temperature for fore-arc basalts (FAB) is 1380 °C at 15 kbar (Shervais *et al.*, 2019) (**Fig. 5**).

The composition of the mantle source evolves from lherzolitic unaffected by slab-derived fluids (similar to MORB mantle) during the earliest subduction-initiation stage, towards more depleted harzburgite progressively modified (metasomatized) by slab-derived fluids as subduction proceeds (Whattam and Stern, 2011). Following the evolution of the mantle source, the erupted magmas evolve from early decompression

melts, known as fore-arc basalts (FAB; Reagan *et al.*, 2010; Shervais *et al.*, 2019), to boninitic lavas (high-Mg andesites) that are more affected by hydrous fluids. This evolution is observed in the Izu-Bonin-Mariana convergent margin (Reagan *et al.*, 2010; Ishizuka *et al.*, 2011; Whattam *et al.*, 2020). The volcanic arc develops when a steady-state or mature subduction is achieved (**Fig. 3**) and the composition of the arc lavas is typically calc-alkaline and LREE-enriched (*e.g.*, Stern, 2010; Stern *et al.*, 2012). In intra-oceanic volcanic arcs, there is usually extension in the back-arc region (**Fig. 3**), which triggers volcanism and the formation of a back-arc basin (*e.g.*, Stern, 2010). These back-arc basin basalts (BABB) are tholeiitic, with MORB-like compositions but slightly more hydrous (*e.g.*, Stern, 2002). Preserved ophiolites usually represent fore-arc lithosphere, since it is more easily emplaced onto incoming continental margins during collision events than the back-arc lithosphere (Casey and Dewey, 1984; Milsom, 2004; Metcalf and Shervais, 2008; Stern *et al.*, 2012).

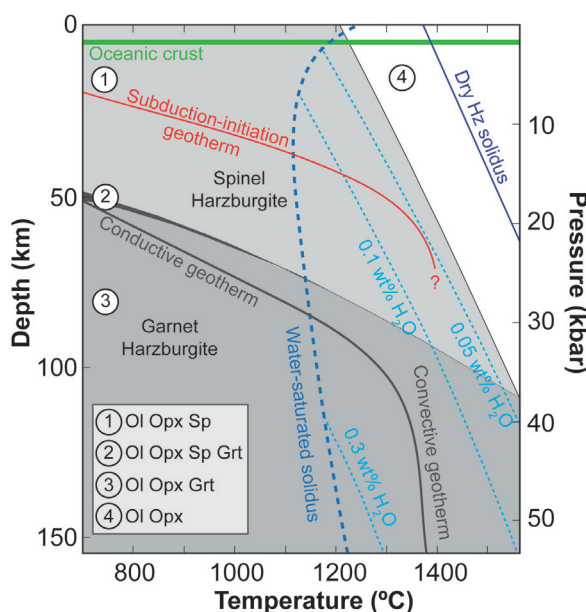


Figure 4. *P-T phase diagram of harzburgite in the system $\text{SiO}_2\text{-MgO-CaO-FeO-Al}_2\text{O}_3$. Modified from Butjosa (2018). Fields of spinel and garnet harzburgites and conductive/convective geotherm were calculated by Butjosa (2018) after the lherzolite fields from Gill (2010). Dry and hydrated harzburgite (Hz) solidus from Maaløe (2004) and the hydrated harzburgite solidus is modified from Green (2015). The theoretical subduction-initiation geotherm is displayed.*

1.2 Ophiolitic chromitites

Ophiolitic (or podiform) chromitites are typically found in the mantellic section of SSZ ophiolites (**Fig. 1**), even though other types of ophiolites, volcanic-arc, mid-ocean ridge, plume, or continental margin ophiolites (**Fig. 2**), may also host rare chromitites (*e.g.*, Thayer, 1964; Leblanc and Nicolas, 1992; Dilek and Furnes, 2011; González-Jiménez *et al.*, 2014a; Arai, 2021 and references therein). Chromitites are mainly composed of Cr-rich spinel with variable composition, of particularly Al due to Al-Cr exchange in the solid solution, that show variable textures. Chromitites usually form tabular to lenticular bodies with very variable sizes (from

cm to hundreds of meters) hosted in harzburgites and typically show a dunite envelope of variable thickness (centimetric to several meters) that bears no apparent correlation in thickness with the size of the chromitite body (e.g., González-Jiménez *et al.*, 2014a; Arai and Miura, 2016). Gabbroic rocks and orthopyroxene-rich pyroxenites are frequently associated with chromitites, either included within or crosscutting them (e.g., Bédard and Hébert, 1998; Proenza *et al.*, 1999, 2001). Chromitites are classified according to their chemistry into two main types: high-Cr ($\text{Cr}\#[\text{Cr}/(\text{Cr}+\text{Al}) \text{ atomic ratio}] > 0.6$) and high-Al ($\text{Cr}\# < 0.6$) (e.g., Arai, 1994; Zhou *et al.*, 1994, 1998, 2014; Arai and Miura, 2016). Generally, high-Cr chromitites are located below the Moho in the ophiolitic sequence, and high-Al chromitites are located in the mantle-crust transition zone (e.g., Proenza *et al.*, 1999).

Chromite grains host a variety of primary inclusions dominated by pargasitic amphibole, diopside, enstatite, olivine, and aspidolite (e.g., Melcher *et al.*, 1997). These inclusions are usually heterogeneously distributed within chromite, have very variable sizes, and can be either mono or polymineralic. Platinum group minerals (PGM) inclusions ($< 30 \mu\text{m}$) are also typical in ophiolitic chromitites and usually associated with base metal minerals (e.g., Gervilla *et al.*, 2005; González-Jiménez *et al.*, 2009, 2014a, 2014b). PGM are characterized by alloys (Os-Ir), sulfides (laurite–erlichmanite), sulfarsenides (irarsite–ruarsite), and arsenides. Secondary processes affecting the chromitites (i.e. serpentinization) that largely affect the silicate matrix also affect these mineral inclusions; secondary minerals are dominated by serpentine, chlorite, magnetite, Ni-sulfides

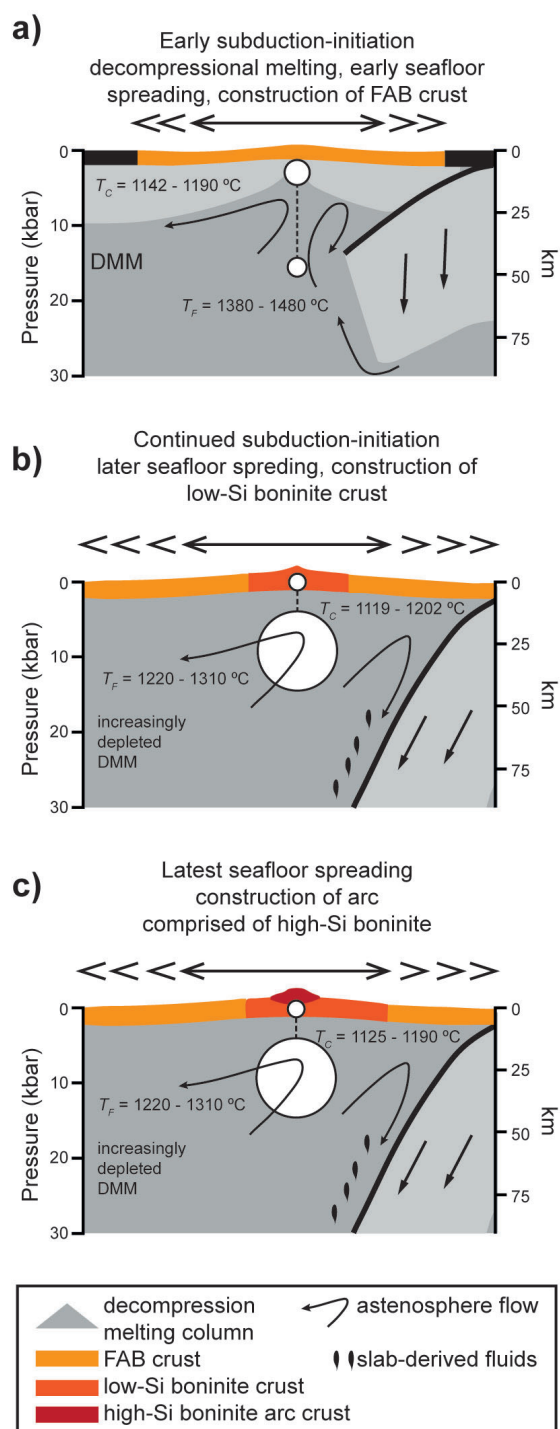


Figure 5. Schematic model showing the magmatic evolution, formation, and crystallization of (a) FAB and (b, c) boninite. Modified from Whattam *et al.* (2020). Formation pressure and temperature constraints for the FAB and boninite are from Shervais *et al.* (2019). The boninite formation temperature is based on the boninite comprising 3 wt% H_2O . White circles represent the range of pressure conditions. Since the pressure for boninite is low (0.2 – 0.4 kbar), the corresponding circle is enlarged $\times 5$. Abbreviations: T_F - formation temperature, T_C - crystallization temperature, DMM - depleted MORB mantle.

(millerite, heazlewoodite), alloys (awaruite), and garnet (uvarovite–andradite).

The origin of ophiolitic chromitites has been actively debated since the first interpretations (Thayer, 1964; Dickey, 1975; Cassard *et al.*, 1981; Lago *et al.*, 1982) and questions such as the chromite concentration mechanisms and the geotectonic settings have not yet been completely resolved (see Melcher *et al.*, 1997; Proenza *et al.*, 1999, 2007; González-Jiménez *et al.*, 2014a; Zhou *et al.*, 2014; Arai, 2021). The proposed genetic models can be grouped into three main categories (reviewed by González-Jiménez *et al.*, 2014a):

1. Fractional crystallization of basaltic melts in magma chambers or conduits in the upper mantle or near the crust-mantle boundary (*e.g.*, Dickey, 1975; Lago *et al.*, 1982; Leblanc and Nicolas, 1992) including variations due to melt-rock interaction (*e.g.*, Zhou *et al.*, 1994; Arai, 1994; Bédard and Hébert, 1998).
2. Mixing or mingling of melts within dunite channels (*e.g.*, Zhou *et al.*, 1994; Gervilla *et al.*, 2005; Zaccarini *et al.*, 2011; González-Jiménez *et al.*, 2014a, 2015).
3. Separation of volatile-rich fluid phases from small fractions of evolving hydrous-silicate melts (*e.g.*, González-Jiménez *et al.*, 2011a; Johan *et al.*, 2017) with an important role for oxygen fugacity (Melcher *et al.*, 1997; Proenza *et al.*, 1999).

Remarkably, all these mechanisms are assumed to occur at low-pressure mantle levels (<20 km depth) (see González-Jiménez *et al.*, 2014a).

1.3 Exotic minerals in ophiolitic chromitites

The discovery of ultra-high pressure (UHP) and super-reduced (SuR) minerals in ophiolitic chromitites, mostly in the Tibet and Polar Urals but also in chromitites from other locations (**Table 1**), represents a challenge for the generally accepted hypotheses for the formation of ophiolitic chromitites and remains a hotly debated topic (Miura *et al.*, 2012; Xu *et al.*, 2015; Xiong *et al.*, 2015; McGowan *et al.*, 2015; Tian *et al.*, 2015; Griffin *et al.*, 2016; Lian *et al.*, 2017; Chen *et al.*, 2018). The earlier reports of diamond grains in nominally low-pressure ophiolitic chromitites date back to the early nineties (Bai *et al.*, 1993), however, these were attributed to anthropogenic contamination and the issue did not attract the interest of the scientific community until the 2000s after the finding of other UHP minerals such as coesite together with SuR phases (*e.g.*, Robinson *et al.*, 2004; Yang *et al.*, 2007, 2015; Griffin *et al.*, 2016). Since then, these exotic mineral assemblages have been described in many ophiolitic chromitites and associated peridotites worldwide (**Table 1**), where UHP-SuR assemblages coexist with typical continental crust-derived minerals (Robinson *et al.*, 2015).

The three recognized exotic mineral groups are (**Table 1**):

1. Ultra-high pressure (UHP) minerals

According to the traditional hypothesis, diamond crystallizes at UHP conditions and indicates

>150 km depth. Diamond grains (50 – 500 μm) have been reported in chromitites associated with polycrystalline coesite, which represents former stishovite polymorph and indicates pressures >10 GPa and >300 km depth (Yang *et al.*, 2007, 2015). Additionally, nitrides (50 - 200 nm), such as TiN and c-BN, and the TiO_2 -II (αPbO_2 -structured) polymorph of rutile included in chromite also indicate >10 GPa pressure (Dobrzhinetskaya *et al.*, 2009). The presence of oriented clinopyroxene lamellae within chromite has been interpreted as indicative of decompression of the Ca-ferrite UHP polymorph of chromite (>12.5 GPa) (Yamamoto *et al.*, 2009). Hence, this association may suggest deep mantle pressures, close to, or within, the Mantle Transition Zone (410 – 660 km) (*e.g.*, Yang *et al.*, 2014, 2015; Griffin *et al.*, 2016).

2. Super-reduced (SuR) phases

Inclusions of carbides (moissanite–SiC, CrC, WC, WCoC, WCoFeNiC), silicides (FeSi), nitrides (TiN, c-BN), native elements (Si, Ni, Cu, Co, Cr, Cu, W), alloys (Fe-Mn, Fe-Cr, Fe-Co), and phosphides evidence super-reduced conditions (Griffin *et al.*, 2016; Xiong *et al.*, 2017a). Associations of these phases (*e.g.*, native Si - moissanite – FeSi) would indicate $f\text{O}_2$ conditions of 4 to 7 orders of magnitude below the Iron-Wüstite (IW) buffer ($\Delta\text{FMQ} = -9$ to -12 ; Dobrzhinetskaya *et al.*, 2009). Some authors (Yang *et al.*, 2015) interpret these super-reduced phases as formed in the Mantle Transition Zone (MTZ, 410 – 660 km depth).

3. Continental crust-derived minerals (crustal)

These include zircon, quartz, corundum, K-feldspar, kyanite, andalusite, almandine garnet, staurolite, topaz, tourmaline, muscovite, biotite, rutile, and titanite (Robinson *et al.*, 2015 and references therein). Zircon is the most relevant mineral of this group since most grains show mineral inclusions (quartz, K-feldspar, biotite, muscovite, rutile) that indicate a continental crust origin and yield much older U-Pb ages than that of the ophiolite, indicating a xenocrystic origin (*e.g.*, Robinson *et al.*, 2015; Proenza *et al.*, 2018). Some of these crustal minerals may also indicate crystallization at deep mantle conditions, for instance, corundum with TiSi inclusions (Robinson *et al.*, 2015).

The finding of these UHP-SuR-crustal mineral assemblages challenged the well-established previous hypothesis for chromite formation and set off the need for new geodynamical models to explain their presence (Robinson *et al.*, 2004, 2015; Yang *et al.*, 2007, 2014, 2015; Dobrzhinetskaya *et al.*, 2009; Yamamoto *et al.*, 2009, 2013; Trumbull *et al.*, 2009; Arai, 2013; Xiong *et al.*, 2015,

Table 1. (Next page) Occurrence of ultra-high pressure (UHP; in violet), super-reduced (SuR; in green), and crustal-derived (in orange) unusual phases in ophiolites and chromitites worldwide. Luobusa (Tibet), Dingqing (Tibet) and Ray-Iz (Polar Urals) data are from Yang *et al.* (2015), Robinson *et al.* (2015), Griffin *et al.* (2016), Xiong *et al.* (2017a) and references therein, Purang (Tibet) from Yang *et al.* (2011) and Xiong *et al.* (2019), Zedang (Tibet) from Xiong *et al.* (2017b), Hegenshan (Inner Mongolia) from Huang *et al.* (2016), Nidar (Ladakh, Himalaya) from Das *et al.* (2017), Myitkyina (Myanmar) from Chen *et al.* (2018), Alapaevsk (Russia) from Zaccarini *et al.* (2016), Semail (Oman) from Miura *et al.* (2012) and Robinson *et al.* (2015), Mirdita (Albania) from Xiong *et al.* (2017c), Ponzati-Karsanti (Turkey) from Lian *et al.* (2017), Orhaneli-Harmancik (Turkey) from Akbulut (2018), Othyrys (Greece) from Zaccarini *et al.* (2019) and Bindi *et al.* (2020), Baja California (Mexico) from González-Jiménez *et al.* (2017), Tehuiztingo (Mexico) from Farré-de-Pablo *et al.* (2019a), Moa-Baracoa (Cuba) from Rojas-Agramonte *et al.* (2016), Proenza *et al.* (2018) and Pujol-Solà *et al.* (2018, 2020a, 2020b), and Bou Azzer data from Pujol-Solà *et al.* (2021).

Ophiolite	Luobusa (Tibet)	Dingqing (Tibet)	Purang (Tibet)	Zedang (Tibet)	Hegenshan (Inner Mongolia)	Nidar (Ladakh, Himalaya)	Myitkyina (Myanmar)	Ray-Iz (Polar Urals)	Alapaevsk (central Urals, Russia)	Semai (Oman)	Mirdita (Albania)	Pozanti-Karsanti (Turkey)	Orhaneli-Harmançik (Turkey)	Othrys (Greece)	Baja California (Mexico)	Tehuizingo (Mexico)	Mon-Baracoa (Cuba)	Rou Azzer (Morocco)
Host rock	Chrom, Harz	Harz	Lherz	Chrom, Dun	Chrom	Harz, Dun	Harz, Lherz	Chrom, Harz	Chrom, Harz	Chrom	Chrom	Chrom	Chrom	Chrom	Chrom	Chrom	Chrom, Harz, Gabbro	Chrom
Diamond	X, O	X	X		X	O	X	X, O			X	X				O	O	
Coesite/ Stishovite	O							X										
TiO ₂ -II	X																	
Cubic-BN	X, O																	
Si-rutile	X																	
BWJ (inverse-spinel structure)	X																	
Clinopyroxene exsolution lamellae	O			O	O			O		O	O	O	O		O		O	O
Amorphous carbon	O					O		O									O	
Moissanite (SiC)	X, O	X	X		X		X	X		X	X	X				O	O	X
Fe-carbide (FeC)	X							X									O	
W-carbide (WC)	X							X									O	
Ti-carbide (TiC)	X							X									O	
Fe-silicide (FeSi)	X							X									O	
Ti-nitride (TiN)	X							X									O	
TAZ (Ti ₃ Al ₂ Zr ₂ Si ₂ O ₁₁)	X																O	
Native Si	X, O						X	X									O	
Native Ni, Co, Cr, Cu	X		X					X									X	X
Iron-Wüstite (Fe-FeO)	X, O	X						X			X							
Alloys (Fe-Mn, Fe-Cr, Fe-Co)	X, O				X			X									X	
Phosphides									O					O				
Almandine	X	X						X		X								
Andalusite	X	X						X										
Biotite	X																X	
Corundum	X, O	X	X					X		X	X						O	
K-feldspar	X									X							X	
Kyanite	X	X						X										
Muscovite	X, O																	
Quartz	X	X			X			X		X	X					O	O	
Rutile	X	X	X		X		X	X		X	X						O	
Titanite	X	X			X			X		X	X						O	
Zircon	X	X	X		X		X	X		X	X			X	X		X	X

*Abbreviations: Chrom – chromitite, Dun – dunitite, Harz – harzburgite, Lherz - lherzolite
 X – indicates the presence of the phase in mineral concentrates
 O – indicates the presence of the phase in situ
 Shaded grey indicates that the phase has not been interpreted as ultra-high-pressure

2017a, 2017b, 2017c; McGowan *et al.*, 2015; Griffin *et al.*, 2016; Zhang *et al.*, 2017; Lian *et al.*, 2017; González-Jiménez *et al.*, 2017; Akbulut, 2018; Proenza *et al.*, 2018), although textures and field relations leave little doubt that most chromitites were formed at shallow mantle levels (*e.g.*, Rollinson, 2008). These models can be summarized into five categories:

- Subduction-recycling model
Chromitites formed in the shallow suboceanic lithospheric mantle are recycled into the deep mantle, eventually reaching the MTZ, where they recrystallize and incorporate the UHP-SuR phases. Afterward, they can be exhumed to shallow depths, together with the host dunites and harzburgites, at spreading centers. Crustal minerals are incorporated during chromite crystallization at low-pressure. This model has been largely used to explain the exotic minerals in the Luobusa chromitites (Tibet; Arai, 2013; McGowan *et al.*, 2015; Griffin *et al.*, 2016).
- Plume model
Chromite crystallizes from high-Cr magmas in the MTZ (15 – 16 GPa, 1600 °C; Yang *et al.*, 2015), incorporating and encapsulating UHP-SuR-crustal phases. UHP and SuR phases are formed in the MTZ but crustal minerals are derived from deep subducted material. Chromite is later transported from the MTZ to mid-ocean ridges by mantle plumes and distributed through mantle convection (Yang *et al.*, 2015; Xu *et al.*, 2015; Xiong *et al.*, 2015). This model has been mostly used to explain the exotic minerals in the Ray-Iz chromitites (Polar Urals; Yang *et al.*, 2015).
- Slab contamination/breakoff model
In this model, crustal minerals derived from subducted slabs are encapsulated into chromite grains that crystallize from rising asthenospheric melts and SSZ melts during subduction-initiation or slab breakoff (Robinson *et al.*, 2015). Diamonds could be derived from the subducted sediments at >150 km depth (Zhou *et al.*, 2014). Chromite grains transported from the deep mantle (MTZ) carry the UHP-SuR phases (Robinson *et al.*, 2015).
- Lightning strikes on exposed chromitite bodies
Based on experimental work, Ballhaus *et al.* (2017, 2018) suggested that some of the UHP-SuR phases reported in chromitites could crystallize after the plasma produced by the impact of lightning strikes on exposed chromitite bodies.
- Cold plumes
Inherited zircon grains and other continental crust-derived minerals within ophiolitic chromitites could be transferred from the subducted slab to the mantle wedge by cold plumes (Proenza *et al.*, 2018). Cold plumes comprise partially molten peridotites, dry solid mantle, and subducted crustal (sedimentary and magmatic) material that can ascent in the mantle wedge (from >100 km depth) as a result of Raleigh-Taylor instabilities caused by hydration and melting in the subduction channel (Proenza *et al.*, 2018).

1.4 Hypothesis and objectives

The topic of this Ph.D. thesis arises from the finding of the UHP-SuR-crustal assemblage in many ophiolitic chromitites worldwide. The leading hypothesis is that this association is widespread in ophiolitic chromitites and, in this pursuit, I have studied the exotic minerals in suprasubduction zone ophiolitic chromitites from the Cretaceous Moa-Baracoa ophiolitic massif in eastern Cuba and the Neoproterozoic Bou Azzer ophiolite in Morocco.

The main goal is to understand the petrological processes that allow the formation or the incorporation of exotic minerals into ophiolitic chromitites and to contextualize them into ophiolite-forming geodynamic processes.

Specific objectives include:

- To identify the presence and characterize exotic minerals in chromitites and associated ophiolitic rocks of different ages.
- To identify the sources of the mantle and continental crust-related exotic minerals.
- To identify the petrogenetic processes responsible for the formation of associations of exotic minerals by geochemical analyses, as well as to estimate the temperature, pressure, and fO_2 conditions of formation.
- To identify the geodynamic processes responsible for the incorporation of these exotic minerals in chromitites and ophiolitic peridotites.
- To offer a comparison of the processes occurring in younger (Cretaceous) ophiolitic chromitites and older (Neoproterozoic) chromitites.

1.5 Areas of study

The two selected areas of study are the Eastern Cuba ophiolites and the Bou Azzer ophiolite, both of which formed in a suprasubduction zone setting but at significantly different times.

1.5.1 Eastern Cuba

The ophiolitic rocks in Cuba outcrop for more than 1000 km along the northern coastline of the island, being the largest ophiolite exposure in the circum-Caribbean region (Iturralde-Vinent *et al.*, 2016 and references therein). The largest chromitite deposits are located in the easternmost ophiolitic massif, known as Mayarí-Baracoa (Proenza *et al.*, 1999), which is divided into three mining districts: Mayarí (high-Cr), Sagua de Tánamo (high-Cr and high-Al), and Moa-Baracoa (high-Al). The Mayarí high-Cr chromitites are interpreted to have formed in a fore-arc setting and the Moa-Baracoa high-Al chromitites in a back-arc setting during Cretaceous times (Proenza *et al.*, 1999, 2001, 2006, 2018; Gervilla *et al.*, 2005; Marchesi *et al.*, 2006, 2007; Garcia-Casco *et al.*, 2006, 2008; González-Jiménez *et al.*, 2011b). The investigations focus on two deposits of the Moa-Baracoa massif: 1) Mercedita, which is the largest ophiolitic chromitite deposit in America

and is hosted in the Moho Transition zone (Proenza *et al.*, 1998, 1999); and 2) Potosí, which is located deeper than Mercedita, below the Moho, and it is crosscut by different generations of gabbroic dikes (Proenza *et al.*, 2001). Zircon grains with ages significantly older (up to 2750 Ma) than that of the ophiolite were already described in these chromitite bodies (Proenza *et al.*, 2014), suggesting the suitability for finding exotic mineral assemblages in these two chromitites.

1.5.2 Bou Azzer

The Neoproterozoic Bou Azzer ophiolite is located in the central Anti-Atlas region of Morocco. It was obducted into the western margin of the West African craton during the Panafrican orogeny (El Hadi *et al.*, 2010; Hefferan *et al.*, 2014). The ophiolite sequence is highly dismembered and has been largely affected by post-magmatic processes, including metamorphism at greenschist facies and low-pressure serpentinization (El Hadi *et al.*, 2010). The original description of the ophiolite (Leblanc, 1972, 1975, 1981) exhibits a 4 – 5 km sequence and comprises from bottom to top: pervasively serpentinized upper mantle peridotites (~2000 m) cross-cut by mafic dikes, a sequence of layered gabbros (~500 m) and pillow lavas (~500 m) intruded by a quartz-diorite stock overlain by a thick Ediacaran to Cambrian volcano-sedimentary sequence (~1500 m) including the *syn*-orogenic Tidline clastic formation. It is interpreted to have formed in a suprasubduction zone setting but it is not clear if it represents fore-arc or back-arc lithosphere (Arenas *et al.*, 2020; Hodel *et al.*, 2020). The strongly serpentinized mantle peridotites host several metric chromitite bodies with massive and semi-massive textures (Ahmed *et al.*, 2005, 2009; El Ghorfi *et al.*, 2007). Chromite grains have unaltered cores that show high-Cr compositions (up to 62 wt.% Cr₂O₃) and allow petrogenetic interpretations (El Ghorfi *et al.*, 2007 and references therein). Additionally, numerous PGM inclusions have been described in these chromitites (Ahmed *et al.*, 2009).

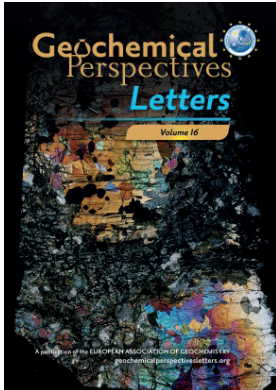
1.6 Published articles

The work of the Ph.D. has been divided into four published articles (**Table 2**). Each article was conceived to clear up specific controversies and unknowns to shed light on the formation and/or incorporation of exotic minerals into the studied ophiolitic chromitites and associated rocks. A summary of each article is provided below.

1.6.1 Article 1

The Potosí chromitite deposit is located in the Moa-Baracoa ophiolitic massif (eastern Cuba), in the mantle-crust transition zone (petrologic Moho) (Proenza *et al.*, 2001). The Moho is located between mantle residual peridotites and layered gabbros of the lower crust, and it is characterized by harzburgites, dunites, chromitites, wehrlites, troctolites, pyroxenites, and crosscutting gabbroic sills and dikes (Marchesi *et al.*, 2006). Previous studies of these chromitites (Proenza *et al.*, 2001) reported unusual mineral chemistry for the chromite, with high contents of TiO₂, FeO, Fe₂O₃,

Table 2. List of publications included in the Ph.D. thesis. The underlined author is the corresponding author. The two journal covers were requested by the editors after the articles' acceptance.

N.	Title	Authors	Journal	Status
1	Fe-Ti-Zr metasomatism in the oceanic mantle due to extreme differentiation of tholeiitic melts (Moa-Baracoa ophiolite, Cuba)	<u>Pujol-Solà, N.</u> , Proenza, J.A., Garcia-Casco, A., González-Jiménez, J.M., Román-Alpiste, M.J., Garrido, C.J., Melgarejo, J.C., Gervilla, F., Llovet, X.	Lithos	Published (2020; v. 358-359, 105420)
2	An Alternative Scenario on the Origin of Ultra-High Pressure (UHP) and Super-Reduced (SuR) Minerals in Ophiolitic Chromitites: A Case Study from the Mercedita Deposit (Eastern Cuba)	<u>Pujol-Solà, N.</u> , Proenza, J., Garcia-Casco, A., González-Jiménez, J., Andreazini, A., Melgarejo, J., Gervilla, F.	Minerals 	Published (2018; v. 8, 433)
3	Diamond forms during low pressure serpentinisation of oceanic lithosphere	<u>Pujol-Solà, N.</u> , Garcia-Casco, A., Proenza, J.A., González-Jiménez, J.M., del Campo, A., Colás, V., Canals, A., Sánchez-Navas, A., Roqué-Rosell, J.	Geochemical Perspectives Letters 	Published (2020; v. 15, 19-24)
4	The chromitites of the Neoproterozoic Bou Azzer ophiolite (Central Anti-Atlas, Morocco) revisited	<u>Pujol-Solà, N.</u> , Domínguez-Carretero, D., Proenza, J.A., Haissen, F., Ikenne, M., González-Jiménez, J.M., Colás, V., Maacha, L., Garcia-Casco, A.	Ore Geology Reviews	Published (2021; v. 134, 104166)

V₂O₃, and MnO, and an uncommon mineral assemblage including Fe-Ni-Cu sulfides, apatite, amphibole, and unidentified oxides of Ti, Zr, Y, Ca, Fe, Hf, and REE along the contact between chromitites and the crosscutting gabbroic dikes. The Fe-Ni-Cu sulfides were studied in detail by González-Jiménez *et al.* (2020). In **Article 1**, a detailed characterization of the mineral phases that formed after the interaction of the chromitites and the evolved gabbroic dikes is presented. The article includes detailed petrography coupled with electron probe microanalyses (EPMA) and trace elements analyses (LA-ICP-MS) of the described minerals, whole-rock geochemical data of the crosscutting gabbroic dikes, and U/Pb LA-ICP-MS dating on seven baddeleyite grains. The genetic interpretation of these unusual HFSE- and REE-bearing phases is offered based on the Fe-Ti-Zr modal metasomatism of the chromitites derived from their interaction with highly evolved tholeiitic melts.

1.6.2 Article 2

The Mercedita deposit is considered the largest and most important chromite deposit in America with calculated reserves >5 Mt (Proenza *et al.*, 1998, 1999). The chromitite bodies are located in the mantle-crust transition zone (petrologic Moho) of the Moa-Baracoa ophiolitic massif, around 250 m below the layered gabbro unit. The chromitite bodies are tabular to lenticular and concordant to the foliation of the host peridotites (Proenza *et al.*, 1999). They show dunite envelopes of variable thickness and the contacts are usually sharp. The chromite has high-Al compositions (Cr# = 0.42 – 0.53) and variable TiO₂ contents (0.12 – 0.48 wt.%). Gabbro sills of variable thickness (cm to >100 m) are included within chromitites and are locally replaced by chromite (Proenza *et al.*, 1999). The chromitites are also crosscut by late gabbroic dikes. It is important to highlight that these gabbroic rocks show no evidence of metamorphism. Chromitites are affected by two stages of post-magmatic evolution related to fluid infiltration: 1) serpentinization, which produced the partial replacement of olivine by serpentine-group minerals, magnetite, and Fe-Ni sulfides, and 2) chloritization, which produced the rims of ferrian chromite around chromite grains, chlorite, and Ni-Cu-sulfides. This article presents the first evidence of UHP-SuR-crustal assemblage minerals within ophiolitic chromitites from the Caribbean area. The exotic mineral phases distinguished *in situ* in thin sections (50 thin sections studied) and in mineral concentrates obtained after hydroseparation of 2.7 kg of chromitites are described and characterized by microRaman spectroscopy, scanning electronic microscopy (SEM-EDS), electron probe microanalyses (EPMA), and X-ray microdiffraction (XRmD) techniques. The obtained data are discussed within the framework of chromitite genesis during the formation and geological evolution of the Caribbean region. Besides, the previously suggested models that were used to explain similar mineral assemblages in other ophiolitic chromitites are evaluated in order to provide an interpretation for the formation of the studied exotic minerals.

1.6.3 Article 3

This article represents the first-ever report of *in situ* diamond within olivine-hosted CH₄-rich fluid inclusions. I have studied 150 inclusions within olivine from low-pressure oceanic gabbro and 16 inclusions within interstitial olivine in a chromitite from the Moa-Baracoa ophiolitic massif, eastern Cuba. The diamond-bearing fluid inclusions were studied through scanning electron microscopy (SEM-EDS), microRaman single spectra, confocal Raman maps, transmission electron microscopy (TEM), and electron energy loss spectroscopy on thin foils prepared by focused ion beam (FIB). I provide evidence of the natural origin of the nanodiamond grains as well as a discussion of the processes and conditions for metastable diamond formation in the oceanic lithosphere. In this line, a mass balance model and thermodynamic calculations using the Perple_X software (Connolly, 2009) are presented, stressing the role of oxygen fugacity in the formation of exotic mineral phases within ophiolitic rocks.

1.6.4 Article 4

The Neoproterozoic Bou Azzer ophiolitic chromitites represent a good window to study old oceanic lithosphere that underwent numerous post-magmatic processes (*e.g.*, El Ghorfi *et al.*, 2007; Ahmed *et al.*, 2009). The composition of chromite is studied in detail by electron probe microanalyses (EPMA) and laser ablation inductively coupled spectrometry (LA-ICP-MS), providing the first trace element characterization for these Moroccan chromitites. Besides, I have studied the whole rock PGE content in chromitites and the PGM, as well as the exotic minerals of the UHP-SuR-crustal assemblage both *in situ* and in mineral concentrates obtained by hydroseparation techniques (4.2 kg sample). The mineral phases were identified and studied by scanning electron microscopy (SEM-EDS), microRaman spectroscopy, and EPMA including X-ray maps. This paper aims to propose a genetic model for the Bou Azzer chromitites, in the context of the complex evolution of their host ophiolite with new petrographic, mineralogical, and geochemical data combined with previous knowledge. For this purpose, the effect of post-magmatic processes on the chromite composition, the parental melts that formed the chromitites, the origin of exotic minerals and PGM, and the possible geodynamic setting for the chromitites formation are discussed. Additionally, a comparison with other Precambrian ophiolitic chromitites elsewhere is provided.

2. General results

2.1 Interaction zone between chromitite and gabbroic intrusions

The main results of the study of the exotic mineralogy in the contact zone between chromitites and highly evolved tholeiitic melts (BABB-like) from the Potosí area, located in the Moho Transition Zone of the Cretaceous Moa-Baracoa suprasubduction zone ophiolite (eastern Cuba), are listed below (**Article 1** in **Table 2**).

1. There are two types of gabbroic dikes: the first type is similar to most gabbroic intrusions within the Moa-Baracoa massif, whereas the second type, which shows pegmatitic textures, is strongly enriched in trace elements, notably in Zr. The mineralogy of the gabbroic dikes mostly includes plagioclase and clinopyroxene with accessory oxides.
2. The interaction zone between the chromitites and the gabbroic melts is characterized by coarse granular textures and strong variability of modal mineralogy. The primary igneous-metasomatic phases include recrystallized Fe³⁺-Ti-rich chromite (metasomatized chromite), Ti-rich amphibole, orthopyroxene, olivine, Mg-ilmenite hosting Zr-bearing minerals and showing zircon coronas, and Fe-Cu-Ni sulfides. The mineral assemblage is variably overprinted by ocean floor alteration that formed secondary serpentine-group minerals, chlorite, ferrian-chromite, magnetite, actinolite-tremolite, rutile, and titanite.
3. The metasomatized chromite has higher Cr# [$\text{Cr}/(\text{Cr}+\text{Al})$] (0.57 – 0.70), higher Fe³⁺# [$\text{Fe}^{3+}/(\text{Fe}^{3+}+\text{Cr}+\text{Al})$] (0.10 – 0.30) and lower Mg# [$\text{Mg}/(\text{Mg}+\text{Fe}^{2+})$] (0.31 – 0.53) than chromite from ordinary chromitites. In addition, the metasomatized chromite is enriched in TiO₂ (1.02 – 4.34 wt.%).
4. Ti-rich amphibole forms large crystals and coronas around chromite grains. The composition corresponds to Ti-rich magnesio-hastingsite, and, to a lesser extent, Ti-rich pargasite and ferri-kaersutite. Orthopyroxene has enstatite composition (En₈₄₋₉₄) and is associated with fine-

- grained olivine with variable composition (Fo_{86-91}).
5. Ilmenite with variable geikielite component (1 – 45 mol% MgTiO_3) forms subhedral to anhedral grains within chromite and at the chromite rims. Ilmenite hosts F-rich apatite and Zr-bearing minerals. Zr-oxides (10 – 80 μm) such as baddeleyite, zirconolite, and srilankite are hosted within relatively small (up to 500 μm in length) ilmenite grains. Zircon coronas are observed around large (up to 0.5 cm length) ilmenite grains in the contact with silicate phases.
 6. Zirconolite composition deviates from the ideal $\text{CaZrTi}_2\text{O}_7$, with very low U and Th contents, a relative enrichment in REE ($\text{REE}_2\text{O}_3 = 9.25 - 10.7$ wt.%), and an exceptionally high Y content (up to 11.06 wt.% Y_2O_3), only comparable with zirconolite from lunar samples.
 7. Trace elements are presented for the different minerals, including chromite, amphibole, clinopyroxene, orthopyroxene, ilmenite, apatite, zircon, and zirconolite. Zircon trace elements show very low contents of U, Th, and Pb, thus ruling out U/Pb dating on the studied grains.
 8. U/Pb dating on baddeleyite grains yielded an age of 134.4 ± 14 Ma.

2.2 Exotic minerals in high-Al chromitites

The main results of the study of the exotic mineralogy in the high-Al chromitites from the Mercedita deposit, located in the most southerly part of the Moa-Baracoa Ophiolitic Massif (eastern Cuba), are listed below (**Article 2** in **Table 2**).

1. Unaltered chromite grains host the typical randomly distributed and occasionally clustered or aligned inclusions for ophiolitic chromitites: olivine, amphibole, Fe-Ni sulfides (commonly millerite), and PGM (laurite, irarsite).
2. There is a transition zone (<10 cm) close to the contact with the gabbro sills in which chromite contains multiple clinopyroxene and plagioclase inclusions that occasionally show the same optical orientation with the clinopyroxene and plagioclase grains from the gabbro, indicating replacement of the gabbro by the chromitite. Similarly, a transition zone is observed close to the dunite host, in which olivine inclusions are much more abundant within chromite and these show the same optical orientation as olivine in dunite.
3. The distinguished exotic minerals include:
 - Mineral inclusions *in situ* in chromite: crystallographically oriented submicrometric lamellae of clinopyroxene (diopside) and rutile. Clinopyroxene is located within chromite grains far from the contact with the gabbro sills whereas rutile lamellae are only found in chromite grains close to the chromitite-gabbro transition.
 - Mineral inclusions in secondary healed fractures (trails) in chromite that can be followed along several grains. The size of the single inclusions ranges from submicrometric to 7 μm and the characterized mineral phases in the trails are graphite-like amorphous C, corundum, and quartz.
 - Subhedral moissanite (SiC) blue grains (80 μm) have been found in the silicate matrix of two replicate thin sections. Single crystal X-ray microdiffraction showed that the studied

moissanite is hexagonal and corresponds to the *6H* polytype, which is the most common polytype of moissanite in nature.

- The identified exotic minerals in the concentrates obtained by hydroseparation consist of native Cu grains with unidentified P- and Na- rich inclusions, Fe-Mn alloys surrounded by Ca-carbonate envelopes, and zircon grains.

2.3 Diamond-bearing fluid inclusions in olivine from gabbro and chromitite

Olivine-hosted secondary fluid inclusions (<1 – 14 μm) arranged in trails that extend across adjacent mineral grains and that represent secondary healed fractures were studied in detail in **Article 3 (Table 2)**. The studied olivine grains are from gabbro and chromitite samples of the upper mantle section of the Moa-Baracoa Ophiolitic Massif. The main results are:

1. Fluid inclusions contain the typical serpentinization phases: serpentine-group minerals, magnetite, and methane. Other daughter minerals identified in some inclusions are diopside, chlorite, amorphous carbon, and calcite. Brucite was not detected in any of the studied inclusions.
2. Diamond was identified in several inclusions by the characteristic Raman peak at 1330 cm^{-1} and it is associated with the serpentinization assemblage (serpentine, magnetite, and methane). Many diamond-bearing inclusions are located below the polished surface of olivine.
3. FIB/TEM studies showed that diamond has sizes between 200 and 300 nm and is completely enveloped by polygonal serpentine and associated with magnetite. Also, these techniques confirmed the lack of polishing debris/resin within the inclusions that would point to an anthropogenic origin of the diamond.
4. The SAED (selected area electron diffraction) pattern and the EELS (electron energy loss spectroscopy) spectra confirm that the carbon allotrope corresponds to diamond.
5. The studied fluid inclusions are dominated by CH_4 in olivine from both gabbros and chromitites, but minor H_2 is distinguished in olivine-hosted inclusions from chromitites.
6. One diamond grain found in interstitial olivine in chromitite is associated with native Si, which was identified by TEM (transmission electron microscopy).

2.4 Neoproterozoic chromitites from Bou Azzer

The chromitites in the Neoproterozoic Bou Azzer ophiolite (Central Anti-Atlas, Morocco) were studied in order to compare the main characteristics and the exotic phases in these older chromitites with the more recent Cretaceous ophiolites from Cuba (**Articles 1-3**). The main results of **Article 4 (Table 2)** are:

1. The studied chromitites show massive, semi-massive, and banded textures. Massive textures

contain >90 vol.% coarse-grained chromite in an altered silicate matrix, whereas semi-massive chromite contains 70 – 80 vol.% chromite. Banded ores show alternate chromite-rich layers with massive or semi-massive textures and silicate-rich layers. Chromitites are variably fractured, can display brecciated textures, and are crosscut by late carbonate and magnetite/hematite veins. Chromite grains include a large variety of globular, elongated, and lamellae-like inclusions and negative crystals with sizes <1 – 60 μm that are typical for ophiolitic chromitites.

2. The unaltered chromite cores show Cr_2O_3 contents ranging from 46.6 to 63.9 wt.%, Al_2O_3 from 7.8 to 21.5 wt.%, and MgO from 9.4 to 18.1 wt.%. The Cr# ratio is strongly variable, from 0.60 to 0.84 and two compositional groups can be distinguished: intermediate-Cr (Cr# = 0.60 – 0.74) and high-Cr (Cr# = 0.79 – 0.84) chromite. Minor and trace element compositions are within the range for ophiolitic chromitites with low Sc (1 – 5 ppm) and Ga (18 – 42 ppm), moderate concentrations of Ti (209 – 370 ppm) and Co (192 – 347 ppm), and higher Zn (407 – 1028 ppm), Ni (565 – 1425 ppm), V (662 – 1161 ppm), and Mn (1020 – 5128 ppm) contents. The high-Cr chromite has lower Ga, V, and Ni, and higher Mn and Sc contents than intermediate-Cr chromite.
3. Chromite cores are generally unaltered and there is variable alteration along rims and fractures, whereas the silicate matrix is completely altered in all the studied samples. The alteration is more intense in the intermediate-Cr chromite than in the high-Cr chromite and in the semi-massive chromitites compared to the massive chromitites.
4. The platinum group elements (PGE) content in the chromitites is between 116 and 313 ppb and there is a preferential enrichment in IPGE (Os-Ir-Ru) compared to PPGE (Pd-Pt-Rh). In the host dunites, the PGE content is between 3 and 30 ppb, which is very low compared with previous studies.
5. 11 grains of platinum group minerals (PGM) with sizes between a few microns to tens of microns were distinguished *in situ* or in mineral concentrates. These are mainly Os-Ir alloys and laurite (RuS_2) with euhedral to anhedral shapes. There is a partial replacement of the primary magmatic PGM by a secondary highly heterogeneous PGM, probably irarsite, which in some cases is intergrown with silicates.
6. The exotic or unusual minerals within these chromitites are:
 - *In situ* crystallographically oriented clinopyroxene lamellae (up to 22 μm long and <1 μm wide) within chromite. Clinopyroxene corresponds to diopside according to the Raman spectra.
 - Diaspore associated with hematite and clinocllore in inclusions (<1 – 15 μm) within chromite. The inclusions are heterogeneously distributed, clustered, or arranged along trails.
 - Super-reduced phases in mineral concentrates include moissanite and native Cu grains.
 - Euhedral to subhedral zircon grains (20 – 50 μm) in mineral concentrates that host apatite or serpentine inclusions.

3. Summary of the overall discussions

3.1 Fe-Ti-Zr metasomatism in the oceanic lithosphere

The metasomatic interaction of gabbroic melts with the Potosí chromitites resulting in the formation of a new exotic assemblage of Fe-Ti-Zr minerals is discussed in **Article 1**. The observed mineralogy in the Potosí metasomatized chromitites shows characteristics that resemble those from SCLM settings, kimberlites, carbonatites, or alkaline basalts. In addition, this is the first report of zirconolite in ophiolitic chromitites and the studied grains have compositions similar to zirconolite hosted in potassic lavas and lunar basalts. Even though these unusual minerals can form in very diverse geodynamic settings, a simple integrated model conceptualized in a suboceanic mantle setting is provided (**Fig. 6**).

The formation of the HFSE-bearing assemblage is explained as follows:

1. Plagioclase, clinopyroxene, and late orthopyroxene crystallized from the gabbroic melt. This crystallization is accompanied by a change in the composition of olivine and the exsolution of a sulfide liquid (see González-Jiménez *et al.*, 2020 for the interpretation of the S-bearing minerals in the Potosí chromitites).
2. Ti-rich amphibole has a magmatic origin, as indicated by the low F and Cl contents. It formed

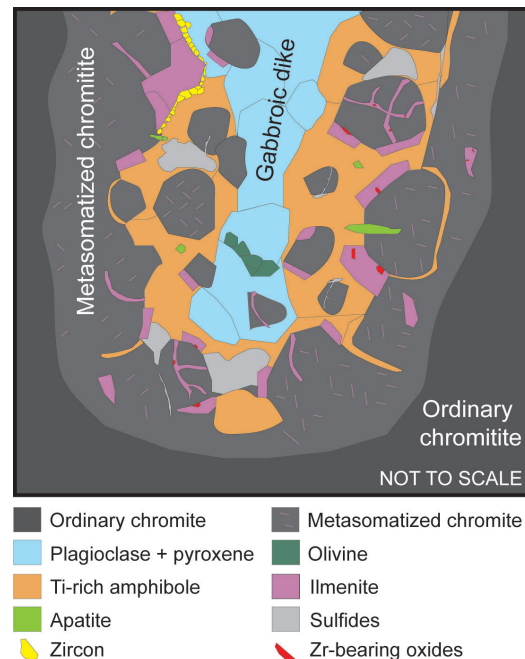


Figure 6. Schematic relations between the observed mineral assemblage in the metasomatized chromitite, located at the interaction zone between the gabbroic dikes and the ordinary ophiolitic chromitite. From Article 1.

after fractional crystallization of a Ti-rich evolved crystallizing/reacting metasomatic melt, which can also explain the enrichment in REE. The trace element composition is typical of SSZ environments (Coltorti *et al.*, 2007).

3. Mg-rich ilmenite crystallized after amphibole crystallization as a result of Fe-Ti saturation in the melt, similar to the srilankite-bearing gabbroic veins that crosscut oceanic peridotites reported by Morishita *et al.* (2004). The interaction of an evolved Ti-rich melt with the host olivine-bearing chromitites explains the Mg-rich composition of ilmenite and the decrease in Mg in the metasomatized chromite and olivine (Lorand and Gregoire, 2010).
4. Apatite crystallized after an increase in P during the magmatic/metasomatic evolution of the gabbroic melts. The F-rich component indicates crystallization from a silicate melt (O'Reilly and Griffin, 2000), whereas the low REE content in apatite indicates late crystallization of this mineral in the metasomatic process.
5. Zr-oxides: zirconolite, baddeleyite, srilankite.
The textural positions of Zr-oxides, located within and along the rims of ilmenite grains hosted within large chromite grains, suggest exsolution from ilmenite, as it occurs in ilmenite from layered intrusions and amphibolites (Bingen *et al.*, 2001). A second generation of sheet-like baddeleyite formed after zircon (Morisset and Scoates, 2008). The formation of zirconolite and srilankite was also related to the availability of Ca and REE in the melts. Besides, zirconolite concentrated the incompatible REE+Y of the late magmatic liquids/fluids, explaining their composition.
6. Zircon coronas around large ilmenite grains suggest high temperature for effective diffusion of Zr in ilmenite (exsolution) and subsequent reaction along grain boundaries with silicate melts (Morisset and Scoates, 2008).

The studied mineralogy indicates that the HFSE-bearing minerals crystallized after MORB melts. These melts formed from derivative liquids after the fractionation of primitive MORB similar to those that built the lower oceanic crust of the Moa-Baracoa ophiolite (Marchesi *et al.*, 2006, 2007). A two-stage model is proposed for the genesis of metasomatic REE- and HFSE- rich melts in Potosí.

1. The crystallization of an evolved MORB in a crystallizing mush produced water-rich residual melts strongly enriched in incompatible elements via intercumulus fractional crystallization.
2. Batches of these evolved melts escaped the solidifying mush and extensively reacted and metasomatized the surrounding chromitites, crystallizing HFSE- and REE-bearing minerals and Fe-Ni-Cu sulfides, and creating strong local heterogeneities in the mineralogy.

These processes occurred in a solidifying mush in dike intrusions, at near-solidus conditions (*e.g.*, Morishita *et al.*, 2004), allowing the stagnation of melts, differentiation, and the metasomatism of the surrounding chromitites. The U/Pb age of baddeleyite suggests an imprecise early Cretaceous age for the metasomatic event (134.4 ± 14 Ma), coeval with the age of magmatism related to ophiolite construction (Rojas-Agramonte *et al.*, 2016; Proenza *et al.*, 2018).

3.2 Exotic minerals in high-Al chromitites from eastern Cuba ophiolites

As stated above, exotic minerals in ophiolitic chromitites are typically classified into three main groups: UHP, SuR, and crustal derived (**Table 1**). Minerals from the three groups were identified in the high-Al chromitites of Mercedita and Potosí (**Articles 2 and 3**). However, UHP conditions were not observed in the ophiolitic rocks and a different hypothesis of formation is discussed.

3.2.1 Nominally UHP mineral phases

The presence of oriented clinopyroxene lamellae within chromite has been largely used as an indicator of UHP conditions (see Griffin *et al.*, 2016 and references therein). This interpretation arises from experimental studies on high-pressure chromite, which showed that clinopyroxene lamellae can exsolve during decompression of the CaFe_2O_4 -structured high-pressure polymorph of chromite (>12.5 GPa, >380 km; Yamamoto *et al.*, 2009). Stishovite or coesite may also form associated with clinopyroxene during this process. However, this interpretation has not been proved yet on natural chromite and other studies suggest that oriented clinopyroxene lamellae in chromite grains do not necessarily involve exsolution from a UHP phase and could form after incorporation of SiO_2 and CaO in liquidus chromite and exsolution of clinopyroxene needles during cooling and annealing (see Ballhaus *et al.*, 2017, 2018). Moreover, Liu *et al.* (2020) demonstrated that clinopyroxene lamellae are not necessarily the result of exsolution upon decompression by showing similar oriented clinopyroxene lamellae in chromitites from the Stillwater Complex, which crystallized at crustal levels. These authors interpreted the lamellae as the result of crystallization of minute melt inclusions encapsulated during the growth of chromite grains or during melt/fluid infiltration along cracks in chromite.

In the Mercedita chromitites, oriented lamellae of clinopyroxene are distinguished in chromite grains that show typical low-pressure chromite Raman spectra. Based on the studies of Ballhaus *et al.* (2017, 2018) that suggest that liquidus chromite can incorporate up to ~ 0.3 wt.% SiO_2 and CaO, the clinopyroxene exsolutions are interpreted as formed during the “normal” cooling of chromite. Actually, this type of exsolutions is very common in chromite, both from ophiolitic and stratiform settings (see Liu *et al.*, 2020). On the other hand, these exsolutions could also form after the encapsulation of minute melt inclusions in the crystallizing chromite (**Fig. 7**; Liu *et al.*, 2020). Our hypothesis is supported by the gabbro sills juxtaposed to, and included in, the chromitites that show no evidence of metamorphism, hence ruling out UHP conditions for the ophiolitic sequence. Oriented rutile lamellae in the Mercedita chromite were found close to the chromitite-gabbro transition, indicating that the contact with the gabbro was a reaction zone that increased the TiO_2 content in the chromitite, which was later exsolved forming the rutile lamellae.

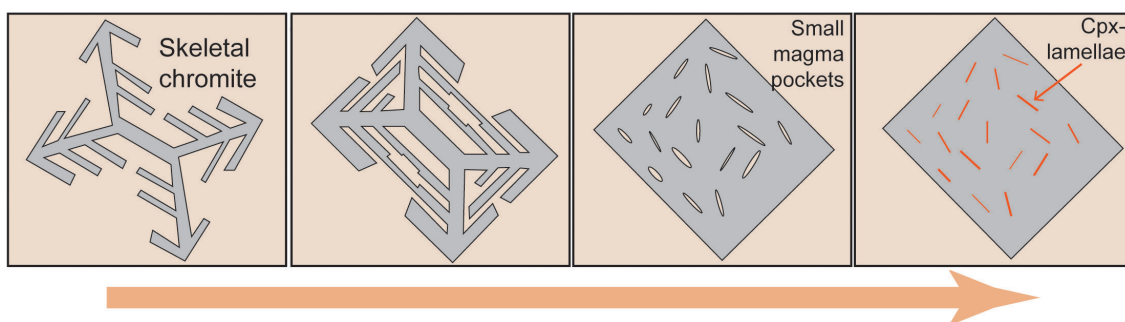


Figure 7. Schematic diagrams showing the evolution of crystallizing chromite and a plausible model for the formation of oriented clinopyroxene inclusions in chromite grains. Modified from Liu *et al.* (2020).

3.2.2 Super-reduced (SuR) conditions and serpentinization

The eastern Cuba chromitites, contain moissanite (SiC), graphite-like amorphous carbon, native Si, native Cu, and Fe-Mn alloys. SuR phases such as the ones reported here have been considered as “unquestionable” evidence for recycling of crustal materials into the Mantle Transition Zone (Yang *et al.*, 2021 and references therein). However, according to several experimental and empirical studies, moissanite can form at super-reduced conditions regardless of the prevailing pressure and temperature conditions (Schmidt *et al.*, 2014; Golubkova *et al.*, 2016; Machev *et al.*, 2018; Ballhaus *et al.*, 2021). Besides, Xiong *et al.* (2017a) described xenocrystic moissanite in the Mount Carmel basaltic complex in Israel and effectively showed that SuR mineral associations do not necessarily reflect UHP conditions. Furthermore, recent experimental studies suggest that some of the super-reduced phases found in ophiolitic chromitites might be unstable at the deep mantle conditions (Ballhaus *et al.*, 2021).

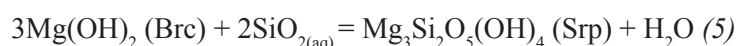
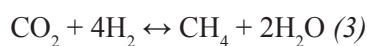
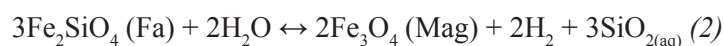
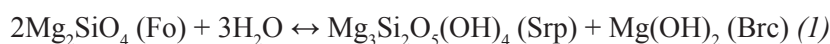
Therefore, moissanite, graphite, native elements, and alloys are interpreted to have formed in a low-pressure and low-temperature environment characterized by ultra-reduced fluids related to serpentinization. A similar interpretation was already suggested by Melcher *et al.* (1997) for the formation of graphite in chromite-hosted inclusions. In fact, CH₄-rich fluids are formed during the serpentinization of ultramafic rocks in submarine and subduction zone environments, with evidence of CH₄ fluid inclusions in olivine from partially serpentinized harzburgite and dunite (Sachan *et al.*, 2007) and the venting of CH₄-rich hydrothermal fluids along the Mid-Atlantic Ridge (MAR) in areas where serpentinized bodies occur on the seafloor (*e.g.*, Bougault *et al.*, 1993; Kelley and Früh-Green, 1999). CH₄ can be generated as a by-product of serpentinization of ultramafic rocks in the mantle wedge above the subducting slab, coupled with the complete consumption of water during hydration of serpentine (Klein *et al.*, 2019 and references therein). The suggested hypothesis is that moissanite and graphite-like amorphous carbon from the Mercedita chromitites (eastern Cuba) precipitated from reduced C-O-H fluids that evolved during serpentinization at low-pressure conditions from H₂O-CO₂-rich fluids that infiltrated the host peridotite (serpentinization reactions are further detailed in section 3.2.3). These low fO_2 conditions were also suitable for the formation of native Si and Cu and Fe-Mn alloys.

3.2.3 Metastable formation of diamond during serpentinization

Even though diamond is commonly regarded as a clear indicator of UHP conditions, recent works (Farré-de-Pablo *et al.*, 2019a) provided evidence that diamond could also grow at low pressures in ophiolitic rocks. However, there was a debate on the natural origin of the diamond grains reported by Farré-de-Pablo *et al.* (2019a) since they were identified in the exposed surface of the samples (Massone, 2019; Yang *et al.*, 2019; Farré-de-Pablo *et al.*, 2019b) and did not meet all the criteria to fully discard anthropogenic contamination (see Litasov *et al.*, 2019, 2020). In this line of study, the finding of nanodiamond in CH₄-bearing fluid inclusions from unmetamorphosed gabbros and chromitites from the Potosí area in the Moa-Baracoa massif provided the definitive evidence for the natural formation of diamond during low-pressure and low-temperature serpentinization (**Article 3**).

The studied diamond grains have an undoubted natural origin because they are hosted in fluid inclusions well below the polished mineral surface. They are associated with a gas phase (CH₄) within the inclusion, surrounded by serpentine, and there is a lack of polishing debris or resin that could indicate anthropogenic contamination during sample preparation (*e.g.*, Dobrzhinetskaya *et al.*, 2014). Besides, nanodiamond coexists with a typical serpentinization mineral assemblage (magnetite and serpentine-group minerals), with metallic Si, and with methane as the single fluid species in the fluid inclusions.

Olivine-hosted fluid inclusions, arranged in trails, represent fluids trapped in secondary healed fractures during the first stages of serpentinization (**Fig. 8**). These fluids initially derived from seawater that infiltrated the oceanic lithosphere associated with sporadic deformation events. Once trapped in the inclusions, the fluids reacted under disequilibrium conditions with the host mineral (olivine), representing a closed-system microreactor (Klein *et al.*, 2019). The following reactions can describe the serpentinization processes (*e.g.*, Lamadrid *et al.*, 2017; Klein *et al.*, 2019; abbreviations after Whitney and Evans, 2010):



Fluids react with the walls of the hosting olivine forming hydrated minerals such as serpentine and brucite (*reaction 1*). As observed in reaction (2), the oxidation of the fayalite component in olivine forms magnetite and generates H₂. The production of hydrogen allows the consumption

of inorganic carbon (CO_2) to form abiotic CH_4 (reaction 3), thus progressively reducing the fluid. If this process continues, it can ultimately reach carbon saturation and precipitate graphite or diamond (reaction 4). As observed in reaction (5), brucite is consumed by the aqueous SiO_2 released from magnetite formation, favoring the formation of serpentine. Hence, explaining the lack of brucite in the studied inclusions. **Figure 8** shows the schematic evolution within one of these fluid inclusions, from the initial trapping of the fluid within olivine to the formation of nanodiamond.

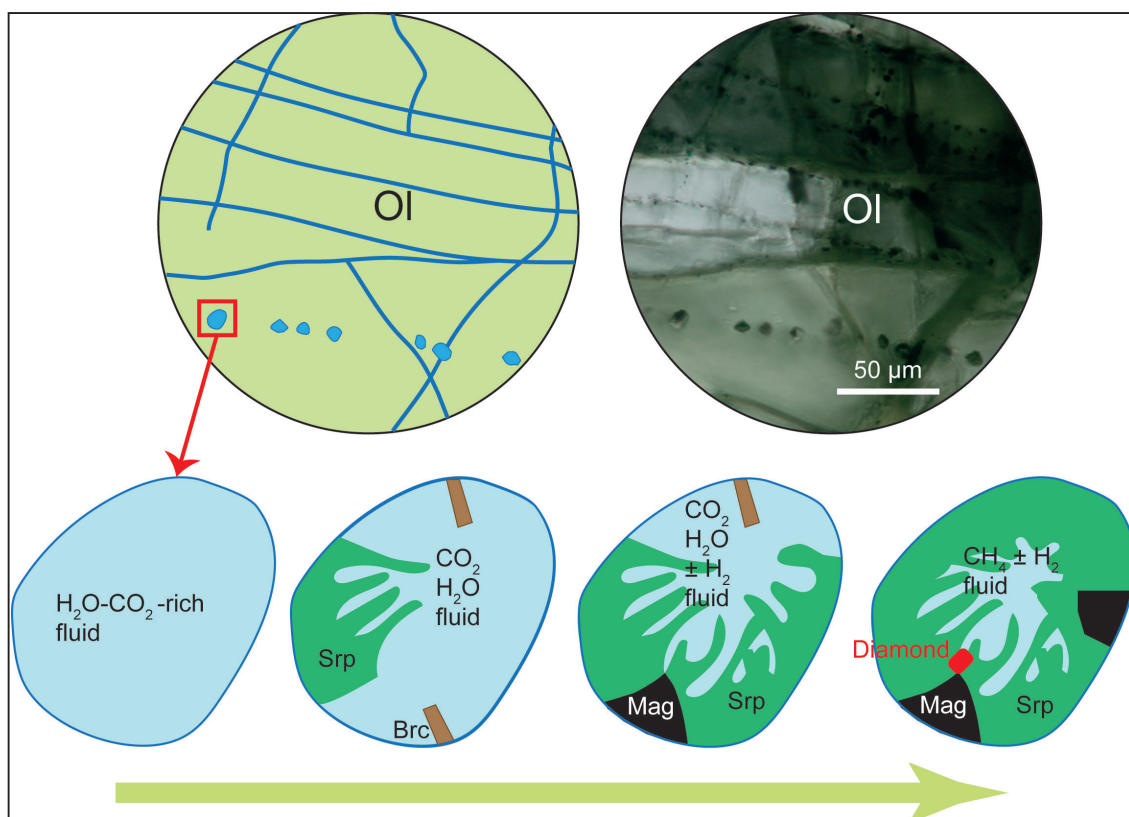


Figure 8. Top: Schematic fractures in an olivine grain that form fluid inclusions upon annealing. Bottom: Schematic evolution of the fluid and mineral components in a fluid inclusion within olivine. The estimated diameter of the inclusion is $8 \mu\text{m}$.

Thermodynamic modeling with the *Perple_X* software (Connolly, 2009) indicates that metastable diamond can grow upon extreme reduction of the fluid ($\log f_{\text{O}_2}$ (MPa) = -45.3; $\Delta \log f_{\text{O}_2}$ [Iron-Magnetite] = -6.5; **Fig. 9**) at a reference P-T point typical for serpentinization (*i.e.* 350 °C and 100 MPa; Klein *et al.*, 2019; Grozeva *et al.*, 2020). Therefore, at least in this case of study, nanodiamond should be classified as a SuR instead of a UHP mineral.

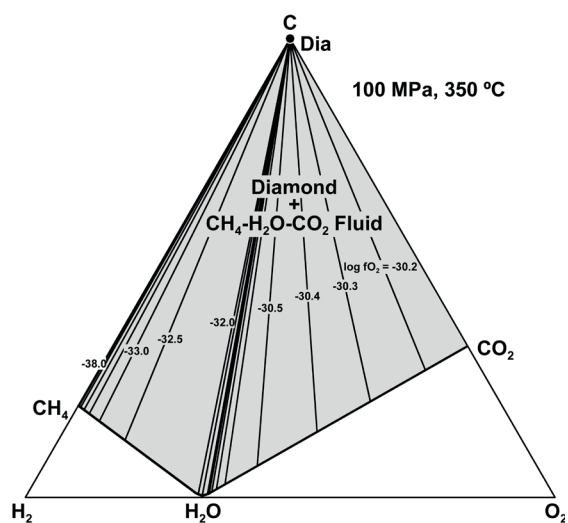


Figure 9. Phase relations in the C-O-H system with indication of f_{O_2} isopleths (black solid lines, log units) for the diamond-(Dia) saturated portion ($\log(a\text{C}) = 0$) of the system at 100 MPa, 350 °C. From Article 3.

The finding of nanodiamond within olivine-hosted fluid inclusions has two main implications:

- The formation of nanodiamond in altered olivine-bearing rocks could be a widespread process in modern and ancient oceanic lithosphere. However, their small size and their scarcity challenge this finding in other locations.
- The presence of diamond and other SuR phases in ophiolitic rocks, and particularly chromitites, cannot be taken as a general indicator of UHP conditions.

3.2.4 Continental crust-derived minerals

The continental crust-derived minerals in the Mercedita chromitites include zircon, quartz, and corundum grains. Proenza *et al.* (2018) also reported the presence of zircon grains with ages from 99 Ma (Cretaceous) to 2750 Ma (Neoproterozoic) in the eastern Cuba chromitites. Except for two zircons that have the age of the ophiolite formation (90 – 125 Ma; Iturralde-Vinent *et al.*, 2016), the recovered zircons represent inherited material. Moreover, these grains host monazite, K-feldspar, quartz, biotite, apatite, and ilmenite inclusions, indicating that zircon crystallized from crustal magmas. Therefore, continental crust-derived minerals in ophiolitic chromitites are explained as xenocrystic material derived from the subducting slab that was entrapped by the chromitite parental melts formed at the supra-subduction zone mantle (Rojas-Agramonte *et al.*, 2016; González-Jiménez *et al.*, 2017), perhaps involving cold plumes (Proenza *et al.*, 2018).

3.3 Comparison of the Bou Azzer Neoproterozoic and the eastern Cuba Cretaceous chromitites

For the comparison of the older Neoproterozoic chromitites from Bou Azzer (Morocco) with the previously studied eastern Cuba chromitites, a detailed characterization of the Bou Azzer chromitites is provided. The topics discussed in **Article 4** are summarized hereafter:

1. Element mobility during alteration

Compositional changes in chromite reflect two alteration trends: first an increase in Cr and Fe²⁺ and a decrease in Al and Mg, followed by an increase in Fe³⁺. A later stage of alteration related to the infiltration of Fe³⁺-rich fluid formed Cr-rich magnetite (Hodel *et al.*, 2017) that was later oxidized to form hematite. The unaltered chromite cores preserve the magmatic composition that overlaps the field for typical ophiolitic chromitites. Also, trace elements are clearly in the range of high-Cr chromitites (González-Jiménez *et al.*, 2017) and show patterns typical for SSZ chromitites.

2. Parental magma compositions

Two types of parental melts were obtained based on the compositions of the unaltered chromitite cores (equations from Kamenetsky *et al.*, 2001 modified by Rollinson, 2008 and Zaccarini *et al.*, 2011). These correspond to fore-arc basalts (FAB) for the intermediate-Cr and boninites for the high-Cr chromitites. The association of these melts only occurs in fore-

arc settings during subduction-initiation (see Reagan *et al.*, 2010; Whattam and Stern, 2011; Whattam *et al.*, 2020).

3. PGE signature and PGM formation

The studied chromitites are enriched in IPGE (Os-Ir-Ru) compared to PPGE (Pd-Pt-Rh), which is reflected in the PGM, dominated by Os-Ir alloys and Os-poor laurite that crystallized contemporaneously. Secondary processes triggered the destabilization and modification of primary PGE, causing the segregation of IPGE nanoparticles within laurite and the formation of secondary irarsite. Dunites hosting the chromitites have very low PGE concentrations, much lower than the harzburgites in the area (Ahmed *et al.*, 2009), indicating very strong leaching.

4. Exotic minerals in the high-Cr chromitites of Bou Azzer

Exotic minerals in the Bou Azzer chromitites include SuR and/or nominally UHP minerals, which are moissanite, native Cu, and oriented clinopyroxene lamellae. Exotic zircon and diasporite have also been identified. The proposed interpretation is that clinopyroxene lamellae have a magmatic origin related to chromite crystallization, whereas SuR phases (moissanite and native Cu) formed during serpentinization in super-reduced microenvironments, while diasporite is linked to the late circulation of low-silica fluids related to rodingitization. Zircon grains, with apatite or serpentine inclusions, could either have formed after the interaction of chromitite with mantle-derived melts or could represent subducted detrital sediments later incorporated into the chromitites. This simple interpretation for the formation of the identified exotic mineral phases completely rules out a UHP origin or deep mantle recycling for the Bou Azzer chromitites.

5. Comparison with Precambrian chromitites elsewhere

There is a very limited number of Precambrian compared to Phanerozoic ophiolitic chromitites (see Table 2 in **Article 4**). I compared the Cr#, the age, and the PGE content in these chromitites, but clear correlations cannot be observed because most chromitites need further studies to assess the effect of post-magmatic processes (metamorphism, serpentinization, hydrothermal alteration) on the chromite composition. The composition of the Bou Azzer chromitites is similar to other Neoproterozoic chromitites from the Arabian-Nubian shield, which are also related to the Panafrican orogeny.

6. Geodynamic setting and tectonic implications

The composition of the studied chromitites, together with the inferred parental melts, indicate that their formation took place in a fore-arc setting during subduction-initiation. In this scenario (**Fig. 10**), intermediate-Cr chromitites formed from FAB melts that were generated by initial spreading of oceanic crust and melting of the nascent mantle wedge, with little or no mass transfer from the subducting slab (**Fig. 10a**). Later, as subduction proceeded, high-Cr chromitites formed from hydrated melts with boninitic affinity (**Fig. 10b**).

Overall, I observed that the formation of exotic minerals in the older Bou Azzer chromitites follows the same processes recognized in the Cretaceous eastern Cuba ophiolitic chromitites.

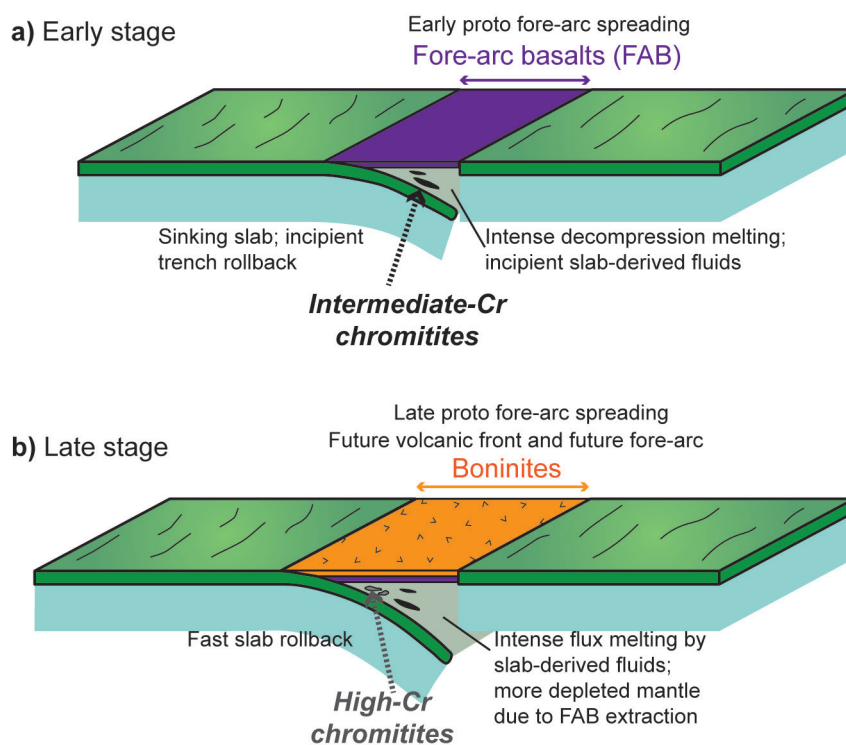


Figure 10. Schematic geodynamic setting for the formation of the Bou Azzer chromitites in a subduction-initiation geodynamic setting. From Article 4.

4. Concluding remarks

1. The intrusion of evolved gabbroic melts within the Potosí chromitites triggered the formation of a unique mineral assemblage characterized by HFSE- and REE-bearing phases including Ti-rich amphibole, Mg-rich ilmenite with inclusions of Zr oxides (baddeleyite, zirconolite, and srilankite), and zircon coronas surrounding ilmenite grains. A two-stage model is proposed for the formation of the metasomatized chromitites: 1) crystallization of an evolved MORB-like melt producing a crystallizing mush plus water-rich residual melts enriched in incompatible elements via intercumulus fractional crystallization; 2) reaction of batches of the evolved residual melts with the surrounding chromitites, triggering the modal metasomatism in the chromitites. This process likely occurred near solidus conditions, in a solidifying mush in dike intrusions, allowing the melts to stagnate, differentiate, and react with the surrounding chromitites. The age of the metasomatic event is 134.4 ± 14 Ma, coeval with the magmatism related to ophiolite construction in eastern Cuba.
2. I discard UHP conditions for the formation and/or evolution of the Cuban ophiolites and suggest a simple low-pressure formation model for the exotic mineral phases reported in the studied ophiolitic chromitites:
 - Chromite-hosted oriented clinopyroxene and rutile exsolution-induced lamellae formed during cooling of chromite and after interaction with adjacent gabbros that show no evidence of UHP conditions.
 - SuR phases, including nanodiamond, moissanite, graphite-like amorphous carbon, native Si, native Cu, and Fe-Mn alloys formed during serpentinization of chromitites and the host peridotites. These phases can precipitate in super-reduced microenvironments (inclusions) within chromite or olivine during the first stages of serpentinization. The formation of hydrated minerals such as serpentine and brucite progressively reduces

- the original oceanic-derived fluids, forming CH₄-rich environments that can reach extremely low fO_2 conditions ($\log fO_2$ (MPa) = -45.3; $\Delta \log fO_2$ [Iron-Magnetite] = -6.5) and eventually reach carbon saturation.
- Continental crust-derived minerals represent xenocrystic material derived from the subducting slab that was entrapped by the chromitite parental melts formed at the supra-subduction zone mantle, perhaps involving cold plumes.
3. The Neoproterozoic Bou Azzer chromitites (Morocco) formed in a subduction-initiation setting with two stages of evolution: 1) formation of intermediate-Cr chromitites from fore-arc basalts (FAB); followed by 2) formation of high-Cr chromitites from boninitic melts. These chromitites contain typical PGM inclusions and unusual (exotic) minerals such as oriented clinopyroxene lamellae, moissanite, native Cu, diaspore, and zircon. These exotic minerals formed after the crystallization of chromite and during the alteration related to the serpentinization of the ultramafic rocks. Therefore, UHP formation and/or evolution for the Bou Azzer ophiolite sequence can be completely ruled out, similar to what is observed in and interpreted for the eastern Cuba ophiolitic chromitites.
 4. Finally, I can unequivocally affirm that diamond and other exotic super-reduced (SuR) minerals described in many ophiolitic chromitites and associated peridotites worldwide, can form at low-pressure conditions, in the stability field of graphite. Therefore, the complex geodynamic models proposed by many authors involving UHP formation of chromite, recycling of the ophiolitic rocks to the Mantle Transition Zone, or formation after lightning strikes (section 1.3) should be reevaluated considering the simpler hypotheses proposed in this Ph.D. thesis.

References

- Ahmed, A.H., Arai, S., Abdel-Aziz, Y.M., Ikenne, M., Rahimi, A., 2009. Platinum-group elements distribution and spinel composition in podiform chromitites and associated rocks from the upper mantle section of the Neoproterozoic Bou Azzer ophiolite, Anti-Atlas, Morocco. *J. African Earth Sci.* 55, 92–104. <https://doi.org/10.1016/j.jafrearsci.2009.02.005>
- Ahmed, A.H., Arai, S., Abdel-Aziz, Y.M., Rahimi, A., 2005. Spinel composition as a petrogenetic indicator of the mantle section in the Neoproterozoic Bou Azzer ophiolite, Anti-Atlas, Morocco. *Precambrian Res.* 138, 225–234. <https://doi.org/10.1016/j.precamres.2005.05.004>
- Aiglsperger, T., Proenza, J.A., Lewis, J.F., Labrador, M., Svojtka, M., Rojas-Purón, A., Longo, F., Durisova, J., 2016. Critical metals (REE, Sc, PGE) in Ni-laterites from Cuba and the Dominican Republic. *Ore Geol. Rev.* 73, 127–147. <https://doi.org/10.1016/j.oregeorev.2015.10.010>
- Akbulut, M., 2018. Investigation of silicate micro-inclusions from Orhaneli and Harmancik chromitites (NW Turkey) new ultrahigh-pressure evidence from western Tethyan ophiolitic chromitites. *Ofioliti* 43, 1–22. <https://doi.org/10.4454/ofioliti.v43i1.453>
- Anonymous, 1972. Penrose field conference on ophiolites. *Geotimes* 17, 24-25.
- Arai, S., 1994. Podiform chromitite in the arc mantle: chromitite xenoliths from the Takashima alkali basalt, south-west Japan arc. *Miner. Deposita* 29, 434–438. <https://doi.org/10.1007/BF01886963>
- Arai, S., 2013. Conversion of low-pressure chromitites to ultrahigh-pressure chromitites by deep recycling: A good inference. *Earth Planet. Sci. Lett.* 379, 81–87. <https://doi.org/10.1016/j.epsl.2013.08.006>
- Arai, S., 2021. Genetic Link between Podiform Chromitites in the Mantle and Stratiform Chromitites in the Crust: A Hypothesis. *Minerals* 11(2), 209. <https://doi.org/10.3390/min11020209>
- Arai, S., Miura, M., 2016. Formation and modification of chromitites in the mantle. *Lithos* 264, 277-295. <https://doi.org/10.1016/j.lithos.2016.08.039>
- Arenas, R., Sánchez Martínez, S., Albert, R., Haissen, F., Fernández-Suárez, J., Pujol-Solà, N., Andonaegui, P., Díez Fernández, R., Proenza, J.A., Garcia-Casco, A., Gerdes, A., 2020. 100 myr cycles of oceanic lithosphere generation in peri-Gondwana: Neoproterozoic–Devonian ophiolites from the NW African–Iberian margin of Gondwana and the Variscan Orogen. *Geol. Soc. London Spec. Publ.* 503, SP503-2020–3. <https://doi.org/10.1144/sp503-2020-3>
- Azer, M.K., 2013. Evolution and economic significance of listwaenites associated with neoproterozoic ophiolites in South Eastern Desert, Egypt. *Geol. Acta* 11, 113–128. <https://doi.org/10.1344/105.000001777>
- Bai W.J., Zhou M.F., Robinson, P.T., 1993. Possibly diamond-bearing mantle peridotites and podiform

- chromitites in the Luobusa and Donqiao ophiolites, Tibet. *Can. J. Earth Sci.* 30, 1650–1659. <https://doi.org/10.1139/e93-143>
- Ballhaus, C., Fonseca, R.O.C., Bragagni, A., 2018. Reply to Comment on “Ultra-high pressure and ultra-reduced minerals in ophiolites may form by lightning strikes”. *Geochem. Persp. Lett.* 7, 3–4. <https://doi.org/10.7185/geochemlet.1810>
- Ballhaus, C., Helmy, H.M., Fonseca, R.O.C., Wirth, R., Schreiber, A., Jöns, N., 2021. Ultra-reduced phases in ophiolites cannot come from Earth’s mantle. *Am. Mineral.* In press.
- Ballhaus, C., Wirth, R., Fonseca, R.O.C., Blanchard, H., Pröll, W., Bragagni, A., Nagel, T., Schreiber, A., Ditttrich, S., Thome, V., Hezel, D.C., Below, R., Cieszynski, H., 2017. Ultra-high pressure and ultra-reduced minerals in ophiolites may form by lightning strikes. *Geochem. Persp. Lett.* 5, 42–46. <https://doi.org/10.7185/geochemlet.1744>
- Bédard, J.H., Hébert, R., 1998. Formation of chromitites by assimilation of crustal pyroxenites and gabbros into peridotitic intrusions: North Arm Mountain massif, Bay of Islands ophiolite, Newfoundland, Canada. *J. Geophys. Res. Solid Earth* 103, 5165–5184. <https://doi.org/10.1029/97JB03291>
- Bindi, L., Zaccarini, F., Ifandi, E., Tsikouras, B., Stanley, C., Garuti, G., Mauro, D., 2020. Grammatikopoulosite, NiVP, a New Phosphide from the Chromitite of the Othrys Ophiolite, Greece. *Minerals* 10, 131. <https://doi.org/10.3390/min10020131>
- Bingen, B., Austrheim, H., Whitehouse, M., 2001. Ilmenite as a Source for Zirconium during High-grade Metamorphism? Textural Evidence from the Caledonides of Western Norway and Implications for Zircon Geochronology. *J. Petrol.* 42, 355–375. <https://doi.org/10.1093/petrology/42.2.355>
- Bougault, H., Charlou, J.L., Fouquet, Y., Needham, H.D., Vaslet, N., Appriou, P., Baptiste, P.J., Rona, P.A., Dmitriev, L., Silantiev, S., 1993. Fast and slow spreading ridges: Structure and hydrothermal activity, ultramafic topographic highs, and CH₄ output. *J. Geophys. Res.* 98, 9643. <https://doi.org/10.1029/93JB00508>
- Buisson, G., Leblanc, M., 1986. Gold bearing listwanites (carbonatized ultramafic rocks) in ophiolite complexes, in: Gallagher, J.M., Ischer, R.A., Neary, C.R., Prichard, H.M. (eds.), *Metallogeny of basic and ultrabasic rocks*. Institute of Mining and Metallurgy, London, pp. 121–132.
- Butjosa, L., 2018. The Petrogenesis of the ophiolitic mélange of Central Cuba: origin and evolution of oceanic lithosphere from abyssal to subduction and suprasubduction zone settings. Ph.D. Thesis, Universitat de Barcelona (UB), Barcelona.
- Butt, C.R.M., Cluzel, D., 2013. Nickel laterite ore deposits: Weathered serpentinites. *Elements* 9, 123–128. <https://doi.org/10.2113/gselements.9.2.123>
- Cárdenas-Párraga, J., Garcia-Casco, A., Harlow, G.E., Blanco-Quintero, I.F., Agramonte, Y.R., Kröner, A., 2012. Hydrothermal origin and age of jadeitites from Sierra del Convento Mélange (Eastern Cuba). *Eur. J. Mineral.* 24, 313–331. <https://doi.org/10.1127/0935-1221/2012/0024-2171>
- Casey, J.F., Dewey, J.F., 1984. Initiation of subduction zones along transform and accreting plate boundaries, triple-junction evolution, and forearc spreading centres—Implications for ophiolitic geology and obduction, in: Gass, G., Lippard, S.J., Shelton, A.W. (eds.), *Ophiolites and Oceanic Lithosphere*. *Geol. Soc. London Spec. Publ.* 13, 269–290. <https://doi.org/GSL.SP.1984.013.01.22>
- Cassard, D., Nicolas, A., Rabinovitch, M., Moutte, J., Leblanc, M., Prinzhofer, A., 1981. Structural classification of chromite pods in southern New Caledonia. *Econ. Geol.* 76, 805–831. <https://doi.org/10.2113/gsecongeo.76.4.805>
- Chen, Y., Yang, J., Xu, Z., Tian, Y., Lai, S., 2018. Diamonds and other unusual minerals from peridotites of the Myitkyina ophiolite, Myanmar. *J. Asian Earth Sci.* 164, 179–193. <https://doi.org/10.1016/j.jseaes.2018.06.018>
- Coleman, R.G., 1977. *Ophiolites*. Springer, Berlin, Heidelberg, 200 pp.
- Coltorti, M., Bonadiman, C., Faccini, B., Grégoire, M., O’Reilly, S.Y., Powell, W., 2007. Amphiboles from suprasubduction and intraplate lithospheric mantle. *Lithos* 99, 68–84. <https://doi.org/10.1016/j.lithos.2007.05.009>
- Connolly, J.A.D., 2009. The geodynamic equation of state: What and how. *Geochemistry, Geophys.*

Geosystems 10. <https://doi.org/10.1029/2009GC002540>

- Das, S., Basu, A.R., Mukherjee, B.K., 2017. In situ peridotitic diamond in Indus ophiolite sourced from hydrocarbon fluids in the mantle transition zone. *Geology* 45, 755–758. <https://doi.org/10.1130/G39100.1>
- Dickey, J.S., 1975. A hypothesis of origin for podiform chromite deposits. *Geochim. Cosmochim. Acta* 39, 1061–1074. [https://doi.org/10.1016/0016-7037\(75\)90047-2](https://doi.org/10.1016/0016-7037(75)90047-2)
- Dilek, Y., 2003. Ophiolite concept and its evolution, in: Dilek, Y., Newcomb, S. (eds.), *Ophiolite Concept and the Evolution of Geological Thought*. *Geol. Soc. Am. Spec. Paper* 373, 1–16. <https://doi.org/10.1130/0-8137-2373-6.1>
- Dilek, Y., Furnes, H., 2011. Ophiolite genesis and global tectonics: Geochemical and tectonic fingerprinting of ancient oceanic lithosphere. *Bull. Geol. Soc. Am.* 123, 387–411. <https://doi.org/10.1130/B30446.1>
- Dilek, Y., Furnes, H., 2014. Ophiolites and their origins. *Elements* 10, 93–100. <https://doi.org/10.2113/gselements.10.2.93>
- Dobrzhinetskaya, L., Wirth, R., Green, H., 2014. Diamonds in Earth's oldest zircons from Jack Hills conglomerate, Australia, are contamination. *Earth Planet. Sci. Lett.* 387, 212–218. <https://doi.org/10.1016/j.epsl.2013.11.023>
- Dobrzhinetskaya, L.F., Wirth, R., Yang, J., Hutcheon, I.D., Weber, P.K., Green, H.W., 2009. High-pressure highly reduced nitrides and oxides from chromitite of a Tibetan ophiolite. *Proc. Natl. Acad. Sci. U.S.A.* 106, 19233–19238. <https://doi.org/10.1073/pnas.0905514106>
- El Ghorfi, M., Melcher, F., Oberthür, T., Boukhari, A.E., Maacha, L., Maddi, A., Mhaili, M., 2007. Platinum group minerals in podiform chromitites of the Bou Azzer ophiolite, Anti Atlas, Central Morocco. *Mineral. Petrol.* 92, 59–80. <https://doi.org/10.1007/s00710-007-0208-2>
- El Hadi, H., Simancas, J.F., Martínez-Poyatos, D., Azor, A., Tahiri, A., Montero, P., Fanning, C.M., Bea, F., González-Lodeiro, F., 2010. Structural and geochronological constraints on the evolution of the Bou Azzer Neoproterozoic ophiolite (Anti-Atlas, Morocco). *Precambrian Res.* 182, 1–14. <https://doi.org/10.1016/j.precamres.2010.06.011>
- Farré-de-Pablo, J., Proenza, J.A., González-Jiménez, J.M., Garcia-Casco, A., Colás, V., Roqué-Rosell, J., Camprubí, A., Sánchez-Navas, A., 2019a. A shallow origin for diamonds in ophiolitic chromitites. *Geology* 47, 75–78. <https://doi.org/10.1130/G45640.1>
- Farré-de-Pablo, J., Proenza, J.A., González-Jiménez, J.M., Garcia-Casco, A., Colás, V., Roqué-Rosell, J., Camprubí, A., Sánchez-Navas, A., 2019b. Reply to Comment on “A shallow origin for diamonds in ophiolitic chromitites”. *Geology* 47, e477–e478. <https://doi.org/10.1130/G46602Y.1>
- Furnes, H., Dilek, Y., 2017. Geochemical characterization and petrogenesis of intermediate to silicic rocks in ophiolites: A global synthesis. *Earth Sci. Rev.* 166, 1–37. <https://doi.org/10.1016/j.earscirev.2017.01.001>
- Furnes, H., Dilek, Y., De Wit, M., 2015. Precambrian greenstone sequences represent different ophiolite types. *Gondwana Res.* 27(2), 649–685. <https://doi.org/10.1016/j.gr.2013.06.004>
- Galley, A. G., Koski, R. A., 1999. Setting and characteristics of ophiolite-hosted volcanogenic massive sulfide deposits, in: Barrie, C.T., Hannington, M.D. (eds.), *Volcanic-associated massive sulphide deposits: processes and examples in modern and ancient settings*. *Rev. Econ. Geol.* 8, pp. 221–246. <https://doi.org/10.5382/Rev.08.10>
- García-Casco, A., Torres-Roldán, R.L., Iturralde-Vinent, M.A., Millán, G., Núñez Cambra, K., Lázaro, C., Rodríguez Vega, A., 2006. High pressure metamorphism of ophiolites in Cuba. *Geol. Acta* 4, 63–88. <https://doi.org/10.1344/105.000000358>
- García-Gasco, A., Iturralde-Vinent, M.A., Pindell, J., 2008. Latest Cretaceous collision/accretion between the Caribbean plate and Caribbeana: Origin of metamorphic terranes in the Greater Antilles. *Int. Geol. Rev.* 50, 781–809. <https://doi.org/10.2747/0020-6814.50.9.781>
- Gervilla, F., Proenza, J.A., Frei, R., González-Jiménez, J.M., Garrido, C.J., Melgarejo, J.C., Meibom, A., Díaz-Martínez, R., Lavaut, W., 2005. Distribution of platinum-group elements and Os isotopes in chromite ores from Mayarí-Baracoa Ophiolitic Belt (eastern Cuba). *Contrib. to Mineral. Petrol.* 150,

- 589–607. <https://doi.org/10.1007/s00410-005-0039-2>
- Gerya, T.V., 2011. Intra-oceanic subduction zones. *Front. Earth Sci.* 4, 23–51. https://doi.org/10.1007/978-3-540-88558-0_2
- Gill, R., 2010. *Igneous Rocks and Processes: A Practical Guide*. First ed. Wiley-Blackwell, Malaysia.
- Golubkova, A., Schmidt, M.W., Connolly, J.A.D., 2016. Ultra-reducing conditions in average mantle peridotites and in podiform chromitites: a thermodynamic model for moissanite (SiC) formation. *Contrib. to Mineral. Petrol.* 171, 1–17. <https://doi.org/10.1007/s00410-016-1253-9>
- González-Jiménez, J.M., Augé, T., Gervilla, F., Bailly, L., Proenza, J.A., Griffin, W.L., 2011a. Mineralogy and geochemistry of platinum-rich chromitites from the mantle-crust transition zone at Ouen Island, New Caledonia Ophiolite. *Can. Mineral.* 49, 1549–1569. <https://doi.org/10.3749/canmin.49.6.1549>
- González-Jiménez, J.M., Camprubí, A., Colás, V., Griffin, W.L., Proenza, J.A., O'Reilly, S.Y., Centeno-García, E., García-Casco, A., Belousova, E., Talavera, C., Farré-de-Pablo, J., Satsukawa, T., 2017. The recycling of chromitites in ophiolites from southwestern North America. *Lithos* 294–295, 53–72. <https://doi.org/10.1016/j.lithos.2017.09.020>
- González-Jiménez, J.M., Gervilla, F., Proenza, J.A., Kerestedjian, T., Augé, T., Bailly, L., 2009. Zoning of laurite (RuS₂) erlichmanite (OsS₂): implications for the origin of PGM in ophiolite chromitites. *Eur. J. Mineral.* 21, 419–432. <https://doi.org/10.1127/0935-1221/2009/0021-1921>
- González-Jiménez, J.M., Griffin, W.L., Gervilla, F., Proenza, J.A., O'Reilly, S.Y., Pearson, N.J., 2014b. Chromitites in ophiolites: How, where, when, why? Part I. A review and new ideas on the origin and significance of platinum-group minerals. *Lithos* 189, 127–139. <https://doi.org/10.1016/j.lithos.2013.06.016>
- González-Jiménez, J.M., Griffin, W.L., Proenza, J.A., Gervilla, F., O'Reilly, S.Y., Akbulut, M., Pearson, N.J., Arai, S., 2014a. Chromitites in ophiolites: How, where, when, why? Part II. The crystallization of chromitites. *Lithos* 189, 140–158. <https://doi.org/10.1016/j.lithos.2013.09.008>
- González-Jiménez, J.M., Locmelis, M., Belousova, E., Griffin, W.L., Gervilla, F., Kerestedjian, T.N., O'Reilly, S.Y., Pearson, N.J., Sergeeva, I., 2015. Genesis and tectonic implications of podiform chromitites in the metamorphosed ultramafic massif of Dobromirski (Bulgaria). *Gondwana Res.* 27, 555–574. <https://doi.org/10.1016/j.gr.2013.09.020>
- González-Jiménez, J.M., Proenza, J.A., Gervilla, F., Melgarejo, J.C., Blanco-Moreno, J.A., Ruiz-Sánchez, R., Griffin, W.L., 2011b. High-Cr and high-Al chromitites from the Sagua de Tánamo district, Mayarí-Cristal ophiolitic massif (eastern Cuba): Constraints on their origin from mineralogy and geochemistry of chromian spinel and platinum-group elements. *Lithos* 125, 101–121. <https://doi.org/10.1016/j.lithos.2011.01.016>
- González-Jiménez, J.M., Proenza, J.A., Pastor-Oliete, M., Saunders, E., Aiglsperger, T., Pujol-Solà, N., Melgarejo, J.C., Gervilla, F., García-Casco, A., 2020. Precious metals in magmatic Fe-Ni-Cu sulfides from the Potosí chromitite deposit, eastern Cuba. *Ore Geol. Rev.* 118, 103339. <https://doi.org/10.1016/j.oregeorev.2020.103339>
- Green, D.H., 2015. Experimental petrology of peridotites, including effects of water and carbon on melting in the Earth's upper mantle. *Phys. Chem. Miner.* 42, 95–122. <https://doi.org/10.1007/s00269-014-0729-2>
- Griffin, W.L., Afonso, J.C., Belousova, E.A., Gain, S.E., Gong, X.H., González-Jiménez, J.M., Howell, D., Huang, J.X., McGowan, N., Pearson, N.J., Satsukawa, T., Shi, R., Williams, P., Xiong, Q., Yang, J.S., Zhang, M., O'Reilly, S.Y., 2016. Mantle recycling: Transition zone metamorphism of Tibetan ophiolitic peridotites and its tectonic implications. *J. Petrol.* 57, 655–684. <https://doi.org/10.1093/petrology/egw011>
- Grozeva, N.G., Klein, F., Seewald, J.S., Sylva, S.P., 2020. Chemical and isotopic analyses of hydrocarbon-bearing fluid inclusions in olivine-rich rocks. *Philos. Trans. A. Math. Phys. Eng. Sci.* 378, 20180431. <https://doi.org/10.1098/rsta.2018.0431>
- Hannington, M.D., 2014. Volcanogenic massive sulfide deposits, in: Scott, S.D. (eds.), *Geochemistry of mineral deposits*. Elsevier, Amsterdam, Treatise on Geochemistry (2nd Ed), 13, pp. 463–488. <https://doi.org/10.1016/B978-0-08-095975-7.01120-7>

- Hannington, M.D., Poulsen, K.H., Thompson, J.F.H., Sillitoe, R.H., 1997. Volcanogenic gold in the massive sulfide environment, in: Barrie, C.T., Hannington, M.D. (eds.), *Volcanic-associated massive sulfide deposits: processes and examples in modern and ancient settings*. *Rev. Econ. Geol.* 8, pp. 325–356. <https://doi.org/10.5382/rev.08.14>
- Harlow, G.E., Sorensen, S.S., 2005. Jade (nephrite and jadeitite) and serpentinite: Metasomatic connections. *Int. Geol. Rev.* 47, 113–146. <https://doi.org/10.2747/0020-6814.47.2.113>
- Hefferan, K., Soulaïmani, A., Samson, S.D., Admou, H., Inglis, J., Saquaque, A., Latifa, C., Heywood, N., 2014. A reconsideration of Pan African orogenic cycle in the Anti-Atlas Mountains, Morocco. *J. African Earth Sci.* 98, 34–46. <https://doi.org/10.1016/j.jafrearsci.2014.03.007>
- Hodel, F., Macouin, M., Triantafyllou, A., Carlut, J., Berger, J., Rouse, S., Ennih, N., Trindade, R.I.F., 2017. Unusual massive magnetite veins and highly altered Cr-spinels as relics of a Cl-rich acidic hydrothermal event in Neoproterozoic serpentinites (Bou Azzer ophiolite, Anti-Atlas, Morocco). *Precambrian Res.* 300, 151–167. <https://doi.org/10.1016/j.precamres.2017.08.005>
- Hodel, F., Triantafyllou, A., Berger, J., Macouin, M., Baele, J.M., Mattielli, N., Monnier, C., Trindade, R.I.F., Ducea, M.N., Chatir, A., Ennih, N., Langlade, J., Pujol, M., 2020. The Moroccan Anti-Atlas ophiolites: Timing and melting processes in an intra-oceanic arc-back-arc environment. *Gondwana Res.* 86, 182–202. <https://doi.org/10.1016/j.gr.2020.05.014>
- Huang, B., Fu, D., Li, S., Ge, M., Zhou, W., 2016. The age and tectonic implications of the Hegenshan ophiolite in Inner Mongolia. *Acta Petrol. Sin.* 32(1), 158–176.
- Ishizuka, O., Tani, K., Reagan, M.K., Kanayama, K., Umino, S., Harigane, Y., Sakamoto, I., Miyajima, Y., Yuasa, M., Dunkley, D.J., 2011. The timescales of subduction initiation and subsequent evolution of an oceanic island arc. *Earth Planet. Sci. Lett.* 306, 229–240. <https://doi.org/10.1016/j.epsl.2011.04.006>
- Iturralde-Vinent, M.A., García-Casco, A., Rojas-Agramonte, Y., Proenza, J.A., Murphy, J.B., Stern, R.J., 2016. The geology of Cuba: A brief overview and synthesis. *GSA Today* 26(10), 4-10. <https://doi.org/10.1130/GSATG296A.1>
- Johan, Z., Martin, R.F., Ettler, V., 2017. Fluids are bound to be involved in the formation of ophiolitic chromite deposits. *Eur. J. Mineral.* 29, 543–555. <https://doi.org/10.1127/ejm/2017/0029-2648>
- Kamenetsky, V.S., Crawford, A.J., Meffre, S., 2001. Factors controlling chemistry of magmatic spinel: An empirical study of associated olivine, Cr-spinel and melt inclusions from primitive rocks. *J. Petrol.* 42, 655–671. <https://doi.org/10.1093/petrology/42.4.655>
- Kelley, D.S., Früh-Green, G.L., 1999. Abiogenic methane in deep-seated mid-ocean ridge environments: Insights from stable isotope analyses. *J. Geophys. Res. Solid Earth* 104, 10439–10460. <https://doi.org/10.1029/1999JB900058>
- Klein, F., Grozeva, N.G., Seewald, J.S., 2019. Abiotic methane synthesis and serpentinitization in olivine-hosted fluid inclusions. *Proc. Natl. Acad. Sci. U.S.A.* 116, 17666–17672. <https://doi.org/10.1073/pnas.1907871116>
- Kushiro, M.J.A., 2007. Origin of magmas in subduction zones: A review of experimental studies. *Proc. Jpn Acad. Ser. B Phys. Biol. Sci.* 83(1), 1-15. <https://doi.org/10.2183/pjab.83.1>
- Lago, B.L., Rabinowicz, M., Nicolas, A., 1982. Podiform Chromite Ore Bodies: a Genetic Model. *J. Petrol.* 23, 103–125. <https://doi.org/10.1093/petrology/23.1.103>
- Lamadrid, H.M., Rimstidt, J.D., Schwarzenbach, E.M., Klein, F., Ulrich, S., Dolocan, A., Bodnar, R.J., 2017. Effect of water activity on rates of serpentinitization of olivine. *Nat. Commun.* 8, 1–9. <https://doi.org/10.1038/ncomms16107>
- Leblanc, M., 1972. Un complexe ophiolitique dans le Précambrien II de l'Anti-Atlas central : Maroc: description interprétation et position stratigraphique, in: *Actes Colloq. Internationl. Corrélations Précambrien. Notes Mém. Serv. Géol. Maroc.*
- Leblanc, M., 1975. Ophiolites précambriennes et gites arsenies de cobalt: Bou Azzer (Maroc). These Dr. d'Etat, Fac. des Sci. Paris VI, Mem. Cent. Geol. Geophys.
- Leblanc, M., 1981. The Late Proterozoic Ophiolites of Bou Azzer (Morocco): Evidence for Pan-African

- Plate Tectonics. *Dev. Precambrian Geol.* 4, 435–451. [https://doi.org/10.1016/S0166-2635\(08\)70022-7](https://doi.org/10.1016/S0166-2635(08)70022-7)
- Leblanc, M., 1991. Platinum-group elements and gold in ophiolitic complexes: distribution and fractionation from mantle to oceanic floor. *Ophiolite Genes. Evol. Ocean. lithosphere. Proc. Conf. Muscat, 1990* 231–260. https://doi.org/10.1007/978-94-011-3358-6_13
- Leblanc, M., Nicolas, A., 1992. Ophiolitic Chromitites. *Int. Geol. Rev.* 34, 653–686. <https://doi.org/10.1080/00206819209465629>
- Lewis, J.F., Draper, G., Proenza, J.A., Espaillat, J., Jiménez, J., 2006. Ophiolite-related ultramafic rocks (serpentinites) in the Caribbean region: A review of their occurrence, composition, origin, emplacement and Ni-laterite soil formation. *Geol. Acta* 4, 237–263. <https://doi.org/10.1344/105.000000368>
- Lian, D., Yang, J., Dilek, Y., Wu, W., Zhang, Z., Xiong, F., Liu, F., Zhou, W., 2017. Deep mantle origin and ultra-reducing conditions in podiform chromitite: Diamond, moissanite, and other unusual minerals in podiform chromitites from the Pozanti-Karsanti ophiolite, southern Turkey. *Am. Mineral.* 102, 1101–1113. <https://doi.org/10.2138/am-2017-5850>
- Litasov, K.D., Bekker, T.B., Kagi, H., Ohfuji, H., 2020. Reply to the comment on “Comparison of enigmatic diamonds from the Tolbachik arc volcano (Kamchatka) and Tibetan ophiolites: Assessing the role of contamination by synthetic materials”. *Gondwana Res.* <https://doi.org/10.1016/j.gr.2019.09.011>
- Litasov, K.D., Kagi, H., Voropaev, S.A., Hirata, T., Ohfuji, H., Ishibashi, H., Makino, Y., Bekker, T.B., Sevastyanov, V.S., Afanasiev, V.P., Pokhilenko, N.P., 2019. Comparison of enigmatic diamonds from the Tolbachik arc volcano (Kamchatka) and Tibetan ophiolites: Assessing the role of contamination by synthetic materials. *Gondwana Res.* 75, 16–27. <https://doi.org/10.1016/j.gr.2019.04.007>
- Liu, X., Su, B.X., Bai, Y., Robinson, P.T., Tang, X., Xiao, Y., Xue, D.S., Cui, M.M., 2020. Genesis of “silicate exsolution lamellae” in chromite of the Stillwater complex: A challenge to the high-pressure crystallization of ophiolitic chromitite. *Lithos* 378–379, 105796. <https://doi.org/10.1016/j.lithos.2020.105796>
- Lorand, J.P., Gregoire, M., 2010. Petrogenesis of Fe-Ti oxides in amphibole-rich veins from the Lherz orogenic peridotite (Northeastern Pyrénées, France). *Contrib. to Mineral. Petrol.* 160, 99–113. <https://doi.org/10.1007/s00410-009-0468-4>
- Maaløe, S., 2004. The solidus of harzburgite to 3 GPa pressure: The compositions of primary abyssal tholeiite. *Mineral. Petrol.* 81, 1–17. <https://doi.org/10.1007/s00710-004-0028-6>
- Machev, P., O’Bannon, E.F., Bozhilov, K.N., Wang, Q., Dobrzhinetskaya, L., 2018. Not all moissanites are created equal: New constraints on moissanite from metamorphic rocks of Bulgaria. *Earth Planet. Sci. Lett.* 498, 387–396. <https://doi.org/10.1016/j.epsl.2018.07.009>
- Marchesi, C., Garrido, C.J., Bosch, D., Proenza, J.A., Gervilla, F., Monié, P., Rodríguez-Vega, A., 2007. Geochemistry of Cretaceous magmatism in eastern Cuba: Recycling of North American Continental sediments and implications for subduction polarity in the Greater Antilles paleo-arc. *J. Petrol.* 48, 1813–1840. <https://doi.org/10.1093/petrology/egm040>
- Marchesi, C., Garrido, C.J., Godard, M., Proenza, J.A., Gervilla, F., Blanco-Moreno, J., 2006. Petrogenesis of highly depleted peridotites and gabbroic rocks from the Mayarí-Baracoa Ophiolitic Belt (eastern Cuba). *Contrib. to Mineral. Petrol.* 151, 717–736. <https://doi.org/10.1007/s00410-006-0089-0>
- Marchesi, C., Garrido, C.J., Proenza, J.A., Hidas, K., Varas-Reus, M.I., Butjosa, L., Lewis, J.F., 2016. Geochemical record of subduction initiation in the sub-arc mantle: Insights from the Loma Caribe peridotite (Dominican Republic). *Lithos* 252–253, 1–15. <https://doi.org/10.1016/j.lithos.2016.02.009>
- Massonne, H.J., 2019. Comment on “A shallow origin for diamonds in ophiolitic chromitites”. *Geology* 47, e476. <https://doi.org/10.1130/G46459C.1>
- Maurizot, P., Sevin, B., Iseppi, M., Giband, T., 2019. Nickel-bearing laterite deposits in accretionary context and the case of New Caledonia: From the large-scale structure of earth to our everyday appliances. *GSA Today* 29(5), 4–10. <https://doi.org/10.1130/GSATG364A.1>
- McGowan, N.M., Griffin, W.L., González-Jiménez, J.M., Belousova, E., Afonso, J.C., Shi, R., McCammon, C.A., Pearson, N.J., O’Reilly, S.Y., 2015. Tibetan chromitites: Excavating the slab graveyard. *Geology* 43, 179–182. <https://doi.org/10.1130/G36245.1>

- Melcher, F., Grum, W., Simon, G., Thalhammer, T. V., Stumpfl, E.F., 1997. Petrogenesis of the ophiolitic giant chromite deposits of Kempirsai, Kazakhstan: A study of solid and fluid inclusions in chromite. *J. Petrol.* 38, 1419–1458. <https://doi.org/10.1093/petroj/38.10.1419>
- Metcalf, R.V., Shervais, J.W., 2008. Supra-subduction zone ophiolites: Is there really an ophiolite conundrum?, in: Wright, J.E., Shervais, J.W. (eds.), *Ophiolites, Arcs, and Batholiths*. Geol. Soc. Am. Spec. Paper 438, 191–222. [https://doi.org/10.1130/2008.2438\(07\)](https://doi.org/10.1130/2008.2438(07))
- Milsom, J., 2004. Forearc ophiolites: A view from the western Pacific. *Geol. Soc. Spec. Publ.* 218, 507–515. <https://doi.org/10.1144/GSL.SP.2003.218.01.26>
- Miura, M., Arai, S., Ahmed, A.H., Mizukami, T., Okuno, M., Yamamoto, S., 2012. Podiform chromitite classification revisited: A comparison of discordant and concordant chromitite pods from Wadi Hilti, northern Oman ophiolite. *J. Asian Earth Sci.* 59, 52–61. <https://doi.org/10.1016/j.jseaes.2012.05.008>
- Miyashiro, A., 1973. The Troodos complex was probably formed in an island arc. *Earth Planet. Sci. Lett.* 19, 218–224. [https://doi.org/10.1016/0012-821X\(73\)90118-0](https://doi.org/10.1016/0012-821X(73)90118-0)
- Miyashiro, A., 1975. Classification, characteristics, and origin of ophiolites. *J. Geol.* 83, 249–281. <https://doi.org/10.1086/628085>
- Monecke, T., Petersen, S., Hannington, M.D., Grant, H., Samson, I., 2016. The minor element endowment of modern seafloor massive sulfide deposits and comparison with deposits hosted in ancient volcanic successions, in: Verplank, P.L., Hitzman, M.W. (eds.), *Rare Earth and Critical Elements in Ore Deposits*, 245–306 pp. *Rev. Econ. Geol.* 18, 365 pp.
- Morishita, T., Maeda, J., Miyashita, S., Matsumoto, T., Dick, H.J.B., 2004. Magmatic srilankite (Ti₂ZrO₆) in gabbroic vein cutting oceanic peridotites: An unusual product of peridotite-melt interactions beneath slow-spreading ridges. *Am. Mineral.* 89, 759–766. <https://doi.org/10.2138/am-2004-5-609>
- Morisset, C.E., Scoates, J.S., 2008. Origin of zircon rims around ilmenite in mafic plutonic rocks of proterozoic anorthosite suites. *Can. Mineral.* 46, 289–304. <https://doi.org/10.3749/canmin.46.2.289>
- Müller, R.D., Sdrolias, M., Gaina, C., Roest, W.R., 2008. Age, spreading rates, and spreading asymmetry of the world's ocean crust. *Geochem. Geophys. Geosyst.* 9(4). <https://doi.org/10.1029/2007GC001743>
- Nicolas, A., 1989. *Structure of Ophiolites and Dynamics of Oceanic Lithosphere*, in: Nicolas, A. (eds.). Dordrecht, the Netherlands, Kluwer Academic Publishers, 367 pp.
- Niu, Y., 1997. Mantle melting and melt extraction processes beneath ocean ridges: Evidence from abyssal peridotites. *J. Petrol.* 38, 1047–1074. <https://doi.org/10.1093/petroj/38.8.1047>
- O'Reilly, S.Y., Griffin, W.L., 2000. Apatite in the mantle: Implications for metasomatic processes and high heat production in Phanerozoic mantle. *Lithos* 53, 217–232. [https://doi.org/10.1016/S0024-4937\(00\)00026-8](https://doi.org/10.1016/S0024-4937(00)00026-8)
- Pearce, J.A., 2014. Immobile element fingerprinting of ophiolites. *Elements* 10, 101–108. <https://doi.org/10.2113/gselements.10.2.101>
- Pearce, J.A., Lippard, S.J., Roberts, S., 1984. Characteristics and tectonic significance of supra-subduction zone ophiolites, in: Kokelaar, B.P., Howells, M.F. (eds.), *Marginal Basin Geology: Volcanic and Associated Sedimentary and Tectonic Processes in Modern and Ancient Marginal Basins*. Geol. Soc. London Spec. Publ. 16, pp. 77–94. <https://doi.org/10.1130/0-8137-2373-6.227>
- Pearce, J.A., Reagan, M.K., 2019. Identification, classification, and interpretation of boninites from Anthropocene to Eoarchean using Si-Mg-Ti systematics. *Geosphere* 15(4), 1008–1037. <https://doi.org/10.1130/GES01661.1>
- Piercey, S.J., 2011. The setting, style, and role of magmatism in the formation of volcanogenic massive sulfide deposits. *Miner. Depos.* 46, 449–471. <https://doi.org/10.1007/s00126-011-0341-z>
- Pirajno, F., Uysal, I., Naumov, E.A., 2020. Oceanic lithosphere and ophiolites: Birth, life and final resting place of related ore deposits. *Gondwana Res.* 88, 333–352. <https://doi.org/10.1016/j.gr.2020.08.004>
- Proenza, J.A., 2015. Mineralogía y Geoquímica de Ni, Co, EGP, Sc, REE en Yacimientos Lateríticos. *Macla* 20, 3–9.
- Proenza, J.A., Díaz-Martínez, R., Iriondo, A., Marchesi, C., Melgarejo, J.C., Gervilla, F., Garrido, C.J.,

- Rodríguez-Vega, A., Lozano-Santacruz, R., Blanco-Moreno, J.A., 2006. Primitive island-arc Cretaceous volcanic rocks in eastern Cuba: The Téneme Formation. *Geol. Acta* 4, 103–121. <https://doi.org/10.1344/105.000000360>
- Proenza, J.A., Gervilla, F., Melgarejo, J., Vera, O., Alfonso, P., Fallick, A., 2001. Genesis of sulfide-rich chromite ores by the interaction between chromitite and pegmatitic olivine-norite dikes in the Potosí Mine (Moa-Baracoa ophiolitic massif, Eastern Cuba). *Miner. Depos.* 36, 658–669. <https://doi.org/10.1007/s001260100193>
- Proenza, J.A., Gervilla, F., Melgarejo, J.C., Bodinier, J.L., 1999. Al- and Cr-rich chromitites from the Mayarí-Baracoa ophiolitic belt (Eastern Cuba): Consequence of interaction between volatile-rich melts and peridotites in suprasubduction mantle. *Econ. Geol.* 94, 547–566. <https://doi.org/10.2113/gsecongeo.94.4.547>
- Proenza, J.A., Gervilla, F., Melgarejo, J.C., Reve, D., Rodriguez, Y.G., 1998. Las cromititas ofiolíticas del yacimiento Mercedita (Cuba). Un ejemplo de cromititas ricas en Al en la zona de transición manto-corteza. *Acta Geol. Hisp.* 33, 179–212.
- Proenza, J.A., González-Jiménez, J.M., Garcia-Casco, A., Belousova, E., Griffin, W.L., Talavera, C., Rojas-Agramonte, Y., Aiglsperger, T., Navarro-Ciurana, D., Pujol-Solà, N., Gervilla, F., O'Reilly, S.Y., Jacob, D.E., 2018. Cold plumes trigger contamination of oceanic mantle wedges with continental crust-derived sediments: Evidence from chromitite zircon grains of eastern Cuban ophiolites. *Geosci. Front.* 9(6), 1921–1936. <https://doi.org/10.1016/j.gsf.2017.12.005>
- Proenza, J.A., González-Jiménez, J.M., Garcia-Casco, A., Belousova, E., Griffin, W.L., Gervilla, F., Rojas-Agramonte, Y., Navarro-Ciurana, D., O'Reilly, S.Y., Talavera-Rodríguez, C., Jacob, D., 2014. Inherited Mantle and Crustal Zircons in Mantle Chromitites (E Cuba): Implications for the Evolution of Oceanic Lithosphere. *Macla* 19.
- Proenza, J.A., Ortega-Gutiérrez, F., Camprubí, A., Tritlla, J., Elías-Herrera, M., Reyes-Salas, M., 2004. Paleozoic serpentinite-enclosed chromitites from Tehuiztingo (Acatlán Complex, southern Mexico): A petrological and mineralogical study. *J. South Am. Earth Sci.* 16, 649–666. <https://doi.org/10.1016/j.jsames.2003.12.003>
- Proenza, J.A., Zaccarini, F., Lewis, J.F., Longo, F., Garuti, G., 2007. Chromian spinel composition and the platinum-group minerals of the PGE-rich Loma Peguera chromitites, Loma Caribe peridotite, Dominican Republic. *Can. Mineral.* 45, 631–648. <https://doi.org/10.2113/gscanmin.45.3.631>
- Pujol-Solà, N., Domínguez-Carretero, D., Proenza, J.A., Haissen, F., Ikenne, M., González-Jiménez, J.M., Colás, V., Maacha, L., Garcia-Casco, A., 2021. The chromitites of the Neoproterozoic Bou Azzer ophiolite (Central Anti-Atlas, Morocco) revisited. *Ore Geol. Rev.* 134, 104166. <https://doi.org/10.1016/j.oregeorev.2021.104166>
- Pujol-Solà, N., Garcia-Casco, A., Proenza, J.A., González-Jiménez, J.M., del Campo, A., Colás, V., Canals, A., Sánchez-Navas, A., Roqué-Rossell, J., 2020b. Diamond forms during low pressure serpentinisation of oceanic lithosphere. *Geochem. Persp. Lett.* 15, 19–24. <https://doi.org/10.7185/geochemlet.2029>
- Pujol-Solà, N., Proenza, J.A., Garcia-Casco, A., González-Jiménez, J., Andreatzini, A., Melgarejo, J., Gervilla, F., 2018. An Alternative Scenario on the Origin of Ultra-High Pressure (UHP) and Super-Reduced (SuR) Minerals in Ophiolitic Chromitites: A Case Study from the Mercedita Deposit (Eastern Cuba). *Minerals* 8(10), 433. <https://doi.org/10.3390/min8100433>
- Pujol-Solà, N., Proenza, J.A., Garcia-Casco, A., González-Jiménez, J.M., Román-Alpiste, M.J., Garrido, C.J., Melgarejo, J.C., Gervilla, F., Llovet, X., 2020a. Fe-Ti-Zr metasomatism in the oceanic mantle due to extreme differentiation of tholeiitic melts (Moa-Baracoa ophiolite, Cuba). *Lithos* 358–359, 105420. <https://doi.org/10.1016/j.lithos.2020.105420>
- Rajendran, S., Nasir, S., Kusky, T.M., Ghulam, A., Gabr, S., El-Ghali, M.A.K., 2013. Detection of hydrothermal mineralized zones associated with listwaenites in Central Oman using ASTER data. *Ore Geol. Rev.* 53, 470–488. <https://doi.org/10.1016/j.oregeorev.2013.02.008>
- Reagan, M.K., Ishizuka, O., Stern, R.J., Kelley, K.A., Ohara, Y., Blichert-Toft, J., Bloomer, S.H., Cash, J., Fryer, P., Hanan, B.B., Hickey-Vargas, R., Ishii, T., Kimura, J.I., Peate, D.W., Rowe, M.C., Woods, M., 2010. Fore-arc basalts and subduction initiation in the Izu-Bonin-Mariana system. *Geochemistry,*

- Geophys. Geosystems 11. <https://doi.org/10.1029/2009GC002871>
- Robinson, P.T., Bai, W.J., Malpas, J., Yang, J.S., Zhou, M.F., Fang, Q.S., Hu, X.F., Cameron, S., Staudigel, H., 2004. Ultra-high pressure minerals in the Luobusa Ophiolite, Tibet, and their tectonic implications. *Geol. Soc. London Spec. Publ.* 226, 247–271. <https://doi.org/10.1144/GSL.SP.2004.226.01.14>
- Robinson, P.T., Trumbull, R.B., Schmitt, A., Yang, J.S., Li, J.W., Zhou, M.F., Erzinger, J., Dare, S., Xiong, F., 2015. The origin and significance of crustal minerals in ophiolitic chromitites and peridotites. *Gondwana Res.* 27, 486–506. <https://doi.org/10.1016/j.gr.2014.06.003>
- Rojas-Agramonte, Y., Garcia-Casco, A., Kemp, A., Kröner, A., Proenza, J.A., Lázaro, C., Liu, D., 2016. Recycling and transport of continental material through the mantle wedge above subduction zones: A Caribbean example. *Earth Planet. Sci. Lett.* 436, 93–107. <https://doi.org/10.1016/j.epsl.2015.11.040>
- Rollinson, H., 2008. The geochemistry of mantle chromitites from the northern part of the Oman ophiolite: Inferred parental melt compositions. *Contrib. to Mineral. Petrol.* 156, 273–288. <https://doi.org/10.1007/s00410-008-0284-2>
- Sachan, H.K., Mukherjee, B.K., Bodnar, R.J., 2007. Preservation of methane generated during serpentinization of upper mantle rocks: Evidence from fluid inclusions in the Nidar ophiolite, Indus Suture Zone, Ladakh (India). *Earth Planet. Sci. Lett.* 257, 47–59. <https://doi.org/10.1016/j.epsl.2007.02.023>
- Schmidt, M.W., Gao, C., Golubkova, A., Rohrbach, A., Connolly, J.A., 2014. Natural moissanite (SiC) – a low temperature mineral formed from highly fractionated ultra-reducing COH-fluids. *Prog. Earth Planet. Sci.* 1, 27. <https://doi.org/10.1186/s40645-014-0027-0>
- Shervais, J.W., Reagan, M., Haugen, E., Almeev, R.R., Pearce, J.A., Prytulak, J., Ryan, J.G., Whattam, S.A., Godard, M., Chapman, T., Li, H., Kurz, W., Nelson, W.R., Heaton, D., Kirchenbaur, M., Shimizu, K., Sakuyama, T., Scott, Y.L., 2019. Magmatic response to subduction initiation: Part 1. Fore-arc basalts of the Izu-Bonin arc from IODP Expedition 352. *Geochemistry, Geophysics, Geosystems* 20, 314–338. <https://doi.org/10.1029/2018GC007731>
- Stern, R.J., 2002. Subduction zones. *Rev. Geophys.* 40, 1012. <https://doi.org/10.1029/2001RG000108>
- Stern, R.J., 2005. Evidence from ophiolites, blueschists, and ultrahigh-pressure metamorphic terranes that the modern episode of subduction tectonics began in Neoproterozoic time. *Geology* 33, 557–560. <https://doi.org/10.1130/G21365.1>
- Stern, R.J., 2010. The anatomy and ontogeny of modern intra-oceanic arc systems. *Geol. Soc. London Spec. Publ.* 338, 7–34. <https://doi.org/10.1144/SP338.2>
- Stern, R.J., Reagan, M., Ishizuka, O., Ohara, Y., Whattam, S., 2012. To understand subduction initiation, study forearc crust: To understand forearc crust, study ophiolites. *Lithosphere* 4, 469–483. <https://doi.org/10.1130/L183.1>
- Thayer, T.P., 1964. Principal features and origin of podiform chromite deposits, and some observations on the Guleman-Soridag district, Turkey. *Econ. Geol.* 59, 1497–1524. <https://doi.org/10.2113/gsecongeo.59.8.1497>
- Tian, Y., Yang, J., Robinson, P.T., Xiong, F., Li, Y., Zhang, Z., Liu, Z., Liu, F., Niu, X., 2015. Diamond Discovered in High-Al Chromitites of the Sartohay Ophiolite, Xinjiang Province, China. *Acta Geol. Sin.* 89, 332–340. <https://doi.org/10.1111/1755-6724.12433>
- Tobón, M., Weber, M., Proenza, J.A., Aiglsperger, T., Betancur, S., Farré-de-Pablo, J., Ramírez, C., Pujol-Solà, N., 2020. Geochemistry of Platinum-Group Elements (PGE) in Cerro Matoso and Planeta Rica Ni-Laterite deposits, Northern Colombia. *Bol. Soc. Geol. Mex.* 72(2), A201219. <http://dx.doi.org/10.18268/BSGM2020v72n3a201219>
- Torró, L., Proenza, J.A., Melgarejo, J.C., Alfonso, P., Farré-de-Pablo, J., Colomer, J.M., Garcia-Casco, A., Gubern, A., Gallardo, E., Cazañas, X., Chávez, C., del Carpio, R., León, P., Nelson, C., Lewis, J.F., 2017. Mineralogy, geochemistry and sulfur isotope characterization of the Cerro de Maimón (Dominican Republic), San Fernando and Antonio (Cuba): Lower Cretaceous VMS deposits associated to the subduction initiation of the Proto-Caribbean lithosphere within a fore-arc. *Ore Geol. Rev.* 72, 794–817. <https://doi.org/10.1016/j.oregeorev.2015.09.017>
- Trumbull, R.B., Yang, J.S., Robinson, P.T., Di Pierro, S., Vennemann, T., Wiedenbeck, M., 2009. The

- carbon isotope composition of natural SiC (moissanite) from the Earth's mantle: New discoveries from ophiolites. *Lithos* 113, 612–620. <https://doi.org/10.1016/j.lithos.2009.06.033>
- Villanova-de-Benavent, C., Proenza, J.A., Galí, S., García-Casco, A., Tauler, E., Lewis, J.F., Longo, F., 2014. Garnierites and garnierites: textures, mineralogy and geochemistry of garnierites in the Falcondo Ni-laterite deposit, Dominican Republic. *Ore Geol. Rev.* 58, 91–109. <https://doi.org/10.1016/j.oregeorev.2013.10.008>
- Wakabayashi, J., Dilek, Y., 2004. What constitutes “emplacement” of an ophiolite?: Mechanisms and relationship to subduction initiation and formation of metamorphic soles. *Geol. Soc. London Spec. Publ.* 218, 427–447. <https://doi.org/10.1144/GSL.SP.2003.218.01.22>
- Wakabayashi, J., Ghatak, A., Basu, A.R., 2010. Suprasubduction-zone ophiolite generation, emplacement, and initiation of subduction: A perspective from geochemistry, metamorphism, geochronology, and regional geology. *Bull. Geol. Soc. Am.* 122, 1548–1568. <https://doi.org/10.1130/B30017.1>
- Walter, M.J., 2003. Melt Extraction and Compositional Variability in Mantle Lithosphere, in: Carlson, R.W. (eds.), *The Mantle and Core. Treatise on Geochemistry* vol. 2. Elsevier, pp. 363–394. <https://doi.org/10.1016/B0-08-043751-6/02008-9>
- Whattam, S.A., Shervais, J.W., Reagan, M.K., Coulthard, D.A., Pearce, J.A., Jones, P., Seo, J., Putirka, K., Chapman, T., Heaton, D., Li, H., Nelson, W.R., Shimizu, K., Stern, R.J., 2020. Mineral compositions and thermobarometry of basalts and boninites recovered during IODP Expedition 352 to the Bonin forearc. *Am. Mineral.* 105, 1490–1507. <https://doi.org/10.2138/am-2020-6640>
- Whattam, S.A., Stern, R.J., 2011. The “subduction initiation rule”: A key for linking ophiolites, intra-oceanic forearcs, and subduction initiation. *Contrib. to Mineral. Petrol.* 162, 1031–1045. <https://doi.org/10.1007/s00410-011-0638-z>
- Whitney, D.L., Evans, B.W., 2010. Abbreviations for names of rock-forming minerals. *Am. Mineral.* 95, 185–187. <https://doi.org/10.2138/am.2010.3371>
- Williams, S., Wright, N.M., Cannon, J., Flament, N., Müller, R.D., 2021. Reconstructing seafloor age distributions in lost ocean basins. *Geosci. Front.* 12, 769–780. <https://doi.org/10.1016/j.gsf.2020.06.004>
- Xiong, F., Liu, Z., Kapsiotis, A., Yang, J., Lenaz, D., Robinson, P.T., 2019. Petrogenesis of lherzolites from the Purang ophiolite, Yarlung-Zangbo suture zone, Tibet: origin and significance of ultra-high pressure and other ‘unusual’ minerals in the Neo-Tethyan lithospheric mantle. *Int. Geol. Rev.* 61(17), 2184–2210. <https://doi.org/10.1080/00206814.2019.1584771>
- Xiong, F., Yang, J., Robinson, P.T., Dilek, Y., Milushi, I., Xu, X., Zhou, W., Zhang, Z., Rong, H., 2017c. Diamonds Discovered from High-Cr Podiform Chromitites of Bulqiza, Eastern Mirdita Ophiolite, Albania. *Acta Geol. Sin.* 91, 455–468. <https://doi.org/10.1111/1755-6724.13111>
- Xiong, F., Yang, J., Robinson, P.T., Xu, X., Liu, Z., Li, Y., Li, J., Chen, S., 2015. Origin of podiform chromitite, a new model based on the Luobusa ophiolite, Tibet. *Gondwana Res.* 27, 525–542. <https://doi.org/10.1016/j.gr.2014.04.008>
- Xiong, Q., Griffin, W.L., Huang, J. X., Gain, S.E.M., Toledo, V., Pearson, N.J., O'Reilly, S.Y., 2017a. Super-reduced mineral assemblages in “ophiolitic” chromitites and peridotites: the view from Mount Carmel. *Eur. J. Mineral.* 29, 557–570. <https://doi.org/10.1127/ejm/2017/0029-2646>
- Xiong, Q., Henry, H., Griffin, W.L., Zheng, J. P., Satsukawa, T., Pearson, N.J., O'Reilly, S.Y., 2017b. High- and low-Cr chromitite and dunite in a Tibetan ophiolite: evolution from mature subduction system to incipient forearc in the Neo-Tethyan Ocean. *Contrib. to Mineral. Petrol.* 172, 45. <https://doi.org/10.1007/s00410-017-1364-y>
- Xu, X.Z., Yang, J.S., Robinson, P.T., Xiong, F.H., Ba, D.Z., Guo, G.L., 2015. Origin of ultrahigh pressure and highly reduced minerals in podiform chromitites and associated mantle peridotites of the Luobusa ophiolite, Tibet. *Gondwana Res.* 27, 686–700. <https://doi.org/10.1016/j.gr.2014.05.010>
- Yamamoto, S., Komiya, T., Hirose, K., Maruyama, S., 2009. Coesite and clinopyroxene exsolution lamellae in chromites: In-situ ultrahigh-pressure evidence from podiform chromitites in the Luobusa ophiolite, southern Tibet. *Lithos* 109, 314–322. <https://doi.org/10.1016/j.lithos.2008.05.003>
- Yamamoto, S., Komiya, T., Yamamoto, H., Kaneko, Y., Terabayashi, M., Katayama, I., Iizuka, T., Maruyama,

- S., Yang, J., Kon, Y., Hirata, T., 2013. Recycled crustal zircons from podiform chromitites in the Luobusa ophiolite, southern Tibet. *Isl. Arc* 22, 89–103. <https://doi.org/10.1111/iar.12011>
- Yang, J., Dobrzhinetskaya, L., Bai, W.J., Fang, Q.S., Robinson, P.T., Zhang, J., Green, H.W., 2007. Diamond- and coesite-bearing chromitites from the Luobusa ophiolite, Tibet. *Geology* 35, 875–878. <https://doi.org/10.1130/G23766A.1>
- Yang, J., Meng, F., Xu, X., Robinson, P.T., Dilek, Y., Makeyev, A.B., Wirth, R., Wiedenbeck, M., Cliff, J., 2015. Diamonds, native elements and metal alloys from chromitites of the Ray-Iz ophiolite of the Polar Urals. *Gondwana Res.* 27, 459–485. <https://doi.org/10.1016/j.gr.2014.07.004>
- Yang, J., Robinson, P.T., Dilek, Y., 2014. Diamonds in ophiolites. *Elements* 10, 127–130. <https://doi.org/10.2113/gselements.10.2.127>
- Yang, J., Simakov, S.K., Moe, K.S., Scribano, V., Lian, D., Wu, W., 2019. Comment on “Comparison of enigmatic diamonds from the tolbachik arc volcano (Kamchatka) and Tibetan ophiolites: Assessing the role of contamination by synthetic materials”. *Gondwana Res.* <https://doi.org/10.1016/j.gr.2019.09.010>
- Yang, J., Wu, W., Lian, D., Rui, H., 2021. Peridotites, chromitites and diamonds in ophiolites. *Nat. Rev. Earth Environ.* 1–15. <https://doi.org/10.1038/s43017-020-00138-4>
- Yang, J., Xu, X.Z., Li, Y., Li, J.Y., Ba, D.Z., Rong, H., Zhang, Z., 2011. Diamonds recovered from peridotite of the Purang ophiolite in the Yarlung-Zangbo suture of Tibet: A proposal for a new type of diamond occurrence. *Acta Petrol. Sin.* 27, 3171–3178.
- Zaccarini, F., Bindi, L., Ifandi, E., Grammatikopoulos, T., Stanley, C., Garuti, G., Mauro, D., 2019. Tsikourasite, $\text{Mo}_3\text{Ni}_2\text{P}_{1+x}$ ($x < 0.25$), a New Phosphide from the Chromitite of the Othrys Ophiolite, Greece. *Minerals* 9, 248. <https://doi.org/10.3390/min9040248>
- Zaccarini, F., Garuti, G., Proenza, J.A., Campos, L., Thalhammer, O.A.R., Aiglsperger, T., Lewis, J.F., 2011. Chromite and platinum group elements mineralization in the Santa Elena Ultramafic Nappe (Costa Rica): Geodynamic implications. *Geol. Acta* 9, 407–423. <https://doi.org/10.1344/105.000001696>
- Zaccarini, F., Pushkarev, E., Garuti, G., Kazakov, I., 2016. Platinum-Group Minerals and Other Accessory Phases in Chromite Deposits of the Alapaevsk Ophiolite, Central Urals, Russia. *Minerals* 6, 108. <https://doi.org/10.3390/min6040108>
- Zhang, Y., Jin, Z., Griffin, W.L., Wang, C., Wu, Y., 2017. High-pressure experiments provide insights into the Mantle Transition Zone history of chromitite in Tibetan ophiolites. *Earth Planet. Sci. Lett.* 463, 151–158. <https://doi.org/10.1016/j.epsl.2017.01.036>
- Zhou, M.F., Robinson, P.T., Bai, W.J., 1994. Formation of podiform chromitites by melt/rock interaction in the upper mantle. *Miner. Depos.* 29, 98–101. <https://doi.org/10.1007/BF03326400>
- Zhou, M.F., Robinson, P.T., Su, B.X., Gao, J.F., Li, J.W., Yang, J.S., Malpas, J., 2014. Compositions of chromite, associated minerals, and parental magmas of podiform chromite deposits: The role of slab contamination of asthenospheric melts in suprasubduction zone environments. *Gondwana Res.* <https://doi.org/10.1016/j.gr.2013.12.011>
- Zhou, M.F., Sun, M., Keays, R.R., Kerrich, R.W., 1998. Controls on platinum-group elemental distributions of podiform chromitites: A case study of high-Cr and high-Al chromitites from Chinese orogenic belts. *Geochim. Cosmochim. Acta* 62, 677–688. [https://doi.org/10.1016/S0016-7037\(97\)00382-7](https://doi.org/10.1016/S0016-7037(97)00382-7)

Appendices

A1. Article 1

Pujol-Solà, N., Proenza, J.A., Garcia-Casco, A., González-Jiménez, J.M., Román-Alpiste, M.J., Garrido, C.J., Melgarejo, J.C., Gervilla, F., Llovet, X., 2020. Fe-Ti-Zr metasomatism in the oceanic mantle due to extreme differentiation of tholeiitic melts (Moa-Baracoa ophiolite, Cuba). *Lithos* 358–359, 105420. <https://doi.org/10.1016/j.lithos.2020.105420>



Research Article

Fe-Ti-Zr metasomatism in the oceanic mantle due to extreme differentiation of tholeiitic melts (Moa-Baracoa ophiolite, Cuba)



Núria Pujol-Solà ^{a,*}, Joaquín A. Proenza ^a, Antonio Garcia-Casco ^{b,c}, José María González-Jiménez ^b, Manuel J. Román-Alpiste ^c, Carlos J. Garrido ^c, Joan Carles Melgarejo ^a, Fernando Gervilla ^{b,c}, Xavier Llovet ^d

^a Departament de Mineralogia, Petrologia i Geologia Aplicada, Facultat de Ciències de la Terra, Universitat de Barcelona, Carrer Martí i Franquès, s/n, 08028 Barcelona, Spain

^b Departamento de Mineralogía y Petrología, Facultad de Ciencias, Universidad de Granada, Avda. Fuentenueva, s/n, 18071 Granada, Spain

^c Instituto Andaluz de Ciencias de la Tierra (CSIC-UGR), Avda. de las Palmeras 4, E-18100 Armilla, Granada, Spain

^d Centres Científics i Tecnològics, Universitat de Barcelona, Carrer de Lluís Solé i Sabarís, 1-3, 08028 Barcelona, Spain

ARTICLE INFO

Article history:

Received 17 November 2019

Received in revised form 28 January 2020

Accepted 9 February 2020

Available online 12 February 2020

Keywords:

ophiolitic chromitites

zircon coronas

HFSE minerals

evolved MORB melt

modal metasomatism

ABSTRACT

Ti-rich amphibole, Mg-rich ilmenite, baddeleyite, zirconolite, srilankite, and zircon are important high-field-strength elements (HFSE) bearing phases in the Potosí chromitite bodies located in the Moho Transition Zone of the Cretaceous Moa-Baracoa suprasubduction zone ophiolite (eastern Cuba). Such HFSE-bearing phases were found in the interaction zone between gabbroic intrusions and chromitite pods. In addition to HFSE-bearing minerals, the studied samples are composed of Fe³⁺ and Ti-rich chromite, olivine (Fo₈₆₋₉₀), clinopyroxene (En₄₄₋₄₉), plagioclase (An₅₁₋₅₆), orthopyroxene (En₈₄₋₉₄), F-rich apatite, and Fe-Cu-Ni sulfides. The studied ilmenite hosting Zr oxides (baddeleyite, zirconolite, and srilankite) contains up to 13 wt.% MgO. The Potosí zirconolite is the first record of this mineral in ophiolitic chromitites and non-metamorphic ophiolite units, and it has relatively high REE contents (up to 10 wt.% of REE₂O₃) and the highest concentrations in Y₂O₃ (up to 11 wt.%) reported so far in zirconolite from terrestrial occurrences. Zircon is observed forming coronas surrounding ilmenite grains in contact with silicate minerals, and is characterized by very low U and Pb contents. The zircons formed after high temperature Zr diffusion in ilmenite (exsolution) and a subsequent reaction along grain boundaries following crystallization. Finally, U-Pb dating of baddeleyite exsolutions within ilmenite yielded an average age of 134.4 ± 14 Ma, which provides the first ever dating for a metasomatic event in Potosí that matches well (within uncertainty) the formation age of the oceanic crust of the eastern Cuba ophiolite. We propose that the occurrence of HFSE- and REE-bearing minerals in the Potosí chromitite deposit is the result of a two stage process: first, water-rich and HFSE-rich residual melts are produced by intercumulus crystal fractionation after an evolved MORB (BABB)-like melt; and secondly, these residual melt fractions escaped the solidifying mush and extensively reacted and metasomatized the surrounding chromitites, crystallizing HFSE- and REE-bearing minerals and Fe-Cu-Ni sulfides.

© 2020 Elsevier B.V. All rights reserved.

1. Introduction

Mantle metasomatism is a process by which the infiltration of melts or fluids through the Earth's upper mantle produces chemical and/or mineralogical modification of peridotites and associated rocks (Bodinier et al., 1990; Constantin, 1999; Menzies and Hawkesworth, 1987). This process leads either to the removal or addition of components of the original rock to varying extents, depending on the

melt-fluid/rock ratio, the compositional nature of the metasomatic agent and the mode of infiltration (i.e., porous flow versus open fractures; O'Reilly and Griffin, 2013). As a result of variable melt/rock ratios through the upper mantle, metasomatism leaves behind different fingerprints in the infiltrated rocks such as newly formed minerals (Bedini et al., 1997; Bodinier et al., 1990). These minerals may be distinct to those originally forming the peridotite, giving rise to the so-called modal metasomatism, or alternatively they are identical to those already existing in the upper mantle rock, which produce the so-called stealth metasomatism (O'Reilly and Griffin, 2013). Recent advances of in-situ microanalytical techniques such as laser ablation ICPMS have allowed to better define the third style of metasomatism, known as cryptic metasomatism, produced under low melt/rock ratios and characterized by the modification of the distribution of major, minor, and trace elements in peridotite-forming minerals (O'Reilly

* Corresponding author.

E-mail addresses: npujolsola@ub.edu (N. Pujol-Solà), japroenza@ub.edu (J.A. Proenza), agcasco@ugr.es (A. Garcia-Casco), jmgonzj@ugr.es (J.M. González-Jiménez), mj.roman@csic.es (M.J. Román-Alpiste), carlos.garrido@csic.es (C.J. Garrido), joan.carles.melgarejo.draper@ub.edu (J.C. Melgarejo), gervilla@ugr.es (F. Gervilla), xavier@ccit.ub.edu (X. Llovet).

and Griffin, 2013 and references therein). To date, most efforts in understanding mantle metasomatism have been focused on the study of ultramafic xenoliths and exhumed ultramafic massifs that have sampled the subcontinental lithospheric mantle (SCLM) underlying cratonic and off-craton regions of the Earth (Bodinier et al., 2008; Coltorti et al., 2004; Le Roux et al., 2007; Lenoir et al., 2001; Soustelle et al., 2009). In the SCLM, these three styles of metasomatism are very well preserved and have been identified to originate via a variety of metasomatic agents, including supercritical fluids and a variety of silicate liquids including silica-saturated, high-Na and high-K alkaline basaltic, as well as kimberlitic and carbonatitic compositions (e.g., Bodinier et al., 1990; Ionov et al., 1999; Coltorti et al., 1999, 2000; Grégoire et al., 2000; Laurora et al., 2001; Dawson, 2002; Lorand et al., 2004; Scamberulli et al., 2009; González-Jiménez et al., 2014a; Akizawa et al., 2017; Tassara et al., 2018). However, modal metasomatism is relatively underexplored in the mantle rocks of “normal oceanic lithosphere”, as numerous studies focused on oceanic islands such as Hawaii, Kerguelen or Canary islands.

Reactive melt percolation, partial dissolution, and melt crystallization are common processes in extensional settings, causing large compositional variations in the lithospheric mantle (Bodinier and Godard, 2003; Kelemen et al., 1995a, 1995b; Rampone et al., 2018; Warren and Shimizu, 2010 and references therein). The resulting lithologies in the thermal boundary layer (TBL) and in the lithospheric mantle include replacive harzburgites, dunites, and impregnated peridotites with plagioclase and pyroxene (Basch et al., 2019a, 2019b; Rampone et al., 2018 and references therein). Ascending melts also lead to the formation of gabbroic rocks (olivine-gabbro, gabbro, gabbrobronite, and ferrogabbro or oxide gabbro), often emplaced as intrusive dikes cross-cutting peridotites in slow- (e.g., Morishita et al., 2004) and fast-spreading environments (e.g., Constantin, 1999). Morishita et al. (2004) reported an example of extreme metasomatism in the slow-spreading SW Indian Ridge, where extremely differentiated mantle-derived melts infiltrate oceanic peridotites thus forming Fe-Ti-rich gabbroic veins with a complex mineral assemblage including srilankite, Mg-rich ilmenite, apatite, and rutile.

Similar processes, such as multi-stage melt infiltration and magma-peridotite interaction, are recorded in many ophiolites (Kelemen et al., 1992, 1995b; Python and Ceuleneer, 2003), especially in the Moho Transition Zone (hereafter MTZ) of ophiolitic sequences. The MTZ, located between residual peridotites and layered crustal gabbros, is characterized by variable thickness but significant lateral continuity of a rock assemblage made of harzburgites, dunites, chromitites, wehrlites, troctolites, pyroxenites, in addition to gabbroic sills and dikes. Many bodies of dunite, wehrlite, troctolite, and websterite originated from impregnation of residual peridotites (e.g., Marchesi et al., 2006), while extensive melt-rock interaction by reactive porous flow leads to selective enrichment in incompatible elements (Basch et al., 2019a).

Eastern Cuban ophiolites are characterized by large exposures of the MTZ, where interaction between residual peridotites and percolating melts have resulted in the formation of dunite bodies and associated chromitites (Marchesi et al., 2006; Proenza et al., 1999a). In the Potosí chromite deposit, Proenza et al. (2001) reported a very peculiar mineral assemblage made up of Fe-Ni-Cu sulfides, apatite, amphibole, and unidentified oxides of Ti, Zr, Y, Ca, Fe, Hf, and REE along the contact between the chromitite pods and intruding gabbroic dikes.

The present study explores in detail the metasomatic assemblage and major and trace element composition of uncommon HFSE-bearing minerals (Mg-rich ilmenite, Hf-bearing baddeleyite, REE-rich zirconolite, srilankite, zircon) found in the interaction zone between gabbroic intrusions and chromitite pods. This is an unprecedented scenario where a highly evolved tholeiitic melt interacted with chromitite in the MTZ, producing a unique metasomatic assemblage enriched in Fe, Ti, Zr, and other high-field-strength elements (HFSE).

2. Geological setting

The Mesozoic Cuban ophiolite belt, that outcrops discontinuously over more than 1,000 km along length of the island (Fig. 1a), represents the largest exposure of ophiolites in the Caribbean region (García-Casco et al., 2006; Iturralde-Vinent, 1996; Iturralde-Vinent et al., 2016; Lewis et al., 2006). This belt represents slices of oceanic lithosphere obducted during Latest Cretaceous to Eocene times as a consequence of the collision of the Caribbean volcanic arc with the Jurassic-Cretaceous passive margins of the continental Maya block and the Bahamas platform (Iturralde-Vinent et al., 2006, 2016; García-Casco et al., 2008a).

In Eastern Cuba, ophiolitic bodies are grouped into the Mayarí-Baracoa Ophiolite Belt (MBOB). This region is characterized by NE-directed tectonic nappes accreted in the Late Cretaceous – Earliest Paleocene (Cobiella-Reguera, 2005; Iturralde-Vinent et al., 2006). These nappes include Early to Late Cretaceous oceanic arc sequences (Marchesi et al., 2007; Proenza et al., 2006), some of them subducted during the latest Cretaceous (García-Casco et al., 2008a and references therein), the MBOB (Proenza et al., 1999b) and closely associated Early Cretaceous low-P and high-P (subduction-related) serpentinite-matrix mélanges (García-Casco et al., 2008b; Blanco-Quintero et al., 2010, 2011; Lázaro et al., 2009, 2016; Cárdenas-Párraga et al., 2017), a Late Cretaceous metamorphic sole (Lázaro et al., 2013, 2015), and high-pressure metamorphosed passive-margin sediments of the Caribbeana terrane (García-Casco et al., 2008a and references therein). The MBOB (170 km long, 10–30 km wide) comprises two allochthonous massifs separated by major fault zones: the Mayarí-Cristal (exposing 5 km of mantle section) to the west and the Moa-Baracoa (2.2 km of peridotites) to the east (Fig. 1b; Proenza et al., 1999a, 1999b; Marchesi et al., 2006). The ophiolite includes the mantle and crustal sequences, is highly dismembered, and represents MOR-like lithosphere formed in the suprasubduction zone setting of the intra-oceanic Caribbean arc (Gervilla et al., 2005; Marchesi et al., 2006, 2007; Proenza et al., 1999b, 2018). More than 250 chromite deposits and occurrences have been described in the MBOB (Gervilla et al., 2005; González-Jiménez et al., 2011; Proenza et al., 1999b). They are divided into three mining districts according to the composition of chromite forming the chromitite ore: Mayarí (high-Cr), Sagua de Tánamo (high-Cr and high-Al) and Moa-Baracoa (high-Al) (Fig. 1b).

2.1. The Moa-Baracoa ophiolitic massif

The Moa-Baracoa massif consists of mantle tectonite harzburgite with subordinate dunite and a MTZ associated with layered gabbros (about 500 m thick) and mafic volcanic rocks (Fig. 1c; Marchesi et al., 2006). Towards the top of the mantle tectonites, harzburgite contains increasing amounts of dunite, gabbro sills, and chromitite, all forming elongated pseudotabular bodies oriented parallel to the foliation of the host harzburgite, as well as discordant dikes of wehrlite, troctolite, olivine gabbro, and pegmatitic gabbro (Flint et al., 1948; Guild, 1947; Marchesi et al., 2006; Proenza et al., 1999a, 1999b, 2001). The peridotites and layered gabbros are in tectonic contact with the pillow basalts of the Morel formation (88–91 Ma; Iturralde-Vinent et al., 2006), which show a back-arc geochemical affinity. Marchesi et al. (2006) established the genetic link between the Morel formation and the cumulate gabbros of the Moa-Baracoa massif. Therefore, the Moa-Baracoa Ophiolite Massif is interpreted to have formed in a back-arc environment (Gervilla et al., 2005; Lázaro et al., 2015; Proenza et al., 2006).

2.2. The Potosí chromitites and the gabbroic intrusions

The Potosí chromitites are located 800 m deeper than the layered gabbros forming the MTZ at the Moa-Baracoa Ophiolitic Massif (Fig. 1c) (Proenza et al., 2001). They form lenses of variable sizes and irregular shapes (tabular to lenticular) hosted in dunite within harzburgite. The bodies are oriented N 40° E to N 74° E with dips

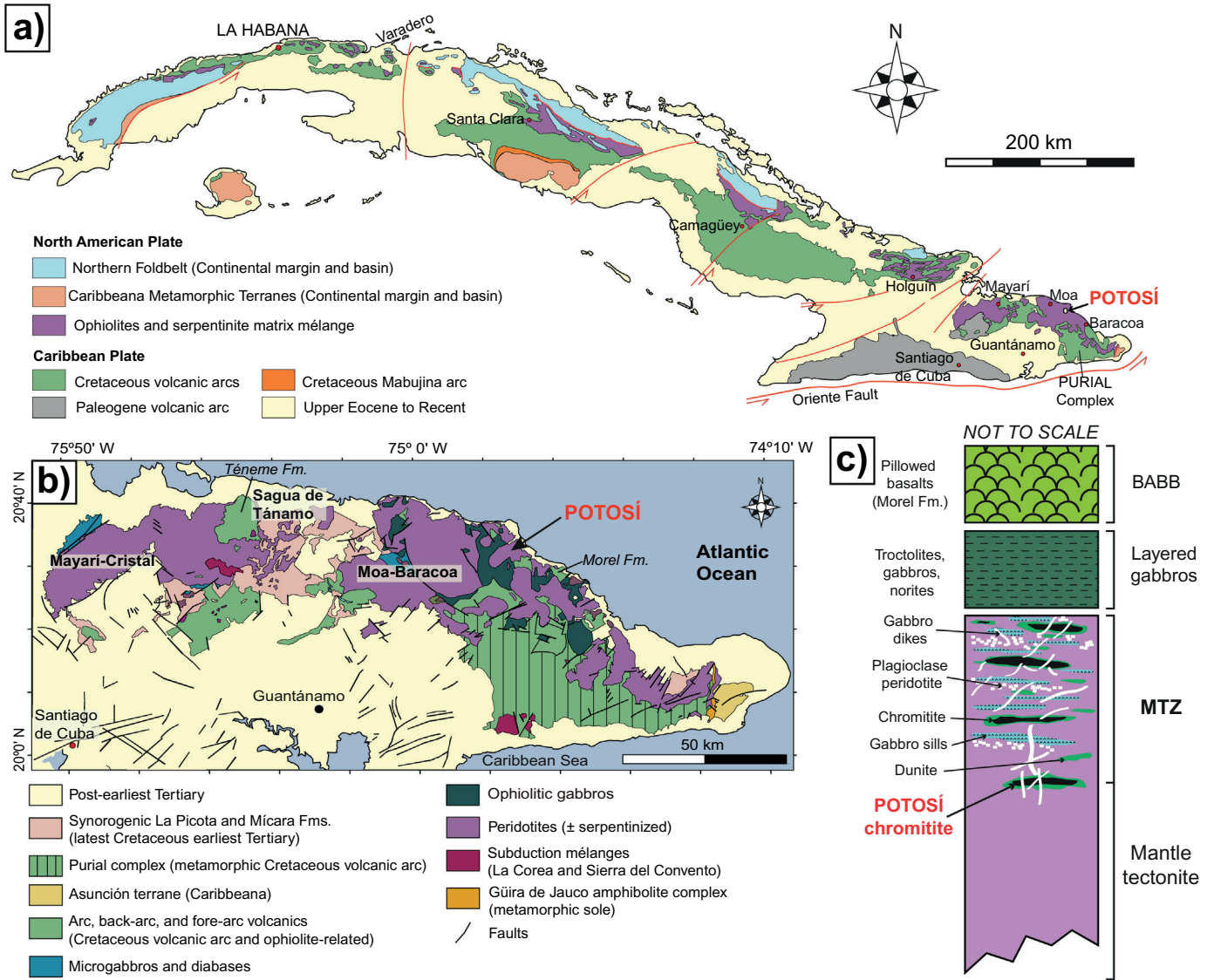


Fig. 1. (a) Generalized geologic-tectonic map of Cuba modified from Iturralde-Vinent et al. (2016); (b) Geological map of the Mayarí-Baracoa Ophiolitic Belt (MBOB) (modified from Pushcharovsky et al., 1988) showing the location of the Potosí deposit; (c) Schematic lithostratigraphic column of Moa-Baracoa with location of Potosí (modified from Marchesi et al., 2006).

between 32° and 45° to the NW, usually filling the foliation of the host peridotites. Several generations of gabbroic intrusions crosscut the chromitite bodies, usually following pull-apart fractures with brecciated zones at their margins (Fig. 2a–d; Proenza et al., 2001). Dikes have highly variable thicknesses, from a few centimeters to 2 m across and locally show a distinct grain-size zoning with pegmatitic textures in the dike cores that reach grain sizes larger than 15 cm (Fig. 2c–e) and finer grain sizes closer to the contacts with chromitite. Disrupted fragments of chromitite occur as inclusions within the gabbroic intrusions (Fig. 2d). The contacts between the chromitites and the gabbroic intrusions may be either neat (Fig. 2e) or gradational, the latter characterized by a brecciated zone where chromite is included within the gabbroic dikes (Fig. 2f).

Chromitite in Potosí can be classified as: i) ordinary podiform chromitite, preexistent to gabbroic intrusions, or ii) metasomatized chromitite, associated with or intruded by gabbroic dikes and denoted as “brecciated chromite ore” and “sulfide-rich chromite ore” by Proenza et al. (2001). Ordinary chromitites represent more than 90 vol.% of the ore body and show mineralogical, textural and chemical

features similar to other Al-rich chromitite bodies in the MBOB (Gervilla et al., 2005; Proenza et al., 1999b) and ophiolitic complexes worldwide (González-Jiménez et al., 2014b; Arai and Miura, 2016 and references in these papers). Metasomatized chromitite is composed mostly of recrystallized Ti- and Fe³⁺- rich chromite, Ti-rich amphibole, orthopyroxene, clinopyroxene, plagioclase, and Fe-Cu-Ni sulfides, the latter formed by fractionation of immiscible sulfide liquid segregated from the mafic intrusions (Proenza et al., 2001).

3. Studied samples and analytical techniques

3.1. Studied samples

A total of 20 hand samples and 38 thin sections were examined for this study (Supplementary material 1), including ordinary chromitite and its host peridotite (5 samples), metasomatized chromitite (11 samples), and gabbroic dikes (4 samples) (Fig. 2a–b). Most samples were taken from the outcrops of old mine works and some were collected in the mine dumps.

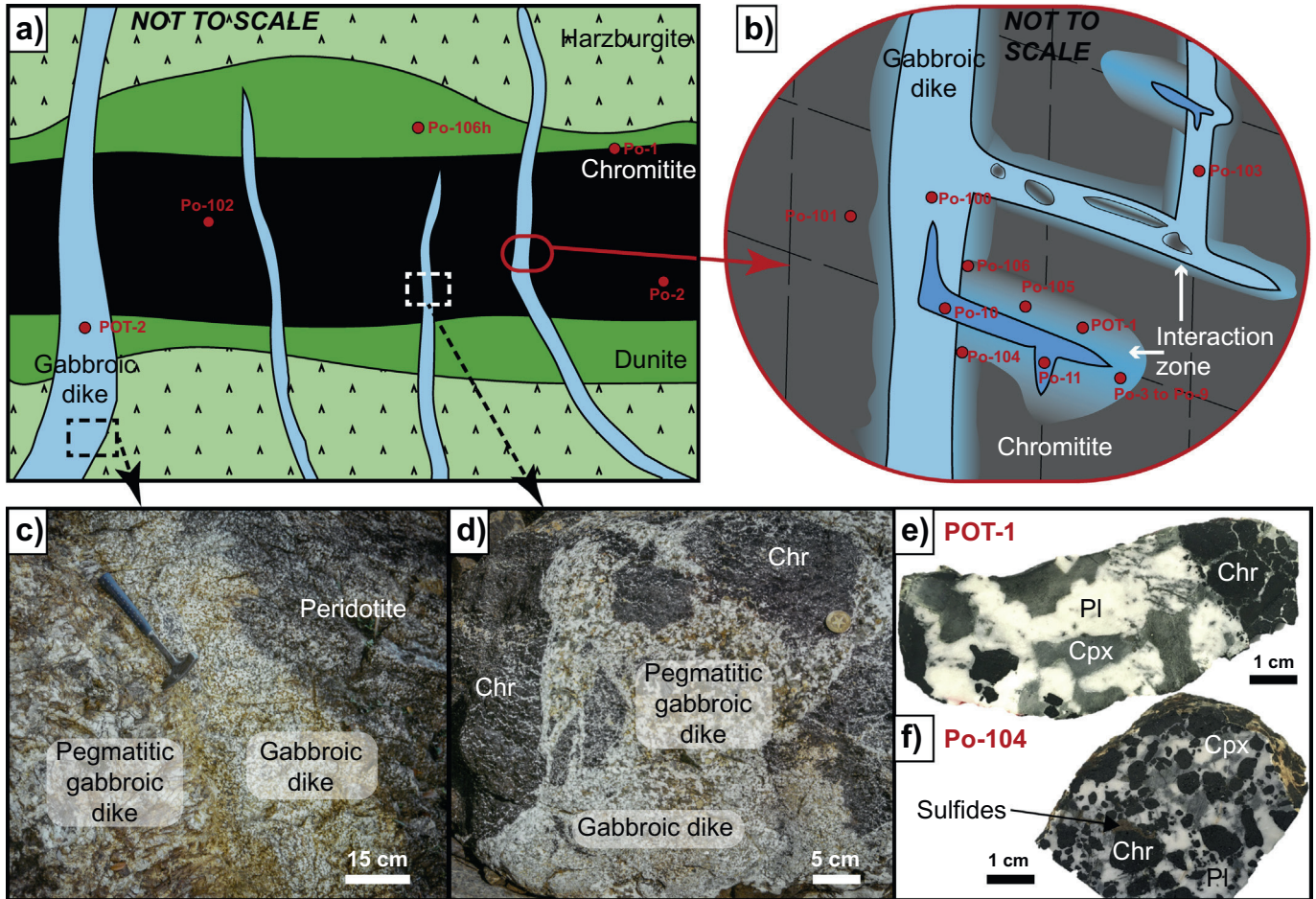


Fig. 2. (a) Schematic cross-section of a chromitite body in Potosí crosscut by multiple generations of gabbroic dikes. Red dots indicate the location of the samples; (b) Detail of the interaction zone between the chromitite and the intruding gabbroic dike. Brighter blue indicates differentiated melts. Red dots indicate the location of the samples; (c) Field relations of a gabbroic dike intruding the peridotite. Note the variation in grain size and the area with pegmatitic texture; (d) Gabbroic dike, with pegmatitic textures, intruding chromitite. Note the disrupted fragments of chromitite as inclusions within the gabbroic dike; (e) Hand sample of the contact between the gabbroic dike and the chromitite; and (f) Hand sample of brecciated chromitite. Abbreviations: Chr – chromite, Pl – plagioclase, Cpx – clinopyroxene.

3.2. Analytical techniques

Modal composition of the POT-2 sample was calculated using point counting on thin section with the software *JMicroVision*. Whole rock geochemical analyses were performed at the Centre for Scientific Instrumentation (CIC) of the University of Granada. Samples were carefully prepared by removing secondary veins and weathering products before crushing and powdering in an agate mill. Major element and Zr concentrations were determined by X-ray fluorescence (XRF) spectrometry on glass beads (~0.6 g of powdered sample diluted in 6 g of $\text{Li}_2\text{B}_4\text{O}_7$) using a Philips Magix Pro (PW-2240). Precision was better than $\pm 1.5\%$ for an analyte concentration of 10 wt.% and the precision for Zr was better than $\pm 4\%$ at 100 ppm concentration. The analyses were recalculated to an anhydrous basis (100 wt.%). Trace elements were analyzed by ICP Mass Spectroscopy (ICP-MS) at the same institution. ~100 mg of sample were digested with $\text{HNO}_3 + \text{HF}$ in a Teflon lined vessel at 180 °C and ~200 psi for 30 min, evaporated to dryness, and subsequently dissolved in 100 ml of 4 vol.% HNO_3 . During analytical sessions, the procedural blanks and reference materials PMS, WSE, UBN, BEN, BR, and AGV were run as unknowns and primary standards to obtain concentrations (Govindaraju, 1994). Precision was better than $\pm 2\%$ and $\pm 5\%$ for analyte concentrations of 50 and 5 ppm, respectively. Major and trace element bulk analyses results are presented in Supplementary material 2.

Polished thin sections were studied in detail by optical microscopy and scanning electron microscopy, using both a Quanta 200 FEI XTE 325/D8395 scanning electron microscope (SEM) and a JEOL JSM-7100 field-emission SEM at the Universitat de Barcelona (CCiTUB). Operating conditions were 15–20 kV accelerating voltage and 5 nA beam current. Quantitative electron microprobe analyses (EMPA) were also conducted at the CCiTUB using both CAMECA SX50 and JEOL JXA-8230 electron microprobes, operating in wavelength-dispersive spectroscopy (WDS) mode. The analytical conditions are described in Supplementary material 3.

Trace element compositions of chromite, ilmenite, clinopyroxene, orthopyroxene, olivine, amphibole, apatite, zircon, and baddeleyite were measured in-situ on polished thin sections (30 μm) by an inductively coupled mass spectrometer Agilent 8800 QQQ ICP-MS interfaced to a laser ablation extraction line Photon Machines Analyte Excite 193 at the Instituto Andaluz de Ciencias de la Tierra (CSIC-UGR, Granada). The analytical conditions are described in Supplementary material 3. Six grains of baddeleyite were analyzed for U/Pb isotopes with the same equipment at the same institution. A spot diameter of 30 μm was used with the same analytical conditions as for zircon. Phalaborwa baddeleyite was used as a reference material and in-house Mogok baddeleyite for secondary/validation. Data (Supplementary material 4) were reduced using Igor Pro iolite 3.6 software, VisualAge DR, ET-Redux, and Isoplot for data presentation.

4. Results

4.1. Petrological features of the gabbroic intrusions

Two types of gabbroic intrusions have been characterized in Potosí (Fig. 3). The first type (POT-2) corresponds to a melagabbro (Fig. 3a)

containing olivine (64%), clinopyroxene (21%), plagioclase (14%), orthopyroxene (<1%), and accessory oxides with a general coarse grain size. Olivine and plagioclase are cumulus minerals and clinopyroxene is intercumulus (mesocumulate texture). Clinopyroxene reaches up to 2 cm in length and develops a poikilitic texture. The major and trace element composition of this type of intrusion (Supplementary

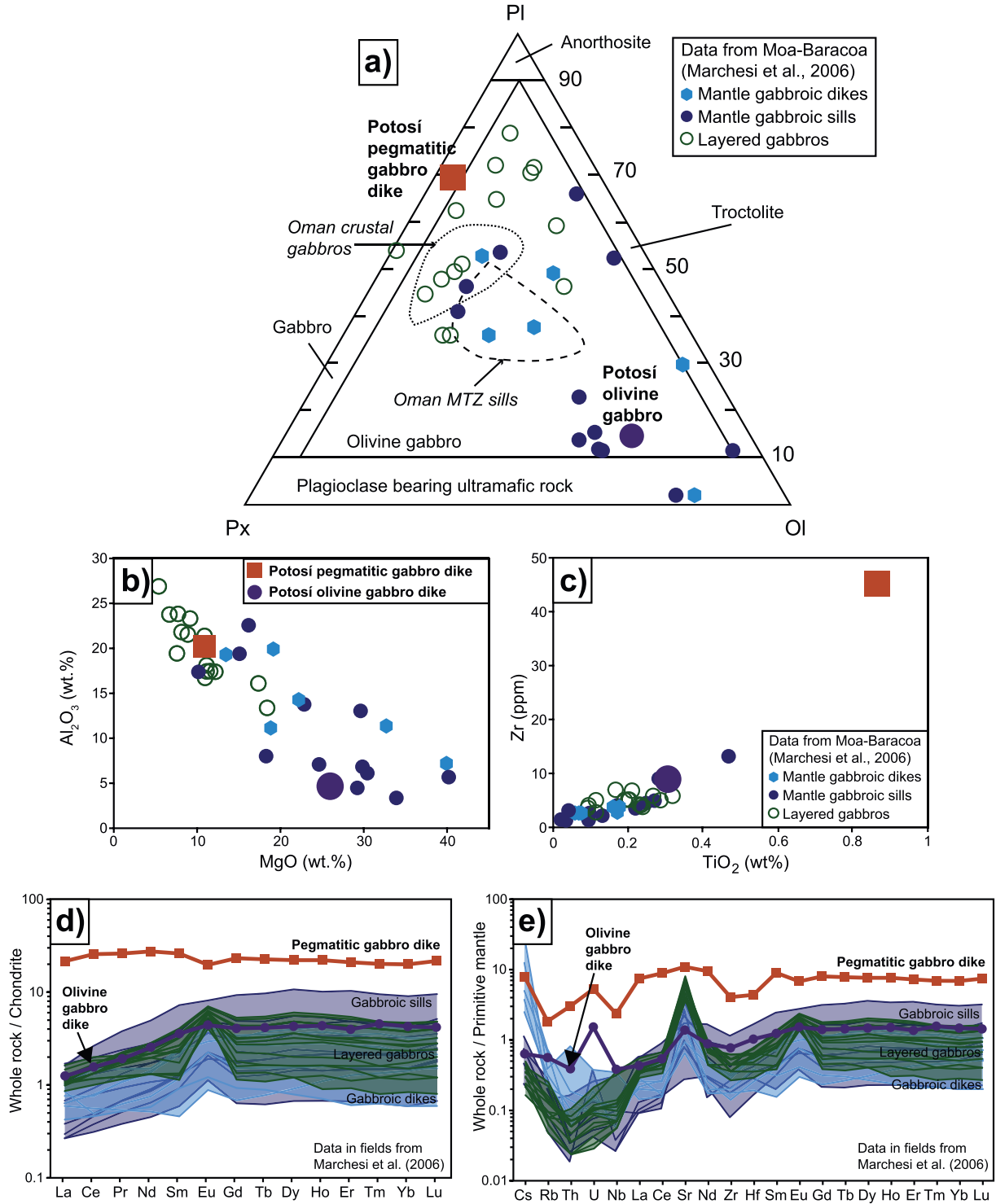


Fig. 3. (a) Modal compositions of the Potosí studied gabbroic dikes compared with gabbro sills and dikes, and layered gabbros from the Moa Baracoa Massif (data from Marchesi et al., 2006); (b–c) Whole rock major and trace element compositions of the Potosí studied gabbroic dikes compared with gabbro sills and dikes, and layered gabbros from the Moa Baracoa Massif (data from Marchesi et al., 2006), (b) Al₂O₃ (wt.%) versus MgO (wt.%), and (c) Zr (ppm) versus TiO₂ (wt.%). All data on anhydrous basis in wt.%; (d) Chondrite-normalized REE patterns of the studied Potosí gabbroic dikes compared with gabbro sills and dikes, and layered gabbros from the Moa Baracoa massif (data from Marchesi et al., 2006). Normalizing values from Sun and McDonough (1989); and (e) Primitive mantle-normalized patterns of the studied Potosí gabbroic dikes compared with gabbro sills and dikes, and layered gabbros from the Moa Baracoa Massif (data from Marchesi et al., 2006). Normalizing values from Sun and McDonough (1989).

material 2) is similar to the primitive sills and dikes crosscutting the MTZ in the Moa-Baracoa massif reported by Marchesi et al. (2006) (Fig. 3b, c). The trace element contents are slightly richer than chondrite and the chondrite-normalized REE pattern shows a slightly positive slope from LREE to MREE and a flat pattern from MREE to HREE (Fig. 3d, e).

The second type of gabbroic intrusion (POT-1) corresponds to a leucogabbro dike with pegmatitic texture (Fig. 2e, 3a) containing plagioclase (70%) and clinopyroxene (28%) crystals up to 3 cm in length

with accessory oxides (around 2%). The major element composition of the dike (Supplementary material 2) is similar to the more evolved gabbroic sills and dikes (Fig. 3b) of the Moa-Baracoa massif (Marchesi et al., 2006). However, it shows an important enrichment in trace elements (Supplementary material 2), notably in Zr (Fig. 3c). The chondrite-normalized REE (Fig. 3d) and primitive mantle-normalized trace element (Fig. 3e) patterns show enrichment by one order of magnitude compared to those of the Moa-Baracoa gabbroic dikes, sills, and layered gabbros (Marchesi et al., 2006).

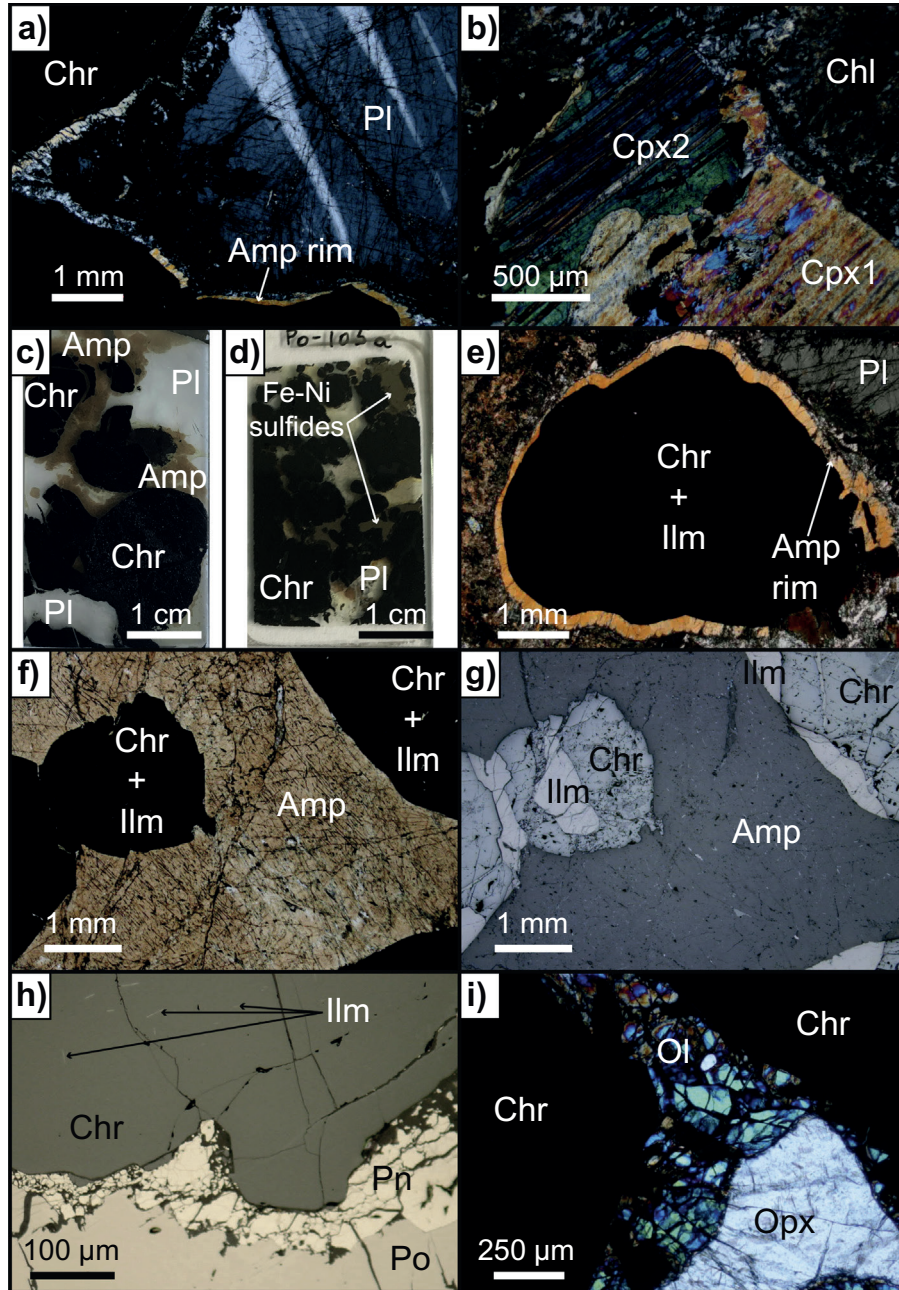


Fig. 4. (a) Transmitted light (crossed nicols) photomicrograph of chromite with amphibole rim and partially altered plagioclase; (b) Transmitted light (crossed nicols) photomicrograph of clinopyroxene 1 (core) and clinopyroxene 2 (rim) surrounded by alteration minerals (probably chlorite); (c) Petrographic thin section of the interaction zone between chromitite and gabbroic dikes, where the main mineralogy includes recrystallized (metasomatized) chromite, amphibole and plagioclase; (d) Petrographic thin section of the interaction zone between chromitite and gabbroic dike, where the main mineralogy includes recrystallized (metasomatized) chromite, plagioclase and Fe-Ni sulfides; (e) Transmitted light (crossed nicols) photomicrograph of recrystallized chromite and ilmenite (opaque) surrounded by an amphibole rim with host plagioclase and alteration minerals; (f) Transmitted light (parallel nicols) photomicrograph of recrystallized chromite and ilmenite (opaque) in equilibrium with brown amphibole hosting multiple oxide inclusions along the cleavage planes; (g) Reflected light photomicrograph of (f)—the opaque minerals in (f) are recrystallized chromite and ilmenite; (h) Reflected light photomicrograph of chromite hosting multiple oriented ilmenite lamellae, in contact with sulfides (pyrrhotite and pentlandite); (i) Transmitted light (crossed nicols) photomicrograph of orthopyroxene in contact with fine-grained olivine within recrystallized chromite. Abbreviations: Chr – chromite, Pl – plagioclase, Amp – amphibole, Cpx – clinopyroxene, Chl – chlorite, Ilm – ilmenite, Ol – olivine, Pn – pentlandite, Po – pyrrhotite, Opx – orthopyroxene.

Plagioclase crystals (up to 2 cm) in the gabbro dike show polysynthetic twinning (Fig. 4a) and partial alteration to (clino)zoisite and fine-grained phyllosilicate aggregates. Fresh plagioclase shows labradorite composition ($An_{51}-An_{56}$) (Supplementary material 5) with limited compositional variation at the grain scale. Clinopyroxene crystals (up to 3 cm) show deformation revealed by folding of the cleavage planes. These crystals host many elongated oxide inclusions along the cleavage planes and show exsolution of orthopyroxene lamellae. The composition of clinopyroxene is relatively narrow, corresponding to the limit between diopside and augite ($En_{44-49}Wo_{48-46}Fs_{8-5}$), with $Mg\# = 0.85-0.92$ and high TiO_2 (0.36–1.05 wt.%) (Supplementary material 5). Some clinopyroxene grains show rims with slightly different extinction angles (Fig. 4b) and higher diopside contents.

4.2. Metasomatized chromitite

The interaction between the pegmatitic gabbro enriched in trace elements and the ordinary chromitite generated unusual mineral phases in the metasomatized chromitite. This type of rock shows strong variability in textures and modal mineralogy at the hand-sample and thin-section scales. Most samples show coarse granular textures with crystals up to 2 cm in length (Fig. 2e, f, 4c, d). The primary igneous-metasomatic phases are Fe^{3+} -Ti-rich chromite, Ti-rich amphibole, orthopyroxene, olivine, Mg-rich ilmenite, and Fe-Cu-Ni sulfides (Fig. 4c, d). This assemblage experienced variable late overprinting that is attributed to ocean floor alteration/metamorphism, which

produced the secondary serpentine-group minerals, chlorite, ferrian-chromite, magnetite, actinolite-tremolite, rutile, and titanite.

Metasomatized chromite forms generally subhedral crystals with sizes ranging between 0.5 and 2 cm (Fig. 4c–e). Locally, octahedral chromite crystals are cemented by sulfides. Chromite is usually associated with amphibole and ilmenite (Fig. 4f, g) and most chromite grains host abundant crystallographically-oriented ilmenite lamellae (Fig. 4h). Metasomatized chromite has higher $Cr\#$ [$Cr/(Cr+Al)$] (0.57–0.70), higher $Fe^{3+}\#$ [$Fe^{3+}/(Fe^{3+}+Cr+Al)$] (0.10–0.30) and lower $Mg\#$ [$Mg/(Mg+Fe^{2+})$] (0.31–0.53) than chromite from ordinary chromitites ($Cr\# = 0.44-0.54$, $Fe^{3+}\# < 0.05$, and $Mg\# = 0.66-0.74$; see also Proenza et al., 2001). It is also enriched in TiO_2 (1.02–4.34 wt.%), Fe^{3+} (up to calculated 21.5 wt.% Fe_2O_3), Fe^{2+} (up to calculated 25.31 wt.% FeO), and V_2O_3 (up to 0.7 wt.%) (Fig. 5) (Supplementary material 6). Two types of metasomatized chromite can be distinguished (Fig. 5):

- (I) Type I bears an intermediate composition between ordinary and metasomatized s.s. chromite (type II, see below) ($Cr\# = 0.57-0.58$, $Fe^{3+}\# = 0.10-0.13$, and $Mg\# = 0.51-0.53$), which roughly corresponds to the “brecciated chromite ore” defined by Proenza et al. (2001).
- (II) Type II ($Cr\# = 0.62-0.70$, $Fe^{3+}\# = 0.19-0.30$, and $Mg\# = 0.31-0.39$) further interacted with the gabbroic dikes and corresponds to the “sulfide-rich chromite ore” (10–30 vol.% Fe-Ni-Cu sulfides) of Proenza et al. (2001).

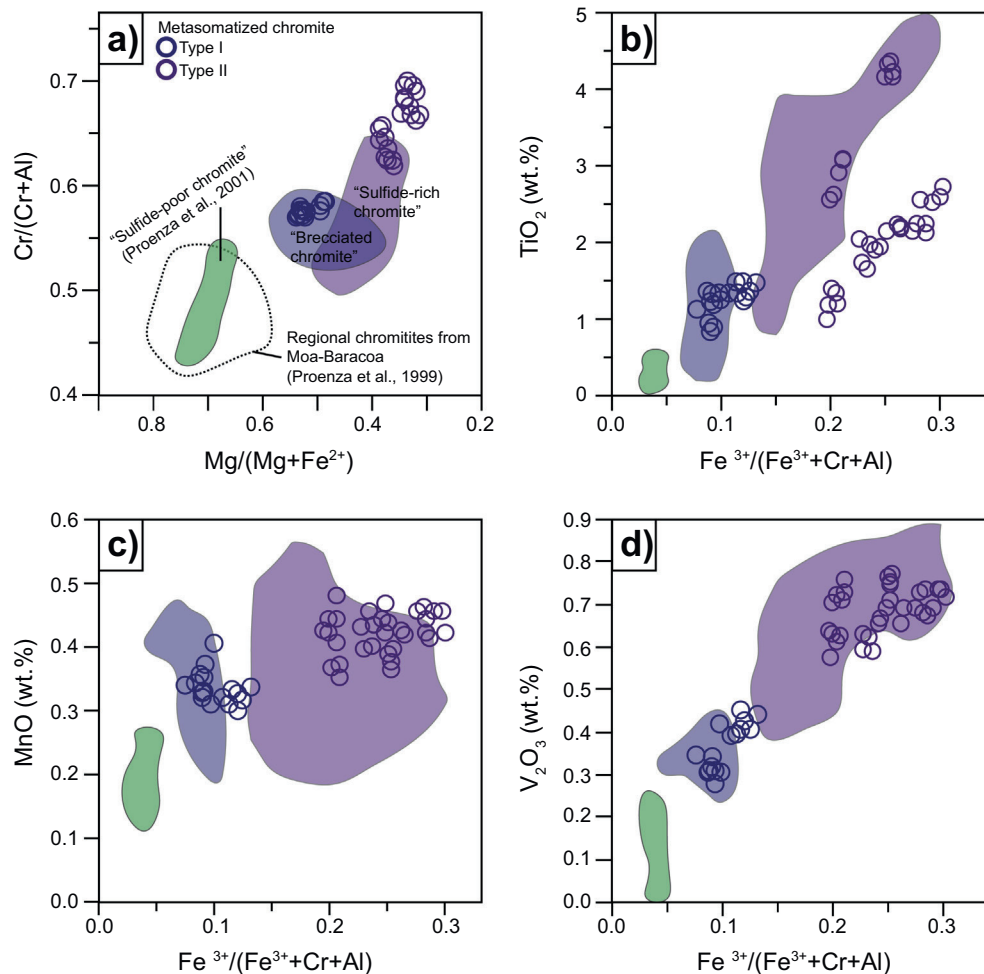


Fig. 5. Composition of chromite from Potosí. (a) Variation of $Cr\#$ [$Cr/(Cr+Al)$] versus $Mg\#$ [$Mg/(Mg+Fe^{2+})$]. The areas represent the compositions of the Potosí ordinary (sulfide-poor chromite ore) and metasomatized chromite (brecciated and sulfide-rich chromite ores) reported by Proenza et al. (2001), and the dashed area is the compositional field of the chromitites from the Moa-Baracoa Massif (Proenza et al., 1999b); (b) TiO_2 versus $Fe^{3+}\#$ [$Fe^{3+}/(Fe^{3+}+Cr+Al)$]; (c) MnO versus $Fe^{3+}\#$; and (d) V_2O_3 versus $Fe^{3+}\#$.

The change in composition from ordinary to type II metasomatized s. s. chromite is defined by an enrichment trend in Cr#, $\text{Fe}^{3+}\#$, and TiO_2 (Fig. 5). In type II metasomatized chromitite the sulfides are usually intergranular to (or forming rims around) chromite (Fig. 4d, h) and are mainly pyrrhotite, pentlandite, chalcopyrite and cubanite, with minor amounts of chalcocite and valleriite (Proenza et al., 2001).

Brown amphibole forms large crystals (up to 2 cm) and coronas around the chromite (Fig. 4a, e). Large crystals usually host a myriad of elongated inclusions (up to 15 μm long) of ilmenite, rutile and titanite following the cleavage planes (Fig. 4f, g). Amphibole composition (Fig. 6a–h) is Ti-rich with TiO_2 ranging between 2.41 and 5.46 wt.%, Mg# between 0.82 and 0.94, Cl up to 0.05 wt.% and F up to 0.5 wt.%, corresponding mainly to Ti-rich magnesio-hastingsite and, to a lesser extent, Ti-rich pargasite and ferri-kaersutite compositions (calculations

following Locock, 2014 and the classification scheme of Hawthorne et al., 2012; Fig. 6a–b; Supplementary material 5).

Orthopyroxene is not abundant and forms grains up to 3 mm that are generally free of inclusions and devoid of zoning with an enstatite composition ($\text{En}_{84-94}\text{Wo}_{4-1}\text{Fs}_{12-5}$), with $\text{Mg}\# = 0.87-0.89$ and high TiO_2 contents (0.23–0.47 wt.%, Supplementary material 5). Orthopyroxenes is in contact with rare fine-grained Fo_{86-91} olivine (up to 200 μm) (Fig. 4i) with NiO ranging between 0.12 and 0.22 wt.% (Supplementary material 5). The higher forsterite contents correspond to typical mantle olivine, including olivine from the regional Moa-Baracoa chromitites (Fo_{90-97} ; Proenza et al., 1999b), while the lower forsterite values are closer to those of gabbroic intrusions (Fo_{74-82} ; Marchesi et al., 2006). Olivine crystals locally include elongated grains of oriented Cr-spinel and ilmenite.

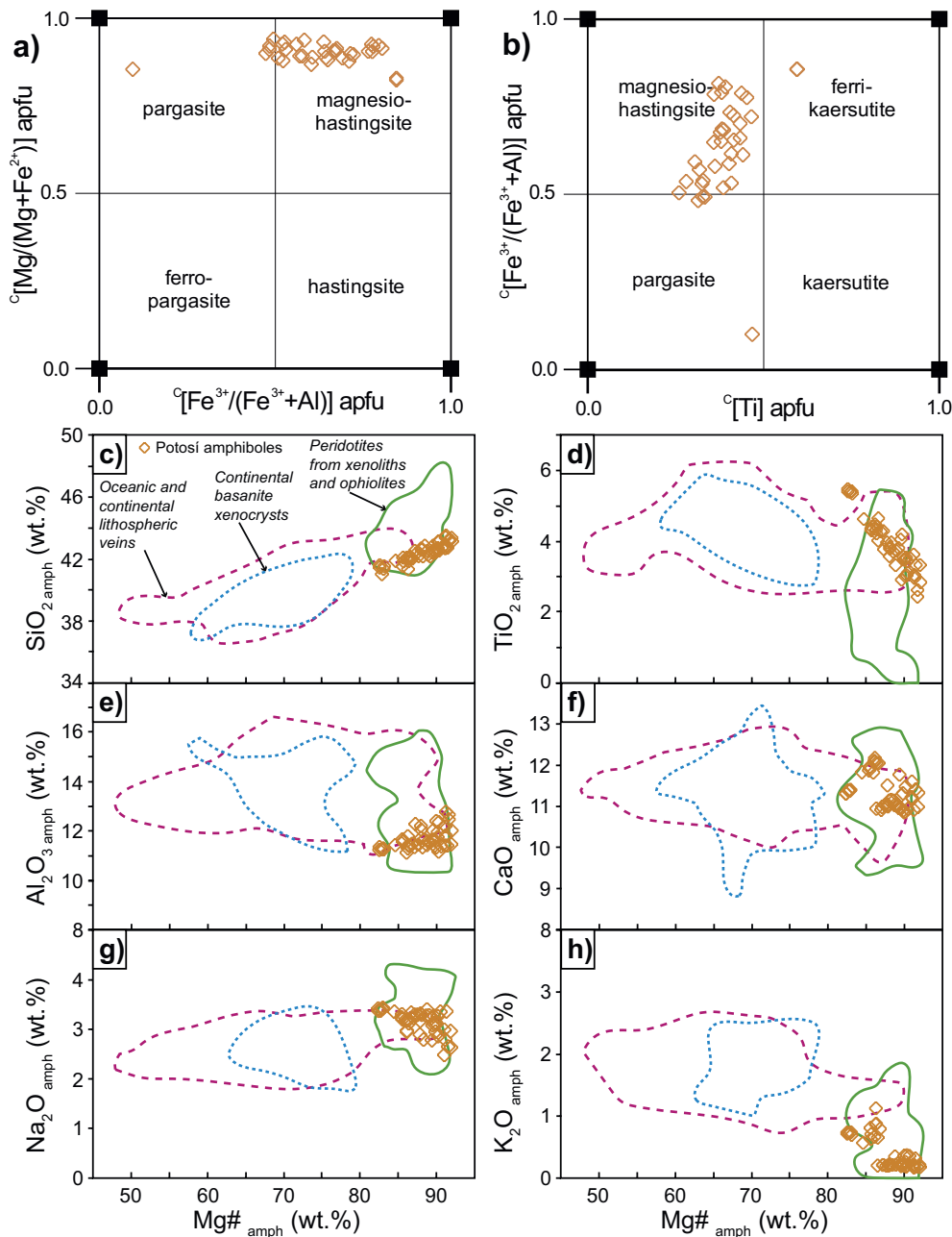


Fig. 6. (a–b) Amphibole classification diagrams according to Hawthorne et al., 2012. (a) Variation of $^c[\text{Mg}/(\text{Mg}+\text{Fe}^{2+})]$ a.p.f.u. versus $^c[\text{Fe}^{3+}/(\text{Fe}^{3+}+\text{Al})]$ a.p.f.u.; (b) $^c[\text{Fe}^{3+}/(\text{Fe}^{3+}+\text{Al})]$ a.p.f.u. versus $^c[\text{Ti}]$ a.p.f.u.; (c–h) Major element variations in amphiboles from Potosí. The fields corresponding to “oceanic and continental lithospheric veins”, “continental basanite xenocrysts”, and “peridotites from xenoliths and ophiolites” are from Pilet et al. (2008). (c) Variation of SiO_2 (wt.%) versus $\text{Mg}\#_{\text{amph}}$ [Mg/(Mg+Fe)]; (d) Variation of TiO_2 (wt.%) versus $\text{Mg}\#_{\text{amph}}$; (e) Variation of Al_2O_3 (wt.%) versus $\text{Mg}\#_{\text{amph}}$; (f) Variation of CaO (wt.%) versus $\text{Mg}\#_{\text{amph}}$; (g) Variation of Na_2O (wt.%) versus $\text{Mg}\#_{\text{amph}}$; and (h) Variation of K_2O (wt.%) versus $\text{Mg}\#_{\text{amph}}$.

Ilmenite forms subhedral to anhedral crystals (up to 1 cm) located at the rims of (Fig. 4g), or within, chromite crystals (Fig. 7a, d, f, h) and forms oriented lamellae in chromite following its crystallographic orientation (Fig. 4h). The content in the geikielite component (Supplementary material 7) varies between 1 and 45 mol% MgTiO₃ (averaging 26 mol%) (Fig. 8a, b). Ilmenite grains are devoid of chemical zoning and compositional variations are independent of textural position, as illustrated by strikingly different geikielitic contents in adjacent grains of ilmenite (Fig. 8a, b).

Several mineral phases occur as inclusions within, or at the rims of, grains of ilmenite. The most abundant is apatite, forming euhedral to subhedral elongated crystals up to 500 μm long (Fig. 9a, b) in contact with or included within ilmenite. Seldom, apatite crystals include sulfide inclusions (Fig. 9b). Apatite contains 0.85–1.52 wt.% F and 0.54–0.77 wt.% Cl, with a Cl/F (molar) ratio between 0.33 and 0.48 (Supplementary material 8). Relatively small (up to 500 μm in length) ilmenite crystals in contact with chromite host accessory Zr-oxides (baddeleyite, zirconolite, and srilankite) (Fig. 7), whereas large ilmenite crystals (up to 0.5 cm long) in contact with silicates (Fig. 9) show zircon coronas. It is noteworthy that Zr-oxides and zircon do not coexist surrounding, or within, a given ilmenite crystal.

Zr oxides form subhedral to anhedral elongated crystals with sizes ranging between 10 and 80 μm long within ilmenite (Fig. 7). Occasionally, Zr oxide inclusions have multiple mineral phases (e.g., baddeleyite and zirconolite or baddeleyite and srilankite; Fig. 7i). Baddeleyite crystals show Hf-enrichment (HfO₂ between 1.52 and 1.96 wt.%) and low Nb, Nd, and U contents (up to 0.06 wt.% Nb₂O₃, up to 0.06 wt.% Nd₂O₃, up to 0.07 wt.% U₂O₃) (Supplementary material 8). Zirconolite composition deviates from the ideal CaZrTi₂O₇ (Fig. 10a), with very low U and Th contents (Fig. 10b), relative enrichment in REE (REE₂O₃ = 9.25–10.7 wt.%) (Fig. 10c) and containing exceptionally high Y (up to 11.06 wt.% of Y₂O₃) (Supplementary material 9). The studied zirconolite contains the highest Y concentrations reported to date in terrestrial zirconolite and the observed dominant coupled substitution is: 2Ca²⁺ + Ti⁴⁺ = 2(REE,Y)³⁺ + (Fe, Mg)²⁺ (Fig. 10d). Two compositional groups of zirconolite are observed with different degrees of coupled substitution (Fig. 10).

Zircon grains (up to 50 μm) usually form rims around large ilmenite crystals, clustering at the contact with silicates (Fig. 9a, d), and they may appear elongated following the rim of ilmenite (Fig. 9e–g). Generally, zircon coronas show granular textures (Fig. 9f) and include ilmenite grains in between. Zircon is devoid of zoning (Appendices 10 and 11) with HfO₂ content ranging between 0.17 and 1.54 wt.%, which is within the range of abundance for natural zircon (0.5–5 wt.%; Belousova et al., 2002). These zircon coronas generally remain unaltered during alteration of ilmenite to rutile and titanite (Fig. 9h, i). Occasionally, zircon is replaced by an aggregate of fine-grained baddeleyite (secondary baddeleyite) together with Mg–Al silicates (Fig. 9c). Figure 11 summarizes the main petrographic features and mineral relations observed in the metasomatized chromitite in Potosí.

4.3. Mineral trace element compositions

Minerals from the metasomatized chromitite show relatively unusual trace element distribution and patterns (Supplementary material 12). Trace elements of chromite normalized to MORB chromite (Fig. 12a) show a positive anomaly in Ti and negative anomaly in Ni, which is not typical in Al-rich ophiolitic chromitites of the Moa-Baracoa massif, usually displaying relatively flat patterns (e.g., Colás et al., 2014). The chondrite-normalized REE patterns of Ti-rich amphibole are characterized by LREE depletion, nearly flat HREE and negative Eu anomalies (Fig. 12b), being similar in shape to (but more enriched than) associated clinopyroxene (Fig. 12c). Clinopyroxene shows two characteristic REE patterns corresponding to the cores and rims of grains. Clinopyroxene cores are particularly depleted in LREE and show strong fractionation from HREE to LREE (Fig. 12c), whereas

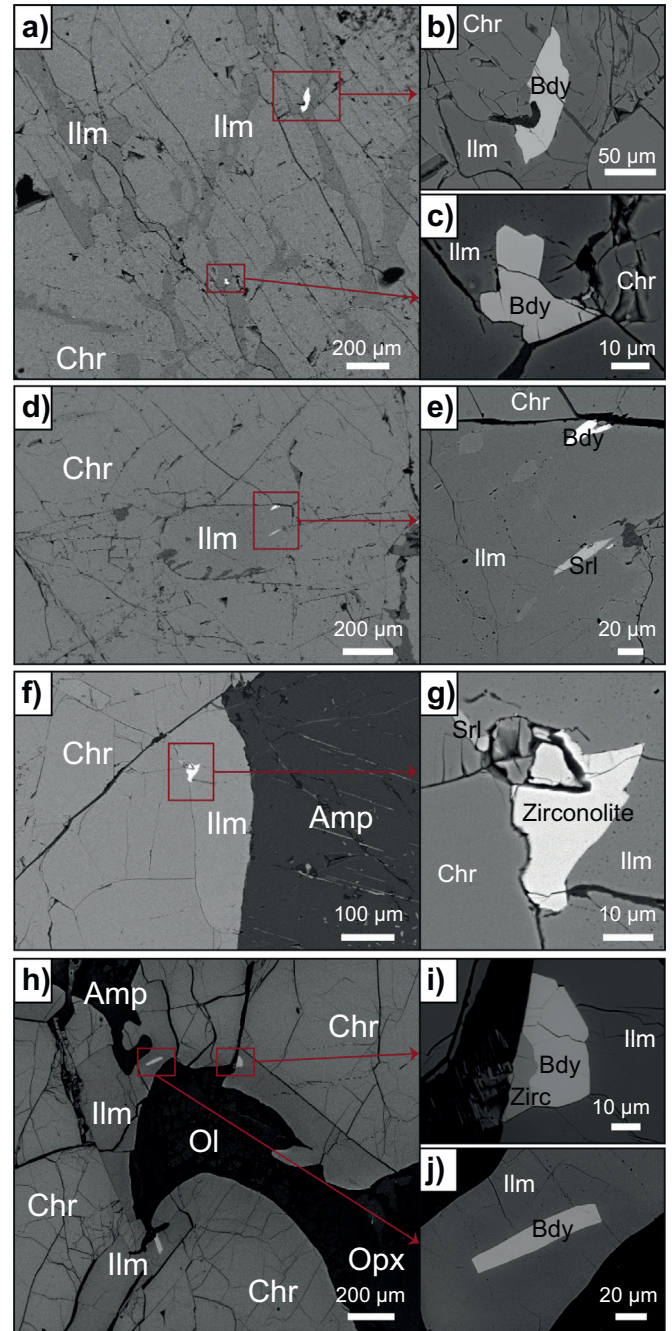


Fig. 7. Backscattered electron images of: (a) Elongated ilmenite crystals within chromite. Note the bright inclusions within ilmenite that correspond to Zr-bearing oxides; (b) Zoom of (a) showing a baddeleyite inclusion within ilmenite in contact with chromite; (c) Second zoom of (a) showing a baddeleyite inclusion within ilmenite in contact with chromite; (d) Ilmenite subrounded crystal hosted in chromite; (e) Zoom of (d) showing elongated inclusions of baddeleyite and probably srilankite within ilmenite; (f) Ilmenite crystal at the border of chromite; (g) Zoom of (f) showing a zirconolite inclusion with minor srilankite in the upper part, hosted in ilmenite in the contact with chromite; (h) Ilmenite crystals in equilibrium with chromite hosting elongated baddeleyite crystals. Note that the interstitial silicate minerals are mainly olivine, with minor orthopyroxene and amphibole; (i) Zoom of (h) showing an inclusion of baddeleyite together with zirconolite; and (j) Second zoom of (h) showing an elongated tabular baddeleyite inclusion within ilmenite. Abbreviations: Chr – chromite, Ilm – ilmenite, Bdy – baddeleyite, Srl – srilankite, Amp – amphibole, Ol – olivine, Opx – orthopyroxene, Zirc – zirconolite.

clinopyroxene rims are characterized by higher trace element contents and larger negative Eu anomalies (Fig. 12c), with patterns depleted in LREE and a flat segment from MREE to HREE. Similar to clinopyroxene

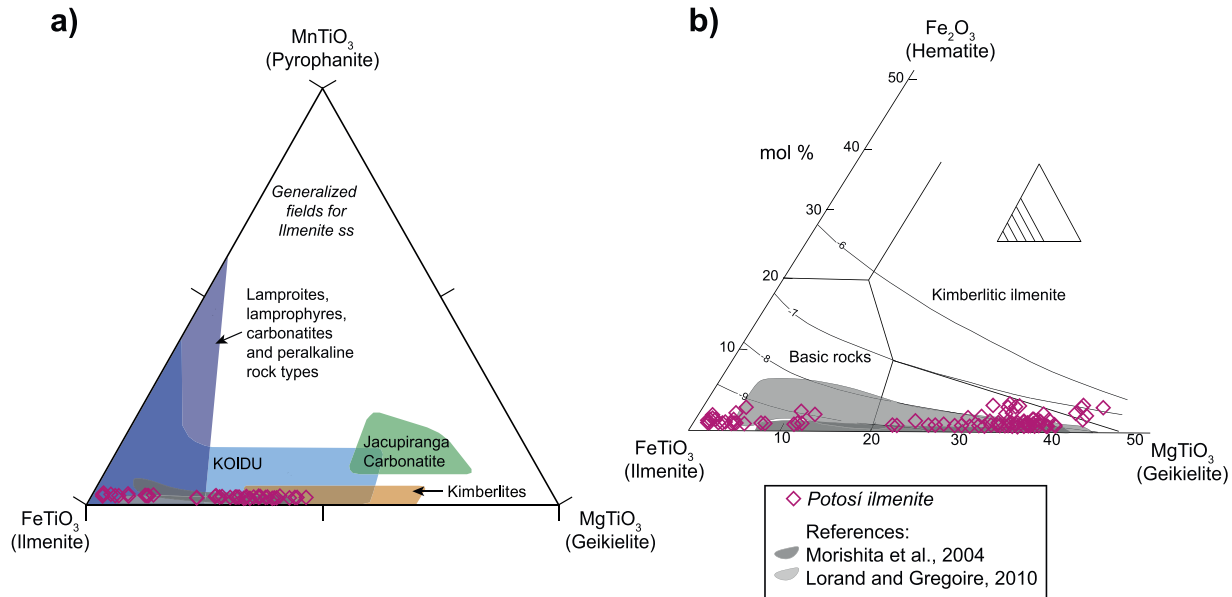


Fig. 8. (a) Ilmenite composition in terms of the pyrophanite (MnTiO_3)–ilmenite (FeTiO_3)–hematite (Fe_2O_3) endmembers. The compositional fields are from Tompkins and Haggerty (1985) and the shaded areas correspond to Morishita et al. (2004) in dark grey and Lorand and Gregoire (2010) in light grey; and (b) Ilmenite composition in terms of the hematite (Fe_2O_3)–ilmenite (FeTiO_3)–hematite (Fe_2O_3) endmembers. Fields for kimberlitic ilmenites and basic rocks are from Mitchell (1977), the shaded areas correspond to Morishita et al. (2004) in dark grey and Lorand and Gregoire (2010) in light grey.

rims, orthopyroxene REE patterns (Fig. 12d) show strong REE fractionation, with a positive slope from LREE to HREE with negative Eu anomalies, but concentrations are one order of magnitude higher and the Eu negative anomaly is stronger.

Ilmenite trace element patterns (Fig. 12e) show positive anomalies in Nb and Ta and strong negative anomalies in Ni. Apatite shows REE patterns with a negative slope from LREE to HREE and slight Eu negative anomalies (Fig. 12f). The main substitution of Ca in the apatite structure is by Y and REE ($\text{REE} + \text{Y} = 161\text{--}405$ ppm).

Zircon shows very low U (up to 54 ppm), Pb (up to 5 ppm), and Th contents (up to 6 ppm) (Supplementary material 12). Its crystallization temperature has been estimated using the Ti-in-zircon thermometer (Ferry and Watson, 2007; Watson et al., 2006), but due to the intimate intergrowth of zircon and ilmenite, the Ti content in nominally clean zircon reaches high values (>4320 ppm) thus resulting in extremely high apparent crystallization temperatures that are not reasonable. The analyzed zircon grains have very pronounced Ce/Ce* (25–218) and the chondrite-normalized REE patterns (Fig. 12g) show a positive steep slope from LREE to HREE with positive Ce and negative Eu anomalies. The chondrite-normalized REE patterns of zirconolite show positive slopes from LREE to MREE and flat segments from MREE to HREE (Fig. 12h) with negative Eu anomalies.

4.4. U/Pb dating

Zircon grains forming coronas around ilmenite crystals are extremely depleted in U and Pb, especially in Pb^{207} , making it difficult to obtain a reliable date. The analyses yielded an average age ($n = 43$) of 369 ± 24 Ma and a secondary cluster at 57 ± 17 Ma. On the other hand, analyses on 7 baddeleyite grains yielded one concordant age and 6 discordant but equivalent ages of 134.4 ± 14 Ma (Appendices 4 and 13).

5. Discussion

5.1. Meaning of the Fe-Ti-Zr minerals in the chromitite: contrasting literature data

We report metasomatic interaction of gabbroic melts with the chromitite located in the MTZ of the Moa-Baracoa ophiolite resulting

in the metasomatism of pre-existing chromitite and the formation of a new exotic assemblage of Fe-Ti-Zr minerals. As noted above, the newly-formed mineral assemblage includes Ti-rich amphibole, Mg-rich ilmenite, Zr oxides, and zircon, and has characteristics that resemble those from SCLM settings, kimberlites, carbonatites or alkaline basalts (e.g., Lorand and Gregoire, 2010). Similar amphibole, usually K-rich, is typical of the MARID (mica-amphibole-rutile-ilmenite-diopside) assemblage in mantle xenoliths from kimberlites (e.g., Dawson and Smith, 1977; Fitzpayne et al., 2018; Grégoire et al., 2002), whereas Mg-rich ilmenite (Fig. 8) is also typical from kimberlites (e.g., Xu et al., 2018). Mg-ilmenite compositions have also been described in megacrysts in alkaline basalts from Algeria (Leblanc et al., 1982), in zirconolite-bearing ultrapotassic veins in mantle xenoliths from the Mt. Melbourne volcanic field in Antarctica (Hornig and Wörner, 1991), in some metasomatized peridotite xenoliths and peridotite massifs (Bodinier et al., 1996; Ionov et al., 1999), as well as in the amphibole-rich veins in the Lherz Massif (Lorand and Gregoire, 2010). The studied ilmenite in Potosí contains particularly low trivalent iron and is devoid of hematite exsolution, with compositions very similar to the ilmenite found in the amphibole veins of the Lherz Massif (Lorand and Gregoire, 2010) both in major (Fig. 8) and trace elements (Fig. 12e). In addition, the chromite trace elements (Fig. 12a) show similarities with accessory chromite from kimberlites and picrites (Yao, 1999).

Zirconolite is a frequent mineral in carbonatites, kimberlites, ultrapotassic metasomatic veins, skarns, as well as many others rock-forming settings (e.g., Williams and Gieré, 1996; Fig. 10). However, the only known occurrence of zirconolite in chromitite is in the Finero SCLM peridotites (Zaccarini et al., 2004). Most zirconolite reported in the literature cluster in a similar compositional field (Fig. 10), but the Potosí zirconolite plots close to zirconolite from potassic lavas (De Hoog and Van Bergen, 2000) and lunar basalts (Rasmussen et al., 2008; Williams and Gieré, 1996). Actually, the Potosí zirconolite contains the highest Y_2O_3 content described to date in terrestrial zirconolite (up to 11.06 wt.% Y_2O_3) and the REE contents are also high (up to 10.7 wt.% REE_2O_3), only comparable with contents in zirconolite from lunar basalts (Rasmussen et al., 2008; Williams and Gieré, 1996). The studied zirconolite contains low amounts of actinides (U, Th) strongly differing from the Finero chromitites' zirconolite (Zaccarini et al., 2004).

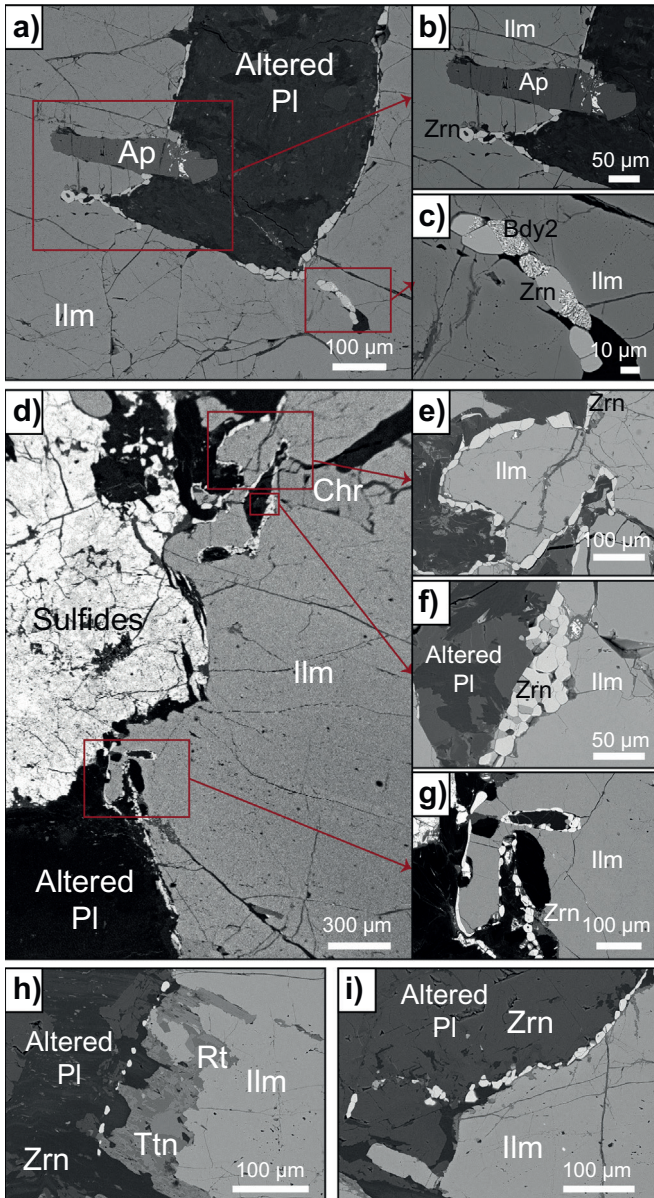


Fig. 9. Backscattered electron images of: (a) Zircon corona around ilmenite in contact with altered plagioclase. Ilmenite hosts a large apatite crystal; (b) Zoom of (a) showing a detail of the apatite crystal including Cu sulfides, and the zircon corona; (c) Second zoom of (a) showing alteration of granular zircon to secondary baddeleyite mixed with silicates; (d) Large ilmenite crystal with zircon coronas along the ilmenite borders in contact with altered silicates. Note that in the region where ilmenite is in contact with sulfides, zircons are not present; (e) Zoom of (d) showing details of zircon grains surrounding ilmenite. Note the elongated shape of zircons; (f) Second zoom of (d) showing the granular texture of zircons forming the coronas. Note the presence of interstitial ilmenite grains within these of zircons and that zircon grains are in contact with altered plagioclase; (g) Third zoom of (d) showing detail of the zircon rims; (h) Ilmenite altered to rutile and titanite. The zircon corona around the primary ilmenite crystal remains immobile and unaltered during ilmenite replacement; and (i) Zircon corona around ilmenite defines ilmenite grain boundaries previous to alteration. Abbreviations: Ap – apatite, Pl – plagioclase, Ilm – ilmenite, Zrn – zircon, Bdy2 – secondary baddeleyite, Chr – chromite, Rt – rutile, Ttn – titanite.

It is a great challenge to reconcile the different settings that this complex mineral assemblage may suggest, including SCLM, kimberlites, carbonatites, alkaline basalts, and those of lunar origin, in the suprasubduction zone ophiolite setting of Moa-Baracoa. In this context, it is essential to consider a simple integrated model that can be conceptualized in a suboceanic mantle setting, as described hereafter.

5.2. Formation of the HFSE-bearing assemblage

The clinopyroxene cores crystallized at an early stage and show trace element compositions (Fig. 12c; Supplementary material 12) similar to those from gabbros sampled from the Mid-Atlantic Ridge (e.g., Coogan et al., 2000). This was followed by the crystallization of plagioclase (that caused depletion in Eu) and the crystallization of the clinopyroxene REE-enriched rims (Fig. 12c) and the orthopyroxene (cf. Bodinier et al., 2008; Drouin et al., 2009; Meyer et al., 1989). During the process, the evolving liquid exsolved a sulfide liquid (Fig. 4d, 11), while relict olivine from the chromitite protolith changed their composition (Fo < 90; Supplementary material 5), chromite recrystallized (Fig. 5; Cr# = 0.57–0.70, Fe³⁺# = 0.10–0.30, and Mg# = 0.31–0.53), and the HFSE-bearing mineral phases (explained hereafter) crystallized.

5.2.1. Ti-rich amphibole

The chemical composition of amphibole (Fig. 6; Supplementary material 5), characterized by high Ti, relatively high F, and low Cl contents indicates a magmatic origin (Coogan et al., 2001; Vanko and Stakes, 1991), though it is texturally late (coronas around plagioclase and clinopyroxene, Fig. 4a, e, and larger interstitial crystals, Fig. 4f, g). Similar compositions are found in oceanic environments, such as gabbros recovered from the Mid Atlantic Ridge (e.g., Coogan et al., 2000, 2001; Cortesogno et al., 2000; Gillis et al., 1993; Koepke et al., 2005) and in olivine-bearing gabbros from the Northern Italy ophiolites (e.g., Tribuzio et al., 1995, 2000, 2014), interpreted as the result of interaction at high temperature with percolating H₂O-rich igneous agents (e.g., Tribuzio et al., 2000). However, these differ with the compositions of amphibole from oceanic veins (compilation by Pilet et al., 2011).

Ti-rich amphibole in oceanic rocks is also typical of low-pressure (< 4 kbar) high temperature (ca. 700–800 °C) ocean floor metamorphism of mafic rocks, as recorded in tectonic blocks of amphibolite (former fore-arc basaltic dykes intruding residual peridotites) from serpentinite mélanges of eastern Cuba (Lázaro et al., 2016). However, amphibole formed during oceanic metamorphism is typically characterized by a high-Cl content (e.g., Currin et al., 2018; Gillis et al., 1993; Gillis and Meyer, 2001; Gillis and Thompson, 1993; Pertsev et al., 2015; Prichard and Cann, 1982; Vanko, 1986), yet the Cl content of the studied amphiboles is low (<0.05 wt.% Cl, <0.016 Cl per 23 O in the amphibole formula), thus dismissing a hydrothermal/metamorphic alteration at the oceanic stage. Furthermore, even if the temperature conditions of formation of Ti-rich amphibole in the studied case cannot be accurately established due to the open-system behavior during metasomatism and the lack of thermodynamic equilibrium in the studied assemblage, the Ti-Al-calcic amphibole thermobarometer of Ernst and Liu (1998) for rutile/titanite/ilmenite-saturated MORB rocks point to magmatic conditions for amphibole formation (ca. 1075 °C, 1 kbar; ca. 925 °C at 5 kbar). Fractional crystallization of a Ti-rich evolved crystallizing/reacting metasomatic melt can satisfactorily explain the enrichment in HREE of amphibole (Fig. 12b; Coogan et al., 2000). On the other hand, the trace-element composition of studied amphibole plots in the suprasubduction environment (Fig. 13; Coltorti et al., 2007), in agreement with the geodynamic position of the studied ophiolitic chromitites in a back-arc position (Proenza et al., 1999b).

5.2.2. Mg-rich ilmenite

Ilmenite probably crystallized during or just right after the formation of amphibole as a result of Fe-Ti saturation of the melt, as indicated by the textural positions of recrystallized chromite, ilmenite, and Ti-rich amphibole. Even though Mg-rich ilmenite is scarce in basaltic rocks of the oceanic lithosphere, it has been observed in srilankite-bearing gabbroic veins that crosscut oceanic peridotites (Morishita et al., 2004).

Since ilmenite appears on the liquidus of strongly fractionated high Fe-Ti melts (Clague et al., 1981; Dick et al., 2000; Juster et al., 1989; Morishita et al., 2004 and references therein), extreme differentiation of a percolating MORB-type melt during its ascent within the

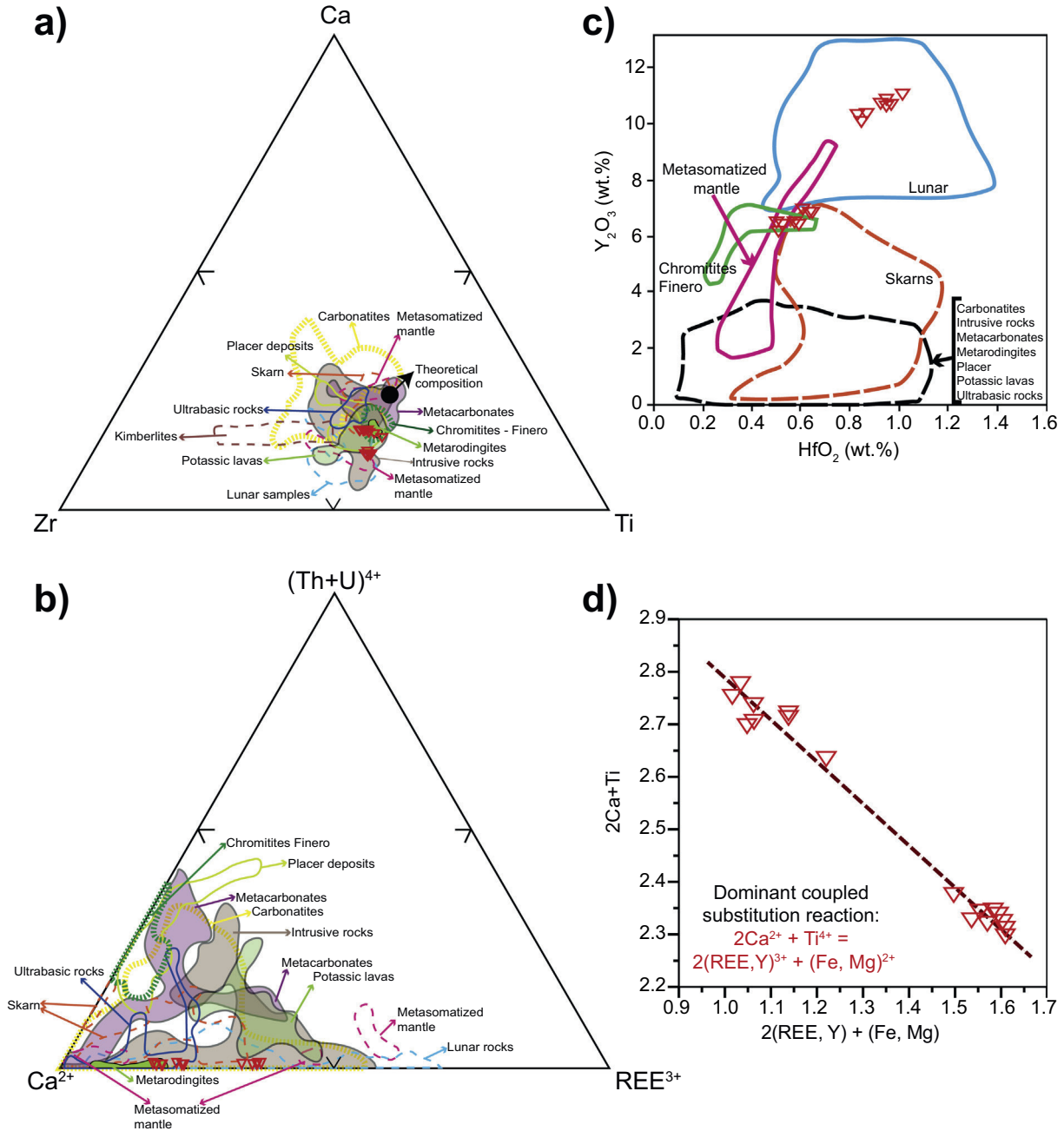


Fig. 10. (a) Ca-Zr-Ti (atom %) diagram of Potosí zirconolites. The reference compositional fields include data from carbonatites (Amores-Casals et al., 2019; Bulakh et al., 1999; Della Ventura et al., 2000; Hurai et al., 2017a, 2017b; Kovalchuk and Shumilova, 2014; Williams and Gieré, 1996), chromitites (Zaccarini et al., 2004), metarodigites (Stucki et al., 2001), intrusive rocks (Bellatreccia et al., 2002; Santos et al., 2015; Williams and Gieré, 1996), kimberlites (Williams and Gieré, 1996), lunar samples (Rasmussen et al., 2008; Williams and Gieré, 1996), metacarbonates (Williams and Gieré, 1996), metasomatized mantle (Della Ventura et al., 2000; Williams and Gieré, 1996), placer deposits (Williams and Gieré, 1996), potassic lavas (De Hoog and van Bergen, 2000; Carlier and Lorand, 2003, 2008), skarns (Pascal et al., 2009; Williams and Gieré, 1996), and ultramafic complexes (Azzone et al., 2009; Williams and Gieré, 1996); (b) Ca²⁺-(Th+U)⁴⁺-REE³⁺ (atom %) diagram of Potosí zirconolites. The reference compositional fields include the same data as (a); (c) Variation of Y₂O₃ (wt.%) versus HfO₂ (wt.%) in the Potosí zirconolites. The reference fields include the same data as (a); (d) Dominant coupled substitution reaction in the Potosí zirconolite. The diagram shows variation of [2Ca+Ti] versus [2(REE+Y)+(Fe+Mg)].

uppermost mantle may be needed (c.f., Morishita et al., 2004). However, Mg-rich ilmenite cannot simply form by fractional crystallization of basaltic liquid, because Mg and Ti have opposite behaviors during this process. Following Lorand and Gregoire (2010), the interaction of an evolved (Fe-) Ti-rich melt with host Ol-bearing chromitite is necessary to explain the observed decrease in Mg in metasomatized/recrystallized chromite and olivine and the corresponding increase in Mg in the crystallizing melt. Furthermore, the preferential uptake of Zr (and Hf) by Ti-rich amphibole (e.g., Tiepolo et al., 2001) causes enrichment in Nb (and Ta) in the residual melt, explaining the positive anomalies in Nb and Ta of

the Potosí ilmenites that crystallized during or shortly after precipitation of Ti-rich amphibole.

5.2.3. Apatite

An increase in P content during the magmatic/metasomatic evolution of the differentiated gabbroic melt explains crystallization of apatite in contact with, or as inclusions within, ilmenite. The Cl content in apatite is within the range of normal apatite from gabbros (Zhang et al., 2017), while the F-rich component of the Potosí apatite indicates magmatic crystallization from an igneous silicate melt (O'Reilly and

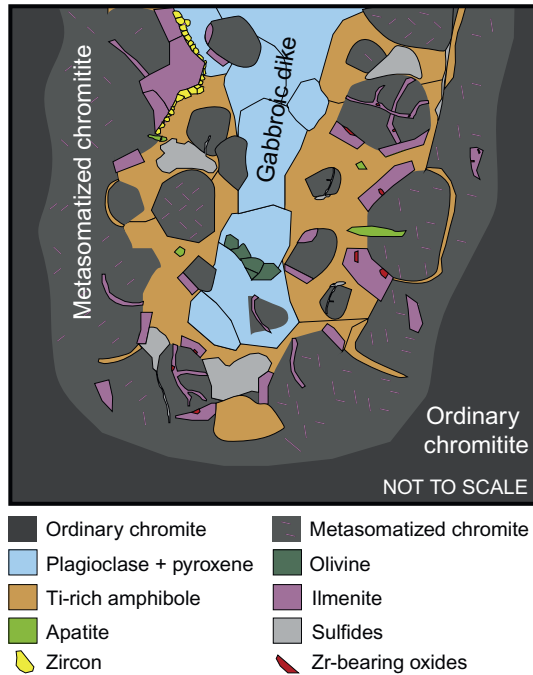


Fig. 11. Schematic relations between the observed mineral assemblage in the metasomatized chromitite, located at the interaction zone between the gabbroic dikes and the ordinary chromitite.

Griffin, 2000), strengthening the idea that seawater-derived fluids did not participate in the metasomatic process of the Potosí chromitite. However, the trace elements in apatite are one order of magnitude depleted compared to typical MORB apatite (Mao et al., 2016) and ophiolitic Fe-gabbro apatite (Tribuzio et al., 2000), indicating a late formation of this mineral in the metasomatic process.

5.2.4. Zr minerals

5.2.4.1. Zr oxides: zirconolite, baddeleyite, and srilankite. The observed textures, with simple and multiple (e.g., baddeleyite and zirconolite or baddeleyite and srilankite; Fig. 7) Zr oxides located within and adjacent to crystal borders of ilmenite hosted within large chromite grains (up to 5 mm), suggest exsolution of Zr oxides from ilmenite (Fig. 7). Direct exchange of Zr^{4+} for Ti^{4+} is possible within the structure of ilmenite (Fujimaki et al., 1984; Jang and Naslund, 2003; McCallum and Charette, 1978; McKay et al., 1986; Morisset and Scoates, 2008; Nakamura et al., 1986; Taylor and McCallister, 1972). Though the amount of Zr in ilmenite is very low (up to 79 ppm; Supplementary material 12), we consider that the exsolution explains the textural relations of Zr oxides, as for similar baddeleyite lamellae/blebs occurring within ilmenite from layered intrusions (Barkov et al., 1995; Heaman and LeCheminant, 1993; Naslund, 1987) and mafic granulite/amphibolite (Bingen et al., 2001). A simultaneous oxidation process, as proposed by Naslund (1987) and Bingen et al. (2001), is not evident in Potosí as far as Mg-ilmenite contains a limited amount of trivalent Fe and lacks hematite exsolutions. A second generation of sheet-like baddeleyite, together with Mg-Al silicates, crystallized after zircon in Potosí (Fig. 9c). Similar textures were reported by Morisset and Scoates (2008), where baddeleyite forms along sealed fractures within zircon and at zircon grain rims. Zirconolite and srilankite likely formed by an exsolution mechanism similar to baddeleyite however it depended on the availability of Ca and REE, which was provided by the evolved melt and/or apatite that also formed in contact with ilmenite. Thus, zirconolite would concentrate incompatible REE+Y of the late magmatic liquids/fluids.

5.2.4.2. Zircon. In many Fe-Ti oxide gabbros, zircon formed from volumetrically small, late-stage, fractionated, Zr-enriched interstitial melt pockets (Scoates and Chamberlain, 1995; Grimes et al., 2009; Beckman et al., 2017; but see also Pietranik et al., 2017, and references therein, for formation of zircon slightly above the wet basaltic solidus after fluid-fluxed partial melting of oceanic gabbros). Zircon occurs in Cuban ophiolitic gabbros and chromitites as magmatic (neofomed) and xenocrystic grains inherited from subducted sedimentary rocks (Proenza et al., 2018; Rojas-Agramonte et al., 2016). However, the studied zircon grains in Potosí are clearly not magmatic s.s. nor xenocrystic, but rather formed *in situ* during metasomatic interaction of chromitite with gabbroic melts, as indicated by textural relations.

Zircon coronas around ilmenite suggest high temperature Zr diffusion in ilmenite (exsolution) and subsequent reaction along grain boundaries under supersolidus to subsolidus conditions following ilmenite crystallization (Morisset and Scoates, 2008). As indicated above, Zr is highly compatible within the ilmenite structure and this mineral is usually considered as one potential source of Zr for zircon formation (Bea et al., 2006; Charlier et al., 2007; Morisset and Scoates, 2008; Sláma et al., 2007). Morisset and Scoates (2008) demonstrated that a reasonable concentration of Zr in ilmenite (345–568 ppm Zr initial concentration) accounts for the observed amount of zircon formed at the rims of ilmenite in mafic plutonic rocks of Proterozoic anorthosite suites. Furthermore, the studied zircon crystals have very low U and Pb contents, consistent with derivation from ilmenite (Morisset and Scoates, 2008; Zack and Brumm, 1998). Formation of zircon after baddeleyite exsolutions in the presence of silica, as proposed by Beckman et al. (2017), cannot be considered here because the observed relationship involves secondary growth of baddeleyite after replacement of granular zircon grains, and the presence of ilmenite interstitial to the granular zircon grains of the coronas is consistent with direct formation of zircon after ilmenite. In this process, silica would be provided by the adjacent silicates and/or the residual melt.

A metamorphic origin for zircon after high-pressure and/or temperature reactions (e.g., Austrheim et al., 2008; Beckman et al., 2014, 2017; Bingen et al., 2001; Kovaleva and Klötzli, 2017; Söderlund et al., 2004) is not considered here due to the lack of evidence for solid-state metamorphic transformation in the studied rocks. Likewise, a hydrothermal origin, similar to the zircons hosted in sealed fractures within chromitites introduced via a network of high-T fluids emanating from gabbroic dikes (Kapsiotis et al., 2016), is also discarded because of the low HfO_2 content of the Potosí zircons (<1.54 wt.%; Supplementary material 11) and the HREE enrichment relative to LREE (Fig. 12g). Hydrothermal zircon usually has high HfO_2 content (3.4 to 4.9 wt.%) (Hoskin and Schaltegger, 2003), high U (550–13,000 ppm) and Th (450–6,000 ppm) (Belousova et al., 2002), and relatively flat chondrite-normalized REE patterns (Hoskin, 2005).

5.3. Fractional crystallization and interaction of evolved melts with chromitite

In the Moa-Baracoa ophiolite, Marchesi et al. (2007) demonstrated that the primitive lower crust layered gabbros and pegmatitic gabbros have similar Sr and Nd isotopic signatures and derived from a common isotopic DMM source, which is similar to that of the Potosí pegmatitic gabbros (in POT-1 sample; $^{87}Sr/^{86}Sr = 0.702581$ and $^{143}Nd/^{144}Nd = 0.513128$; unpublished data). It is then conceivable that the Potosí pegmatitic gabbro dikes formed from derivative liquids after the crystal fractionation of primitive MORB similar to those that built the Moa-Baracoa lower oceanic crust and the more primitive olivine gabbro dikes intruding Potosí chromitites. Like oceanic Fe-Ti gabbros in slow-spreading mid-ocean ridges (Chen et al., 2019; Dick et al., 2000), Potosí gabbros have an assemblage composed of clinopyroxene and plagioclase – with multiple oxide inclusions – that is distinctive of gabbroic rocks derived from MOR-like basaltic melts (with BABB-like trace element signature, Fig. 3). Under the quartz-fayalite-magnetite oxygen

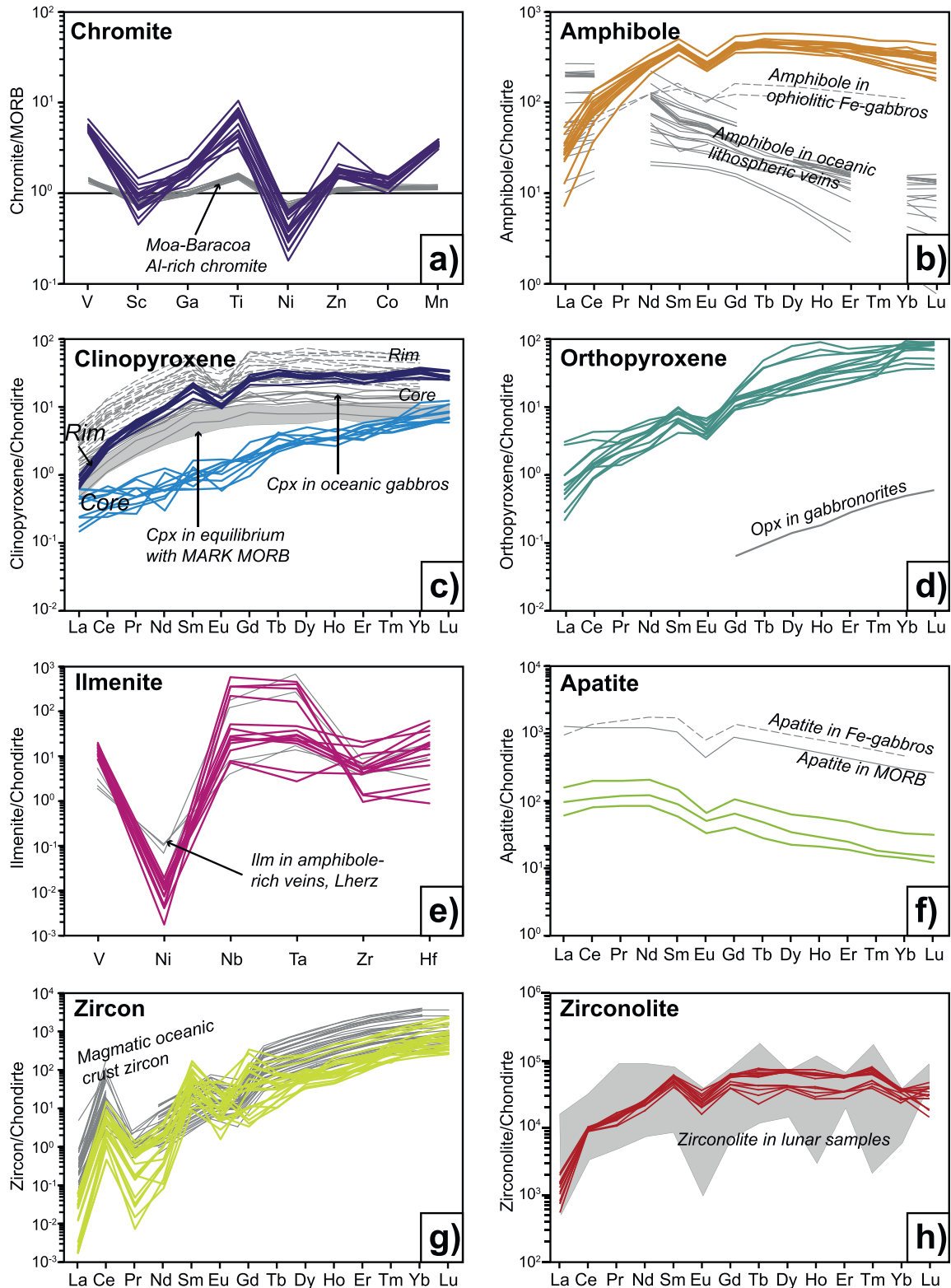


Fig. 12. (a) Chromite trace elements normalized to accessory MORB chromite (Pagé and Barnes, 2009). The regional Moa-Baracoa Al-rich chromite data is from Colás et al. (2014); (b) Amphibole REE normalized to chondrite C1 (Sun and McDonough, 1989). Amphibole in ophiolitic Fe-gabbros is from Tribuzio et al. (2000) and amphibole in oceanic lithosphere veins is a compilation by Pilet et al. (2011); (c) Clinopyroxene REE normalized to chondrite C1. Note the different patterns in the core and rim of clinopyroxene. Clinopyroxene in oceanic gabbros is from Coogan et al. (2000) and clinopyroxene in equilibrium with MARK MORB is from Reynolds and Langmuir (1997); (d) Orthopyroxene REE normalized to chondrite C1. Orthopyroxene in gabbro-norites is from Secchiari et al. (2018); (e) Ilmenite trace elements normalized to chondrite C1. Mg-rich ilmenites in amphibole-rich veins from Lherz are from Lorand and Gregoire (2010); (f) Apatite REE normalized to chondrite C1. Apatite in ophiolitic Fe-gabbros is from Tribuzio et al. (2000) and apatite in MORB is from Mao et al. (2016); (g) Zircon REE normalized to chondrite C1. Magmatic oceanic crust zircons are from Grimes et al. (2009); and (h) Zirconolite REE normalized to chondrite C1. Lunar zirconolite is from Williams and Gieré (1996) and Rasmussen et al. (2008).

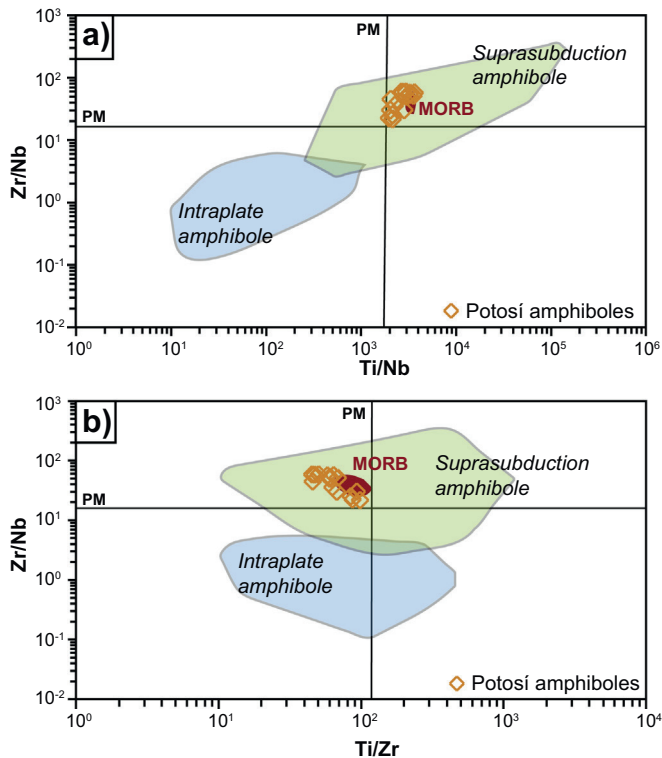


Fig. 13. Classification diagrams of amphiboles: (a) Zr/Nb vs Ti/Nb; and (b) Zr/Nb vs Ti/Zr. Fields for intraplate and suprasubduction amphiboles are from Coltorti et al. (2007).

buffer condition, primitive MORB crystallizes olivine, clinopyroxene, plagioclase and, upon further cooling below c. 1100 °C, Fe-Ti oxides forming oxide gabbros (e.g. Chen et al., 2019), in agreement with the mineral assemblage observed in Potosí gabbro dikes. The low anorthite content of plagioclase (An_{51-56} ; Supplementary material 5) and a rather high Mg# (85–90 mol.%) of Potosí pegmatitic gabbros are consistent with crystallization from a rather anhydrous (<0.5 wt.%) evolved MORB melt for a liquidus temperature of c. 1100 °C (Berndt et al., 2004; Feig et al., 2006). However, their high contents in REE and incompatible trace elements (Fig. 12, Supplementary material 12), their unfractionated trace element patterns and the strong enrichments in trace elements in the rims of high-Mg# clinopyroxene cannot solely be accounted by crystal fractionation. These geochemical features are symptomatic of post cumulus fractionation of melts in a solidifying crystal-melt mush and entrapment of residual evolved melts upon cooling (e.g. Bédard, 1994; Bodinier et al., 1986; Borghini and Rampone, 2007; Garrido et al., 2006; Langmuir, 1989). This trapped melt mechanism is well documented in continental igneous layered intrusions (Cawthorn and Tegner, 2017; Ibanez-Mejia and Tissot, 2019). In this process, the residual melts are progressively and effectively isolated from early cumulus minerals due to physical or kinetic barriers and evolve via intercumulus fractional crystallization upon cooling. Borghini and Rampone (2007) successfully modeled trace element enrichment in MORB-type primitive olivine-rich cumulates from the Erro-Tobio mantle peridotite by small-scale migration of residual evolved melt by crystal fractionation and entrapment of low fractions (5–10%). The resulting melts are enriched in REE, Ti and Zr accounting for the occurrence of accessory interstitial Ti-amphibole and Fe-Ti oxide cumulates without requiring an exotic REE- and HFSE-rich melt (Borghini and Rampone, 2007).

Proenza et al. (2001) proposed that the intrusion of gabbroic dikes into chromitites triggered the crystallization of sulfide-rich chromite ores. Here, we propose a two-stage model for the genesis of metasomatic REE- and HFSE-rich melt in Potosí chromitites. In a first stage,

crystallization of evolved MORB in a crystallizing mush produced via intercumulus fractional crystallization water-rich residual melts strongly enriched in incompatible elements. In a second stage, batches of these evolved melts escaped the solidifying mush and extensively reacted and metasomatized the surrounding chromitites, crystallizing HFSE- and REE-bearing minerals and Fe-Cu-Ni sulfides. We envisage that this process occurred in a solidifying mush in dike intrusions –in a nearly closed system or with low rate of magma supply– at near solidus conditions in the conductive oceanic mantle lithosphere, allowing melts to stagnate, slowly cool and differentiate, and the residual melts to leak and react with the surrounding chromitites and peridotites (e.g. Morishita et al., 2004).

During crystallization in the crystal mush, residual melt fractions produced via an inter-cumulus fractional crystallization were progressively enriched in FeO, TiO₂, HFSE, and H₂O, promoting crystallization of HFSE- and REE-bearing minerals and, upon sulfide liquid immiscibility, the Fe-Cu-Ni sulfide assemblage described by Proenza et al. (2001). To yield residual melts with enough H₂O (2–6 wt.%) to stabilize amphibole after a primitive MORB composition (0.10–0.20 wt.% of H₂O) requires over 90% fractional crystallization driven by anhydrous mineral fractionation up to near solidus conditions (Gillis and Meyer, 2001; Tribuzio et al., 2000). This substantial degree of fractionation generated via intercumulus fractional crystallization generated near-solidus water-rich buoyant silicic melt fractions that were strongly enriched in Zr and other HFSE until the onset of zircon and baddeleyite saturation (<900 °C for melts with H₂O >2 wt.%; Ibanez-Mejia and Tissot, 2019). These residual melts percolated the crystallizing mush and were progressively trapped leading to the strong whole-rock trace element enrichments of the Potosí pegmatitic gabbro dikes.

Locally, batches of these HFSE-enriched residual melts escaped the crystallizing mush and tapped into the surrounding chromitites. These water-rich siliceous residual melts were in strong disequilibrium with the surrounding chromitites, leading to extensive reaction with chromitites and metasomatism, and to the rapid consumption of the melts via melt-consuming melt-rock reactions. The substantial compositional variations in the studied minerals, especially in ilmenite, and the heterogeneous distribution of the accessory Zr-bearing minerals indicates strong local heterogeneities in SiO₂, MgO, and HFSE, which is compatible with a kinetically-inhibited restricted system that evolved by rapid melt-rock reactions at decreasing melt mass. During this stage, Zr-bearing minerals (baddeleyite, zirconolite, srilankite) may have formed by exsolution after Zr-rich ilmenite, forming zircon coronas and likely involving residual silica-rich melt/fluids at temperatures below the zircon saturation. These HFSE-rich residual melt that formed the particular mineral assemblage of the Potosí metasomatized chromitites derives from a BABB-like melt (MORB-like melt) in a suprasubduction environment (Marchesi et al., 2006, 2007; Proenza et al., 2001).

The U/Pb age of baddeleyite is indicative of the age of the metasomatic event (134.4 ± 14 Ma) that was coeval with the oceanic stage in back-arc suprasubduction settings. Similar ages were reported in igneous zircon grains from a Fe-Ti-rich gabbro intruding the mantle peridotite section of the Moa-Baracoa massif (124 ± 1 Ma; Rojas-Agramonte et al., 2016) and two zircons recovered from the Potosí ordinary chromitite (99 ± 21 Ma and 118 ± 8 Ma, Proenza et al., 2018). The metasomatic event is hence consistent with magmatism related to ophiolite construction, generally considered to have taken place at 90–125 Ma (Iturralde-Vinent, 1996; Iturralde-Vinent et al., 2006).

6. Concluding remarks

The interaction between chromitites and gabbroic intrusions in Potosí (eastern Cuba ophiolite) triggered the formation of a particular HFSE-mineral assemblage including Ti-rich amphibole, Mg-rich ilmenite with inclusions of Zr oxides, such as baddeleyite, zirconolite and srilankite, and zircon coronas surrounding ilmenite grains. These

mineral phases related to the metasomatized chromitite are also REE-rich. We propose a two-stage model for the formation of the HFSE- and REE-bearing minerals in the Potosí metasomatized chromitites: (1) crystallization of evolved MORB-like melt (BABB-like melt in a suprasubduction environment) in a crystallizing mush, producing water-rich residual melts enriched in incompatible elements via intercumulus fractional crystallization; (2) reaction of batches of the evolved residual melts that escaped the solidifying mush, with the surrounding chromitites, giving place to the observed metasomatism and the formation of HFSE- and REE-bearing minerals and Fe-Cu-Ni sulfides. This process likely occurred near solidus conditions in a nearly closed system (or with a low rate magma supply), which allowed the melts to stagnate, slowly cool, differentiate, and react with the surrounding chromitites. The age of the metasomatic event is 134.4 ± 14 Ma, coeval with the magmatism related to ophiolite construction in eastern Cuba.

Declaration of Competing Interest

The authors declare that they have no known competing financial interests or personal relationships that could have appeared to influence the work reported in this paper.

Acknowledgments

This research was financially supported by the Spanish Project CGL2015-65824 granted by the Spanish “Ministerio de Economía y Competitividad” to J.A.P., the project RTI2018-099157-A-I00 granted by the “Ministerio de Ciencia, Innovación y Universidades”, the Ramón y Cajal Fellowship RYC-2015-17596 to J.M.G.-J., a FPU Ph.D. grant to N.P.-S. by the “Ministerio de Educación” of the Spanish Government, and received support for analyses at CIC from the University of Granada. Reviewers Michel Grégoire and Valentin Basch, and *Lithos* editor Marco Scambelluri are deeply acknowledged for their constructive criticism that has helped to greatly improve the quality of the present manuscript.

Appendix A. Supplementary data

Supplementary data to this article can be found online at <https://doi.org/10.1016/j.lithos.2020.105420>.

References

- Akizawa, N., Miyake, A., Ishikawa, A., Tamura, A., Terada, Y., Uesugi, K., Takeuchi, A., Arai, S., Tanaka, C., Igami, Y., Suzuki, K., Kogiso, T., 2017. Metasomatic PGE mobilization by carbonatitic melt in the mantle: evidence from sub- μm -scale sulphidecarbonaceous glass inclusions in Tahitian harzburgite xenolith. *Chem. Geol.* 475, 87–104. <https://doi.org/10.1016/j.chemgeo.2017.10.037>.
- Amores-Casals, S., Melgarejo, J.C., Bambi, A., Gonçalves, A.O., Morais, E.A., Manuel, J., Buta Neto, A., Costanzo, A., Martí Molist, J., 2019. Lamprophyre-carbonatite magma mingling and subsolidus processes as key controls on critical element concentration in carbonatites—The Bonga Complex (Angola). *Minerals* 9 (10), 601. <https://doi.org/10.3390/min9100601>.
- Arai, S., Miura, M., 2016. Formation and modification of chromitites in the mantle. *Lithos* 264, 277–295. <https://doi.org/10.1016/j.lithos.2016.08.039>.
- Austrheim, H., Putnis, C.V., Engvik, A.K., Putnis, A., 2008. Zircon coronas around Fe-Ti oxides: a physical reference frame for metamorphic and metasomatic reactions. *Contrib. Mineral. Petrol.* 156 (4), 517–527. <https://doi.org/10.1007/s00410-008-0299-8>.
- Azzone, R.G., Ruberti, E., Enrich, G.E., Gomes, C.B., 2009. Zr- and Ba-rich minerals from the Ponte Nova alkaline mafic-ultramafic massif, southeastern Brazil: indication of an enriched mantle source. *Can. Mineral.* 47 (5), 1087–1103. <https://doi.org/10.3749/canmin.47.5.1087>.
- Barkov, A.Y., Pakhomovskii, Y.A., Men'shikov, Y.P., 1995. Baddeleyite: new occurrences from two mafic-ultramafic layered intrusions, Russia. *Mineral. Mag.* 59 (2), 349–353. <https://doi.org/10.1180/minmag.1995.059.395.18>.
- Basch, V., Rampone, E., Crispini, L., Ferrando, C., Hedefonse, B., Godard, M., 2019a. Multi-stage reactive formation of troctolites in slow-spreading oceanic lithosphere (Erro-Tobbio, Italy): a combined field and petrochemical study. *J. Petrol.* 60 (5), 873–906. <https://doi.org/10.1093/petrology/egz019>.
- Basch, V., Rampone, E., Borghini, G., Ferrando, C., Zanetti, A., 2019b. Origin of pyroxenites in the oceanic mantle and their implications on the reactive percolation of depleted melts. *Contrib. Mineral. Petrol.* 174 (12), 97. <https://doi.org/10.1007/s00410-019-1640-0>.
- Bea, F., Montero, P.G., Gonzalez-Lodeiro, F., Talavera, C., Molina, J.F., Scarrow, J.H., Whitehouse, M.J., Zinger, T., 2006. Zircon thermometry and U–Pb ion-microprobe dating of the gabbros and associated migmatites of the Variscan Toledo Anatectic Complex, Central Iberia. *J. Geol. Soc.* 163 (5), 847–855. <https://doi.org/10.1144/0016-76492005-143>.
- Beckman, V., Möller, C., Söderlund, U., Corfu, F., Pallon, J., Chamberlain, K.R., 2014. Metamorphic zircon formation at the transition from gabbro to eclogite in Trollheimen-Surnadalen, Norwegian Caledonides. *Geol. Soc.* 390 (1), 403–424. <https://doi.org/10.1144/SP390.26> London, Special Publications.
- Beckman, V., Möller, C., Söderlund, U., Andersson, J., 2017. Zircon growth during progressive recrystallization of Gabbro to Garnet Amphibolite, Eastern segment, Sveconorwegian Orogen. *J. Petrol.* 58 (1), 167–187. <https://doi.org/10.1093/petrology/egx009>.
- Bédard, J.H., 1994. A procedure for calculating the equilibrium distribution of trace elements among the minerals of cumulate rocks, and the concentration of trace elements in the coexisting liquids. *Chem. Geol.* 118 (1–4), 143–153. [https://doi.org/10.1016/0009-2541\(94\)90173-2](https://doi.org/10.1016/0009-2541(94)90173-2).
- Bedini, R.M., Bodinier, J.L., Dautria, J.M., Morten, L., 1997. Evolution of LILE-enriched small melt fractions in the lithospheric mantle: a case study from the East African Rift. *Earth Planet. Sci. Lett.* 153, 67–83. [https://doi.org/10.1016/S0012-821X\(97\)00167-2](https://doi.org/10.1016/S0012-821X(97)00167-2).
- Bellatreccia, F., Ventura, G.D., Williams, C.T., Lumpkin, G.R., Smith, K.L., Colella, M., 2002. Non-metamict zirconolite polytypes from the feldspathoid-bearing alkalisyenitic ejecta of the Vico volcanic complex (Latium, Italy). *Eur. J. Mineral.* 14 (4), 809–820. <https://doi.org/10.1127/0935-1221/2002/0014-0809>.
- Belousova, E., Griffin, W.L., O'Reilly, S.Y., Fisher, N.L., 2002. Igneous zircon: trace element composition as an indicator of source rock type. *Contrib. Mineral. Petrol.* 143 (5), 602–622. <https://doi.org/10.1007/s00410-002-0364-7>.
- Berndt, J., Koepke, J., Holtz, F., 2004. An experimental investigation of the influence of water and oxygen fugacity on differentiation of MORB at 200 MPa. *J. Petrol.* 46, 135–167. <https://doi.org/10.1093/petrology/egh066>.
- Bingen, B., Austrheim, H., Whitehouse, M., 2001. Ilmenite as a source for zirconium during high-grade metamorphism? Textural evidence from the Caledonides of western Norway and implications for zircon geochronology. *J. Petrol.* 42 (2), 355–375. <https://doi.org/10.1093/petrology/42.2.355>.
- Blanco-Quintero, I.F., García-Casco, A., Rojas-Agramonte, Y., Rodríguez-Vega, A., Lázaro, C., Iturralde-Vinent, M.A., 2010. Metamorphic evolution of subducted hot oceanic crust (La Corea Melange, Cuba). *Am. J. Sci.* 310 (9), 889–915. <https://doi.org/10.2475/11.2010.01>.
- Blanco-Quintero, I.F., Rojas-Agramonte, Y., García-Casco, A., Kröner, A., Mertz, D.F., Lázaro, C., Blanco-Moreno, J., Renne, P.R., 2011. Timing of subduction and exhumation in a subduction channel: evidence from slab melts from La Corea mélange (eastern Cuba). *Lithos* 127, 86–100. <https://doi.org/10.1016/j.lithos.2011.08.009>.
- Bodinier, J.L., Godard, M., 2003. Orogenic, ophiolitic, and abyssal peridotites. In: Carlson, R. (Ed.), *Treatise on Geochemistry, 2: Mantle and Core*. Elsevier, Amsterdam, pp. 103–170.
- Bodinier, J.L., Guiraud, M., Dupuy, C., Dostal, J., 1986. Geochemistry of basic dikes in the Lanzo massif (Western Alps): petrogenetic and geodynamic implications. *Tectonophysics* 128, 77–95. [https://doi.org/10.1016/0040-1951\(86\)90309-4](https://doi.org/10.1016/0040-1951(86)90309-4).
- Bodinier, J.L., Vasseur, G., Vernières, J., Dupuy, C., Fabries, J., 1990. Mechanisms of mantle metasomatism: geochemical evidence from the Lherz orogenic peridotite. *J. Petrol.* 31 (3), 597–628. <https://doi.org/10.1093/petrology/31.3.597>.
- Bodinier, J.L., Merlet, C., Bedini, R.M., Simien, F., Remaidi, M., Garrido, C.J., 1996. Distribution of niobium, tantalum, and other highly incompatible trace elements in the lithospheric mantle: the spinel paradox. *Geochim. Cosmochim. Acta* 60, 545–550. doi: 510.1016/0016-7037(1995)00431-00439.
- Bodinier, J.L., Garrido, C.J., Chanefo, I., Bruguier, O., Gervilla, F., 2008. Origin of pyroxenite-peridotite veined mantle by refertilization reactions: evidence from the Ronda peridotite (Southern Spain). *J. Petrol.* 49 (5), 999–1025. <https://doi.org/10.1093/petrology/egn014>.
- Borghini, G., Rampone, E., 2007. Postcumulus processes in oceanic-type olivine-rich cumulates: the role of trapped melt crystallization versus melt/rock interaction. *Contrib. Mineral. Petrol.* 154 (6), 619–633. <https://doi.org/10.1007/s00410-007-0217-5>.
- Bulakh, A.G., Nesterov, A.R., Anastasenko, G.F., Anisimov, I.S., 1999. Crystal morphology and intergrowths of calzirtite $\text{Ca}_2\text{Zr}_5\text{Ti}_2\text{O}_{16}$, zirkelite $(\text{Ti,Ca,Zr})\text{O}_{2-x}$, zirconolite $\text{CaZrTi}_2\text{O}_7$ in phosphorites and carbonatites of the Kola Peninsula (Russia). *Neues Jb. Mineral. Monat.* 1, 11–20.
- Cárdenas-Párraga, J., García-Casco, A., Proenza, J.A., Harlow, G.E., Blanco-Quintero, I.F., Lázaro, C., Villanova-de-Benavent, C., Núñez Cambra, K., 2017. Trace-element geochemistry of transform-fault serpentinite in high-pressure subduction mélanges (eastern Cuba): Implications for subduction initiation. *Int. Geol. Rev.* 59 (16), 2041–2064. <https://doi.org/10.1080/00206814.2017.1308843>.
- Carlier, G., Lorand, J.P., 2003. Petrogenesis of a zirconolite-bearing Mediterranean-type lamproite from the Peruvian Altiplano (Andean Cordillera). *Lithos* 69 (1), 15–35. [https://doi.org/10.1016/S0024-4937\(03\)00045-8](https://doi.org/10.1016/S0024-4937(03)00045-8).
- Carlier, G., Lorand, J.P., 2008. Zr-rich accessory minerals (titanite, perrierite, zirconolite, baddeleyite) record strong oxidation associated with magma mixing in the south Peruvian potassic province. *Lithos* 104 (1–4), 54–70. <https://doi.org/10.1016/j.lithos.2007.11.008>.
- Cawthorn, R.G., Tegner, C., 2017. Modeling incompatible trace-element abundances in plagioclase in the Skaergaard intrusion using the trapped liquid shift effect. *Contrib. Mineral. Petrol.* 172, 93. <https://doi.org/10.1007/s00410-017-1411-8>.
- Charlier, B., Skår, Ø., Korneliussen, A., Duchesne, J.C., Vander Auwera, J., 2007. Ilmenite composition in the Tellnes Fe–Ti deposit, SW Norway: fractional crystallization, postcumulus evolution and ilmenite–zircon relation. *Contrib. Mineral. Petrol.* 154 (2), 119–134. <https://doi.org/10.1007/s00410-007-0186-8>.
- Chen, Y., Niu, Y., Wang, X., Gong, H., Guo, P., Gao, Y., Shen, F., 2019. Petrogenesis of ODP Hole 735B (Leg 176) oceanic plagiogranite: partial melting of gabbro or advanced

- extent of fractional crystallization? *Geochem. Geophys. Geosyst.* 20, 2717–2732. <https://doi.org/10.1029/2019gc008320>.
- Clague, D.A., Frey, F.A., Thompson, G., Rindge, S., 1981. Minor and trace element geochemistry of volcanic rocks dredged from the Galapagos Spreading Center Role of crystal fractionation and mantle heterogeneity. *J. Geophys. Res.* 86, 9469–9482. <https://doi.org/10.1029/JB086iB10p09469>.
- Cobiella-Reguera, J.L., 2005. Emplacement of Cuban ophiolites. *Geol. Acta* 3, 273–294.
- Colás, V., González-Jiménez, J.M., Griffin, W.L., Fanlo, I., Gervilla, F., O'Reilly, S.Y., Pearson, N.J., Kerestédjian, T., Proenza, J.A., 2014. Fingerprints of metamorphism in chromite: new insights from minor and trace elements. *Chem. Geol.* 389, 137–152. <https://doi.org/10.1016/j.chemgeo.2014.10.001>.
- Coltorti, M., Bonadiman, C., Hinton, R.W., Siena, F., Upton, B.G.J., 1999. Carbonatite metasomatism of the oceanic upper mantle: evidence from clinopyroxenes and glasses in ultramafic xenoliths of Grande Comore, Indian Ocean. *J. Petrol.* 40, 303–320. <https://doi.org/10.1093/ptro/40.1.303>.
- Coltorti, M., Beccaluva, L., Bonadiman, C., Salvini, L., Siena, F., 2000. Glasses in mantle xenoliths as geochemical indicators of metasomatic agents. *Earth Planet. Sci. Lett.* 183, 303–320. [https://doi.org/10.1016/S0012-821X\(00\)00274-0](https://doi.org/10.1016/S0012-821X(00)00274-0).
- Coltorti, M., Beccaluva, L., Bonadiman, C., Faccini, B., Ntafos, T., Siena, F., 2004. Amphibole genesis via metasomatic reaction with clinopyroxene in mantle xenoliths from Victoria Land, Antarctica. *Lithos* 75, 115–139. <https://doi.org/10.1016/j.lithos.2003.12.021>.
- Coltorti, M., Bonadiman, C., Faccini, B., Grégoire, M., O'Reilly, S.Y., Powell, W., 2007. Amphiboles from suprasubduction and intraplate lithospheric mantle. *Lithos* 99 (1–2), 68–84. <https://doi.org/10.1016/j.lithos.2007.05.009>.
- Constantin, M., 1999. Gabbroic intrusions and magmatic metasomatism in harzburgites from the Garret transform fault: implications for the nature of the mantle-crust transition at fast-spreading ridges. *Contrib. Mineral. Petrol.* 136 (1–2), 111–130. <https://doi.org/10.1007/s004100050527>.
- Coogan, L.A., Saunders, A.D., Kempton, P.D., Norry, M.J., 2000. Evidence from oceanic gabbros for porous melt migration within a crystal mush beneath the Mid-Atlantic Ridge. *Geochem. Geophys. Geosyst.* 1 (9). <https://doi.org/10.1029/2000GC000072>.
- Coogan, L.A., Wilson, R.N., Gillis, K.M., MacLeod, C.J., 2001. Near-solidus evolution of oceanic gabbros: insights from amphibole geochemistry. *Geochim. Cosmochim. Acta* 65 (23), 4339–4357. [https://doi.org/10.1016/S0016-7037\(01\)00714-1](https://doi.org/10.1016/S0016-7037(01)00714-1).
- Cortesogno, L., Gaggero, L., Zanetti, A., 2000. Rare earth and trace elements in igneous and high-temperature metamorphic minerals of oceanic gabbros (MARK area, Mid-Atlantic Ridge). *Contrib. Mineral. Petrol.* 139 (4), 373–393. <https://doi.org/10.1007/s004100000147>.
- Currin, A., Wolff, P.E., Koepke, J., Almeev, R.R., Zhang, C., Zihlmann, B., Ildefonse, B., Teagle, D.A.H., 2018. Chlorine-rich amphibole in deep layered gabbros as evidence for brine/rock interaction in the lower oceanic crust: A case study from the Wadi Wariyah, Samail Ophiolite, Sultanate of Oman. *Lithos* 323, 125–136. <https://doi.org/10.1016/j.lithos.2018.09.015>.
- Dawson, J.B., 2002. Metasomatism and partial melting in upper-mantle peridotite xenoliths from Lashaine volcano, northern Tanzania. *J. Petrol.* 43, 1749–1777. <https://doi.org/10.1093/ptro/43.9.1749>.
- Dawson, J.B., Smith, J.V., 1977. The MARID (mica-amphibole-rutile-ilmenite-diopside) suite of xenoliths in kimberlite. *Geochim. Cosmochim. Acta* 41 (2), 309–323. [https://doi.org/10.1016/0016-7037\(77\)90239-3](https://doi.org/10.1016/0016-7037(77)90239-3).
- De Hoog, J.C.M., Van Bergen, M.J., 2000. Volatile-induced transport of HFSE, REE, Th and U in arc magmas: evidence from zirconolite-bearing vesicles in potassic lavas of Lewotolo volcano (Indonesia). *Contrib. Mineral. Petrol.* 139, 465–502. <https://doi.org/10.1007/s004100000146>.
- Della Ventura, G., Bellatreccia, F., Williams, C.T., 2000. Zirconolite with significant REE₂Nb(Mn,Fe)O₇ from a xenolith of the Laacher See eruptive center, Eifel volcanic region, Germany. *Can. Mineral.* 38 (1), 57–65.
- Dick, H.J.B., Natland, J.H., Alt, J.C., Bach, W., Bideau, D., Gee, J.S., Haggas, S., Hertogen, J.G.H., Hirth, G., Holm, P.M., Ildefonse, B., Iturrino, G.J., John, B.E., Kelley, D.S., Kikawa, E., Kingdon, A., LeRux, P.J., Maeda, J., Meyer, P.S., Miller, D.J., Naslund, H.R., Niu, Y.-L., Robinson, P.T., Snow, J., Stephen, R.A., Trimby, P.W., Worm, H.-U., Yoshinobu, A., 2000. A long in situ section of the lower ocean crust: results of ODP Leg 176 drilling at the Southwest Indian Ridge. *Earth Planet. Sci. Lett.* 179, 31–51. [https://doi.org/10.1016/S0012-821X\(00\)00102-3](https://doi.org/10.1016/S0012-821X(00)00102-3).
- Drouin, M., Godard, M., Ildefonse, B., Bruguier, O., Garrido, C.J., 2009. Geochemical and petrographic evidence for magmatic impregnation in the oceanic lithosphere at Atlantid Massif, Mid-Atlantic Ridge (IODP Hole U1309D, 30 N). *Chem. Geol.* 264 (1–4), 71–88. <https://doi.org/10.1016/j.chemgeo.2009.02.013>.
- Ernst, W.G., Liu, J., 1998. Experimental phase-equilibrium study of Al- and Ti-contents of calcic amphibole in MORB—A semiquantitative thermobarometer. *Am. Mineral.* 83 (9–10), 952–969. <https://doi.org/10.2138/am-1998-9-1004>.
- Feig, S.T., Koepke, J., Snow, J.E., 2006. Effect of water on tholeiitic basalt phase equilibria: an experimental study under oxidizing conditions. *Contrib. Mineral. Petrol.* 152, 611–638. <https://doi.org/10.1007/s00410-006-0123-2>.
- Ferry, J.M., Watson, E.B., 2007. New thermodynamic models and revised calibrations for the Ti-in-zircon and Zr-in-rutile thermometers. *Contrib. Mineral. Petrol.* 154 (4), 429–437. <https://doi.org/10.1007/s00410-007-0201-0>.
- Fitzpayne, A., Giuliani, A., Hergt, J., Phillips, D., Janney, P., 2018. New geochemical constraints on the origins of MARID and PIC rocks: Implications for mantle metasomatism and mantle-derived potassic magmatism. *Lithos* 318, 478–493. <https://doi.org/10.1016/j.lithos.2018.08.036>.
- Flint, D.E., de Albear, J.F., Guild, P.W., 1948. *Geology and chromite deposits of the Camagüey district, Camagüey Province, Cuba*. US Geol. Surv. Bull. 954-B, 39–63.
- Fujimaki, H., Tatsumoto, M., Aoki, K.I., 1984. Partition coefficients of Hf, Zr, and REE between phenocrysts and groundmasses. *J. Geophys. Res. Solid Earth* 89 (S02), B662–B672. <https://doi.org/10.1029/JB089iS02p0662>.
- García-Casco, A., Torres-Roldán, R.L., Iturralde-Vinent, M.A., Millán, G., Núñez Cambra, K., Lázaro, C., Rodríguez Vega, A., 2006. High pressure metamorphism of ophiolites in Cuba. *Geol. Acta* 4, 63–88. <https://doi.org/10.1344/105.000000358>.
- García-Casco, A., Iturralde-Vinent, M.A., Pindell, J., 2008a. Latest Cretaceous collision/accretion between the Caribbean Plate and Caribbeana: origin of metamorphic terranes in the Greater Antilles. *Int. Geol. Rev.* 50, 781–809. <https://doi.org/10.2747/0020-6814.50.9.781>.
- García-Casco, A., Lázaro, C., Rojas-Agramonte, Y., Kröner, A., Torres Roldán, R.L., Núñez, K., Millán, G., Neubauber, F., Quintero, I., 2008b. Partial melting and counterclockwise P-T path of subducted oceanic crust (Sierra del Convento, E Cuba). *J. Petrol.* 49, 129–161. <https://doi.org/10.1093/ptro/49.1.129>.
- Garrido, C.J., Bodinier, J.-L., Burg, J.-P., Zeilinger, G., Hussain, S.S., Dawood, H., Chaudhry, M.N., Gervilla, F., 2006. Petrogenesis of Mafic Garnet Granulite In The Lower Crust of The Kohistan Paleo-Arc Complex (Northern Pakistan): Implications For Intra-Crustal Differentiation of Island Arcs And Generation of Continental Crust. *J. Petrol.* 47, 1873–1914. <https://doi.org/10.1093/ptro/47.10.1873>.
- Gervilla, F., Proenza, J.A., Frei, R., González-Jiménez, J.M., Garrido, C.J., Melgarejo, J.C., Meibom, A., Díaz-Martínez, R., Lavaut, W., 2005. Distribution of platinum-group elements and Os isotopes in chromite ores from Mayarí-Baracoa Ophiolitic Belt (eastern Cuba). *Contrib. Mineral. Petrol.* 150, 589–607. <https://doi.org/10.1007/s00410-005-0039-2>.
- Gillis, K.M., Meyer, P.S., 2001. Metasomatism of oceanic gabbros by late stage melts and hydrothermal fluids: Evidence from the rare earth element composition of amphiboles. *Geochem. Geophys. Geosyst.* 2 (3). <https://doi.org/10.1029/2000GC000087>.
- Gillis, K.M., Thompson, G., 1993. Metabasalts from the Mid-Atlantic Ridge: new insights into hydrothermal systems in slow-spreading crust. *Contrib. Mineral. Petrol.* 113 (4), 502–523. <https://doi.org/10.1007/BF00698319>.
- Gillis, K.M., Thompson, G., Kelley, D.S., 1993. A view of the lower crustal component of hydrothermal systems at the Mid-Atlantic Ridge. *J. Geophys. Res. Solid Earth* 98 (B11), 19597–19619. <https://doi.org/10.1029/93JB01717>.
- González-Jiménez, J.M., Proenza, J.A., Gervilla, F., Melgarejo, J.C., Blanco-Moreno, J.A., Ruiz-Sánchez, R., Griffin, W.L., 2011. High-Cr and high-Al chromitites from the Sagua de Tanamo district, Mayarí-Cristal Ophiolitic Massif (eastern Cuba): constraints on their origin from mineralogy and geochemistry of chromian spinel and platinum group elements. *Lithos* 125, 101–121. <https://doi.org/10.1016/j.lithos.2011.01.016>.
- González-Jiménez, J.M., Griffin, W.L., Proenza, J.A., Gervilla, F., O'Reilly, S.Y., Akbulut, M., Pearson, N.J., Arai, S., 2014a. Chromitites in ophiolites: how, where, when, why? Part II. The crystallization of chromitites. *Lithos* 189, 140–158. <https://doi.org/10.1016/j.lithos.2013.09.008>.
- González-Jiménez, J.M., Villaseca, C., Griffin, W.L., O'Reilly, S.Y., Belousova, E., Ancochea, E., Pearson, N.J., 2014b. Significance of ancient sulphides PGE and Re-Os signatures in the mantle beneath Calatrava, Central Spain. *Contrib. Mineral. Petrol.* 168, 1047. <https://doi.org/10.1007/s00410-014-1047-x>.
- Govindaraju, K., 1994. Compilation of working values and sample description for 383 geo-standards. *Geostand. Geoanal. Res.* 18, 1–158. <https://doi.org/10.1111/j.1751-908X.1994.tb00502.x>.
- Grégoire, M., Lorand, J.-P., O'Reilly, S.Y., Cottin, J.Y., 2000. Armalcolite-bearing, Ti-rich metasomatic assemblages in harzburgitic xenoliths from the Kerguelen Islands: implications for the oceanic mantle budget of high-field strength elements. *Geochim. Cosmochim. Acta* 64, 673–694. [https://doi.org/10.1016/S0016-7037\(99\)00345-2](https://doi.org/10.1016/S0016-7037(99)00345-2).
- Grégoire, M., Bell, D., Le Roex, A., 2002. Trace element geochemistry of phlogopite-rich mafic mantle xenoliths: their classification and their relationship to phlogopite-bearing peridotites and kimberlites revisited. *Contrib. Mineral. Petrol.* 142 (5), 603–625. <https://doi.org/10.1007/s00410-001-0315-8>.
- Grimes, C.B., John, B.E., Cheadle, M.J., Mazdab, F.K., Wooden, J.L., Swapp, S., Schwartz, J.J., 2009. On the occurrence, trace element geochemistry, and crystallization history of zircon from in situ oceanic lithosphere. *Contrib. Mineral. Petrol.* 158 (6), 757. <https://doi.org/10.1007/s00410-009-0409-2>.
- Guild, P.W., 1947. *Petrology and structure of the Moa Chromite District, Oriente province, Cuba*. Am. Geophys. Union 28, 218–264.
- Hawthorne, F.C., Oberti, R., Harlow, G.E., Maresch, W.V., Martin, R.F., Schumacher, J.C., Welch, M.D., 2012. Nomenclature of the amphibole supergroup. *Am. Mineral.* 97 (11–12), 2031–2048. <https://doi.org/10.2138/am.2012.4276>.
- Heaman, L.M., LeCheminant, A.N., 1993. Paragenesis and U-Pb systematics of baddeleyite (ZrO₂). *Chem. Geol.* 110 (1–3), 95–126. [https://doi.org/10.1016/0009-2541\(93\)90249-1](https://doi.org/10.1016/0009-2541(93)90249-1).
- Hornig, I., Wörner, G., 1991. Zirconolite-bearing ultrapotassic veins in a mantle xenolith from Mt. Melbourne Volcanic Field, Victoria Land, Antarctica. *Contrib. Mineral. Petrol.* 106, 355–366. <https://doi.org/10.1007/BF00324563>.
- Hoskin, P.W., 2005. Trace-element composition of hydrothermal zircon and the alteration of Hadean zircon from the Jack Hills, Australia. *Geochim. Cosmochim. Acta* 69 (3), 637–648. <https://doi.org/10.1016/j.gca.2004.07.006>.
- Hoskin, P.W., Schaltegger, U., 2003. The composition of zircon and igneous and metamorphic petrogenesis. *Rev. Mineral. Geochem.* 53 (1), 27–62. <https://doi.org/10.2113/0530027>.
- Hurai, V., Huraiová, M., Gajdošová, M., Konečný, P., Slobodník, M., Siegfried, P.R., 2017a. Compositional variations of zirconolite from the Evate apatite deposit (Mozambique) as an indicator of magmatic-hydrothermal conditions during post-orogenic collapse of Gondwana. *Mineral. Petrol.* 1–18. <https://doi.org/10.1007/s00110-017-0538-7>.
- Hurai, V., Paquette, J.L., Huraiová, M., Slobodník, M., Hvozd'ara, P., Siegfried, P., Gajdošová, M., Milovská, S., 2017b. New insights into the origin of the Evate apatite-iron oxide-carbonate deposit, Northeastern Mozambique, constrained by mineralogy, textures, thermochronometry, and fluid inclusions. *Ore Geol. Rev.* 80, 1072–1091. <https://doi.org/10.1016/j.oregeorev.2016.09.017>.

- Ibanez-Mejia, M., Tissot, F.L., 2019. Extreme Zr stable isotope fractionation during magmatic fractional crystallization. *Sci. Adv.* 5 (12). <https://doi.org/10.1126/sciadv.aax8648> eaax8648.
- Ionov, D.A., Gregoire, M., Ashchepkov, I., 1999. Feldspar–Ti oxide metasomatism in off-cratonic continental and oceanic upper mantle. *Earth Planet. Sci. Lett.* 165, 37–44. [https://doi.org/10.1016/S0012-821X\(98\)00253-2](https://doi.org/10.1016/S0012-821X(98)00253-2).
- Iturralde-Vinent, M., 1996. Geología de las ofiolitas de Cuba. In: Iturralde-Vinent, M. (Ed.), *Ofiolitas y arcos volcánicos de Cuba: IGCP Project 432, Miami, USA*, pp. 83–120.
- Iturralde-Vinent, M.A., Díaz-Otero, C., Rodríguez-Vega, A., Díaz-Martínez, R., 2006. Tectonic implications of paleontologic dating of Cretaceous-Danian sections of Eastern Cuba. *Geol. Acta* 4, 89–102. <https://doi.org/10.1344/105.000000359>.
- Iturralde-Vinent, M.A., García-Casco, A., Rojas-Agramonte, Y., Proenza, J.A., Murphy, J.B., Stern, R.G., 2016. The geology of Cuba: a brief overview and synthesis. *GSA Today* 26 (10), 4–10. <https://doi.org/10.1130/GSATG296A.1>.
- Jang, Y.D., Naslund, H.R., 2003. Major and trace element variation in ilmenite in the Skaergaard intrusion: petrologic implications. *Chem. Geol.* 193 (1–2), 109–125. [https://doi.org/10.1016/S0009-2541\(02\)00224-3](https://doi.org/10.1016/S0009-2541(02)00224-3).
- Juster, T.C., Grove, T.L., Perfit, M.R., 1989. Experimental constraints on the generation of Fe-Ti basalts, andesites and rhyodacites at the Galapagos Spreading Center, 85°W and 95°W. *J. Geophys. Res.* 94, 9215–9247. <https://doi.org/10.1029/JB094iB07p09251>.
- Kapsiotis, A., Ewing Rassios, A., Antonelou, A., Tzamos, E., 2016. Genesis and multi-episodic alteration of zircon-bearing chromitites from the ayios stefanos mine, othris Massif, Greece: assessment of an unconventional hypothesis on the origin of zircon in ophiolitic chromitites. *Minerals* 6 (4), 124. <https://doi.org/10.3390/min6040124>.
- Kelemen, P.B., Dick, H.J., Quick, J.E., 1992. Formation of harzburgite by pervasive melt/rock reaction in the upper mantle. *Nature* 358 (6388), 635. <https://doi.org/10.1038/358635a0>.
- Kelemen, P.B., Hitehead, J.A., Aharonov, E., Jordahl, K.A., 1995a. Experiments on flow focusing in soluble porous media, with applications to melt extraction from the mantle. *J. Geophys. Res.* 100, 475–496. <https://doi.org/10.1029/94JB02544>.
- Kelemen, P.B., Shimizu, N., Salters, V.J., 1995b. Extraction of mid-ocean-ridge basalt from the upwelling mantle by focused flow of melt in dunite channels. *Nature* 375 (6534), 747. <https://doi.org/10.1038/375747a0>.
- Koepke, J., Feig, S., Snow, J., 2005. Late stage magmatic evolution of oceanic gabbros as a result of hydrous partial melting: evidence from the Ocean Drilling Program (ODP) Leg 153 drilling at the Mid-Atlantic Ridge. *Geochem. Geophys. Res.* 6 (2). <https://doi.org/10.1029/2004GC000805>.
- Kovalchuk, N.S., Shumilova, T.G., 2014. Rare Earth and Zirconium-Niobium mineralization in diamondiferous carbonates of Fuerteventura (Spain). *IG Komi SC UB RAS* 10, 28–34.
- Kovaleva, E., Klötzli, U., 2017. NanoSIMS study of seismically deformed zircon: Evidence of Y, Yb, Ce, and P redistribution and resetting of radiogenic Pb. *Am. Mineral.* 102 (6), 1311–1327. <https://doi.org/10.2138/am-2017-5975>.
- Langmuir, C.H., 1989. Geochemical consequences of in situ crystallization. *Nature* 340, 199–205. <https://doi.org/10.1038/340199a0>.
- Laurora, A., Mazzucchelli, M., Rivalenti, G., Vannucci, R., Zanetti, A., Barbieri, M.A., Cingolani, C., 2001. Metasomatism and melting in carbonated peridotite xenoliths from the mantle wedge: the Gobernador Gregores case (Southern Patagonia). *J. Petrol.* 42, 69–87. <https://doi.org/10.1093/ptrology/42.1.69>.
- Lázaro, C., García-Casco, A., Neubauer, F., Rojas-Agramonte, Y., Kröner, A., Iturralde-Vinent, M.A., 2009. Fifty-five-million-year history of oceanic subduction and exhumation in the northern edge of the Caribbean plate (Sierra del Convento mélange, Cuba). *J. Metamorph. Geol.* 27, 19–40. <https://doi.org/10.1111/j.1525-1314.2008.00800.x>.
- Lázaro, C., Blanco-Quintero, I.F., Rojas-Agramonte, Y., Proenza, J.A., Núñez-Cambra, K., García-Casco, A., 2013. First description of a metamorphic sole related to ophiolite obduction in the northern Caribbean: Geochemistry and petrology of the Güira de Jaico amphibolite complex (eastern Cuba) and tectonic implications. *Lithos* 179, 193–210. <https://doi.org/10.1016/j.lithos.2013.08.019>.
- Lázaro, C., García-Casco, A., Blanco-Quintero, I.F., Rojas-Agramonte, Y., Corsini, M., Proenza, J.A., 2015. Did the Turonian-Coniacian plume pulse trigger subduction initiation in the Northern Caribbean? Constraints from ⁴⁰Ar/³⁹Ar dating of the Moa-Baracoa metamorphic sole (eastern Cuba). *Int. Geol. Rev.* 57 (5–8), 919–942. <https://doi.org/10.1080/00206814.2014.924037>.
- Lázaro, C., Blanco-Quintero, I.F., Proenza, J.A., Rojas-Agramonte, Y., Neubauer, F., Núñez-Cambra, K., García-Casco, A., 2016. Petrogenesis and ⁴⁰Ar/³⁹Ar dating of proforearc crust in the Early Cretaceous Caribbean arc: the La Tinta mélange (eastern Cuba) and its easterly correlation in Hispaniola. *Int. Geol. Rev.* 58 (4), 1020–1040. <https://doi.org/10.1080/00206814.2015.1118647>.
- Le Roux, V., Bodinier, J.L., Tommasi, A., Alard, O., Dautria, J.M., Vauchez, A., Riches, A.J.V., 2007. The Lherz spinel Iherzolite: reformed rather than pristine mantle. *Earth Planet. Sci. Lett.* 259 (3–4), 599–612. <https://doi.org/10.1016/j.epsl.2007.05.026>.
- Leblanc, M., Dautria, J.M., Girod, M., 1982. Magnesian ilmenite xenoliths in a basanite from Tahalra, Ahaggar (Southern Algeria). *Contrib. Mineral. Petrol.* 79 (4), 347–354. <https://doi.org/10.1007/BF01132063>.
- Lenoir, X., Garrido, C.J., Bodinier, J.L., Dautria, J.M., Gervilla, F., 2001. The recrystallization front of the Ronda peridotite: evidence for melting and thermal erosion of subcontinental lithospheric mantle beneath the Alboran Basin. *J. Petrol.* 42 (1), 141–158. <https://doi.org/10.1093/ptrology/42.1.141>.
- Lewis, J.F., Draper, G., Proenza, J.A., Espaillet, J., Jiménez, J., 2006. Ophiolite-related ultramafic rocks (serpentinites) in the Caribbean region: a review of their occurrence, composition, origin, emplacement and nickel laterite soils. *Geol. Acta* 4, 237–263. <https://doi.org/10.1344/105.000000368>.
- Locock, A.J., 2014. An Excel spreadsheet to classify chemical analyses of amphiboles following the IMA 2012 recommendations. *Comput. Geosci.* 62, 1–11. <https://doi.org/10.1016/j.cageo.2013.09.011>.
- Lorand, J.P., Gregoire, M., 2010. Petrogenesis of Fe–Ti oxides in amphibole-rich veins from the Lherz orogenic peridotite (Northeastern Pyrénées, France). *Contrib. Mineral. Petrol.* 160 (1), 99–113. <https://doi.org/10.1007/s00410-009-0468-4>.
- Lorand, J.-P., Delpech, G., Grégoire, M., Moine, B., O'Reilly, S.Y., Cottin, J.Y., 2004. Platinum-group elements and the multistage metasomatic history of Kerguelen lithospheric mantle (South Indian Ocean). *Chem. Geol.* 208, 195–215. <https://doi.org/10.1016/j.chemgeo.2004.04.012>.
- Mao, M., Rukhlov, A.S., Rowins, S.M., Spence, J., Coogan, L.A., 2016. Apatite trace element compositions: a robust new tool for mineral exploration. *Econ. Geol.* 111 (5), 1187–1222. <https://doi.org/10.2113/econgeo.111.5.1187>.
- Marchesi, C., Garrido, C.J., Godard, M., Proenza, J.A., Gervilla, F., Blanco-Moreno, J., 2006. Petrogenesis of highly depleted peridotites and gabbroic rocks from the Mayarí-Baracoa Ophiolitic Belt (eastern Cuba). *Contrib. Mineral. Petrol.* 151 (6), 717. <https://doi.org/10.1007/s00410-006-0089-0>.
- Marchesi, C., Garrido, C.J., Bosch, D., Proenza, J.A., Gervilla, F., Monié, P., Rodríguez-Vega, A., 2007. Geochemistry of Cretaceous magmatism in eastern Cuba: recycling of North American continental sediments and implications for subduction polarity in the Greater Antilles Paleo-arc. *J. Petrol.* 48, 1813–1840. <https://doi.org/10.1093/ptrology/egm040>.
- McCallum, I.S., Charette, M.P., 1978. Zr and Nb partition coefficients: implications for the genesis of mare basalts, KREEP and sea floor basalts. *Geochim. Cosmochim. Acta* 42 (6), 859–869. [https://doi.org/10.1016/0016-7037\(78\)90098-4](https://doi.org/10.1016/0016-7037(78)90098-4).
- McKay, G., Wagstaff, J., Yang, S.R., 1986. Zirconium, hafnium, and rare earth element partition coefficients for ilmenite and other minerals in high-Ti lunar mare basalts: An experimental study. *J. Geophys. Res. Solid Earth* 91 (B4), 229–237. <https://doi.org/10.1029/JB091iB04pD229>.
- Menzies, M.A., Hawkesworth, C.J., 1987. *Mantle metasomatism*. Academic Press London.
- Meyer, P.S., Dick, H.J., Thompson, G., 1989. Cumulate gabbros from the Southwest Indian Ridge, 54 S–17° E: implications for magmatic processes at a slow spreading ridge. *Contrib. Mineral. Petrol.* 103 (1), 44–63. <https://doi.org/10.1007/BF00371364>.
- Mitchell, R.H., 1977. Geochemistry of magnesian ilmenites from kimberlites in South Africa and Lesotho. *Lithos* 10 (1), 29–37. [https://doi.org/10.1016/0024-4937\(77\)90028-7](https://doi.org/10.1016/0024-4937(77)90028-7).
- Morishita, T., Maeda, J., Miyashita, S., Matsumoto, T., Dick, H.J., 2004. Magmatic srilankite (Ti₂ZrO₆) in gabbroic vein cutting oceanic peridotites: an unusual product of peridotite-melt interactions beneath slow-spreading ridges. *Am. Mineral.* 89 (5–6), 759–766. <https://doi.org/10.2138/am-2004-5-609>.
- Morisset, C.E., Scoates, J.S., 2008. Origin of zircon rims around ilmenite in mafic plutonic rocks of Proterozoic anorthosite suites. *Can. Mineral.* 46 (2), 289–304. <https://doi.org/10.3749/canmin.46.2.289>.
- Nakamura, Y., Fujimaki, H., Nakamura, N., Tatsumoto, M., McKay, G.A., Wagstaff, J., 1986. Hf, Zr, and REE partition coefficients between ilmenite and liquid: implications for lunar petrogenesis. *J. Geophys. Res. Solid Earth* 91 (B4), 239–250. <https://doi.org/10.1029/JB091iB04pD239>.
- Naslund, H.R., 1987. Lamellae of baddeleyite and Fe–Cr-spinel in ilmenite from the Basistoppen sill, East Greenland. *Can. Mineral.* 25 (1), 91–96.
- O'Reilly, S.Y., Griffin, W.L., 2000. Apatite in the mantle: implications for metasomatic processes and high heat production in Phanerozoic mantle. *Lithos* 53 (3–4), 217–232. [https://doi.org/10.1016/S0024-4937\(00\)00026-8](https://doi.org/10.1016/S0024-4937(00)00026-8).
- O'Reilly, S.Y., Griffin, W.L., 2013. Mantle metasomatism. In: Harlov, D.E., Austrheim, H. (Eds.), *Metasomatism and the Chemical Transformation of Rock: The Role of Fluids in Terrestrial and Extraterrestrial Processes*. Lecture Notes in Earth System Sciences. Springer-Verlag, Berlin, Heidelberg, pp. 471–533. https://doi.org/10.1007/978-3-642-28394-9_12.
- Pagé, P., Barnes, S.J., 2009. Using trace elements in chromites to constrain the origin of podiform chromitites in the Theford Mines ophiolite, Québec, Canada. *Econ. Geol.* 104 (7), 997–1018. <https://doi.org/10.2113/econgeo.104.7.997>.
- Pascal, M.L., Di Muro, A., Fontelles, M., Principe, C., 2009. Zirconolite and calzirtite in banded forsterite-spinel-calcite skarn ejecta from the 1631 eruption of Vesuvius: inferences for magma-wallrock interactions. *Mineral. Mag.* 73 (2), 333–356. <https://doi.org/10.1180/minmag.2009.073.2.333>.
- Pertsev, A.N., Aranovich, L.Y., Prokofiev, V.Y., Bortnikov, N.S., Cipriani, A., Simakin, S.S., Borisovskiy, S.E., 2015. Signatures of residual melts, magmatic and seawater-derived fluids in oceanic lower-crust gabbro from the Vema lithospheric section, Central Atlantic. *J. Petrol.* 56 (6), 1069–1088. <https://doi.org/10.1093/ptrology/egv028>.
- Pietranik, A., Storey, C., Koepke, J., Lasalle, S., 2017. Zircon record of fractionation, hydrous partial melting and thermal gradients at different depths in oceanic crust (ODP Site 735B, South-West Indian Ocean). *Contrib. Mineral. Petrol.* 172 (2–3), 10. <https://doi.org/10.1007/s00410-016-1324-y>.
- Pilet, S., Baker, M.B., Stolper, E.M., 2008. Metasomatized lithosphere and the origin of alkaline lavas. *Science* 320 (5878), 916–919. <https://doi.org/10.1126/science.1156563>.
- Pilet, S., Baker, M.B., Müntener, O., Stolper, E.M., 2011. Monte Carlo simulations of metasomatic enrichment in the lithosphere and implications for the source of alkaline basalts. *J. Petrol.* 52 (7–8), 1415–1442. <https://doi.org/10.1093/ptrology/egr007>.
- Prichard, H.T., Cann, J.R., 1982. Petrology and mineralogy of dredged gabbro from Gettysburg Bank, Eastern Atlantic. *Contrib. Mineral. Petrol.* 79 (1), 46–55. <https://doi.org/10.1007/BF00376960>.
- Proenza, J.A., Gervilla, F., Melgarejo, J.C., 1999a. La Moho Transition Zone en el macizo ofiolítico Moa-Baracoa (Cuba): Un ejemplo de interacción magma/peridotita. *Rev. Soc. Geol. Esp.* 12 (3–4), 309–327.
- Proenza, J., Gervilla, F., Melgarejo, J.C., Bodinier, J.L., 1999b. Al- and Cr-rich chromitites from the Mayarí-Baracoa Ophiolitic Belt (eastern Cuba): consequence of interaction between volatile-rich melts and peridotite in suprasubduction mantle. *Econ. Geol.* 94, 547–566. <https://doi.org/10.2113/gsecongeo.94.4.547>.
- Proenza, J., Gervilla, F., Melgarejo, J., Vera, O., Alfonso, P., Fallick, A., 2001. Genesis of sulfide-rich chromite ores by the interaction between chromitite and pegmatitic

- olivine-norite dikes in the Potosi Mine (Moa-Baracoa ophiolitic massif, eastern Cuba). *Mineral. Deposita* 36 (7), 658–669. <https://doi.org/10.1007/s001260100193>.
- Proenza, J.A., Díaz-Martínez, R., Iriondo, A., Marchesi, C., Melgarejo, J.C., Gervilla, F., Garrido, C.J., Rodríguez-Vega, A., Lozano-Santacruz, R., Blanco-Moreno, J.A., 2006. Primitive Cretaceous island-arc volcanic rocks in eastern Cuba: the Téneme Formation. *Geol. Acta* 4 (1–2), 103–121. <https://doi.org/10.1344/105.000000360>.
- Proenza, J.A., González-Jiménez, J.M., García-Casco, A., Belousova, E., Griffin, W.L., Talavera, C., Rojas-Agramonte, Y., Aiglsperger, T., Navarro-Ciurana, D., Pujol-Solà, N., Gervilla, F., O'Reilly, S.Y., Jacob, D.E., 2018. Cold plumes trigger contamination of oceanic mantle wedges with continental crust-derived sediments: Evidence from chromitite zircon grains of eastern Cuban ophiolites. *Geosci. Front.* 9 (6), 1921–1936. <https://doi.org/10.1016/j.gsf.2017.12.005>.
- Pushcharovsky, Y. (Ed.), 1988. *Mapa geológico de Cuba escala 1:250000: Academias de Ciencias de Cuba y la URSS*.
- Python, M., Ceuleneer, G., 2003. Nature and distribution of dykes and related melt migration structures in the mantle section of the Oman ophiolite. *Geochem. Geophys. Geosyst.* 4 (7). <https://doi.org/10.1029/2002GC000354>.
- Rampone, E., Borghini, G., Basch, V., 2018. Melt migration and melt-rock reaction in the Alpine-Apennine peridotites: Insights on mantle dynamics in extending lithosphere. *Geosci. Front.* <https://doi.org/10.1016/j.gsf.2018.11.001> In Press.
- Rasmussen, B., Fletcher, I.R., Muhling, J.R., 2008. Pb/Pb geochronology, petrography and chemistry of Zr-rich accessory minerals (zirconolite, tranquillityite and baddeleyite) in mare basalt 10047. *Geochim. Cosmochim. Acta* 72 (23), 5799–5818. <https://doi.org/10.1016/j.gca.2008.09.010>.
- Reynolds, J.R., Langmuir, C.H., 1997. Petrological systematics of the Mid-Atlantic Ridge south of Kane: Implications for ocean crust formation. *J. Geophys. Res. Solid Earth* 102 (B7), 14915–14946. <https://doi.org/10.1029/97JB00391>.
- Rojas-Agramonte, Y., García-Casco, A., Kemp, A., Kröner, A., Proenza, J.A., Lázaro, C., Liu, D., 2016. Recycling and transport of continental material through the mantle wedge above subduction zones: A Caribbean example. *Earth Planet. Sci. Lett.* 436, 93–107. <https://doi.org/10.1016/j.epsl.2015.11.040>.
- Santos, J.J.A., Pimenta, A.C.S., Rosa, M.L.S., Conceição, H., 2015. *Primeira ocorrência de zirconolita na Província Alcalina do Sul do da Bahia: intrusão científica do Complexo Alcalino Floresta Azul, Bahia, NE Brasil. Scientia Plena* 11 (9).
- Scamberulli, M., Vannucci, R., De Stefano, A., Preite-Martínez, M., Rivalenti, G., 2009. CO₂ fluid and silicate glass as monitors of alkali basalt/peridotite interaction in the mantle wedge beneath Gobernador Gregores, Southern Patagonia. *Lithos* 107, 121–133. <https://doi.org/10.1016/j.lithos.2008.06.015>.
- Scotese, J.S., Chamberlain, K.R., 1995. Baddeleyite (ZrO₂) and zircon (ZrSiO₄) from anorthositic rocks of the Laramie anorthosite complex, Wyoming: Petrologic consequences and U–Pb ages. *Am. Mineralogist* 80 (11–12), 1317–1327. <https://doi.org/10.2138/am-1995-11-1223>.
- Secchiari, A., Montanini, A., Bosch, D., Macera, P., Cluzel, D., 2018. The contrasting geochemical message from the New Caledonia gabbro-norites: insights on depletion and contamination processes of the sub-arc mantle in a nascent arc setting. *Contrib. Mineral. Petrol.* 173 (8), 66. <https://doi.org/10.1007/s00410-018-1496-8>.
- Sláma, J., Košler, J., Pedersen, R.B., 2007. Behaviour of zircon in high-grade metamorphic rocks: evidence from Hf isotopes, trace elements and textural studies. *Contrib. Mineral. Petrol.* 154 (3), 335–356. <https://doi.org/10.1007/s00410-007-0196-6>.
- Söderlund, P., Söderlund, U., Möller, C., Gorbatshev, R., Rodhe, A., 2004. Petrology and ion microprobe U–Pb chronology applied to a metabasic intrusion in southern Sweden: a study on zircon formation during metamorphism and deformation. *Tectonics* 23 (5). <https://doi.org/10.1029/2003TC001498>.
- Soustelle, V., Tommasi, A., Bodinier, J.L., Garrido, C.J., Vauchez, A., 2009. Deformation and reactive melt transport in the mantle lithosphere above a large-scale partial melting domain: the Ronda Peridotite massif, Southern Spain. *J. Petrol.* 50, 1235–1266. <https://doi.org/10.1093/ptrology/egp032>.
- Stucki, A., Trommsdorff, V., Günther, D., 2001. Zirconolite in metarodingites of Penninic Mesozoic ophiolites Central Alps. *Schweiz. Mineral. Petrogr. Mitt.* 81 (2), 257–265.
- Sun, S.S., McDonough, W.F., 1989. Chemical and isotopic systematics of oceanic basalts: implications for mantle composition and processes. *Geol. Soc. Lond., Spec. Publ.* 42 (1), 313–345. <https://doi.org/10.1144/GSL.SP.1989.042.01.19>.
- Tassara, S., González-Jiménez, J.M., Reich, M., Saunders, E., Luguet, A., Morata, D., Grégoire, M., van Acken, D., Schilling, M.E., Barra, F., Nowell, G., Corgne, A., 2018. Highly siderophile elements mobility in the subcontinental lithospheric mantle beneath southern Patagonia. *Lithos* 314, 579–596. <https://doi.org/10.1016/j.lithos.2018.06.022>.
- Taylor, L.A., McCallister, R.H., 1972. An experimental investigation of the significance of zirconium partitioning in lunar ilmenite and ulvöspinel. *Earth Planet. Sci. Lett.* 17 (1), 105–109. [https://doi.org/10.1016/0012-821X\(72\)90264-6](https://doi.org/10.1016/0012-821X(72)90264-6).
- Tiepolo, M., Bottazzi, P., Foley, S.F., Oberti, R., Vannucci, R., Zanetti, A., 2001. Fractionation of Nb and Ta from Zr and Hf at mantle depths: the role of titanian pargasite and kaersutite. *J. Petrol.* 42 (1), 221–232. <https://doi.org/10.1093/ptrology/42.1.221>.
- Tompkins, L.A., Haggerty, S.E., 1985. Groundmass oxide minerals in the Koidu kimberlite dikes, Sierra Leone, West Africa. *Contrib. Mineral. Petrol.* 91 (3), 245–263. <https://doi.org/10.1007/BF00413351>.
- Tribuzio, R., Riccardi, M.P., Ottolini, L., 1995. Trace element redistribution in high-temperature deformed gabbros from East Ligurian ophiolites (Northern Apennines, Italy): constraints on the origin of syndeformation fluids. *J. Metamorph. Geol.* 13 (3), 367–377. <https://doi.org/10.1111/j.1525-1314.1995.tb00226.x>.
- Tribuzio, R., Tiepolo, M., Thirlwall, M.F., 2000. Origin of titanian pargasite in gabbroic rocks from the Northern Apennine ophiolites (Italy): insights into the late-magmatic evolution of a MOR-type intrusive sequence. *Earth Planet. Sci. Lett.* 176 (3–4), 281–293. [https://doi.org/10.1016/S0012-821X\(00\)00014-5](https://doi.org/10.1016/S0012-821X(00)00014-5).
- Tribuzio, R., Renna, M.R., Dallai, L., Zanetti, A., 2014. The magmatic-hydrothermal transition in the lower oceanic crust: clues from the Ligurian ophiolites, Italy. *Geochim. Cosmochim. Acta* 130, 188–211. <https://doi.org/10.1016/j.gca.2014.01.010>.
- Vanko, D.A., 1986. High-chlorine amphiboles from oceanic rocks; product of highly-saline hydrothermal fluids? *Am. Mineral.* 71 (1–2), 51–59.
- Vanko, D.A., Stakes, D.S., 1991. Fluids in oceanic layer 3: evidence from veined rocks, Hole 735B, Southwest Indian Ridge. *Proceedings of the Ocean Drilling Program - Scientific Results*. vol. 118, pp. 181–215. <https://doi.org/10.2973/odp.proc.sr.118.121.1991>.
- Warren, J.M., Shimizu, N., 2010. Cryptic variations in abyssal peridotite compositions: evidence for shallow-level melt infiltration in the oceanic lithosphere. *J. Petrol.* 51 (1–2), 395–423. <https://doi.org/10.1093/ptrology/egp096>.
- Watson, E.B., Wark, D.A., Thomas, J.B., 2006. Crystallization thermometers for zircon and rutile. *Contrib. Mineral. Petrol.* 151 (4), 413. <https://doi.org/10.1007/s00410-006-0068-5>.
- Williams, C.T., Gieré, R., 1996. Zirconolite: a review of localities worldwide, and a compilation of its chemical compositions. *Bull. British Nat. History Mus. (Geological Service)* 52, 1–24.
- Xu, J., Melgarejo, J.C., Castillo-Oliver, M., 2018. Ilmenite as a recorder of kimberlite history from mantle to surface: examples from Indian kimberlites. *Mineral. Petrol.* 112 (2), 569–581. <https://doi.org/10.1007/s00710-018-0616-5>.
- Yao, S., 1999. *Chemical Composition of Chromites from Ultramafic Rocks: Application to Mineral Exploration and Petrogenesis*. (PhD thesis). Macquarie University, Sydney (174 pp).
- Zaccarini, F., Stumpfl, E.F., Garuti, G., 2004. Zirconolite and Zr–Th–U minerals in chromitites of the Finero complex, Western Alps, Italy: evidence for carbonatite-type metasomatism in a subcontinental mantle plume. *Can. Mineral.* 42 (6), 1825–1845. <https://doi.org/10.2113/gscanmin.42.6.1825>.
- Zack, T., Brumm, R., 1998. Ilmenite/liquid partition coefficients of 26 trace elements determined through ilmenite/clinopyroxene partitioning in garnet pyroxenites. *Int. Kimberlite Conf.* 7 (1), 986–988.
- Zhang, C., Koepke, J., Albrecht, M., Horn, I., Holtz, F., 2017. Apatite in the dike-gabbro transition zone of mid-ocean ridge: Evidence for brine assimilation by axial melt lens. *Am. Mineral.* 102 (3), 558–570. <https://doi.org/10.2138/am-2017-5906>.

Supplementary data

Appendix 1. Table summarizing the studied samples from Potosí.

Sample	Description	Zone	Thin section	SEM-EDS	EPMA	LA-ICP-MS
Po-1	Chromitite-Harzburgite contact	Ordinary chromitite	Po-1		X	
Po-2	Massive chromitite	Ordinary chromitite	Po-2			
Po-3	Chromitite in the interaction zone	Metasomatized chromitite	Po-3 Po-3-1 Po-3-3 Po-3-4	X X	X	
Po-4	Chromitite in the interaction zone	Metasomatized chromitite	Po-4 Po-4-1 Po-4-2		X X	
Po-5	Chromitite in the interaction zone	Metasomatized chromitite	Po-5 Po-5-2			
Po-6	Chromitite in the interaction zone	Metasomatized chromitite	Po-6 Po-6-1 Po-6-2 Po-6-3			
Po-7	Chromitite in the interaction zone	Metasomatized chromitite	Po-7 Po-7-2		X	
Po-8	Chromitite in the interaction zone	Metasomatized chromitite	Po-8			
Po-9	Chromitite in the interaction zone	Metasomatized chromitite	Po-9			
Po-10	Pegmatitic gabbro	Gabbroic intrusive	Po-10		X	
Po-11	Pegmatitic gabbro	Gabbroic intrusive				
Po-100	Gabbro	Gabbroic intrusive				
Po-101	Massive chromitite - 10cm from the gabbro	Ordinary chromitite	Po-101			
Po-102	Disseminated chromitite	Ordinary chromitite	Po-102		X	
Po-103	Pegmatitic gabbro	Gabbroic intrusive	Po-103		X	
Po-104	Brecciated chromitite	Metasomatized chromitite	Po-104		X	
Po-105	Chromitite in the interaction zone	Metasomatized chromitite	Po-105a Po-105b	X X	X	X
Po-106	Chromitite in the interaction zone	Metasomatized chromitite	Po-106			
Po-106	Regional peridotite	Ordinary chromitite	Po-106host		X	
POT-1	Chromitite in the interaction zone	Metasomatized chromitite	POT-1 POT-1(II) POT-2 POT-3 POT-4 POT-5 POT-6	X X X X	X X X X X X	X X
POT-2	Olivine gabbro	Gabbroic intrusive	POT-2(II)	X	X	

Appendix 2. Whole rock analyses of gabbroic dikes.

Sample	POT-1	POT-2
SiO ₂ (wt.%)	39.77	40.64
TiO ₂	0.8	0.29
Al ₂ O ₃	18.7	4.41
Fe ₂ O _{3T}	6.51	17.9
MnO	0.04	0.26
MgO	9.92	24.33
CaO	13.97	5.82
Na ₂ O	2.6	0.35
K ₂ O	0.02	-
P ₂ O ₅	0.11	0.02
Total	92.44	94.02

Sample	POT-1	POT-2
Li (ppm)	6.8	2.0
Rb	1.17	0.36
Cs	0.062	0.005
Be	0.23	0.05
Sr	231	29
Ba	6.3	1.6
Sc	23	26
V	202	94
Cr	19475	435
Co	35	110
Ni	532	691
Cu	480	86
Zn	30	96
Ga	13.5	4.5
Y	35.4	7.0
Nb	1.7	0.3
Ta	0.36	0.27
Zr	149.2	5.0
Hf	1.35	0.32
Mo	0.10	0.04
Sn	0.61	0.25
Tl	0.024	0.003
Pb	1.16	0.48
U	0.11	0.03
Th	0.26	0.03
La	5.11	0.30
Ce	15.7	1.0
Pr	2.5	0.2
Nd	12.8	1.2
Sm	3.99	0.55
Eu	1.14	0.26
Gd	4.76	0.84
Tb	0.84	0.16
Dy	5.63	1.09
Ho	1.25	0.25
Er	3.47	0.66
Tm	0.51	0.12
Yb	3.39	0.73
Lu	0.55	0.11

Appendix 3. Electron Microprobe analyses and LA-ICP-MS analyses conditions.

Electron Probe Micro Analyses

Quantitative electron microprobe analyses (EMPA) were obtained at the Universitat de Barcelona (CCiTUB) using both CAMECA SX50 and JEOL JXA-8230 electron microprobes, operating in wavelength-dispersive spectroscopy (WDS) mode. Analytical conditions for silicates, spinels, oxides, and apatite analyses were 20 kV accelerating voltage, 10-20 nA beam current, 1-2 μm beam diameter, and 10 s counting time per element. Natural and synthetic standards used were Cr_2O_3 (Cr), wollastonite (Si and Ca), corundum (Al), rutile (Ti), albite (Na), periclase (Mg), hematite (Fe), rhodonite (Mn), orthoclase (K), apatite (P), celestine (Sr), NiO (Ni), sphalerite (Zn), yttrium-aluminum garnet (Y), ZrO_2 (Zr), CaF (F), NaCl (Cl), CeO_2 (Ce), UO_2 (U), REE glass (Nd), and pure metals for V, Nb and Hf. The correction procedure XPP (Pouchou and Pichoir, 1991) was used to convert specimen intensity ratios into concentrations.

Analytical conditions for zirconolite analyses were 25 kV accelerating voltage and 80 nA beam current. Background positions were carefully adjusted and peak-overlap corrections were applied for the main REE peak overlaps using the method described by Fialin et al. (1997). Analytical standards included natural and synthetic silicates, oxides and REE glasses as follows: periclase (Mg), corundum (Al), wollastonite (Si and Ca), orthoclase (K), rutile (Ti), Cr_2O_3 (Cr), rhodonite (Mn), hematite (Fe), yttrium-aluminum garnet (Y), ZrO_2 (Zr), LaB_6 (La), CeO_2 (Ce), REE glasses (Pr, Nd, Sm, Eu, Gd, Tb, Dy, Ho, Er, Tm, Yb, Lu), UO_2 (U) and ThO_2 (Th) (the REE glasses consist of Si-Al-Ca based glasses each containing four of the 14 REEs). Metals were used for Sc, Nb and Hf. The correction procedure PAP (Pouchou and Pichoir, 1991) was used to convert specimen intensity ratios into concentrations.

X-ray maps of selected areas were collected on the Potosí thin sections using the following analytical conditions: 20 kV accelerating voltage, 50 nA beam current, focused spot, stage-scanning mode, 0.8 μm pixel size, 512 x 512 pixel number, and 10 ms counting time per pixel. The following elements were mapped: Si, Al, Y, Ti, Cr, U, F, Na, Mg, Mn, Fe, Ni, Ca, K, and Zr.

Olivine and plagioclase compositions were normalized to 4 and 8 O respectively, and $Fe_{total} = Fe^{2+}$. Orthopyroxene and clinopyroxene were normalized to 6 O, the distribution of cations in the T, M1 and M2-sites was carried out by stoichiometry and Fe^{3+}/Fe^{2+} ratio was estimated following Morimoto (1988). Amphibole was normalized to 23 O, the H_2O content was determined assuming $(OH + F + Cl) = 2$ a.p.f.u., and the distribution of cations in the A, B, C, and T sites was performed by stoichiometry and Fe^{3+} was estimated for electroneutrality after cation normalization (Hawthorne et al., 2012). Chromite and ilmenite were normalized to 4 and 3 O respectively and the Fe^{3+}/Fe^{2+} ratio was stoichiometrically recalculated according to Carmichael's (1967). Apatite was normalized to 25 anions (O, OH, Cl, F).. Baddeleyite and zircon compositions were normalized to 2 and 4 O respectively. Zirconolite composition was calculated favoring $REEZrM_{5+}M_{2+}O_7$ in the calculation sequence because it yields better results for REE-zirconolites, instead of $CaZr M_{5+}M_{2+}O_7$ commonly used for U-Th zirconolites (Gieré et al., 1998; Hurai et al., 2017). All iron is considered as divalent because only electron microprobe analyses are available. Mineral and end-member abbreviations are after Whitney and Evans (2010).

LA-ICP-MS analyses

Trace element compositions of chromite, ilmenite, clinopyroxene, orthopyroxene, olivine, amphibole, apatite, zircon and baddeleyite were measured in-situ on polished thin sections by an inductively coupled mass spectrometer Agilent 8800 QQQ ICP-MS interfaced to a laser ablation extraction line Photon Machines Analyte Excite 193 at the Instituto Andaluz de Ciencias de la Tierra (CSIC-UGR, Granada). Ablation conditions were set up to get the maximum sensibility on analysis, minimize interactions and interferences, and to get accurate location analysis, avoiding mixed areas, fractures and irregularities over the ablated area. 50 μm spot size beam was used for chromite, ilmenite, amphibole, and apatite, 85 μm for clinopyroxene, 65 μm for orthopyroxene, 30 μm for baddeleyite, and 15 μm in raster mode during 30 s for zircon due to its low concentration of trace elements. Surface nebulization of chromite, ilmenite, clinopyroxene, orthopyroxene, amphibole, and apatite does not require high pulse energy on the laser beam and a fluence of 8 J/cm^2 was used over a total laser energy of 7

mJ, 20% attenuation, and repetition rate of 10 Hz, which is the most common RP used when analyzing depleted samples. For zircon the fluence was 10 J/cm².

The ablation mode was static spot and performed as automatic driven positioning. The same conditions were used both for chromite and ilmenite because, over initial signal monitoring for three different masses, sensibility was the same using the same ablation conditions. Auto-tuning calibration was performed before analyses, using NIST611 SRM synthetic glass. A continuous raster at 1 µm/s was programmed to avoid temporary low signal when performing continuous Auto-tuning. This process is more than 20 minutes long when calibrating the instrument to have the higher sensibility over masses that will not show more than 100 CPS as maximum. Masses used for tuning must encompass all masses to analyse, usually a low mass (7), half weight mass (59) and high mass (232). For zircon analyses the used masses were 90-208-238. After tuning, a signal monitor over low signal masses must be done in order to adjust certain type of acquisition conditions, especially the Ar Carrier gas flow (1.5 l/min), sampling depth (4 mm) and N₂ addition flow (0.05 l/min), which is added to increase sensibility over heavy masses. Integration time for all analyses acquisition was 60 milliseconds for each mass. Samples were located on a double volume ablation cell, with He carrier flow of 1.2 l/min (1 l/min main flow, 0.2 l/min auxiliary gas flow). Unknown samples and standard material were ablated in sequence of one primary standard (NIST611 SRM for chromite and ilmenite and 91500 for zircon) every 4 unknown samples. Interleaved secondary /validation standard (BIR1G synthetic glass, IAG-USGS for chromite and ilmenite and Plesovice for zircon) was also included. Data were subsequently reduced using Igor Pro iolite 3.6 software (Paton et al., 2011) using one element of previous EPMA data as internal standard.

References

Carmichael, I.S.E., 1967. The iron-titanium oxides of salic volcanic rocks and their associated ferromagnesian silicates. *Contributions to Mineralogy and Petrology* 14, 36–64. <https://doi.org/10.1007/BF0037098>.

- Fialin, M., Outrequin, M., Staub, P., 1997. A new tool to treat peak overlaps in electron-probe microanalysis of rare-earth-element L-series X-rays. *European Journal of Mineralogy* 9, 965-968. <https://doi.org/10.1127/ejm/9/5/0965>.
- Gieré, R., Williams, C.T., Lumpkin, G.R., 1998. Chemical characteristics of natural zirconolite. *Schweizerische Mineralogische und Petrographische Mitteilungen* 78, 433–459.
- Hawthorne, F.C., Oberti, R., Harlow, G.E., Maresch, W.V., Martin, R.F., Schumacher, J.C., Welch, M.D., 2012. IMA report: nomenclature of the amphibole supergroup. *American Mineralogist* 97, 2031–2048. <https://doi.org/10.2138/am.2012.4276>.
- Hurai, V., Huraiová, M., Gajdošová, M., Konečný, P., Slobodník, M., Siegfried, P.R., 2017. Compositional variations of zirconolite from the Evate apatite deposit (Mozambique) as an indicator of magmatic-hydrothermal conditions during post-orogenic collapse of Gondwana. *Mineralogy and Petrology* 1-18. <https://doi.org/10.1007/s00710-017-0538-7>.
- Morimoto, N. (1988). Nomenclature of pyroxenes. *Mineralogy and Petrology* 39(1), 55-76. <https://doi.org/10.1007/BF01226262>.
- Paton, C., Hellstrom, J., Paul, B., Woodhead, J., Hergt, J., 2011. Iolite: Freeware for the visualisation and processing of mass spectrometric data. *Journal of Analytical Atomic Spectrometry* 26(12), 2508-2518. <https://doi.org/10.1039/C1JA10172B>.
- Pouchou, J.L., Pichoir, F., 1991. Quantitative analysis of homogeneous or stratified microvolumes applying the model PAP, *in* Heinrich, K.F.J., and Newbury, D.E. eds., *Electron Probe Quantitation*. Plenum Press, New York, 31-75. https://doi.org/10.1007/978-1-4899-2617-3_4.
- Whitney, D.L., Evans, B.W., 2010. Abbreviations for names of rock-forming minerals. *American Mineralogist* 95, 185–187. <https://doi.org/10.2138/am.2010.3371>.

Bottle/plate	Data for Wehenill plot				Data for Tera-Wasserburg plot				Dates				Concentrations							
	$^{207}\text{Pb}/^{235}\text{U}$	2σ	$^{206}\text{Pb}/^{238}\text{U}$	2σ	$^{238}\text{U}/^{206}\text{Pb}$	$^{238}\text{U}/^{206}\text{Pb}$	$^{207}\text{Pb}/^{206}\text{Pb}$	2σ	Error	Correlation	Age $^{207}\text{Pb}/^{235}\text{U}$	Age $^{206}\text{Pb}/^{238}\text{U}$	Age $^{207}\text{Pb}/^{235}\text{U}$	Age $^{206}\text{Pb}/^{238}\text{U}$	U	SD U	Th	SD Th	Pb	SD Pb
POT105-2	1	6.2	0.024	0.025	0.06507	43.40278	0	1.3	0.12642	1900	475	80	-10000	23000	0.72	0.35	2.1	2.2	470	350
POT105-3	0.4	1.2	0.023	0.015	0.4927	43.47826	-0.14	0.28	-0.9927	380	490	48	-88000	9300	35.8	8.9	0.8	1.2	140	340
POT1-1	3.6	4.3	0.024	0.017	0.073538	28.35539	0.47	0.76	0.82694	1480	410	55	-1.50E+03	7.80E+03	194	46	1	2.1	40	350
POT1-2	0.3	1.8	0.022	0.017	0.074648	29.51389	-1.2	1.6	-0.040728	1210	225	55	-45000	46000	61	15	1.3	1.9	500	500
POT1-3	2.8	1.8	0.022	0.014	0.19357	35.12397	-0.4	1.7	0.85196	1730	140	42.5	-18000	34000	45	11	-0.15	0.19	150	210
POT1-4	2.8	3.7	0.024	0.01	0.04979	28.92562	0.11	2	0.082598	1200	650	32	0.00E+00	1.20E+04	29.1	5.8	-0.13	0.2	110	110
POT1-5	0.56	0.25	0.0239	0.0023	0.78128	17.36111	0.101	0.056	0.86325	440	75	7	1420	870	16.8	1.8	0.7	1.6	20	250

Sample	Po-105a 04					POT-6 01					POT-5 03					POT-5 04									
	amp-cr-1	amp-cr-2	amp-cr-3	amp-cr-4	amp-cr-5	amp-1	amp-2	amp-3	amp-4	amp-5	amp-rim-1	amp-rim-2	amp-rim-3	amp-rim-4	amp-rim-5	amp-rim-1	amp-rim-2	amp-rim-3	amp-rim-4	amp-rim-5	amp-1	amp-2	amp-3	amp-4	amp-5
SiO ₂	41.87	42.07	41.83	42.07	42.12	42.38	42.16	42.49	42.18	42.05	42.85	42.57	42.86	43.38	43.12	42.65	42.31	42.85	42.66	43.16	43.12	43.11	43.50	43.24	
TiO ₂	4.61	4.29	4.39	4.46	4.63	3.46	3.95	3.55	3.95	4.00	2.89	3.00	3.01	3.03	3.09	3.77	3.75	3.69	3.56	2.60	2.82	3.02	2.94	2.41	
Al ₂ O ₃	11.44	11.58	11.57	11.13	11.40	11.41	11.35	11.65	11.45	11.41	12.02	12.40	12.77	12.19	12.36	12.05	12.28	11.67	12.21	12.47	12.02	11.96	11.83	12.66	
Cr ₂ O ₃	1.59	1.42	1.53	1.54	1.52	1.29	1.51	1.40	1.26	1.44	1.34	1.21	1.20	1.30	1.24	1.34	1.28	1.36	1.36	1.30	1.51	1.29	0.96	0.67	
V ₂ O ₅	0.15	0.13	0.17	0.19	0.17	0.09	0.11	0.16	0.13	0.12	0.16	0.17	0.09	0.14	0.13	0.13	0.11	0.12	0.12	0.13	0.13	0.15	0.12	0.14	
FeO _t	5.42	5.16	5.02	4.86	4.68	5.40	5.60	5.77	5.91	6.09	5.34	5.73	5.68	5.18	5.37	6.25	6.17	5.96	5.89	5.59	5.38	5.63	5.62	5.70	
MnO	0.07	0.07	0.07	0.06	0.06	0.11	0.11	0.10	0.11	0.11	0.12	0.08	0.13	0.10	0.11	0.11	0.12	0.11	0.10	0.09	0.14	0.14	0.09	0.13	
MgO	16.66	16.99	16.77	16.82	16.78	17.19	16.86	17.04	16.69	16.28	17.11	16.96	16.98	17.20	17.16	16.67	16.41	16.66	16.71	17.23	17.45	16.98	17.41	17.56	
CaO	11.82	11.93	11.95	11.81	12.04	11.26	11.13	10.94	11.02	10.94	11.76	11.31	11.18	11.59	11.47	11.03	10.98	11.15	11.50	11.40	11.32	11.38	11.36	11.32	
Na ₂ O	3.33	3.28	3.18	3.17	3.10	3.09	3.27	3.25	3.27	3.17	2.76	2.93	2.77	2.46	2.84	3.15	3.27	2.87	2.63	2.63	2.61	2.63	2.67	2.56	
K ₂ O	0.56	0.62	0.70	0.66	0.65	0.20	0.21	0.20	0.19	0.20	0.19	0.21	0.21	0.17	0.20	0.21	0.21	0.21	0.20	0.17	0.17	0.18	0.16	0.16	
F	0.37	0.29	bdl	bdl	bdl	bdl	0.10	0.14	bdl	bdl	0.14	0.09	0.22	0.18	bdl	0.11	0.17	0.26	0.28	bdl	0.10	0.11	0.18	0.13	
Cl	0.02	0.01	0.03	0.03	0.02	0.02	bdl	0.01	0.01	0.01	bdl	0.01	bdl	0.02	0.01	bdl	bdl	bdl	bdl	bdl	bdl	bdl	bdl	bdl	
Total	97.82	97.87	96.93	96.43	96.41	96.12	96.53	96.95	96.37	96.00	96.86	96.94	97.41	97.20	97.33	97.71	97.26	97.03	97.65	97.09	97.07	96.84	97.13	96.99	
O=	23	23	23	23	23	23	23	23	23	23	23	23	23	23	23	23	23	23	23	23	23	23	23	23	
Analyse	amp-cr-1	amp-cr-2	amp-cr-3	amp-cr-4	amp-cr-5	amp-1	amp-2	amp-3	amp-4	amp-5	amp-rim-1	amp-rim-2	amp-rim-3	amp-rim-4	amp-rim-5	amp-rim-1	amp-rim-2	amp-rim-3	amp-rim-4	amp-1	amp-2	amp-3	amp-4	amp-5	
Si	6.072	6.086	6.081	6.133	6.117	6.169	6.136	6.145	6.143	6.154	6.188	6.141	6.143	6.217	6.177	6.127	6.113	6.192	6.136	6.187	6.191	6.213	6.241	6.201	
Ti	0.503	0.467	0.480	0.489	0.506	0.379	0.432	0.386	0.433	0.440	0.314	0.325	0.324	0.327	0.333	0.407	0.407	0.401	0.385	0.280	0.304	0.327	0.317	0.260	
Al	1.955	1.974	1.982	1.912	1.951	1.958	1.947	1.986	1.965	1.968	2.046	2.108	2.157	2.059	2.087	2.040	2.091	1.987	2.070	2.107	2.034	2.032	2.000	2.140	
Cr	0.182	0.163	0.176	0.178	0.175	0.149	0.174	0.160	0.146	0.167	0.152	0.138	0.136	0.148	0.140	0.152	0.147	0.155	0.155	0.148	0.171	0.147	0.109	0.075	
V	0.018	0.016	0.019	0.022	0.020	0.010	0.013	0.018	0.015	0.014	0.019	0.020	0.010	0.017	0.015	0.015	0.012	0.014	0.013	0.015	0.015	0.015	0.017	0.016	
Fe ²⁺	0.000	0.006	0.000	0.000	0.000	0.232	0.190	0.277	0.207	0.189	0.213	0.284	0.331	0.264	0.250	0.263	0.227	0.250	0.217	0.333	0.321	0.281	0.315	0.339	
Fe ³⁺	0.657	0.618	0.610	0.592	0.568	0.425	0.492	0.421	0.513	0.556	0.432	0.407	0.350	0.357	0.393	0.488	0.519	0.471	0.492	0.338	0.325	0.398	0.360	0.344	
Mn	0.009	0.009	0.009	0.008	0.007	0.014	0.013	0.012	0.014	0.014	0.015	0.010	0.016	0.013	0.013	0.013	0.015	0.013	0.012	0.011	0.017	0.017	0.011	0.016	
Mg	3.601	3.664	3.634	3.655	3.633	3.730	3.658	3.674	3.624	3.552	3.683	3.647	3.628	3.675	3.664	3.570	3.534	3.589	3.583	3.682	3.735	3.648	3.724	3.754	
Ca	1.836	1.849	1.861	1.845	1.873	1.756	1.735	1.695	1.720	1.715	1.819	1.748	1.717	1.780	1.760	1.698	1.700	1.726	1.772	1.751	1.741	1.757	1.746	1.739	
Na	0.936	0.920	0.896	0.896	0.873	0.872	0.923	0.911	0.923	0.899	0.773	0.819	0.770	0.684	0.789	0.877	0.916	0.776	0.800	0.731	0.727	0.735	0.743	0.712	
K	0.103	0.115	0.130	0.122	0.120	0.038	0.038	0.036	0.036	0.037	0.034	0.039	0.038	0.032	0.037	0.038	0.038	0.038	0.036	0.032	0.031	0.032	0.030	0.029	
F	0.170	0.134				0.047	0.047	0.063	0.063	0.003	0.063	0.040	0.102	0.084	0.004	0.051	0.077	0.118	0.128		0.048	0.051	0.084	0.061	
Cl	0.005	0.003	0.007	0.006	0.006	0.006	0.000	0.003	0.003	0.003	0.003	0.004	0.004	0.004	0.003					1.5613	1.5613	1.5605	1.5609	1.562	
Mg#	0.85	0.86	0.86	0.86	0.86	0.90	0.88	0.90	0.88	0.86	0.90	0.90	0.91	0.91	0.90	0.88	0.87	0.88	0.88	0.92	0.92	0.90	0.91	0.92	
Prefix	Chromi	Chromi	Chromi	Chromi	Chromi	Ferri-	Ferri-	Ferri-	Ferri-	Ferri-	Magnes	Magnes	Magnes	Magnes	Magnes	Magnes	Magnes	Magnes	Magnes	Ferri-	Ferri-	Ferri-	Ferri-	Ferri-	
Classificat	Kaersut	Pargasi	Pargasi	Pargasi	Kaersut	Magnes	Magnes	Magnes	Magnes	Magnes	Pargasi	Magnes	Magnes	Magnes	Magnes	Magnes	Magnes	Magnes	Magnes	Magnes	Magnes	Magnes	Magnes	Magnes	Pargasi
ion	ite	ite	ite	ite	ite	io	io	io	io	io	ite	io	io	io	ite	io	io	io	io	io	io	io	io	ite	ite

Sample	Po-105a 01						POT-2 03						Po-105a 01					
	cpx-2	cpx-3	cpx-1-in1	cpx-2-1	cpx-2-2	cpx-2-3	cpx-2-4	cpx-2-5	opx-1	opx-2	opx-3	opx-4	opx-5	opx-6	opx-7	opx-8	opx-9	cpx-1
SiO ₂	53.17	53.76	51.93	51.88	52.11	51.89	51.08	51.76	55.11	55.22	55.78	55.25	55.75	55.32	56.29	55.40	55.61	53.09
TiO ₂	0.54	0.36	0.63	0.60	0.60	0.55	0.52	0.57	0.38	0.41	0.45	0.42	0.43	0.30	0.43	0.47	0.57	0.57
Al ₂ O ₃	1.38	1.01	2.53	2.75	2.95	2.87	2.98	2.97	1.23	1.16	1.28	1.39	1.16	1.17	0.79	1.18	1.31	1.45
Cr ₂ O ₃	0.47	0.39	0.99	1.01	1.12	0.98	1.04	1.04	0.35	0.26	0.33	0.35	0.30	0.30	0.27	0.27	0.45	0.45
V ₂ O ₅	0.03	0.06	0.05	0.05	0.08	0.06	0.04	0.06	0.03	bdl	bdl	0.04	bdl	0.03	bdl	0.05	0.07	0.05
FeO†	2.93	2.73	3.29	3.20	3.78	4.04	3.81	3.88	8.33	8.22	8.39	8.51	8.53	8.51	7.63	8.63	8.13	3.10
MnO	0.09	0.10	0.09	0.12	0.15	0.17	0.15	0.13	0.25	0.22	0.21	0.20	0.17	0.21	0.21	0.24	0.22	0.11
MgO	17.11	17.40	15.98	16.16	16.18	16.22	15.97	16.03	32.90	32.45	33.38	33.01	33.17	33.28	34.16	32.64	32.66	17.18
CaO	23.52	23.83	23.61	23.41	22.68	22.29	22.99	22.63	1.60	1.51	0.70	1.07	0.62	0.74	0.55	1.30	1.21	23.32
Na ₂ O	0.49	0.42	0.39	0.46	0.62	0.40	0.49	0.46	bdl	bdl	bdl	bdl	bdl	bdl	bdl	bdl	bdl	0.44
K ₂ O	bdl	bdl	bdl	bdl	bdl	bdl	bdl	bdl	bdl	bdl	bdl	bdl	bdl	bdl	bdl	0.02	bdl	bdl
F	0.08	bdl	bdl	bdl	bdl	bdl	bdl	bdl	bdl	0.13	bdl	0.09	bdl	bdl	bdl	bdl	bdl	bdl
Cl	bdl	bdl	bdl	bdl	bdl	bdl	bdl	bdl	bdl	bdl	bdl	bdl	bdl	bdl	bdl	bdl	bdl	bdl
Total	100.01	100.24	99.63	99.83	100.49	99.59	99.87	99.66	100.51	99.78	100.74	100.60	100.31	100.27	100.41	100.39	100.08	99.96
O=	6	6	6	6	6	6	6	6	6	6	6	6	6	6	6	6	6	6
Analyse	cpx-2	cpx-3	cpx-1-in1	cpx-2-1	cpx-2-2	cpx-2-3	cpx-2-4	cpx-2-5	opx-1	opx-2	opx-3	opx-4	opx-5	opx-6	opx-7	opx-8	opx-9	cpx-1
Si	1.937	1.951	1.907	1.899	1.896	1.906	1.894	1.901	1.916	1.935	1.930	1.919	1.938	1.924	1.945	1.929	1.938	1.935
Ti	0.015	0.010	0.017	0.017	0.016	0.015	0.014	0.016	0.010	0.011	0.012	0.011	0.011	0.011	0.008	0.011	0.012	0.016
Al	0.059	0.043	0.110	0.119	0.127	0.124	0.129	0.129	0.051	0.048	0.052	0.057	0.048	0.048	0.032	0.048	0.054	0.062
Cr	0.013	0.011	0.029	0.029	0.032	0.029	0.030	0.030	0.010	0.007	0.009	0.010	0.008	0.008	0.007	0.007	0.007	0.013
V	0.001	0.002	0.001	0.001	0.002	0.002	0.001	0.002	0.001	0.004	0.005	0.001	0.001	0.001	0.001	0.001	0.002	0.002
Fe ²⁺	0.057	0.052	0.039	0.051	0.057	0.031	0.058	0.040	0.088	0.054	0.055	0.072	0.046	0.071	0.054	0.062	0.035	0.054
Fe ³⁺	0.032	0.031	0.062	0.047	0.058	0.093	0.059	0.079	0.154	0.187	0.188	0.175	0.202	0.176	0.167	0.189	0.202	0.040
Mn	0.003	0.003	0.003	0.004	0.005	0.005	0.005	0.004	0.007	0.007	0.006	0.006	0.005	0.006	0.006	0.007	0.006	0.003
Mg	0.929	0.941	0.875	0.882	0.878	0.888	0.873	0.877	1.705	1.695	1.722	1.709	1.719	1.726	1.760	1.695	1.697	0.933
Ca	0.918	0.927	0.929	0.918	0.884	0.877	0.903	0.890	0.060	0.057	0.026	0.040	0.023	0.028	0.020	0.048	0.045	0.910
Na	0.035	0.029	0.028	0.032	0.044	0.029	0.035	0.033										0.031
K																		
F	0.010								0.014			0.010						
Cl																		
Total	4.000	4.000	4.000	4.000	4.000	4.000	4.000	4.000	4.000	4.000	4.000	4.000	4.000	4.000	4.000	4.000	4.000	4.000
Mg#	0.91	0.92	0.90	0.90	0.88	0.88	0.88	0.88	0.88	0.88	0.88	0.87	0.87	0.87	0.89	0.87	0.88	0.91
Prefix	Chromian	Chromian	Chromian	Chromian	Chromian	Chromian	Chromian	Chromian	Chromian	Enstatite	Enstatite	Enstatite	Enstatite	Enstatite	Enstatite	Enstatite	Enstatite	Chromian
Classification	Diopside	Diopside	Diopside	Diopside	Diopside	Diopside	Diopside	Diopside	Enstatite	Enstatite	Enstatite	Enstatite	Enstatite	Enstatite	Enstatite	Enstatite	Enstatite	Diopside
Px %Ca	47.34	47.43	48.69	48.28	46.99	46.30	47.60	47.08	2.96	2.84	1.30	1.99	1.15	1.38	2.42	2.27	2.27	46.89
Px %Mg	47.92	48.18	45.86	46.37	46.64	46.88	46.01	46.41	84.66	84.79	86.23	85.37	86.16	85.98	87.69	84.66	85.47	48.07
Px %Fe	4.74	4.39	5.45	5.35	6.36	6.83	6.40	6.51	12.39	12.38	12.47	12.64	12.69	12.64	11.29	12.92	12.26	5.04

Sample Analyse	Po-105a 01										POT-6 01										POT-5 03									
	ol-1	ol-2	ol-3	ol-4	ol-5	ol-6	ol-8	ol-9	ol-10	pl-1	pl-2	pl-3	pl-4	pl-5	pl-6	pl-7	pl-8	pl-9	pl-10	pl-1	pl-2	pl-3	pl-4	pl-5						
SiO ₂	40.43	39.99	40.29	40.16	40.12	40.44	40.20	40.45	40.39	53.93	53.30	53.14	53.66	53.60	53.97	53.87	53.88	53.73	54.01	53.51	53.29	53.55	53.35	53.49						
TiO ₂	bdl	bdl	bdl	bdl	bdl	bdl	bdl	bdl	bdl	0.10	0.12	0.14	0.08	0.10	0.11	0.12	0.08	0.14	0.11	0.09	0.06	0.08	0.07	0.08						
Al ₂ O ₃	bdl	bdl	bdl	bdl	bdl	0.03	bdl	bdl	0.03	28.94	28.63	29.19	29.34	29.11	29.10	29.01	28.98	28.89	29.00	29.15	29.19	29.15	29.24	29.49						
Cr ₂ O ₃	bdl	bdl	bdl	0.04	bdl	bdl	bdl	bdl	bdl	bdl	bdl	bdl	bdl	bdl	bdl	bdl	bdl	bdl	bdl	bdl	bdl	bdl	bdl							
V ₂ O ₅	bdl	bdl	0.03	bdl	bdl	bdl	bdl	bdl	bdl	bdl	bdl	bdl	bdl	bdl	bdl	bdl	bdl	bdl	0.03	bdl	bdl	bdl	bdl							
FeO _T	10.27	10.15	9.84	8.57	10.10	9.35	9.59	9.98	10.02	0.10	0.07	0.12	0.07	0.09	0.08	0.07	0.10	0.04	0.07	0.08	0.09	0.11	0.11							
MnO	0.18	0.14	0.15	0.11	0.14	0.14	0.14	0.13	0.15	bdl	bdl	bdl	bdl	0.02	bdl	bdl	bdl	bdl	bdl	bdl	bdl	bdl	bdl							
MgO	49.60	49.84	49.41	50.77	49.80	50.52	50.23	49.76	49.57	bdl	bdl	bdl	bdl	bdl	bdl	bdl	bdl	bdl	bdl	bdl	bdl	bdl	bdl							
CaO	0.03	0.02	0.03	0.02	bdl	0.02	0.01	0.02	0.03	11.39	12.11	11.66	11.50	11.40	11.27	11.15	11.21	11.10	11.00	11.75	11.81	11.83	11.75							
Na ₂ O	bdl	bdl	bdl	bdl	bdl	bdl	bdl	bdl	bdl	5.46	5.12	5.45	5.33	5.29	5.57	5.64	5.62	5.56	5.60	5.20	5.20	5.34	5.24							
K ₂ O	bdl	bdl	bdl	bdl	bdl	bdl	bdl	bdl	bdl	0.04	0.05	0.04	0.04	0.05	0.05	0.04	0.05	0.04	0.05	0.03	0.03	0.03	0.04							
F	bdl	0.11	bdl	bdl	bdl	bdl	bdl	bdl	bdl	0.22	bdl	bdl	0.12	bdl	bdl	0.27	bdl	0.21	bdl	bdl	0.20	bdl	0.17							
Cl	bdl	bdl	bdl	0.01	bdl	0.01	bdl	bdl	bdl	bdl	0.07	0.02	bdl	bdl	bdl	bdl	bdl	bdl	bdl	bdl	bdl	bdl	bdl							
Total	100.52	100.25	99.74	99.69	100.16	100.52	100.17	100.34	100.19	100.24	99.48	99.78	100.14	99.67	100.16	100.17	99.94	99.71	99.88	99.90	99.88	100.10	99.76	100.29						
O=																														
Si	0.989	0.982	0.991	0.983	0.984	0.985	0.984	0.989	0.990	2.440	2.431	2.415	2.427	2.432	2.438	2.439	2.439	2.441	2.444	2.426	2.421	2.424	2.422	2.419						
Ti	0.004	0.003	0.003	0.002	0.003	0.003	0.003	0.003	0.003	0.003	0.004	0.005	0.003	0.003	0.004	0.004	0.003	0.005	0.004	0.004	0.003	0.002	0.003	0.003						
Al	1.808	1.824	1.811	1.853	1.821	1.835	1.833	1.814	1.810	1.543	1.539	1.564	1.564	1.557	1.549	1.548	1.546	1.547	1.547	1.557	1.563	1.555	1.564	1.572						
Cr				0.001					0.001	0.002																				
V				0.000																										
Fe ²⁺	0.210	0.208	0.202	0.176	0.207	0.190	0.196	0.204	0.205	0.004	0.003	0.005	0.002	0.003	0.003	0.003	0.004	0.001	0.003	0.003	0.004	0.004	0.005	0.004						
Fe ³⁺										0.000	0.000	0.000	0.000	0.000	0.000	0.000	0.000	0.000	0.000	0.000	0.000	0.000	0.000	0.000						
Mn	0.004	0.003	0.003	0.002	0.003	0.003	0.003	0.003	0.003	0.003	0.004	0.005	0.003	0.003	0.004	0.004	0.003	0.005	0.004	0.004	0.003	0.002	0.003	0.003						
Mg	1.808	1.824	1.811	1.853	1.821	1.835	1.833	1.814	1.810	1.543	1.539	1.564	1.564	1.557	1.549	1.548	1.546	1.547	1.547	1.557	1.563	1.555	1.564	1.572						
Ca	0.001	0.000	0.001	0.001	0.001	0.001	0.000	0.000	0.001	0.552	0.592	0.568	0.557	0.554	0.545	0.541	0.544	0.540	0.533	0.571	0.575	0.574	0.571	0.565						
Na										0.479	0.453	0.480	0.467	0.465	0.488	0.495	0.493	0.490	0.491	0.465	0.458	0.469	0.456	0.459						
K										0.003	0.003	0.002	0.002	0.003	0.003	0.002	0.003	0.002	0.003	0.002	0.002	0.002	0.002	0.002						
F		0.009							0.031				0.018			0.039		0.030			0.028			0.025						
Cl				0.000		0.001				0.006	0.002																			
Total	3.011	3.018	3.009	3.016	3.016	3.014	3.016	3.011	3.010	5.025	5.024	5.039	5.023	5.020	5.030	5.032	5.033	5.027	5.026	5.026	5.025	5.031	5.023	5.024						
Classification										Labradorite	Labradorite	Labradorite	Labradorite	Labradorite	Labradorite	Labradorite	Labradorite	Labradorite	Labradorite	Labradorite	Labradorite	Labradorite	Labradorite	Labradorite						
Pl %An										53.41	56.50	54.05	54.28	54.19	52.63	52.10	52.28	52.33	51.91	55.02	55.57	54.94	55.50	55.03						
Ol %Fo	0.90	0.90	0.90	0.91	0.90	0.91	0.90	0.90	0.90																					

Appendix 6. Major element composition of chromite from Potosí.

Sample	POT-1_01					POT-1_03					POT-1_05					Po-105a_01					Po-105a_03										
	chr-1	chr-2	chr-3	chr-4	chr-5	chr-1	chr-2	chr-3	chr-4	chr-5	chr-1	chr-2	chr-3	chr-4	chr-5	chr-1	chr-2	chr-3	chr-4	chr-5	chr-1	chr-2	chr-3	chr-4	chr-5	chr-1	chr-2	chr-3	chr-4	chr-5	
SiO ₂	2.69	2.57	2.24	2.53	2.50	1.67	2.09	1.93	2.21	1.91	0.28	0.03	2.11	2.16	2.21	2.23	2.55	2.60	2.91	3.07	3.10	bdl	bdl	bdl	bdl	bdl	4.29	4.17	4.17	4.26	4.34
TiO ₂	0.72	0.74	0.73	0.69	0.68	0.62	0.69	0.67	0.65	0.66	0.68	0.70	0.71	0.69	0.73	0.71	0.72	0.71	0.72	0.71	0.73	0.76	0.77	0.77	0.76	0.75	0.77	0.77	0.76	0.75	0.77
Al ₂ O ₃	10.66	10.88	11.00	10.81	10.85	10.70	10.79	10.94	10.82	10.90	10.85	11.19	11.19	11.12	10.82	13.01	13.05	13.05	12.97	13.05	13.10	12.51	12.39	12.59	12.33	12.27	12.51	12.39	12.59	12.33	12.27
Cr ₂ O ₃	31.73	32.03	32.98	32.42	33.29	37.63	36.25	37.00	35.26	36.97	33.66	34.10	36.07	34.73	33.97	37.14	36.99	36.13	35.56	35.61	35.61	31.39	31.95	31.67	31.52	31.59	31.39	31.95	31.67	31.52	31.59
FeO _T	44.74	44.64	43.72	43.61	43.21	39.43	41.21	40.83	41.92	40.06	43.47	42.51	41.29	42.08	43.08	36.87	36.92	37.50	37.91	37.81	37.81	40.27	41.06	40.48	40.56	40.81	40.27	41.06	40.48	40.56	40.81
MnO	0.42	0.45	0.44	0.45	0.42	0.46	0.47	0.44	0.43	0.43	0.41	0.46	0.44	0.42	0.46	0.42	0.37	0.41	0.37	0.35	0.35	0.39	0.40	0.42	0.36	0.37	0.39	0.40	0.42	0.36	0.37
MgO	6.61	6.63	6.61	6.84	6.87	6.73	6.60	6.82	6.79	6.93	6.82	7.03	7.11	6.90	6.83	8.16	8.38	8.17	8.16	8.38	8.18	8.34	8.29	8.20	8.36	8.18	8.34	8.29	8.20	8.36	8.18
CoO	0.09	0.10	0.08	0.14	0.10	0.06	0.08	0.07	0.08	0.11	0.08	0.08	0.06	0.09	0.08	0.08	0.08	0.08	0.08	0.09	0.04	0.10	0.08	0.11	0.07	0.07	0.10	0.08	0.11	0.07	0.07
NiO	0.12	0.12	0.06	0.11	0.11	0.10	0.12	0.11	0.12	0.07	0.15	0.16	0.13	0.14	0.12	0.11	0.10	0.15	0.09	0.10	0.10	0.12	0.14	0.14	0.14	0.18	0.12	0.14	0.14	0.14	0.18
ZnO	0.08	0.06	0.06	0.09	0.10	0.08	0.07	0.10	0.05	0.08	0.07	0.14	0.09	0.08	0.12	0.11	0.08	0.10	0.13	0.11	0.11	0.08	0.05	0.05	0.12	0.07	0.08	0.05	0.05	0.12	0.07
Total O=4	97.85	98.24	97.92	97.76	98.14	97.76	98.37	98.91	98.33	98.35	98.34	98.52	99.23	98.46	98.43	99.16	99.32	99.11	99.16	99.36	98.26	99.29	98.58	98.46	98.64	98.26	99.29	98.58	98.46	98.64	
Sample	chr-1	chr-2	chr-3	chr-4	chr-5	chr-1	chr-2	chr-3	chr-4	chr-5	chr-1	chr-2	chr-3	chr-4	chr-5	chr-1	chr-2	chr-3	chr-4	chr-5	chr-1	chr-2	chr-3	chr-4	chr-5	chr-1	chr-2	chr-3	chr-4	chr-5	
Cr _T	0.855	0.859	0.887	0.873	0.893	1.018	0.973	0.986	0.945	0.992	0.901	0.909	0.956	0.928	0.909	0.971	0.964	0.945	0.930	0.928	0.928	0.827	0.835	0.833	0.830	0.831	0.827	0.835	0.833	0.830	0.831
Ti	0.069	0.066	0.057	0.065	0.064	0.043	0.053	0.049	0.056	0.049	0.054	0.055	0.054	0.056	0.057	0.063	0.064	0.072	0.076	0.077	0.077	0.108	0.104	0.104	0.107	0.109	0.108	0.104	0.104	0.107	0.109
V	0.012	0.012	0.012	0.011	0.011	0.010	0.011	0.011	0.011	0.011	0.011	0.011	0.011	0.011	0.012	0.011	0.011	0.011	0.011	0.012	0.012	0.012	0.012	0.012	0.012	0.012	0.012	0.012	0.012	0.012	0.012
Al	0.428	0.435	0.441	0.434	0.434	0.432	0.432	0.435	0.433	0.436	0.433	0.445	0.442	0.443	0.432	0.507	0.507	0.506	0.509	0.509	0.492	0.483	0.494	0.484	0.482	0.492	0.483	0.494	0.484	0.482	
Fe ³⁺	0.554	0.549	0.532	0.539	0.522	0.442	0.464	0.458	0.487	0.451	0.534	0.513	0.470	0.493	0.521	0.371	0.375	0.380	0.384	0.384	0.384	0.440	0.449	0.439	0.448	0.444	0.440	0.449	0.439	0.448	0.444
Fe ²⁺	0.722	0.718	0.712	0.703	0.704	0.687	0.706	0.694	0.702	0.686	0.697	0.686	0.687	0.696	0.699	0.649	0.643	0.658	0.664	0.657	0.657	0.683	0.686	0.687	0.681	0.693	0.683	0.686	0.687	0.681	0.693
Mn	0.012	0.013	0.013	0.013	0.012	0.013	0.013	0.013	0.012	0.012	0.012	0.013	0.012	0.012	0.013	0.012	0.010	0.011	0.011	0.010	0.010	0.010	0.011	0.011	0.011	0.010	0.011	0.011	0.011	0.010	0.010
Mg	0.336	0.335	0.335	0.347	0.347	0.343	0.334	0.343	0.343	0.351	0.344	0.353	0.355	0.347	0.345	0.402	0.412	0.403	0.402	0.411	0.411	0.414	0.408	0.406	0.415	0.406	0.414	0.408	0.406	0.415	0.406
Co	0.002	0.003	0.002	0.004	0.003	0.002	0.002	0.002	0.002	0.003	0.002	0.002	0.002	0.003	0.002	0.002	0.002	0.002	0.002	0.001	0.001	0.003	0.002	0.003	0.002	0.002	0.003	0.002	0.003	0.002	0.002
Ni	0.003	0.003	0.002	0.003	0.003	0.003	0.003	0.003	0.003	0.002	0.004	0.004	0.003	0.004	0.003	0.003	0.003	0.003	0.004	0.003	0.003	0.003	0.004	0.004	0.004	0.005	0.003	0.004	0.004	0.004	0.005
Zn	0.002	0.001	0.002	0.002	0.003	0.002	0.002	0.002	0.003	0.002	0.002	0.003	0.002	0.002	0.003	0.003	0.003	0.002	0.002	0.003	0.003	0.002	0.001	0.001	0.001	0.002	0.002	0.001	0.001	0.001	0.002
divcat	1.077	1.074	1.066	1.073	1.071	1.050	1.061	1.056	1.064	1.056	1.061	1.063	1.062	1.064	1.065	1.071	1.072	1.080	1.084	1.085	1.085	1.116	1.112	1.113	1.115	1.117	1.116	1.112	1.113	1.115	1.117
trivcat	1.837	1.843	1.860	1.846	1.849	1.892	1.869	1.879	1.865	1.880	1.869	1.867	1.868	1.864	1.861	1.849	1.847	1.831	1.823	1.821	1.821	1.759	1.767	1.766	1.761	1.757	1.759	1.767	1.766	1.761	1.757
totcat	2.995	2.995	2.995	2.995	2.995	2.996	2.995	2.995	2.995	2.995	2.995	2.995	2.995	2.995	2.995	2.995	2.995	2.995	2.995	2.995	2.995	2.995	2.995	2.995	2.995	2.995	2.995	2.995	2.995	2.995	2.995
Mg#	0.32	0.32	0.32	0.33	0.33	0.33	0.32	0.33	0.33	0.34	0.33	0.34	0.34	0.33	0.33	0.38	0.39	0.38	0.38	0.38	0.38	0.38	0.37	0.37	0.378	0.369	0.38	0.37	0.37	0.378	0.369
Cr#	0.67	0.66	0.67	0.67	0.67	0.70	0.69	0.69	0.69	0.69	0.68	0.67	0.68	0.68	0.68	0.66	0.66	0.65	0.65	0.65	0.65	0.63	0.63	0.63	0.632	0.633	0.63	0.63	0.63	0.632	0.633
Fe ³⁺ #	0.30	0.30	0.29	0.29	0.28	0.23	0.25	0.24	0.26	0.24	0.29	0.27	0.25	0.26	0.28	0.20	0.20	0.21	0.21	0.21	0.21	0.25	0.25	0.25	0.254	0.253	0.25	0.25	0.25	0.254	0.253

Sample Analyse	POT-5 03					POT-5 04				
	chr-1	chr-2	chr-3	chr-4	chr-5	chr-1	chr-2	chr-3	chr-4	chr-5
SiO ₂	bdl	bdl	0.03	bdl	bdl	bdl	0.03	bdl		
TiO ₂	1.30	1.03	1.39	1.17	1.19	1.73	1.94	2.05		
V ₂ O ₅	0.62	0.64	0.63	0.58	0.63	0.6	0.59	0.63		
Al ₂ O ₃	12.55	12.51	12.82	12.41	12.44	14	13.5	13.7		
Cr ₂ O ₃	38.62	39.65	38.26	38.81	38.42	34.2	34.1	33.9		
FeO _t	37.68	37.38	37.86	36.80	37.51	38.7	39.4	39		
MnO	0.44	0.43	0.45	0.42	0.48	0.43	0.4	0.4		
MgO	7.03	6.85	6.74	7.01	6.98	7.49	7.58	7.43		
CoO	0.12	0.09	0.06	0.09	0.08	0.11	0.09	0.09		
NiO	0.05	0.03	0.06	0.05	0.08	0.13	0.13	0.09		
ZnO	0.16	0.14	0.13	0.10	0.09	0.05	0.09	0.07		
Total	98.57	98.74	98.43	97.45	97.90	97.3	97.9	97.4		
O=4										
Sample	chr-1	chr-2	chr-3	chr-4	chr-5	chr-1	chr-2	chr-3		
Cr	1.025	1.053	1.018	1.042	1.027	0.908	0.903	0.902		
Ti	0.033	0.026	0.035	0.030	0.030	0.044	0.049	0.052		
V	0.010	0.010	0.010	0.009	0.010	0.010	0.010	0.010		
Al	0.497	0.495	0.509	0.497	0.496	0.554	0.532	0.544		
Fe ³⁺	0.391	0.378	0.381	0.382	0.395	0.431	0.447	0.429		
Fe ²⁺	0.667	0.672	0.685	0.663	0.665	0.655	0.658	0.668		
Mn	0.013	0.012	0.013	0.012	0.014	0.012	0.011	0.011		
Mg	0.352	0.343	0.338	0.355	0.352	0.375	0.378	0.372		
Co	0.003	0.002	0.002	0.003	0.002	0.003	0.002	0.003		
Ni	0.001	0.001	0.002	0.001	0.002	0.003	0.003	0.003		
Zn	0.004	0.003	0.003	0.003	0.002	0.001	0.002	0.002		
divcat	1.040	1.033	1.042	1.036	1.037	1.050	1.055	1.059		
trivcat	1.913	1.926	1.908	1.920	1.918	1.892	1.882	1.875		
totcat	2.996	2.995	2.996	2.996	2.996	2.996	2.996	2.996		
Mg#	0.345	0.34	0.331	0.35	0.35	0.36	0.37	0.36		
Cr#	0.674	0.68	0.667	0.68	0.67	0.62	0.63	0.62		
Fe ³⁺ #	0.204	0.2	0.2	0.2	0.21	0.23	0.24	0.23		

Sample	OTROS											OTROS										
	ilm-1	ilm-2	ilm-3	ilm-4	ilm-5	ilm-6	ilm-7	ilm-8	ilm-9	ilm-10	ilm-11	ilm-12	ilm-13	ilm-14	ilm-15	ilm-16	ilm-17	ilm-18	ilm-19	ilm-20	ilm-21	
SiO ₂	bd	bd	bd	bd	bd	bd	bd	bd	bd	bd	bd	bd	bd	bd	bd	bd	bd	bd	bd	bd	bd	
Al ₂ O ₃	0.19	0.15	0.13	0.11	0.15	0.07	0.11	0.12	0.08	0.15	0.16	0.16	0.16	0.16	0.16	0.16	0.16	0.16	0.16	0.16	0.16	
Cr ₂ O ₃	0.24	0.30	0.25	0.26	0.26	0.27	0.27	0.29	0.24	0.27	0.30	0.30	0.30	0.30	0.30	0.30	0.30	0.30	0.30	0.30	0.30	
TiO ₂	53.16	54.30	54.29	54.23	54.18	54.31	54.31	54.28	54.04	54.11	54.27	54.27	54.27	54.27	54.27	54.27	54.27	54.27	54.27	54.27	54.27	
MgO	7.07	9.54	9.94	9.76	9.54	9.66	9.47	9.43	9.61	9.49	9.43	9.43	9.43	9.43	9.43	9.43	9.43	9.43	9.43	9.43	9.43	
Na ₂ O	bd	bd	bd	bd	bd	bd	bd	bd	bd	bd	bd	bd	bd	bd	bd	bd	bd	bd	bd	bd	bd	
V ₂ O ₅	bd	bd	bd	bd	bd	bd	bd	bd	bd	bd	bd	bd	bd	bd	bd	bd	bd	bd	bd	bd	bd	
MnO	0.76	0.56	0.56	0.50	0.62	0.61	0.63	0.58	0.55	0.47	0.61	0.61	0.61	0.61	0.61	0.61	0.61	0.61	0.61	0.61	0.61	
FeO ₁	34.68	31.51	30.75	31.06	31.31	31.17	31.53	31.64	31.08	31.49	31.64	31.64	31.64	31.64	31.64	31.64	31.64	31.64	31.64	31.64	31.64	
NiO	bd	bd	bd	bd	bd	bd	bd	bd	bd	bd	bd	bd	bd	bd	bd	bd	bd	bd	bd	bd	bd	
ZnO	bd	bd	bd	bd	bd	bd	bd	bd	bd	bd	bd	bd	bd	bd	bd	bd	bd	bd	bd	bd	bd	
CaO	0.11	0.03	0.03	0.03	0.00	0.00	0.00	0.00	0.00	0.01	0.01	0.01	0.01	0.01	0.01	0.01	0.01	0.01	0.01	0.01	0.01	
Total	96.2	96.4	95.9	95.9	96.1	96.1	96.3	96.3	95.6	96.0	96.4	96.4	96.4	96.4	96.4	96.4	96.4	96.4	96.4	96.4	96.4	
FeO	34.3	31.2	30.5	30.9	31.1	31.0	31.3	31.4	30.9	31.2	31.4	31.4	31.4	31.4	31.4	31.4	31.4	31.4	31.4	31.4	31.4	
Fe ₂ O ₃	0.4	0.3	0.3	0.2	0.3	0.2	0.2	0.3	0.2	0.3	0.3	0.3	0.3	0.3	0.3	0.3	0.3	0.3	0.3	0.3	0.3	
Total Fe	96.2	96.4	96.0	95.9	96.1	96.1	96.3	96.4	95.6	96.0	96.4	96.4	96.4	96.4	96.4	96.4	96.4	96.4	96.4	96.4	96.4	
Calc																						

Sample	OTROS											OTROS										
	ilm-1	ilm-2	ilm-3	ilm-4	ilm-5	ilm-6	ilm-7	ilm-8	ilm-9	ilm-10	ilm-11	ilm-12	ilm-13	ilm-14	ilm-15	ilm-16	ilm-17	ilm-18	ilm-19	ilm-20	ilm-21	
Si	0.000	0.002	0.000	0.000	0.000	0.000	0.001	0.001	0.001	0.001	0.001	0.001	0.001	0.001	0.001	0.001	0.001	0.001	0.001	0.001	0.001	
Al	0.006	0.004	0.004	0.003	0.004	0.002	0.003	0.003	0.002	0.004	0.005	0.005	0.005	0.005	0.005	0.005	0.005	0.005	0.005	0.005	0.005	
Cr	0.005	0.006	0.005	0.005	0.005	0.005	0.005	0.006	0.005	0.005	0.006	0.006	0.006	0.006	0.006	0.006	0.006	0.006	0.006	0.006	0.006	
Ti	0.991	0.992	0.993	0.994	0.993	0.995	0.994	0.993	0.995	0.993	0.992	0.992	0.992	0.992	0.992	0.992	0.992	0.992	0.992	0.992	0.992	
Mg	0.261	0.345	0.360	0.355	0.347	0.351	0.343	0.342	0.351	0.345	0.342	0.342	0.342	0.342	0.342	0.342	0.342	0.342	0.342	0.342	0.342	
Na																						
V																						
Mn	0.016	0.011	0.012	0.010	0.013	0.013	0.013	0.012	0.011	0.010	0.013	0.013	0.013	0.013	0.013	0.013	0.013	0.013	0.013	0.013	0.013	
Fe ²⁺	0.711	0.634	0.620	0.629	0.633	0.631	0.637	0.639	0.633	0.637	0.638	0.638	0.638	0.638	0.638	0.638	0.638	0.638	0.638	0.638	0.638	
Fe ³⁺	0.008	0.006	0.005	0.004	0.005	0.004	0.004	0.005	0.004	0.005	0.006	0.006	0.006	0.006	0.006	0.006	0.006	0.006	0.006	0.006	0.006	
Ni																						
Zn	0.003	0.001	0.001	0.000	0.000	0.000	0.000	0.000	0.000	0.000	0.000	0.000	0.000	0.000	0.000	0.000	0.000	0.000	0.000	0.000	0.000	
Ca	2.000	2.000	2.000	2.000	2.000	2.000	2.000	2.000	2.000	2.000	2.000	2.000	2.000	2.000	2.000	2.000	2.000	2.000	2.000	2.000	2.000	
totcat	71.66	63.80	62.36	63.15	63.64	63.35	64.01	64.22	63.49	64.07	64.11	64.11	64.11	64.11	64.11	64.11	64.11	64.11	64.11	64.11	64.11	
Fe ₂ O ₃	26.32	34.75	36.22	35.60	34.83	35.21	34.48	34.35	35.19	34.70	34.35	34.35	34.35	34.35	34.35	34.35	34.35	34.35	34.35	34.35	34.35	
FeO ₃	0.41	0.30	0.26	0.20	0.24	0.18	0.21	0.23	0.18	0.26	0.28	0.28	0.28	0.28	0.28	0.28	0.28	0.28	0.28	0.28	0.28	

Appendix 8. Major element composition of apatite and baddeleyite from Potosí.

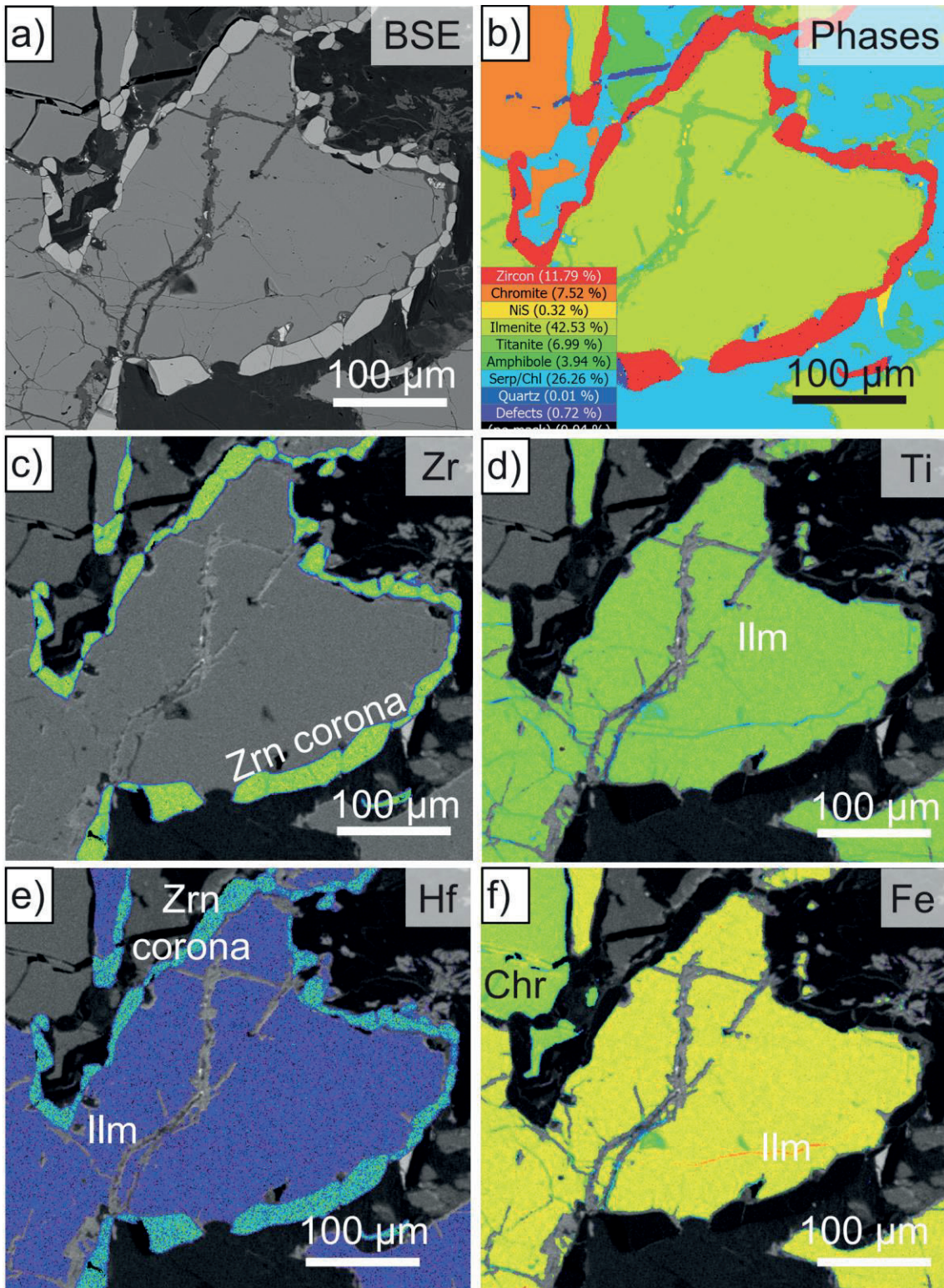
Mineral Sample	Apatite														
	#1	#2	#3	#4	#5	#6	#7	#8	#9	#10	#11	#12	#13	#14	#15
P ₂ O ₅	41.19	40.55	42.25	41.99	40.90	41.89	41.92	42.30	41.14	42.03	42.00	41.85	39.80	41.73	42.06
SiO ₂	0.22	0.28	0.20	0.26	0.34	0.34	0.23	0.21	0.57	0.26	0.27	0.29	2.48	0.28	0.20
Al ₂ O ₃	-	-	-	-	-	-	-	-	-	-	-	-	-	-	-
TiO ₂	-	-	-	-	-	-	-	-	-	-	-	-	-	-	-
ZrO ₂	-	-	-	-	-	-	-	-	-	-	-	-	-	-	-
HfO ₂	-	-	-	-	-	-	-	-	-	-	-	-	-	-	-
Cr ₂ O ₃	-	-	-	-	-	-	-	-	-	-	-	-	-	-	-
Nb ₂ O ₅	-	-	-	-	-	-	-	-	-	-	-	-	-	-	-
Ce ₂ O ₃	0.55	0.63	0.23	0.18	0.18	0.20	0.10	0.22	0.27	0.31	0.24	0.22	0.19	0.26	0.15
Nd ₂ O ₃	-	-	-	-	-	-	-	-	-	-	-	-	-	-	-
U ₂ O ₅	-	-	-	-	-	-	-	-	-	-	-	-	-	-	-
MgO	-	-	-	-	-	-	-	-	-	-	-	-	-	-	-
CaO	54.02	54.56	55.48	55.45	55.84	55.49	55.81	55.27	55.53	55.29	55.29	55.45	52.00	55.81	55.65
MnO	0.04	0.03	0.01	0.03	bdl	bdl	0.06	bdl	bdl	bdl	0.03	bdl	0.11	bdl	0.01
FeO†	0.00	0.08	0.11	0.05	0.07	0.07	0.07	0.13	0.16	0.15	0.18	0.10	0.91	0.10	0.00
Na ₂ O	0.43	0.40	0.12	0.14	0.13	0.11	0.11	0.13	0.12	0.13	0.11	0.12	0.11	0.11	0.17
F	4.40	4.28	2.06	2.28	2.20	2.43	2.17	2.25	1.97	2.19	2.15	2.13	2.01	2.14	2.29
Cl	0.47	0.46	0.52	0.58	0.56	0.57	0.57	0.53	0.55	0.72	0.77	0.78	0.75	0.60	0.56
Total	101.31	101.27	100.98	100.97	100.21	101.10	101.03	101.04	100.30	101.09	101.04	100.94	98.36	101.03	101.09
O=F,Cl	1.96	1.91	0.98	1.09	1.05	1.15	1.04	1.07	0.95	1.09	1.08	1.07	1.02	1.04	1.09
Total	99.35	99.36	100.00	99.87	99.15	99.94	99.99	99.98	99.35	100.00	99.96	99.87	97.34	99.99	100.00
Sample	#1	#2	#3	#4	#5	#6	#7	#8	#9	#10	#11	#12	#13	#14	#15
P	5.676	5.616	5.833	5.801	5.721	5.780	5.793	5.832	5.740	5.806	5.805	5.793	5.624	5.777	5.804
Si	0.035	0.045	0.032	0.042	0.056	0.055	0.037	0.035	0.095	0.042	0.045	0.047	0.415	0.045	0.032
Ti	-	-	-	-	-	-	-	-	-	-	-	-	-	-	-
Zr	-	-	-	-	-	-	-	-	-	-	-	-	-	-	-
Hf	-	-	-	-	-	-	-	-	-	-	-	-	-	-	-
Cr	-	-	-	-	-	-	-	-	-	-	-	-	-	-	-
Ce	0.033	0.038	0.014	0.011	0.011	0.012	0.006	0.013	0.016	0.019	0.014	0.013	0.011	0.016	0.009
Mg	-	-	-	-	-	-	-	-	-	-	-	-	-	-	-
Ca	9.420	9.563	9.693	9.695	9.885	9.689	9.761	9.642	9.805	9.667	9.671	9.712	9.298	9.776	9.718
Mn	0.005	0.005	0.002	0.005	0.000	0.000	0.008	0.000	0.000	0.000	0.004	0.000	0.015	0.001	0.001
Fet	0.000	0.011	0.015	0.007	0.009	0.009	0.009	0.018	0.022	0.021	0.024	0.014	0.127	0.013	0.000
Na	0.134	0.128	0.039	0.043	0.043	0.036	0.036	0.041	0.037	0.041	0.035	0.039	0.034	0.034	0.053
F	2.264	2.216	1.060	1.179	1.151	1.253	1.118	1.157	1.027	1.132	1.110	1.102	1.062	1.108	1.180
Cl	0.130	0.126	0.144	0.159	0.156	0.158	0.157	0.147	0.153	0.200	0.212	0.216	0.213	0.165	0.155
OH	0.000	0.000	0.000	0.000	0.000	0.000	0.000	0.000	0.000	0.000	0.000	0.000	0.000	0.000	0.000
Total	17.698	17.747	16.832	16.941	17.032	16.992	16.925	16.884	16.896	16.927	16.921	16.936	16.799	16.936	16.951

Mineral Sample	Baddeleyite															
	#1	#2	#3	#4	#5	#6	#7	#8	#9	#10	#11	#12	#13	#14	#15	#16
P ₂ O ₅	0.02	0.03	0.25	0.19	0.33	0.33	0.33	0.00	0.04	0.00	0.02	2.20	0.04	0.43	0.00	0.03
SiO ₂	bdl	bdl	bdl	bdl	bdl	bdl	bdl	bdl	bdl	bdl	bdl	bdl	0.39	0.02	0.01	bdl
Al ₂ O ₃	1.51	1.55	1.50	1.77	1.54	1.69	1.57	1.32	1.31	1.08	1.19	2.55	1.64	1.60	0.66	0.58
TiO ₂	96.75	96.71	95.81	95.30	95.01	95.29	95.13	96.61	97.20	97.21	96.87	88.10	95.81	89.89	97.57	97.45
HfO ₂	1.59	1.61	1.58	1.52	1.54	1.61	1.55	1.85	1.84	1.81	1.96	1.69	1.66	1.72	1.83	1.77
Cr ₂ O ₃	0.35	0.33	0.35	0.34	0.35	0.36	0.34	0.24	0.21	0.25	0.21	0.09	0.09	0.10	0.13	0.13
Nb ₂ O ₅	bdl	0.02	0.02	0.03	bdl	0.01	0.00	0.00	bdl	bdl	0.01	0.01	0.01	0.01	0.06	bdl
Ce ₂ O ₃	-	-	-	-	-	-	-	-	-	-	-	-	-	-	-	-
Nd ₂ O ₃	bdl	0.05	0.03	0.02	0.02	0.06	0.01	bdl	0.02	0.03	bdl	0.03	0.00	0.02	0.02	bdl
U ₂ O ₃	0.01	0.07	bdl	bdl	bdl	0.05	bdl	bdl	0.06	bdl	bdl	bdl	0.05	0.05	bdl	0.01
MgO	0.01	0.03	0.03	0.09	0.04	0.03	0.04	0.02	0.03	0.03	0.03	1.94	0.05	0.07	0.04	0.03
CaO	0.01	0.02	bdl	bdl	bdl	0.01	bdl	bdl	0.03	0.02	bdl	0.35	bdl	0.02	0.01	0.00
MnO	0.03	0.01	bdl	0.03	0.01	0.01	0.02	bdl	0.03	0.01	0.01	0.03	0.02	0.01	bdl	0.02
FeO _t	1.09	1.07	1.09	1.21	1.13	1.06	1.10	0.79	0.93	0.92	1.02	1.51	0.58	0.76	0.56	0.46
Na ₂ O	-	-	-	-	-	-	-	-	-	-	-	-	-	-	-	-
F	-	-	-	-	-	-	-	-	-	-	-	-	-	-	-	-
Cl	-	-	-	-	-	-	-	-	-	-	-	-	-	-	-	-
Total	101.37	101.49	100.65	100.49	99.97	100.51	100.09	100.82	101.69	101.36	101.31	98.89	99.97	94.67	100.89	100.49
O=F,Cl	-	-	-	-	-	-	-	-	-	-	-	-	-	-	-	-
Total	-	-	-	-	-	-	-	-	-	-	-	-	-	-	-	-
Sample	#1	#2	#3	#4	#5	#6	#7	#8	#9	#10	#11	#12	#13	#14	#15	#16
P	0.000	0.001	0.005	0.004	0.007	0.007	0.007	0.000	0.001	0.000	0.000	0.044	0.001	0.009	0.000	0.001
Si	0.000	0.000	0.000	0.000	0.000	0.000	0.000	0.000	0.000	0.000	0.000	0.009	0.001	0.000	0.000	0.000
Al	0.023	0.023	0.023	0.027	0.024	0.026	0.024	0.020	0.020	0.016	0.018	0.038	0.025	0.026	0.010	0.009
Ti	0.954	0.952	0.949	0.944	0.946	0.944	0.946	0.959	0.957	0.961	0.958	0.855	0.855	0.944	0.971	0.974
Zr	0.009	0.009	0.009	0.009	0.009	0.009	0.009	0.011	0.011	0.010	0.011	0.010	0.010	0.011	0.011	0.010
Hf	0.006	0.005	0.006	0.005	0.006	0.006	0.006	0.004	0.003	0.004	0.003	0.001	0.001	0.002	0.002	0.002
Ce	-	-	-	-	-	-	-	-	-	-	-	-	-	-	-	-
Mg	0.000	0.001	0.001	0.003	0.001	0.001	0.001	0.000	0.001	0.001	0.001	0.058	0.001	0.002	0.001	0.001
Ca	0.000	0.000	0.000	0.000	0.000	0.000	0.000	0.000	0.001	0.000	0.000	0.007	0.000	0.001	0.000	0.000
Mn	0.001	0.000	0.000	0.000	0.000	0.000	0.000	0.000	0.000	0.000	0.000	0.000	0.000	0.000	0.000	0.000
Fet	-	-	-	-	-	-	-	-	-	-	-	-	-	-	-	-
Na	-	-	-	-	-	-	-	-	-	-	-	-	-	-	-	-
F	-	-	-	-	-	-	-	-	-	-	-	-	-	-	-	-
Cl	-	-	-	-	-	-	-	-	-	-	-	-	-	-	-	-
OH	-	-	-	-	-	-	-	-	-	-	-	-	-	-	-	-
Total	0.993	0.991	0.993	0.992	0.993	0.993	0.993	0.994	0.994	0.992	0.991	1.022	0.996	0.995	0.995	0.997

Appendix 9. Composition of zirconolite from Potosí.

Zirconolite																	
Analyse	#1	#2	#3	#4	#5	#6	#7	#8	#9	#10	#11	#12	#13	#14	#15	#16	#17
Nb ₂ O ₅	0.07	0.09	0.09	0.04	0.08	0.02	0.03	0.07	0.04	0.02	0.01	0.00	0.04	0.03	0.03	0.01	0.02
SiO ₂	0.08	0.31	0.16	0.50	0.11	0.26	0.53	0.34	0.12	0.26	0.76	0.61	0.50	0.38	0.70	1.12	0.90
TiO ₂	31.72	31.80	31.91	31.38	31.59	31.79	31.59	31.74	31.54	34.68	33.95	34.70	34.93	35.21	34.14	35.19	34.00
ZrO ₂	31.66	32.04	32.24	31.83	32.21	32.11	32.31	32.41	31.64	36.64	35.87	35.35	35.01	33.86	34.14	32.17	35.08
HfO ₂	0.95	0.94	0.95	0.95	1.01	0.87	0.83	0.85	0.93	0.50	0.52	0.59	0.51	0.64	0.61	0.64	0.57
ThO ₂	bdl	bdl	bdl	bdl	bdl	bdl	0.06	bdl	bdl	bdl	bdl	bdl	bdl	bdl	bdl	bdl	bdl
UO ₂	bdl	bdl	bdl	bdl	bdl	bdl	0.05	bdl	0.05	0.08	bdl	bdl	0.05	0.05	bdl	bdl	bdl
Al ₂ O ₃	0.49	0.50	0.47	0.50	0.47	0.54	0.53	0.57	0.50	0.58	0.64	0.60	0.53	0.53	0.48	0.57	0.56
Sc ₂ O ₃	bdl	bdl	bdl	bdl	bdl	bdl	bdl	bdl	bdl	bdl	bdl	bdl	bdl	bdl	bdl	bdl	bdl
Cr ₂ O ₃	0.68	0.51	0.48	0.49	0.46	0.45	0.45	0.49	0.62	0.71	0.75	0.74	0.75	0.78	0.61	0.70	0.69
Y ₂ O ₃	10.77	10.73	10.89	10.93	11.06	10.40	10.38	10.13	10.76	6.54	6.45	6.45	6.20	6.86	7.01	6.88	6.54
La ₂ O ₃	bdl	0.04	bdl	0.04	bdl	0.03	0.04	bdl	0.05	bdl	bdl	0.03	bdl	0.04	0.06	0.06	bdl
Ce ₂ O ₃	0.65	0.68	0.69	0.68	0.66	0.66	0.65	0.65	0.67	0.54	0.51	0.63	0.72	0.70	0.74	0.69	0.62
Pr ₂ O ₃	0.15	0.17	0.18	0.14	0.15	0.17	0.17	0.12	0.16	0.11	0.10	0.12	0.16	0.19	0.17	0.17	0.11
Nd ₂ O ₃	1.30	1.38	1.38	1.35	1.43	1.42	1.34	1.30	1.34	0.74	0.91	0.99	1.17	1.20	1.42	1.22	1.04
Sm ₂ O ₃	1.07	1.08	1.07	1.08	1.06	1.04	1.01	0.99	1.04	0.60	0.57	0.68	0.75	0.87	0.82	0.80	0.66
Eu ₂ O ₃	0.16	0.18	0.24	0.18	0.21	0.18	0.20	0.16	0.16	0.00	0.12	0.13	0.10	0.14	0.15	0.13	0.23
Gd ₂ O ₃	1.46	1.45	1.39	1.46	1.50	1.39	1.41	1.33	1.42	0.80	0.80	0.92	0.92	1.04	1.16	1.04	0.96
Tb ₂ O ₃	0.30	0.33	0.31	0.28	0.29	0.25	0.25	0.27	0.25	0.07	0.12	0.13	0.10	0.16	0.18	0.18	0.13
Dy ₂ O ₃	2.07	2.03	2.11	2.01	1.96	1.99	2.02	1.95	2.01	1.05	1.08	1.17	1.09	1.18	1.22	1.23	1.10
Ho ₂ O ₃	0.40	0.43	0.47	0.41	0.35	0.42	0.42	0.39	0.40	0.32	0.22	0.22	0.18	0.27	0.19	0.25	0.17
Er ₂ O ₃	1.12	1.09	1.14	1.07	1.11	1.05	1.10	1.09	1.12	0.71	0.63	0.65	0.52	0.65	0.65	0.65	0.56
Tm ₂ O ₃	0.22	0.23	0.21	0.18	0.19	0.22	0.23	0.19	0.19	0.18	0.15	0.13	0.12	0.11	0.15	0.15	0.09
Yb ₂ O ₃	0.71	0.73	0.73	0.72	0.68	0.75	0.69	0.67	0.72	0.74	0.69	0.65	0.52	0.45	0.56	0.51	0.50
Lu ₂ O ₃	0.08	0.10	0.12	0.14	0.11	0.05	0.09	0.11	0.09	0.07	0.11	0.06	0.08	0.11	0.04	0.09	0.06
REE ₂ O ₃	9.71	9.92	10.07	9.74	9.71	9.61	9.63	9.25	9.59	5.92	6.01	6.50	6.46	7.11	7.51	7.17	6.21
MgO	0.51	0.58	0.53	0.71	0.55	0.61	0.52	0.51	0.52	0.42	0.76	0.57	0.39	0.41	0.38	0.87	0.57
CaO	5.51	5.55	5.52	5.43	5.41	5.62	5.62	5.85	5.58	8.74	8.47	8.63	8.69	8.16	8.26	7.58	8.38
MnO	0.06	0.08	0.06	0.06	0.06	0.07	0.07	0.05	0.05	0.06	0.04	0.06	0.07	0.07	0.05	0.07	bdl
FeO	6.57	6.50	6.50	6.60	6.64	6.49	6.39	6.28	6.50	6.07	6.00	6.14	6.22	6.82	5.98	7.52	6.04
Total	98.85	99.59	99.89	99.22	99.44	98.93	99.01	98.59	98.46	101.26	100.29	100.99	100.37	100.93	99.92	100.53	99.63
O=7																	
Analyse	#1	#2	#3	#4	#5	#6	#7	#8	#9	#10	#11	#12	#13	#14	#15	#16	#17
Nb	0.002	0.003	0.003	0.001	0.002	0.001	0.001	0.002	0.001	0.001	0.000	0.000	0.001	0.001	0.001	0.000	0.001
Si	0.005	0.020	0.010	0.032	0.007	0.017	0.035	0.022	0.008	0.016	0.047	0.038	0.031	0.024	0.044	0.069	0.056
Ti	1.564	1.554	1.559	1.539	1.552	1.560	1.548	1.558	1.561	1.604	1.578	1.605	1.626	1.639	1.609	1.632	1.592
Zr	1.012	1.015	1.022	1.012	1.026	1.022	1.027	1.031	1.015	1.099	1.081	1.061	1.057	1.022	1.043	0.967	1.065
Hf	0.018	0.018	0.018	0.018	0.019	0.016	0.015	0.016	0.017	0.009	0.009	0.010	0.009	0.011	0.011	0.011	0.010
Th							0.001										
U							0.001		0.001	0.001			0.001	0.001			
Al	0.038	0.039	0.036	0.038	0.036	0.041	0.041	0.044	0.039	0.042	0.047	0.044	0.039	0.039	0.036	0.041	0.041
Cr	0.035	0.026	0.024	0.025	0.024	0.023	0.023	0.025	0.032	0.034	0.037	0.036	0.037	0.038	0.030	0.034	0.034
Y	0.376	0.371	0.377	0.379	0.384	0.361	0.360	0.352	0.377	0.214	0.212	0.211	0.204	0.226	0.234	0.226	0.217
La		0.001		0.001		0.001	0.001		0.001				0.001	0.001	0.001	0.001	
Ce	0.016	0.016	0.016	0.016	0.016	0.016	0.016	0.015	0.016	0.012	0.011	0.014	0.016	0.016	0.017	0.015	0.014
Pr	0.003	0.004	0.004	0.003	0.004	0.004	0.004	0.003	0.004	0.002	0.002	0.003	0.004	0.004	0.004	0.004	0.002
Nd	0.031	0.032	0.032	0.032	0.033	0.033	0.031	0.030	0.031	0.016	0.020	0.022	0.026	0.026	0.032	0.027	0.023
Sm	0.024	0.024	0.024	0.024	0.024	0.023	0.023	0.022	0.024	0.013	0.013	0.015	0.017	0.019	0.019	0.018	0.015
Eu	0.004	0.004	0.005	0.004	0.005	0.004	0.004	0.004	0.004	0.000	0.003	0.003	0.002	0.003	0.003	0.003	0.005
Gd	0.032	0.031	0.030	0.032	0.033	0.030	0.030	0.029	0.031	0.016	0.016	0.019	0.019	0.021	0.024	0.021	0.020
Tb	0.006	0.007	0.007	0.006	0.006	0.005	0.005	0.006	0.005	0.001	0.002	0.003	0.002	0.003	0.004	0.004	0.003
Dy	0.044	0.042	0.044	0.042	0.041	0.042	0.042	0.041	0.043	0.021	0.021	0.023	0.022	0.024	0.025	0.024	0.022
Ho	0.008	0.009	0.010	0.008	0.007	0.009	0.009	0.008	0.008	0.006	0.004	0.004	0.003	0.005	0.004	0.005	0.003
Er	0.023	0.022	0.023	0.022	0.023	0.022	0.023	0.022	0.023	0.014	0.012	0.013	0.010	0.013	0.013	0.013	0.011
Tm	0.004	0.005	0.004	0.004	0.004	0.004	0.005	0.004	0.004	0.003	0.003	0.003	0.002	0.002	0.003	0.003	0.002
Yb	0.014	0.014	0.015	0.014	0.014	0.015	0.014	0.013	0.014	0.014	0.013	0.012	0.010	0.009	0.011	0.010	0.010
Lu	0.002	0.002	0.002	0.003	0.002	0.001	0.002	0.002	0.002	0.001	0.002	0.001	0.001	0.002	0.001	0.002	0.001
REE	0.212	0.213	0.217	0.211	0.212	0.209	0.209	0.200	0.210	0.119	0.122	0.136	0.134	0.148	0.161	0.150	0.131
Mg	0.050	0.056	0.051	0.069	0.053	0.060	0.050	0.050	0.051	0.038	0.070	0.052	0.036	0.037	0.035	0.080	0.053
Ca	0.387	0.387	0.384	0.379	0.379	0.393	0.392	0.409	0.393	0.576	0.561	0.569	0.576	0.541	0.554	0.501	0.559
Mn	0.004	0.004	0.003	0.003	0.003	0.004	0.004	0.003	0.003	0.003	0.002	0.003	0.004	0.004	0.003	0.004	
Fe	0.360	0.353	0.353	0.360	0.363	0.354	0.348	0.343	0.358	0.312	0.310	0.316	0.322	0.353	0.313	0.388	0.314
Total	4.065	4.061	4.059	4.069	4.061	4.063	4.056	4.057	4.068	4.070	4.079	4.083	4.078	4.085	4.076	4.105	4.076

Appendix 10. X-ray maps of zircon coronas around ilmenite.



Appendix 11. Major element composition of zircon from Potosí.

Sample	POT-1 01					POT-1 03				
Analyse	#-1	#-2	#-3	#-4	#-5	#-1	#-2	#-3	#-4	#-5
SiO ₂	31.85	31.91	32.45	32.20	32.23	31.84	32.56	31.98	31.14	31.72
TiO ₂	0.16	0.21	0.19	0.25	0.13	0.00	0.01	0.02	0.17	0.15
ZrO ₂	64.54	65.57	65.62	65.63	65.76	65.83	66.17	65.85	65.37	65.10
HfO ₂	1.54	1.44	1.34	1.40	1.35	0.92	0.95	0.94	1.52	1.37
Al ₂ O ₃	bdl	bdl	bdl	bdl	bdl	bdl	bdl	bdl	bdl	bdl
Fe ₂ O ₃	0.33	0.46	0.29	0.44	0.36	bdl	bdl	bdl	bdl	bdl
Y ₂ O ₃	bdl	bdl	bdl	bdl	bdl	bdl	bdl	bdl	bdl	bdl
Nb ₂ O ₃	bdl	0.10	bdl	0.09	bdl	bdl	0.05	bdl	0.01	0.04
MgO	bdl	0.02	bdl	bdl	0.02	bdl	bdl	bdl	0.05	0.10
CaO	0.01	0.02	0.04	0.02	0.02	bdl	bdl	0.04	0.34	0.36
Total	98.43	99.73	99.93	100.03	99.86	98.59	99.73	98.83	98.59	98.85
O=4										
Sample	#-1	#-2	#-3	#-4	#-5	#-1	#-2	#-3	#-4	#-5
Si	0.99	0.99	1.00	0.99	0.99	0.99	0.99	1.00	0.99	0.99
Ti	0.00	0.01	0.00	0.01	0.00	0.00	0.01	0.00	0.01	0.00
Zr	0.98	0.99	0.98	0.98	0.99	0.98	0.99	0.98	0.98	0.99
Hf	0.01	0.01	0.01	0.01	0.01	0.01	0.01	0.01	0.01	0.01
Fe	0.01	0.01	0.01	0.01	0.01	0.01	0.01	0.01	0.01	0.01
Total	2.00	2.00	2.00	2.00	2.00	2.00	2.00	2.00	2.00	2.00

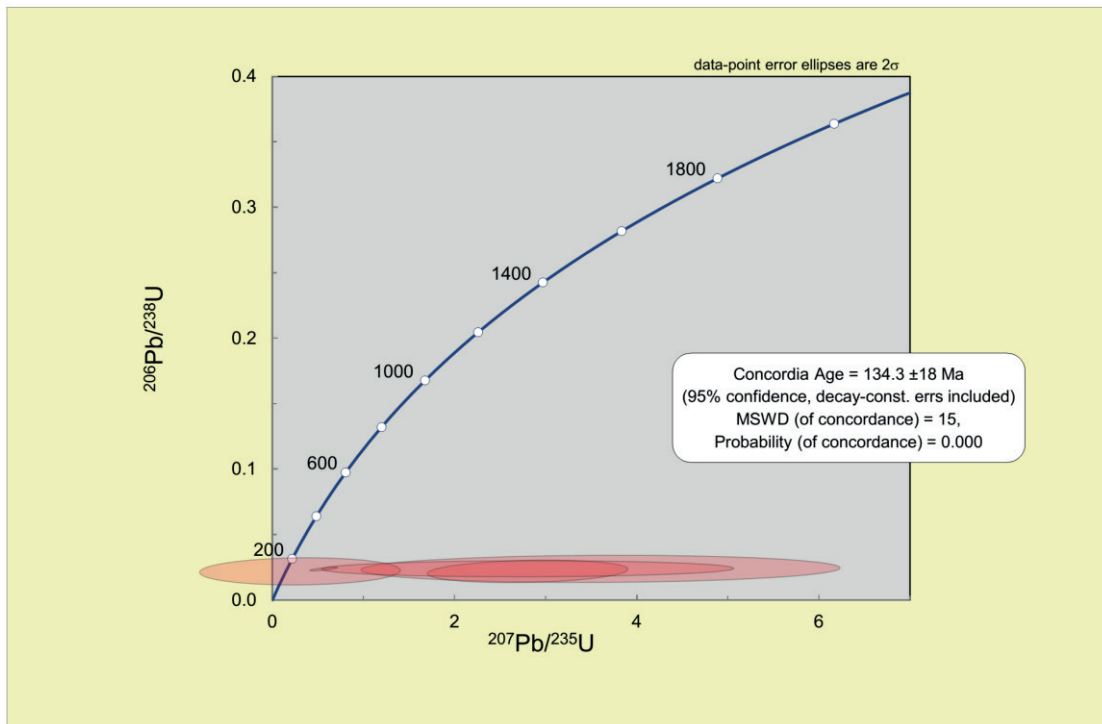
Sample Mineral	POT-1			POT-1			POT-1																	
	ilm	ilm	ilm	ap	ap	ap	193700	17800	19300	201400	198800	198300	183000	194500	188000	195100	195200	200600	198300	194400	197600	195400	196400	
Si	13400	11500	9600	11000	11400	10400	770	606	542	580														
Ti	-	-	-	-	-	-	bdl	5.6	18	0.368														
Mn	6480	6770	5950	5700	5550	4710	-	-	-	-	-	-	-	-	-	-	-	-	-	-	-	-	-	-
Rb	-	-	-	-	-	-	-	-	-	-	-	-	-	-	-	-	-	-	-	-	-	-	-	-
Cs	-	-	-	-	-	-	-	-	-	-	-	-	-	-	-	-	-	-	-	-	-	-	-	-
Sr	-	-	-	-	-	-	-	-	-	-	-	-	-	-	-	-	-	-	-	-	-	-	-	-
Ba	-	-	-	-	-	-	-	-	-	-	-	-	-	-	-	-	-	-	-	-	-	-	-	-
Sc	45	90	59	68	75	84	bdl	bdl	0.009	0.009														
V	470	613	706	1020	900	999	2.0	1.3	1.2	0.174														
Cr	1387	1067	1174	1950	1241	1985	-	-	-	-	-	-	-	-	-	-	-	-	-	-	-	-	-	-
Co	14	10	19	26	28	22	-	-	-	-	-	-	-	-	-	-	-	-	-	-	-	-	-	-
Ni	44	41.1	75	196	117	110	-	-	-	-	-	-	-	-	-	-	-	-	-	-	-	-	-	-
Cu	2.7	1.51	2.9	100	0.100	bdl	-	-	-	-	-	-	-	-	-	-	-	-	-	-	-	-	-	-
Zn	18	7.8	23	37	14	5.9	-	-	-	-	-	-	-	-	-	-	-	-	-	-	-	-	-	-
Ga	bdl	0.11	0.8	bdl	3.1	1.3	-	-	-	-	-	-	-	-	-	-	-	-	-	-	-	-	-	-
Y	0.03	0.31	bdl	0.070	bdl	bdl	61	23	32	0.0198														
Nb	87	1.88	6.7	12	4.7	3.2	bdl	0.045	0.041	bdl														
Ta	5.6	0.059	0.51	0.64	0.41	0.39	bdl	bdl	bdl	bdl														
Zr	3.6	15.2	19.3	79	26	21	0.900	bdl	0.140	0.005														
Hf	0.19	1.74	1.12	3.8	4.9	3.1	bdl	0.080	0.017	bdl														
Sn	3.2	6	7.2	5.7	6.7	6.7	-	-	-	-	-	-	-	-	-	-	-	-	-	-	-	-	-	-
Pb	0.3	0.18	0.06	bdl	bdl	0.170	0.115	0.020	0.025	bdl														
U	bdl	0.061	0.15	bdl	bdl	bdl	0.055	0.012	0.027	bdl														
Th	bdl	bdl	0.009	bdl	bdl	bdl	0.350	0.126	0.234	bdl														
La	0.31	0.02	0.049	bdl	0.320	bdl	36	14	22	0.001														
Ce	0.38	0.22	0.21	0.100	0.330	bdl	116	47	64	0.004														
Pr	bdl	0.026	0.035	0.028	0.011	bdl	18	7.7	11	bdl														
Nd	bdl	0.21	bdl	0.007	0.130	0.200	92	38	54	bdl														
Sm	bdl	0.1	bdl	bdl	bdl	bdl	22	8.6	13	bdl														
Eu	bdl	0.44	0.049	bdl	0.12	bdl	3.7	1.9	2.8	bdl														
Gd	bdl	0.06	bdl	0.024	bdl	bdl	21	8.0	13	bdl														
Tb	bdl	0.007	bdl	0.0050	bdl	bdl	2.9	1.0	1.7	bdl														
Dy	bdl	0.021	bdl	0.055	bdl	bdl	15	5.5	8.4	0.005														
Ho	bdl	0.100	bdl	0.026	bdl	bdl	3.1	1.2	1.6	0.001														
Er	bdl	0.018	bdl	bdl	bdl	0.035	7.8	3.0	3.9	0.003														
Tm	bdl	0.049	0.007	0.016	bdl	bdl	0.930	0.383	0.450	bdl														
Yb	bdl	0.060	bdl	0.270	0.025	0.0160	5.4	2.3	2.7	bdl														
Lu	0.050	0.032	0.024	0.059	0.060	0.045	0.770	0.300	0.368	bdl														
Hg	158	211	65	bdl	110	47	149	201	146	52														
Ge	1.0	2.3	bdl	bdl	3.6	bdl	-	-	-	-														
W	bdl	bdl	bdl	bdl	1.1	bdl	-	-	-	-														

Sample Mineral	Po-105a										Po-105a															
	opx	opx	opx	opx	opx	opx	opx	opx	opx	opx	opx	opx	opx	opx	opx	opx	opx	opx	opx	opx						
Si	3830	3150	3290	2780	3160	3290	3070	2640	2620	2789	3368	3240	1400	1090	1220	1010	1100	2860	1135	1138	920	995	4400	1109	950	
Ti	3990	3000	2530	1766	1830	1928	2320	2570	2810	1676	1644	1703	577	537	252	142	272	975	1004	897	989	891	914	1020	1320	
Mn	bdl	0.082	0.057	0.027	0.019	0.012	bdl	0.022	0.003	bdl	bdl	0.011	0.68	0.55	1.01	0.62	0.4	0.83	0.91	0.84	2.1	1.53	0.94	0.71	0.91	
Rb	0.216	0.237	0.331	0.32	0.448	0.511	0.79	1.3	0.87	0.66	0.125	0.395	2.51	2.56	5.8	2.38	1.85	5.72	2.97	4.7	4.47	3.69	2.65	3.48	1.69	
Sr	0.036	0.041	0.021	0.052	0.053	0.066	0.031	0.094	0.045	0.02	0.015	bdl	0.15	bdl	0.69	0.11	0.16	0.217	0.27	0.19	0.39	0.19	0.1	0.27	0.25	
Ba	60.7	60.4	58.5	58.3	55	59.7	52.1	43.7	46.2	60.8	56.5	54.6	41.7	42.5	29	25.4	30.9	119.2	59.9	53.7	50.1	60	53.1	48.7	48.7	
V	179	162.1	160.1	157.9	155.3	157.2	139	125	122	151.6	137.9	137	144	149	128	138	120	295	224	195	177	183	233	217	226	
Cr	3480	2890	2750	2149	2105	2180	2280	2270	2240	2331	2130	2260	4130	4190	3370	2960	3140	3900	5530	5190	4960	5160	5130	5130	5410	
Co	58.6	51.6	53.7	51.2	50.7	49.4	42.5	40.1	38	61.7	55.3	55.4	-	-	-	-	-	-	-	-	-	-	-	-	-	
Ni	406	360	359	338	335	325	287	266	257	356.4	334	334	-	-	-	-	-	-	-	-	-	-	-	-	-	
Cu	0.22	0.18	0.32	0.007	0.55	0.07	bdl	bdl	bdl	0.96	0.24	1.8	-	-	-	-	-	-	-	-	-	-	-	-	-	
Zn	41.8	35.6	39.8	37.3	38.5	36.7	30.7	28.5	27.6	57.5	55.2	52.5	-	-	-	-	-	-	-	-	-	-	-	-	-	
Ga	-	-	-	-	-	-	-	-	-	-	-	-	-	-	-	-	-	-	-	-	-	-	-	-	-	
Y	52.2	52.3	53.1	51.6	63.9	51.5	70.7	66.1	49.7	45.8	33.9	28.9	3.79	2.82	2.57	2.04	3	3.54	9.1	6.06	10	9.4	8.8	5.91	10.5	
Nb	bdl	0.015	bdl	bdl	0.001	bdl	0.001	bdl	bdl	bdl	bdl	bdl	5.39	4.96	4.21	2.7	2.01	28.6	6.45	5.2	4.38	4.77	12.6	5.7	5.65	
Ta	0.009	0.013	0.0018	bdl	bdl	bdl	0.0066	bdl	0.0023	0.0042	bdl	0.0027	0.046	0.027	0.015	0.017	0.045	0.021	0.023	0.014	0.014	0.015	0.04	bdl	bdl	
Zr	22.3	18.85	23.9	17.7	24.2	18.9	27.5	29.69	20.5	12.88	10.67	9.59	bdl	bdl	bdl	bdl	bdl	0.0068	bdl	bdl	bdl	bdl	0.0022	bdl	bdl	
Hf	0.92	0.78	0.78	0.93	1.44	1.12	0.84	0.95	0.73	0.64	0.565	0.45	7.7	6.8	3.18	2.7	3	59.9	3.84	2.6	3.15	2.93	3.8	3.64	6.9	
Hf	-	-	-	-	-	-	-	-	-	-	-	-	0.181	0.266	0.067	0.09	0.18	2.37	0.113	0.112	0.156	0.081	0.117	0.085	0.149	
Sn	-	-	-	-	-	-	-	-	-	-	-	-	-	-	-	-	-	-	-	-	-	-	-	-	-	
Pb	0.04	0.022	0.07	0.05	0.068	0.007	0.057	0.07	0.002	0.044	bdl	0.062	0.37	0.4	1.4	0.395	0.46	0.134	0.147	0.204	0.165	0.15	0.179	0.25	0.17	
U	bdl	0.0047	0.009	0.011	0.0034	bdl	bdl	0.015	bdl	bdl	bdl	bdl	0.0073	bdl	0.0031	0.0076	bdl	0.0069	bdl	bdl	0.007	bdl	0.003	bdl	0.0029	
Th	0.02	0.025	0.0204	0.009	0.024	0.043	0.11	0.118	0.057	0.018	0.016	0.013	0.0046	bdl	0.013	0.005	0.009	bdl	0.01	0.0035	bdl	bdl	bdl	bdl	bdl	
La	0.128	0.125	0.74	0.106	0.24	0.144	0.239	0.67	0.175	0.068	0.052	0.171	0.035	0.056	0.078	0.027	0.041	0.201	0.071	0.106	0.113	0.0576	0.2	0.147	0.148	
Ce	0.91	0.905	2.7	0.772	1.45	1	1.38	2.05	0.851	0.566	0.537	0.81	0.169	0.148	0.148	0.078	0.087	1.52	0.281	0.42	0.228	0.206	0.621	0.349	0.36	
Pr	0.263	0.216	0.428	0.22	0.285	0.319	0.407	0.289	0.218	0.176	0.16	0.135	0.0255	0.0323	0.0152	0.0103	0.007	0.422	0.053	0.045	0.048	0.045	0.115	0.046	0.061	
Nd	2.25	1.97	3.1	1.85	2.08	2.15	2.7	2.09	1.44	1.15	1.21	1.13	0.51	0.21	0.19	0.107	0.13	3.39	0.46	0.36	0.32	0.28	0.632	0.32	0.283	
Sm	1.56	1.54	1.22	1.31	1.5	1.35	1.26	1.06	0.91	1.04	0.97	0.65	0.104	0.25	0.077	bdl	0.016	2.05	0.35	0.18	0.06	0.094	0.3	0.133	0.13	
Eu	0.265	0.286	0.32	0.279	0.33	0.37	0.404	0.248	0.198	0.247	0.214	0.235	0.079	0.099	0.016	0.0281	0.013	0.59	0.067	0.06	0.092	0.037	0.4	0.08	0.048	
Gd	3.62	3.09	3.49	2.93	2.77	2.88	2.67	1.93	1.9	2.56	2.19	2.14	4	3.19	0.18	0.12	0.21	4.42	0.37	0.36	0.25	0.2	0.72	0.42	0.31	
Tb	1.87	1.43	1.46	0.714	0.65	0.704	0.597	0.544	0.427	0.675	0.564	0.476	0.09	0.096	0.0537	0.033	0.046	0.793	0.147	0.159	0.063	0.096	0.275	0.129	0.098	
Dy	20.7	13.8	13	6.25	6.61	6.75	5.82	5.17	4.65	4.85	3.85	4	0.86	0.77	0.47	0.27	0.231	5.64	1.06	0.75	0.542	0.86	2.38	0.73	0.96	
Ho	5.28	4.12	3.36	1.99	2.07	1.85	1.82	1.61	1.35	1.5	1.07	1.028	0.202	0.2	0.181	0.07	0.077	1.35	0.218	0.152	0.187	0.2	0.54	0.198	0.273	
Er	12.3	10.38	10.5	7.3	8.2	6.93	5.9	5.55	4.5	5.88	3.87	3.81	0.84	0.89	0.91	0.26	0.41	3.8	0.83	0.65	0.59	0.68	2.37	0.89	0.7	
Tm	2.05	1.68	1.82	1.5	1.49	1.24	1.06	0.931	0.795	1.16	0.864	0.753	0.157	0.157	0.16	0.087	0.13	0.639	0.125	0.153	0.073	0.108	0.349	0.1097	0.143	
Yb	14.3	12.95	15.3	13.6	14.14	11.9	9.2	7.7	6.35	16.37	13.1	12.95	2	1.27	1.97	1.1	1.13	4.74	1.26	1.03	0.91	0.9	2.45	0.96	1.24	
Lu	2.29	2.15	2.4	1.85	2.14	1.85	1.35	1.08	0.962	2.3	1.84	1.78	0.317	0.285	0.4	0.309	0.214	0.64	0.185	0.176	0.174	0.172	0.233	0.18	0.212	
Hg	-	-	-	-	-	-	-	-	-	-	-	-	-	-	-	-	-	-	-	-	-	-	-	-	-	-
Ge	-	-	-	-	-	-	-	-	-	-	-	-	-	-	-	-	-	-	-	-	-	-	-	-	-	-
W	-	-	-	-	-	-	-	-	-	-	-	-	-	-	-	-	-	-	-	-	-	-	-	-	-	-

Sample Mineral	Po-105a										Po-105a									
	cpX	cpX	cpX	cpX	cpX	cpX	cpX	cpX	cpX	cpX	cpX-rim	cpX-rim	cpX-rim	cpX-rim	cpX-rim	cpX-rim	cpX-rim	cpX-rim	cpX-rim	cpX-rim
Si	-	-	-	-	-	-	-	-	-	-	-	-	-	-	-	-	-	-	-	-
Ti	860	920	855	1240	1180	395	280	770	449	754	791	3380	3410	3020	3240	3740	3280	3510	3700	3690
Min	1120	1040	1093	1040	1090	615	465	469	720	508	423	1188	1188	1035	1096	1023	1077	1040	883	951
Rb	1.1	0.87	0.89	1.18	0.83	1.01	0.71	0.62	0.84	1.24	0.66	1.53	1.17	1.51	1.49	0.92	0.93	0.8	1.05	0.78
Cs	0.038	0.157	0.092	0.18	0.147	0.051	0.014	0.074	0.079	0.14	0.083	0.01	0.015	0.0138	0.0032	0.007	0.021	0.013	bdl	0.01
Sr	2	2.13	2.39	3.5	2.74	3.72	4.03	3.03	2.63	3.78	3.05	5.92	5.61	6.5	6.2	5.29	5.42	4.89	5.29	4.66
Ba	0.07	0.24	0.15	0.07	0.2	0.6	0.27	0.17	0.15	0.35	0.22	0.17	0.065	0.98	0.36	0.1	0.036	0.056	0.19	0.048
Se	58.9	61.6	56.4	65.1	62.9	19.5	23.1	40.8	44.6	47.9	46.7	138	137.9	115.2	127	156	119.1	138	145.6	126.9
V	238	199	188	227	239	117	98	188	137	179.9	194	372	373	338	360	364	377	384	351	345
Cr	6180	4950	5440	4980	5340	2130	1220	4350	3970	4900	4300	5800	6990	6630	6860	6610	7260	7260	6150	6200
Co	-	-	-	-	-	-	-	-	-	-	-	-	-	-	-	-	-	-	-	-
Ni	-	-	-	-	-	-	-	-	-	-	-	-	-	-	-	-	-	-	-	-
Cu	-	-	-	-	-	-	-	-	-	-	-	-	-	-	-	-	-	-	-	-
Zn	-	-	-	-	-	-	-	-	-	-	-	-	-	-	-	-	-	-	-	-
Ga	12.1	9.3	13	9.6	11.3	5.3	3.74	4.09	8.4	5.06	3	4.7	4.5	4.65	4.94	4.24	5.46	4.95	4.33	3.73
Y	4	5.24	5.1	6.98	6.3	1.72	1.3	4.71	2.25	4.33	5.4	39.8	40.3	37.8	40.5	37	39.9	43.4	39.1	41.9
Nb	0.033	0.017	bdl	0.018	bdl	0.015	bdl	0.068	0.018	0.029	0.012	bdl	0.07	0.009	0.01	0.042	0.02	0.029	0.053	0.037
Ta	bdl	bdl	bdl	bdl	bdl	bdl	bdl	bdl	bdl	bdl	bdl	0.0045	0.0055	0.012	0.0032	0.011	0.012	0.0068	0.012	0.0126
Zr	5.4	5.94	6.63	7.8	7.4	1.71	1.67	3.6	3.3	8.4	8.4	70.8	53.8	41.4	50.4	72.4	47.2	59.1	72.9	46.7
Hf	0.17	0.158	0.088	0.143	0.163	0.034	0.018	0.121	0.071	0.224	0.224	3.07	2.44	2.09	2.46	3.83	2.2	2.5	3.33	2.47
Sn	-	-	-	-	-	-	-	-	-	-	-	-	-	-	-	-	-	-	-	-
Pb	0.073	0.135	0.135	0.096	0.084	0.127	0.112	0.35	0.27	0.19	0.121	1.5	2.66	0.52	0.292	0.99	0.67	0.88	0.193	2.14
U	bdl	bdl	0.008	bdl	bdl	bdl	bdl	0.0029	0.007	0.01	bdl	bdl	bdl	0.0064	bdl	0.0026	bdl	bdl	bdl	0.0065
Th	bdl	bdl	0.013	0.006	0.005	bdl	bdl	0.005	bdl	0.01	0.009	0.004	0.0031	0.028	0.028	0.012	0.009	bdl	0.005	0.002
La	0.132	0.09	0.115	0.105	0.061	0.031	0.032	0.041	0.041	0.066	0.041	0.201	0.18	0.224	0.241	0.163	0.169	0.152	0.156	0.238
Ce	0.299	0.316	0.224	0.32	0.255	0.074	0.045	0.144	0.113	0.12	0.199	1.65	2	1.99	2	1.514	1.78	1.83	1.41	1.93
Pr	0.058	0.082	0.061	0.088	0.054	0.0056	0.0162	0.041	0.013	0.041	0.0358	0.56	0.616	0.516	0.614	0.473	0.586	0.625	0.505	0.55
Nd	0.29	0.27	0.14	0.59	0.398	0.103	0.086	0.154	0.08	0.26	0.23	4.64	4.6	4.6	4.85	4.2	4.8	4.91	4.26	4.69
Sm	0.029	0.16	0.2	0.138	0.34	0.013	0.012	0.174	0.088	0.081	0.152	3.32	3.01	2.6	3.51	2.62	3.17	3.29	2.62	3.08
Eu	0.052	0.088	0.034	0.067	0.148	0.022	0.009	0.059	0.042	0.032	0.089	0.78	0.59	0.64	0.616	0.645	0.59	0.81	0.56	0.638
Gd	0.24	0.38	0.27	0.63	0.46	0.057	0.04	0.26	0.22	0.077	0.35	5.32	6.2	5.26	5.3	5	5.05	5.73	5.3	5.1
Tb	0.078	0.146	0.083	0.148	0.141	0.0296	0.027	0.05	0.026	0.075	0.101	1.12	1.33	1.1	1.19	1.1	1.19	1.33	1.12	1.21
Dy	0.58	0.98	0.76	1.29	1.19	0.184	0.126	0.56	0.36	0.66	0.758	6.83	8.12	6.73	7.51	6.74	7	7.06	7.15	7.38
Ho	0.157	0.183	0.207	0.25	0.229	0.061	0.052	0.165	0.088	0.23	0.202	1.75	1.78	1.679	1.78	1.51	1.842	1.79	1.81	1.86
Er	0.63	0.76	0.56	0.98	0.85	0.3	0.172	0.54	0.368	0.51	0.544	5.03	4.47	3.8	4.26	3.66	4.3	4.95	4.68	4.63
Tm	0.104	0.134	0.125	0.176	0.09	0.062	0.047	0.138	0.087	0.11	0.157	0.82	0.715	0.686	0.736	0.752	0.85	0.809	0.776	0.848
Yb	0.78	1.01	0.99	1.28	1.16	0.73	0.427	1.37	0.69	1.28	1.57	6.54	5.32	4.43	5.87	5.42	6.32	6.04	5.99	5.56
Lu	0.134	0.151	0.173	0.22	0.134	0.119	0.072	0.292	0.15	0.283	0.28	0.89	0.67	0.65	0.721	0.714	0.87	0.847	0.86	0.742
Hg	-	-	-	-	-	-	-	-	-	-	-	-	-	-	-	-	-	-	-	-
Ce	-	-	-	-	-	-	-	-	-	-	-	-	-	-	-	-	-	-	-	-
W	-	-	-	-	-	-	-	-	-	-	-	-	-	-	-	-	-	-	-	-

Sample	POT-1															
Mineral	zm	zm	zm	zm	zm	zm	zm	zm	zm	zm	zm	zm	zm	zm	zm	zm
Si	-	-	-	-	-	-	-	-	-	-	-	-	-	-	-	-
Ti	1410	25900	48000	52000	36000	32000	6900	12700	30000	9900	9300	200	1300	6500	-	-
Mn	-	-	-	-	-	-	-	-	-	-	-	-	-	-	-	-
Rb	-	-	-	-	-	-	-	-	-	-	-	-	-	-	-	-
Cs	-	-	-	-	-	-	-	-	-	-	-	-	-	-	-	-
Sr	-	-	-	-	-	-	-	-	-	-	-	-	-	-	-	-
Ba	-	-	-	-	-	-	-	-	-	-	-	-	-	-	-	-
Sc	466	650	4440	1230	750	6200	6000	13300	19300	81000	9430	5280	3200	2100	-	-
V	1.3	28	65	308	376	520	85	123	65.5	46	314	7.1	18	17	-	-
Cr	-	-	-	-	-	-	-	-	-	-	-	-	-	-	-	-
Co	-	-	-	-	-	-	-	-	-	-	-	-	-	-	-	-
Ni	-	-	-	-	-	-	-	-	-	-	-	-	-	-	-	-
Cu	-	-	-	-	-	-	-	-	-	-	-	-	-	-	-	-
Zn	-	-	-	-	-	-	-	-	-	-	-	-	-	-	-	-
Ga	2.1	22	bdl	bdl	bdl	2.9	3	bdl	0.53	3.3	3.22	0.06	bdl	2.4	-	-
Y	80	68	106	150	77	184	186	143	117	164	554	639	520	332	-	-
Nb	0.2	0.26	1.6	1.09	2.1	bdl	bdl	970	57	18	0.73	1.02	0.46	0.82	-	-
Ta	bdl	0.5	2.4	1	2.2	6.2	1.9	2.7	6.7	2.2	0.72	0.09	0.1	bdl	-	-
Zr	1640000	2300000	450000	2180000	1450000	2150000	2430000	1270000	3050000	2730000	3170000	3860000	3180000	2450000	-	-
Hf	5700	5520	1760	4100	3700	11600	8600	4000	5000	5600	5850	6950	6680	5400	-	-
Sn	-	-	-	-	-	-	-	-	-	-	-	-	-	-	-	-
Pb	1.5	23	54	3	0.41	6.4	4.9	3.4	2.7	6.6	5.8	5.3	1.9	bdl	-	-
U	2.6	3.03	0.22	1.9	1.17	3.2	2.7	2.53	3.5	5.1	4.1	4	2.93	4.9	-	-
Th	1.6	0.71	0.22	0.45	1.07	1.95	2	2.1	0.63	2.2	5	6.07	4.6	2.9	-	-
La	bdl	bdl	0.0029	0.0064	0.0065	0.014	0.0031	0.012	0.015	0.007	0.0074	bdl	bdl	bdl	-	-
Ce	0.28	0.92	1.22	5.4	4.4	3.2	1.71	3.1	4.8	3	5	0.87	0.94	0.7	-	-
Pr	0.0014	0.0026	0.017	0.071	0.048	0.057	0.0171	0.076	0.069	0.048	0.096	0.0031	0.0045	bdl	-	-
Nd	0.039	0.17	0.05	1.59	0.95	0.74	0.48	0.7	0.9	1.06	2	0.15	0.18	bdl	-	-
Sm	1.3	2.3	2.9	20.5	9.3	4.8	1.5	4.4	11.5	6.2	15.4	4.2	2.8	1.8	-	-
Eu	0.16	0.35	0.26	1.58	0.71	0.31	0.64	0.09	0.41	2.9	0.7	0.55	0.54	0.36	-	-
Gd	2.3	0.68	2	8	6.7	25	29	6	20	53	67	29.3	18	4.9	-	-
Tb	0.38	0.58	0.78	1.93	1.17	2.7	2.58	2.87	1.27	3	7.7	6.03	4.2	2.2	-	-
Dy	10.3	8.2	14.5	25.8	13	15.7	13.6	13.7	12.3	17.9	60	56.5	41	36	-	-
Ho	2.88	2.41	4.3	4.59	3.5	7.6	9.3	5.3	4.2	7.9	25.3	24.9	17.9	11.3	-	-
Er	18.1	13.8	23.3	24.8	17.3	33.8	38	25	16.1	27.2	95	100	77	51	-	-
Tm	7.4	4.52	7.1	6	4.6	8.1	8.1	3.8	4.3	6.82	23.2	26.6	18.9	13.8	-	-
Yb	64	51.2	46.2	42.4	46	109.6	98	72	53	75.8	229	275	205	172	-	-
Lu	9.6	8.4	8.2	6.8	10.1	20.2	23.3	8.15	12.3	15.7	52.5	58.8	41.4	28	-	-
Hg	-	-	-	-	-	-	-	-	-	-	-	-	-	-	-	-
Ce	-	-	-	-	-	-	-	-	-	-	-	-	-	-	-	-
W	-	-	-	-	-	-	-	-	-	-	-	-	-	-	-	-

Appendix 13. Concordia age of baddeleyite U/Pb dating.





A2. Article 2

Pujol-Solà, N., Proenza, J., Garcia-Casco, A., González-Jiménez, J., Andreazini, A., Melgarejo, J., Gervilla, F., 2018. An Alternative Scenario on the Origin of Ultra-High Pressure (UHP) and Super-Reduced (SuR) Minerals in Ophiolitic Chromitites: A Case Study from the Mercedita Deposit (Eastern Cuba). *Minerals* 8, 433. <https://doi.org/10.3390/min8100433>

Article

An Alternative Scenario on the Origin of Ultra-High Pressure (UHP) and Super-Reduced (SuR) Minerals in Ophiolitic Chromitites: A Case Study from the Mercedita Deposit (Eastern Cuba)

Núria Pujol-Solà ^{1,*}, Joaquín A. Proenza ¹ , Antonio Garcia-Casco ^{2,3},
José María González-Jiménez ² , Aleu Andreazini ⁴, Joan Carles Melgarejo ¹  and
Fernando Gervilla ^{2,3}

¹ Departament de Mineralogia, Petrologia i Geologia Aplicada, Facultat de Ciències de la Terra, Universitat de Barcelona, Martí i Franquès s/n, 08028 Barcelona, Spain; japrozena@ub.edu (J.A.P.); joan.carles.melgarejo.draper@ub.edu (J.C.M.)

² Departamento de Mineralogía y Petrología, Facultad de Ciencias de la Tierra, Universidad de Granada, Avda. Fuentenueva, s/n, 18071 Granada, Spain; agcasco@ugr.es (A.G.-C.); jmgonzj@ugr.es (J.M.G.-J.); gervilla@ugr.es (F.G.)

³ Instituto Andaluz de Ciencias de la Tierra (CSIC-UGR), Avda. de las Palmeras 4, 18100 Armilla, Granada, Spain

⁴ Centro de Instrumentación Científica, Universidad de Granada, Campus Universitario de Fuentenueva, Paseo Prof. Juan Ossorio, s/n, 18003 Granada, Spain; aleuan@gmail.com

* Correspondence: npujolsola@ub.edu; Tel.: +34-93-402-1341

Received: 31 July 2018; Accepted: 27 September 2018; Published: 1 October 2018



Abstract: The origin of the assemblage of ultra-high pressure (UHP), super-reduced (SuR) and several crustally derived phases in ophiolitic chromitites is still hotly debated. In this paper, we report, for the first time, this assemblage of phases in ophiolitic chromitites of the Caribbean. We studied the Mercedita chromitite deposit in the eastern Cuban ophiolitic complexes. The mineral phases were characterized using microRaman spectroscopy, energy-dispersive spectroscopy with a scanning electron microscope (SEM-EDS), X-ray microdiffraction and electron microprobe analyses. Mineral concentrates were prepared using hydroseparation techniques. We have identified oriented clinopyroxene lamellae in chromite, oriented rutile lamellae in chromite, moissanite hosted in the altered matrix of the chromitite, graphite-like amorphous carbon, corundum and SiO₂ hosted in healed fractures in chromite grains, and native Cu and Fe–Mn alloy recovered in heavy-mineral concentrates obtained by hydroseparation. This assemblage may correspond to UHP–SuR conditions, implying recycling of chromitite in the mantle or formation of the chromite grains at deep mantle depths, followed by emplacement at a shallow level in the mantle. However, the chromitite bodies contain gabbro sills oriented parallel to the elongation of the chromitite lenses, and these show no evidence of HP/UHP metamorphism. Therefore, the identified “exotic” phases may not be indicative of UHP. They formed independently as oriented clinopyroxene lamellae in chromite during cooling (clinopyroxene and rutile), in super-reduced microenvironments during the serpentinization processes, and by transference of subducted crustal material to the mantle wedge via cold plumes.

Keywords: moissanite; inclusions; Mercedita; serpentinization; super-reducing conditions; chromitites; ophiolites; Cuba

1. Introduction

Minerals indicative of super-reducing (SuR) environments, e.g., native elements, alloys, carbides, nitrides and phosphides, and those formed at ultra-high pressure (UHP), e.g., diamond, TiO₂-II, pseudomorphs after coesite and stishovite, are increasingly being reported in peridotites and associated chromitites from ophiolite complexes, along with minerals that typically form in the continental crust, e.g., zircon, quartz, K-feldspar, almandine, andalusite, apatite and kyanite [1–12]. The origin of minerals considered “exotic” to the ophiolitic rocks is currently the subject of many frontline studies and remains a hotly debated topic.

Some investigators have proposed that peridotites and associated chromitites form near the MTZ-Moho Transition Zone (petrologic Moho) in a suprasubduction environment and incorporate crustal minerals in the shallow mantle. The rocks are subsequently recycled into the ultra-deep mantle (>410 km, and perhaps even deeper, to a mantle-core depth) by continued subduction, where SuR and UHP minerals become incorporated, e.g., [6,13–15]. Rapid exhumation of the deep-seated chromitites and host peridotites carrying SuR, UHP and continental-crust-derived minerals is related to the generation of low-viscosity upwelling channels created during the opening of marginal basins in island arcs or continental arcs as a result of retraction of subducting slabs during the rollback process [14,15]. In this model, crustal minerals are already present in the chromitite, which forms in a mantle wedge contaminated by subducted material with a crustal component after the ascent of cold plumes derived from the subducting slabs [12,16].

Others have suggested that SuR, UHP and continental-crust-derived minerals correspond to material present in the slab graveyard located at the bottom of the upper mantle, near the mantle-transition zone. This subducted material is incorporated in chromite crystallizing from melts originating from rising deep-seated mantle plumes [5,6,17,18] or, alternatively, asthenosphere-derived melts that rise along slab-windows [4,19].

In addition, the role of fluids has been highlighted [20] in the formation of ophiolitic chromite deposits. According to this metasomatic model, localized super-reducing environments favor the disequilibrium crystallization of UHP minerals, forming very unusual paragenesis in the oceanic crust. The authors propose that chromite formation requires a SuR subsolidus in a low-pressure environment with a temperature above 800 °C.

Yet other investigators [21,22] have synthesized SuR and UHP mineral assemblages from plasma generated by electric discharges at >5700 °C, suggesting that these minerals in ophiolitic rocks can originate after obduction by lightning strikes. This short review indicates that the SuR and UHP assemblages may not record a deep origin and may not support an emplacement history involving mantle lithologies.

Here, we provide the first-ever report of SuR minerals in ophiolitic rocks from the Caribbean, in fact from the Mercedita chromitite deposit, in eastern Cuba. This mineral assemblage, which occurs with continental-crust-derived minerals, is described and evaluated in the framework of chromitite genesis during the formation and geological evolution of the Caribbean region. Our work leads to an evaluation of the various models proposed for the origin of this unusual paragenesis.

2. Geological Setting

The Mercedita chromitite deposit is located in eastern Cuba (Figure 1a), part of the Mayarí-Baracoa ophiolitic belt. It is associated with Cretaceous HP serpentinite-matrix subduction mélanges (Sierra del Convento and La Coreá), Early to Late Cretaceous volcanic arc sequences, and a Late Cretaceous metamorphic sole (the Güira de Jauco Amphibolite Complex) related to the onset of ophiolite obduction [16,23–39] (Figure 1a,b). The synorogenic La Picota and Mícará formations date oceanic arc-terrane collision and exhumation during latest Cretaceous to earliest Paleocene times, prior to the final northeasterly verging collision with the Bahamas platform and accretion of tectonic pile onto the North American plate (Figure 1b) [23,27,28,35,36]. The Cuban Ophiolite Belt represents oceanic lithosphere obducted onto the North American continental paleomargin owing to northward collision

between the Caribbean plate and the passive margins of the Maya block and the Bahamas platform during the latest Cretaceous to Late Eocene [23,27,28].

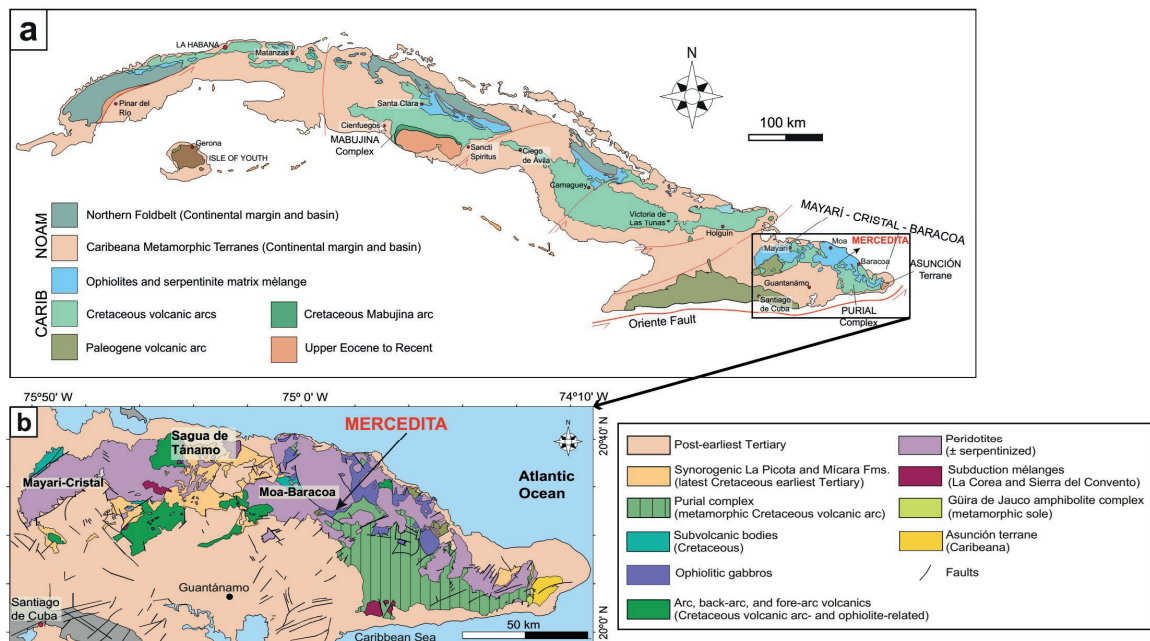


Figure 1. (a) Generalized geologic-tectonic map of Cuba; (b) Schematic geological map of the Mayari-Baracoa Ophiolitic Belt (MBOB) showing the location of the Mercedita Mine.

2.1. Eastern Cuba Ophiolites

The Mayari-Baracoa ophiolite belt, in the eastern part of the Cuban Ophiolite Belt, outcrops for more than 1000 km along the Cuban coastline (Figure 1a,b) and represents the largest exposure of oceanic lithosphere in the circum-Caribbean region, e.g., [24,37]. The allochthonous Mayari-Baracoa belt is divided by major fault zones into two different massifs: the Mayari-Cristal massif in the west and the Moa-Baracoa massif in the east (Figure 1b), having mantle sections of more than 5 km and about 2.2 km in thickness respectively [24,38]. The ophiolite assemblage is highly dismembered; the dominant lithology is harzburgitic tectonite with subordinate dunite, chromitite, layered gabbro and discordant microgabbro, pyroxenite, troctolite, wehrlite, and diabase bodies [24,37–39] in both massifs. The Cuban ophiolites have supra-subduction zone geochemical signature [24,38,40–42] related to the intra-oceanic Greater Antilles arc, developed during the lower to upper Cretaceous.

2.2. The Moa-Baracoa Ophiolitic Massif

The Moa-Baracoa ophiolitic massif consists of harzburgitic tectonites with minor dunite and the petrologic Moho crosscut by gabbroic dikes associated with layered gabbros. These lithologies are in tectonic contact with pillow basalts of the Morel Formation (88–91 Ma), which have a back-arc geochemical affinity and are related to cumulate gabbros [25,40,42]. These findings strongly indicate a back-arc environment scenario for the formation of the Moa-Baracoa massif [30,33,40,41].

Numerous high-Al ($0.41 < Cr\# < 0.54$) chromitite bodies are hosted in the mantle tectonites [24]. These bodies have tabular to lenticular shape, are concordant to the host peridotite foliation, and show a dunite envelope of variable thickness [24]. The melts inferred to have been in equilibrium with such Al-rich chromitite are similar in composition to back-arc basin basalts (BABB) [24,41,43].

2.3. The Mercedita Deposit

The Mercedita deposit, located in the most southerly part of the Moa-Baracoa massif (Figure 1b), is considered the largest and most important podiform chromite deposit in America [44], with

calculated reserves exceeding 5 million tons. The largest chromitite body is 600 m long, 250 m wide, and up to 20 m thick [24,44]. Tabular to lenticular bodies of chromitite of variable size (Figure 2a) are crosscut by normal faults. The lenses are invariably parallel to the foliation and lineation of host peridotite and are located in the mantle-crust transition zone, characterized by the interlayering of ultramafic and gabbroic rocks. Dunite (from few centimeters to a few meters in thickness) systematically envelopes the chromitite bodies, though chromitite-harzburgite contacts are locally developed. The contact between chromitite and peridotites is generally sharp and only locally gradational [44].

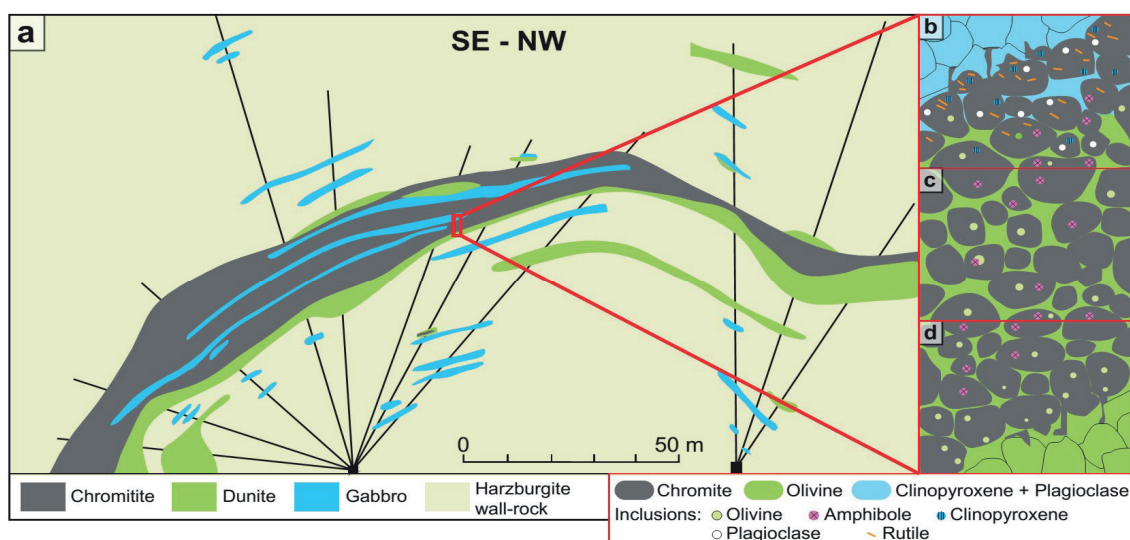


Figure 2. (a) Cross-section through the Mercedita chromitite. The relationships between chromitite, dunite, gabbros and harzburgite were interpreted from holes drilled upward from the roof of the mine's galleries; (b) Mineral inclusions in Mercedita chromite grains near the contact with gabbro; (c) Mineral inclusions in Mercedita chromite grains in the inner part of the chromitite body; (d) Mineral inclusions in Mercedita chromite grains near the dunite envelope. (b–d) Are not to scale.

The chromitite lenses usually include gabbro sills of variable size (Figure 2a), from centimeters to >100 m in length. These have the same orientation as the chromitite bodies [44]. The layers of gabbro are locally replaced by the chromitite, an observation also supported by the chemical variations observed in the composition of chromite, which shows increasing Ti and Al towards the gabbro bodies [24]. Later gabbro and pegmatitic gabbro dikes crosscut the chromitite bodies and are sheared or displaced by normal faults with NE-SW and NW-SE orientations [24,44]. Interestingly, similar relationships between chromitites and gabbro sills parallel to the chromitite bodies have been described in nearby Cayo Guam chromite deposit (Moa-Baracoa massif, Cuba [45]), Camagüey (Cuba [46]), and in the Coto Block (Philippines [47]).

Chromitite shows two types of texture [44]: massive compact and massive anhedral chromite in an altered olivine matrix. However, other textures include deformed nodular, mylonitic (locally in shear zones) and cataclastic (locally along normal faults) varieties. Pull-apart fractures are abundant in the lenses.

3. Materials and Methods

3.1. Sampling

50 thin sections from chromite samples (including drill cores) collected from the Mercedita high-Al chromitite deposit have been selected and carefully studied for this article.

3.2. Hydroseparation

Chromitite samples (2.7 kg) were crushed and powdered using an agate mill. The powder was sieved using various mesh-sizes and hydroseparated (HS Lab, Barcelona, Spain). The grains obtained were mounted as polished monolayers (five concentrates) on resin blocks (SimpliMet 1000). For details of the procedure, see [48].

3.3. Scanning Electron Microscopy (SEM)

After studying the polished thin sections with petrographic microscope, selected samples were examined with a scanning electron microscope (SEM) using both a Quanta 200 FEI XTE 325/D8395 and a JEOL JSM-7100 field-emission scanning electron microscope equipped with an energy-dispersive spectrometer (EDS) at the Serveis Científics i Tecnològics, Universitat de Barcelona (CCiTUB), Spain. The operating conditions were 15 keV accelerating voltage and 5 nA in backscattered electron (BSE) mode.

3.4. MicroRAMAN Spectroscopy

The “exotic” mineral phases were characterized using microRaman directly in the polished thin sections with a HORIBA Jobin LabRaman HR 800 dispersive spectrometer equipped with an Olympus BXFM optical microscope in the Serveis Científics i Tecnològics, Universitat de Barcelona (CCiTUB). Raman spectra were obtained using a non-polarized 532 nm laser, a 100× objective, with five measurements lasting 10 s. The Si band at $\sim 520\text{ cm}^{-1}$ was used for calibration. The spectra were processed using the LabSpec[®] software (Jobin Yvon) (Villeneuve-d’Ascq, France).

3.5. Electron Microprobe Analysis (EMP)

Electron microprobe analyses of chromite were carried out using a CAMECA SX-50 electron microprobe at the Serveis Científics i Tecnològics, Universitat de Barcelona (CCiTUB). The instrument is equipped with four wavelength-dispersive spectrometers (WDS) and one energy-dispersive spectrometer (EDS). The WDS analyses were performed using an acceleration voltage of 20 keV, a beam current of 15 nA, a beam diameter of 1–2 μm and a dwell time of 10 s. Calibration standards were Cr_2O_3 (Cr), corundum (Al), rutile (Ti), periclase (Mg), hematite (Fe), rhodonite (Mn), NiO (Ni), and metallic V. The detection limits were 350 ppm for Cr, 100 ppm for Al, 250 ppm for Ti, 180 ppm for Mg, and 150 ppm for Fe, Mn, Ni and V. The PAP correction procedure [49] was used for obtaining concentrations.

3.6. X-ray Micro Diffraction

Moissanite crystals were analyzed on the thin section by X-ray microdiffraction (μXRD) using a D8 DISCOVER μMR powder diffractometer in Bragg–Brentano $\theta/2\theta$ geometry of 154.1 mm of radius, $\text{Cu K}\alpha_1$ radiation ($\lambda = 1.54056\text{ \AA}$), operated at 50 kV and 1 mA, and with a 0.1 mm collimator at the Centro de Instrumentación Científica (CIC) of the University of Granada. During analysis, the sample was spun at 1 revolution per minute. Crystals were scanned from 25° to $56^\circ 2\theta$ with a step size of 0.02° and a time of 240 s per step, using a Pilatus3-100K Detector (Villigen, Switzerland) at a distance of 151.58 mm. The software Diffrac.EVA was used to integrate the frames and generate the diffractograms, to detect the peaks, and to assign mineral phases and their corresponding d_{hkl} to each peak.

4. Results

4.1. Ore Texture and Mineralogy

The chromitite lenses (Figure 2) mainly consist of subhedral to anhedral grains of chromite 0.5 mm to 1 cm across, and intergranular olivine partially or completely altered to serpentine-group minerals and minor chlorite (Figure 2c,d). The serpentine phase displays a pseudomorphic mesh

texture after olivine, indicating that lizardite is the main phase. However, in some samples chrysotile and antigorite were also recognized [50]. The chromite grains contain inclusions of euhedral olivine (50–200 μm) and amphibole (30–100 μm) (Figure 2c). Other accessory mineral phases are Fe–Ni sulfides (commonly, millerite) and platinum-group minerals (PGM: laurite, irarsite). The inclusions in chromite are generally monomineralic and randomly distributed in the grains, even though they can appear locally clustered or aligned. Olivine inclusions are more abundant near the contact with the dunite envelope (Figure 2d) and show the same optical orientation as olivine crystals in dunite, indicating dunite replacement by chromitite, previously documented by [44].

Near the contact with gabbro sills a <10 cm transition zone develops where chromite “invades” the intergranular space between clinopyroxene and plagioclase grains of the gabbro (Figure 2b). In this zone, clinopyroxene and plagioclase inclusions (<100 μm) in chromite crystals are common; the clinopyroxene inclusions are in optical continuity with clinopyroxene crystals of the adjacent gabbro, indicating that chromitite replaced the gabbro sills [44].

Chromitites are affected by two stages of post-magmatic evolution: serpentinization and chloritization. Serpentinization produced the partial to total replacement of olivine by serpentine-group minerals, magnetite and Fe–Ni sulfides. A second stage produced a thin rim of ferrian chromite, chlorite and sulfides of Ni (millerite) and Cu (chalcopyrite, chalcocite).

Far from the alteration-induced rim and cracks, the spinel consists of high-Al chromite [$0.42 < \text{Cr}\# = \text{Cr}/(\text{Cr} + \text{Al}) < 0.53$; $0.58 < \text{Mg}\# = \text{Mg}/(\text{Mg} + \text{Fe}^{2+}) < 0.77$] (Table 1). Its composition is generally homogeneous (except for lens 6), overlapping the compositional field of podiform “ophiolitic” chromitite (Figure 3a,d). The ranges of concentration of major element oxides are (in wt %): 34.76–42.5 Cr_2O_3 , 24.44–33.14 Al_2O_3 , 12.96–18.51 MgO , up to 6.36 FeO , 8.21–16.92 Fe_2O_3 , 0.07–0.28 V_2O_3 , 0.02–0.29 NiO , and up to 0.34 MnO . The TiO_2 contents are variably high (0.12–0.48 wt %, Figure 3b), overlapping that of chromite crystallized from MORB-type basalts (Figure 3c). This is explained by the fact that the BABB melts from which chromite crystallized had analogous compositions to MORB-type melts [55].

Table 1. Representative electron microprobe analyses of chromite from the Mercedita mine.

Sample	G-12-27	G-12-6	G-12-2	G-12-8	G-12-12	G-12-18	G-15-4	L2-7	L2-8	L3-2	L3-8	L3-7	L3-11	L6-1
TiO₂ (wt %)	0.33	0.33	0.33	0.33	0.40	0.28	0.31	0.31	0.32	0.20	0.21	0.29	0.20	0.28
Al₂O₃	31.03	31.02	31.77	30.53	31.38	30.49	30.44	29.37	29.56	32.04	32.78	31.19	32.98	26.19
V₂O₃	0.16	0.16	0.15	0.19	0.18	0.14	0.10	0.19	0.15	0.14	0.09	0.16	0.07	0.19
Cr₂O₃	37.02	36.49	35.88	37.25	38.30	35.80	37.42	36.88	37.09	35.11	35.29	36.20	35.77	41.22
Fe₂O₃ *	3.38	3.43	3.19	3.14	0.00	3.14	3.35	4.61	3.56	4.18	3.74	2.88	2.01	4.18
FeO *	11.73	11.62	11.12	11.98	14.47	16.92	11.09	12.29	12.55	11.37	9.88	11.85	11.35	11.17
MgO	16.59	16.50	16.90	16.29	14.10	12.96	16.82	15.84	15.55	16.82	17.84	16.21	16.75	16.26
MnO	0.17	0.21	0.12	0.11	0.18	0.30	0.13	0.25	0.26	0.08	0.16	0.16	0.20	0.17
NiO	0.17	0.13	0.18	0.20	0.24	0.10	0.14	0.13	0.14	0.20	0.20	0.18	0.24	0.23
Sum	100.59	99.90	99.64	100.02	99.25	100.13	99.81	99.89	99.21	100.14	100.18	99.12	99.57	99.89
Ti (a.p.f.u.)	0.06	0.06	0.06	0.06	0.07	0.05	0.05	0.06	0.06	0.04	0.04	0.05	0.03	0.05
Al	8.48	8.52	8.70	8.41	8.75	8.56	8.37	8.16	8.26	8.74	8.85	8.63	9.00	7.35
V	0.03	0.03	0.03	0.03	0.03	0.03	0.02	0.04	0.03	0.03	0.02	0.03	0.01	0.04
Cr	6.78	6.72	6.59	6.88	7.17	6.74	6.90	6.87	6.95	6.42	6.40	6.72	6.55	7.76
Fe³⁺	0.59	0.60	0.56	0.55	0.00	0.56	0.59	0.82	0.64	0.73	0.64	0.51	0.35	0.75
Fe²⁺	5.73	5.73	5.85	5.67	4.97	4.60	5.85	5.56	5.49	5.80	6.10	5.67	5.78	5.77
Mg	0.03	0.04	0.02	0.02	0.04	0.06	0.03	0.05	0.05	0.01	0.03	0.03	0.04	0.03
Mn	2.27	2.27	2.16	2.34	2.86	3.37	2.16	2.42	2.49	2.20	1.89	2.33	2.20	2.22
Ni	0.03	0.02	0.03	0.04	0.04	0.02	0.03	0.02	0.03	0.04	0.04	0.03	0.04	0.04
#Cr	0.44	0.44	0.43	0.45	0.45	0.44	0.45	0.46	0.46	0.42	0.42	0.44	0.42	0.51
#Mg	0.72	0.72	0.73	0.71	0.63	0.58	0.73	0.70	0.69	0.73	0.76	0.71	0.72	0.72

a.p.f.u. = atoms per formula unit; *: Calculated.

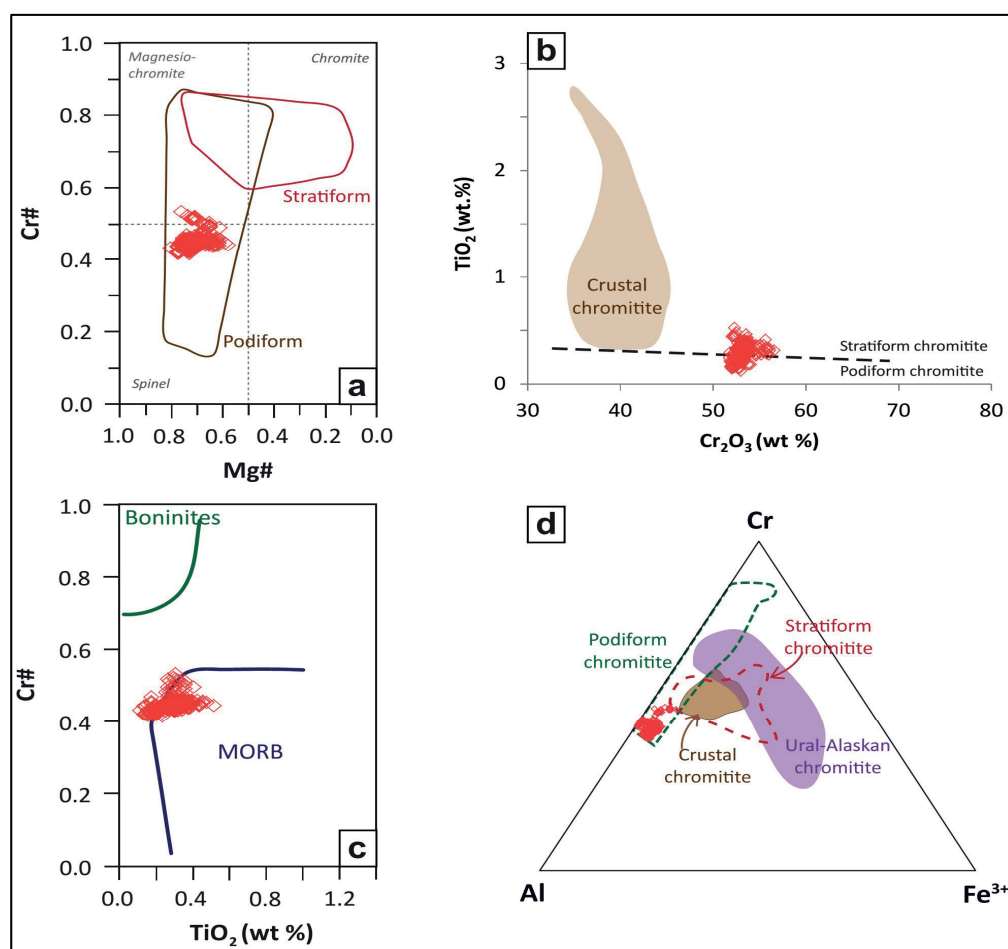


Figure 3. Mercedita chromite composition diagrams: (a) Cr# [Cr/(Cr + Al)] versus Mg# [Mg/(Mg + Al)]; (b) TiO₂ versus Cr₂O₃ (wt %) diagram showing the compositional fields for podiform, stratiform and crustal chromitite; (c) Cr# versus TiO₂ (wt %) showing the type of melt in equilibrium; (d) Fe³⁺–Cr–Al ternary diagram showing the fields for different types of chromitites. Compositional fields are after [51,52] in (a), after [53,54] in (b), (d) and after [55] in (c).

4.2. Mineral Inclusions Identified In Situ in the Chromitite

4.2.1. Oriented Clinopyroxene and Rutile Lamellae in Chromite

Submicrometric lamellae of clinopyroxene with a preferred crystallographic orientation are included in chromite grains located far from the interaction zone with the gabbro dikes (Figure 4a–c). These elongate crystals are usually 10 μm long and less than 1 μm wide, follow the (111) crystallographic planes of chromite (Figure 4b,c) and are variably distributed in most of the samples studied. The energy-dispersive spectra obtained using the field-emission electron microscope (FESEM) on relatively large grains (e.g., Figure 4d) indicate a diopside or Ca-rich enstatite composition (the signal of the host chromite is recorded in the spectra to some extent), but further Raman analyses show spectra compatible with diopside (Figure 4e, after subtracting the chromite signal), with peaks at 242, 326, 391, 667, 857, 1011 and 1269 cm⁻¹, which are analogous with those described by [12,56].

Rutile lamellar crystals 5–80 μm across are present in chromite following the (111) crystallographic plane (Figure 5a,b,d). The elongate crystals define three different main orientations in chromite (Figure 5b). The EDS spectra obtained in the larger crystals (Figure 5c) clearly show that only Ti and O are present; the Raman spectra show peaks at 239, 246, 441 and 609 cm⁻¹ (Figure 5e) corresponding to rutile (e.g., RUFF ID: R110109). However, it is noteworthy that rutile inclusions are only found in chromite grains located near the contact with the gabbro sills described by [24,44].

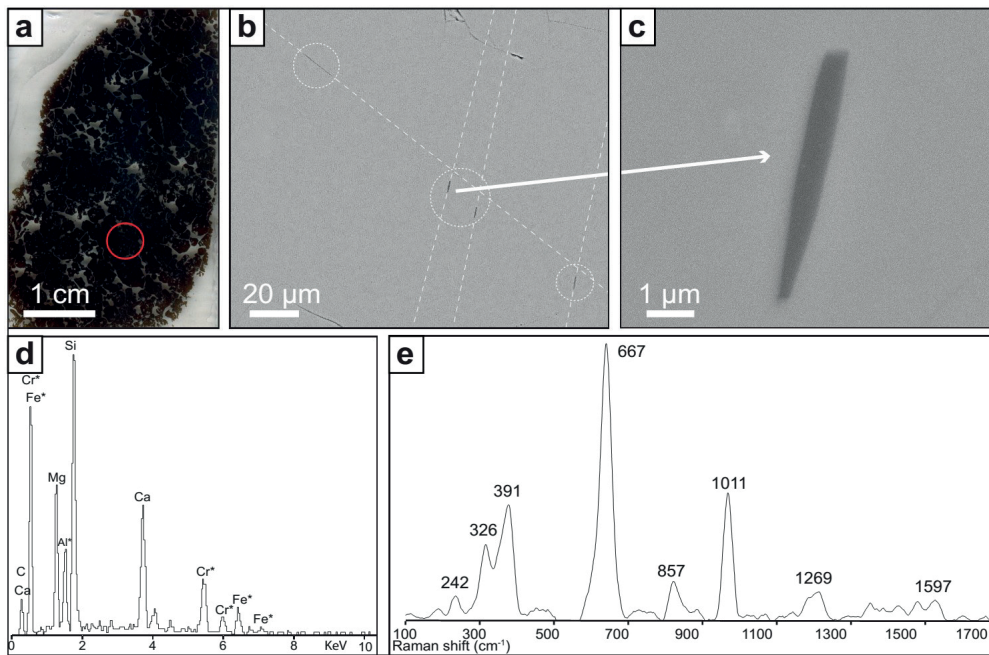


Figure 4. Oriented clinopyroxene lamellae in the Mercedita chromite: (a) Thin section containing the clinopyroxene lamellae showed in the images (b,c). The location of the studied lamellae is showed with a red circle; (b) Backscattered electron (BSE) image of oriented pyroxene lamellae defining two main directions; (c) Zoom of one sub-micron clinopyroxene lamellae of image (b); (d) Energy-Dispersive Spectroscopy (EDS) spectra of the clinopyroxene of image (b), showing qualitatively its chemical composition. The elements marked with an asterisk correspond to the chromite host; (e) Raman spectra of the diopside after subtraction of the chromite background.

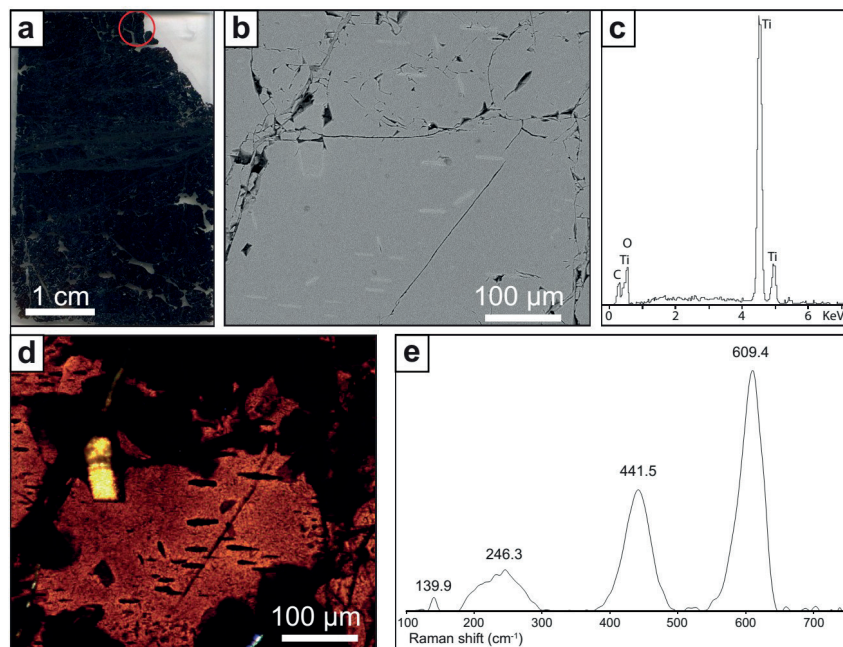


Figure 5. Rutile laminar crystals oriented in the Mercedita chromite in contact with the gabbro: (a) Thin section containing the rutile crystals in the images (b,d). The location of the images (b,c) is shown with a red circle; (b) Backscattered electron (BSE) image of oriented rutile crystals defining three main directions; (c) Energy-Dispersive Spectroscopy (EDS) spectra of the rutile of image (b), showing qualitatively its chemical composition; (d) Transmitted light optical microscope image of rutile crystals included in chromite; (e) Raman spectra of rutile after subtraction of the chromite background.

4.2.2. Mineral Inclusions in Healed Fractures in Chromite

Chromite grains host multiple trails of inclusions (Figure 6a–c) that can be followed across several grains. The inclusions range from a submicrometric size to 7 μm . The mineral species hosted in these trails are described hereafter.

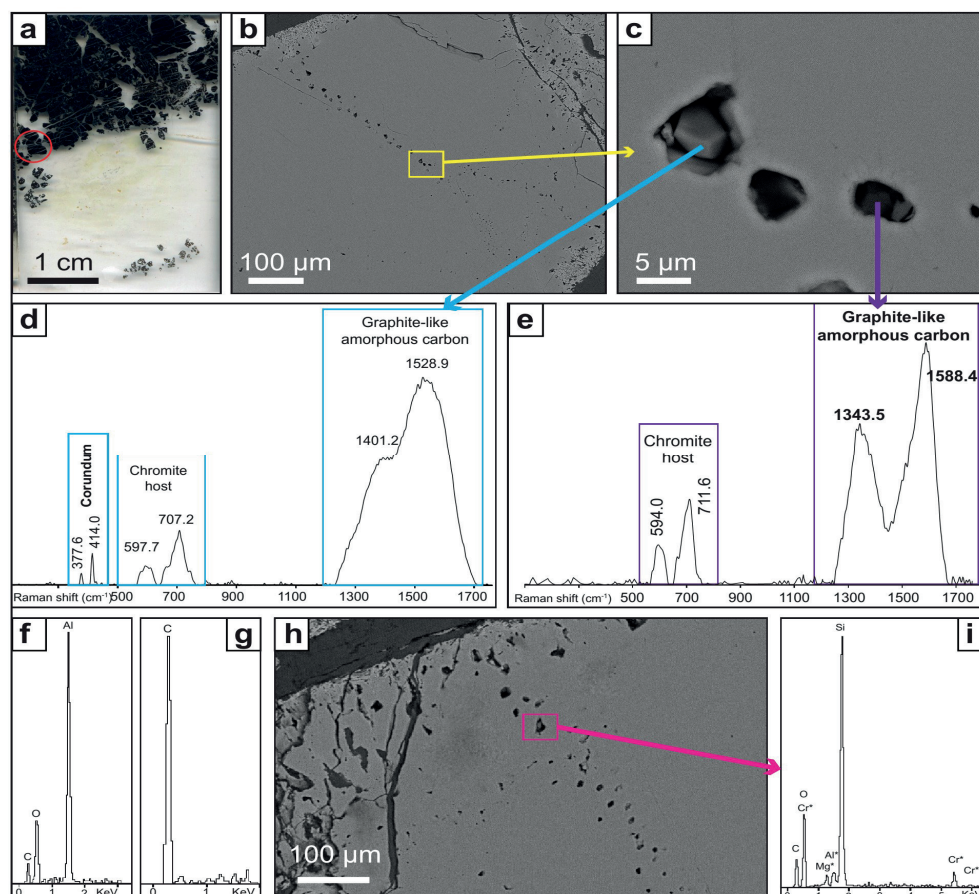


Figure 6. Inclusion trails in chromite grains: (a) Thin section containing the inclusion trails in images (b,c). The location of the inclusions in the section is shown with a red circle; (b) Backscattered electron (BSE) image of a trail of inclusions; (c) Detail of three inclusions hosting corundum and graphite-like amorphous carbon, BSE image. (d) Raman spectra of corundum, the host chromite and graphite-like amorphous carbon surrounding the corundum crystal; (e) Raman spectra of the carbon-bearing inclusion in image (c), showing the host chromite and graphite-like amorphous carbon; (f) Energy-Dispersive Spectroscopy (EDS) spectra of the corundum crystal of image (d), showing qualitatively its chemical composition; (g) Energy-Dispersive Spectroscopy (EDS) spectra of the carbon-bearing inclusion in image (c); (h) BSE image of inclusion trail close to the chromite alteration rim; (i) Energy-Dispersive Spectroscopy (EDS) spectra of the SiO_2 crystal of image (h), showing qualitatively its chemical composition.

Subhedral corundum grains up to 5 μm in size (Figure 6c) have been characterized by Raman spectroscopy (Figure 6d, in which the characteristic spectrum appears together with that of the host chromite), and by EDS (Figure 6f). Corundum is surrounded by amorphous carbon, which also appears in the Raman spectra.

Carbon inclusions up to 5 μm across are common in the chromite trails (Figure 6c). The main species of carbon is graphite-like disordered carbon, which is characterized by the D and G Raman bands at about 1350 and 1580 cm^{-1} , respectively (Figure 6d,e). The inclusions show a variable degree of disorder in the stacking sequence. The EDS spectra of these inclusions show that C is the only element present (Figure 6g).

Grains of SiO₂ also have been identified (Figure 6h,i). These inclusions, up to 7 μm across, are usually located close to the ferrian chromite rims. They have been characterized by EDS (Figure 6i). However, it has not been possible to obtain the corresponding Raman spectra owing to strong fluorescence.

4.2.3. Moissanite in the Silicate Matrix

Moissanite crystals have been found in situ in two replicated thin sections (elaborated after the same rock slab) (Figure 7a). The SiC grains are located in the altered matrix of chromitite (Figure 7b,c) that mainly consists of aggregates of fine-grained hydrated minerals including serpentine-group minerals, clinocllore and minor hornblende.

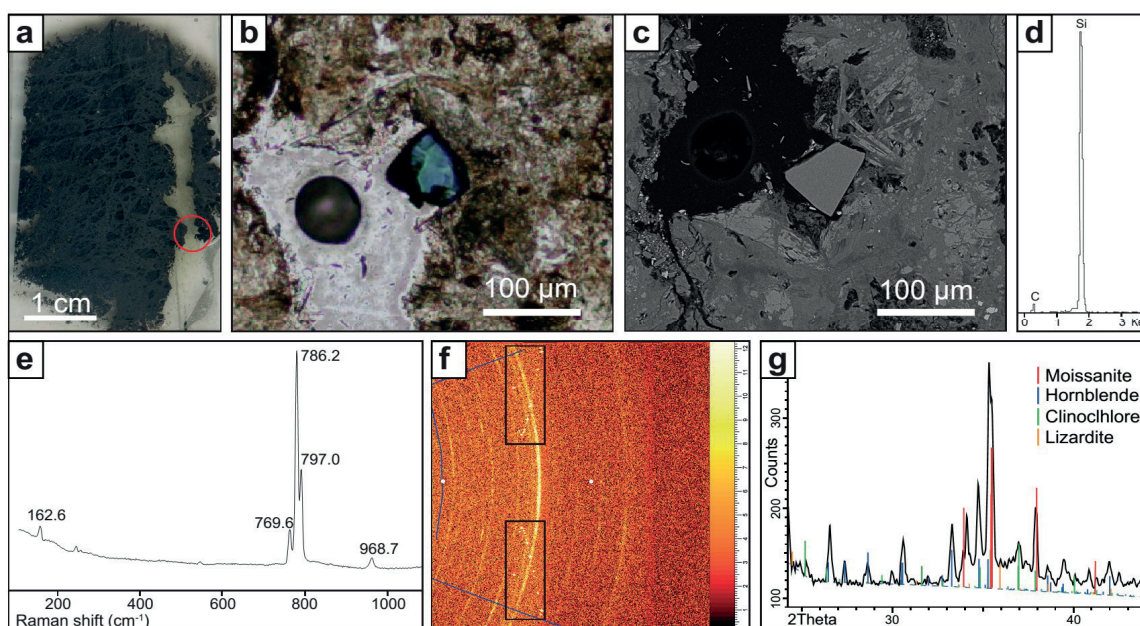


Figure 7. Moissanite crystal hosted in the chromitite altered silicate matrix: (a) Thin section containing the moissanite crystal in images (b,c). The location of the moissanite crystal in the thin section is showed with a red circle; (b) Transmitted light optical microscope image of the moissanite crystal. Note that the crystals show the typical natural moissanite blue color; (c) Backscattered electron (BSE) image of the same moissanite crystal in (b); (d) Energy-Dispersive Spectroscopy (EDS) spectra of the moissanite crystal of images (b,c), showing qualitatively its chemical composition; (e) Raman spectra of the moissanite crystal; (f) Single crystal X-ray microdiffraction pattern of moissanite; (g) Integration of the diffraction pattern with peak identification.

The crystals are subhedral, with a grain size of about 80 μm (Figure 7b,c) showing the typical blue color in transmitted light. The EDS spectra show peaks of Si and C only (Figure 7d). The Raman spectra, with peaks at 162, 769, 786, 797 and 968 cm⁻¹, confirms that the mineral is moissanite. Single crystal X-ray microdiffraction (Figure 7f) shows that SiC has a hexagonal structure that corresponds to the 6H polytype (Figure 7g), the most common polytype of moissanite [57].

Synthetic SiC used in polishing the sample has a maximum grain-size (21.8 μm—P800) significantly smaller than that of the observed moissanite crystals (up to 80 μm). We believe that the sample was not contaminated during thin-section preparation. In addition, moissanite grains with similar morphological characteristics (crystal, habit size and color) have been reported from the chromitites of various Neotethyan ophiolites (e.g., Oman, Ponzati-Karsanti in Turkey, Luobusa, Sarohay and Hegenshan in Tibet and Ray-Iz in Polar Urals [4,19,58–60]). These grains have been interpreted as natural moissanite and not due to anthropogenic contamination.

4.3. Mineralogy of Heavy Mineral Concentrates Obtained by Hydroseparation

Euhedral grains of native Cu up to 100 μm (Figure 8a,b) are very common in the mineral concentrates. Even though the EDS spectra of these grains show a small oxygen peak (Figure 8b), electron-microprobe analyses show that the grain is native Cu (99–100 wt % Cu). Unidentified inclusions up to 15 μm in length and rich in P and Na are hosted in the native Cu grains (Figure 8c). To our knowledge, their qualitative composition does not correspond to any known mineral. The grains also show an overgrowth of SiO_2 (Figure 8d).

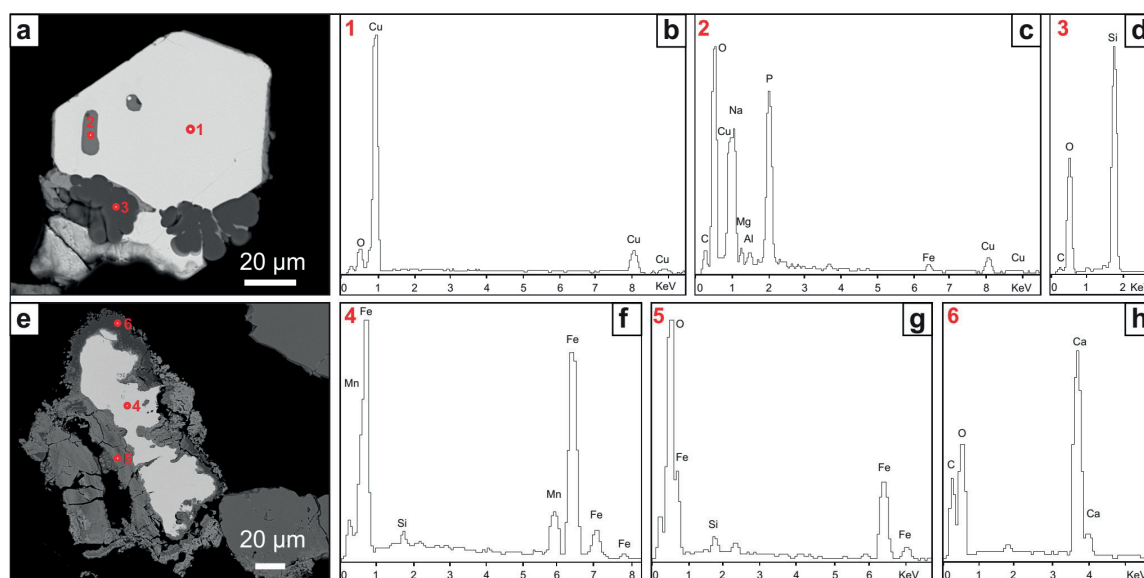


Figure 8. Metallic alloys found in the mineral concentrates of chromitite samples: (a) Backscattered electron (BSE) image of a metallic grain showing inclusions and mineral growth in the lower border. Numbers indicate the position of the EDS spectra of images (b–d); (b) Energy-Dispersive Spectroscopy (EDS) spectra of center of the bright grain of image (a) (1); (c) EDS spectra of the inclusion (2); (d) EDS spectra of the mineral growth in the lower border of the crystal (3); (e) Backscattered electron (BSE) image of a metallic grain surrounded by other mineral phases. Numbers indicate the position of the EDS spectra of images (f–h); (f) EDS spectra of center of the bright grain of image (e) (4); (g) EDS spectra of the border (5); (h) EDS spectra of the outer border of the crystal (6).

Elongate grains (up to 125 μm) of a Fe–Mn alloy (Figure 8e) have been characterized by EDS (Figure 8f; the Si peak corresponds to the glue used to mount the grains in the polished section). These grains are surrounded by an inner layer of Fe oxide (Figure 8g) and an outer layer of Ca-carbonate (Figure 8h). The texture indicates a replacement relationship.

In addition, it should be mentioned that euhedral grains of zircon have been identified [16] in heavy-mineral concentrates from the Mercedita chromitites.

5. Discussion

5.1. Origin of Oriented Clinopyroxene and Rutile Lamellae in Chromite

The Mercedita chromitites contain inclusions of clinopyroxene with preferred orientation in chromite, a petrographic feature that has been observed in other ophiolitic chromitites (Table 2). Such inclusions have been interpreted as the exsolution of silicate components lodged in the structure of high-temperature and high-pressure chromite (or their high-pressure polymorphs) [6,61,62], whether these pyroxene lamellae are associated [61] or not [12,63] with minerals that typically form at high pressure (e.g., coesite >30 GPa; [64] and references therein). According to the models proposed in the literature, such petrographic feature could correspond to (1) chromite that originated at low

pressure in the shallow mantle, and then experienced recycling in the deep mantle, at which point they could dissolve a silicate component. Once returned to the surface, the new spinel reverted back to low-pressure chromite and released the dissolved silicate component in the form of pyroxene lamellae [12,14,15,61,63,65]. It is also possible (2) that a high-pressure polymorph of chromite already containing high amounts of SiO₂ and CaO in its structure had crystallized near the bottom of the upper mantle or at the mantle transition and was carried upwards by deep-seated mantle plumes or asthenospheric melts, that experienced decompression to low-pressure chromite while releasing clinopyroxene lamellae, e.g., [6,19].

These interpretations seem to be consistent with the results of recent experimental work; magnesiochromite can incorporate only <0.5 wt % CaO at 12–15 GPa and minor amounts (<1–2 wt %) of SiO₂ at <16 GPa, whereas the structure of the high-pressure polymorph calcium ferrite (CF-type, CaFe₂O₄) can accommodate higher amounts of SiO₂ (~3–5 wt % at 14–18 GPa in the MgCr₂O₄–Mg₂SiO₄ system and up to ~11–14 wt % in the MgAl₂O₄–Mg₂SiO₄ system) and CaO (~7–8 wt % at 14–18 GPa) [66,67]. The calcium ferrite polymorph is stable in the P-T region between 12.5 and 20 GPa at ~1400–1600 °C, and it could release SiO₂ and CaO in the form of pyroxene lamellae upon decompression [66–68].

It is worth noting that we have not identified exsolution-induced lamellae of coesite or other UHP minerals in the Mercedita chromitite (Table 2). This lack of coesite in our samples can be related to the mechanism of formation of the clinopyroxene lamellae. Silica will only exsolve from chromite once CaO and SiO₂ have been completely consumed to form clinopyroxene and MgSiO₃ [66]. Therefore, the absence of coesite lamellae in the Mercedita chromitites may simply reflect the fact that not all the CaO and SiO₂ were consumed.

However, the Mercedita chromitites are juxtaposed to, and also include, gabbro sills that show no evidence of HP/UHP metamorphism, ruling out the recycling of the whole ophiolitic sequence, including chromitite, gabbro and their dunite envelope and host harzburgite. In turn, the Mercedita chromitite could consist of an accumulation of UHP chromite grains brought from the lower mantle to the top of the petrologic Moho upon its arrival to the shallow part of the lithosphere, as suggested by [6,19]. We must point out that there is no evidence for such magmatic activity related to mantle plume in eastern Cuba ophiolites [40,42], leading us to rule out this possibility. In addition, the Mercedita chromite grains yielded micro-Raman spectra with positions at 591–596 and 712–717 cm⁻¹, which are similar to the peaks observed for low-pressure cubic chromite and magnesiochromite and strongly differ from the peaks observed in the high-pressure chromite polymorph (Figure 9), which suggests that they were not derived from a high-pressure polymorph. In any case, clinopyroxene exsolution in chromite grains do not necessarily involve exsolution from a UHP phase. In fact, the liquidus chromite can concentrate significant amount of SiO₂ and CaO (~0.3 wt % each) that is more than enough to exsolve clinopyroxene lamellae during solid-state processes of annealing (see [22]).

Another interesting observation is that chromite grains in the vicinity of gabbro sills juxtaposed or included in the Mercedita chromitite body also contain rutile lamellae with preferred crystallographic orientation. These types of inclusions have been described in chromitites of the Bushveld layered complex in South Africa [69] as well as in other ophiolitic chromitites, e.g., [70]. Such type of inclusions is interpreted as the result of exsolution of TiO₂ from the chromite structure upon cooling, owing to the low solubility of Ti in the structure of chromite at a low temperature [70,71]. The presence of these inclusions in Mercedita chromite indicates that the contact between the gabbro sills and the chromitites was a reaction zone with a relatively high availability of titanium. Since the composition of chromite is broadly constant except in the proximity of the gabbros (see profiles in Figure 4 in [24], the local increase in Ti must be attributed to the presence of the gabbros.

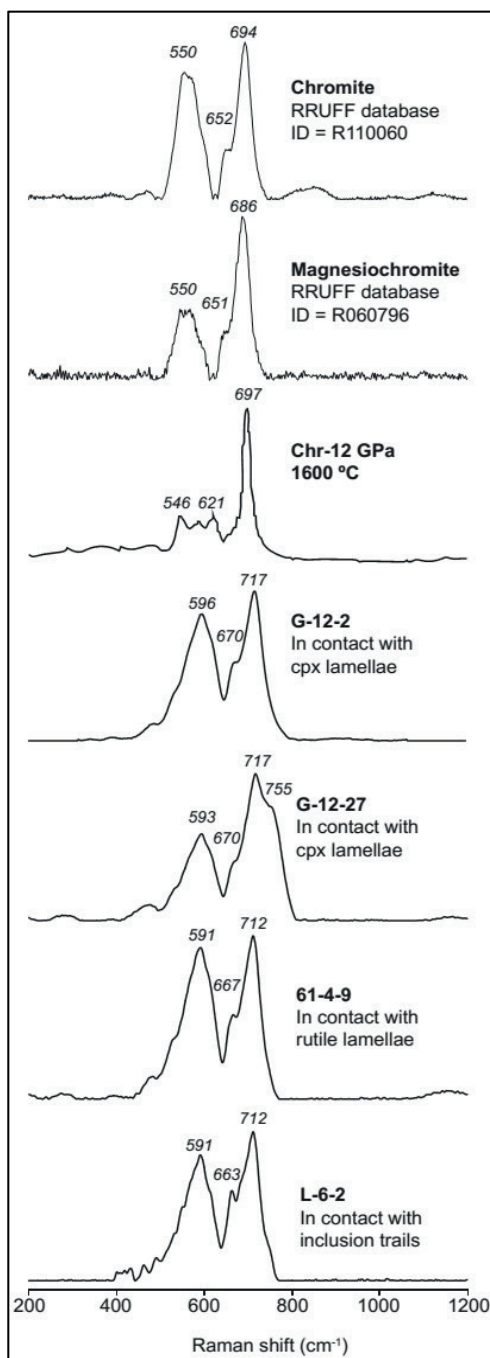


Figure 9. Raman spectra of chromite in the Mercedita chromitites. Spectra of chromite and magnesiochromite from natural examples and experimental works are shown by comparison. The spectrum for high-pressure chromite polymorph (Chr-12 GPa, 1600 °C) is from [67].

Table 2. Occurrence of UHP (Ultra-High Pressure), SuR (Super-Reduced) and Crustal-derived “exotic” mineral phases in worldwide ophiolites and chromitites. Luobusa (Tibet), Dingqing (Tibet) and Ray-Iz (Polar Urals) data is from [15,72] and references therein, Purang (Tibet) data from [73], Zedang (Tibet) data from [74], Semail (Oman) data from [4,62], Mirdita (Albania) data from [75], Pozanti-Karsanti (Turkey) data from [10], Orhaneli-Harmancik (Turkey) data from [11], Myitkyina (Myanmar) data from [76], Baja California (Mexico) data from [12] and Moa-Baracoa (Cuba) data from [16] and this study.

Ophiolite	Luobusa (Tibet)	Dingqing (Tibet)	Purang (Tibet)	Zedang (Tibet)	Ray-Iz (Polar Urals)	Semail (Oman)	Mirdita (Albania)	Pozanti-Karsanti (Turkey)	Orhaneli-Harmancik (Turkey)	Myitkyina (Myanmar)	Baja California (Mexico)	Moa-Baracoa (Cuba)
Host Rock	Chrom, Harz	Harz	Peridotite	Chrom, Dun	Chrom, Harz	Chrom	Chrom	Chrom	Chrom	Peridotite	Chrom	Chrom, Harz
Diamond	×	×	×		×		×			×		
Coesite/Stishovite pseudomorph TiO2 II (α -PbO ₂ structure)	×				×							
Cubic-BN	×											
Si-rutile	×											
BWJ (inverse-spinel structure)	×											
CF-chromite Clinopyroxene exsolution lamellae	×			×	×	×		×			×	×
Amorphous carbon	×				×							×
Moissanite (SiC)	×				×	×		×		×		×
Fe-carbide (FeC)	×				×							×
W-carbide (WC)	×				×							×
Ti-carbide (TiC)	×				×							×
Fe-silicide (FeSi)	×				×							×
Ti-nitride (TiN)	×				×							×
TAZ (Ti ₄ Al ₂ (Zr,Si)O ₁₁)	×				×					×		×
Native Si	×				×							×
Native Ni, Co, Fe, Cr, Zn, PGE	×				×							×
Iron-Wüstite (Fe-FeO)	×				×							×
Alloys (Fe-Mn, Fe-Cr, Fe-Co)	×				×							×
Alm garnet	×				×							×
Andalusite	×				×							×
Amphibole	×			×	×	×						×
Apatite	×				×	×						×
Biotite	×				×	×						×
Corundum	×				×	×						×
K-feldspar	×				×	×						×
Kyanite	×				×	×						×
Ilmenite	×				×	×						×
Muscovite	×				×	×						×
Plagioclase	×				×	×						×
Quartz	×				×	×						×
Rutile	×				×	×		×		×		×
Titanite	×				×	×		×		×		×
Zircon	×				×	×		×		×		×

×: Indicates the presence of the mineral in the ophiolite (peridotites and/or chromitites).

5.2. The SuR Assemblage

The Mercedita chromitite contains moissanite (SiC), native Cu and a Fe–Mn alloy surrounded by an iron oxide and CaCO₃ (Figures 7 and 8). Similar phases have been reported in other ophiolitic chromitites (Table 2) and interpreted as part of a super-reducing (SuR) assemblage [3,4,6–8,10,14,15,17]. Although only recently reported in ophiolitic chromitites [58,77], moissanite has already been found in a variety of terrestrial and extraterrestrial rocks, including meteorites [78] and references therein, kimberlites and associated diamond [57,79–82], volcanic breccias and tuff [72,83,84], high- and low-grade metamorphic rocks [59,85], and limestones [86,87]. According to experimental and empirical data, the formation of SiC only occurs at a fugacity of oxygen 6.5–7 log units below the iron-wüstite buffer (IW) [88,89]. This observation, together with the common association of the SiC with inclusions of native Si and other minerals such as diamond and coesite that typically form at UHP conditions, has led some authors [3,6,15] to suggest that moissanite found in ophiolitic peridotites and chromitites formed from highly reducing fluids present near the top of the Mantle Transition Zone. However, some [89] have shown that moissanite can be deposited at low pressure and low temperature (3.5 GPa and <700–800 °C) by ultra-reducing fluids released during the initial stages of serpentinization of olivine in peridotites. In this model, C-rich fluids provided by dehydration of the sedimentary lid of the subducting slab reacted with peridotite, trapping H₂O in the hydrous alteration-induced minerals and thus progressively reducing fluids. CH₄-rich fluids are associated with serpentinization of ultramafic rocks in the submarine and subduction zone environments. CH₄ fluid inclusions occur in olivine from partially serpentinized harzburgite and dunite [90]. Production of CH₄ during serpentinization in the sub-seafloor is a widely accepted process [91]. In addition, CH₄ can be generated as a by-product of serpentinization of peridotites in the mantle wedge overlying the subducting oceanic slab, as a result of the complete consumption of water during formation of serpentine [90] and references therein.

The observation of large crystals of moissanite up to 80 µm across in the serpentinized silicate matrix of Mercedita chromitites is consistent with their formation related to serpentinization fluids. Furthermore, the presence of C in the system during serpentinization is also consistent with inclusions of graphite-like amorphous carbon in sealed cracks in many Mercedita chromite grains. These highly reducing fluids released during serpentinization may be also responsible for the formation of native Cu grains and the Fe–Mn alloy, which are stable at ΔFMQ between –9 and –12, as suggested by [92] for the ophiolitic chromitites of Kempirsai and [89] for the Luobusa chromitites. In addition, Ref. [93] described Fe–Ni and Ni–P alloys that also record extremely low conditions of oxygen fugacity and interpreted them to result from serpentinization.

5.3. Minerals Typical of the Continental Crust

Mineral concentrates from the Mercedita chromitite contain zircon, corundum, and quartz (Table 2). According to [16], zircon yields an age between 289 ± 9 Ma (early Permian) and 310 ± 10 Ma (late Carboniferous), much older than the time of ophiolite formation (90–125 Ma); [23,25]. The zircon contains a suite of inclusions (monazite, K-feldspar, quartz, biotite, apatite and occasional ilmenite) typical of any zircon crystallized from a crustal magma. A crustal origin of the zircon is also consistent with its Hf isotopic composition, with εHf(t) ranging from –5.57 to –3.67 [16]. Interestingly, xenocrystic zircon of the same age has been reported in associated oceanic gabbros and volcanic arc lavas in Cuba [94] indicating the recycling of crustal zircon through the mantle wedge above the paleo-subducting slab of the Greater Antilles Arc.

5.4. Pros and Cons of Existing Models in Order to Explain the SuR and Associated Minerals in Mercedita

Table 2 summarizes the occurrence of UHP, SuR and crustal-derived phases discovered in chromitites and associated peridotites from the mantle section of ophiolitic complexes. Various models have been proposed to explain the presence of these “exotic” minerals.

(i) The Subduction-Recycling Model.

Chromitites and host peridotites are formed at shallow depth; the assemblage is subducted into the Mantle Transition Zone, and later exhumed to a shallow depth together with its host dunite and harzburgite at spreading centers as a mantle diapir [9,13–15,63]. In this model, SuR phases and coexisting UHP minerals are incorporated into chromitite during the UHP event at the Mantle Transition Zone, whereas the crustal minerals are trapped during crystallization of chromite at low pressure in the upper mantle [12,14,15]. This model has been largely considered to explain the mineral phases found in the Luobusa chromitites (Tibet). However, it has limitations. It does not explain the presence of unmetamorphosed gabbro sills included in the Mercedita chromitites. Moreover, it cannot explain why SuR minerals are closely linked to serpentinization-related minerals, which are not stable at the Mantle Transition Zone or even shallower depths.

(ii) The Plume Model.

Chromite grains formed from high-Cr magmas in the Mantle Transition Zone (15–16 GPa and 1600 °C, [6]) or the lower part of the upper mantle are proposed to encapsulate UHP and SuR phases. Later, these grains migrate upward in a mantle plume and are incorporated in the magma system beneath a spreading center [5,6,17,18,66,95]. According to this model, crustal minerals encapsulated in chromitite were brought to the MTZ through earlier subduction, and SuR and UHP minerals formed at or near the top of the MTZ. This model has been used to explain the mineral phases recovered in the Ray-Iz ophiolitic chromitites (Polar Urals [6]). However, besides requiring an specific geological setting of mantle plume plus spreading center, recent experimental studies [67] have shown that Cr is preferentially partitioned into garnet at pressure conditions of the MTZ, preventing chromite (or its high-pressure polymorph) to directly crystallize from melts at these depths. Moreover, it has been suggested that chromite (or its high-pressure polymorph) is not stable at the reducing conditions of the MTZ, and that such conditions would imply a complete loss of oxygen, forming aluminum spinel and native Cr and Fe [89]. As with the previously discussed model, this model has limitations as well. It fails to explain the formation of the mineral phases in the Mercedita chromitite. Firstly, the model predicts the formation of Cr-rich chromite, whereas the Mercedita chromite is Al-rich. Secondly, the model cannot explain the presence of gabbros juxtaposed and included in the chromitite. Thirdly, there is no evidence of magmatic activity related to mantle plume in eastern Cuba ophiolites. Finally, it does not explain the coexistence of serpentinization-related minerals with SuR phases.

(iii) The Slab Contamination Model.

The presence of continental crust-derived minerals in chromitites and ophiolites reflects the subduction of metasedimentary rocks. These rocks were subducted into the deep mantle and reacted with highly reduced phases. Later, rollback and breakoff of a subducting slab creates a slab window through which asthenosphere rises and melts, generating Cr-rich mafic magmas [4,19]. The formation of the chromitite bodies is related to local slab tear, allowing rapid uprise of asthenospheric melts into the supra-subduction mantle wedges. In this model, chromite grains are interpreted to be transported against gravity attached to H₂O-rich pools segregated from the basaltic melt [19]. Nevertheless, exsolution of volatiles to transport chromite grains necessary to form the chromitite bodies would only occur at very low pressures in the shallow mantle [96], hence, making unlikely the transport of chromite (a dense mineral) for tens of hundreds of kilometers from the slab window to the shallow mantle. For Mercedita chromitite bodies, and similar to previous models, slab contamination fails to explain the relation of reduced mineral phases with serpentinization processes.

(iv) Lightning Strikes Exposed Chromitite Bodies.

On the basis of experimental work using 30 kA electric discharges corresponding to natural cloud-to-ground lightning strikes [21,22], some have suggested that a suite of minerals of the SuR assemblage (such as moissanite and other carbides, silicides, alloys, and silicate and oxide spherules) can form in ophiolitic chromitite in response to lightning strikes. According to these authors, chromitite bodies within ophiolites are highly conductive and, hence, the thermal effect of a lightning strike could penetrate deeply if they are exposed at the Earth's surface. The derived >6000 K (5700 °C) thermal effect would produce plasma from which the aforementioned SuR phases and diamond precursors crystallize. However, if these high temperatures were reached during lightning (either experimental or natural), one could expect that chromite would melt and thus producing microstructural and chemical modifications, which have not been identified in natural chromites. It is worth to note that these experiments were performed using a silicate material, not chromite, therefore limiting its applicability to natural chromite as long as lightning strikes must have affected the entire rock and not only the silicate matrix. In addition, these authors state that "other high-pressure phases like coesite and stishovite may also form even though they are not found here", therefore leaving unexplained how plasma ejecta could form coesite intimately intergrown with diopside, as reported as oriented inclusions in the Tibetan chromitites, e.g., [65]. Moreover, the Mercedita chromitites were not exposed to lightning strikes and to the formation of fulgurite at the high altitude, in excess of 4000 m, suggested by [21,22] for the Tibetan case. The limited applicability of this model to explain the SuR minerals in the Mercedita chromitites is, again, the fact that SuR minerals occur associated with serpentine minerals, in both the silicate matrix and in fractures at Mercedita. These minerals formed at less than 700 °C, while fractures were annealed by recrystallization of chromite at subsolidus conditions during their passage through the shallow mantle and their final emplacement into the continental margin. These observations therefore rule out an origin of SuR minerals related to vaporization at the high temperatures proposed by Ballhaus and co-workers. Moreover, this model cannot explain the presence of minerals derived from the continental crust.

(v) The Cold Plumes Model.

Cold plumes comprise partially molten hydrated peridotite, dry solid mantle, and subducted oceanic crust [30,97] and references therein. Cold plumes rise in the mantle wedge as a result of Raleigh-Taylor instabilities caused by hydration and melting in the subduction channel [97]. The rise from a depth greater than 100 km brings asthenospheric and lithospheric mantle and subducted crustal material to shallow mantle levels, creating mineralogical and lithological heterogeneities in the mantle wedge. These heterogeneities may include bodies of podiform chromitite. Cold plumes are an excellent mechanism to transfer subducted crystals of zircon of crustal origin toward the mantle wedge [98], whereas others [16] explain the presence of crustal zircon in the Mayarí-Baracoa ophiolitic belt by this mechanism. Although this mechanism explains the presence of continental-crust-derived mineral phases, it fails to explain UHP and SuR minerals. For the case of the Mercedita chromitite, the presence of the crustal minerals can be explained by this model but the association of SuR phases and serpentinization-related minerals and the presence of the clinopyroxene lamellae along crystallographic planes of chromite cannot be explained.

6. Concluding Remarks

"Exotic" mineral phases in the Mercedita chromitite could be interpreted as providing evidence of high-pressure and ultra-reduced conditions (graphite-like amorphous carbon, clinopyroxene exsolution lamellae, moissanite, native elements, and alloys). However, the juxtaposition of chromitite bodies with unmetamorphosed gabbro sills rules out the possibility of deep recycling of the ophiolitic sequence. Evidence of a mantle plume, asthenospheric rise or lightning strikes can also hardly be invoked to the case of the ophiolites of eastern Cuba.

A simpler explanation for the formation of the “exotic” phases in the Mercedita chromitites can be offered. Clinopyroxene and rutile exsolution-induced lamellae formed during cooling of chromite after interaction with adjacent gabbros. The SuR phases (moissanite, native Cu, Fe–Mn alloy) formed during the serpentinization processes, where super-reduced microenvironments are created at low temperature and low pressure. Finally, crustal phases (corundum, quartz, zircon) represent sediment-derived xenocrystic grains delivered into the mantle wedge by cold plumes.

Author Contributions: J.A.P. conceived the ideas for this study; J.A.P., J.C.M. and F.G. participated in the field work and sample collection; A.A. designed the strategy for the XRD analyses; N.P.-S., J.A.P., A.G.-C. and J.M.G.-J. analyzed and discussed the resulting data; N.P.-S., J.A.P., A.G.-C. and J.M.G.-J. wrote the paper.

Funding: This research was financially supported by the Spanish Project CGL2015-65824 granted by the Spanish “Ministerio de Economía y Competitividad” to J.A.P., the Ramón y Cajal Fellowship RYC-2015-17596 to J.M.G.-J. and a FPU Ph.D grant to N.P.-S. by the Ministerio de Educación of the Spanish Government.

Acknowledgments: We want to thank three anonymous reviewers and the academic editor for their criticism that greatly improved our manuscript.

Conflicts of Interest: The authors declare no conflict of interest.

References

- Robinson, P.T.; Bai, W.J.; Malpas, J.; Yang, J.S.; Zhou, M.F.; Fang, Q.S.; Hu, X.F.; Cameron, S.; Staudigel, H. Ultra-high pressure minerals in the Luobusa ophiolite, Tibet, and their tectonic implications. *Geol. Soc. Lond. Spec. Publ.* **2004**, *226*, 247–271. [[CrossRef](#)]
- Yang, J.S.; Dobrzhinetskaya, L.; Bai, W.J.; Fang, Q.S.; Robinson, P.T.; Zhang, J.; Green, H.W. Diamond- and coesite-bearing chromitites from the Luobusa ophiolite, Tibet. *Geology* **2007**, *35*, 875–878. [[CrossRef](#)]
- Dobrzhinetskaya, L.F.; Wirth, R.; Yang, J.; Hutcheon, I.D.; Weber, P.K.; Green, H.W. High-pressure highly reduced nitrides and oxides from chromitite of a Tibetan ophiolite. *Proc. Natl. Acad. Sci. USA* **2009**, *106*, 19233–19238. [[CrossRef](#)] [[PubMed](#)]
- Robinson, P.T.; Trumbull, R.B.; Schmitt, A.; Yang, J.S.; Li, J.W.; Zhou, M.F.; Erzinger, J.; Dare, S.; Xiong, F. The origin and significance of crustal minerals in ophiolitic chromitites and peridotites. *Gondwana Res.* **2015**, *27*, 486–506. [[CrossRef](#)]
- Xu, X.; Yang, J.; Robinson, P.T.; Xiong, F.; Ba, D.; Guo, G. Origin of ultrahigh pressure and highly reduced minerals in podiform chromitites and associated mantle peridotites of the Luobusa ophiolite, Tibet. *Gondwana Res.* **2015**, *27*, 686–700. [[CrossRef](#)]
- Yang, J.S.; Meng, F.; Xu, S.; Robinson, P.T.; Dilek, Y.; Makeyev, A.B.; Wirth, R.; Wiedenbeck, M.; Cliff, J. Diamonds, native elements and metal alloys from chromitite of the Ray-Iz ophiolite of the Polar Urals. *Gondwana Res.* **2015**, *27*, 459–485. [[CrossRef](#)]
- Zhang, R.Y.; Yang, J.S.; Ernst, W.G.; Jahn, B.M.; Iizuka, Y.; Guo, G.L. Discovery of in situ super-reducing, ultrahigh-pressure phases in the Luobusa ophiolitic chromitites, Tibet: New insights into the deep upper mantle and mantle transition zone. *Am. Mineral.* **2016**, *101*, 1285–1294. [[CrossRef](#)]
- Xiong, F.; Yang, J.; Robinson, P.T.; Xu, X.; Ba, D.; Li, Y.; Zhang, Z.; Rong, H. Diamonds and other exotic minerals recovered from peridotites of the Dangqiong Ophiolite, western Yarlung–Zangbo suture zone, Tibet. *Acta Geol. Sin.* **2016**, *90*, 425–439.
- Xiong, F.; Yang, J.; Dilek, Y.; Xu, X.; Zhang, Z. Origin and significance of diamonds and other exotic minerals in the Dingqing ophiolite peridotites, eastern Bangong–Nujiang suture zone, Tibet. *Lithosphere* **2017**, *10*, 142–155. [[CrossRef](#)]
- Lian, D.; Yang, J.; Dilek, Y.; Wu, W.; Zhang, Z.; Xiong, F.; Liu, F.; Zhou, W. Diamond, moissanite and other unusual minerals in podiform chromitites from Pozanti-Karsanti ophiolite, southern Turkey: Implications for deep mantle origin and ultra-reducing conditions in podiform chromitite. *Am. Mineral.* **2017**, *112*, 1101–1114.
- Akbulut, M. Investigation of silicate micro-inclusions from Orhaneli and Harmancik chromitites (NW Turkey): New ultrahigh-pressure evidence from Western Tethyan ophiolitic chromitites. *Ophioliti* **2018**, *43*, 1–22.

12. González-Jiménez, J.M.; Camprubi, A.; Colás, V.; Griffin, W.L.; Proenza, J.A.; O'Reilly, S.Y.; Centeno-García, E.; García-Casco, A.; Belousova, E.; Talavera, C.; et al. The recycling of chromitites in ophiolites from southwestern North America. *Lithos* **2017**, *294*, 53–72. [[CrossRef](#)]
13. Arai, S. Conversion of low-pressure chromitites to ultrahigh-pressure chromitites by deep recycling: A good inference. *Earth Planet. Sci. Lett.* **2013**, *397*, 81–87. [[CrossRef](#)]
14. McGowan, N.M.; Griffin, W.L.; González-Jiménez, J.M.; Belousova, E.A.; Afonso, J.; Shi, R.; McCammon, C.A.; Pearson, N.J.; O'Reilly, S.Y. Tibetan chromitites: Excavating the slab graveyard. *Geology* **2015**, *43*, 179–182. [[CrossRef](#)]
15. Griffin, W.L.; Afonso, J.C.; Belousova, E.A.; Gain, S.E.; Gong, X.H.; González-Jiménez, J.M.; Howell, D.; Huang, J.X.; McGowan, N.; Pearson, N.J.; et al. Mantle recycling: Transition zone metamorphism of Tibetan ophiolitic peridotites and its tectonic implications. *J. Petrol.* **2016**, *57*, 655–684. [[CrossRef](#)]
16. Proenza, J.A.; González-Jiménez, J.M.; García-Casco, A.; Belousova, E.; Griffin, W.L.; Talavera, C.; Rojas-Agramonte, Y.; Aiglsperger, T.; Navarro-Ciurana, D.; Pujol-Solà, N.; et al. Cold plumes trigger contamination of oceanic mantle wedges with continental crust-derived sediments: Evidence from chromitite zircon grains of eastern Cuban Ophiolites. *Geosci. Front.* **2018**, in press. [[CrossRef](#)]
17. Yang, J.S.; Robinson, P.T.; Dilek, Y. Diamonds in ophiolites. *Elements* **2014**, *10*, 127–130. [[CrossRef](#)]
18. Xiong, F.; Yang, J.; Robinson, P.T.; Xu, X.; Liu, Z.; Li, Y.; Li, J.; Chen, S. Origin of podiform chromitite, a new model based on the Luobusa ophiolite, Tibet. *Gondwana Res.* **2015**, *27*, 525–542. [[CrossRef](#)]
19. Zhou, M.F.; Robinson, P.T.; Su, B.X.; Gao, J.F.; Li, J.W.; Yang, J.S.; Malpas, J. Compositions of chromite, associated minerals, and parental magmas of podiform chromite deposits: The role of slab contamination of asthenospheric melts in suprasubduction zone environments. *Gondwana Res.* **2014**, *26*, 262–283. [[CrossRef](#)]
20. Johan, Z.; Martin, R.F.; Ettler, V. Fluids are bound to be involved in the formation of ophiolitic chromite deposits. *Eur. J. Mineral.* **2017**, *27*, 543–555. [[CrossRef](#)]
21. Ballhaus, C.; Wirth, R.; Fonseca, R.O.C.; Blanchard, H.; Pröll, W.; Bragagni, A.; Nagel, T.; Schreiber, A.; Dittrich, S.; Thome, V.; et al. Ultra-high pressure and ultra-reduced minerals in ophiolites may form by lightning strikes. *Geochem. Persp. Lett.* **2017**, *5*, 42–46. [[CrossRef](#)]
22. Ballhaus, C.; Fonseca, R.O.C.; Bragagni, A. Reply to Comment on “Ultra-high pressure and ultra-reduced minerals in ophiolites may form by lightning strikes” by Griffin et al. 2018: No evidence for transition zone metamorphism in the Luobusa ophiolite. *Geochem. Persp. Lett.* **2018**, *7*, 3–4. [[CrossRef](#)]
23. Iturralde-Vinent, M. (Ed.) Introduction to Cuban geology and geophysics. In *Ophiolitas y Arcos Volcánicos de Cuba*; International Geological Correlation Programme: Miami, FL, USA, 1996; Volume 364, pp. 3–35.
24. Proenza, J.A.; Gervilla, F.; Melgarejo, J.C.; Bodinier, J.L. Al- and Cr-rich chromitites from the Mayarí-Baracoa ophiolitic belt (eastern Cuba); consequence of interaction between volatile-rich melts and peridotites in suprasubduction mantle. *Econ. Geol.* **1999**, *94*, 547–566. [[CrossRef](#)]
25. Iturralde-Vinent, M.A.; Díaz-Otero, C.; Rodríguez-Vega, A.; Díaz-Martínez, R. Tectonic implications of paleontologic dating of Cretaceous–Danian sections of Eastern Cuba. *Geol. Acta* **2006**, *4*, 89–102.
26. García-Casco, A.; Torres-Roldán, R.L.; Iturralde-Vinent, M.A.; Millán, G.; Núñez Cambra, K.; Lázaro, C.; Rodríguez Vega, A. High pressure metamorphism of ophiolites in Cuba. *Geol. Acta* **2006**, *4*, 63–88.
27. García-Casco, A.; Iturralde-Vinent, M.A.; Pindell, J. Latest Cretaceous collision/accretion between the Caribbean Plate and Caribbeana: Origin of metamorphic terranes in the Greater Antilles. *Int. Geol. Rev.* **2008**, *50*, 781–809. [[CrossRef](#)]
28. García-Casco, A.; Lázaro, C.; Torres-Roldán, R.L.; Núñez Cambra, K.; Rojas Agramonte, Y.; Kröner, A.; Neubauer, F.; Millán, G.; Blanco-Quintero, I. Partial melting and counterclockwise P-T path of subducted oceanic crust (Sierra del Convento mélange, Cuba). *J. Petrol.* **2008**, *49*, 129–161. [[CrossRef](#)]
29. Lázaro, C.; García-Casco, A.; Rojas-Agramonte, Y.; Kröner, A.; Neubauer, F.; Iturralde-Vinent, M. Fifty-five-million-year history of oceanic subduction and exhumation at the northern edge of the Caribbean plate (Sierra del Convento mélange, Cuba). *J. Metamorph. Geol.* **2009**, *27*, 19–40. [[CrossRef](#)]
30. Blanco-Quintero, I.F.; Gerya, T.V.; García-Casco, A.; Castro, A. Subduction of young oceanic plates: A numerical study with application to aborted thermal-chemical plumes. *Geochem. Geophys.* **2011**, *12*, 10.
31. Blanco-Quintero, I.F.; Proenza, J.A.; García-Casco, A.; Tauler, E.; Galí, S. Serpentinites and serpentinites within a fossil subduction channel: La Corea mélange, eastern Cuba. *Geol. Acta* **2011**, *9*, 389–405.

32. Blanco-Quintero, I.F.; Rojas-Agramonte, Y.; García-Casco, A.; Kröner, A.; Mertz, D.F.; Lázaro, C.; Blanco-Moreno, J.; Renne, P.R. Timing of subduction and exhumation in a subduction channel: Evidence from slab melts from La Corea mélangé (eastern Cuba). *Lithos* **2011**, *127*, 86–100. [[CrossRef](#)]
33. Lázaro, C.; García-Casco, A.; Blanco-Quintero, I.F.; Rojas-Agramonte, Y.; Corsini, M.; Proenza, J.A. Did the Turonian–Coniacian plume pulse trigger subduction initiation in the Northern Caribbean? Constraints from ⁴⁰Ar/³⁹Ar dating of the Moa-Baracoa metamorphic sole (eastern Cuba). *Int. Geol. Rev.* **2015**, *57*, 919–942. [[CrossRef](#)]
34. Cárdenas-Párraga, J.; García-Casco, A.; Proenza, J.A.; Harlow, G.E.; Blanco-Quintero, I.F.; Lázaro, C.; Villanova-de-Benavent, C.; Núñez Cambra, K. Trace-element geochemistry of transform-fault serpentinite in high-pressure subduction mélanges (eastern Cuba): Implications for subduction initiation. *Int. Geol. Rev.* **2017**, *59*, 2041–2064. [[CrossRef](#)]
35. Iturralde-Vinent, M.A.; Diaz Otero, C.; García-Casco, A.; Van Hinsbergen, D.J.J. Paleogene foredeep basin deposits of North-Central Cuba: A record of arc-continent collision between the Caribbean and North American plate. *Int. Geol. Rev.* **2008**, *50*, 863–884. [[CrossRef](#)]
36. Van Hinsbergen, D.J.J.; Iturralde-Vinent, M.A.; Van Geffen, P.W.; García-Casco, A.; Van Benthem, S. Structure of the accretionary prism, and the evolution of the Paleogene northern Caribbean subduction zone in the region of Camagüey, Cuba. *J. Struct. Geol.* **2009**, *31*, 1130–1144. [[CrossRef](#)]
37. Lewis, J.F.; Draper, G.; Proenza, J.A.; Espaillet, J.; Jiménez, J. Ophiolite-related ultramafic rocks (serpentinites) in the Caribbean region: A review of their occurrence, composition, origin, emplacement and nickel laterite soils. *Geol. Acta* **2006**, *4*, 237–263.
38. Marchesi, C.; Garrido, C.J.; Godard, M.; Proenza, J.A.; Gervilla, F.; Blanco-Moreno, J. Petrogenesis of highly depleted peridotites and gabbroic rocks from the Mayarí-Baracoa Ophiolitic Belt (eastern Cuba). *Contrib. Mineral. Petrol.* **2006**, *151*, 717–736. [[CrossRef](#)]
39. Iturralde-Vinent, M.A.; García-Casco, A.; Rojas-Agramonte, Y.; Proenza, J.A.; Murphy, J.B.; Stern, R.G. The geology of Cuba: A brief overview and synthesis. *GSA Today* **2016**, *26*, 4–10. [[CrossRef](#)]
40. Proenza, J.A.; Díaz-Martínez, R.; Iriondo, A.; Marchesi, C.; Melgarejo, J.C.; Gervilla, F.; Garrido, C.J.; Rodríguez-Vega, A.; Lozano-Santacruz, R.; Blanco-Moreno, J.A. Primitive island-arc Cretaceous volcanic rocks in eastern Cuba: The Téneme Formation. *Geol. Acta* **2006**, *4*, 103–121.
41. Gervilla, F.; Proenza, J.A.; Frei, R.; González-Jiménez, J.M.; Garrido, C.J.; Melgarejo, J.C.; Meibom, A.; Díaz-Martínez, R.; Lavaut, W. Distribution of platinum-group elements and Os isotopes in chromite ores from Mayarí-Baracoa Ophiolitic Belt (eastern Cuba). *Contrib. Mineral. Petrol.* **2005**, *150*, 589–607. [[CrossRef](#)]
42. Marchesi, C.; Garrido, C.J.; Bosch, D.; Proenza, J.A.; Gervilla, F.; Monié, P.; Rodríguez-Vega, A. Geochemistry of Cretaceous magmatism in eastern Cuba: Recycling of North American continental sediments and implications for subduction polarity in the Greater Antilles Paleo-arc. *J. Petrol.* **2007**, *48*, 1813–1840. [[CrossRef](#)]
43. González-Jiménez, J.M.; Proenza, J.A.; Gervilla, F.; Melgarejo, J.C.; Blanco-Moreno, J.A.; Ruiz-Sánchez, R.; Griffin, W.L. High-Cr and high-Al chromitites from the Sagua de Tánamo district, Mayarí-Cristal Ophiolitic Massif (eastern Cuba): Constraints on their origin from mineralogy and geochemistry of chromian spinel and platinum group elements. *Lithos* **2011**, *125*, 101–121. [[CrossRef](#)]
44. Proenza, J.A.; Gervilla, F.; Melgarejo, J.C.; Revé, D.; Rodríguez, G. Las cromititas ofiolíticas del yacimiento Mercedita (Cuba). Un ejemplo de cromitas ricas en Al en la zona de transición manto-corteza. *Acta Geol. Hisp.* **1998**, *33*, 179–212.
45. Guild, P.W. Petrology and structure of the Moa Chromite District, Oriente province, Cuba. *Trans. Am. Geophys. Union* **1947**, *28*, 218–246. [[CrossRef](#)]
46. Flint, D.E.; de Albear, J.F.; Guild, P.W. *Geology and Chromite Deposits of the Camagüey District, Camagüey Province, Cuba*; U.S. Geological Survey Bull: Washington, DC, USA, 1948; Volume 954-B, pp. 39–63.
47. Leblanc, M.; Violette, J.F. Distribution of aluminium-rich and chromium-rich chromite pods in ophiolite peridotites. *Econ. Geol.* **1983**, *78*, 293–301. [[CrossRef](#)]
48. Aiglsperger, T.; Proenza, J.A.; Zaccarini, F.; Lewis, J.F.; Garuti, G.; Labrador, M.; Longo, F. Platinum group minerals (PGM) in the Falcondo Ni laterite deposit, Loma Caribe peridotite (Dominican Republic). *Miner. Depos.* **2015**, *50*, 105–123. [[CrossRef](#)]
49. Pouchou, J.L.; Pichoir, F. Quantitative analysis of homogeneous or stratified microvolumes applying the model PAP. In *Electron Probe Quantitation*; Heinrich, K.J., Newbury, D.E., Eds.; Plenum Press: New York, NY, USA, 1991; pp. 31–75, ISBN 978-1-4899-2619-7.

50. Proenza, J.A.; Alfonso, P.; Melgarejo, J.C.; Gervilla, F.; Tritlla, J.; Fallick, A.E. D., O and C isotopes in podiform chromitites as fluid tracers for hydrothermal alteration processes of the Mayarí-Baracoa Ophiolitic Belt, eastern Cuba. *J. Geochem. Explor.* **2003**, *78–79*, 1–6. [[CrossRef](#)]
51. Irvine, T.N. Chromian spinel as a petrogenetic indicator: Part 2. Petrologic applications. *Can. J. Earth Sci.* **1967**, *4*, 71–103. [[CrossRef](#)]
52. Leblanc, M.; Nicolas, A. Ophiolitic chromitites. *Int. Geol. Rev.* **1992**, *34*, 653–686. [[CrossRef](#)]
53. Bonavia, F.F.; Diella, V.; Ferrario, A. Precambrian podiform chromitites from Kenticha Hill, southern Ethiopia. *Econ. Geol.* **1993**, *88*, 198–202. [[CrossRef](#)]
54. Arai, S.; Uesugi, J.; Ahmed, A.H. Upper crustal podiform chromitite from the northern Oman ophiolite as the stratigraphically shallowest chromitite in ophiolite and its implication for Cr concentration. *Contrib. Mineral. Petrol.* **2004**, *147*, 145–154. [[CrossRef](#)]
55. Arai, S. Chemistry of chromian spinel in volcanic rocks as a potential guide to magma chemistry. *Mineral. Mag.* **1992**, *56*, 173–184. [[CrossRef](#)]
56. Prencipe, M.; Mantovani, L.; Tribaudino, M.; Bersani, D.; Lottici, P.P. The Raman spectrum of diopside: A comparison between ab initio calculated and experimentally measured frequencies. *Eur. J. Mineral.* **2012**, *24*, 457–464. [[CrossRef](#)]
57. Shiryaev, A.A.; Griffin, W.L.; Stoyanov, E. Moissanite (SiC) from kimberlites: Polytypes, trace elements, inclusions and speculations on origin. *Lithos* **2011**, *122*, 152–164. [[CrossRef](#)]
58. Trumbull, R.B.; Yang, J.S.; Robinson, P.T.; Di Pierro, S.; Vennemann, T.; Wiedenbeck, M. The carbon isotope composition of natural SiC (moissanite) from the Earth's mantle: New discoveries from ophiolites. *Lithos* **2009**, *113*, 612–620. [[CrossRef](#)]
59. Xu, S.T.; Wu, W.P.; Xiao, W.S.; Yang, J.S.; Chen, J.; Ji, S.Y.; Liu, Y.C. Moissanite in serpentinite from the Dabie Mountains in China. *Mineral. Mag.* **2008**, *72*, 899–908. [[CrossRef](#)]
60. Tian, Y.; Yang, J.; Robinson, P.T.; Xiong, F.; Yuan, L.I.; Zhang, Z.; Liu, Z.; Liu, F.; Niu, X. Diamond discovered in high-Al chromitites of the Sartohay Ophiolite, Xinjiang Province, China. *Acta Geol. Sin.* **2015**, *89*, 332–340.
61. Yamamoto, S.; Komiya, T.; Hirose, K.; Maruyama, S. Coesite and clinopyroxene exsolution lamellae in chromites: In-situ ultrahigh-pressure evidence from podiform chromitites in the Luobusa ophiolite, southern Tibet. *Lithos* **2009**, *109*, 314–322. [[CrossRef](#)]
62. Miura, M.; Arai, S.; Ahmed, A.H.; Mizukami, T.; Okuno, M.; Yamamoto, S. Podiform chromitite classification revisited: A comparison of discordant and concordant chromitite pods from Wadi Hilti, northern Oman ophiolite. *J. Asian Earth Sci.* **2012**, *59*, 52–61. [[CrossRef](#)]
63. Arai, S.; Miura, M. Formation and modification of chromitites in the mantle. *Lithos* **2016**, *264*, 277–295. [[CrossRef](#)]
64. Ono, S.; Kikegawa, T.; Higo, Y.; Tange, Y. Precise determination of the phase boundary between coesite and stishovite in SiO₂. *Phys. Earth Planet. Int.* **2017**, *264*, 1–6. [[CrossRef](#)]
65. Satsukawa, T.; Griffin, W.L.; Piazzolo, S.; O'Reilly, S.Y. Messengers from the deep: Fossil wadsleyite–chromite microstructures from the Mantle Transition Zone. *Sci. Rep.* **2015**, *5*, 16484. [[CrossRef](#)] [[PubMed](#)]
66. Wu, Y.; Xu, M.; Jin, Z.; Fei, Y.; Robinson, P.T. Experimental constraints on the formation of the Tibetan podiform chromitites. *Lithos* **2016**, *245*, 109–117. [[CrossRef](#)]
67. Zhang, Y.F.; Jin, Z.M.; Griffin, W.L.; Wang, C.; Wu, Y. High-pressure experiments provide insights into the Mantle Transition Zone history of chromitite in Tibetan ophiolites. *Earth Planet. Sci. Lett.* **2017**, *463*, 151–158. [[CrossRef](#)]
68. Chen, M.; Shu, J.; Xie, X.; Mao, H.K. Natural CaTi₂O₄-structured FeCr₂O₄ polymorph in the Suizhou meteorite and its significance in mantle mineralogy. *Geochim. Cosmochim. Acta* **2003**, *67*, 3937–3942. [[CrossRef](#)]
69. Cameron, E.N. Titanium-bearing oxide minerals of the Critical Zone of the Eastern Bushveld Complex. *Am. Miner.* **1979**, *64*, 140–150.
70. Arai, S.; Yurimoto, H. Podiform chromitites of the Tari–Misaka ultramafic complex, Southwest Japan, as mantle–melt interaction products. *Econ. Geol.* **1994**, *89*, 1279–1288. [[CrossRef](#)]
71. Augé, T. Chromite deposits in the northern Oman ophiolite: Mineralogical constraints. *Miner. Depos.* **1987**, *22*, 1–10. [[CrossRef](#)]
72. Xiong, Q.; Griffin, W.L.; Huang, J.X.; Gain, S.E.; Toledo, V.; Pearson, N.J.; O'Reilly, S.Y. Super-reduced mineral assemblages in “ophiolitic” chromitites and peridotites: The view from Mount Carmel. *Eur. J. Mineral.* **2017**, *29*, 557–570. [[CrossRef](#)]

73. Yang, J.S.; Xu, X.Z.; Li, Y.; Li, J.Y.; Ba, D.Z.; Rong, H.; Zhang, Z.M. Diamonds recovered from peridotite of the Purang ophiolite in the Yarlung-Zangbo suture of Tibet: A proposal for a new type of diamond occurrence. *Acta Petrol. Sin.* **2011**, *27*, 3171–3178.
74. Xiong, Q.; Henry, H.; Griffin, W.L.; Zheng, J.P.; Satsukawa, T.; Pearson, N.J.; O'Reilly, S.Y. High-and low-Cr chromitite and dunite in a Tibetan ophiolite: Evolution from mature subduction system to incipient forearc in the Neo-Tethyan Ocean. *Contrib. Mineral. Petrol.* **2017**, *172*, 45. [[CrossRef](#)]
75. Xiong, F.; Yang, J.; Robinson, P.T.; Dilek, Y.; Milushi, I.; Xu, X.; Zhou, W.; Zhang, Z.; Rong, H. Diamonds Discovered from High-Cr Podiform Chromitites of Bulqiza, Eastern Mirdita Ophiolite, Albania. *Acta Geol. Sin. Eng. Ed.* **2017**, *91*, 455–468. [[CrossRef](#)]
76. Chen, Y.; Yang, J.; Xu, Z.; Tian, Y.; Lai, S. Diamonds and other unusual minerals from peridotites of the Myitkyina ophiolite, Myanmar. *J. Asian Earth Sci.* **2018**, *164*, 179–193. [[CrossRef](#)]
77. Bai, W.J.; Robinson, P.T.; Fang, Q.; Hu, X.F.; Zhou, M.F. The PGE and base-metal alloys in the podiform chromitites of the Luobusa ophiolite, southern Tibet. *Can. Mineral.* **2000**, *38*, 585–598. [[CrossRef](#)]
78. Alexander, C.M.O. Presolar SiC in chondrites: How variable and how many sources? *Geochim. Cosmochim. Acta* **1993**, *57*, 2869–2888. [[CrossRef](#)]
79. Moore, R.O.; Otter, M.L.; Rickard, R.S.; Harris, J.W.; Gurney, J.J. The occurrence of moissanite and ferro-periclase as inclusions in diamond. In Proceedings of the 4th International Kimberlite Conference, Perth, Australia, 11–15 August 1986; pp. 409–411.
80. Moore, R.O.; Gurney, J.J. Mineral inclusions in diamond from the Monastery kimberlite, South Africa. *Kimberl. Relat. Rocks* **1989**, *2*, 1029–1041.
81. Leung, I.S. Silicon carbide cluster entrapped in a diamond from Fuxian, China. *Am. Mineral.* **1990**, *75*, 1110–1119.
82. Kaminsky, F. Mineralogy of the lower mantle: A review of 'super-deep' mineral inclusions in diamond. *Earth Sci. Rev.* **2012**, *110*, 127–147. [[CrossRef](#)]
83. Di Pierro, S.; Gnos, E.; Grobety, B.H.; Armbruster, T.; Bernasconi, S.M.; Ulmer, P. Rock-forming moissanite (natural alpha-silicon carbide). *Am. Mineral.* **2003**, *88*, 1817–1821. [[CrossRef](#)]
84. Dobrzhinetskaya, L.; Mukhin, P.; Wang, Q.; Wirth, R.; O'Bannon, E.; Zhao, W.; Eppelbaum, L.; Sokhonchuk, T. Moissanite (SiC) with metal-silicide and silicon inclusions from tuff of Israel: Raman spectroscopy and electron microscope studies. *Lithos* **2017**, *310–311*, 355–368. [[CrossRef](#)]
85. Machev, P.; O'Bannon, E.; Bozhilov, K.; Wang, Q.; Dobrzhinetskaya, L. Not all moissanites are created equal: New constraints on moissanite from metamorphic rocks of Bulgaria. *Earth Planet. Sci. Lett.* **2018**, *498*, 387–396. [[CrossRef](#)]
86. Gnoevaja, N.; Grozdanov, L. Moissanite from Triassic rocks, NW Bulgaria. *Proc. Bulg. Geol. Soc.* **1965**, *26*, 89–95.
87. Shiryaev, A.A.; Wiedenbeck, M.; Reutsky, V.; Polyakov, V.B.; Mel'nik, N.N.; Lebedev, A.A.; Yakimova, R. Isotopic heterogeneity in synthetic and natural silicon carbide. *J. Phys. Chem. Solids* **2008**, *69*, 2492–2498. [[CrossRef](#)]
88. Schmidt, M.W.; Gao, C.; Golubkova, A.; Rohrbach, A.; Connolly, J.A. Natural moissanite (SiC)—A low temperature mineral formed from highly fractionated ultra-reducing COH-fluids. *Prog. Earth Planet. Sci.* **2014**, *1*, 27. [[CrossRef](#)]
89. Golubkova, A.; Schmidt, M.W.; Connolly, J.A. Ultra-reducing conditions in average mantle peridotites and in podiform chromitites: A thermodynamic model for moissanite (SiC) formation. *Contrib. Mineral. Petrol.* **2016**, *171*, 41. [[CrossRef](#)]
90. Sachan, H.K.; Mukherjee, B.K.; Bodnar, R.J. Preservation of methane generated during serpentinization of upper mantle rocks: Evidence from fluid inclusions in the Nidar ophiolite, Indus Suture Zone, Ladakh (India). *Earth Planet. Sci. Lett.* **2007**, *257*, 47–59. [[CrossRef](#)]
91. Kelley, D.S.; Früh-Green, G.L. Abiogenic methane in deep-seated mid-ocean ridge environments: Insights from stable isotope analyses. *J. Geophys. Res.* **1999**, *104*, 10439–10460. [[CrossRef](#)]
92. Melcher, F.; Grum, W.; Simon, G.; Thalhammer, T.V.; Stumpfl, E. Petrogenesis of the ophiolitic giant chromite deposit of Kempirsai, Kazakhstan: A study of solid and fluid inclusions in chromite. *J. Petrol.* **1997**, *10*, 1419–1458. [[CrossRef](#)]
93. Proenza, J.A. Mineralizaciones de Cromita en la Faja Ofiolítica Mayarí-Baracoa (Cuba). Ejemplo del Yacimiento Mercedita. Ph.D. Thesis, Universitat de Barcelona, Barcelona, Spain, February 1998; p. 227.

94. Rojas-Agramonte, Y.; Williams, I.S.; Arculus, R.; Kröner, A.; García-Casco, A.; Lázaro, C.; Buhre, S.; Wong, J.; Geng, H.; Morales Echevarría, C.; et al. Ancient xenocrystic zircon in young volcanic rocks of the southern Lesser Antilles island arc. *Lithos* **2017**, *290*, 228–252. [[CrossRef](#)]
95. Ruskov, T.; Spirov, I.; Georgieva, M.; Yamamoto, S.; Green, H.W.; McCammon, C.A.; Dobrzhinetskaya, L.F. Mossbauer spectroscopy studies of the valence state of iron in chromite from the Luobusa massif of Tibet: Implications for a highly reduced deep mantle. *J. Metamorph. Geol.* **2010**, *28*, 551–560. [[CrossRef](#)]
96. Matveev, S.; Ballhaus, C. Role of water in the origin of podiform chromitite deposits. *Earth Planet. Sci. Lett.* **2002**, *203*, 235–243. [[CrossRef](#)]
97. Gerya, T.V.; Yuen, D. Rayleigh–Taylor instabilities from hydration and melting propel “cold plumes” at subduction zones. *Earth Planet. Sci. Lett.* **2003**, *212*, 47–62. [[CrossRef](#)]
98. Rojas-Agramonte, Y.; Garcia-Casco, A.; Kemp, A.; Kröner, A.; Proenza, J.A.; Lázaro, C.; Liu, D. Recycling and transport of continental material through the mantle wedge above subduction zones: A. Caribbean example. *Earth Planet. Sci. Lett.* **2016**, *436*, 93–107. [[CrossRef](#)]



© 2018 by the authors. Licensee MDPI, Basel, Switzerland. This article is an open access article distributed under the terms and conditions of the Creative Commons Attribution (CC BY) license (<http://creativecommons.org/licenses/by/4.0/>).

A3. Article 3

Pujol-Solà, N., Garcia-Casco, A., Proenza, J.A., González-Jiménez, J.M., del Campo, A., Colás, V., Canals, A., Sánchez-Navas, A., Roqué-Rosell, J., 2020. Diamond forms during low pressure serpentinisation of oceanic lithosphere. *Geochemical Perspectives Letters* 15, 19–24. <https://doi.org/10.7185/geochemlet.2029>

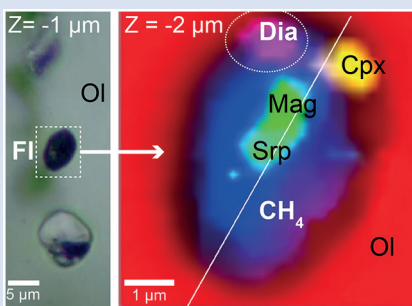
Diamond forms during low pressure serpentinisation of oceanic lithosphere

N. Pujol-Solà^{1*}, A. Garcia-Casco^{2,3}, J.A. Proenza^{1,4}, J.M. González-Jiménez²,
A. del Campo⁵, V. Colás⁶, À. Canals¹, A. Sánchez-Navas², J. Roqué-Rossell^{1,4}



doi: 10.7185/geochemlet.2029

Abstract



Diamond is commonly regarded as an indicator of ultra-high pressure conditions in Earth System Science. This canonical view is challenged by recent data and interpretations that suggest metastable growth of diamond in low pressure environments. One such environment is serpentinisation of oceanic lithosphere, which produces highly reduced CH_4 -bearing fluids after olivine alteration by reaction with infiltrating fluids. Here we report the first ever observed *in situ* diamond within olivine-hosted, CH_4 -rich fluid inclusions from low pressure oceanic gabbro and chromitite samples from the Moa-Baracoa ophiolitic massif, eastern Cuba. Diamond is encapsulated in voids below the polished mineral surface forming a typical serpentinisation array, with methane, serpentine and magnetite, providing definitive evidence for its metastable growth upon low temperature and low pressure alteration of oceanic lithosphere and super-reduction of infiltrated fluids.

Thermodynamic modelling of the observed solid and fluid assemblage at a reference P-T point appropriate for serpentinisation (350 °C and 100 MPa) is consistent with extreme reduction of the fluid to $\log f\text{O}_2$ (MPa) = -45.3 ($\Delta \log f\text{O}_2$ [Iron-Magnetite] = -6.5). These findings imply that the formation of metastable diamond at low pressure in serpentinised olivine is a widespread process in modern and ancient oceanic lithosphere, questioning a generalised ultra-high pressure origin for ophiolitic diamond.

Received 6 June 2020 | Accepted 31 July 2020 | Published 10 September 2020

Introduction

The discovery of nano- to micrometre scale grains of diamond separated from ophiolitic rocks has recently attracted the attention of geoscientists due to its potential evidence for lithosphere recycling down to, or below, the mantle Transition Zone (e.g., Yang *et al.*, 2007, 2015; Griffin *et al.*, 2016). The earlier reports of diamond in nominally low pressure ophiolitic rocks date back to the early 1990s, when diamond was found in heavy mineral concentrates obtained from Tibetan ophiolites (Bai *et al.*, 1993). These were initially considered to be due to contamination during sample preparation. The debate, however, rejuvenated after findings of other UHP minerals such as coesite together with super-reduced phases in many chromitites and associated peridotites of ophiolites worldwide (e.g., Griffin *et al.*, 2016). Far-reaching geodynamic models have been proposed based on the assumption that diamond growth took place at UHP conditions in these rocks (e.g., Barron *et al.*, 1996; Xiong *et al.*, 2019 and references therein). Recently, the finding of *in situ* diamond in chromite-hosted fluid inclusions from ophiolitic chromitites by Farré-de-Pablo *et al.*, (2019a) provided the first evidence

for empirical (Simakov *et al.*, 2015, 2020), experimental (Simakov *et al.*, 2008) and theoretical (Manuella, 2013; Simakov, 2018) work on low pressure growth of diamond. However, the debate on the natural origin of diamond continued (e.g., Farré-de-Pablo *et al.*, 2019b; Massonne, 2019; Yang *et al.*, 2019). In this regard, Litasov *et al.* (2019a,b) have recently claimed that most diamonds, if not all, from ophiolitic rocks are not natural but instead have a synthetic origin, and emphasised the need to identify diamond below the polished surface of the host mineral. In this study we report for the first time *in situ* diamond grains hosted below the polished surface of magmatic olivine from a low pressure gabbro sill of the upper mantle section of the Moa-Baracoa Ophiolitic Massif, eastern Cuba (Supplementary Information; Figs. S-1–S-4, Table S-1), where super-reduced phases formed during serpentinisation have been previously reported (Pujol-Solà *et al.*, 2018). Diamond grains, which are also present in olivine of associated chromitite, occur in secondary inclusions within olivine. Our observations provide conclusive evidence for the natural formation of metastable diamond at low P (<200 MPa) and low T (<350 °C) during serpentinisation of oceanic mafic and ultramafic rocks, and allow a word of caution

1. Department of Mineralogy, Petrology and Applied Geology, University of Barcelona, Martí i Franquès s/n, 08028 Barcelona, Spain
2. Department of Mineralogy and Petrology, University of Granada, Av. Fuentenueva s/n, 18071 Granada, Spain
3. Andalusian Earth Science Institute (IACT), Spanish Research Council (CSIC)–University of Granada, Av. de las Palmeras 4, 18100 Armilla, Spain
4. Institut de Nanociència i Nanotecnologia, IN2UB Facultat de Química, University of Barcelona, Diagonal 645, 08028 Barcelona, Spain
5. Instituto de Cerámica y Vidrio – CSIC. C. Kelsen, 5, Campus de Cantoblanco, 28049 Madrid, Spain
6. Institute of Geology, National Autonomous University of Mexico, Ciudad Universitaria, 04510 Ciudad de México, Mexico

* Corresponding author (email: npujolsola@ub.edu)



on the development of generalised geodynamic models of mantle convection and lithosphere recycling into the deep mantle based on diamond and super-reduced phases alone.

Results

We have studied approximately 150 inclusions (96 below the polished surface) in olivine from 5 gabbro thin sections and 16 inclusions (8 below the surface) hosted in olivine in chromitite (representative inclusions in Table S-2). The inclusions align along trails that extend across adjacent mineral grains and delineate healed fractures (Fig. 1a–d). The distribution of these trails is heterogeneous, with some olivine grains showing a high density of trails cross-cutting each other. Inclusions are typically spheroidal, with sizes ranging between <1 μm and 14 μm in diameter (Figs. 1a–d, S-2).

Diamond grains were identified with the characteristic Raman peak at 1330 cm⁻¹ with a slight downshift from the typical band to 1326 cm⁻¹ (n = 17; Table S-2) lining the walls of inclusions (Fig. 1e–f). These very small (200–300 nm) diamond grains were better characterised by confocal Raman maps at different depths (Fig. 1e–h). Nanodiamond is usually associated with methane, serpentine (lizardite, polygonal serpentine, chrysotile), and magnetite (Fig. 1h). Daughter minerals include diopside, chlorite, graphite-like amorphous C, and calcite (Table S-2, Fig. S-5). Brucite was not identified in any of the studied inclusions, similar to other locations (e.g., Sachan *et al.*, 2007). However, brucite is a widespread product in olivine-hosted fluid inclusions in ophiolitic samples (e.g., Klein *et al.*, 2019; Grozeva *et al.*, 2020).

TEM observations of a thin foil extracted by focused ion beam (FIB) (Fig. 2a) reveal that nanodiamond is clearly surrounded by polygonal serpentine and associated with magnetite (Fig. 2b,c). The selected area electron diffraction (SAED) pattern of a grain a few hundreds of nanometres in size confirms its diamond structure (with a reciprocal distance of 5 nm⁻¹ corresponding to the d₁₁₁-spacing of 2 Å; Fig. 2d), while the corresponding electron energy loss spectrum (EELS) indicates that C-type is the diamond allotrope (sp³-hybridised C atoms; Fig. 2e). No polishing debris was observed in the studied inclusions, suggesting no contamination during ion milling of the thin foil except for sublimated Pt used to protect the area. The observed pore space in the inclusions (Figs. 2a, S-6) was likely filled by methane, as indicated by Raman spectroscopy measurements (Table S-2).

Sub-surface fluid inclusions lack water and are dominated by methane (Table S-2), similarly to olivine-hosted fluid inclusions described by Klein *et al.* (2019). In chromitite, diamond grains have been found in 5 sealed fracture-filling inclusions within interstitial magmatic olivine. One inclusion studied by TEM (Fig. S-7) revealed a <1 μm-sized diamond crystal co-existing with the super-reduced phase native Si. In addition, H₂ was identified by Raman spectroscopy in another inclusion (Table S-2). Nevertheless, the phase assemblages are similar to those of the studied inclusions in olivine from the associated gabbro, with serpentine and magnetite (Fig. S-4, Table S-2).

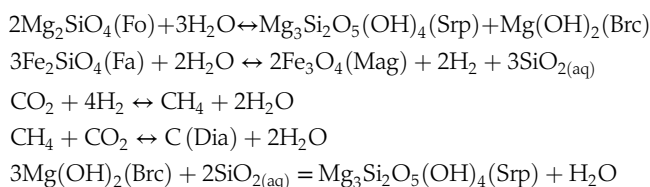
Natural Origin of the Studied Diamond

The natural *vs.* anthropogenic origin of ophiolitic diamond is a hotly debated topic. Whereas in other samples the natural origin of diamond has not been firmly proved (Massonne, 2019), here we provide several lines of evidence for a natural origin. Our most significant evidence is that diamond is hosted within olivine well below the mineral's polished surface (Fig. 1). Such an observation meets the basic requirements for *in situ* mineral

grains, as suggested by Massonne (2019). Additional evidence includes: (1) that diamond was found within CH₄-bearing fluid inclusions forming linear arrays (healed fractures) in olivine and surrounded by serpentine (Figs. 1–2), and (2) lack of polishing debris and/or resin artificially incorporated (e.g., Dobrzhinetskaya *et al.*, 2014).

Processes and Conditions for Diamond Formation

The olivine-hosted inclusion trails represent fluids trapped in healed fractures. Fluid infiltration in oceanic lithosphere is commonly associated with sporadic deformation events that trigger an increase of porosity by (micro-)fracturing during cooling below the brittle-ductile transition of olivine (Klein *et al.*, 2019). In this scenario, fluid-rock interaction changes from a general open system during initial infiltration to closed system micro-reactors once the inclusions are sealed. At the initial trapping pressure and temperature and during subsequent cooling, the trapped aqueous fluids react with the olivine walls of the inclusion, triggering a number of reactions that ultimately result in growth of hydrated minerals and changes in fluid composition. Comprehensive thermodynamic models of these processes in ultramafic and oceanic rocks (McCullom and Bach, 2009; Klein *et al.*, 2019) show that below ~350 °C (at <200 MPa) in the stability field of serpentine + brucite “serpentinisation” of the walls of olivine hosting fluid inclusions consumes H₂O in the fluid and generates H₂ through precipitation of Fe³⁺-rich phases, particularly magnetite, so that consumption of inorganic carbon (CO₂) and formation of abiotic CH₄ takes place. In the 6 component system MgO-FeO-SiO₂-C-O₂-H₂, the formation of phase assemblages made of serpentine, brucite, magnetite, diamond and CH₄-fluid from an initial assemblage made of olivine and H₂O-CO₂ fluid can be described by a number of linearly independent reactions. Assuming 11 phase components (Fo, Fa, Mag, Mg-Srp, Mg-Brc, H₂O, CO₂, CH₄, H₂, SiO_{2(aq)}, C abbreviations after Whitney and Evans, 2010) appropriate for the low temperature stage of reaction progress, and excluding magnesite for simplicity, the dimension of the reaction space is 5. Among many, the following set of five linearly independent reactions obtained with the software CSpace (Torres-Roldán *et al.*, 2000) describes the process (commonly used as coupled reactions during serpentinisation, e.g., Lamadrid *et al.*, 2017; Klein *et al.*, 2019):



As a whole, this set of reactions (and any other independent set, provided that it contains all phase components considered) indicates that the hydration process of olivine triggers the formation of magnetite by oxidation of Fe²⁺ (from component fayalite), liberating H₂ that ultimately favours the consumption of CO₂ and the formation of CH₄ and C. A bulk mass balance can be obtained after combination of these reactions correspondingly multiplied by a given stoichiometric coefficient. The number of combinations is hence infinite, and combinations that yield zero brucite are possible. A defined mass balance can be calculated only if additional constraints are imposed, such as the bulk composition of the system as long as the relative contribution of the above reactions to the integrated mass balance is a function of the original compositions of olivine and fluid and the initial fluid-olivine ratio. For initial H₂O-rich fluid and olivine

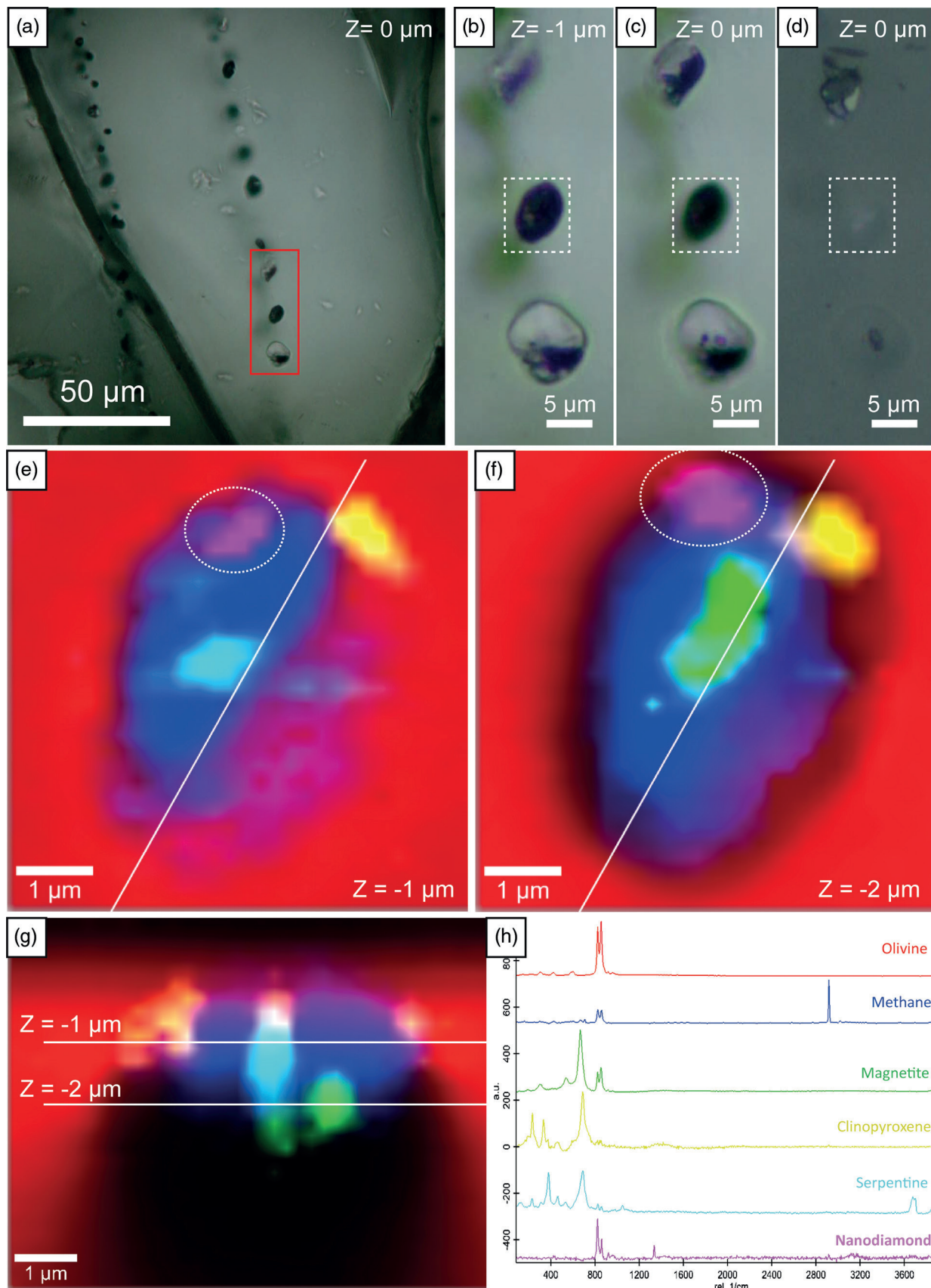


Figure 1 (a) Transmitted light photomicrograph (TLP) of olivine hosting a trail of secondary fluid inclusions. The red area defines the zoom in (b-d). (b, c) TLP of fluid inclusions below the surface of olivine with focus at Z (depth) = -1 and 0 μm respectively. (d) Reflected light photomicrograph of (c), showing that the central inclusion is completely below the surface. White rectangles mark the area of (e-g). (e) Fluid inclusion confocal Raman map at Z = -1 μm; different colours represent different phases. (f) Confocal Raman map for the same inclusion at Z = -2 μm. (g) Z-stack of (e, f) showing the inclusion profile. (h) Raman spectra of the identified phases (colour coded). Mapping conditions: 6 × 6 μm, 30 × 30 spectra, $T_{\text{int}} = 2$ s, 2 mW, 100× objective.

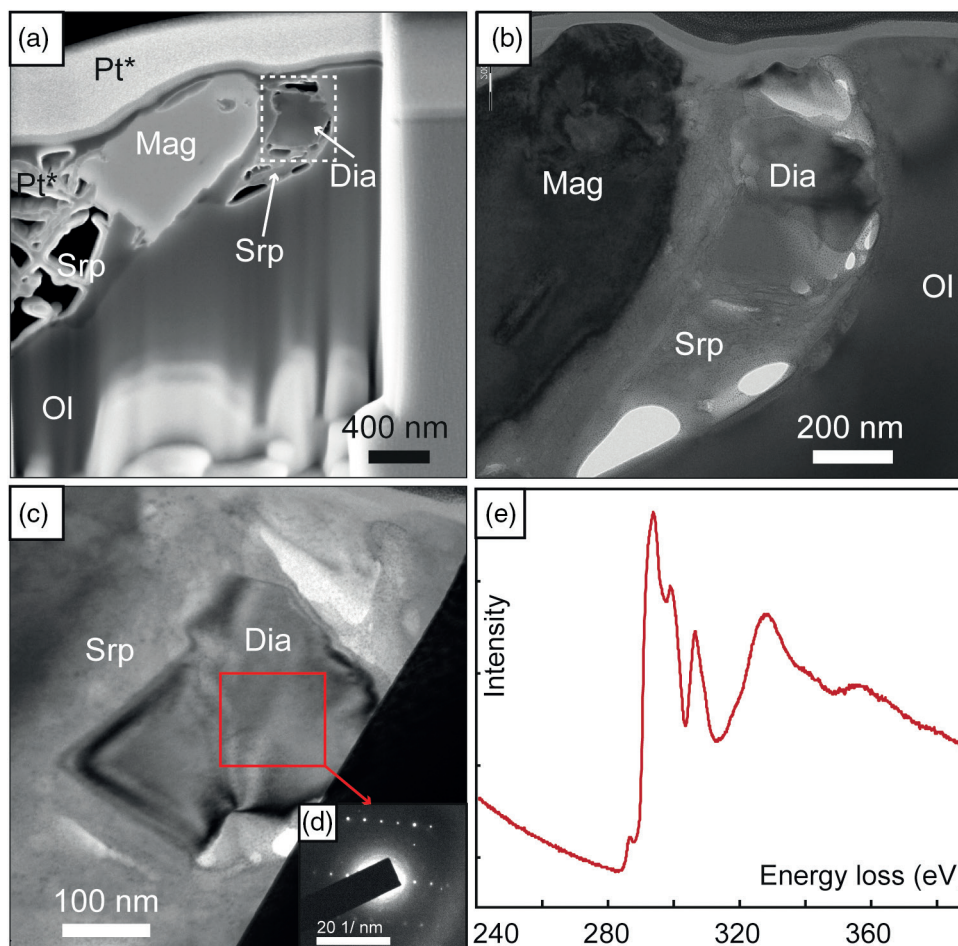
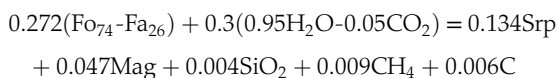


Figure 2 (a) Field emission scanning electron microscope image of olivine-hosted inclusion thinned by focused ion beam. (b,c) TEM image of the diamond and the surrounding serpentine and magnetite; the red square shows the selected area electron diffraction (SAED). (d) SAED pattern confirming the diamond structure of the crystal (the nearly horizontal rows of reflections have indices 111 with d spacing of 2 Å). (e) Electron energy loss near-edge structure of the C K-edge for the diamond showing a major peak due to its sp³ bonding. Abbreviations: Dia-Diamond, Mag-magnetite, Ol-olivine, Srp-serpentine, Pt*-platinum deposited during sample preparation.

with the composition of the studied gabbro (Table S-1), the observed stable brucite-lacking assemblage serpentine + magnetite + diamond + CH₄-rich fluid can be reached for specific olivine-fluid ratios, such as in the following example obtained using the software CSpace:



This reaction completely consumes both reactants. Under natural conditions in the fluid inclusion, olivine is in excess once H₂O and CO₂ are completely exhausted. Hence, thermodynamic calculations for a closed system fluid inclusion must consider an olivine-fluid ratio higher than 0.27:0.3. A bulk composition with an initial olivine:fluid ratio of 0.7:0.3 produces an assemblage of 51.3 vol. % Ol (Fo = 0.76), 40.2 vol. % antigorite, 6.8 vol. % magnetite, 1.5 vol. % CH₄ and 0.12 vol. % diamond at 100 MPa and 350 °C using the *Perple_X* software (Connolly, 2009). According to the low P conditions at which serpentinisation occurs, the stable C allotrope should be graphite. However, it has been demonstrated that nanodiamond can form at super-reducing conditions (e.g., Manuella, 2013; Simakov, 2018). Hence, in the above thermodynamic calculations, diamond has been used instead of graphite in order to simulate its metastable formation. The corresponding calculated log(*f*O₂; MPa) is as low as -45.3, ($\Delta\log f\text{O}_2[\text{Iron-Magnetite}] = -6.5$; Frost, 1991),

consistent with thermodynamic calculations in the diamond-COH fluid system at 350 °C and 100 MPa (Fig. 3; cf. Schmidt *et al.*, 2014).

Admittedly, calculations in a more complex system, with additional components and minerals (e.g., CaO, clinopyroxene, talc, carbonates *etc.*) and constraints (e.g., dissolved silica in the fluid), and at other P-T conditions over which serpentinisation takes place, would yield a more intricate picture of the basic process outlined above and different absolute values of *f*O₂ (e.g., Klein *et al.*, 2019). However, a highly reduced environment (particularly at lower T, see e.g., Klein *et al.*, 2019) should develop if CH₄ is to be the main fluid species in the inclusions, making possible the metastable formation of nanodiamond in low pressure, olivine-bearing oceanic rocks during low T infiltration of H₂O-CO₂ fluid mixtures.

The undoubted natural origin of diamond hosted with serpentine, magnetite and CH₄ in sealed fluid inclusions within magmatic olivine from a gabbro sill and associated chromitite should be related to the generalised release of CH₄ during hydrothermal alteration (partial hydration) of shallow oceanic lithosphere (e.g., Klein *et al.*, 2019). This finding implies that the formation of nanodiamond in altered olivine-bearing rocks can be a widespread process. The presence of diamond (Farré-de-Pablo *et al.*, 2019a) and other highly reduced phases (e.g., metallic Si, moissanite; Pujol-Solà *et al.*, 2018) in these rocks, in

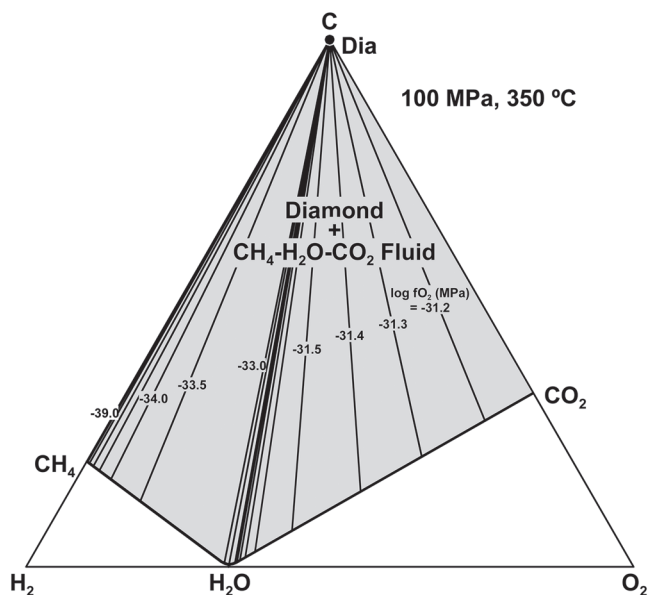


Figure 3 Phase relations in the C-O-H system (see methods in SI for details) with indication of fO_2 isopleths (black solid lines, log-units) for the diamond-(Dia) saturated portion ($\log(aC) = 0$) of the system at 100 MPa, 350 °C.

particular chromitites, cannot hence be taken as a general indication of ultra-high pressure conditions (e.g., Yang *et al.*, 2007, 2015; Griffin *et al.*, 2016). The small size of diamond (<1 μm) and its scarcity in the fluid inclusions are important handicaps in searching for “the needle in the haystack”, thus explaining its apparent absence in other case studies of altered oceanic rocks.

Acknowledgements

We thank the editor H.R. Marschall and the reviewers F. Klein, I. Graham and C. Ballhaus for their constructive comments. This research was funded by Fondo Europeo de Desarrollo Regional (FEDER) Funds, Spanish Projects CGL2015-65824, RTI2018-099157-A-I00, PID2019-105625RB-C21, and A.RNM.186.UGR18. Additional funding was provided by the Ramón y Cajal Fellowship RYC-2015-17596 to JMGJ, a FPU-PhD grant to NPS, the Mexican research programs CONACYT-Ciencia Básica (A1-S-14574) and UNAM-PAPIIT grant IA-101419, and received support for analyses at CIC from the University of Granada.

Editor: Horst R. Marschall

Additional Information

Supplementary Information accompanies this letter at <http://www.geochemicalperspectivesletters.org/article2029>.



© 2020 The Authors. This work is distributed under the Creative Commons Attribution Non-Commercial No-Derivatives 4.0

License, which permits unrestricted distribution provided the original author and source are credited. The material may not be adapted (remixed, transformed or built upon) or used for commercial purposes without written permission from the author. Additional information is available at <http://www.geochemicalperspectivesletters.org/copyright-and-permissions>.

Cite this letter as: Pujol-Solà, N., Garcia-Casco, A., Proenza, J.A., González-Jiménez, J.M., del Campo, A., Colás, V., Canals, À., Sánchez-Navas, A., Roqué-Rossell, J. (2020) Diamond forms during low pressure serpentinisation of oceanic lithosphere. *Geochem. Persp. Let.* 15, 19–24.

References

- BAI, W.J., ZHOU, M.F., ROBINSON, P.T. (1993) Possibly diamond-bearing mantle peridotites and podiform chromitites in the Luobusa and Dongqiao ophiolites, Tibet. *Canadian Journal of Earth Sciences* 30, 1650–1659.
- BARRON, L.M., LISHMUND, S.R., OAKES, G.M., BARRON, B.J., SUTHERLAND, F.L. (1996) Subduction model for the origin of some diamonds in the Phanerozoic of eastern New South Wales. *Australian Journal of Earth Sciences* 43, 257–267.
- CONNOLLY, J.A.D. (2009) The geodynamic equation of state: What and how. *Geochemistry, Geophysics, Geosystems* 10, doi: [10.1029/2009GC002540](https://doi.org/10.1029/2009GC002540).
- DOBZHINETSKAYA, L., WIRTH, R., GREEN, H. (2014) Diamonds in Earth's oldest zircons from Jack Hills conglomerate, Australia, are contamination. *Earth and Planetary Science Letters* 387, 212–218.
- FARRÉ-DE-PABLO, J., PROENZA, J.A., GONZÁLEZ-JIMÉNEZ, J.M., GARCÍA-CASCO, A., COLÁS, V., ROQUÉ-ROSSELL, J., CAMPRUBÍ, A., SÁNCHEZ-NAVAS, A. (2019a) A shallow origin for diamonds in ophiolitic chromitites. *Geology* 47, 75–78.
- FARRÉ-DE-PABLO, J., PROENZA, J.A., GONZÁLEZ-JIMÉNEZ, J.M., GARCÍA-CASCO, A., COLÁS, V., ROQUÉ-ROSSELL, J., CAMPRUBÍ, A., SÁNCHEZ-NAVAS, A. (2019b) A shallow origin for diamonds in ophiolitic chromitites: REPLY. *Geology* 47, e477–e478, doi: [10.1130/G46602Y.1](https://doi.org/10.1130/G46602Y.1).
- FROST, B.R. (1991) Introduction to oxygen fugacity and its petrologic importance. *Reviews in Mineralogy and Geochemistry* 25, 1–9.
- GRIFFIN, W.L., AFONSO, J.C., BELOUSOVA, E.A., GAIN, S.E., GONG, X.H., GONZÁLEZ-JIMÉNEZ, J.M., HOWELL, D., HUANG, J.X., MCGOWAN, N., PEARSON, N.J., SATSUAWA, T., SHI, R., WILLIAMS, P., XIONG, Q., YANG, J.S., ZHANG, M., O'REILLY, S.Y. (2016) Mantle Recycling: Transition Zone Metamorphism of Tibetan Ophiolitic Peridotites and its Tectonic Implications. *Journal of Petrology* 57, 655–684.
- GROZEVA, N.G., KLEIN, F., SEEWALD, J.S., SYLVA, S.P. (2020) Chemical and isotopic analyses of hydrocarbon-bearing fluid inclusions in olivine-rich rocks. *Philosophical Transactions of the Royal Society A: Mathematical, Physical and Engineering Sciences* 378, 20180431.
- KLEIN, F., GROZEVA, N.G., SEEWALD, J.S. (2019) Abiotic methane synthesis and serpentinization in olivine-hosted fluid inclusions. *Proceedings of the National Academy of Sciences of the United States of America* 116, 17666–17672.
- LAMADRID, H.M., RIMSTDT, J.D., SCHWARZENBACH, E.M., KLEIN, F., ULRICH, S., DOLOCANI, A., BODNAR, R.J. (2017) Effect of water activity on rates of serpentinization of olivine. *Nature Communications* 8, 1–9.
- LITASOV, K.D., KAGI, H., VOROPAEV, S.A., HIRATA, T., OHFUJI, H., ISHIBASHI, H., MAKINO, Y., BEKKER, T.B., SEVASTYANOV, V.S., AFANASIEV, V.P., POKHILENKO, N.P. (2019a) Comparison of enigmatic diamonds from the Tolbachik arc volcano (Kamchatka) and Tibetan ophiolites: Assessing the role of contamination by synthetic materials. *Gondwana Research* 75, 16–27.
- LITASOV, K.D., KAGI, H., BEKKER, T.B., HIRATA, T., MAKINO, Y. (2019b) Cuboctahedral type Ib diamonds in ophiolitic chromitites and peridotites: the evidence for anthropogenic contamination. *High Pressure Research* 39, 480–488.
- MANUELLA, F.C. (2013) Can nanodiamonds grow in serpentinite-hosted hydrothermal systems? A theoretical modelling study. *Mineralogical Magazine* 77, 3163–3174.
- MASSONNE, H.J. (2019) Comment: A shallow origin for diamonds in ophiolitic chromitites. *Geology* 47, e476, doi: [10.1130/G46459C.1](https://doi.org/10.1130/G46459C.1).
- MCCOLLOM, T.M., BACH, W. (2009) Thermodynamic constraints on hydrogen generation during serpentinization of ultramafic rocks. *Geochimica et Cosmochimica Acta* 73, 856–875.
- PUJOL-SOLÀ, N., PROENZA, J., GARCÍA-CASCO, A., GONZÁLEZ-JIMÉNEZ, J., ANDREAZINI, A., MELGAREJO, J., GERVILLA, F. (2018) An Alternative Scenario on the Origin of Ultra-High Pressure (UHP) and Super-Reduced (SuR) Minerals in Ophiolitic Chromitites: A Case Study from the Mercedita Deposit (Eastern Cuba). *Minerals* 8, 433, doi: [10.3390/min8100433](https://doi.org/10.3390/min8100433).
- SACHAN, H.K., MUKHERJEE, B.K., BODNAR, R.J. (2007) Preservation of methane generated during serpentinization of upper mantle rocks: Evidence from fluid inclusions in the Nidar ophiolite, Indus Suture Zone, Ladakh (India). *Earth and Planetary Science Letters* 257, 47–59.
- SCHMIDT, M.W., GAO, C., GOLUBKOVA, A., ROHRBACH, A., CONNOLLY, J.A. (2014) Natural moissanite (SiC) – a low temperature mineral formed from highly



- fractionated ultra-reducing COH-fluids. *Progress in Earth and Planetary Science* 1, 27.
- SIMAKOV, S.K. (2018) Nano- and micron-sized diamond genesis in nature: An overview. *Geoscience Frontiers* 9, 1849–1858.
- SIMAKOV, S.K., DUBINCHUK, V.T., NOVIKOV, M.P., DROZDOVA, I.A. (2008) Formation of diamond and diamond-type phases from the carbon-bearing fluid at PT parameters corresponding to processes in the Earth's crust. *Doklady Earth Sciences* 421, 835–837.
- SIMAKOV, S.K., KOUCHI, A., MEL'NIK, N.N., SCRIBANO, V., KIMURA, Y., HAMA, T., SUZUKI, N., SATTO, H., YOSHIZAWA, T. (2015) Nanodiamond finding in the hyblean shallow mantle xenoliths. *Scientific Reports* 5, 10765, doi: [10.1038/srep10765](https://doi.org/10.1038/srep10765).
- SIMAKOV, S.K., SCRIBANO, V., MEL'NIK, N.N., BARONE, G. (2020) Sicilian serpentinite xenoliths containing abiotic organics with nanodiamond clusters as key model for prebiotic processes. *Geoscience Frontiers (in press)*, doi: [10.1016/j.gsf.2020.04.008](https://doi.org/10.1016/j.gsf.2020.04.008).
- TORRES-ROLDÁN, R.L., GARCÍA-CASCO, A., GARCÍA-SÁNCHEZ, P.A. (2000) CSpace: An integrated workplace for the graphical and algebraic analysis of phase assemblages on 32-bit Wintel platforms. *Computers and Geosciences* 26, 779–793.
- WHITNEY, D.L., EVANS, B.W. (2010) Abbreviations for names of rock-forming minerals. *American Mineralogist* 95, 185–187.
- XIONG, F., LIU, Z., KAPSIOTIS, A., YANG, J., LENAŽ, D., ROBINSON, P.T. (2019) Petrogenesis of lherzolites from the Purang ophiolite, Yarlung-Zangbo suture zone, Tibet: origin and significance of ultra-high pressure and other 'unusual' minerals in the Neo-Tethyan lithospheric mantle. *International Geology Review* 61, 2184–2210.
- YANG, J.S., DOBRZHINETSAYA, L., BAI, W.J., FANG, Q.S., ROBINSON, P.T., ZHANG, J., GREEN, H.W. (2007) Diamond- and coesite-bearing chromitites from the Luobusa ophiolite, Tibet. *Geology* 35, 875–878.
- YANG, J., MENG, F., XU, X., ROBINSON, P.T., DILEK, Y., MAKEYEV, A.B., WIRTH, R., WIEDENBECK, M., CLIFF, J. (2015) Diamonds, native elements and metal alloys from chromitites of the Ray-Iz ophiolite of the Polar Urals. *Gondwana Research* 27, 459–485.
- YANG, J., LIAN, D., ROBINSON, P.T., QIU, T., XIONG, F., WU, W. (2019) Comment to: A shallow origin for diamonds in ophiolitic chromitites. *Geology* 47, e475, doi: [10.1130/G46446C.1](https://doi.org/10.1130/G46446C.1).

Diamond forms during low-pressure serpentinisation of oceanic lithosphere

N. Pujol-Solà, A. Garcia-Casco, J.A. Proenza, J.M. González-Jiménez, A. del Campo, V. Colás, A. Canals, A. Sánchez-Navas, J. Roqué-Rossell

Supplementary Information

The Supplementary Information includes:

- Geological Setting and Petrography
- Methods
- Tables S-1 and S-2
- Figures S-1 to S-7
- Supplementary Information References

Geological Setting and Petrography

The diamond-bearing samples were collected in the Potosí chromitite mining area (20°33'N, 74°45'W) within the Moa-Baracoa Ophiolitic Massif (MBOM; Fig. S-1a), eastern Cuba (Proenza *et al.*, 1999), which forms part of the ca. 1000 km long Cuban ophiolite belt (Late Jurassic - Cretaceous; Iturralde-Vinent *et al.*, 2016 and references therein). The MBOM consists of mantle harzburgites with subordinate dunites and a well-preserved Moho Transition Zone (MTZ), layered gabbros (Fig. S-1b) and mafic volcanic rocks (Marchesi *et al.*, 2006). The mantle tectonites of the MTZ contain elongate dunite bodies, chromitites and gabbroic sill intrusions following the fabric of the host harzburgite, as well as discordant dikes of gabbro, wehrlite and troctolite (Proenza *et al.*, 1999).

In the Potosí area, chromitite bodies are crosscut by several generations of gabbroic intrusions that locally triggered metasomatism in adjacent chromitites (Proenza *et al.*, 2001; González-Jiménez *et al.*, 2020; Pujol-Solà *et al.*, 2020). Diamond grains were found in a gabbro sill formed by a primary assemblage of

olivine (64% vol.; Fo₇₄), clinopyroxene (21% vol.; En₃₇₋₄₆Wo₄₉₋₄₁Fs₁₅₋₉), plagioclase (14% vol.; An₅₉₋₆₄), orthopyroxene (1% vol.; En₇₄₋₇₅) and accessory oxides that show a non-oriented coarse-grained magmatic texture (Figs. S-2, S-3, Table S-1). Diamond was also identified in interstitial magmatic olivine of associated chromitite bodies (Fig. S-4) described in detail by Pujol-Solà *et al.* (2020).

Methods

1. Sample preparation

Olivine gabbro and chromitite samples were collected from the Potosí area in the Moa-Baracoa massif, eastern Cuba. Thin sections were prepared at the University of Barcelona (UB) and the University of Granada (UGR). Thin sections were polished using diamond abrasive paste of 1 µm and 1/4 µm particle size and epoxy resin. Different sets of duplicated thin sections were prepared using Al₂O₃ or amorphous colloidal silica as carbon-free polishing materials in order to exclude contamination. In addition, ultrasonic baths were performed to remove any remaining polishing debris from the thin sections. Special doubly polished sections approximately 100 µm thick were also prepared for fluid inclusion studies using the same diamond abrasives and using polyester resin.

2. Scanning electron microscopy

Samples were studied in detail by optical microscopy and scanning electron microscopy, using a Quanta 200 FEI XTE 325/D8395 scanning electron microscope (SEM) and a JEOL JSM-7100 field-emission scanning SEM at the University of Barcelona (CCiTUB), and also using a GEMINI field-emission scanning SEM at the University of Granada. Operating conditions were 15 – 20 kV accelerating voltage and 5 nA beam current.

3. Electron probe microanalyses (EPMA)

Quantitative electron microprobe analyses (EMPA) were conducted at the CCiTUB using a JEOL JXA-8230 electron microprobe and in the Centre for Scientific Instrumentation of the University of Granada (CIC-UGR) using a CAMECA SX100 operated in wavelength-dispersive spectroscopy (WDS) mode. Analytical conditions were 20 kV accelerating voltage, 10-20 nA beam current, 1-2 µm beam diameter, and 10 s counting time per element. Natural and synthetic standards used were Cr₂O₃ (Cr), wollastonite (Si and Ca), corundum (Al), rutile (Ti), albite (Na), periclase (Mg), hematite (Fe), rhodonite (Mn), orthoclase (K), NiO (Ni), sphalerite (Zn), CaF (F), and NaCl (Cl) at the CCiTUB; and albite (Na), diopside (Si), wollastonite (Ca), vanadinite (Cl), sanidine (K), TiO₂ (Ti), rhodonite (Mn), CaF₂ (F), Fe₂O₃ (Fe), and synthetic periclase (Mg), Al₂O₃ (Al), Cr₂O₃ (Cr), and NiO (Ni) at the CIC-UGR. The correction procedure PAP (Pouchou and Pichoir, 1991) was used to convert specimen intensity ratios into concentrations. The chemical data for Cr-spinel were stoichiometrically recalculated in order to distinguish FeO from Fe₂O₃ according to the procedure described by Carmichael (1966).

X-ray maps of selected areas were collected with the CAMECA SX100 machine on thin sections using the following analytical conditions: 20 kV accelerating voltage, 300 nA beam current, focused spot, stage-scanning mode, 2 - 8 µm pixel size, and 20 - 30 ms counting time per pixel. The following elements were



mapped: Si, Al, Ba, Ti, Cr, Na, Mg, Mn, Fe, Ni, Ca, K, Cl, Zr, Zn, P, S, and O. The images were treated with DWImager software (Torres-Roldán and Garcia Casco, unpublished; see Garcia-Casco, 2007) and consist of the X-Ray signals of the elements (colour-coded; expressed in counts) and with polish defects, voids and all other mineral masked out. A grey-scale base-layer, calculated with the expression $\Sigma(\text{counts}_i \cdot A_i)$ (where A is atomic number, and i is Si, Ti, Al, Cr, Fe, Mn, Mg, Ca, Na and K), underlies the images and contains the basic textural information of the scanned areas. Phase abundance maps were created after the manipulation of the histograms of elemental maps.

4. Micro-Raman spectroscopy

Micro-Raman spectra of the solid and fluid inclusions in olivine were obtained using different instruments: a) HORIBA JobinYvon LabRam HR 800 dispersive spectrometer equipped with an Olympus BXFM optical microscope at CCiTUB. Non polarized Raman spectra were obtained in confocal geometry by applying a 532 nm laser, using a 100x objective (beam size around 2 μm), with 3 - 5 measurement repetitions for 10 - 15 seconds each. The Si band at $\sim 520 \text{ cm}^{-1}$ was used for calibration. The obtained spectra were processed using the LabSpec® software (JobinYvon; Villeneuve-d'Ascq, France); b) JASCO NRS-5100 dispersive spectrometer equipped with an Olympus Optical microscope at CIC-UGR. The spectra conditions were the same as above. The obtained spectra were processed using the Spectra Manager™ II Software and KnowItAll® JASCO Software. The micro-Raman maps were made in two-dimensional mode in the thin sections with 1 μm step and focus at different depth.

Mapping and cross-sections of selected inclusions were taken with a confocal Raman microscope (CRM) at the Instituto de Cerámica y Vidrio (CSIC – Madrid) with spectral resolution of 0.02 cm^{-1} , coupled with an AFM instrument (Witec ALPHA 300RA), with laser excitation at 532 nm and a 100 \times objective lens (NA = 0.95). The incident laser power was 2 - 6 mW. The optical diffraction resolution was limited to about 200 nm laterally and 500 nm vertically. The samples were mounted in a piezo-driven scan platform having 4 nm lateral and 0.5 nm vertical positioning accuracy, also equipped with an active vibration isolation system, active 0.7 - 1000 Hz. The images were processed and analysed with the software WiTec Project Plus 2.08.

Some inclusions below the polished mineral's surface do not show Raman signal of CH_4 (or of any other gas species) probably related to the low density of the gas within the inclusion and the detection limit of the Raman analyses (see Grozeva *et al.*, 2020).

5. Focused ion beam (FIB)

A selected inclusion containing diamond hosted in the olivine gabbro was prepared as an electro-transparent thin-foil at the Barcelona Research Center in Multiscale Science and Engineering, from the Polytechnical University of Catalonia (UPC), using a double-beam workstation (Neon40, CarlZeiss) equipped with a Schotky FE-SEM and FIB Ga^+ columns. The selected inclusion was coated with a thin slip ($\sim 100 \text{ nm}$) of Pt by means of e-beam assisted gas deposition as a protection layer for milling and polishing of the thin-foil. Then, the sample was milled by means of Ga ion bombardment until 1 μm thickness. The thin-foil was then lift-out and transferred to a TEM grid using a Kleindiek® micromanipulator with a tungsten tip and fixed into the TEM grid by ion-beam assisted Pt deposition. Finally, the inclusion area within the thin-foil was polished until electron transparency was achieved (down to $\sim 80 \mu\text{m}$).

A second diamond inclusion within olivine from chromitite was prepared as a thin-foil at the Laboratorio de Microscopías Avanzadas (LMA) from the Universidad de Zaragoza, using a dual beam



Helios Nanolab 650 equipped with a FE-SEM and FIB Ga⁺ column. For the thin-foil preparation, the thin section was firstly coated with a thin (a few μm) layer of Pd and the area of the inclusion was also coated with a Pt layer by means of e-beam assisted gas deposition for protection of the interest area. The preparation of the thin-foil followed the same process as described above, but it was transferred to the grid using an Omniprobe® nanomanipulator.

6. Transmission electron microscopy (TEM)

The TEM study on the first thin-foil (olivine gabbro) was performed at the CCiTUB with a JEOL JEM-2100 LaB₆ transmission electron microscope (TEM) with energy dispersed analysis of X-rays (EDX), operated at 200 kV in STEM mode and beam size of ~ 15 nm, with an Oxford Instruments INCA x-sight spectrometer with Si (Li) detector. Images were acquired using a Gatan CCD Camera Orius SC1000 and processed with the DigitalMicrograph™ Software (v. 1.71.38).

The second thin-foil (chromitite) was studied using a FEI Titan G2 TEM equipped with Field Emission cannon XFEG, with spherical correction for the objective lens and working at 300 kV at the CIC-UGR. The microscope is equipped with four energy-dispersive analyses of X-rays (EDX) detectors (FEI microanalysis Super X) that allowed to perform elemental maps, and high angle-annular dark field detector (HAADF) that allowed to obtain high Z contrast mages. High-magnification electron microscopy (HMEM) images and selected area electron diffraction (SAED) patterns were also acquired. Images were processed with Digital Micrograph® Software (v. 1.71.38) and maps with INCA® Microanalysis Suite Software (v. 4.09).

7. Electron energy loss spectroscopy (EELS)

The electron energy loss spectroscopy (EELS) was performed at the CIC-UGR using a Zeiss Libra 120 plus LaB₆ transmission electron microscope with Omega energy filtering, operating at 120 kV. Analyses were done at 80000x magnification with 1 - 2 μA current emission on an area of 300 nm of diameter.

8. Thermodynamic calculations

The thermodynamic calculations were performed using Perple_X 6.8.3 (Connolly, 2009; <http://www.perplex.ethz.ch/>) and the internally consistent thermodynamic database of Holland and Powell (2011) extended to include super-reduced phases (cr_hp11ver_metal.dat). In the above database we removed graphite in order to simulate the metastable formation of diamond. The solution models considered were olivine (Holland and Powell, 1998) and C-O-H fluid (Connolly and Cesare, 1993). All other minerals involved in the calculations were treated as pure phases. Phase relations for olivine-hosted CH₄-rich fluid inclusions were computed at 100 MPa and 350 °C in the system MgO-FeO-SiO₂-C-O₂-H₂ (MFSCOH). The bulk composition of the fluid inclusion-olivine ensemble corresponds to an initial assemblage of 0.7:0.3 molar mix of magmatic olivine (F_{0.74}, (Mg_{1.48}Fe_{0.52})SiO₄) and H₂O-rich fluid (X_{H₂O} = 0.95, 0.95H₂O:0.05CO₂). The phase relations for diamond-COH fluid (Fig. 3) were computed in the C-O-H system and contoured for oxygen fugacity isopleths calculated for a diamond-buffered fluid (Connolly and Cesare, 1993).



Tables S-1 to S-2**Table S-1** Representative electron microprobe analyses of olivine in the studied samples.

Sample	POT-2(II)					POT-2B					POT-3				
	ol-1	ol-2	ol-3	ol-4	ol-5	ol-1	ol-2	ol-3	ol-4	ol-5	ol-1	ol-2	ol-3	ol-4	ol-5
SiO ₂ (wt.%)	38.26	38.17	38.03	37.70	37.75	37.59	37.55	37.45	37.65	38.02	40.54	40.47	40.68	40.49	40.59
TiO ₂	bdl	bdl	bdl	bdl	bdl	0.02	bdl	bdl	0.02	bdl	bdl	bdl	bdl	bdl	0.02
Al ₂ O ₃	bdl	bdl	bdl	bdl	bdl	bdl	0.02	0.03	bdl	bdl	bdl	bdl	0.02	bdl	0.03
Cr ₂ O ₃	bdl	bdl	bdl	bdl	bdl	bdl	bdl	bdl	bdl	bdl	bdl	0.06	0.05	0.03	bdl
FeO _T	24.03	24.19	24.23	24.15	24.22	24.78	24.33	24.70	24.30	24.28	9.90	9.96	9.61	10.03	9.70
MnO	0.35	0.34	0.36	0.37	0.36	0.36	0.39	0.38	0.38	0.38	0.14	0.16	0.16	0.17	0.16
MgO	37.79	37.76	37.45	37.34	37.47	36.80	36.80	36.47	36.86	37.25	48.75	48.55	48.70	48.94	48.74
NiO	0.15	0.14	0.16	0.15	0.16	0.14	0.18	0.15	0.12	0.15	0.27	0.28	0.26	0.28	0.29
CaO	0.05	0.04	0.03	0.02	0.03	0.03	0.03	0.05	0.04	0.02	0.02	0.02	0.02	0.03	0.02
Total	100.63	100.64	100.26	99.73	99.99	99.73	99.31	99.23	99.37	100.10	99.62	99.49	99.50	99.97	99.55
Cations per 4 oxygens															
Si	0.997	0.996	0.996	0.994	0.993	0.994	0.995	0.995	0.997	0.998	0.999	0.998	1.002	0.995	0.999
Ti						0.000			0.000						0.000
Al							0.001	0.001					0.001		0.001
Cr												0.001	0.001	0.001	
Fe ²⁺	0.524	0.528	0.531	0.532	0.533	0.548	0.539	0.549	0.538	0.533	0.204	0.206	0.198	0.206	0.200
Mn	0.008	0.008	0.008	0.008	0.008	0.008	0.009	0.008	0.009	0.008	0.003	0.003	0.003	0.004	0.003
Mg	1.468	1.469	1.463	1.467	1.469	1.450	1.454	1.445	1.455	1.458	1.790	1.786	1.787	1.792	1.789
Ni	0.003	0.003	0.003	0.003	0.003	0.003	0.004	0.003	0.003	0.003	0.005	0.005	0.005	0.005	0.006
Ca	0.001	0.001	0.001	0.001	0.001	0.001	0.001	0.001	0.001	0.001	0.000	0.000	0.000	0.001	0.001
Total	3.002	3.004	3.003	3.006	3.007	3.005	3.003	3.003	3.002	3.001	3.001	3.000	2.997	3.003	2.999
Fo	0.74	0.74	0.73	0.73	0.73	0.73	0.73	0.72	0.73	0.73	0.90	0.90	0.90	0.90	0.90
Ni (ppm)	1288	1143	1366	1257	1310	1137	1529	1301	1040	1260	2309	2323	2178	2319	2468



Figures S-1 to S-7

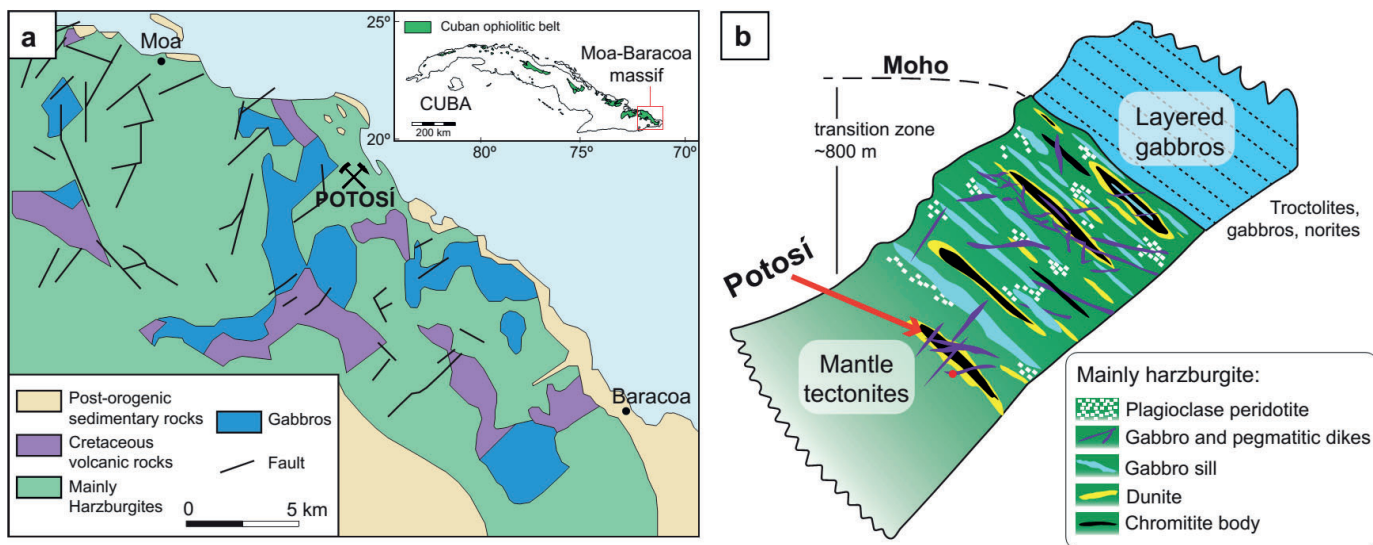


Figure S-1 (a) Geological map of the Moa-Baracoa massif in eastern Cuba, modified from Proenza *et al.* (2001). The inset in the upper right shows the location within the Cuba Island. (b) Schematic column of the ophiolitic sequence in the Moa Baracoa Massif (eastern Cuba) showing the position of the Potosí chromitites, modified from Marchesi *et al.* (2006).

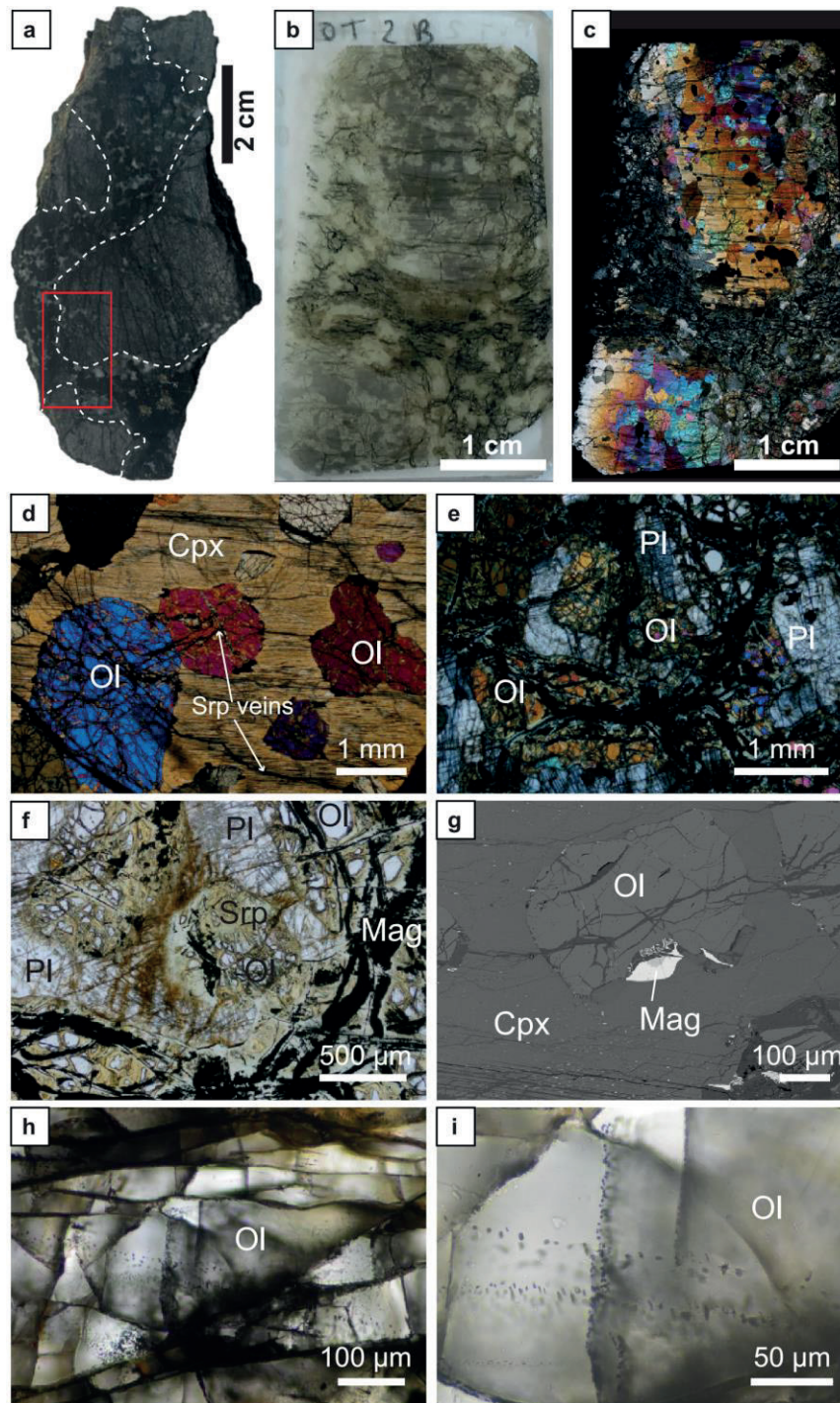


Figure S-2 (a) Diamond-bearing olivine gabbro hand sample. The red rectangle marks the area of the thin section in b-c. (b) Thin section of the olivine gabbro. (c) Thin section of the olivine gabbro in crossed nicols. Note the poikilitic texture of the sample. (d) Transmitted light (crossed nicols) photomicrograph of the olivine gabbro showing the poikilitic texture of clinopyroxene and olivine. (e) Transmitted light (crossed nicols) photomicrograph of the olivine gabbro showing the poikilitic texture of partially altered plagioclase and olivine. (f) Transmitted light photomicrograph of partially serpentinised olivine with serpentine-group minerals and magnetite veins. (g) Backscattered electron image of an olivine chadacryst with magnetite in a larger poikilitic clinopyroxene crystal. (h) Transmitted light photomicrograph of olivine hosting multiple trails of fluid inclusions with crosscutting relations. (i) Transmitted light photomicrograph of a close up of fluid inclusion trails hosted in olivine. Abbreviations: Cpx – clinopyroxene, Mag – magnetite, Ol – olivine, Pl – plagioclase, Srp – serpentine.

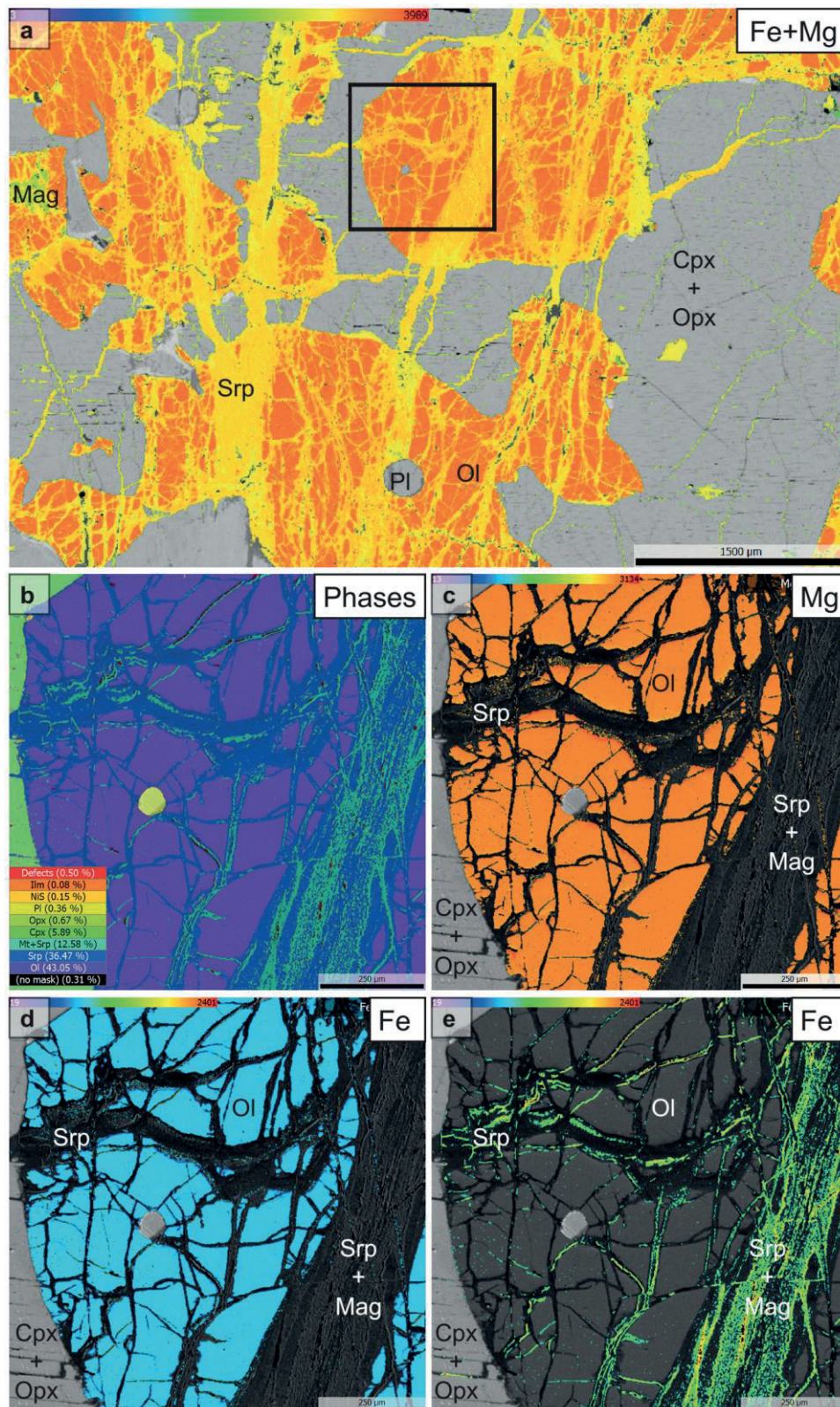


Figure S-3 Electron microprobe X-ray maps of the olivine gabbro. **(a)** Fe+Mg element map of olivine crystals and serpentine veins cross cutting the sample. The black square marks the area of the detailed maps b-e. **(b)** Phase map of the analysed area. **(c)** Mg map of olivine. **(d)** Fe map of olivine. **(e)** Fe map of the serpentine veins containing magnetite. Abbreviations: Cpx – clinopyroxene, Opx – orthopyroxene, Mag – magnetite, Ol – olivine, Pl – plagioclase, Srp – serpentine.

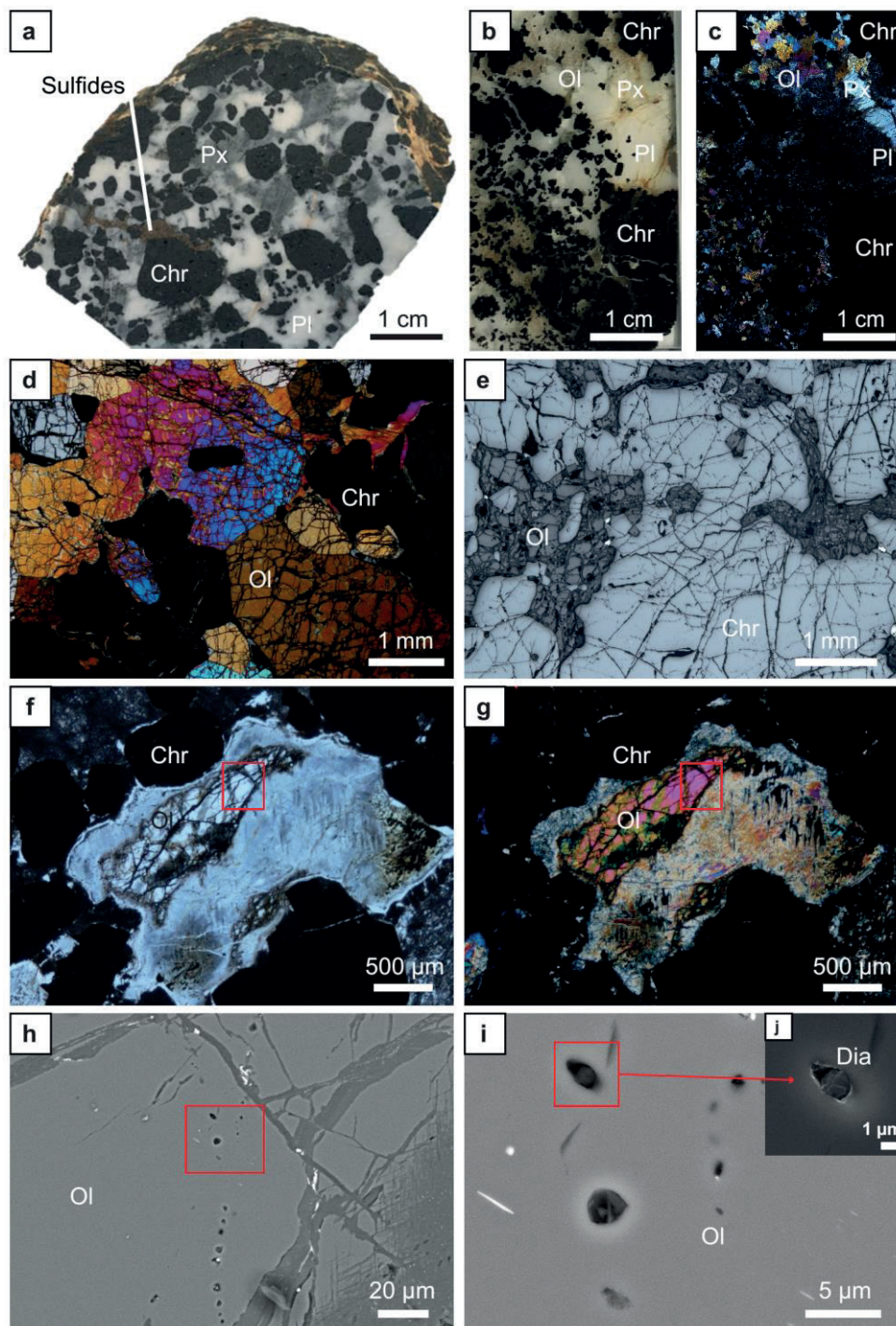


Figure S-4 (a) Diamond-bearing chromitite hand sample. (b) Thin section of the chromitite. (c) Thin section of the chromitite in crossed nicols. (d) Transmitted light (crossed nicols) microphotograph of chromitite showing interstitial magmatic olivine. (e) Reflected light microphotograph of chromite and interstitial olivine. (f) Transmitted light microphotograph of partially altered olivine hosting inclusion trails. (g) Transmitted light (crossed nicols) microphotograph of partially altered olivine hosting inclusion trails. The red rectangle marks the area of image h. (h) Backscattered electron image of inclusion trails hosted within olivine. The red rectangle marks the area of image i. (i) Backscattered electron image of inclusions hosting diamond and native Si (top) and serpentine (center): needle-like crystal is ilmenite and the bright dot is chromite. (j) Zoom of i showing a secondary electron image of the inclusion hosting diamond and native Si. Abbreviations: Chr – chromite, Dia - diamond, Mag – magnetite, Ol – olivine, Pl – plagioclase, Px – pyroxene.

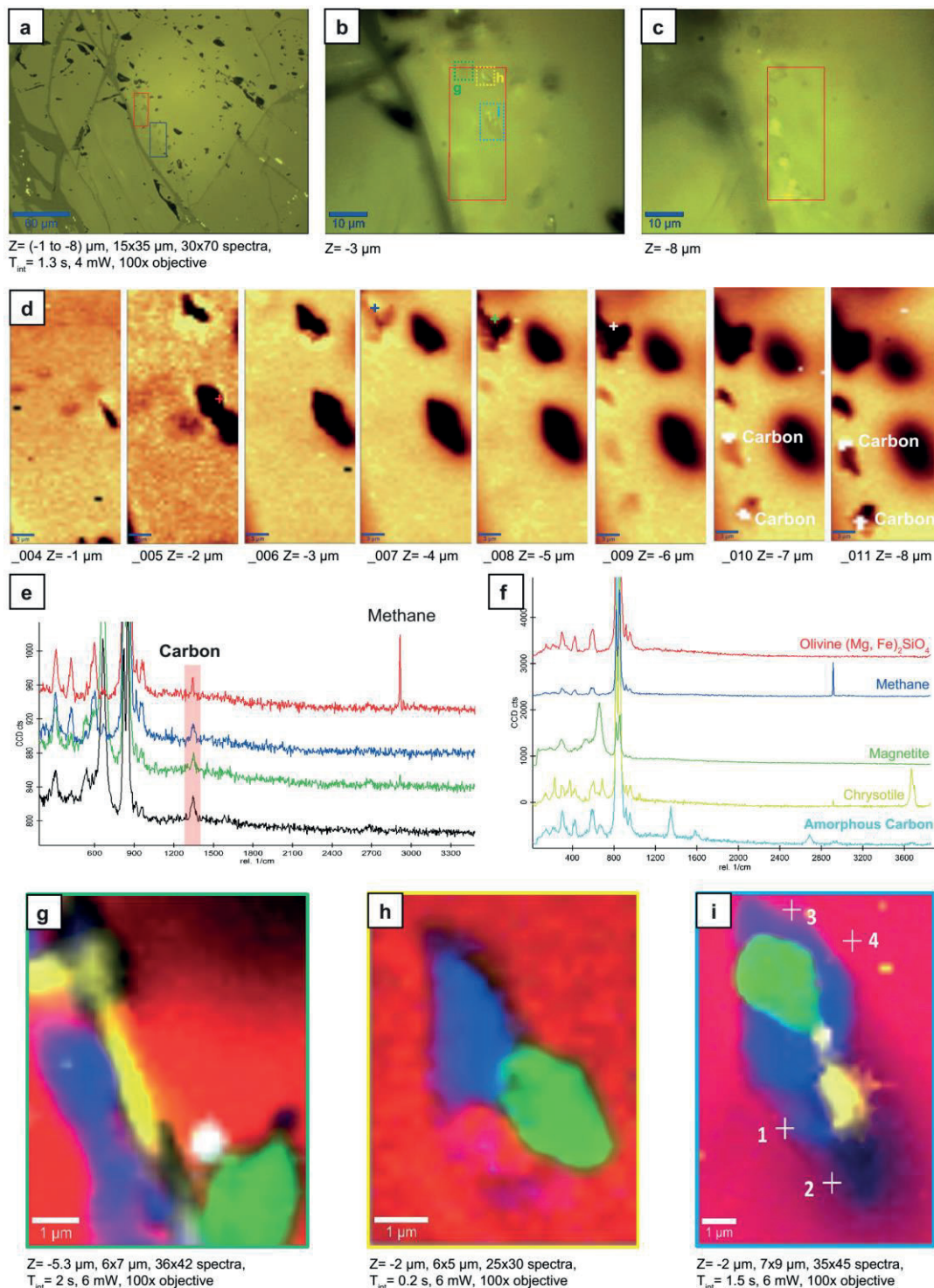


Figure S-5 Confocal Raman maps of fluid inclusions. **(a)** Reflected light microphotograph of inclusion trails hosted in olivine from the gabbro. **(b)** Zoom of **(a)** showing the inclusions at Z (depth) = $-3 \mu\text{m}$. **(c)** Image **(b)** with focus at $Z = -8 \mu\text{m}$. Note that the inclusions that are shown in **(b)** and **(c)** are different. **(d)** Z -stack in the area in red in **(b)** and **(c)** from $Z = -1 \mu\text{m}$ to $Z = -8 \mu\text{m}$. Amorphous carbon has been recognized in 5 inclusions. **(e)** Amorphous carbon Raman patterns corresponding to the inclusions in the Z -stack of **(d)**. The colors correspond to the analyzed points showed in **(d)**. **(f)** Raman spectra for the different phases observed in the inclusion maps **(g)**-**(i)**. **(g)** X-Y Raman map of the inclusion denoted by the green square in **(b)**. **(h)** X-Y Raman map of the inclusion denoted by the yellow square in **(b)**. **(i)** X-Y Raman map of the inclusion denoted by the blue square in **(b)**.

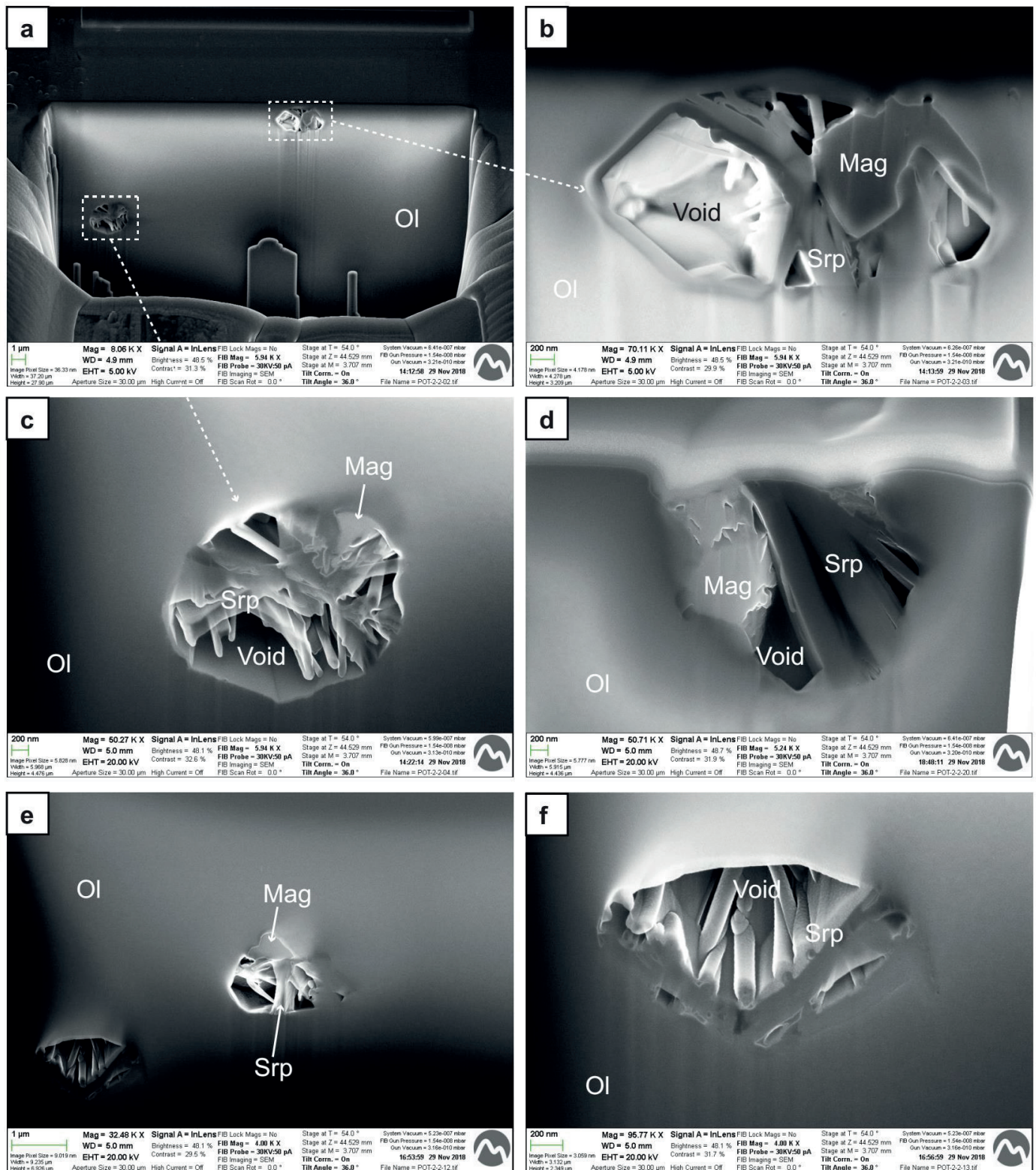


Figure S-6 Backscattered electron images of inclusions hosted within olivine cut with focused ion beam (FIB). Most inclusions contain serpentine and magnetite. Abbreviations: Mag – magnetite, Ol – olivine, Srp – serpentine.

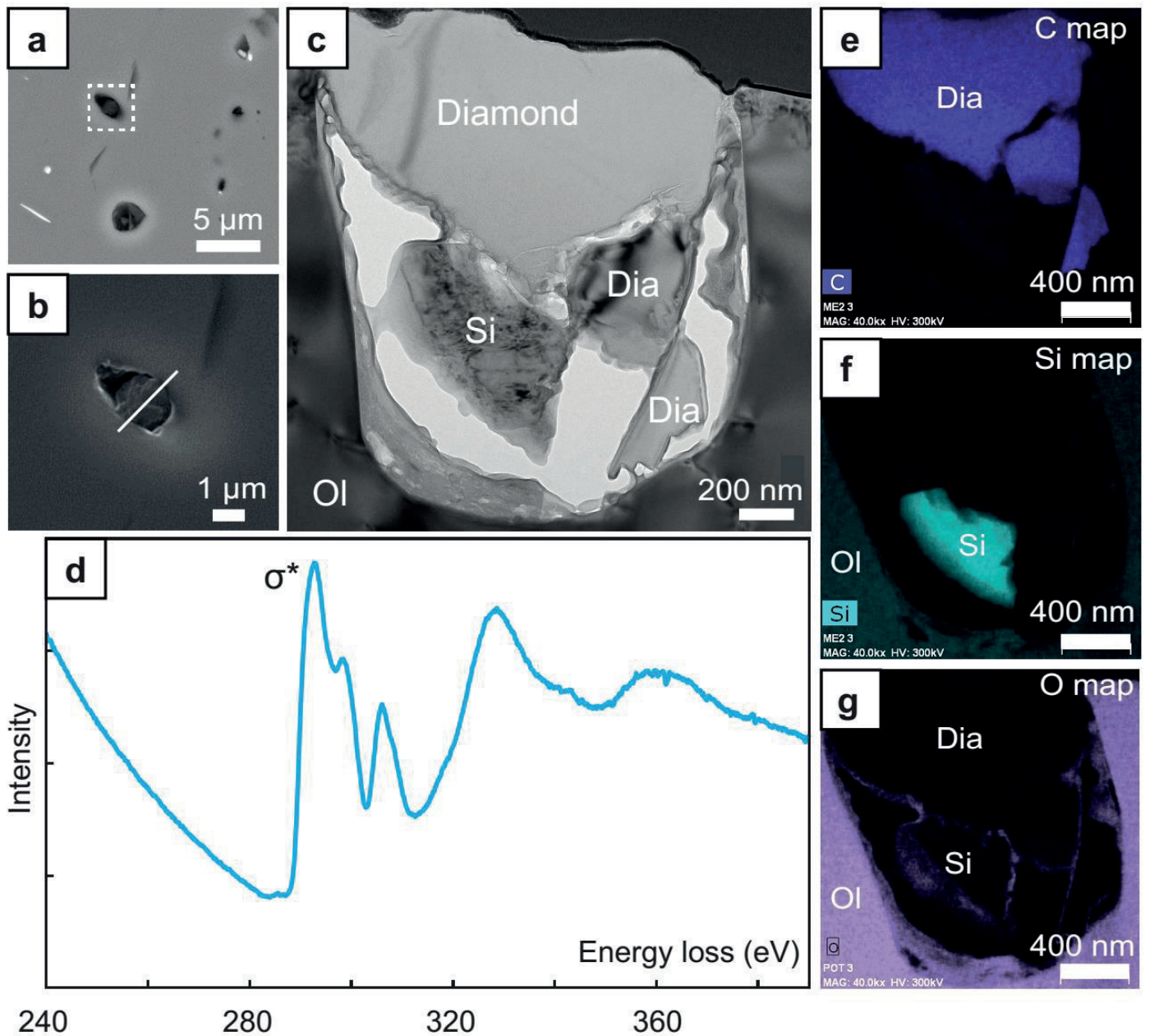


Figure S-7 Diamond hosted in interstitial olivine in chromitite. **(a)** Field-emission scanning electron microscope (FE-SEM) back-scattered image showing the location of a diamond grain in olivine. **(b)** Detailed FE-SEM secondary electron image of the diamond grain cut with focused ion beam (FIB). **(c)** Transmission electron microscopy (TEM) image showing the grains of diamond and native Si. **(d)** ELNES of C-K at the diamond grain, indicating the sp^3 hybridization of C by the presence of a strong σ^* peak at about 290 eV, but no Π^* peak. **(e-g)** TEM X-ray maps of C, Si and O, respectively. Abbreviations: Dia- diamond, Ol – olivine, Si – native silicon.

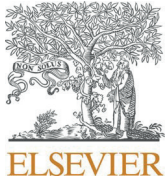
Supplementary Information References

- Carmichael, I.S.E. (1966) The iron-titanium oxides of salic volcanic rocks and their associated ferromagnesian silicates. *Contributions to Mineralogy and Petrology* 14, 36–64.
- Connolly, J.A.D. (2009) The geodynamic equation of state: What and how. *Geochemistry, Geophysics, Geosystems* 10.
- Connolly, J.A.D., Cesare, B. (1993) C-O-H-S fluid composition and oxygen fugacity in graphitic metapelites. *Journal of Metamorphic Geology* 11, 379–388.
- García-Casco, A. (2007) Magmatic paragonite in trondhjemitites from the Sierra del Convento mélange, Cuba. *American Mineralogist* 92, 1232–1237.
- González-Jiménez, J.M., Proenza, J.A., Pastor-Oliete, M., Saunders, E., Aiglsperger, T., Pujol-Solà, N., Melgarejo, J.C., Gervilla, F., García-Casco, A. (2020) Precious metals in magmatic Fe-Ni-Cu sulfides from the Potosí chromitite deposit, eastern Cuba. *Ore Geology Reviews* 118, 103339.
- Grozeva, N.G., Klein, F., Seewald, J.S., Sylva, S.P. (2020) Chemical and isotopic analyses of hydrocarbon-bearing fluid inclusions in olivine-rich rocks. *Philosophical transactions. Series A, Mathematical, physical, and engineering sciences* 378, 20180431.
- Holland, T.J.B., Powell, R. (1998). An internally consistent thermodynamic data set for phases of petrological interest. *Journal of Metamorphic Geology* 16, 309–343.
- Holland, T.J.B., Powell, R. (2011) An improved and extended internally consistent thermodynamic dataset for phases of petrological interest, involving a new equation of state for solids. *Journal of Metamorphic Geology* 29, 333–383.
- Iturralde-Vinent, M.A., García-Casco, A., Rojas-Agramonte, Y., Proenza, J.A., Murphy, J.B., Stern, R.J. (2016) The geology of Cuba: A brief overview and synthesis. *GSA Today* 4–10.
- Marchesi, C., Garrido, C.J., Godard, M., Proenza, J.A., Gervilla, F., Blanco-Moreno, J. (2006) Petrogenesis of highly depleted peridotites and gabbroic rocks from the Mayarí-Baracoa Ophiolitic Belt (eastern Cuba). *Contributions to Mineralogy and Petrology* 151, 717–736.
- Pouchou, J.-L., Pichoir, F. (1991) Quantitative Analysis of Homogeneous or Stratified Microvolumes Applying the Model “PAP.” *Electron Probe Quantitation* 31–75.
- Proenza, J., Gervilla, F., Melgarejo, J., Vera, O., Alfonso, P., Fallick, A. (2001) Genesis of sulfide-rich chromite ores by the interaction between chromitite and pegmatitic olivine-norite dikes in the Potosí Mine (Moa-Baracoa ophiolitic massif, Eastern Cuba). *Mineralium Deposita* 36, 658–669.
- Proenza, J., Gervilla, F., Melgarejo, J.C., Bodinier, J.L. (1999) Al- and Cr-rich chromitites from the Mayari-Baracoa ophiolitic belt (Eastern Cuba): Consequence of interaction between volatile-rich melts and peridotites in suprasubduction mantle. *Economic Geology* 94, 547–566.
- Pujol-Solà, N., Proenza, J.A., García-Casco, A., González-Jiménez, J.M., Román-Alpiste, M.J., Garrido, C.J., Melgarejo, J.C., Gervilla, F., Llovet, X. (2020) Fe-Ti-Zr metasomatism in the oceanic mantle due to extreme differentiation of tholeiitic melts (Moa-Baracoa ophiolite, Cuba). *Lithos* 358–359, 105420.



A4. Article 4

Pujol-Solà, N., Domínguez-Carretero, D., Proenza, J.A., Haissen, F., Ikenne, M., González-Jiménez, J.M., Colás, V., Maacha, L., Garcia-Casco, A., 2021. The chromitites of the Neoproterozoic Bou Azzer ophiolite (Central Anti-Atlas, Morocco) revisited. *Ore Geology Reviews*. In press. <https://doi.org/10.1016/j.oregeorev.2021.104166>

Contents lists available at [ScienceDirect](https://www.sciencedirect.com)

Ore Geology Reviews

journal homepage: www.elsevier.com/locate/oregeorev

The chromitites of the Neoproterozoic Bou Azzer ophiolite (central Anti-Atlas, Morocco) revisited

Núria Pujol-Solà^{a,*}, Diego Domínguez-Carretero^a, Joaquín A. Proenza^a, Faouziya Haissen^b, Moha Ikenne^c, José María González-Jiménez^{d,e}, Vanessa Colás^f, Lhou Maacha^g, Antonio Garcia-Casco^{d,e}

^a Departament de Mineralogia, Petrologia i Geologia Aplicada, Facultat de Ciències de la Terra, Universitat de Barcelona, Carrer Martí i Franquès, s/n, 08028 Barcelona, Spain

^b LGAGE, Département de Géologie, Faculté des Sciences Ben M'sik, Université Hassan II, Casablanca, Morocco

^c LAGAGE, Faculty of Sciences, Ibn Zohr University, Agadir, Morocco

^d Departamento de Mineralogía y Petrología, Facultad de Ciencias, Universidad de Granada, Avda. Fuentenueva, s/n, 18071 Granada, Spain

^e Instituto Andaluz de Ciencias de la Tierra (CSIC-UGR), Avda. de las Palmeras 4, E-18100 Armilla, Granada, Spain

^f Instituto de Geología, Universidad Nacional Autónoma de México, Ciudad Universitaria, 04510 Ciudad de México, Mexico

^g MANAGEM Group, 191, bd Mohamed Zerktouni, angle bd., Massira Alkhadra, Twin Center Tour, A-20100 Casablanca, Morocco

ARTICLE INFO

Keywords:

Ophiolitic chromitites
Unusual ("exotic") mineral assemblages
Trace elements
Platinum group minerals (PGM)
Subduction-initiation
Fore-arc basalts (FAB)

ABSTRACT

The Neoproterozoic Bou Azzer ophiolite in the Moroccan Anti-Atlas Panafrican belt hosts numerous chromitite orebodies within the peridotite section of the oceanic mantle. The chromitites are strongly affected by serpentinization and metamorphism, although they still preserve igneous relicts amenable for petrogenetic interpretation. The major, minor and trace element composition of unaltered chromite cores reveal two compositional groups: intermediate-Cr ($Cr\# = 0.60 - 0.74$) and high-Cr ($Cr\# = 0.79 - 0.84$) and estimates of parental melt compositions suggest crystallization from pulses of fore-arc basalts (FAB) and boninitic melts, respectively, that infiltrated the oceanic supra-subduction zone (SSZ) mantle. A platinum group elements (PGE) mineralization dominated by Ir-Ru-Os is recognized in the chromitites, which has its mineralogical expression in abundant inclusions of Os-Ir alloys and coexisting magmatic laurite (RuS_2) and their products of metamorphic alteration. Unusual mineral phases in chromite, not previously reported in this ophiolite, include super-reduced and/or nominally ultra-high pressure minerals moissanite (SiC), native Cu and silicates (oriented clinopyroxene lamellae), but "exotic" zircon and diaspore have also been identified. We interpret that clinopyroxene lamellae have a magmatic origin, whereas super-reduced phases originated during serpentinization processes and diaspore is linked to late circulation of low-silica fluids related to rodingitization. Zircon grains, on the other hand, with apatite and serpentine inclusions, could either have formed after the interaction of chromitite with mantle-derived melts or could represent subducted detrital sediments later incorporated into the chromitites. We offer a comparison of the Bou Azzer chromitites with other Precambrian ophiolitic chromitites worldwide, which are rather scarce in the geological record. The studied chromitites are very similar to the Neoproterozoic chromitites reported in the Arabian-Nubian shield, which are also related to the Panafrican orogeny. Thus, we conclude that the Bou Azzer chromitites formed in a subduction-initiation geodynamic setting with two-stages of evolution, with formation of FAB-derived intermediate-Cr chromitites in the early stage and formation of boninite-derived high-Cr chromitites in the late stage.

* Corresponding author.

E-mail addresses: npujolsola@ub.edu (N. Pujol-Solà), ddominguezcarretero@gmail.com (D. Domínguez-Carretero), japroenza@ub.edu (J.A. Proenza), faouziya.haissen@gmail.com (F. Haissen), m.ikenne@uiz.ac.ma (M. Ikenne), jmgonzj@ugr.es (J.M. González-Jiménez), vcolas86@gmail.com (V. Colás), l.maacha@managemgroup.com (L. Maacha), agcasco@ugr.es (A. Garcia-Casco).

<https://doi.org/10.1016/j.oregeorev.2021.104166>

Received 4 February 2021; Received in revised form 4 April 2021; Accepted 11 April 2021

Available online 20 April 2021

0169-1368/© 2021 Elsevier B.V. All rights reserved.

1. Introduction

The presence of chromitites is one of the characteristics shared by most ophiolites worldwide (Leblanc and Nicolas, 1992 and references therein). These bodies of rocks made almost exclusively by chromite are usually hosted in peridotites that represent the upper mantle section of the ophiolite (e.g., González-Jiménez et al., 2014a; Arai and Miura, 2016). Recent observation of unusual (“exotic”) mineral assemblages (Table 1) typical of continental crust rocks (e.g., Yamamoto et al., 2013; Robinson et al., 2015; González-Jiménez et al., 2015a, 2017a; Proenza et al., 2018) or formed under super-reduced (SuR) conditions either at ultra-high pressure (UHP) or low-pressure (e.g., Bai et al., 1993; Yang et al., 2014, 2015; Griffin et al., 2016; Pujol-Solà et al., 2018, 2020a; Xiong et al., 2019; Farré-de-Pablo et al., 2019a) have been profusely used for the formulation, testing, and establishment of models on the lithosphere-asthenosphere system dynamics (Arai, 2013; Yang et al., 2014, 2015; McGowan et al., 2015; Robinson et al., 2015; Griffin et al., 2016). Far-reaching geodynamic models derived from these findings propose that the ophiolitic mantle—or at least portions of it—experiences UHP conditions prevailing in the Mantle Transition Zone (410–660 km depth) or deeper down to the mantle-core boundary before it returns to the shallow lithospheric oceanic mantle (e.g., Arai, 2013; McGowan et al., 2015; Griffin et al., 2016). However, new works have shown that some SuR/UHP minerals (e.g., moissanite, nano-to-micron-sized diamond, native Si) found in ophiolitic chromitite orebodies form, instead, under super-reduced conditions prevailing in the shallow mantle during ocean-floor metamorphic processes of serpentinization of ultramafic/mafic rocks at low pressure and low temperature (Pujol-Solà et al., 2018, 2020a; Farré-de-Pablo et al., 2019a, 2019b). Besides, the identification of continental-derived zircons in some ophiolitic chromitites and associated gabbros has been used as a tool to track the recycling and transport of continental material through the mantle wedge above subduction zones (Rojas-Agramonte et al., 2016; González-Jiménez et al., 2017a; Proenza et al., 2018).

Most of the recent advances in these issues come from the study of the well-exposed Phanerozoic examples (e.g., González-Jiménez et al., 2014a; Yang et al., 2015; Robinson et al., 2015; Griffin et al., 2016; Proenza et al., 2018). However, there is still great uncertainty and limited information regarding the less-abundant Archaean and Proterozoic chromitite-bearing ophiolites. To date, the oldest known chromitite-bearing ophiolites are located in China (the 2.5 Ga old Zunhua and Dongwanzi ophiolites; Kusky et al., 2004a, 2004b) and in Brazil (the 2.1 Ga old Santa Luz ophiolite; Oliveira et al., 2007). Examples of relatively well-studied Proterozoic chromitite-bearing ophiolites include those from Outokumpu-Jormua in Finland (1.95 Ga; Peltonen et al., 2008) and from the Arabian-Nubian shield in Saudi Arabia and Egypt (0.87 Ga - Pallister et al., 1988; and 0.75 Ga - Ali et al., 2010, respectively). The study of preserved Precambrian ophiolitic chromitites is significant to understand the chemical evolution of the oceanic mantle (e.g., Arai and Ahmed, 2018).

The Neoproterozoic (759 and 697 Ma; El Hadi et al., 2010; Hodel et al., 2020) Bou Azzer ophiolitic sequence, located in the Panafrikan Anti-Atlas belt (Morocco) associated with a long-lived oceanic-arc (760–640 Ma, Triantafyllou et al., 2020 and references therein), has been extensively studied since the 1970s (i.e. Leblanc, 1972, 1975, 1981; Bodinier et al., 1984; Saquaque et al., 1989). The Bou Azzer peridotites host chromitite orebodies that have been the focus of detailed studies (Ikenne et al., 2005; El Ghorfi et al., 2007; Ahmed et al., 2009). The general assumption is that these chromitites and their hosting mantle peridotites formed in a suprasubduction zone (SSZ) setting (Bodinier et al., 1984; Naidoo et al., 1991; Ikenne et al., 2005; Ahmed et al., 2009; Walsh et al., 2012; Hefferan et al., 2014; Arenas et al., 2020; Hodel et al., 2020), although the precise location of their formation within the arc environment, fore-arc (e.g., Saquaque et al., 1989; Naidoo et al., 1991; Ahmed et al., 2005; El Hadi et al., 2010; Walsh et al., 2012; Arenas et al., 2020) vs. back-arc position (e.g., Bodinier et al., 1984;

Triantafyllou et al., 2018; Hodel et al., 2020) is still debated. Recently, Arenas et al. (2020) identified MORB-like and boninitic compositions within the mafic rocks of the Bou Azzer crustal sequence, and interpreted that the ophiolite formed in a subduction-initiation geodynamic setting, where magmas evolve from MORB-like (FAB) to boninite-like as subduction proceeds (Whattam and Stern, 2011).

This paper aims to propose a genetic model for the Bou Azzer chromitites in the context of the complex evolution of their host ophiolite with new petrographic, mineralogical and geochemical data combined with previous knowledge. We provide the first-ever trace element data for chromite forming these chromitites as well as a detailed characterization of mineral phases within chromitite not previously reported, including PGM, minerals of the SuR-nominally UHP association such as moissanite (SiC), native Cu and silicates (oriented clinopyroxene lamellae), and exotic minerals such as zircon and diaspore. Furthermore, we compare the Bou Azzer chromitites with other published data of Precambrian ophiolitic chromitites worldwide.

2. Geological setting

2.1. The Bou Azzer ophiolite

The Bou Azzer ophiolite is located in the central part of the Panafrikan Anti-Atlas belt of Morocco (Fig. 1a). The ophiolitic rocks crop out in the core of a NW-SE directed recumbent antiform (Fig. 1a), affected by later folds and disturbed by thrusts and faults (El Hadi et al., 2010). Even though the ophiolite sequence is highly dismembered, the original description of the ophiolite (Leblanc, 1972, 1975, 1981) exhibits a 4–5 km sequence and comprises from bottom to top: pervasively serpentinized upper mantle peridotites (~2000 m) cross-cut by mafic dikes (Fig. 1b), a sequence of layered gabbros (~500 m) and pillow lavas (~500 m) intruded by a quartz-diorite stock overlain by a thick, Ediacaran to Cambrian volcano-sedimentary sequence (~1500 m) including the syn-orogenic Tiddline clastic Formation (Leblanc, 1972, 1975, 1981; Bodinier et al., 1984; Hefferan et al., 1992; Thomas et al., 2004; Gasquet et al., 2005; Ahmed et al., 2005; Gahlan et al., 2006; El Hadi et al., 2010).

The age of the ophiolite is still controversial; SHRIMP U-Pb zircon dating yielded 697 ± 6 Ma in a metagabbro located in the Boumane complex (El Hadi et al., 2010) and LA-ICP-MS U-Pb zircon dating yielded 759 ± 2 Ma in a layered metagabbro from the crustal section at Ait Ahmane (Hodel et al., 2020). These differences suggest that the younger age obtained by El Hadi et al. (2010) may correspond to the volcanic arc stage (Triantafyllou et al., 2018, 2020; Hodel et al., 2020) or may be indicative of a long-lived construction of the oceanic lithosphere. The ophiolitic sequence is intruded by two groups of arc-related granitoids: 1) syn-orogenic granitoids emplaced during arc-continent collision (632–659 Ma; El Hadi et al., 2010; Inglis et al., 2005); 2) Late-orogenic granitoids represented by the Bleida granodiorite dated at 579 Ma (Inglis et al., 2004). Low- to medium-grade metamorphic assemblages overprint the Bou Azzer ophiolite (Leblanc, 1981; Saquaque et al., 1989; Hefferan et al., 2000; El Hadi et al., 2010).

The ophiolitic bodies in the region are interpreted as the suture of the Panafrikan orogen (Leblanc, 1972, 1976, 1981; Leblanc and Lancelot, 1980; Saquaque et al., 1989; Hefferan et al., 2002; Soulimani et al., 2006; Bousquet et al., 2008; El Hadi et al., 2010). According to Walsh et al. (2012), the Panafrikan cycle started with a northward-dipping subduction (ca. 760 Ma), triggering the formation of oceanic lithosphere and a volcanic arc. The consumption of oceanic lithosphere triggered the collision of the volcanic arc with Gondwana at 660–600 Ma (Villeneuve and Cornée, 1994; Thomas et al., 2002; Gasquet et al., 2005, 2008) and the obduction of the ophiolitic sequence onto the margin of Gondwana (Michard et al., 2010; Walsh et al., 2012; Hefferan et al., 2014). During the Variscan orogeny (Late Paleozoic), the region was deformed and the Anti-Atlas Mountain Belt formed, triggering the exhumation of these Precambrian rocks (also known as inliers) (e.g.,

Table 1

Occurrence of ultra-high pressure (UHP), super-reduced (SuR) and crustal-derived unusual phases in ophiolites and chromitites worldwide. Luobusa (Tibet), Dingqing (Tibet) and Ray-Iz (Polar Urals) data are from Yang et al. (2015), Griffin et al. (2016), Xiong et al. (2017a) and references therein, Purang (Tibet) from Yang et al. (2017a) and (Xiong et al., 2019), Zedang (Tibet) from Xiong et al. (2017b), Hegenshan (Inner Mongolia) from Huang et al. (2016), Nidar (Ladakh, Himalaya) from Das et al. (2017), Myitkyina (Myanmar) from Chen et al. (2018), Alapaevsk (Russia) from Zaccarini et al. (2016), Semall (Oman) from Mitura et al. (2012) and Robinson et al. (2015), Mirdita (Albania) from Xiong et al. (2017c), Ponzati-Karsanti (Turkey) from Akbulut (2018), Othyrus (Greece) from Zaccarini et al. (2019) and Bindi et al. (2020), Baja California (Mexico) from González-Jiménez et al. (2017a), Tehuitzingo (Mexico) from Farré-de-Pablo et al. (2019a), Moa-Baracoa (Cuba) from Rojas-Agramonte et al. (2016), Proenza et al. (2018) and Pujol-Solà et al. (2018), (Pujol-Solà et al., 2020a), and Bou Azzer data from the present study. Host rock abbreviations: Chrom – chromitite, Harz – harzburgite, Dun – dunite, Lherz - lherzölitite. X - indicates the presence of the mineral in the ophiolite.

Host rock	Luobusa (Tibet)	Dingqing (Tibet)	Purang (Tibet)	Zedang (Tibet)	Hegenshan (Inner Mongolia)	Nidar (Ladakh, Himalaya)	Myitkyina (Myanmar)	Ray-Iz (Polar Urals)	Alapaevsk (central Urals, Russia)	Semall (Oman)	Mirdita (Albania)	Pozanti-Karsanti (Turkey)	Othaneli-Harmancik (Turkey)	Othyrus (Greece)	Beja California (Mexico)	Tehuitzingo (Mexico)	Moa-Baracoa (Cuba)	Bou Azzer (Morocco)
Diamond	X	X	X	X	X	X	X	X	X	X	X	X	X	X	X	X	X	X
Coesite/ Stishovite pseudomorph	X							X										
TiO ₂ -II (α-PbO ₂ structure)	X																	
Cubic-BN	X																	
Si-rutile	X																	
BWJ (inverse-spinel structure)	X																	
CF-chromite	X		X	X	X			X	X	X	X	X	X	X	X	X	X	X
Clinopyroxene exsolution lamellae	X					X		X								X	X	
Amorphous carbon																		
Moissanite (SiC)	X		X		X		X	X	X	X	X	X					X	X
Fe-carbide (FeC)	X							X	X									
W-carbide (WC)	X							X	X									
Ti-carbide (TiC)	X							X	X									
Fe-silicide (FeSi)	X							X	X									
Ti-nitride (TiN)	X							X	X									
TAZ (Ti ₄ Al ₂ Zr ₂ SiO ₁₁)	X							X	X									
Native Si	X							X	X									
Native Ni, Co, Cr, Cu	X							X	X									
Iron-Wustite (Fe-FeO)	X							X	X									
Alloys (Fe-Mn, Fe-Co)	X							X	X									
Phosphides									X					X				
Almandine	X	X						X	X									
Andalusite	X	X						X	X									
Biotite	X	X						X	X									
Corundum	X	X						X	X									
K-feldspar	X	X						X	X									
Kyanite	X	X						X	X									
Muscovite	X	X						X	X									
Quartz	X	X						X	X									
Rutile	X	X					X	X	X									
Titanite	X	X					X	X	X									
Zircon	X	X					X	X	X						X			

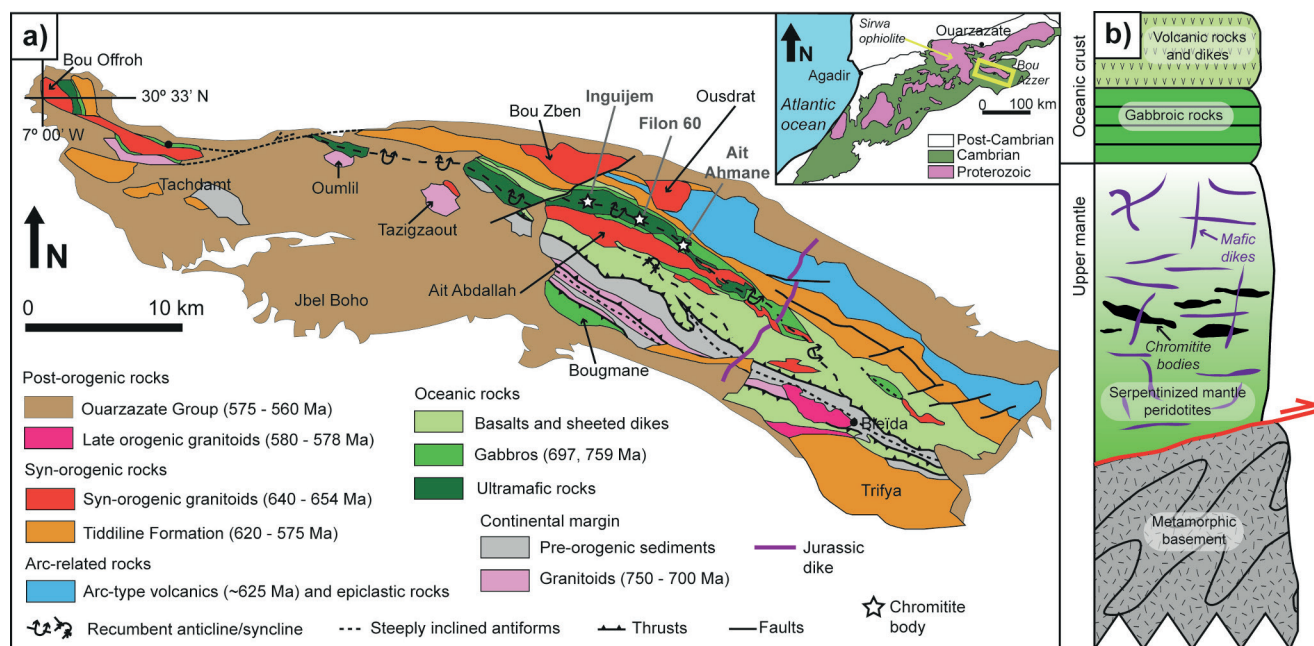


Fig. 1. (a) Generalized geologic-tectonic map of the Bou Azzer inlier showing the location of the chromitite orebodies (modified from El Hadi et al., 2010; Soulaïmani et al., 2018). The inset in the upper right corner (modified from Soulaïmani et al., 2018) shows the location of the Bou Azzer and Sirwa ophiolites within the Panafrican Anti-Atlas belt. (b) Schematic column of the Bou Azzer ophiolite showing the location of the chromitite orebodies.

Thomas et al., 2002; Walsh et al., 2002, 2012).

2.2. Chromite deposits

The Bou Azzer chromitite orebodies are hosted in pervasively serpentinized harzburgitic mantle peridotites (Fig. 1a; Ikenne et al., 2005; El Ghorfi et al., 2007; Ahmed et al., 2009). The bodies display elongated irregular shapes from almost tabular to lenticular, with sizes ranging from several cm to few tens of meters, with average length of 3–4 m and they are concordant to sub-concordant to the mantellic foliation of the host peridotite (Ahmed et al., 2009). Chromitites predominantly consist of massive-textured ore, and semi-massive and banded ore to a lesser extent (Figs. 2 and 3) and are usually enveloped by completely serpentinized dunite of variable thickness (El Ghorfi et al., 2007). Massive chromitites (Figs. 2a-c and 3a-b) are almost totally formed by chromite (>90 vol%) with minor interstitial altered silicate matrix, semi-massive chromitite ores (Figs. 2e and 3c-d) contain 70–80 vol% chromite crystals embedded in an altered silicate matrix (Fig. 3d) and banded chromitites (Fig. 2d-f) are characterized by alternating chromite-rich layers with massive (Fig. 2f) to semi-massive (Fig. 2e) textures and serpentine-rich layers. The silicate matrix is formed by secondary minerals, mainly chlorite and serpentine, but also talc, magnetite and carbonates in veins (Ahmed et al., 2009). Chromite crystals in the different textured chromitites show rare inclusions of olivine, usually serpentinized, clinopyroxene (Cr-diopside), calcic amphibole (chromian edenite), and Cr- and Fe³⁺-garnet (uvarovite-andradite) (El Ghorfi et al., 2007). The chromitite orebodies are crosscut by centimetric veins of massive magnetite (Gahlan et al., 2006; Ahmed et al., 2009), suggesting leaching by a Cl-rich hydrothermal event at temperatures below 350 °C during formation of these late veins (Hodel et al., 2017).

3. Studied samples and analytical techniques

We studied representative samples from three chromitite mining sites in the Bou Azzer ophiolite: Inguijem, Filon 60 and Ait Ahmane (Figs. 1 and 2), including massive chromitites from individual pods (n = 4), semi-massive chromitites (n = 2), banded chromitites (n = 1) and the host dunites. Polished thin sections were studied by optical and electron

microscopy using a Quanta 200 FEI XTE 325/D8395 scanning electron microscope (SEM) equipped with an INCA Energy 250 EDS microanalysis system and a JEOL JSM-7100 field-emission SEM at the Centres Científics i Tecnològics de la Universitat de Barcelona (CCiTUB). Operating conditions were 20 kV accelerating voltage. Micro-Raman spectra were obtained with a HORIBA JobinYvon LabRam HR 800 dispersive spectrometer equipped with an Olympus BXM optical microscope at the CCiTUB. Non polarized Raman spectra were obtained in confocal geometry by applying a 532 nm laser, using a 100x objective (beam size around 2 μm), with 3–5 measurement repetitions for 10–15 s each. The Si band at ~520 cm⁻¹ was used for calibration. The obtained spectra were processed using the LabSpec® software (JobinYvon; Villeneuve-d'Ascq, France).

Quantitative electron microprobe analyses (EMPA) on chromite and platinum group minerals (PGM) were also conducted at the CCiTUB using a JEOL JXA-8230 operating in wavelength-dispersive spectrometry (WDS) mode. Analytical conditions are described in detail in Appendix 1. X-ray (XR) images of chromite (512 × 512 pixels, 0.52 × 0.52 μm pixel size and 266.24 × 266.24 μm total area) and platinum group minerals (three images of 300 × 300 pixels: 0.22 μm pixel size and 66 × 66 μm total area, 0.08 μm pixel size and 24 × 24 μm total area and 0.1 μm pixel size and 30 × 30 μm total area) were obtained with the same a JEOL JXA-8230 electron microprobe operated at 20 kV and 20 nA in spot mode with focused electron beam and counting time of 20 to 60 ms/pixel. The images were treated with DWImager software (Torres-Roldán & Garcia Casco, unpublished; see Garcia-Casco, 2007). Minor and trace elements in chromite were analyzed using a Resolution M-50 Excimer laser coupled to a ThermoCap Qc inductively coupled mass spectrometer at the Laboratorio de Estudios Isotópicos (LEI) from the Centro de Geociencias, UNAM (Mexico). The analytical conditions and procedure are described in Appendix 1.

A representative sample (m = 4.2 kg) of massive chromitite from the Inguijem deposit was crushed, sieved and processed using hydro-separation (HS Lab, Universitat de Barcelona; <http://www.hslab-barcelona.com/>) to obtain mineral concentrates. The resulting concentrates were mounted as polished monolayers on resin blocks (SimpliMet 1000) in order to identify mineral phases. Whole-rock platinum-group elements (PGE) analyses were performed on 8 chromitite and 5 dunite

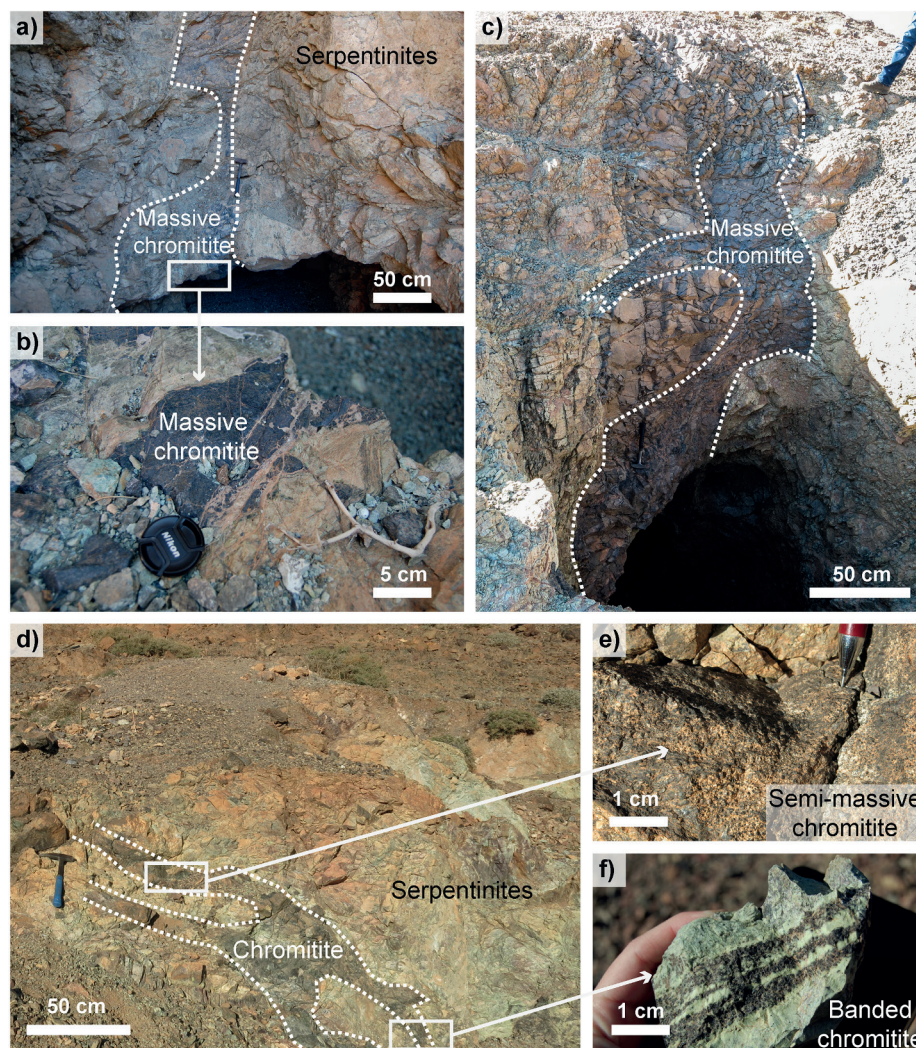


Fig. 2. Outcrops showing the studied chromitite orebodies. (a) Massive chromitite body in Inguijem. (b) Close up of the massive chromitite in Inguijem. (c) Massive chromitite body from Filon 60. (d) Banded chromitites in Ait Ahmane. (e) Close up of disseminated chromitite in the rims of the massive-banded chromitite bodies of (d). (f) Close up of banded chromitite shown in (d).

samples at Genalysis Ltd (Perth, Western Australia) after nickel sulfide fire assay collection, following the method described by Chan and Finch (2001). The analytical procedure is described in detail in Appendix 1.

4. Results

4.1. Petrography and mineralogy of chromitites

The chromitites from Bou Azzer consist of chromite in an altered silicate matrix, variations in the relative proportions between chromite and the matrix result in the different observed textures (Fig. 3). The Inguijem orebody only contains massive chromitites, whereas Filon 60 is formed by massive chromitites and semi-massive chromitites. Banded chromitites were only observed in Ait Ahmane, where the chromite-rich layers show either massive or semi-massive textures; hence, these samples have been grouped and are described with the two main types.

Massive chromitites (Fig. 3a-b) are formed by coarse-grained (>500 μm) anhedral chromite that shows reddish to black color, pervasive pull-apart fractures (Fig. 3b) and occasional brecciated textures. The chromite grains are generally unaltered (Fig. 4a-d), with limited alteration in the porous rims (brighter phase under the scanning microscope; Fig. 4b) and along fractures that are occasionally filled by late hematite (Fig. 4b). Chromite grains from the Inguijem chromitite orebody (Fig. 4a-b) and

from Ait Ahmane are more altered than in Filon 60 (Fig. 4c-d), where alteration is restricted to very narrow rims (Fig. 4c) and along fractures (Fig. 4d) although some samples show strong brecciation (Fig. 4c).

Semi-massive chromitites (Fig. 3c-d) are formed by subhedral to anhedral chromite crystals (~500 μm) that are slightly to strongly fractured. Darker unaltered cores under the scanning microscope are generally surrounded by altered brighter rims (Fig. 4e-f) and the alteration is also evident along fractures. Just as observed in massive chromitites, the alteration is less strong in the semi-massive chromitites from Filon 60 (Fig. 4g-h), where it is very restricted along fractures (Fig. 4g) and occasionally in the rims (Fig. 4h), compared to Ait Ahmane (Fig. 4e-f). Nevertheless, the degree of alteration is higher in semi-massive chromitites (Fig. 4e-h) than in massive varieties (Fig. 4a-d).

A large variety of globular, elongated to lamellae-like inclusions and negative crystals, with sizes ranging from few micrometers to 60 μm with average sizes around 10 μm , have been observed in chromite crystals both from massive and semi-massive chromitites. These contain mainly serpentinized olivine, sulfides (*in situ* pyrite and sphalerite; galena and arsenopyrite in mineral concentrates) and platinum group minerals (PGM) in chromite; and andradite, millerite and a Pb-Ni-S phase in the altered silicate matrix. Appendix 2 contains the list of accessory minerals identified both *in situ* and in mineral concentrates.

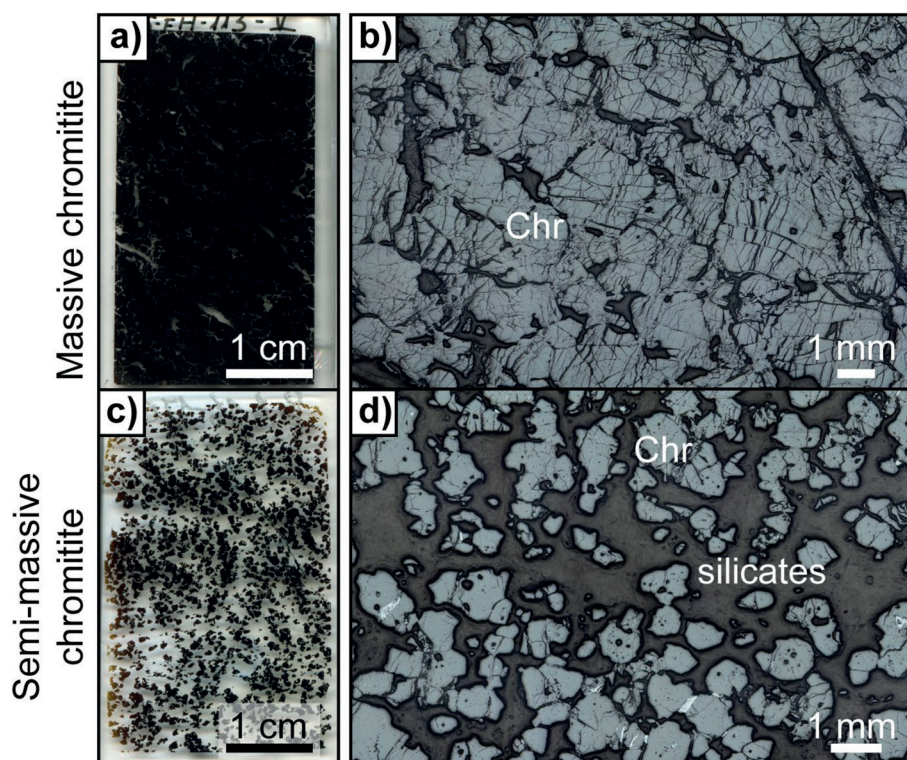


Fig. 3. Textures of chromitites. (a) Thin section of massive chromitite. (b) Reflected light microphotograph of massive chromitite showing pervasive pull-apart fractures and a matrix formed by altered silicates. (c) Thin section of semi-massive chromitite. (d) Reflected light microphotograph of semi-massive chromitite. The matrix is made of silicates, mostly chlorite and serpentine. Abbreviation: Chr – chromite.

4.1.1. Platinum-group minerals

Up to 11 different PGM grains have been distinguished *in situ* in thin sections or recovered in the mineral concentrates. The grain sizes range from a few to several tens of micrometers (Fig. 5). Laurite (RuS₂) (Fig. 5a-b) and Os-Ir alloys (Fig. 5c-e) are the most abundant phases, followed by a highly heterogeneous Ir-As-S phase, probably irarsite (Fig. 5f). PGM grains show euhedral (Fig. 5a), subhedral (Fig. 5c-f) to anhedral shapes (Fig. 5b) and some grains show partial replacement by secondary PGM (Fig. 5b, e), which can either occur at the rims (Fig. 5e) or within the crystal forming nano-blebs of PGE alloys (Fig. 5b). Furthermore, PGM also occur intergrown with alteration minerals such as chlorite (Fig. 5f).

4.1.2. Unusual mineral assemblages

Less common mineral phases found as inclusions within chromite grains consist of submicrometric clinopyroxene lamellae (up to 22 μm long and <1 μm wide) variably distributed following the (111) crystallographic planes of the unaltered chromite cores (Fig. 6a-c). Raman analyses (Fig. 6c) show spectra compatible with diopside after subtracting the chromite signal, with peaks at 328, 394, 563, 669, 1012 and 1045 cm⁻¹. Diaspore was found associated with hematite and clinocllore in inclusions within chromite (Fig. 6d-e). Diaspore and hematite have been identified by Raman spectroscopy (Fig. 6f) with characteristic peaks at 153, 329 and 448 cm⁻¹, and 226, 293, 410, 500, and 662 cm⁻¹, respectively. This type of inclusions, with sizes between <1 μm and 15 μm, are arranged along trails that can be followed across different grains and are distributed heterogeneously (Fig. 6d, g-h), with clinocllore present in most of them (Fig. 6h). The same types of inclusions were identified in chromitites from the three studied deposits, Inguijem, Filon 60 and Ait Ahmane.

Other unusual mineral phases have been identified in mineral concentrates obtained by hydroseparation. These include super-reduced minerals (Fig. 6i-k), zircon (Fig. 6l-m) and diaspore (Fig. 6n). The

moissanite grain of Fig. 6i (~30 μm) was identified with Raman spectroscopy and shows the typical peaks at 150, 768, 789, and 965 cm⁻¹ (Fig. 6j). Anhedral grains of native Cu, occasionally including chromite, were also recovered (Fig. 6k). Euhedral to subhedral grains of zircon (n = 6) with sizes between 20 and 50 μm, too small for *in situ* dating, have apatite (Fig. 6l) and serpentine inclusions (Fig. 6m). Other inclusions typically found in zircon grains recovered from chromitites, such as quartz, K-feldspar and mica (e.g., Robinson et al., 2015; Proenza et al., 2018), have not been identified in the studied grains. Diaspore was found both *in situ* and in the mineral concentrates (Fig. 6n).

4.2. Chromite composition

Unaltered chromite cores from the Bou Azzer chromitites have Cr₂O₃ contents ranging from 46.6 to 63.9 wt%, Al₂O₃ from 7.8 to 21.5 wt% and MgO from 9.4 to 18.1 wt% (Fig. 7a; Appendix 3). The Cr# [Cr/(Cr + Al) atomic ratio] is strongly variable, from 0.60 to 0.83, and the Mg# [Mg/(Mg + Fe²⁺) atomic ratio] ranges from 0.60 to 0.84 (Fig. 7b). According to the chemistry, unaltered chromite can be divided in two groups: intermediate-Cr chromite (Cr# = 0.60–0.74 and Mg# = 0.61–0.82; sampled from Inguijem and Ait Ahmane deposits) and high-Cr chromite (Cr# = 0.79–0.84 and Mg# = 0.48–0.66; sampled from Filon 60 deposit; Figs. 1 and 2). The grouping of unaltered chromite into intermediate-Cr (Cr# = 0.6–0.75) and high-Cr (Cr# > 0.75) chromite (Fig. 7) better fits with the classification proposed by Liu et al. (2019) for chromitites into three categories: high-Cr, intermediate and high-Al (e.g., Uysal et al., 2016, 2018; Chen et al., 2018; Liu et al., 2019) than with the custom classification into high-Cr (Cr# > 0.6) and high-Al (Cr# < 0.6) (e.g., Arai, 1994; Arai and Miura, 2016).

Altered chromite rims (Fig. 8; Appendices 3 and 4) show higher Cr and Fe²⁺ but lower Al and Mg, than unaltered chromite cores, generally progressing towards Cr-rich chromite. Altered chromite, derived from both intermediate-Cr and high-Cr chromite, reach Cr₂O₃ contents of 70

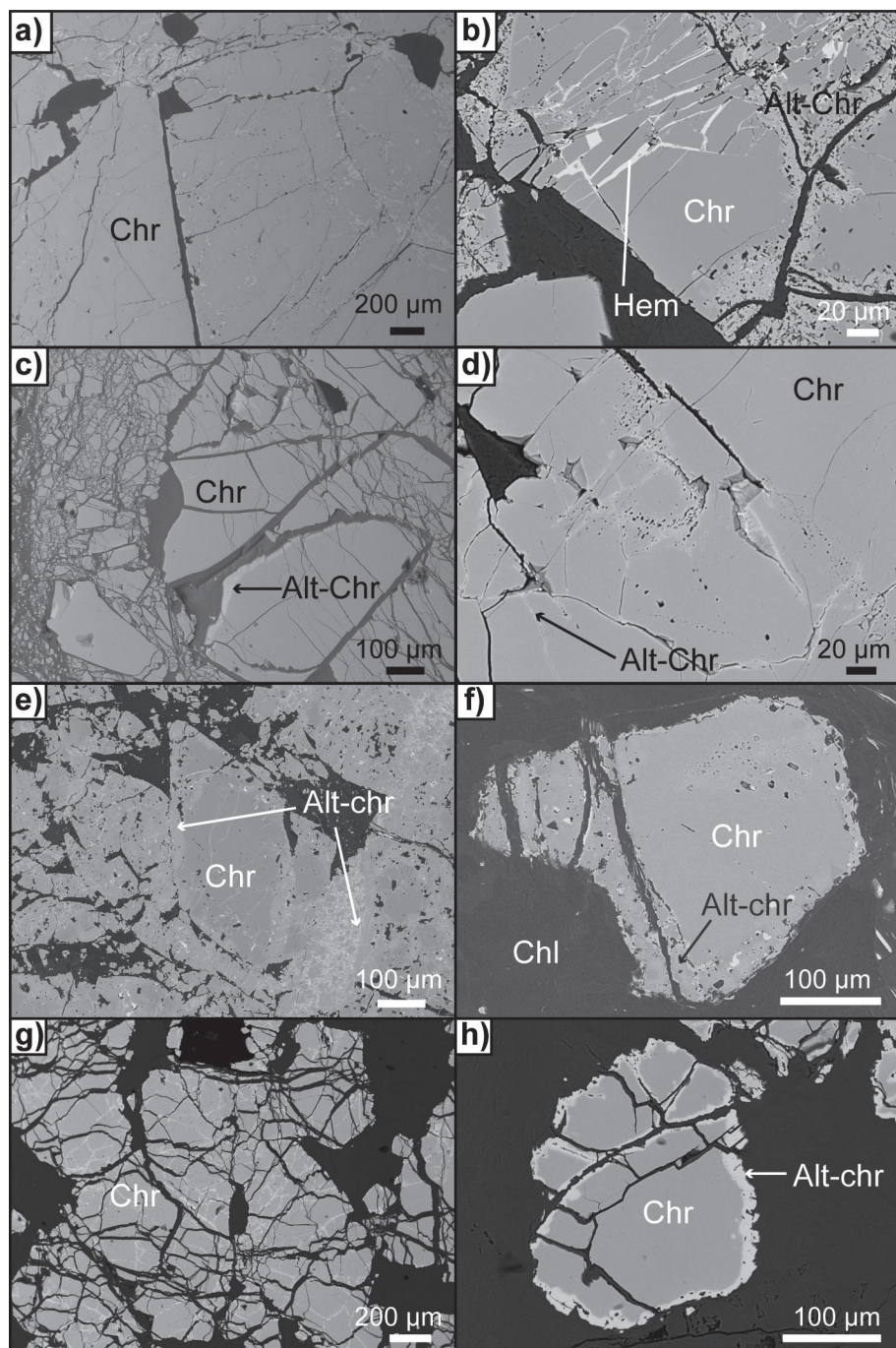


Fig. 4. Backscattered electron images of chromitites. (a) Unaltered massive chromitite from the Inguijem deposit. (b) Chromite with alteration rims and fractures filled by late hematite veins (massive chromitite from Inguijem). (c) Massive chromitite from Filon 60. Large unaltered chromite grains with thin altered rims in the center in contact with a brecciated area in the left part. (d) Chromite from Filon 60 showing alteration along fractures (brighter phase). (e) Chromite grains from Ait Ahmane semi-massive chromitites showing thick rims of altered chromite. (f) Semi-massive chromitite from Ait Ahmane showing alteration rims. (g) Strongly fractured semi-massive chromitite from Filon 60. The chromite grains show alteration along fractures. (h) Single chromite grain from the Ait Ahmane semi-massive chromitites showing alteration along fractures and rims. Abbreviations: Chr – chromite, Alt-Chr – altered chromite, Chl – chlorite, and Hem – hematite.

wt%. The $Fe^{3+}\#$ [$Fe^{3+}/(Fe^{2+}+Fe^{3+})$ atomic ratio] in the altered porous chromite rims (Appendix 3) remains similar to that of unaltered chromite (Fig. 8), except in semi-massive chromitite samples in which ferrian chromite [$Fe^{2+}(Fe^{3+},Cr)_2O_4$] developed. Two clear alteration trends can be observed (Fig. 8): first an increase in Cr followed by an increase in Fe^{3+} . The analyzed hematite is relatively enriched in Cr_2O_3 (up to 7 wt %; Appendix 3) and represents the final product of alteration.

Minor and trace element compositions of unaltered chromite cores (Fig. 9; Appendix 5) shows low Sc (1–5 ppm) and Ga (18–42 ppm) contents, moderate concentrations of Ti (209–370 ppm) and Co (192–347 ppm), and higher Zn (407–1028 ppm), Ni (565–1425 ppm), V (662–1161 ppm), and Mn (1020–5128 ppm) contents. The Ti and Co contents (Fig. 9) are within the same range for both intermediate-Cr and high-Cr chromite; however, it is remarkable that high-Cr chromite

shows lower contents of Ga, V and Ni and higher contents of Mn and Sc compared to intermediate-Cr chromite. Similar relationships were already observed in ophiolitic chromitites showing different compositions in terms of Cr# from Cuba and Dominican Republic by Proenza et al. (2011). The altered chromite rims (Appendix 5) exhibit enrichment (at ppm levels) of Ni, V, Zn, and Mn, which is typically observed in chromitites elsewhere (e.g., Colás et al., 2019 and references therein).

4.3. Platinum group elements (PGE) in the Bou Azzer chromitites

4.3.1. Bulk-rock contents of PGE

Bulk-rock PGE contents in chromitites are between 116 and 313 ppb (Appendix 6), being the IPGE (Ir-Os-Ru: 94–265 ppb) more abundant than PPGE (Pd-Pt-Rh: 11–48 ppb). Chondrite-normalized patterns

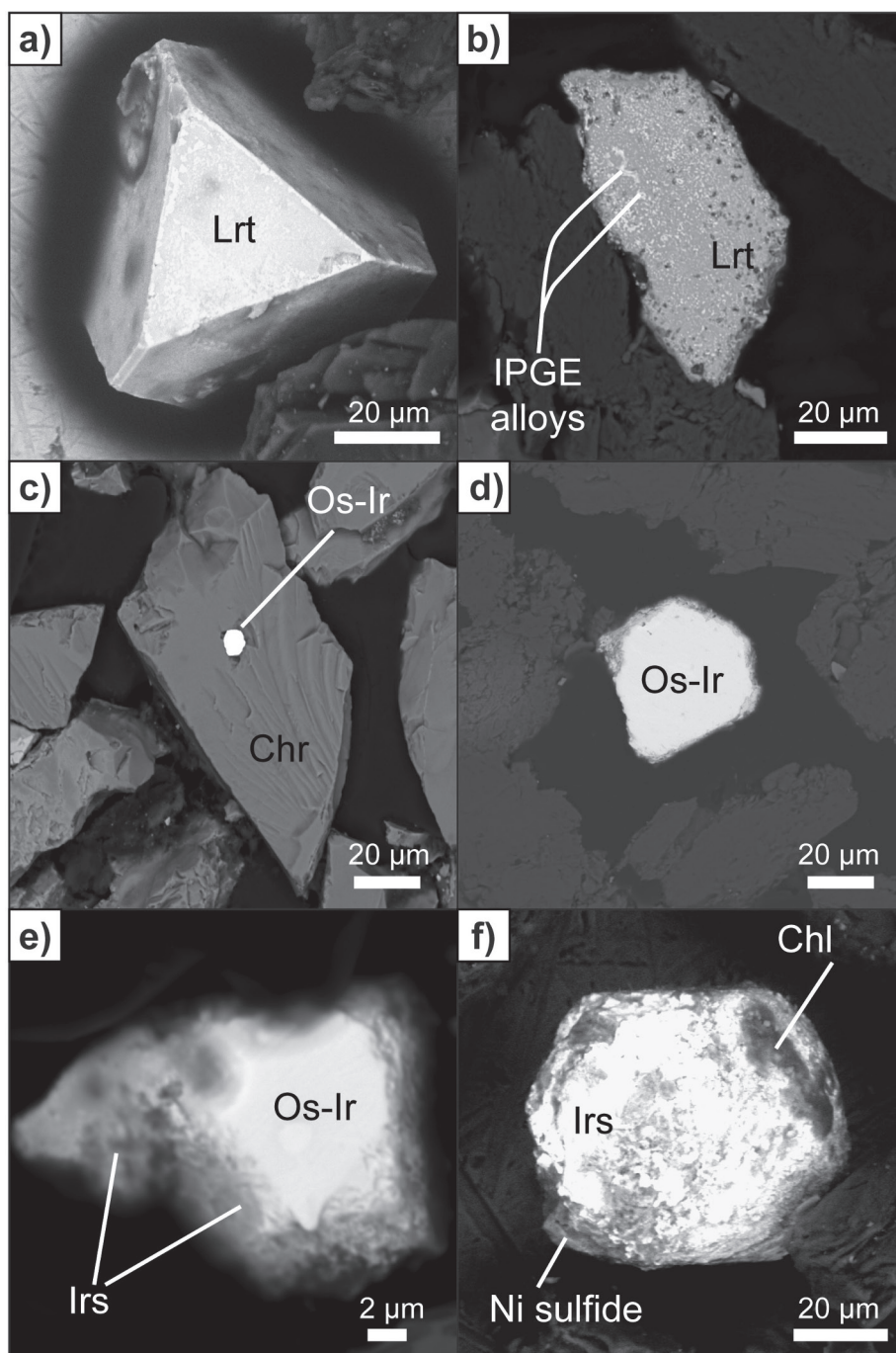


Fig. 5. Backscattered electron images of representative platinum group minerals (PGM) in the Bou Azzer chromitites. (a) Euhedral laurite grain. (b) Laurite grain partially replaced by IPGE nano-blebs. (c) Euhedral Os-Ir alloy grain hosted in chromite. (d) Os-Ir alloy. (e) Os-Ir alloy with a rim of secondary irarsite. (f) Irarsite grain intergrown with chlorite and a Ni-sulfide. Abbreviations: Chr – chromite, Lrt – laurite, Irs – irarsite, and Chl – chlorite.

(Fig. 10a) show a positive slope to flat line from Os to Ru and a negative slope from Ru to Pd. In addition, four samples show a negative anomaly in Pt (Fig. 10a). These results compare well with previous data from the Bou Azzer chromitites (El Ghorfi et al., 2007; Ahmed et al., 2009). PGE contents in the host dunites are low (Σ PGE = 3–30 ppb; Appendix 6), especially compared with previous results by Ahmed et al. (2009), who reported PGE values in the Bou Azzer host-rocks of chromitites ranging from 22 to 60 ppb. In general, the Bou Azzer dunites hosting the chromitites show a positive slope from Os to Ru and a negative slope from Ru to Pd (Fig. 10b), but they do not show preferential enrichment in IPGE nor PPGE.

4.3.2. Platinum group minerals (PGM) composition

Four grains of alloys from the Bou Azzer chromitites were analyzed by electron microprobe (Appendix 7) and classify mostly as native Os with relevant concentration of Ir (Fig. 11a). The average composition is between $\text{Os}_{0.70}\text{Ir}_{0.23}\text{Ru}_{0.05}\text{Pt}_{0.02}$ and $\text{Os}_{0.44}\text{Ir}_{0.39}\text{Ru}_{0.17}$. The chemical composition of magmatic laurite is very close to the laurite end-member composition (RuS_2 ; Fig. 11b), containing low amounts of Os and Ir in solid solution, up to 6.70 and 3.18 wt%, respectively (Appendix 7). Laurite shows low PPGE contents, up to 1.16 wt% Rh, 0.43 wt% Pd and 0.51 wt% Pt. The composition ranges from $(\text{Ru}_{0.98}\text{Ir}_{0.02}\text{Os}_{0.02}\text{Rh}_{0.01})_{\Sigma=1.03}\text{S}_{1.96}$ to $(\text{Ru}_{0.88}\text{Os}_{0.06}\text{Ir}_{0.03}\text{Rh}_{0.02})_{\Sigma=0.99}\text{S}_{2.03}$ ($n = 15$; Appendix 7). X-ray maps of a single magmatic idiomorphic laurite grain (Appendix 8a) show

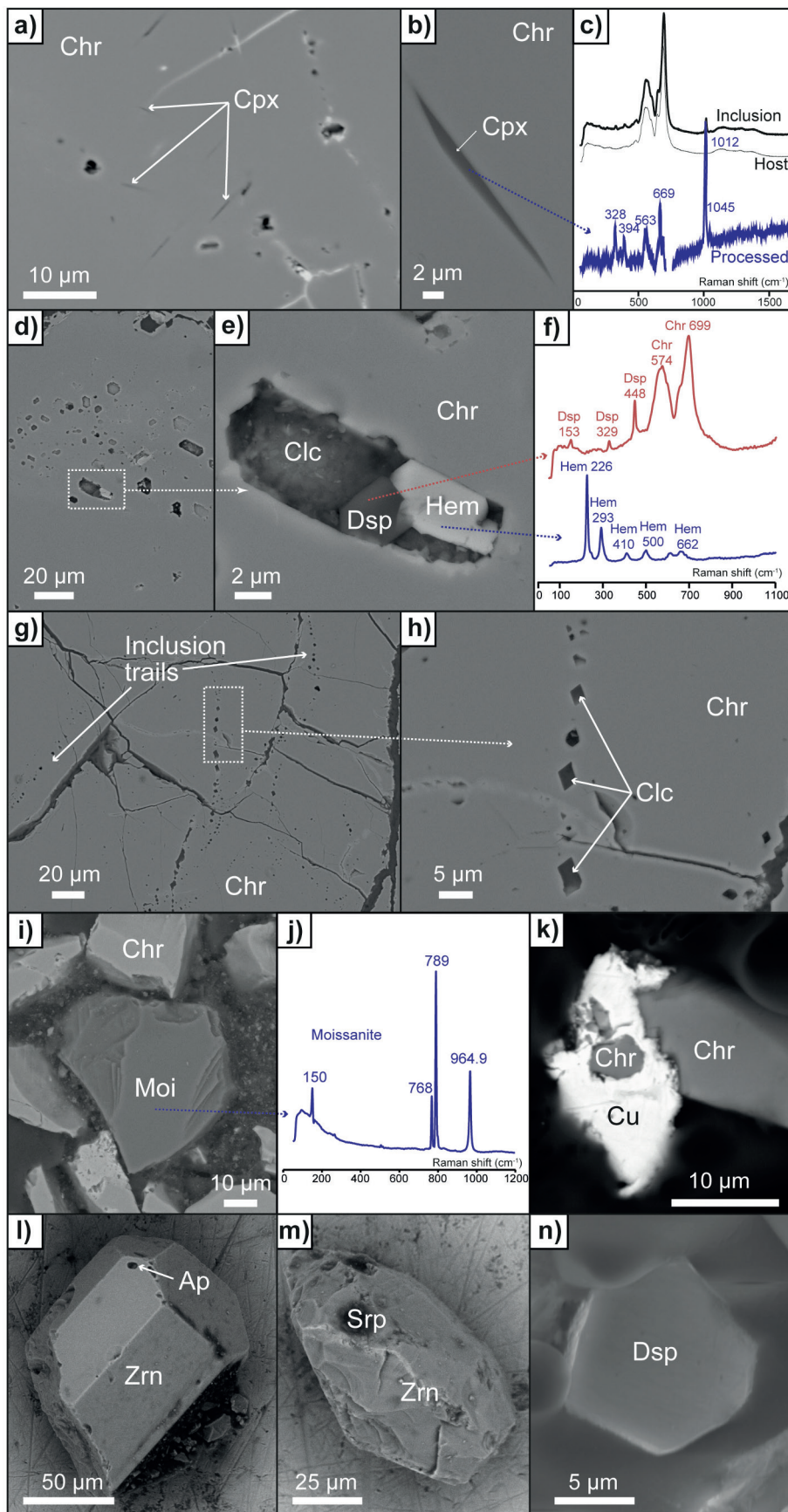


Fig. 6. Unusual mineral phases identified in the Bou Azzer chromitites. (a) Oriented clinopyroxene lamellae hosted within chromite (backscattered electron image). (b) Close up of a clinopyroxene lamellae (backscattered electron image). (c) Raman spectra of (from top to bottom) clinopyroxene inclusion within chromite, chromite host and the processed spectra that corresponds to diopside. (d) Mineral inclusions within a chromite grain (backscattered electron image). (e) Close up of one inclusion in (d) that hosts clinocllore, diaspore and hematite (backscattered electron image). (f) Raman spectra of the different minerals in the inclusion in (e) showing the typical spectra of diaspore and hematite. (g) Inclusion trails in chromitite (backscattered electron image). (h) Close up of (g) showing in detail one of the inclusion trails filled by clinocllore (backscattered electron image). (i) Moissanite grain within a mineral concentrate obtained by hydroseparation (backscattered electron image). (j) Raman spectrum of the moissanite grain. (k) Native Cu attached to chromite (backscattered electron image). (l) Subhedral zircon grain with an apatite inclusion (backscattered electron image). (m) Anhedral zircon grain with a serpentine inclusion (backscattered electron image). (n) Euhedral diaspore grain in a mineral concentrate (backscattered electron image). Abbreviations: Chr – chromite, Cpx – clinopyroxene, Clc – clinocllore, Dsp – diaspore, Hem – hematite, Moi – moissanite, Cu – native Cu, Ap – apatite, Zrn – zircon, and Srp – serpentine.

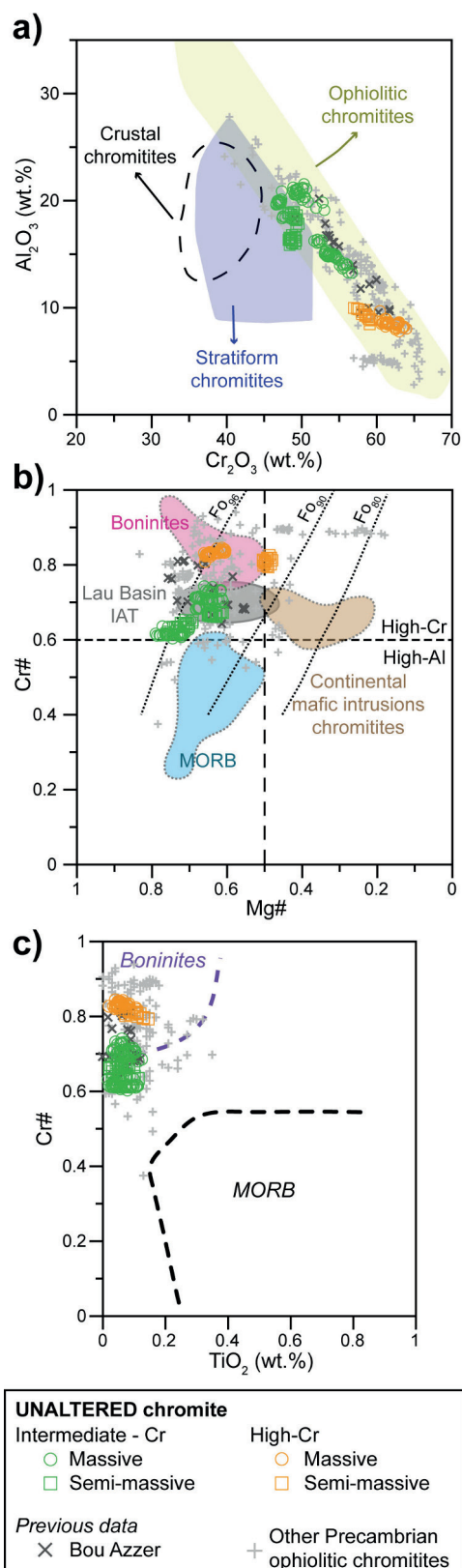


Fig. 7. Composition of the Bou Azzer unaltered chromite cores. (a) Al₂O₃ (wt. %) vs. Cr₂O₃ (wt. %). (b) Cr# [Cr/(Cr + Al)] vs. Mg# [Mg/(Mg + Fe²⁺)]. Dashed lines represent the composition of olivine in equilibrium with chromite at 1200 °C (Dick and Bullen, 1984). (c) Cr# vs. TiO₂ (wt. %). Data sources for chromian spinel of different tectonic settings are Irvine (1967), Leblanc and Nicolas (1992), Arai (1992), Bonavia et al. (1993), Kamenetsky et al. (2001), and Proenza et al. (2007).

significant zoning. Electron microprobe analyses revealed that some laurite grains are partially altered, showing Ru concentrations up to 70.21 wt%, Os between 1.61 and 4.93 wt%, Ir between 1.06 and 2.82 wt %, up to 1.42 wt% Rh, up to 0.50 wt% Pt, and up to 0.34 wt% Pd (Appendix 7). One grain of altered laurite shows an inverse correlation between Ru and S contents, indicating the transformation of the sulfide into an alloy (X-ray maps of Appendix 8b). A third type of PGM is observed surrounding the alloys (Fig. 5e-f; Appendix 8c), sometimes intergrown with silicates. This phase was too heterogeneous to obtain a well-defined composition, but the analyses confirm the presence of Ir-As-S, probably corresponding to secondary irarsite.

5. Discussion

In this section, petrological, mineralogical and geochemical data are discussed in order to explore the effects of alteration on element mobility, to determine the parental melts for chromitites, to examine the origin and significance of PGE/PGM and unusual mineral phases within the chromitites, to compare with other Precambrian chromites, and to ultimately provide a genetic model for the formation of the Bou Azzer chromitites.

5.1. Effects of metamorphism and alteration on mobility of major and minor elements

As the Bou Azzer ophiolite is variably affected by post-magmatic processes, including metamorphism, serpentinization and carbonation (e.g., Gahlan et al., 2006; Fanlo et al., 2015; Hodel et al., 2017), interpretations based on the composition of chromite in terms of primary magmatic processes require an assessment of the potential effects of alteration on element mobility. The intermediate-Cr chromite cores are partially mantled by wide rims of porous altered chromite (Fig. 4b, e-f; Appendix 4), which is texturally very similar to the “porous chromite” reported in chromitites affected by greenschist to amphibolite-facies metamorphism elsewhere (e.g., Gervilla et al., 2012; González-Jiménez et al., 2015a, 2015b, 2017b; Colás et al., 2016, 2019; Hernández-González et al., 2020). The “porous chromite” in the Bou Azzer chromitites is enriched in Cr and Fe²⁺ and depleted in Al and Mg when compared to the unaltered chromite cores (Fig. 8; Appendix 3). On the other hand, alteration is restricted to thin homogeneous ferrian chromite rims in high-Cr chromite (Fig. 4c, h). Semi-massive chromitites show more evolved alteration than massive chromitites due to stronger interaction (i.e. lower chromite/silicate ratio) with the fluids altering the host peridotites (e.g., Proenza et al., 2004; González-Jiménez et al., 2015a; Gervilla et al., 2012; Colás et al., 2019).

The textural and chemical evidences suggest two different stages of alteration (Fig. 8), similar to the alteration reported in many other ophiolitic chromitites (Proenza et al., 2004; Gervilla et al., 2012; Colás et al., 2014, 2019, 2020; González-Jiménez et al., 2015a, 2015b, 2017b; Hernández-González et al., 2020): first, Cr and Fe²⁺ increase under water-saturated reduced conditions accompanied by a volume reduction of ~43% (Gervilla et al., 2012) in order to form the porous chromite (Fig. 8a); and afterwards, oxidizing conditions prompt the formation of ferrian chromite (Fig. 8b). A latter stage of alteration involved the circulation of Fe³⁺-rich fluids that formed Cr-magnetite, as reported in the Bou Azzer serpentinites by Hodel et al. (2017). This magnetite veins were later oxidized forming hematite, explaining the Cr-rich composition of the studied Bou Azzer hematite (Appendix 3).

Regarding the composition of unaltered chromite cores, both intermediate-Cr and high-Cr chromite overlap the field typical for ophiolitic chromitites (Fig. 7a). The Ti content (Fig. 9a) is similar for the two types of chromite and relatively low when compared with other high-Cr (Cr# >0.6) ophiolitic chromitites (González-Jiménez et al., 2014a, 2017a and references therein), ruling out the addition of Ti during metamorphism noted in other greenschist to amphibolite facies metamorphosed ophiolitic chromitites (e.g., Colás et al., 2014;

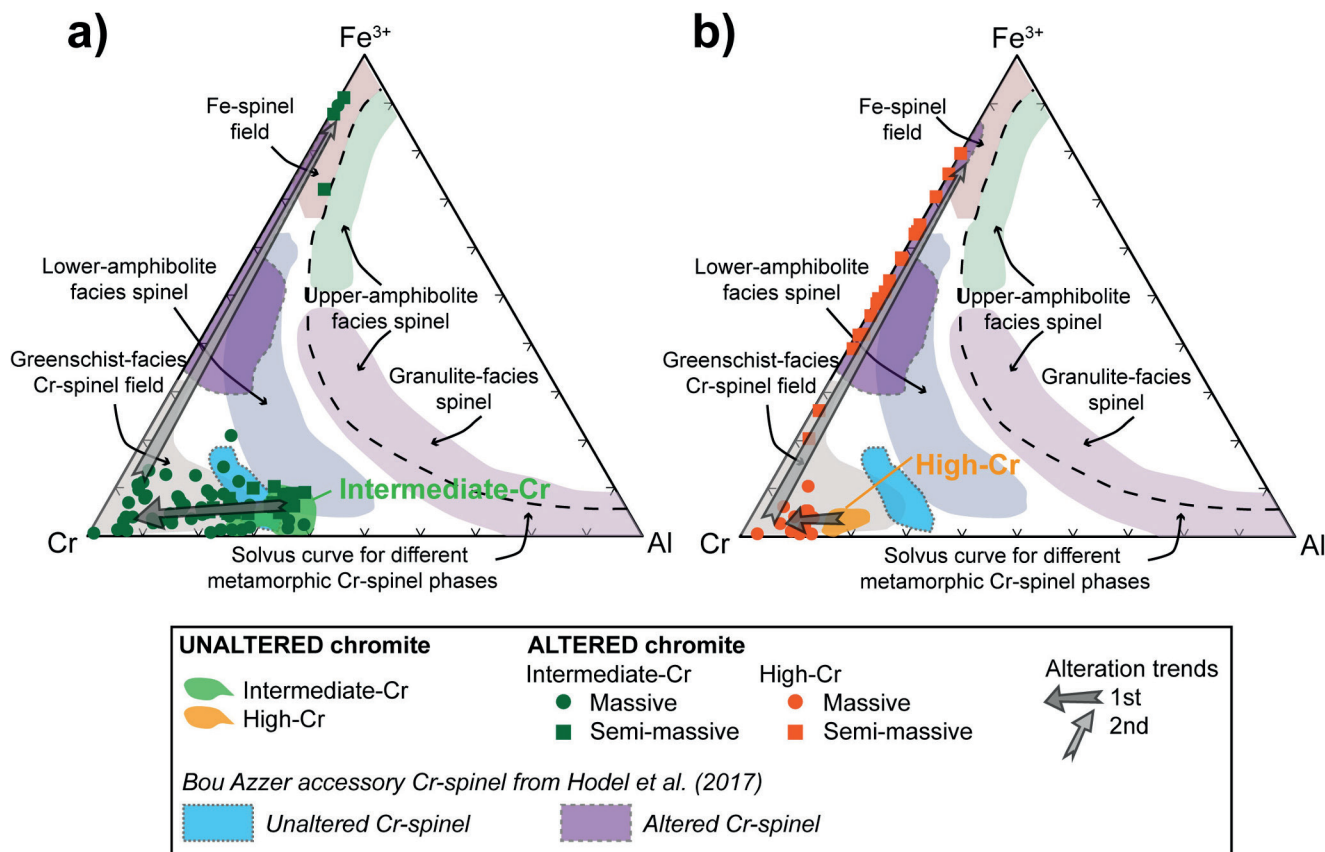


Fig. 8. Fe^{3+} -Cr-Al ternary diagram of the Bou Azzer unaltered and altered chromite. (a) Intermediate-Cr chromite. (b) High-Cr chromite. Fields for unaltered and altered accessory spinel in the Bou Azzer serpentinites are from Hodel et al. (2017). Spinel compositional fields from different metamorphic facies are from Purvis et al. (1972), Evans and Frost (1975) and Suita and Strieder (1996).

González-Jiménez et al., 2015a and references therein). Trace elements contents in intermediate-Cr and high-Cr chromite cores are within the range for primary igneous chromite (Fig. 9), suggesting that the primary chromite composition is preserved and that high-Cr chromitites are not the alteration product after intermediate-Cr chromitites, allowing petrogenetic interpretations related to the formation of the deposits (see below). Altered chromite rims exhibits the typical Ni, V, Zn, and Mn enrichment at ppm levels (Appendix 5) related to the formation of Cr and Fe^{2+} -rich porous chromite (Colás et al., 2019 and references therein). MORB-normalized trace element patterns of unaltered intermediate-Cr and high-Cr chromite are very similar to those of chromitites from the oceanic supra-subduction zone (SSZ) mantle, in particular to fore-arc chromitites (Fig. 12), suggesting that the minor and trace elements contents in the unaltered chromite cores represent the magmatic fingerprint of a fore-arc environment.

5.2. Parental magma compositions

In the Cr# versus Mg# and Cr# versus TiO_2 plots (Fig. 7b-c), the composition of the Bou Azzer intermediate-Cr chromite falls between the fields defined by Cr-spinel in boninites and mid-oceanic ridge basalts (MORB). In contrast, the composition of the high-Cr chromite plots within the field defined by Cr-spinel in boninites. Using the Al_2O_3 and the TiO_2 compositions of unaltered chromite cores (Appendix 3), we have estimated the composition of the corresponding melts in equilibrium using the equations for chromite with $Cr\# > 0.6$ by Kamenetsky et al. (2001) modified by Rollinson (2008) for Al_2O_3 and by Zaccarini et al. (2011) for the TiO_2 content. The Al_2O_3 contents were estimated with the equation $(Al_2O_3)_{melt} = 4.6455 \cdot \ln(Al_2O_3)_{spinel} - 0.3616$, while TiO_2 contents were estimated with the expression $(TiO_2)_{melt} = 1.089$

$(TiO_2)_{spinel} + 0.089$. The FeO/MgO ratios were estimated using the Maurel and Maurel's (1982) empirical expression: $\ln(FeO/MgO)_{spinel} = 0.47 - 1.07Al\#_{spinel} + 0.64Fe^{3+}\#_{spinel} + \ln(FeO/MgO)_{melt}$, with FeO and MgO in wt.%, $Al\# = Al/(Cr + Al + Fe^{3+})$ and $Fe^{3+}\# = Fe^{3+}/(Cr + Al + Fe^{3+})$.

As expected, we have identified two different parental melts for the two types of studied chromitites (Fig. 13). Intermediate-Cr chromitites yield average 12.87 wt% of Al_2O_3 , 0.16 wt% of TiO_2 and 0.90 FeO/MgO ratio, which is similar to MORB melts in terms of Al_2O_3 content (Fig. 13a; e.g., Gale et al., 2013) but not in terms of TiO_2 (Fig. 13b; typical MORB 1.68 wt% TiO_2 ; Gale et al., 2013). The low Ti content in MORB-akin melts, together with low Ti/V and Yb/V ratios, is characteristic of fore-arc basalts (FAB; Reagan et al., 2010). According to Shervais et al. (2019), FAB involve a more depleted source than NMORB source mantle, usually recording up to 23% melting. On the other hand, high-Cr chromitites yield average 9.69 wt% of Al_2O_3 , 0.16 wt% of TiO_2 and 1.08 FeO/MgO ratio, corresponding to typical boninitic parental melt compositions (Fig. 13c; e.g., Hickey and Frey, 1982; Dick and Bullen, 1984; Kelemen et al., 2004). The PGE contents in the intermediate-Cr and high-Cr chromitites are similar (Fig. 10a) despite having formed after two different parental melts. This feature could either indicate that these melts originated from the same source (e.g., Zaccarini et al., 2011; González-Jiménez et al., 2015a) or could be the result of higher degree of partial melting (than for typical MORB) in the depleted mantle that originated the FAB melts that formed the intermediate-Cr chromitites (e.g., Shervais et al., 2019).

5.3. PGE signature and PGM formation

The distribution of PGE in the upper mantle is mainly controlled by

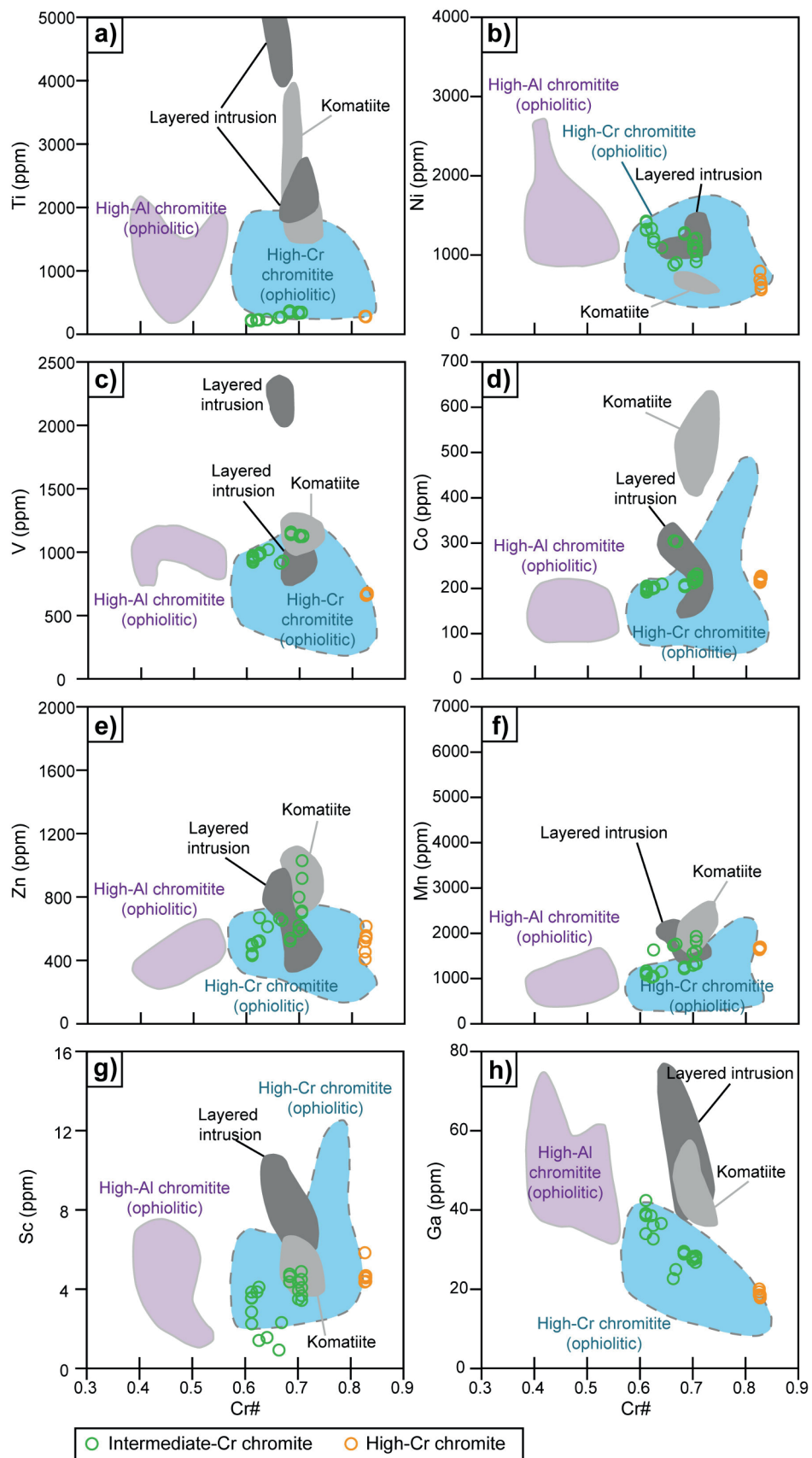


Fig. 9. Variations in terms of Ti, Ni, V, Co, Zn, Mn, Sc, and Ga vs. Cr# [Cr/(Cr + Al)] in the Bou Azer chromite. Fields are from González-Jiménez et al. (2017a) and references therein.

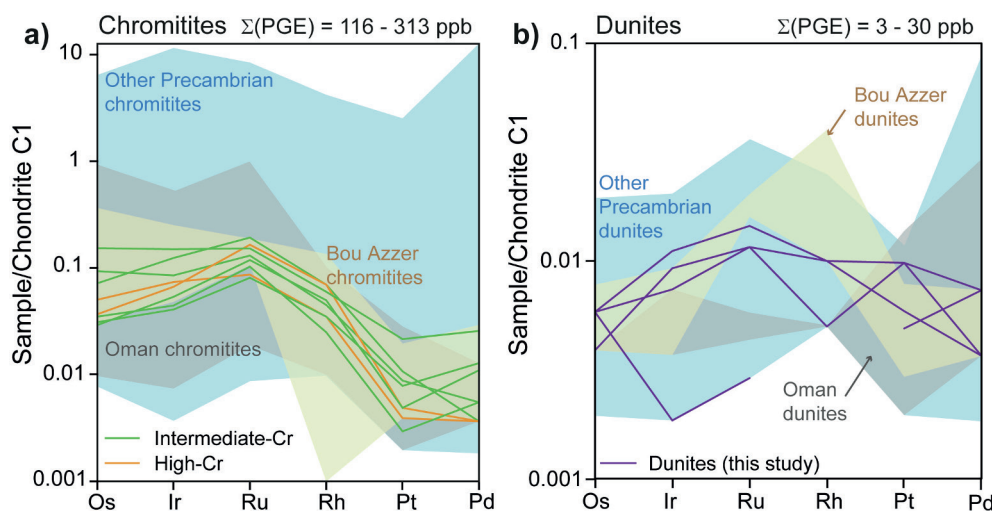


Fig. 10. (a) C1 chondrite-normalized (Naldrett and Duke, 1980) patterns of PGE in Bou Azzer chromitites and comparison with other mantle-hosted chromitites. Previous data from Bou Azzer (brown field) from El Ghorfi et al. (2007) and Ahmed et al. (2009). Data from other Precambrian chromitites including Egypt, Saudi Arabia, Ethiopia and Finland (blue field) from Bonavia et al. (1993), Vuollo et al. (1995), Prichard et al. (2008), Ahmed et al. (2012), Ahmed (2013), and Habtoor et al. (2017). Data from Oman chromitites (grey field) from Ahmed and Arai (2002). (b) C1 chondrite-normalized (Naldrett and Duke, 1980) patterns of PGE in the Bou Azzer dunites. Previous data from Bou Azzer (brown field) from Ahmed et al. (2009), data from other Precambrian dunites include Egypt and Saudi Arabia ophiolites (blue field) from Prichard et al. (2008), Ahmed et al. (2012), Ahmed (2013), and Habtoor et al. (2017), and Oman dunites (grey field) from Ahmed and Arai (2002).

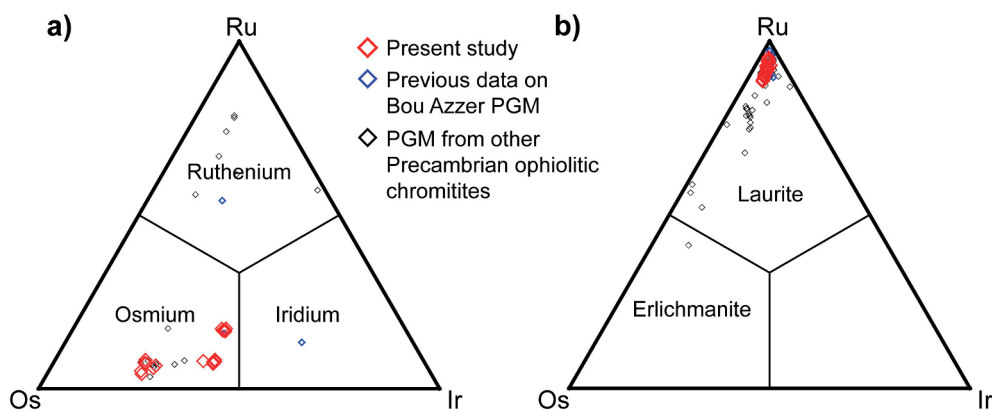


Fig. 11. Classification of platinum group minerals (PGM) found in Bou Azzer chromitites in terms of Ru, Os and Ir for (a) alloys and (b) unaltered laurite. Data in blue are previously reported PGM in the Bou Azzer chromitites (El Ghorfi et al., 2007) and data in grey are from other Precambrian ophiolitic chromitites: Outokumpu (Finland; Liipo, 1999), SE Desert (Egypt; Ahmed, 2007), Pampean Ranges (Argentina; Proenza et al., 2008), Al'Ays (Saudi Arabia; Prichard et al., 2008), and Bir Tuluha (Saudi Arabia; Habtoor et al., 2017).

the accessory base metal sulfides and PGM disseminated within the mantle peridotites (O'Driscoll and González-Jiménez, 2016 and references therein). During partial melting of mantle peridotites, PGE fractionates into two groups: the most refractory IPGE (Ir-Os-Ru) remain trapped within sulfides or PGM in the mantle residue, while the more mobile PPGE (Pd-Pt-Rh) are transferred to the silicate melt (Bockrath et al., 2004a). However, if moderate to high degrees of mantle partial melting (20–25%) are achieved, such as in suprasubduction zones (Barnes et al., 1985; Prichard et al., 1996; O'Hara et al., 2001), it is possible to extract the IPGE by dissolution of IPGE-bearing sulfides and PGM of the mantle residue, thus forming chromitites enriched in IPGE relative to PPGE (Bockrath et al., 2004a; Prichard et al., 2008; González-Jiménez et al., 2014b).

In the Bou Azzer chromitites, there is a clear enrichment in IPGE relative to PPGE (Fig. 10a; El Ghorfi et al., 2007; Ahmed et al., 2009), similar to what is observed in the Oman chromitites (Fig. 10a; Ahmed and Arai, 2002) and in other high-Cr ($Cr\# > 0.6$) chromitites elsewhere (González-Jiménez et al., 2014a, 2014b). This enrichment is reflected in the mineralogy, characterized by Ru-Os-Ir bearing minerals, such as laurite and Os-Ir alloys (Fig. 5). The origin of chromite-hosted PGM may be linked to chromite crystallization, since it preferentially incorporates trivalent Cr and Fe from the magma, producing a local decrease of fO_2 that reduces the solubility of the dissolved IPGE in the magma and triggers the crystallization of nano-nuggets of IPGE at the chromite rims (Mungall, 2005; Gervilla et al., 2005; Finnigan et al., 2008; González-Jiménez et al., 2014b). According to O'Driscoll and González-Jiménez

(2016), chromite and IPGE nuggets crystallize most likely from S-undersaturated melts with low fS_2 in supra-subduction environments. Experimental works (Brenan and Andrews, 2001; Andrews and Brenan, 2002; Bockrath et al., 2004b) demonstrated that Os-free laurite precipitates in equilibrium with Os-Ir alloys at the T- fS_2 - fO_2 -P conditions predominating during chromite formation in the upper mantle. Therefore, the Bou Azzer Os-poor laurite grains (Os content between 1 and 6 at.%) would have crystallized contemporaneously with the Os-Ir alloys, as indicated by petrographic observations.

Metamorphism, serpentinization and hydrothermal alteration in the Bou Azzer ophiolitic sequence triggered the destabilization and modification of the primary PGM assemblage. One of the first modifications is the segregation of IPGE nanoparticles from primary laurite grains (Fig. 5b; Appendix 8b) due to the decrease in fS_2 associated with serpentinization that favors the formation of PGE alloys instead of sulfides (Garuti and Zaccarini, 1997; Jiménez-Franco et al., 2020 and references therein). Another modification of the primary PGM assemblage is the formation of secondary Ir-As-S phases, which have only been found as spongy envelopes around Os-Ir alloys (Fig. 5e; Appendix 8c) or coexisting with chlorite (Fig. 5f). The formation of these secondary phases requires an increase in the a_{As} of the system (e.g., Thalhammer et al., 1990; Malitch et al., 2001; González-Jiménez et al., 2010, 2012), which could be caused by post-serpentinization Cl-rich hydrothermal fluids that circulated in the Bou Azzer area between 380 and 240 Ma (Gasquet et al., 2005; Hodel et al., 2017).

The dunites hosting the Bou Azzer chromitites have PGE contents

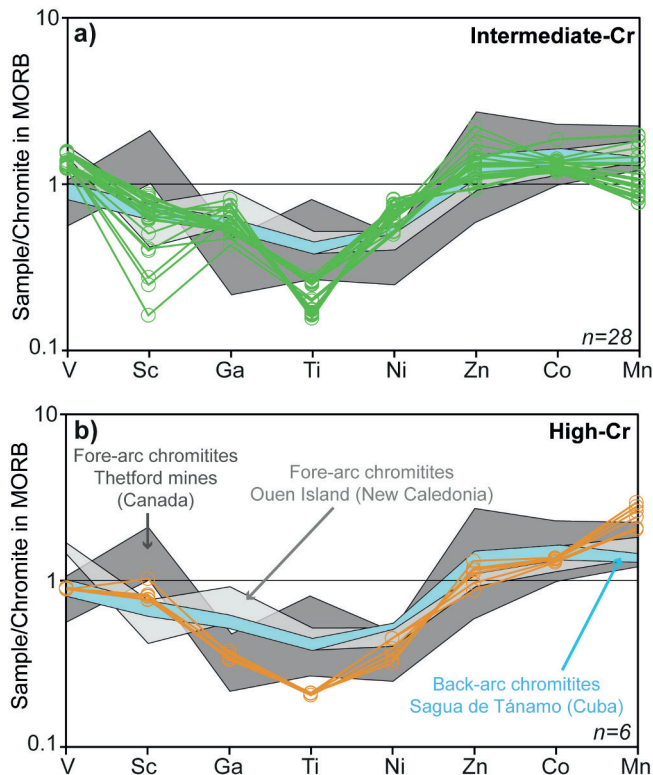


Fig. 12. Spider diagrams showing the composition of minor and trace elements of chromite from Bou Azzer. (a) Intermediate-Cr chromite. (b) High-Cr chromite. Data are normalized to MORB (Pagé and Barnes, 2009) and compared with representative Thetford mines fore-arc chromitites (Pagé and Barnes, 2009), Ouen Island fore-arc chromitites and Sagua de Tánamo back-arc chromitites (González-Jiménez et al., 2015a).

(3–30 ppb) much lower than previously reported (22–53 ppb, Ahmed et al., 2009). The chondrite-normalized patterns are generally flat, except for Ru positive anomalies (Fig. 10b). When compared to ophiolitic dunites elsewhere, the PGE contents in the studied dunites are remarkably low and the chondrite-normalized patterns also differ due to the Ru positive anomaly (e.g., Barnes et al., 1985; Leblanc, 1981; Lorand et al., 1999; Ahmed and Arai, 2002; Proenza et al., 2004). Previous studies of PGE in the Bou Azzer serpentinized peridotites also reported positive Ru-Rh anomalies (Ahmed et al., 2009). These authors found that the chondrite-normalized PGE patterns for dunites were similar to the ones corresponding to Co-Ni-Fe-bearing arsenides. Therefore, these Ru-Rh anomalies were explained after the presence of disseminated arsenides in dunites (Ahmed et al., 2009). The low PGE contents of dunites, lower than in spatially related harzburgites (40–68 ppb PGE in Bou Azzer harzburgites; Ahmed et al., 2009) may indicate very strong leaching in dunites. The presence of disseminated arsenides also supports intense fluid circulation in the studied serpentinites. Such leaching could have been a key process regarding the formation of PGE mineralization, such as the Au-Pd deposit of Bleida Far West in the south-eastern part of the Bou Azzer inlier (El Ghorfi et al., 2006).

5.4. Origin and significance of unusual (“exotic”) mineral assemblages

Unusual minerals distinguished *in situ* in chromite include oriented clinopyroxene lamellae and polymineralic inclusions of diasporite, hematite and clinocllore. Other minerals identified in the mineral concentrates include moissanite, native Cu and zircon grains with apatite or serpentine inclusions (Fig. 6). Several of these unusual mineral phases have been commonly interpreted as indicators of UHP conditions and sourced from the mantle transition zone in many ophiolitic rocks

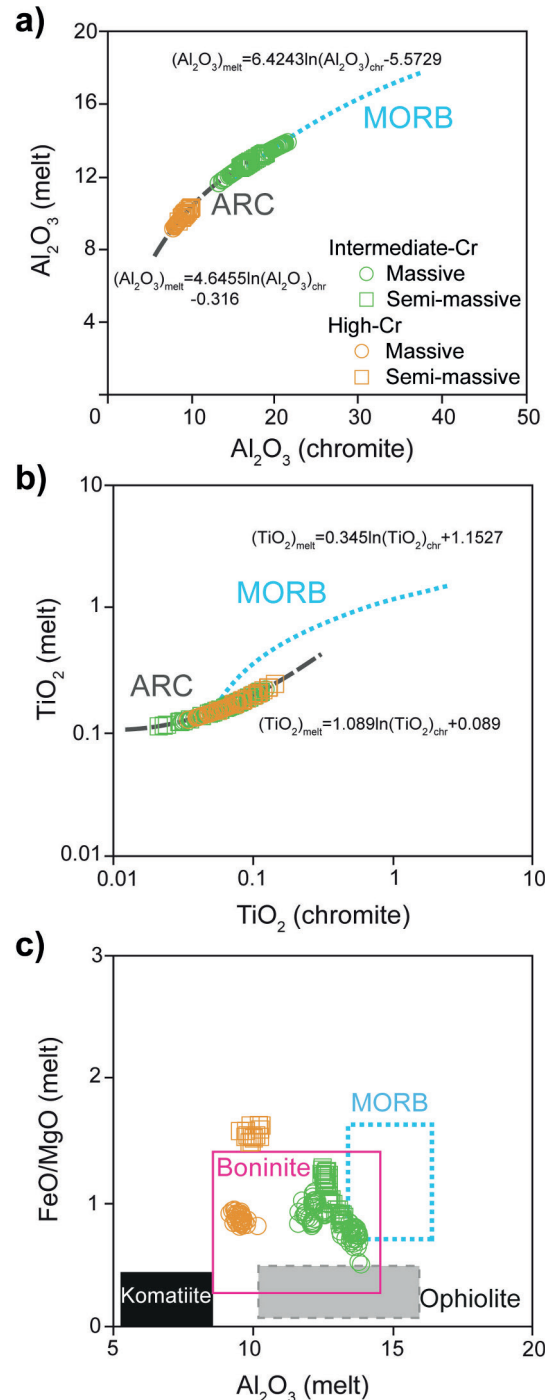


Fig. 13. Calculated composition of melts in equilibrium with Bou Azzer chromitites, compared with spinel-melt relationship for MORB and arc lavas (Kamenetsky et al., 2001). Equations from Kamenetsky et al. (2001) modified by Rollinson (2008) and Zaccarini et al. (2011). (a) Al_2O_3 melt vs. Al_2O_3 spinel. (b) TiO_2 melt vs. TiO_2 spinel. (c) FeO/MgO melt ratio vs. Al_2O_3 melt. Tectonic compositional fields are from Barnes and Röeder (2001).

worldwide (Table 1), but such models have been challenged by recent studies (Pujol-Solà et al., 2018, 2020a; Farré-de-Pablo et al., 2019a). The occurrence of similar mixed mineral assemblages of continental crust and super-reduced (SUR) and/or ultra-high pressure (UHP) origin as the ones in Bou Azzer is revised in Table 1.

Studies on high-pressure chromite showed that oriented clinopyroxene lamellae could form as exsolutions, together with coesite, after the $CaFe_2O_4$ -structured (Ca-ferrite) polymorph of chromite (>12.5 GPa,

Table 2

Comparison of Precambrian ophiolitic chromitites worldwide. Zunhua and Dongwazi (China) data are from Huang et al. (2004), Kusky et al. (2004a) and Kusky et al. (2004b), Santa Luz (Brazil) from Oliveira et al. (2007), Outokumpu (Finland) from Liipo et al. (1995), Liipo (1999), Vuollo et al. (1995) and Peltonen et al. (2008), Miaowan (China) from Peng et al. (2012), Eastern Sayan (Russia) from Khain et al. (2002) and Kiseleva and Zhmodik (2017), Jebel Rahid (Sudan) from Abdel Rahman et al. (1990) and Haldar (2017), Bir Tuluha (Saudi Arabia) from Pallister et al. (1988) and Habtoor et al. (2017), Capané (Dom Feliciano, Brazil) from Marques et al. (2003), Arena et al. (2018) and Werle et al. (2020), Kenticha Hill (Ethiopia) from Bonavia et al. (1993) and Yibas et al. (2003), Wadi Al Hwanet (Saudi Arabia) from Pallister et al. (1988) and Ahmed et al. (2012), Bou Azzer (Morocco) from Ikenne et al. (2005), El Ghorfi et al. (2007), Ahmed et al. (2009), Hodel et al. (2020) and the present study, Quatipuru (Brazil) from Paixão et al. (2008), Paixão (2009) and Hodel et al. (2019), South Eastern Egypt Desert from Kröner et al. (1992), Ahmed et al. (2001), Saleh (2006), Ahmed (2007), Ahmed (2013), and Hamdy and Lebda (2011), Al'Ays (Saudi Arabia) from Bakor et al. (1976), Pallister et al. (1988) and Prichard et al. (2008), Central Eastern Egypt Desert from Ahmed et al. (2001), Ahmed (2007) and Andresen et al. (2009), Hoggar (Algeria) from Caby (2003) and Augé et al. (2012), Tapo Massif (Peru) from Castroviejo et al. (2009), Tassinari et al. (2011) and Colás et al. (2017), Halaban (Saudi Arabia) from Stacey et al. (1984), Ahmed and Hariri (2001) and Abuamarah (2020), Pampean Ranges (Argentina) from Escayola et al. (2007) and Proenza et al. (2008), Pirapora (Brazil) from Hackspacher et al. (2000) and Tassinari et al. (2001), and Marlborough (Australia) from Bruce et al. (2000).

Ophiolite belt	Country	Age (Ma)	Orebody length	Chromitite host rock	Textures	Geodynamic setting	Cr#	∑PGE(ppb) in chromitites	PGM
Zunhua & Dongwanzi	China	2547 ± 10 Re-Os (TIMS) Model age of chromite from podiform chromitite	1–20 m	Harzburgites Dunites	Disseminated Banded Nodular Orbicular	SSZ	0.88–0.90	–	–
Santa Luz	Brazil	2085 ± 12 (minimum age) U-Pb (SHRIMP) Zircon from aplite dikes	–	Serpentinites Harzburgites	Massive Disseminated	MOR	0.60–0.70	–	–
Outokumpu	Finland	1959 ± 5 1971 ± 15 U-Pb (TIMS) Zircon from gabbros and plagiogranites	–	Serpentinites	Massive Nodular	MOR	0.59–0.60	71–336	Laurite Irarsite-Osarsite
Miaowan	China	1118 ± 24 974 ± 11 U-Pb (LA-ICP-MS) Zircon from gabbros	–	Harzburgites Dunites	Disseminated Nodular Orbicular	SSZ	–	–	–
Eastern Sayan	Russia	1019 ± 1 Pb-Pb (TIMS) Zircon from plagiogranites	<10 m	Dunites Harzburgites	Massive Disseminated	MOR + SSZ	0.59–0.90	88–1189	Os-Ir-Ru Alloys Laurite Irarsite-Osarsite- Ruarsite Hollingworthite (RhAsS) Native Osmium Ir-Ru-Rh sulfoarsenides
Jebel Rahid	Sudan	860 ± 17 K-Ar in hornblende from metagabbros 740 ± 15 K-Ar in metabasalts (whole rock)	~50 m	Dunites Harzburgites	Massive	SSZ	0.85	–	–
Bir Tuluha	Saudi Arabia	847 ± 14 823 ± 11 U-Pb (Two-stage MS) Model ages of zircon grains from plagiogranites	2–10 m	Dunites	Massive Banded	SSZ	0.72–0.81	142–217	Laurite
Capané (Dom Feliciano)	Brazil	793 ± 0.9 757 ± 2.1 715 ± 2.2 U-Pb (LA-ICP-MS) Zircon grains from rodingites	–	Serpentinites	Massive Nodular	MOR	–	–	–
Kenticha Hill	Ethiopia	789 ± 36 Sm-Nd (INAA) Whole-rock age from metavolcanics	<30 cm	Serpentinites	Massive	SSZ (FA)	0.87–0.91	116–205	–
Wadi Al Hwanet	Saudi Arabia	780 ± 11 U-Pb (Two-stage MS) Model age of zircon grains from gabbros	5–20 m	Harzburgites	Massive	SSZ	0.61–0.81	204–967	Laurite
Bou Azzer	Morocco	759 ± 2 U-Pb (LA-ICP-MS) Zircon from metagabbros	<5 m	Harzburgites	Massive Banded Semimassive	SSZ (FA)	0.60–0.83	116–313	Laurite Os alloys Irarsite Ir-Os-Ru-Pt-Ni sulfo-arsenide
Quatipuru	Brazil		1–10 m			MOR or OCT	0.42–0.61	66–176	–

(continued on next page)

Table 2 (continued)

Ophiolite belt	Country	Age (Ma)	Orebody length	Chromitite host rock	Textures	Geodynamic setting	Cr#	∑PGE(ppb) in chromitites	PGM
		757 ± 49 Sm-Nd (TIMS) Model age of gabbro and diabase dikes		Harzburgites Dunites	Massive Disseminated Nodular				
Southern Eastern Desert	Egypt	741 ± 21 Pb-Pb (TIMS) Zircon from gabbros	<30 m	Harzburgites Dunites	Massive Disseminated Nodular Anti-nodular	SSZ	0.57–0.90	77–320	Laurite- Erlichmannite Os-Ir alloys Irsite-Osarsite
Al'Ays	Saudi Arabia	740 ± 11 U-Pb (Two-stage MS) Model age of zircon grains from plagiogranites	–	Harzburgites Dunites	Massive	SSZ (BAB)	0.60–0.90	131–10463	Os-Ir-Ru Alloys Laurite Irsite Ir-Ni-Fe alloys Hollingworthite (RhAsS) Rh antimonides Rh arsenides Pt-Pd alloys Pt-Pd arsenides
Central Eastern Desert	Egypt	737 ± 1.2 U-Pb (TIMS) Zircon from gabbros	<30 m	Harzburgites Dunites	Massive Disseminated Nodular Anti-nodular	SSZ	0.53–0.82	58–365	Laurite Irsite-Osarsite Sperryllite (PtAs) PdAs Pt-Pd-Fe alloy Ir-Rh alloy Ruarsite Os-Ru-Ir alloys Os-Ir-Ru sulfarsenides Os-Ir-Ru arsenides
Hoggar	Algeria	730 U-Pb (TIMS) Zircon from plagiogranite	<250 m	Serpentinites	Massive Disseminated Schlieren	MOR	0.48–0.52	–	Ruarsite Os-Ru-Ir alloys Os-Ir-Ru sulfarsenides Os-Ir-Ru arsenides
Tapo Massif	Peru	718 ± 47 Sm-Nd (TIMS) Chromite from chromitites and whole-rock from gabbros	<100 m	Serpentinites	Massive Disseminated	MOR	0.49–0.50	up to 148	–
Halaban	Saudi Arabia	694 ± 8 Pb-Pb (TIMS) Zircon from gabbros	–	Harzburgites Dunites	Massive Disseminated Nodular	SSZ (FA)	–	–	–
Pampean Ranges	Argentina	647 ± 77 Sm-Nd (TIMS) Whole-rock age from basalts, pyroxenites and dunite dikes	10's of meters	Harzburgites	Massive Lobate Brecciated Disseminated	SSZ (BAB)	0.48–0.56	11–49	Os Alloys Laurite- Erlichmannite Irsite Native Pt Pt tellurides Unnamed Ru, Pt, Ir oxi-hydroxides
Pirapora	Brazil	628 ± 9 U-Pb (LA-ICP-MS) Zircon and monazite grains from metabasalts	2–3 m	Dunites	Massive	SSZ (BAB)	–	–	–
Marlborough	Australia	562 ± 22 Sm-Nd (MC-ICP-MS) Whole-rock age from basalts and gabbros	–	Serpentinites	Massive	MOR	0.37–0.44	–	–

Abbreviations: SSZ – supra-subduction zone, BAB – back-arc basin, MOR – mid-ocean ridge, FA – fore-arc, and OCT – ocean-continent transition.

>380 km; Yamamoto et al., 2009; McGowan et al., 2015). These experiments have been taken as one of the bases for proposing UHP conditions in ophiolitic chromitites worldwide (e.g., Arai, 2013; Griffin et al., 2016; González-Jiménez et al., 2017a; Akbulut, 2018). However, recent findings of similar “exsolution” in shallow ophiolitic chromitites (Mercedita, Cuba; Pujol-Solà et al., 2018; Table 1) and layered chromitites of the Stillwater complex (Liu et al., 2020), challenge this interpretation and point instead to silicate-liquid interactions. Indeed, no evidence of UHP metamorphism is found in the ultramafic and mafic rocks of the Bou Azzer ophiolite, where greenschist facies are commonplace (Hefferan et al., 2002; El Hadi et al., 2010). In terms of trace elements, the Bou Azzer chromitites are similar to typical low-pressure SSZ chromitites (Fig. 12). Furthermore, other UHP mineral phases such as coesite, TiO₂-II or cubic-BN (Table 1; Xiong et al., 2017a)

have not been identified in the studied thin sections nor in the mineral concentrates. Therefore, we interpret that the oriented clinopyroxene lamellae in the Bou Azzer chromite grains (Fig. 6a-c) did not form after the decompression of the UHP Ca-ferrite polymorph of chromite (cf. Yamamoto et al., 2009). On the other hand, there is no field evidence that the parental melts of the chromitites interacted with silicate melts (i.e. gabbroic rocks; cf. Pujol-Solà et al., 2018, 2020b). Hence, we interpret that these lamellae represent clinopyroxene that crystallized from silicate melt inclusions trapped at the crystallographic planes of the growing chromite grains (Liu et al., 2020).

Diaspore, associated with hematite and clinocllore, is observed in inclusion trails within the Bou Azzer chromite (Fig. 6d-h). Diaspore is not a common mineral in serpentinized rocks, but it could form under extremely low a_{SiO_2} by desilication of chlorite (Frost and Beard, 2007).

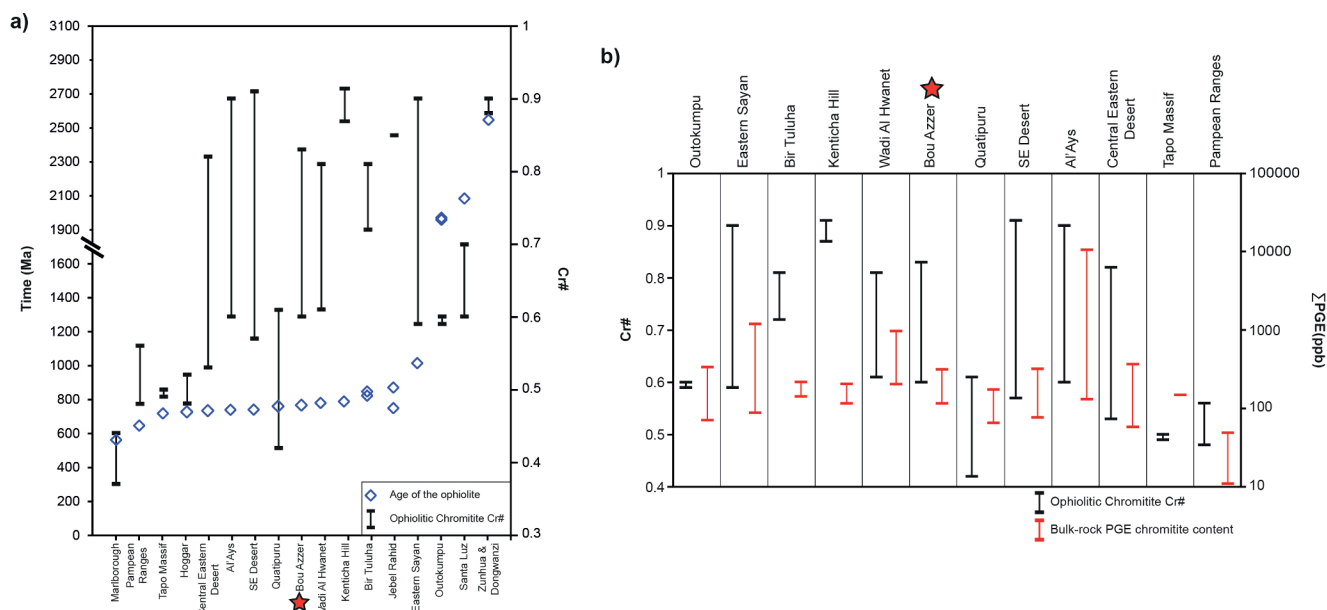


Fig. 14. Comparison between different Precambrian ophiolitic chromitites. (a) Age and Cr#. (b) Σ PGE and Cr#. Zunhua and Dongwazi (China) data are from [Kusky et al. \(2004a, b\)](#), Santa Luz (Brazil) from [Oliveira et al. \(2007\)](#), Outokumpu (Finland) from [Liipo et al. \(1995\)](#), Vuollo et al. (1995) and [Peltonen et al. \(2008\)](#), Eastern Sayan (Russia) from [Khain et al. \(2002\)](#) and [Kiseleva and Zhmodik \(2017\)](#), Jebel Rahid (Sudan) from [Abdel Rahman et al. \(1990\)](#) and [Haldar \(2017\)](#), Bir Tuluha (Saudi Arabia) from [Pallister et al. \(1988\)](#) and [Habtoor et al. \(2017\)](#), Kenticha Hill (Ethiopia) from [Bonavia et al. \(1993\)](#) and [Yibas et al. \(2003\)](#), Wadi Al Hwanet (Saudi Arabia) from [Pallister et al. \(1988\)](#) and [Ahmed et al. \(2012\)](#), Bou Azzer (Morocco) from [Ikenne et al. \(2005\)](#), [El Ghorfi et al. \(2007\)](#), [Ahmed et al. \(2009\)](#), [Hodel et al. \(2020\)](#), and the present study, Quatipuru (Brazil) from [Paixão et al. \(2008\)](#), [Paixão \(2009\)](#) and [Hodel et al. \(2019\)](#), South Eastern Egypt Desert from [Kröner et al. \(1992\)](#), [Ahmed et al. \(2001\)](#), [Saleh \(2006\)](#), [Hamdy and Lebda \(2011\)](#), and [Ahmed \(2013\)](#), Al'Ays (Saudi Arabia) from [Pallister et al. \(1988\)](#) and [Prichard et al. \(2008\)](#), Central Eastern Egypt Desert from [Ahmed et al. \(2001\)](#) and [Andresen et al. \(2009\)](#), Hoggar (Algeria) from [Caby \(2003\)](#) and [Augé et al. \(2012\)](#), Tapo Massif (Peru) from [Castroviejo et al. \(2009\)](#), [Tassinari et al. \(2011\)](#) and [Colás et al. \(2017\)](#), Pampean Ranges (Argentina) from [Escayola et al. \(2007\)](#) and [Proenza et al. \(2008\)](#), and Marlborough (Australia) from [Bruce et al. \(2000\)](#).

The formation of diasporite may be driven by late seawater infiltration and indicates serpentinization at very low temperature conditions ($T < 50$ °C; [Frost and Beard, 2007](#)). Therefore, the aligned inclusions are interpreted as secondary healed fractures where serpentinization-related fluids circulated (e.g., [Farré-de-Pablo et al., 2019a, 2019b; Pujol-Solà et al., 2018, 2020a](#)). Fluid circulation is also evidenced by late hematite ([Fig. 4b](#)) and carbonate veins that crosscut the chromitite orebodies. Andradite, formed after the alteration of diopside ([Frost and Beard, 2007](#)), has been distinguished in the altered silicate matrix ([Appendix 2](#)) and can also be associated with low- T (< 225 °C) serpentinization fluids ([Frost and Beard, 2007](#)). These late fluids enriched in Al, Fe^{3+} and Ca may be related to rodingitization of the surrounding mafic rocks, as in the Halaban ophiolite in Saudi Arabia ([Abuamarah, 2020](#)) and in the Eastern Desert of Egypt ([Mubarak et al., 2020](#)). In Bou Azzer, rodingites are reported in association with silver mineralization ([Leblanc and Lbouabi, 1988](#)).

SuR phases, including diamond, moissanite and native elements, are quite common in mineral concentrates from ophiolitic chromitites worldwide ([Table 1](#)). Globally, these have been interpreted as formed at the mantle transition zone (410–660 km depth; e.g., [Lian et al., 2017](#)). However, we interpret that the SuR phases (moissanite and native Cu) recovered in the Bou Azzer mineral concentrates ([Fig. 6i-k](#)) formed during serpentinization processes as there is no evidence of UHP conditions in Bou Azzer. Empirical observations ([Pujol-Solà et al., 2018](#)) and thermodynamic calculations ([Pujol-Solà et al., 2020a; Ballhaus et al., 2020](#)) indicate that SuR phases can form during serpentinization (350 °C and 100 MPa) in super-reduced microenvironments (inclusions) in which oxygen fugacity can be as low as fO_2 (MPa) = -45.3 ($\Delta \log fO_2[\text{Iron-Magnetite}] = -6.5$; [Pujol-Solà et al., 2020a](#)).

Zircon grains hosting serpentine inclusions (denoting the former presence of ferro-magnesian minerals, notably olivine; [Fig. 6m](#)) recovered from the Bou Azzer chromitites could have crystallized at shallow mantle levels during the formation of the chromitites or during further

interaction with silicate melts, as reported in other chromitites ([Pujol-Solà et al., 2020b](#)). The presence of apatite inclusions within other recovered zircon grains ([Fig. 6l](#)) may however indicate crystallization from a continental crustal magma. These potentially xenocrystic zircon grains may hence be linked to the transference of detrital zircon from subducted sediments to the upper mantle wedge and lateral encapsulation within chromite ([Robinson et al., 2015; Rojas-Agramonte et al., 2016; González-Jiménez et al., 2017a; Proenza et al., 2018; Torró et al., 2018](#)). Subduction of WAC (West African Craton)-derived sediments accumulated on top of the subducting oceanic lithosphere ahead the craton could facilitate the transfer of detrital zircons to the mantle wedge and their incorporation to the chromite-forming magmas.

Overall, we suggest a simple crystallization process for the Bou Azzer chromitites, discarding UHP crystallization ([Yang et al., 2014, 2015](#)) or recycling of low-pressure UHP chromitites to great depth via mantle convection ([Arai, 2013; Griffin et al., 2016](#)). In contrast, we observe that the unusual mineralogy formed during the serpentinization of the chromitites and the host peridotites, from relatively high temperature conditions forming chlorite, moissanite and native Cu, to lower temperature conditions, forming andradite and diasporite.

5.5. Comparison with other Precambrian ophiolitic chromitites

Precambrian ophiolites are quite common in the geological record, even though in most cases, they are strongly altered, dismembered and characterized as “greenstone belts” ([Furnes et al., 2015](#)). Most of these Precambrian ophiolites are subduction-related, generated in fore-arc or back-arc environments ([Furnes et al., 2015](#)). [Table 2](#) reports the occurrence of chromitite orebodies within 21 Precambrian ophiolitic sequences of South America, Asia, Africa, Europe, and Australia, together with the studied ophiolitic sequence from Morocco, spanning from 2500 to 560 Ma (see the [Table 2](#) caption for references). When compared to the more abundant Phanerozoic supra-subduction zone

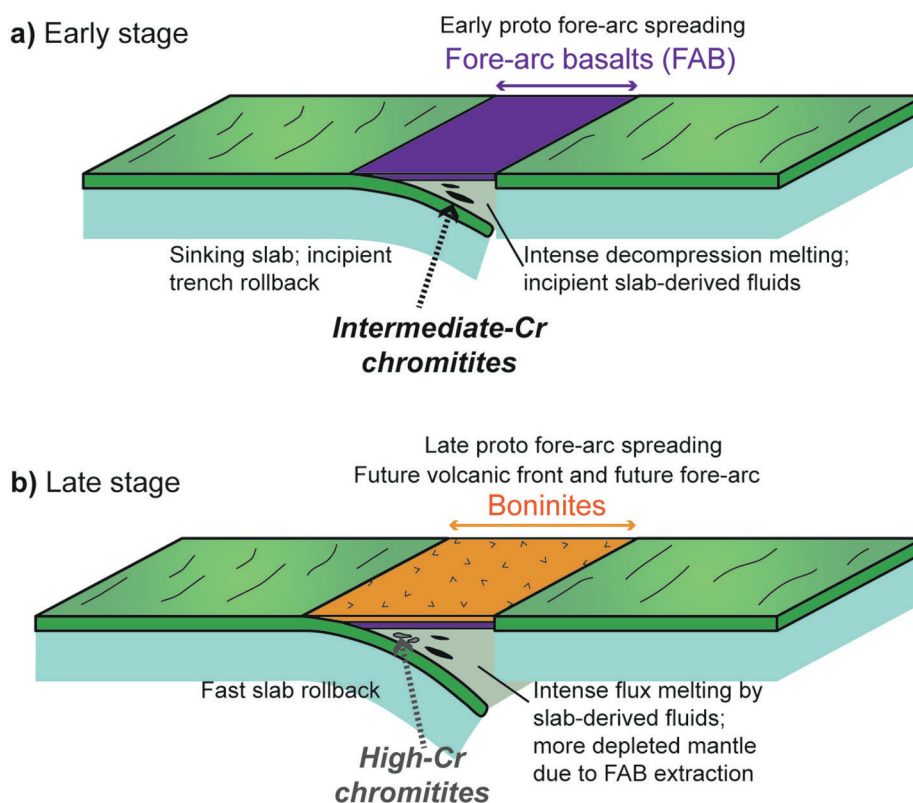


Fig. 15. Schematic geodynamic setting for the formation of the Bou Azzer chromitites in a subduction-initiation geodynamic setting. Based on Whattam and Stern (2011), Torró et al. (2017) and Pandey et al. (2019).

ophiolites (e.g., Furnes et al., 2015), it is striking the limited number of locations of Precambrian chromitites. In fact, most known economic chromitite deposits are Late Paleozoic to younger (Stowe, 1994; Arai and Ahmed, 2018).

Precambrian chromitites are mostly typically show massive textures and are centimetric to metric in size, with some exceptions such as the chromitites from the Hoggar ophiolite (Algeria) that reach 250 m in length (Augé et al., 2012) and those from the Tapo Massif (Peru) that reach around a hundred meters in length (Castroviejo et al., 2009; Colás et al., 2017) (Table 2). Regarding Cr#, it is highly variable, from 0.37 (Marlborough chromitites, Australia; Bruce et al., 2000) to 0.91 (Kenticha Hill chromitites, Ethiopia; Bonavia et al., 1993), though most orebodies are high-Cr ($Cr\# > 0.6$; Table 2; Fig. 14a). A clear correlation between the composition of the chromitites and the age of the host ophiolite is not observed (Fig. 14a). However, younger chromitites generally have lower Cr# ($Cr\# < 0.7$) than older chromitites (Fig. 14a), as already observed by Arai and Ahmed (2018). In order to establish a potential correlation, and since the compositional information is in many cases partial and the post-magmatic chemical variations are not assessed, further studies on some of these Precambrian ophiolitic chromitites are needed.

The observed range of PGE content in Precambrian chromitites is very large, from 11 ppb (Pampean Ranges, Argentina; Proenza et al., 2008) to 10 ppm (Al'Ays, Saudi Arabia; Prichard et al., 2008; Table 2), still, most orebodies have Σ PGE at ppb levels (Fig. 14b). The observed enrichment in PGE in Al'Ays chromitites (Saudi Arabia; 131–10463 ppb; Prichard et al., 2008) or in Sayan chromitites (Russia; 88–1189 ppb; Kiseleva and Zhmodik, 2017) is anomalous and could be related to post-magmatic processes such as metamorphism. Laurite is the most important PGM in most chromitites (Table 2), followed by Os alloys and erlichmanite, indicating an enrichment in IPGE regarding PPG, which is typical in mantle-hosted SSZ chromitites (e.g., González-Jiménez et al., 2014b). Even though a relationship between the Cr# of chromite

and the PGE content is typically observed (e.g., González-Jiménez et al., 2014b), we do not observe a clear trend in the reviewed Precambrian chromitites (Fig. 14b). To the authors' knowledge, mineral associations nominally indicative of UHP or SuR conditions have not been described in the reviewed Precambrian ophiolitic chromitites listed in Table 2, except for the Zunhua Archean chromitites, where Kusky et al. (2019) reported UHP polymorphs of chromite and rutile (TiO₂-II). On the other hand, most chromitites formed in a supra-subduction zone setting, but fore-arc or back-arc locations have not been determined, strengthening the need of further studies on these chromitites.

In terms of Cr# (Fig. 14a), the composition of the studied Bou Azzer chromitites is very similar to Neoproterozoic chromitites from Egypt (e.g., Ahmed, 2007; Ali et al., 2020), Sudan (Abdel Rahman et al., 1990) and Saudi Arabia (e.g., Pallister et al., 1988). The corresponding ophiolitic bodies belong to the Arabian-Nubian shield and are related to the Panafrican orogeny as much as the Moroccan Anti-Atlas. However, in north-western African ophiolites, chromitites have only been described in Bou Azzer and not in other ophiolites such as the Khzama sequence in the Sirwa inlier (e.g., Hodel et al., 2020; Chaib et al., 2021) and this may be related to the scarcity of chromitites in Precambrian ophiolites as stated above (e.g., Stowe, 1994). In the South American margin of Gondwana, Neoproterozoic ophiolitic chromitites have been reported in Peru (Tapo Massif: 718 Ma; Colás et al., 2017), Brazil (Capané: 793–715 Ma, Quatipuru: 757 Ma, and Pirapora: 628 Ma; Marques et al., 2003; Arena et al., 2018; Paixão et al., 2008; Paixão, 2009; Hodel et al., 2019; Hackspacher et al., 2000; Tassinari et al., 2001) and Argentina (Pampean Ranges: 647 Ma; Proenza et al., 2008). Even though some authors (Paixão et al., 2008) attempted to correlate the Neoproterozoic Araguaia belt in Brazil (Quatipuru ophiolite) with the NW African Mauritanide-Basseride-Rockelide belts, the well-studied ophiolitic chromitites in South America have compositions richer in Al₂O₃ than the Bou Azzer chromitites (Table 2). These differences, coupled with a general lack of geological data regarding the geodynamic

setting of the ophiolites and the Neoproterozoic suture zones, makes it very difficult to relate the South American ophiolites to the Moroccan Bou Azzer ophiolite.

5.6. Geodynamic setting and tectonic implications

Arenas et al. (2020) have recently proposed a geodynamic model for the Neoproterozoic-Devonian margin of Gondwana in which the generation of accreted oceanic lithosphere seems to occur at 100 Ma intervals, as recorded by the age of obducted Neoproterozoic to Devonian ophiolites in Morocco and Iberia. In this model, all these ophiolites were collectively generated in the supra-subduction *peri*-Gondwanan realm during the opening of fore-arc and back-arc basins. Other authors have interpreted the formation of the Bou Azzer ophiolite in an intra-oceanic arc setting (e.g., Gasquet et al., 2005; El Hadi et al., 2010; Walsh et al., 2012; Hodel et al., 2020). However, there is still debate on whether there is one or multiple magmatic arcs (Admou et al., 2013; Soulaïmani et al., 2018; Triantafyllou et al., 2018, 2020) and whether the ophiolite formed in a fore-arc (e.g., Saquaque et al., 1989; Naidoo et al., 1991; Ahmed et al., 2005; El Hadi et al., 2010; Walsh et al., 2012; Arenas et al., 2020) or a back-arc setting (e.g., Bodinier et al., 1984; Triantafyllou et al., 2018; Hodel et al., 2020).

The composition of unaltered chromite cores from the Bou Azzer chromitites reveals the presence of two compositional groups of chromitites: intermediate-Cr (Cr# = 0.60–0.74) and high-Cr (Cr# = 0.79–0.84) chromitites (Fig. 7). This distinction was not reported in previous studies of the Bou Azzer chromitites (e.g., Ikenne et al., 2005; El Ghorfi et al., 2007; Ahmed et al., 2009) but it is highly relevant because it translates into two types of parental melts for the studied chromitites. Intermediate-Cr chromitites yield parental melts similar to MORB but with lower TiO₂ contents (the low Ti content in the chromitites is also observed in the trace elements in Fig. 9a) corresponding to FAB melts, whereas high-Cr chromitites yield boninitic parental melts. This association of melts only occurs in fore-arc regions during subduction-initiation (Reagan et al., 2010; Whattam and Stern, 2011; Torró et al., 2017; Shervais et al., 2019; Liu et al., 2019; Pandey et al., 2019; Whattam et al., 2020). In this setting, extension of the upper plate due to rollback of the sinking plate contributes to a stronger interaction of the mantle flowing to the nascent mantle wedge with fluids from the subducting plate, triggering a higher degree of melting, which is translated into a depletion of Ti, and possibly into an increase in the PGE content in the released melts when compared to typical MORB (Reagan et al., 2010; Shervais et al., 2019). In the Izu-Bonin Mariana (IBM) fore-arc, FAB occur stratigraphically below and <2 Ma older than the associated boninite sequence (Reagan et al., 2010, 2013). In Bou Azzer, intense deformation, alteration and metamorphism obscure the stratigraphy of the volcanic sequence.

Trace elements contents in the studied unaltered chromite cores show patterns very similar to fore-arc chromitites (Fig. 12). Additionally, the magmatic rocks that form the Bou Azzer ophiolitic crustal sequence (gabbroic rocks and undifferentiated volcanic rocks and dikes) show characteristics of a subduction-initiation ophiolite formed in a fore-arc environment (Arenas et al., 2020). Therefore, the origin of the Bou Azzer chromitites is conceptualized within a subduction-initiation ophiolite model (Whattam and Stern, 2011). In this context, chromitites formed in the fore-arc during the early stages of a Neoproterozoic intra-oceanic arc developed ahead the West African Craton margin. Similar studies have also interpreted the formation of chromitite bodies with different compositions in a subduction-initiation geodynamic setting (e.g., Moghadam et al., 2015; Zhang et al., 2016, 2020; Uysal et al., 2018). According to the subduction-initiation model, from early to more mature stages of subduction, melts evolve from FAB to boninites and island arc tholeiites to calc-alkaline arc magmas (Reagan et al., 2010; Whattam and Stern, 2011; Ishizuka et al., 2014; Shervais et al., 2019; Whattam et al., 2020). In this setting, during early stages of intra-oceanic subduction (Fig. 15a) intermediate-Cr chromitites formed from

FAB melts that were generated by initial spreading of oceanic crust and melting of the nascent mantle wedge. At this stage, there is little or no mass transfer from the subducting slab (Fig. 15a; Liu et al., 2019). Later, as subduction proceeded, high-Cr chromitites precipitated from hydrated melts with boninitic affinity that migrate through the mantle wedge in the fore-arc (Fig. 15b; e.g., Shervais, 2001; Dilek and Furnes, 2014; Moghadam et al., 2015).

Our interpretation of the geodynamic setting of formation of the Bou Azzer ophiolite in the fore-arc clearly differs from the recent proposal of a back-arc SSZ setting by Hodel et al. (2020). In the studied North Ait Ahmane ophiolitic sequence (Fig. 1), high-Cr chromitites (Filon 60 deposit) are located in between chromitites with intermediate-Cr composition (Ingujem and Ait Ahmane deposits). This interesting feature can be related to imbrication of the ophiolitic sequence during the obduction onto the WAC passive margin (El Hadi et al., 2010), hence repeating the serpentinized harzburgite sequence as suggested by Arenas et al. (2020) based on its unusual thickness.

6. Concluding remarks

We interpret that the Bou Azzer chromitites formed in a subduction-initiation geodynamic setting with two-stages of evolution, including formation of intermediate-Cr chromitites from fore-arc basalts (FAB) in the early stage and formation of high-Cr chromitites from boninitic melts in the ensuing stage. The studied chromitites are enriched in IPGE with respect to PPGE as observed in the magmatic PGM: Os-poor laurite and Os-Ir alloys. Unusual mineral phases in the studied chromite grains include clinopyroxene lamellae, moissanite, native Cu, diaspore, and zircon, and these were formed during shallow magmatic crystallization or via different stages of post-magmatic alteration related to serpentinization, rather than having UHP origin. Precambrian ophiolitic chromitites are quite rare compared to Phanerozoic ophiolitic chromitites and tend to be richer in Cr, while the PGE content is highly variable and clear trends related to the ophiolites age cannot be defined. The studied chromitites are very similar to Neoproterozoic ophiolitic chromitites of the Arabian-Nubian shield, also related to the Panafrican orogeny.

Declaration of competing interest

The authors declare that they have no known competing financial interests or personal relationships that could have appeared to influence the work reported in this paper

Acknowledgments

This research was financially supported by the Fondo Europeo de Desarrollo Regional (FEDER) Funds, the Spanish Projects CGL2015–65824, RTI2018-099157-A-I00, PID2019-105625RB-C21, and A.RNM.186.UGR18. Additional funding was provided by a FPU-PhD grant to NPS by the “Ministerio de Educación” of the Spanish Government, the Ramón y Cajal Fellowship RYC-2015-17596 to JMGJ, and the Mexican research programs CONACYT-Ciencia Básica A1-S-14574 and UNAM-PAPIIT grant IA-101419 to VC. The help extended by MANAGEMENT mining company is greatly acknowledged. We are also indebted to Thomas Aiglsperger, Lidia Butjosa and Cristina Villanova-de-Benavent for their participation during fieldwork, to Aleu Andreazini for his support during sample preparation, to Xavier Llovet from the Centres Científics i Tecnològics of the Universitat of Barcelona (CCiTUB) for his careful help with EMPA, and to Carlos Ortega-Obregón from the Laboratorio de Estudios Isotópicos of the Centro de Geociencias (UNAM, Mexico) for his help with the LA-ICP-MS analyses on chromite. Ben-Xun Su, one anonymous reviewer, and editors Ibrahim Uysal and Franco Pirajno are deeply acknowledged for their constructive criticism that has helped to improve the manuscript.

Appendix A. Supplementary data

Supplementary data to this article can be found online at <https://doi.org/10.1016/j.oregeorev.2021.104166>.

References

- Abdel Rahman, E.M., Harms, U., Schandelmeyer, H., Franz, G., Darbyshire, D.P.F., Horn, P., Müller-Sohnius, D., 1990. A new ophiolite occurrence in NW Sudan? constraints on Late Proterozoic tectonism. *Terra Nov.* 2, 363–376. <https://doi.org/10.1111/j.1365-3121.1990.tb00088.x>.
- Abuamarah, B.A., 2020. Petrogenetic evolution of Cryogenian Halaban ophiolite, Saudi Arabia: A fragment of fore-arc oceanic lithosphere mantle. *Lithos* 356–357, 105303. <https://doi.org/10.1016/j.lithos.2019.105303>.
- Admou, H., Razin, P., Egal, E., Youbi, N., Soulaïmani, A., Blein, O., Chévrement, P., Gasquet, D., Barbanson, L., Bouabdelli, M., 2013. Notice explicative carte géol. Maroc (1/50 000), feuille d'Aït Ahmane. Notes et Mem. Serv. Geol. Maroc 533.
- Ahmed, A.H., 2007. Diversity of platinum-group minerals in podiform chromitites of the late Proterozoic ophiolite, Eastern Desert, Egypt: Genetic implications. *Ore Geol. Rev.* 32, 1–19. <https://doi.org/10.1016/j.oregeorev.2006.05.008>.
- Ahmed, A.H., 2013. Highly depleted harzburgite-dunite-chromitite complexes from the Neoproterozoic ophiolite, south Eastern Desert, Egypt: A possible recycled upper mantle lithosphere. *Precambrian Res.* 233, 173–192. <https://doi.org/10.1016/j.precamres.2013.05.001>.
- Ahmed, A.H., Arai, S., 2002. Unexpectedly high-PGE chromitite from the deeper mantle section of the northern Oman ophiolite and its tectonic implications. *Contrib. to Mineral. Petrol.* 143, 263–278. <https://doi.org/10.1007/s00410-002-0347-8>.
- Ahmed, A.H., Arai, S., Abdel-Aziz, Y.M., Ikenne, M., Rahimi, A., 2009. Platinum-group elements distribution and spinel composition in podiform chromitites and associated rocks from the upper mantle section of the Neoproterozoic Bou Azzer ophiolite, Anti-Atlas, Morocco. *J. African Earth Sci.* 55, 92–104. <https://doi.org/10.1016/j.jafrearsci.2009.02.005>.
- Ahmed, A.H., Arai, S., Abdel-Aziz, Y.M., Rahimi, A., 2005. Spinel composition as a petrogenetic indicator of the mantle section in the Neoproterozoic Bou Azzer ophiolite, Anti-Atlas, Morocco. *Precambrian Res.* 138, 225–234. <https://doi.org/10.1016/j.precamres.2005.05.004>.
- Ahmed, A.H., Arai, S., Attia, A.K., 2001. Petrological characteristics of podiform chromitites and associated peridotites of the Pan African Proterozoic ophiolite complexes of Egypt. *Miner. Depos.* 36, 72–84. <https://doi.org/10.1007/s001260050287>.
- Ahmed, A.H., Harbi, H.M., Habtoor, A.M., 2012. Compositional variations and tectonic settings of podiform chromitites and associated ultramafic rocks of the Neoproterozoic ophiolite at Wadi Al Hwanet, northwestern Saudi Arabia. *J. Asian Earth Sci.* 56, 118–134. <https://doi.org/10.1016/j.jseas.2012.05.002>.
- Ahmed, Z., Hariri, M.H., 2001. Neoproterozoic Ophiolites as Developed in Saudi Arabia and their Oceanic and Pericontinental Domains. *Arab. J. Sci. Eng.* 33, 17–54.
- Akbulut, M., 2018. Investigation of silicate micro-inclusions from Orhaneli and Harmancik chromitites (NW Turkey) new ultrahigh-pressure evidence from western tethyan ophiolitic chromitites. *Ophioliti* 43, 1–22. <https://doi.org/10.4454/ofioliti.v43i1.453>.
- Ali, K.A., Azer, M.K., Gahlan, H.A., Wilde, S.A., Samuel, M.D., Stern, R.J., 2010. Age constraints on the formation and emplacement of Neoproterozoic ophiolites along the Allaqi-Heiani Suture, South Eastern Desert of Egypt. *Gondwana Res.* 18, 583–595. <https://doi.org/10.1016/j.gr.2010.03.002>.
- Ali, R.A.M., Pitcairn, I.K., Maurice, A.E., Azer, M.K., Bakhit, B.R., Shahien, M.G., 2020. Petrology and geochemistry of ophiolitic ultramafic rocks and chromitites across the Eastern Desert of Egypt: Insights into the composition and nature of a Neoproterozoic mantle and implication for the evolution of SSZ system. *Precambrian Res.* 337, 105565. <https://doi.org/10.1016/j.precamres.2019.105565>.
- Andresen, A., El-Rus, M.A.A., Myhre, P.I., Boghdady, G.Y., Corfu, F., 2009. U-Pb TIMS age constraints on the evolution of the Neoproterozoic Meatiq Gneiss Dome, Eastern Desert, Egypt. *Int. J. Earth Sci.* 98, 481–497. <https://doi.org/10.1007/s00531-007-0276-x>.
- Andrews, D.R.A., Brenan, J.M., 2002. Phase-equilibrium constraints on the magmatic origin of laurite + Ru-Os-Ir alloy. *Can. Mineral.* 40, 1705–1716. <https://doi.org/10.2113/gscanmin.40.6.1705>.
- Arai, S., 1992. Chemistry of chromian spinel in volcanic rocks as a potential guide to magma chemistry. *Mineral. Mag.* 56, 173–184. <https://doi.org/10.1180/minmag.1992.056.383.04>.
- Arai, S., 1994. Characterization of spinel peridotites by olivine-spinel compositional relationships: Review and interpretation. *Chem. Geol.* 113, 191–204. [https://doi.org/10.1016/0009-2541\(94\)90066-3](https://doi.org/10.1016/0009-2541(94)90066-3).
- Arai, S., 2013. Conversion of low-pressure chromitites to ultrahigh-pressure chromitites by deep recycling: A good inference. *Earth Planet. Sci. Lett.* 379, 81–87. <https://doi.org/10.1016/j.epsl.2013.08.006>.
- Arai, S., Ahmed, A.H., 2018. Secular change of chromite concentration processes from the archaic to the phanerozoic. In: *Processes and Ore Deposits of Ultramafic-Mafic Magmas through Space and Time*. Elsevier, pp. 139–157. <https://doi.org/10.1016/B978-0-12-811159-8.00006-8>.
- Arai, S., Miura, M., 2016. Formation and modification of chromitites in the mantle. *Lithos* 264, 277–295. <https://doi.org/10.1016/j.lithos.2016.08.039>.
- Arena, K.R., Hartmann, L.A., Lana, C., 2018. U-Pb-Hf isotopes and trace elements of metasomatic zircon delimit the evolution of neoproterozoic Capané ophiolite in the southern Brasiliano Orogen. *Int. Geol. Rev.* 60, 911–928. <https://doi.org/10.1080/00206814.2017.1355269>.
- Arenas, R., Sánchez Martínez, S., Albert, R., Haissen, F., Fernández-Suárez, J., Pujol-Solà, N., Andonaegui, P., Díez Fernández, R., Proenza, J.A., García-Casco, A., Gerdes, A., 2020. 100 myr cycles of oceanic lithosphere generation in peri-Gondwana: Neoproterozoic–Devonian ophiolites from the NW African–Iberian margin of Gondwana and the Variscan Orogen. *J. Geol. Soc. London, Spec. Publ.* 503, SP503-2020–3. <https://doi.org/10.1144/sp503-2020-3>.
- Augé, T., Joubert, M., Bailly, L., 2012. Typology of mafic-ultramafic complexes in Hoggar, Algeria: Implications for PGE, chromite and base-metal sulphide mineralisation. *J. African Earth Sci.* 63, 32–47. <https://doi.org/10.1016/j.jafrearsci.2011.10.002>.
- Bai, W.J., Zhou, M.F., Robinson, P.T., 1993. Possibly diamond-bearing mantle peridotites and podiform chromitites in the Luobusa and Donqiao ophiolites, Tibet. *Can. J. Earth Sci.* 30, 1650–1659. <https://doi.org/10.1139/e93-143>.
- Bakor, A.R., Gass, I.G., Neary, C.R., 1976. Jabal al Wask, northwest Saudi Arabia: An Eocambrian back-arc ophiolite. *Earth Planet. Sci. Lett.* 30, 1–9. [https://doi.org/10.1016/0012-821X\(76\)90002-9](https://doi.org/10.1016/0012-821X(76)90002-9).
- Ballhaus, C., Helmy, H.M., Fonseca, R.O.C., Wirth, R., Schreiber, A., Jöns, N., 2020. Ultra-reduced phases in ophiolites cannot come from Earth's mantle. *Am. Mineral.* In press.
- Barnes, S.J., Naldrett, A.J., Gorton, M.P., 1985. The origin of the fractionation of platinum-group elements in terrestrial magmas. *Chem. Geol.* 53, 303–323. [https://doi.org/10.1016/0009-2541\(85\)90076-2](https://doi.org/10.1016/0009-2541(85)90076-2).
- Barnes, S.J., Röeder, P.L., 2001. The Range of Spinel Compositions in Terrestrial Mafic and Ultramafic Rocks. *J. Petrol.* 42, 2279–2302. <https://doi.org/10.1093/petrology/42.12.2279>.
- Bindi, L., Zaccarini, F., Ifandi, E., Tsikouras, B., Stanley, C., Garuti, G., Mauro, D., 2020. Grammatikopouloisite, NiVP, a New Phosphide from the Chromitite of the Othrys Ophiolite, Greece. *Minerals* 10, 131. <https://doi.org/10.3390/min10020131>.
- Bockrath, C., Ballhaus, C., Holzheid, A., 2004a. Fractionation of the platinum-group elements during mantle melting. *Science* 305, 1951–1953. <https://doi.org/10.1126/science.1100160>.
- Bockrath, C., Ballhaus, C., Holzheid, A., 2004b. Stabilities of laurite RuS₂ and monosulfide liquid solution at magmatic temperature. *Chem. Geol.* 208 (1–4), 265–271. <https://doi.org/10.1016/j.chemgeo.2004.04.016>.
- Bodinier, J.L., Dupuy, C., Dostal, J., 1984. Geochemistry of Precambrian ophiolites from Bou Azzer, Morocco. *Contrib. to Mineral. Petrol.* 87, 43–50. <https://doi.org/10.1007/BF00371401>.
- Bonavia, F.F., Diella, V., Ferrario, A., 1993. Precambrian podiform chromitites from Kenticha hill, Southern Ethiopia. *Econ. Geol.* 88, 198–202. <https://doi.org/10.2113/gsecongeo.88.1.198>.
- Bousquet, R., El Mamoun, R., Saddiqi, O., Goffé, B., Möller, A., Madi, A., 2008. Mélanges and ophiolites during the Pan-African orogeny: The case of the Bou-Azzer ophiolite suite (Morocco). *Geol. Soc. Spec. Publ.* 297, 233–247. <https://doi.org/10.1144/SP297.11>.
- Brenan, J.M., Andrews, D., 2001. Higher-temperature stability of laurite and Ru-Os-Ir alloy and their role in PGE fractionation in mafic magmas. *Can. Mineral.* 39, 341–360. <https://doi.org/10.2113/gscanmin.39.2.341>.
- Bruce, M.C., Niu, Y., Harbort, T.A., Holcombe, R.J., 2000. Petrological, geochemical and geochronological evidence for a Neoproterozoic ocean basin recorded in the Marlborough terrane of the northern New England Fold Belt. *Aust. J. Earth Sci.* 47, 1053–1064. <https://doi.org/10.1046/j.1440-0952.2000.00833.x>.
- Caby, R., 2003. Terrane assembly and geodynamic evolution of central-western Hoggar: A synthesis. *J. African Earth Sci.* 37, 133–159. <https://doi.org/10.1016/j.jafrearsci.2003.05.003>.
- Castroviejo, R., Rodrigues, J.F., Carrascal, R., Chirif, H., Acosta, J., Uribe, R., 2009. *Mineralogía del Macizo Ultramáfico de Tapo (Cordillera Oriental Andina, Perú)*. *Macfa* 11, 55–56.
- Chaïb, U., Ait Lahna, A., Admou, H., Youbi, N., El Moume, W., Tassinari, C.C.G., Mata, J., Basei, M.A.S., Sato, K., Marzoli, A., Bodinier, J.L., Gärtner, A., Boumehdi, M.A., Bensalah, M.K., Soulaïmani, A., Hefferan, K., Maacha, L., Bajddi, A., 2021. Geochemistry and Geochronology of the Neoproterozoic Backarc Basin Khzama Ophiolite (Anti-Atlas Mountains, Morocco): Tectonomagmatic Implications. *Minerals* 11, 56. <https://doi.org/10.3390/min11010056>.
- Chan, T.K., Finch, I.J., 2001. Determination of platinum-group elements and gold by inductively coupled plasma mass spectrometry. In: *Australian Platinum Conference*. Perth, Western Australia, pp. 1–9.
- Chen, Y., Yang, J., Xu, Z., Tian, Y., Lai, S., 2018. Diamonds and other unusual minerals from peridotites of the Myitkyina ophiolite, Myanmar. *J. Asian Earth Sci.* 164, 179–193. <https://doi.org/10.1016/j.jseas.2018.06.018>.
- Colás, V., González-Jiménez, J.M., Camprubí, A., Proenza, J.A., Griffin, W.L., Fanlo, I., O'Reilly, S.Y., Gervilla, F., González-Partida, E., 2019. A reappraisal of the metamorphic history of the Tehuizingo chromitite, Puebla state, Mexico. *Int. Geol. Rev.* 61, 1706–1727. <https://doi.org/10.1080/00206814.2018.1542633>.
- Colás, V., González-Jiménez, J.M., Griffin, W.L., Fanlo, I., Gervilla, F., O'Reilly, S.Y., Pearson, N.J., Kerestédjian, T., Proenza, J.A., 2014. Fingerprints of metamorphism in chromite: New insights from minor and trace elements. *Chem. Geol.* 389, 137–152. <https://doi.org/10.1016/j.chemgeo.2014.10.001>.
- Colás, V., Padrón-Navarta, J.A., González-Jiménez, J.M., Fanlo, I., Sanchez López-Vizcaíno, V., Castroviejo, R., Gervilla, F., 2017. The role of silica in the hydrous metamorphism of chromite. *Ore Geol. Rev.* 90, 274–286. <https://doi.org/10.1016/j.oregeorev.2017.02.025>.
- Colás, V., Padrón-Navarta, J.A., González-Jiménez, J.M., Griffin, W.L., Fanlo, I., O'Reilly, S.Y., Gervilla, F., Proenza, J.A., Pearson, N.J., Escayola, M.P., 2016. Compositional effects on the solubility of minor and trace elements in oxide spinel

- minerals: Insights from crystal-crystal partition coefficients in chromite exsolution. *Am. Mineral.* 101, 1360–1372. <https://doi.org/10.2138/am-2016-5611>.
- Colás, V., Subías, I., González-Jiménez, J.M., Proenza, J.A., Fanlo, I., Camprubí, A., Griffin, W.L., Gervilla, F., O'Reilly, S.Y., Escayola, M.F., 2020. Metamorphic fingerprints of Fe-rich chromitites from the Eastern Pampean Ranges, Argentina. *Bol. Soc. Geol. Mex.* 72(3), A08042. 10.18268/BSGM2020v72n3a080420.
- Das, S., Basu, A.R., Mukherjee, B.K., 2017. In situ peridotitic diamond in Indus ophiolite sourced from hydrocarbon fluids in the mantle transition zone. *Geology* 45, 755–758. <https://doi.org/10.1130/G39100.1>.
- Dick, H.J.B., Bullen, T., 1984. Chromian spinel as a petrogenetic indicator in abyssal and alpine-type peridotites and spatially associated lavas. *Contrib. to Mineral. Petrol.* 86, 54–76. <https://doi.org/10.1007/BF00373711>.
- Dilek, Y., Furnes, H., 2014. Ophiolites and their origins. *Elements* 10, 93–100. <https://doi.org/10.2113/gselements.10.2.93>.
- El Ghorfi, M., Melcher, F., Oberthür, T., Boukhari, A.E., Maacha, L., Maddi, A., Mhaïli, M., 2007. Platinum group minerals in podiform chromitites of the Bou Azzer ophiolite, Anti Atlas, Central Morocco. *Mineral. Petrol.* 92, 59–80. <https://doi.org/10.1007/s00710-007-0208-2>.
- El Ghorfi, M., Oberthür, T., Melcher, F., Lüders, V., El Boukhari, A., Maacha, L., Ziadi, R., Baoutoul, H., 2006. Gold-palladium mineralization at Bleïda Far West, Bou Azzer-El Graara Inlier, Anti-Atlas, Morocco. *Miner. Depos.* 41, 549–564. <https://doi.org/10.1007/s00126-006-0077-3>.
- El Hadi, H., Simancas, J.F., Martínez-Poyatos, D., Azor, A., Tahiri, A., Montero, P., Fanning, C.M., Bea, F., González-Lodeiro, F., 2010. Structural and geochronological constraints on the evolution of the Bou Azzer Neoproterozoic ophiolite (Anti-Atlas, Morocco). *Precambrian Res.* 182, 1–14. <https://doi.org/10.1016/j.precamres.2010.06.011>.
- Escayola, M.P., Pimentel, M.M., Armstrong, R., 2007. Neoproterozoic backarc basin: Sensitive high-resolution ion microprobe U-Pb and Sm-Nd isotopic evidence from the Eastern Pampean Ranges, Argentina. *Geology* 35, 495–498. <https://doi.org/10.1130/G23549A.1>.
- Evans, B.W., Frost, B.R., 1975. Chrome-spinel in progressive metamorphism—a preliminary analysis. *Geochim. Cosmochim. Acta* 39, 959–972. [https://doi.org/10.1016/0016-7037\(75\)90041-1](https://doi.org/10.1016/0016-7037(75)90041-1).
- Fanlo, I., Gervilla, F., Colás, V., Subías, I., 2015. Zn-, Mn- and Co-rich chromian spinels from the Bou-Azzer mining district (Morocco): Constraints on their relationship with the mineralizing process. *Ore Geol. Rev.* 10.1016/j.oregeorev.2015.05.006.
- Farré-de-Pablo, J., Proenza, J.A., González-Jiménez, J.M., García-Casco, A., Colás, V., Roqué-Rosell, J., Camprubí, A., Sánchez-Navas, A., 2019a. A shallow origin for diamonds in ophiolitic chromitites. *Geology* 47, 75–78. <https://doi.org/10.1130/G45640.1>.
- Farré-de-Pablo, J., Proenza, J.A., González-Jiménez, J.M., García-Casco, A., Colás, V., Roqué-Rosell, J., Camprubí, A., Sánchez-Navas, A., 2019b. Reply to Comment on “A shallow origin for diamonds in ophiolitic chromitites”. *Geology* 47, e477–e478. <https://doi.org/10.1130/G46602Y.1>.
- Finnigan, C.S., Brennan, J.M., Mungall, J.E., McDonough, W.F., 2008. Experiments and Models Bearing on the Role of Chromite as a Collector of Platinum Group Minerals by Local Reduction. *J. Petrol.* 49, 1647–1665. <https://doi.org/10.1093/petrology/egn041>.
- Frost, B.R., Beard, J.S., 2007. On Silica Activity and Serpentinization. *J. Petrol.* 48, 1351–1368. <https://doi.org/10.1093/petrology/egm021>.
- Furnes, H., Dilek, Y., De Wit, M., 2015. Precambrian greenstone sequences represent different ophiolite types. *Gondwana Res.* 27 (2), 649–685. <https://doi.org/10.1016/j.jgr.2013.06.004>.
- Gahlan, H.A., Arai, S., Ahmed, A.H., Ishida, Y., Abdel-Aziz, Y.M., Rahimi, A., 2006. Origin of magnetite veins in serpentinite from the Late Proterozoic Bou-Azzer ophiolite, Anti-Atlas, Morocco: An implication for mobility of iron during serpentinization. *J. African Earth Sci.* 46, 318–330. <https://doi.org/10.1016/j.jafrearsci.2006.06.003>.
- Gale, A., Dalton, C.A., Langmuir, C.H., Su, Y., Schilling, J.G., 2013. The mean composition of ocean ridge basalts. *Geochemistry. Geophys. Geosystems* 14, 489–518. <https://doi.org/10.1029/2012GC004334>.
- García-Casco, A., 2007. Magmatic paragonite in trondhjemites from the Sierra del Convento mélange. *Cuba. Am. Mineral.* 92, 1232–1237. <https://doi.org/10.2138/am.2007.2598>.
- Garuti, G., Zaccarini, F., 1997. In situ alteration of platinum-group minerals at low temperature: evidence from serpentinized and weathered chromitite of the Vourinos complex, Greece. *Can. Mineral.* 35, 611–626.
- Gasquet, D., Ennih, N., Liégeois, J.P., Soulaïmani, A., Michard, A., 2008. The pan-African belt. *Lect. Notes Earth Sci.* 116, 33–64. https://doi.org/10.1007/978-3-540-77076-3_2.
- Gasquet, D., Levrès, G., Cheilletz, A., Azizi-Samir, M.R., Mouttaqi, A., 2005. Contribution to a geodynamic reconstruction of the Anti-Atlas (Morocco) during Pan-African times with the emphasis on inversion tectonics and metallogenic activity at the Precambrian-Cambrian transition. *Precambrian Res.* 140, 157–182. <https://doi.org/10.1016/j.precamres.2005.06.009>.
- Gervilla, F., Padrón-Navarta, J.A., Kerestédjian, T., Sergeeva, I., González-Jiménez, J.M., Fanlo, I., 2012. Formation of ferrian chromite in podiform chromitites from the Golyamo Kamenyane serpentinite, Eastern Rhodopes, SE Bulgaria: A two-stage process. *Contrib. to Mineral. Petrol.* 164, 643–657. <https://doi.org/10.1007/s00410-012-0763-3>.
- Gervilla, F., Proenza, J.A., Frei, R., González-Jiménez, J.M., Garrido, C.J., Melgarejo, J. C., Meibom, A., Díaz-Martínez, R., Lavaut, W., 2005. Distribution of platinum-group elements and Os isotopes in chromite ores from Mayarí-Baracoa Ophiolitic Belt (eastern Cuba). *Contrib. to Mineral. Petrol.* 150, 589–607. <https://doi.org/10.1007/s00410-005-0039-2>.
- González-Jiménez, J.M., Camprubí, A., Colás, V., Griffin, W.L., Proenza, J.A., O'Reilly, S. Y., Centeno-García, E., García-Casco, A., Belousova, E., Talavera, C., Farré-de-Pablo, J., Satsukawa, T., 2017a. The recycling of chromitites in ophiolites from southwestern North America. *Lithos* 294–295, 53–72. <https://doi.org/10.1016/j.lithos.2017.09.020>.
- González-Jiménez, J.M., Gervilla, F., Kerestédjian, T., Proenza, J.A., 2010. Alteration of Platinum-Group and Base-Metal Mineral Assemblages in Ophiolite Chromitites from the Dobromirski Massif, Rhodope Mountains (Bulgaria). *Resour. Geol.* 60, 315–334. <https://doi.org/10.1111/j.1751-3928.2010.00138.x>.
- González-Jiménez, J.M., Griffin, W.L., Gervilla, F., Kerestédjian, T.N., O'Reilly, S.Y., Proenza, J.A., Pearson, N.J., Sergeeva, I., 2012. Metamorphism disturbs the Re-Os signatures of platinum-group minerals in ophiolite chromitites. *Geology* 40, 659–662. <https://doi.org/10.1130/G33064.1>.
- González-Jiménez, J.M., Griffin, W.L., Gervilla, F., Proenza, J.A., O'Reilly, S.Y., Pearson, N.J., 2014a. Chromitites in ophiolites: How, where, when, why? Part I. A review and new ideas on the origin and significance of platinum-group minerals. *Lithos* 189, 127–139. <https://doi.org/10.1016/j.lithos.2013.06.016>.
- González-Jiménez, J.M., Griffin, W.L., Proenza, J.A., Gervilla, F., O'Reilly, S.Y., Akbulut, M., Pearson, N.J., Arai, S., 2014b. Chromitites in ophiolites: How, where, when, why? Part II. The crystallization of chromitites. *Lithos* 189, 140–158. <https://doi.org/10.1016/j.lithos.2013.09.008>.
- González-Jiménez, J.M., Locmelis, M., Belousova, E., Griffin, W.L., Gervilla, F., Kerestédjian, T.N., O'Reilly, S.Y., Pearson, N.J., Sergeeva, I., 2015a. Genesis and tectonic implications of podiform chromitites in the metamorphosed ultramafic massif of Dobromirski (Bulgaria). *Gondwana Res.* 27, 555–574. <https://doi.org/10.1016/j.gr.2013.09.020>.
- González-Jiménez, J.M., Proenza, J.A., Martini, M., Camprubí, A., Griffin, W.L., O'Reilly, S.Y., Pearson, N.J., 2017b. Deposits associated with ultramafic-mafic complexes in Mexico: the Loma Baya case. *Ore Geol. Rev.* 81, 1053–1065. <https://doi.org/10.1016/j.oregeorev.2015.05.014>.
- González-Jiménez, J.M., Reich, M., Camprubí, A., Gervilla, F., Griffin, W.L., Colás, V., O'Reilly, S.Y., Proenza, J.A., Pearson, N.J., Centeno-García, E., 2015b. Thermal metamorphism of mantle chromites and the stability of noble-metal nanoparticles. *Contrib. to Mineral. Petrol.* 170, 1–20. <https://doi.org/10.1007/s00410-015-1169-9>.
- Griffin, W.L., Afonso, J.C., Belousova, E.A., Gain, S.E., Gong, X.-H., González-Jiménez, J. M., Howell, D., Huang, J.-X., McGowan, N., Pearson, N.J., Satsukawa, T., Shi, R., Williams, P., Xiong, Q., Yang, J.-S., Zhang, M., O'Reilly, S.Y., 2016. Mantle Recycling: Transition Zone Metamorphism of Tibetan Ophiolitic Peridotites and its Tectonic Implications. *J. Petrol.* 57, 655–684. <https://doi.org/10.1093/petrology/egw011>.
- Habtoor, A.M., Ahmed, A.H., Akizawa, N., Harbi, H., Arai, S., 2017. Chemical homogeneity of high-Cr chromitites as indicator for widespread invasion of boninitic melt in mantle peridotite of Bir Tuluha ophiolite, Northern Arabian Shield. *Saudi Arabia. Ore Geol. Rev.* 90, 243–259. <https://doi.org/10.1016/j.oregeorev.2017.03.010>.
- Hackspacher, P.C., Dantas, E.L., Spoladore, A., Hutcheson Fetter, A., Fario de Oliveira, M.A., 2000. Evidence of Neoproterozoic backarc basin development in the Central Ribeira belt, southeastern Brazil: New geochronological and geochemical constraints from de Sao Roque - Açungui groups. *Rev. Bras. Geociências* 30, 110–114.
- Haldar, S.K., 2017. Deposits of Africa. *Platinum-Nickel-Chromium Deposits*. Elsevier 63–96. <https://doi.org/10.1016/b978-0-12-802041-8.00003-1>.
- Hamdy, M.M., Lebda, E.M.M., 2011. Al-compositional variation in ophiolitic chromitites from the south Eastern Desert of Egypt: Petrogenetic implications. *J. Geol. Min. Res.* 3, 232–250.
- Hefferan, K.P., Admou, H., Hilal, R., Karson, J.A., Saquaque, A., Juteau, T., Bohn, M.M., Samson, S.D., Kornprobst, J.M., 2002. Proterozoic blueschist-bearing mélange in the Anti-Atlas mountains, Morocco. *Precambrian Res.* 118, 179–194. [https://doi.org/10.1016/S0301-9268\(02\)00109-2](https://doi.org/10.1016/S0301-9268(02)00109-2).
- Hefferan, K.P., Admou, H., Karson, J.A., Saquaque, A., 2000. Anti-Atlas (Morocco) role in Neoproterozoic Western Gondwana reconstruction. *Precambrian Res.* 103, 89–96. [https://doi.org/10.1016/S0301-9268\(00\)00078-4](https://doi.org/10.1016/S0301-9268(00)00078-4).
- Hefferan, K.P., Karson, J.A., Saquaque, A., 1992. Proterozoic collisional basins in a Pan-African suture zone, Anti-Atlas mountains, Morocco. *Precambrian Res.* 54, 295–319. [https://doi.org/10.1016/0301-9268\(92\)90075-Y](https://doi.org/10.1016/0301-9268(92)90075-Y).
- Hefferan, K.P., Soulaïmani, A., Samson, S.D., Admou, H., Inglis, J., Saquaque, A., Latifa, C., Heywood, N., 2014. A reconsideration of Pan African orogenic cycle in the Anti-Atlas Mountains, Morocco. *J. African Earth Sci.* 98, 34–46. <https://doi.org/10.1016/j.jafrearsci.2014.03.007>.
- Hernández-González, J.S., Butjosa, L., Pujol-Solà, N., Aiglsperger, T., Weber, M., Escayola, M., Ramírez-Cárdenas, C., Blanco-Quintero, I.F., González-Jiménez, J.M., Proenza, J.A., 2020. Petrology and geochemistry of high-Al chromitites from the Medellín Metaharzburgitic Unit (MMU), Colombia. *Bol. Soc. Geol. Mex.* 72, A120620. <https://doi.org/10.18268/BSGM2020v72n3a120620>.
- Hickey, R.L., Frey, F.A., 1982. Geochemical characteristics of boninite series volcanics: implications for their source. *Geochim. Cosmochim. Acta* 46, 2099–2115. [https://doi.org/10.1016/0016-7037\(82\)90188-0](https://doi.org/10.1016/0016-7037(82)90188-0).
- Hodel, F., Macouin, M., Triantafyllou, A., Carlut, J., Berger, J., Rousse, S., Ennih, N., Trindade, R.I.F., 2017. Unusual massive magnetite veins and highly altered Cr-spinels as relics of a Cl-rich acidic hydrothermal event in Neoproterozoic serpentinites (Bou Azzer ophiolite, Anti-Atlas, Morocco). *Precambrian Res.* 300, 151–167. <https://doi.org/10.1016/j.precamres.2017.08.005>.
- Hodel, F., Triantafyllou, A., Berger, J., Macouin, M., Baele, J.M., Mattielli, N., Monnier, C., Trindade, R.I.F., Ducea, M.N., Chatir, A., Ennih, N., Langlade, J., Poujol, M., 2020. The Moroccan Anti-Atlas ophiolites: Timing and melting processes

- in an intra-oceanic arc-back-arc environment. *Gondwana Res.* 86, 182–202. <https://doi.org/10.1016/j.gr.2020.05.014>.
- Hodel, F., Trindade, R.I.F., Macouin, M., Meira, V.T., Dantas, E.L., Paixão, M.A.P., Rospabé, M., Castro, M.P., Queiroga, G.N., Alkmim, A.R., Lana, C.C., 2019. A Neoproterozoic hyper-extended margin associated with Rodinia's demise and Gondwana's build-up: The Araguaia Belt, central Brazil. *Gondwana Res.* 66, 43–62. <https://doi.org/10.1016/j.gr.2018.08.010>.
- Huang, B., Fu, D., Li, S., Ge, M., Zhou, W., 2016. The age and tectonic implications of the Hegenshan ophiolite in Inner Mongolia. *Acta Petrol. Sin.* 32 (1), 158–176.
- Huang, X., Li, J., Kusky, T.M., Chen, Z., 2004. Microstructures of the Zunhua 2.50 Ga Podiform Chromite, North China Craton and Implications for the Deformation and Rheology of the Archean Oceanic Lithospheric Mantle. *Dev. Precambrian Geol.* 13, 321–337. [https://doi.org/10.1016/S0166-2635\(04\)13010-7](https://doi.org/10.1016/S0166-2635(04)13010-7).
- Ikenne, M., Madi, A., Gasquet, D., Cheilletz, A., Hilal, R., Mortaji, A., Mhali, E., 2005. Petrogenetic significance of podiform chromitites from the Neoproterozoic ophiolitic complex of Bou Azzer (Anti-Atlas, Morocco). *Africa Geosci. Rev.* 12, 131–143.
- Inglis, J.D., D'Lemos, R.S., Samson, S.D., Admou, H., 2005. Geochronological constraints on Late Precambrian intrusion, metamorphism, and tectonism in the Anti-Atlas mountains. *J. Geol.* 113, 439–450. <https://doi.org/10.1086/430242>.
- Inglis, J.D., MacLean, J.S., Samson, S.D., D'Lemos, R.S., Admou, H., Hefferan, K., 2004. A precise U-Pb zircon age for the Bleida granodiorite, Anti-Atlas, Morocco: Implications for the timing of deformation and terrane assembly in the eastern Anti-Atlas. *J. African Earth Sci.* 39, 277–283. <https://doi.org/10.1016/j.jafrearsci.2004.07.041>.
- Irvine, T.N., 1967. Chromian spinel as a petrogenetic indicator: Part 2. Petrologic applications. *Can. J. Earth Sci.* 4, 71–103. <https://doi.org/10.1139/e67-004>.
- Ishizuka, O., Tani, K., Reagan, M.K., 2014. Izu-Bonin-Mariana forearc crust as a modern ophiolite analogue. *Elements* 10, 115–120. <https://doi.org/10.2113/gselements.10.2.115>.
- Jiménez-Franco, A., González-Jiménez, J.M., Roqué, J., Proenza, J.A., Gervilla, F., Nieto, F., 2020. Nanoscale constraints on the in situ transformation of Ru–Os–Ir sulfides to alloys at low temperature. *Ore Geol. Rev.* 124, 103640 <https://doi.org/10.1016/j.oregeorev.2020.103640>.
- Kamenetsky, V.S., Crawford, A.J., Meffre, S., 2001. Factors controlling chemistry of magmatic spinel: An empirical study of associated olivine, Cr-spinel and melt inclusions from primitive rocks. *J. Petrol.* 42, 655–671. <https://doi.org/10.1093/ptrology/42.4.655>.
- Kelemen, P.B., Yogodzinski, G.M., Scholl, D.W., 2004. Along-strike variation in the Aleutian Island Arc: Genesis of high Mg# andesite and implications for continental crust. *Geophysical Monograph Series*. Blackwell Publishing Ltd 223–276. <https://doi.org/10.1029/138GM11>.
- Khain, E.V., Bibikova, E.V., Kröner, A., Zhuravlev, D.Z., Sklyarov, E.V., Fedotova, A.A., Kravchenko-Berezhnoy, I.R., 2002. The most ancient ophiolite of the Central Asian fold belt: U-Pb and Pb-Pb zircon ages for the Dunzhugur Complex, Eastern Sayan, Siberia, and geodynamic implications. *Earth Planet. Sci. Lett.* 199, 311–325. [https://doi.org/10.1016/S0012-821X\(02\)00587-3](https://doi.org/10.1016/S0012-821X(02)00587-3).
- Kiseleva, O., Zhmodik, S., 2017. PGE mineralization and melt composition of chromitites in Proterozoic ophiolite complexes of Eastern Sayan, Southern Siberia. *Geosci. Front.* 8, 721–731. <https://doi.org/10.1016/j.gsf.2016.04.003>.
- Kröner, A., Todt, W., Hussein, I.M., Mansour, M., Rashwan, A.A., 1992. Dating of late Proterozoic ophiolites in Egypt and the Sudan using the single grain zircon evaporation technique. *Precambrian Res.* 59, 15–32. [https://doi.org/10.1016/0301-9268\(92\)90049-T](https://doi.org/10.1016/0301-9268(92)90049-T).
- Kusky, T.M., Li, J., Glass, A., Huang, X.N., 2004a. Origin and emplacement of Archean ophiolites of the central orogenic belt. *North China Craton. Dev. Precambrian Geol.* 13, 223–274. [https://doi.org/10.1016/S0166-2635\(04\)13007-7](https://doi.org/10.1016/S0166-2635(04)13007-7).
- Kusky, T.M., Li, J.H., Raharimahafa, T., Carlson, R.W., 2004b. Re-Os Isotope Chemistry and Geochronology of Chromite from Mantle Podiform Chromites from the Zunhua Ophiolitic Mélange Belt, N. China: Correlation with the Dongwanzi Ophiolite. *Dev. Precambrian Geol.* 13, 275–282. [https://doi.org/10.1016/S0166-2635\(04\)13008-9](https://doi.org/10.1016/S0166-2635(04)13008-9).
- Kusky, T.M., Wang, L., Huang, Y., Robinson, P., Wirth, R., Ning, W., 2019. Deep subduction in the Archean indicated by ultrahigh-pressure polymorphs of chromite and rutile in Archean ophiolitic podiform chromite. In: *Goldschmidt 2019 Abstracts Proceedings*.
- Leblanc, M., 1972. Un complexe ophiolitique dans le Précambrien II de l'Anti-Atlas central : Maroc : description interprétation et position stratigraphique. *Actes Colloq. International. Corrélations Précambrien. Notes Mém. Serv. Géol. Maroc*.
- Leblanc, M., 1975. Ophiolites précambriennes et gîtes arsenies de cobalt : Bou Azzer (Maroc). These Dr. d'Etat, Fac. des Sci. Paris VI, Mem. Cent. Geol. Geophys.
- Leblanc, M., 1976. Proterozoic oceanic crust at Bou Azzer. *Nature* 261, 34–35. <https://doi.org/10.1038/261034a0>.
- Leblanc, M., 1981. The Late Proterozoic Ophiolites of Bou Azzer (Morocco): Evidence for Pan-African Plate Tectonics. *Dev. Precambrian Geol.* 4, 435–451. [https://doi.org/10.1016/S0166-2635\(08\)70022-7](https://doi.org/10.1016/S0166-2635(08)70022-7).
- Leblanc, M., Lancelot, J.R., 1980. Interprétation géodynamique du domaine pan-africain (Précambrien terminal) de l'Anti-Atlas (Maroc) à partir de données géologiques et géochronologiques. *Can. J. Earth Sci.* 17, 142–155. <https://doi.org/10.1139/e80-012>.
- Leblanc, M., Lbouabi, M., 1988. Native silver mineralization along a rodingite tectonic contact between serpentinite and quartz diorite (Bou Azzer, Morocco). *Econ. Geol.* 83, 1379–1391. <https://doi.org/10.2113/econgeo.83.7.1379>.
- Leblanc, M., Nicolas, A., 1992. Ophiolitic Chromitites. *Int. Geol. Rev.* 34, 653–686. <https://doi.org/10.1080/00206819209465629>.
- Lian, D., Yang, J., Dilek, Y., Wu, W., Zhang, Z., Xiong, F., Liu, F., Zhou, W., 2017. Deep mantle origin and ultra-reducing conditions in podiform chromitite: Diamond, moissanite, and other unusual minerals in podiform chromitites from the Pozanti-Karsanti ophiolite, southern Turkey. *Am. Mineral.* 102, 1101–1113. <https://doi.org/10.2138/am-2017-5850>.
- Liipo, J., 1999. Platinum-group minerals from the Paleoproterozoic chromitite, Outokumpu ophiolite complex, eastern Finland. *Ofoliti* 22 (2), 119–215. <https://doi.org/10.4454/ofoliti.v24i2.102>.
- Liipo, J., Vuollo, J., Nykänen, V., Piirainen, T., Pekkarinen, L., Tuokko, I., 1995. Chromites from the early Proterozoic Outokumpu-Jormua Ophiolite Belt: a comparison with chromites from Mesozoic ophiolites. *Lithos* 36, 15–27. [https://doi.org/10.1016/0024-4937\(95\)00002-W](https://doi.org/10.1016/0024-4937(95)00002-W).
- Liu, X., Su, B.X., Bai, Y., Robinson, P.T., Tang, X., Xiao, Y., Xue, D.-S., Cui, M.-M., 2020. Genesis of "silicate exsolution lamellae" in chromite of the Stillwater complex: A challenge to the high-pressure crystallization of ophiolitic chromitite. *Lithos* 378–379, 105796. <https://doi.org/10.1016/j.lithos.2020.105796>.
- Liu, X., Su, B.X., Xiao, Y., Chen, C., Uysal, I., Jing, J.J., Zhang, P.F., Chu, Y., Lin, W., Asamoah Sakyi, P., 2019. Initial subduction of Neo-Tethyan ocean: Geochemical records in chromite and mineral inclusions in the Pozanti-Karsanti ophiolite, southern Turkey. *Ore Geol. Rev.* 110, 102926 <https://doi.org/10.1016/j.oregeorev.2019.05.012>.
- Lorand, J.P., Pattou, L., Gros, M., 1999. Fractionation of Platinum-group Elements and Gold in the Upper Mantle: a Detailed Study in Pyrenean Orogenic Lherzolites. *J. Petrol.* 40, 957–981. <https://doi.org/10.1093/ptrology/40.6.957>.
- Malitch, K.N., Melcher, F., Mühlhans, H., 2001. Palladium and gold mineralization in podiform chromitite at Kraubath, Austria. *Mineral. Petrol.* 73, 247–277. <https://doi.org/10.1007/s007100170002>.
- Marques, J., Roisenberg, A., Jost, H., Frantz, J.C., Dos, R., Teixeira, S., 2003. Geologia e geoquímica das rochas metaltramáficas da antiforme Capané, suite metamórfica Porongos. *RS. Rev. Bras. Geociências* 33, 83–94.
- Maurel, C., Maurel, P., 1982. Étude expérimentale de la distribution de l'aluminium entre bain silicaté basique et spinelle chromifère. Implications petrogenétiques: teneur en chrome des spinelles. *Bull. Mineral.* 105, 197–202. <https://doi.org/10.3406/bulmi.1982.7605>.
- McGowan, N.M., Griffin, W.L., González-Jiménez, J.M., Belousova, E., Afonso, J.C., Shi, R., McCammon, C.A., Pearson, N.J., O'Reilly, S.Y., 2015. Tibetan chromitites: Excavating the slab graveyard. *Geology* 43, 179–182. <https://doi.org/10.1130/G36245.1>.
- Michard, A., Soulaïmani, A., Hoepffner, C., Ouanaïmi, H., Baïdder, L., Rjimat, E.C., Saddiqi, O., 2010. The South-Western Branch of the Variscan Belt: Evidence from Morocco. *Tectonophysics* 492 (1–4), 1–24. <https://doi.org/10.1016/j.tecto.2010.05.021>.
- Miura, M., Arai, S., Ahmed, A.H., Mizukami, T., Okuno, M., Yamamoto, S., 2012. Podiform chromitite classification revisited: A comparison of discordant and concordant chromitite pods from Wadi Hilti, northern Oman ophiolite. *J. Asian Earth Sci.* 59, 52–61. <https://doi.org/10.1016/j.jseaes.2012.05.008>.
- Moghadam, H.S., Khedr, M.Z., Arai, S., Stern, R.J., Ghorbani, G., Tamura, A., Ottley, C.J., 2015. Arc-related harzburgite-dunite-chromitite complexes in the mantle section of the Sabzevar ophiolite, Iran: A model for formation of podiform chromitites. *Gondwana Res.* 27, 575–593. <https://doi.org/10.1016/j.gr.2013.09.007>.
- Mubarak, H.S., Azer, M.K., Surour, A.A., Moussa, H.E., Asimow, P.D., Kabesh, M.M.L., 2020. Mineralogical and geochemical study of rodingites and associated serpentized peridotite, Eastern Desert of Egypt. *Arabian-Nubian Shield. Lithos* 374–375, 105720. <https://doi.org/10.1016/j.lithos.2020.105720>.
- Mungall, J.E., 2005. Magmatic geochemistry of the platinum-group elements. In: *Exploration from Platinum-Group Elements Deposits*. Mungall, J.E. (Ed.), Short Course Series — Mineralogical Association of Canada. pp. 1–34.
- Naidoo, D.D., Bloomer, S.H., Saquaque, A., Hefferan, K., 1991. Geochemistry and significance of metavolcanic rocks from the Bou Azzer-El Graara ophiolite (Morocco). *Precambrian Res.* 53, 79–97. [https://doi.org/10.1016/0301-9268\(91\)90006-V](https://doi.org/10.1016/0301-9268(91)90006-V).
- Naldrett, A.J., Duke, J.M., 1980. Platinum metals in magmatic sulfide ores. *Science* 208, 1417–1424. <https://doi.org/10.1126/science.208.4451.1417>.
- O'Driscoll, B., González-Jiménez, J.M., 2016. Petrogenesis of the platinum-group minerals. *Rev. Mineral. Geochemistry* 81, 489–578. <https://doi.org/10.2138/rmg.2016.81.09>.
- O'Hara, M.J., Fry, N., Prichard, H.M., 2001. Minor phases as carriers of trace elements in non-modal crystal-liquid separation processes II: Illustrations and bearing on behaviour of REE, U, Th and the PGE in igneous processes. *J. Petrol.* 42, 1887–1910. <https://doi.org/10.1093/ptrology/42.10.1887>.
- Oliveira, E.P., Escayola, M., Souza, Z.S., Bueno, J.F., De Souza, Glaucus, Araújo, M., Mcnaughton, N., 2007. The Santa Luz chromite-periodotite and associated mafic dykes, Bahia-Bra-zil: remnants of a transitional-type ophiolite related to the paleoproterozoic (>2.1 Ga) Rio Itapicuru greenstone belt? *Rev. Bras. Geociências* 37, 894–905.
- Pagé, P., Barnes, S.J., 2009. Using Trace Elements in Chromites to Constrain the Origin of Podiform Chromitites in the Thetford Mines Ophiolite, Quebec. *Canada. Econ. Geol.* 104, 997–1018. <https://doi.org/10.2113/econgeo.104.7.997>.
- Paixão, M.A.P., 2009. *Complexo ofiolítico Quatipuru, Pará, Brazil. PhD Thesis. Universidade de Brasília, Brasília (DF)*.
- Paixão, M.A.P., Nilson, A.A., Dantas, E.L., 2008. The neoproterozoic quatipuru ophiolite and the Araguaia fold belt, central-northern Brazil, compared with correlatives in NW Africa. *Geol. Soc. London. Spec. Publ.* 294, 297–318. <https://doi.org/10.1144/SP294.16>.
- Pallister, J.S., Stacey, J.S., Fischer, L.B., Premo, W.R., 1988. Precambrian ophiolites of Arabia: geologic settings, U/Pb geochronology, Pb-isotope characteristics, and implications for continental accretion. *Precambrian Res.* 38, 1–54. [https://doi.org/10.1016/0301-9268\(88\)90092-7](https://doi.org/10.1016/0301-9268(88)90092-7).

- Pandey, D.K., Pandey, A., Whattam, S.A., 2019. Relict subduction initiation along a passive margin in the northwest Indian Ocean. *Nat. Commun.* 10, 1–10. <https://doi.org/10.1038/s41467-019-10227-8>.
- Peltonen, P., Kontinen, A., Huhma, H., Kuronen, U., 2008. Outokumpu revisited: New mineral deposit model for the mantle peridotite-associated Cu-Co-Zn-Ni-Ag-Au sulphide deposits. *Ore Geol. Rev.* 33, 559–617. <https://doi.org/10.1016/j.oregeorev.2007.07.002>.
- Peng, S., Kusky, T.M., Jiang, X.F., Wang, L., Wang, J.P., Deng, H., 2012. Geology, geochemistry, and geochronology of the Miaowan ophiolite, Yangtze craton: Implications for South China's amalgamation history with the Rodinian supercontinent. *Gondwana Res.* 21, 577–594. <https://doi.org/10.1016/j.gr.2011.07.010>.
- Prichard, H.M., Lord, R.A., Neary, C.R., 1996. A model to explain the occurrence of platinum- and palladium-rich ophiolite complexes. *J. Geol. Soc. London.* 153, 323–328. <https://doi.org/10.1144/gsjgs.153.2.0323>.
- Prichard, H.M., Neary, C.R., Fisher, P.C., O'Hara, M.J., 2008. PGE-rich podiform chromitites in the Al 'Ays ophiolite complex, Saudi Arabia: An example of critical mantle melting to extract and concentrate PGE. *Econ. Geol.* 103, 1507–1529. <https://doi.org/10.2113/gsecongeo.103.7.1507>.
- Proenza, J.A., Escayola, M., María González-Jiménez, J., Jackson, S., 2011. Discriminación de Cromititas Ophiolíticas a Partir de Elementos Menores y Trazas: un Estudio Mediante LA-ICP-MS. *Macla* 15, 169–170.
- Proenza, J.A., González-Jiménez, J.M., García-Casco, A., Belousova, E., Griffin, W.L., Talavera, C., Rojas-Agramonte, Y., Aiglsperger, T., Navarro-Ciurana, D., Pujol-Solà, N., Gervilla, F., O'Reilly, S., Jacob, D.E., 2018. Cold plumes trigger contamination of oceanic mantle wedges with continental crust-derived sediments: Evidence from chromitite zircon grains of eastern Cuban ophiolites. *Geosci. Front.* 9, 1921–1936. <https://doi.org/10.1016/j.gsf.2017.12.005>.
- Proenza, J.A., Ortega-Gutiérrez, F., Camprubí, A., Tritilla, J., Elías-Herrera, M., Reyes-Salas, M., 2004. Paleozoic serpentinite-enclosed chromitites from Tehuizingo (Acatlán Complex, southern Mexico): A petrological and mineralogical study. *J. South Am. Earth Sci.* 16, 649–666. <https://doi.org/10.1016/j.jsames.2003.12.003>.
- Proenza, J.A., Zaccarini, F., Escayola, M., Cábana, C., Schalamuk, A., Garuti, G., 2008. Composition and textures of chromite and platinum-group minerals in chromitites of the western ophiolitic belt from Pampean Ranges of Córdoba, Argentina. *Ore Geol. Rev.* 33, 32–48. <https://doi.org/10.1016/j.oregeorev.2006.05.009>.
- Proenza, J.A., Zaccarini, F., Lewis, J.F., Longo, F., Garuti, G., 2007. Chromian spinel composition and the platinum-group minerals of the PGE-rich Loma peguera chromitites, Loma Caribe peridotite, Dominican Republic. *Can. Mineral.* 45, 631–648. <https://doi.org/10.2113/gscanmin.45.3.631>.
- Pujol-Solà, N., García-Casco, A., Proenza, J.A., González-Jiménez, J.M., del Campo, A., Colás, V., Canals, A., Sánchez-Navas, A., Roqué-Rossell, J., 2020a. Diamond forms during low pressure serpentinisation of oceanic lithosphere. *Geochem. Persp. Lett.* 15, 19–24. <https://doi.org/10.7185/geochemlet.2029>.
- Pujol-Solà, N., Proenza, J.A., García-Casco, A., González-Jiménez, J., Andreazini, A., Melgarejo, J., Gervilla, F., 2018. An Alternative Scenario on the Origin of Ultra-High Pressure (UHP) and Super-Reduced (SuR) Minerals in Ophiolitic Chromitites: A Case Study from the Mercedita Deposit (Eastern Cuba). *Minerals* 8, 433. <https://doi.org/10.3390/min8100433>.
- Pujol-Solà, N., Proenza, J.A., García-Casco, A., González-Jiménez, J.M., Román-Alpiste, M.J., Garrido, C.J., Melgarejo, J.C., Gervilla, F., Llovet, X., 2020b. Fe-Ti-Zr metasomatism in the oceanic mantle due to extreme differentiation of tholeiitic melts (Moa-Baracoa ophiolite, Cuba). *Lithos* 358–359, 105420. <https://doi.org/10.1016/j.lithos.2020.105420>.
- Purvis, A.C., Nesbitt, R.W., Hallberg, J.A., 1972. The geology of part of the Carr Boyd rocks complex and its associated nickel mineralization, Western Australia. *Econ. Geol.* 67, 1093–1113. <https://doi.org/10.2113/gsecongeo.67.8.1093>.
- Reagan, M.K., Ishizuka, O., Stern, R.J., Kelley, K.A., Ohara, Y., Blichert-Toft, J., Bloomer, S.H., Cash, J., Fryer, P., Hanan, B.B., Hickey-Vargas, R., Ishii, T., Kimura, J. I., Peate, D.W., Rowe, M.C., Woods, M., 2010. Fore-arc basalts and subduction initiation in the Izu-Bonin-Mariana system. *Geochemistry, Geophys. Geosystems* 11. <https://doi.org/10.1029/2009GC002871>.
- Reagan, M.K., McClelland, W.C., Girard, G., Goff, K.R., Peate, D.W., Ohara, Y., Stern, R. J., 2013. The geology of the southern Mariana fore-arc crust: Implications for the scale of Eocene volcanism in the western Pacific. *Earth Planet. Sci. Lett.* 380, 41. <https://doi.org/10.1016/j.epsl.2013.08.013>.
- Robinson, P.T., Trumbull, R.B., Schmitt, A., Yang, J.S., Li, J.W., Zhou, M.F., Erzinger, J., Dare, S., Xiong, F., 2015. The origin and significance of crustal minerals in ophiolitic chromitites and peridotites. *Gondwana Res.* 27, 486–506. <https://doi.org/10.1016/j.jgr.2014.06.003>.
- Rojas-Agramonte, Y., García-Casco, A., Kemp, A., Kröner, A., Proenza, J.A., Lázaro, C., Liu, D., 2016. Recycling and transport of continental material through the mantle wedge above subduction zones: A Caribbean example. *Earth Planet. Sci. Lett.* 436, 93–107. <https://doi.org/10.1016/j.epsl.2015.11.040>.
- Rollinson, H., 2008. The geochemistry of mantle chromitites from the northern part of the Oman ophiolite: Inferred parental melt compositions. *Contrib. to Mineral. Petrol.* 156, 273–288. <https://doi.org/10.1007/s00410-008-0284-2>.
- Saleh, G.M., 2006. The chromite deposits associated with ophiolite complexes. Southeastern Desert, Egypt: Petrological and geochemical characteristics and mineralization. *Chinese J. Geochemistry* 25, 307–317. <https://doi.org/10.1007/s11631-006-0307-5>.
- Saquaque, A., Admou, H., Karson, J., Hefferan, K., Reuber, I., 1989. Precambrian accretionary tectonics in the Bou Azzer-El Graara region, Anti-Atlas, Morocco. *Geology* 17, 1107–1110. [https://doi.org/10.1130/0091-7613\(1989\)0172.3.co;2](https://doi.org/10.1130/0091-7613(1989)0172.3.co;2).
- Shervais, J.W., 2001. Birth, death, and resurrection: The life cycle of suprasubduction zone ophiolites. *Geochemistry, Geophys. Geosystems* 2. [https://doi.org/10.1029/2000GC000080@10.1002/\(ISSN\)1525-2727.GERMI](https://doi.org/10.1029/2000GC000080@10.1002/(ISSN)1525-2727.GERMI).
- Shervais, J.W., Reagan, M., Haugen, E., Almeev, R.R., Pearce, J.A., Prytulak, J., Ryan, J. G., Whattam, S.A., Godard, M., Chapman, T., Li, H., Kurz, W., Nelson, W.R., Heaton, D., Kirchenbaur, M., Shimizu, K., Sakuyama, T., Scott, Y.L., 2019. Magmatic response to subduction initiation: Part 1. Fore-arc basalts of the Izu-Bonin arc from IODP Expedition 352. *Geochemistry, Geophysics, Geosystems* 20, 314–338. <https://doi.org/10.1029/2018GC007731>.
- Soulaimani, A., Jaffal, M., Maacha, L., Kchikach, A., Najine, A., Saidi, A., 2006. Magnetic modelling of the Bou Azzer-El Graara ophiolite (central Anti-Atlas, Morocco). Geodynamic implications of the Panafrican reconstruction. *Comptes Rendus - Geosci.* 338, 153–160. <https://doi.org/10.1016/j.crte.2005.10.001>.
- Soulaimani, A., Ouanaïm, H., Saddiqi, O., Baïdier, L., Michard, A., 2018. The Anti-Atlas Pan-African Belt (Morocco): Overview and pending questions. *Comptes Rendus - Geosci.* 350, 279–288. <https://doi.org/10.1016/j.crte.2018.07.002>.
- Stacey, J.S., Stoeser, D.B., Greenwood, W.R., Fischer, L.B., 1984. U-Pb zircon geochronology and geological evolution of the Halabon - Al Amar region of the eastern Arabian Shield, Kingdom of Saudi Arabia. *J. Geol. Soc. London.* 141, 1043–1055. <https://doi.org/10.1144/gsjgs.141.6.1043>.
- Stowe, C.W., 1994. Compositions and tectonic settings of chromite deposits through time. *Econ. Geol.* 89, 528–546. <https://doi.org/10.2113/gsecongeo.89.3.528>.
- Suita, M.T.D.F., Strieder, A.J., 1996. Cr-spinels from Brazilian mafic-ultramafic complexes: Metamorphic modifications. *Int. Geol. Rev.* 38, 245–267. <https://doi.org/10.1080/00206819709465333>.
- Tassinari, C.C.G., Castroviejo, R., Rodrigues, J.F., Acosta, J., Pereira, E., 2011. A Neoproterozoic age for the chromitite and gabbro of the Tapo ultramafic Massif, Eastern Cordillera, Central Peru and its tectonic implications. *J. South Am. Earth Sci.* 32, 429–437. <https://doi.org/10.1016/j.jsames.2011.03.008>.
- Tassinari, C.C.G., Munhá, J.M.U., Ribeiro, A., Correia, C.T., 2001. Neoproterozoic oceans in the Ribeira belt (southeastern Brazil): The Pirapora do bom Jesus ophiolitic complex. *Episodes* 24, 245–251. <https://doi.org/10.18814/epiugs/2001/v24i4/004>.
- Thalhammer, O.A.R., Prochaska, W., Mühlhans, H.W., 1990. Solid inclusions in chromite-spinels and platinum group element concentrations from the hochgrössen and kraubath ultramafic massifs (Austria) - their relationships to metamorphism and serpentinization. *Contrib. to Mineral. Petrol.* 105, 66–80. <https://doi.org/10.1007/BF00329067>.
- Thomas, R.J., Chevallier, L.P., Gresse, P.G., Harmer, R.E., Eglinton, B.M., Armstrong, R. A., De Beer, C.H., Martini, J.E.J., De Kock, G.S., Macey, P.H., Ingram, B.A., 2002. Precambrian evolution of the Sirwa Window, Anti-Atlas Orogen, Morocco. *Precambrian Res.* 118, 1–57. [https://doi.org/10.1016/S0301-9268\(02\)00075-X](https://doi.org/10.1016/S0301-9268(02)00075-X).
- Thomas, R.J., Fekkak, A., Ennih, N., Errami, E., Loughlin, S.C., Gresse, P.G., Chevallier, L. P., Liégeois, J.P., 2004. A new lithostratigraphic framework for the Anti-Atlas Orogen, Morocco. *J. African Earth Sci.* 39, 217–226. <https://doi.org/10.1016/j.jafrearsci.2004.07.046>.
- Torró, L., Proenza, J.A., Marchesi, C., García-Casco, A., Lewis, J.F., 2017. Petrogenesis of meta-volcanic rocks from the Maimón Formation (Dominican Republic): Geochemical record of the nascent Greater Antilles paleo-arc. *Lithos* 278–281, 255–273. <https://doi.org/10.1016/j.lithos.2017.01.031>.
- Torró, L., Proenza, J.A., Rojas-Agramonte, Y., García-Casco, A., Yang, J.H., Yang, Y.H., 2018. Recycling in the subduction factory: Archaean to Permian zircons in the oceanic Cretaceous Caribbean island-arc (Hispaniola). *Gondwana Res.* 54, 23–37. <https://doi.org/10.1016/j.gr.2017.09.010>.
- Triantafyllou, A., Berger, J., Baelle, J.M., Bruguier, O., Diot, H., Ennih, N., Monnier, C., Plissart, G., Vanduycke, S., Watlet, A., 2018. Intra-oceanic arc growth driven by magmatic and tectonic processes recorded in the Neoproterozoic Bougnane arc complex (Anti-Atlas, Morocco). *Precambrian Res.* 304, 39–63. <https://doi.org/10.1016/j.precamres.2017.10.022>.
- Triantafyllou, A., Berger, J., Baelle, J.M., Mattielli, N., Ducea, M.N., Sterckx, S., Sanson, S., Hodel, F., Ennih, N., 2020. Episodic magmatism during the growth of a Neoproterozoic oceanic arc (Anti-Atlas, Morocco). *Precambrian Res.* 339, 105610. <https://doi.org/10.1016/j.precamres.2020.105610>.
- Uysal, I., Akmaz, R.M., Saka, S., Kapsiotis, A., 2016. Coexistence of compositionally heterogeneous chromitites in the Antalya-Isparta ophiolitic suite, SW Turkey: A record of sequential magmatic processes in the sub-arc lithospheric mantle. *Lithos* 248–251, 160–174. <https://doi.org/10.1016/j.lithos.2016.01.021>.
- Uysal, I., Kapsiotis, A., Akmaz, R.M., Saka, S., Seitz, H.M., 2018. The Guleman ophiolitic chromitites (SE Turkey) and their link to a compositionally evolving mantle source during subduction initiation. *Ore Geol. Rev.* 93, 98–113. <https://doi.org/10.1016/j.oregeorev.2017.12.017>.
- Villeneuve, M., Cornée, J.J., 1994. Structure, evolution and paleogeography of the West African craton and bordering belts during the Neoproterozoic. *Precambrian Res.* 69, 307–326. [https://doi.org/10.1016/0301-9268\(94\)90094-9](https://doi.org/10.1016/0301-9268(94)90094-9).
- Vuollo, J., Liipo, J., Nykanen, V., Piirainen, T., Pekkarinen, L., Tuokko, I., Ekdahl, E., 1995. Early proterozoic podiform chromitite in the Outokumpu Ophiolite complex, Finland. *Econ. Geol.* 90, 445–452. <https://doi.org/10.2113/gsecongeo.90.2.445>.
- Walsh, G.J., Aleinikoff, J.N., Benziane, F., Yazidi, A., Armstrong, T.R., 2002. U-Pb zircon geochronology of the Paleoproterozoic Tagragra de Tata inlier and its Neoproterozoic cover, western Anti-Atlas, Morocco. *Precambrian Res.* 117, 1–20. [https://doi.org/10.1016/S0301-9268\(02\)00044-X](https://doi.org/10.1016/S0301-9268(02)00044-X).
- Walsh, G.J., Benziane, F., Aleinikoff, J.N., Harrison, R.W., Yazidi, A., Burton, W.C., Quick, J.E., Saadane, A., 2012. Neoproterozoic tectonic evolution of the Jebel Saghro and Bou Azzer-El Graara inliers, eastern and central Anti-Atlas, Morocco. *Precambrian Res.* 216–219, 23–62. <https://doi.org/10.1016/j.precamres.2012.06.010>.

- Werle, M., Hartmann, L.A., Queiroga, G.N., Lana, C., Pertille, J., Michelin, C.R.L., Remus, M.V.D., Roberts, M.P., Castro, M.P., Leandro, C.G., Savian, J.F., 2020. Oceanic crust and mantle evidence for the evolution of Tonian-Cryogenian ophiolites, southern Brasiliano Orogen. *Precambrian Res.* 351, 105979 <https://doi.org/10.1016/j.precamres.2020.105979>.
- Whattam, S.A., Shervais, J.W., Reagan, M.K., Coulthard, D.A., Pearce, J.A., Jones, P., Seo, J., Putirka, K., Chapman, T., Heaton, D., Li, H., Nelson, W.R., Shimizu, K., Stern, R.J., 2020. Mineral compositions and thermobarometry of basalts and boninites recovered during IODP Expedition 352 to the Bonin forearc. *Am. Mineral.* 105, 1490–1507. <https://doi.org/10.2138/am-2020-6640>.
- Whattam, S.A., Stern, R.J., 2011. The “subduction initiation rule”: A key for linking ophiolites, intra-oceanic forearcs, and subduction initiation. *Contrib. to Mineral. Petrol.* 162, 1031–1045. <https://doi.org/10.1007/s00410-011-0638-z>.
- Xiong, F., Liu, Z., Kapsiotis, A., Yang, J., Lenaz, D., Robinson, P.T., 2019. Petrogenesis of lherzolites from the Purang ophiolite, Yarlung-Zangbo suture zone, Tibet: origin and significance of ultra-high pressure and other ‘unusual’ minerals in the Neo-Tethyan lithospheric mantle. *Int. Geol. Rev.* 61, 2184–2210. <https://doi.org/10.1080/00206814.2019.1584771>.
- Xiong, F., Yang, J., Robinson, P.T., Dilek, Y., Milushi, I., Xu, X., Zhou, W., Zhang, Z., Rong, H., 2017a. Diamonds Discovered from High-Cr Podiform Chromitites of Bulqiza, Eastern Mirdita Ophiolite, Albania. *Acta Geol. Sin.* 91, 455–468. <https://doi.org/10.1111/1755-6724.13111>.
- Xiong, Q., Griffin, W.L., Huang, J.-X., Gain, S.E.M., Toledo, V., Pearson, N.J., O’Reilly, S. Y., 2017b. Super-reduced mineral assemblages in “ophiolitic” chromitites and peridotites: the view from Mount Carmel. *Eur. J. Mineral.* 29, 557–570. <https://doi.org/10.1127/ejm/2017/0029-2646>.
- Xiong, Q., Henry, H., Griffin, W.L., Zheng, J.-P., Satsukawa, T., Pearson, N.J., O’Reilly, S. Y., 2017c. High- and low-Cr chromitite and dunite in a Tibetan ophiolite: evolution from mature subduction system to incipient forearc in the Neo-Tethyan Ocean. *Contrib. to Mineral. Petrol.* 172, 45. <https://doi.org/10.1007/s00410-017-1364-y>.
- Yamamoto, S., Komiya, T., Hirose, K., Maruyama, S., 2009. Coesite and clinopyroxene exsolution lamellae in chromites: In-situ ultrahigh-pressure evidence from podiform chromitites in the Luobusa ophiolite, southern Tibet. *Lithos* 109, 314–322. <https://doi.org/10.1016/j.lithos.2008.05.003>.
- Yamamoto, S., Komiya, T., Yamamoto, H., Kaneko, Y., Terabayashi, M., Katayama, I., Iizuka, T., Maruyama, S., Yang, J., Kon, Y., Hirata, T., 2013. Recycled crustal zircons from podiform chromitites in the Luobusa ophiolite, southern Tibet. *Isl. Arc* 22, 89–103. <https://doi.org/10.1111/iar.12011>.
- Yang, J., Meng, F., Xu, X., Robinson, P.T., Dilek, Y., Makeyev, A.B., Wirth, R., Wiedenbeck, M., Cliff, J., 2015. Diamonds, native elements and metal alloys from chromitites of the Ray-Iz ophiolite of the Polar Urals. *Gondwana Res.* 27, 459–485. <https://doi.org/10.1016/j.gr.2014.07.004>.
- Yang, J., Xu, X.Z., Li, Y., Li, J.Y., Ba, D.Z., Rong, H., Zhang, Z., 2011. Diamonds recovered from peridotite of the Purang ophiolite in the Yarlung-Zangbo suture of Tibet: A proposal for a new type of diamond occurrence. *Acta Petrol. Sin.* 27, 3171–3178.
- Yang, J.S., Robinson, P.T., Dilek, Y., 2014. Diamonds in ophiolites. *Elements* 10, 127–130. <https://doi.org/10.2113/gselements.10.2.127>.
- Yibas, B., Reimold, W.U., Anhaeusser, C.R., Koerberl, C., 2003. Geochemistry of the mafic rocks of the ophiolitic fold and thrust belts of southern Ethiopia: Constraints on the tectonic regime during the Neoproterozoic (900–700 MA). *Precambrian Res.* 121, 157–183. [https://doi.org/10.1016/S0301-9268\(02\)00197-3](https://doi.org/10.1016/S0301-9268(02)00197-3).
- Zaccarini, F., Bindi, L., Ifandi, E., Grammatikopoulos, T., Stanley, C., Garuti, G., Mauro, D., 2019. Tsikourasite, Mo₃Ni₂P_{1+x} (x < 0.25), a New Phosphide from the Chromitite of the Othrys Ophiolite, Greece. *Minerals* 9, 248. <https://doi.org/10.3390/min9040248>.
- Zaccarini, F., Garuti, G., Proenza, J.A., Campos, L., Thalhammer, O.A.R., Aiglsperger, T., Lewis, J.F., 2011. Chromite and platinum group elements mineralization in the Santa Elena Ultramafic Nappe (Costa Rica): Geodynamic implications. *Geol. Acta* 9, 407–423. <https://doi.org/10.1344/105.000001696>.
- Zaccarini, F., Pushkarev, E., Garuti, G., Kazakov, I., 2016. Platinum-Group Minerals and Other Accessory Phases in Chromite Deposits of the Alapaevsk Ophiolite, Central Urals, Russia. *Minerals* 6, 108. <https://doi.org/10.3390/min6040108>.
- Zhang, P.F., Uysal, I., Zhou, M.F., Su, B.X., Avci, E., 2016. Subduction initiation for the formation of high-Cr chromitites in the Kop ophiolite, NE Turkey. *Lithos* 260, 345–355. <https://doi.org/10.1016/j.lithos.2016.05.025>.
- Zhang, P.F., Zhou, M.F., Yumul Jr, G.P., 2020. Coexistence of high-Al and high-Cr chromite orebodies in the Acoje block of the Zambales ophiolite, Philippines: Evidence for subduction initiation. *Ore Geol. Rev.* 126, 103739 <https://doi.org/10.1016/j.oregeorev.2020.103739>.

Supplementary data

Appendix 1. Analytical techniques.

Electron microprobe analyses (EMPA)

Quantitative analyses of chromite and platinum group minerals (PGM) were performed using a five-channel JEOL JXA-8230 electron microprobe at the *Centres Científics i Tecnològics de la Universitat de Barcelona* (CCiTUB). The analytical conditions were 15 - 20 kV accelerating voltage, 10 - 20 nA beam current, 1 - 2 μm beam diameter, and 10 - 20 s counting time per element, using WDS detectors and XPP matrix correction (Pouchou and Pichoir, 1990). The results for chromite were stoichiometrically recalculated to distinguish FeO and Fe₂O₃ according to the procedure described by Carmichael (1967). The measurements and the calibrations for chromite and PGM analyses were performed using natural and synthetic standards and are shown in Tables A and B.

Table A. Standards used for chromite measurements on EMPA.

Element	Standard	X-ray	Crystal	Channel
Si	Diopside	Ka	TAP	1
Al	Kyanite	Ka	TAP	1
Cr	Cr ₂ O ₃	Ka	PETJ	2
Ti	Rutile	Ka	PETJ	2
Mg	Periclase	Ka	TAPH	3
Co	Co	Ka	LIFH	4
Fe	Fe ₂ O ₃	Ka	LIFH	4
V	V	Ka	LIFH	4
Ni	NiO	Ka	LIFL	5
Zn	Sphalerite	Ka	LIFL	5
Mn	Rhodonite	Ka	LIFL	5

Table B. Standards used for PGM measurements on EMPA.

Element	Standard	X-ray	Crystal	Channel
Ru	Ru	La	PETJ	1
Rh	Rh	La	PETJ	1
Pd	Pd	Lb	PETJ	1
S	Chalcopyrite	Ka	PETJ	2
As	GaAs	Lb	TAPH	3
Cr	Cr ₂ O ₃	Ka	LIFH	4
Fe	Chalcopyrite	Ka	LIFH	4
Co	Co	Ka	LIFH	4
Ni	Ni	Ka	LIFH	4
Cu	Chalcopyrite	Ka	LIFL	5
Pt	Pt	La	LIFL	5
Ir	Ir	La	LIFL	5
Os	Os	La	LIFL	5

Laser ablation inductively coupled plasma mass spectrometry (LA-ICP-MS)

Minor and trace elements in chromite were obtained at the *Laboratorio de Estudios Isotópicos (LEI) del Centro de Geociencias, UNAM (Mexico)* using a Resolution M-50 Excimer laser coupled to a ThermoICap Qc inductively coupled mass spectrometer (ICP-MS). Chromite analyses were focused on the masses ^{45}Sc , ^{47}Ti , ^{51}V , ^{55}Mn , ^{59}Co , ^{60}Ni , ^{66}Zn and ^{71}Ga (Table C), and were conducted using $\sim 44\ \mu\text{m}$ beam diameter, 5 Hz frequency, and fluence of $6\ \text{J}/\text{cm}^2$ during 100 s (40 s for the He gas blank and 60 s on the chromite).

Table C. Results of repeated analyses of the GOR132-G and G15-28 (Mercedita, Cuba) standards by laser ablation ICP-MS and comparison with literature values.

	^{45}Sc (ppm)	^{47}Ti	^{51}V	^{55}Mn	^{59}Co	^{60}Ni	^{66}Zn	^{71}Ga
GOR132-1	34.5	1347	226	1154	104.1	1356	81.7	11.4
GOR132-2	34.3	1340	227	1156	102.0	1330	78.2	11.4
GOR132-3	33.9	1369	227	1138	99.7	1319	88.0	10.5
GOR132-4	34.3	1366	223	1140	99.0	1294	82.6	11.2
GOR132-5	34.1	1416	226	1145	99.8	1290	74.4	11.3
GOR132-6	32.8	1422	218	1140	99.8	1284	79.5	11.0
GOR132-7	33.5	1409	220	1137	99.2	1273	78.0	10.6
Minimum	32.8	1340	218	1137	99.0	1273	74.4	10.5
Maximum	34.5	1422	227	1156	104	1356	88.0	11.4
Mean	33.9	1381	224	1144	101	1307	80.3	11.1
Median	34.1	1369	226	1140	99.8	1294	79.5	11.2
Std. dev.	0.61	33.90	3.59	7.98	1.86	29.48	4.31	0.35
Rel. Dev. (%)	1.79	2.45	1.60	0.70	1.85	2.26	5.37	3.15
Comparison of preferred published value and analyzed value								
Jochum et al. 2006 (LA-ICP-MS)	36.50	1834	214	1193	92.70	1187	76.80	10.40
Diff. publ. value & this study ^a	2.59	452.71	-9.90	48.79	-7.81	-119.57	-3.54	-0.65
Dev. publ. value & this study ^b	7.09	24.68	-4.63	4.09	-8.43	-10.07	-4.61	-6.29
LEI (Mexico)								
G15-28-1	3.65	1128	1010	1162	210	1703	593	53.1
G15-28-2	1.86	1085	977	1138	215	1481	586	51.1
G15-28-3	2.14	1066	970	1119	211	1477	626	49.3
G15-28-4	3.70	976	811	893	169	1248	479	43.9
G15-28-5	3.32	1145	969	1140	207	157	525	52.6
G15-28-6	3.60	1126	954	1137	208	1630	535	51.7
G15-28-7	3.92	1119	964	1130	207	1591	551	52.6
Minimum	1.86	976	811	893	169	1248	479	43.9
Maximum	3.92	1145	1010	1162	215	1703	626	53.1
Mean	3.17	1092	950	1103	204	1531	556	50.6
Median	3.60	1119	969	1137	208	1587	551	51.7
Std. dev.	0.82	58.0	63.9	93.2	15.54	148	49.3	3.22
Rel. Dev. (%)	25.94	5.31	6.72	8.45	7.62	9.67	8.86	6.36
GEMOC (Australia)								
Mean	4.32	1640	935	1041	189	1324	436	50.1
Std. Dev.	1.11	114	30.8	33.4	6.07	136	33	1.85
Rel. Dev. (%)	25.8	6.97	3.29	3.21	3.22	10.3	7.59	3.68
Comparison of analyzed values from GEMOC and from LEI								
Diff. publ. value & this study ^c	1.15	548	-15	-62	-15	-207	-121	0
Dev. publ. value & this study ^d	26.6	33.4	-1.6	-6.0	-8.1	-15.7	-27.7	-1.0
Ratio publ. value & this study ^e	0.6	0.6	0.5	0.5	0.5	0.5	0.4	0.5

Note: Al of the NIST610 glass was used as internal standard

(a) Difference between values published by Jochum et al. (2006) and analyzed values. All values determined by laser ablation

(b) Deviation between values by Jochum et al. (2006) and analyzed values

- (c) Difference between values analyzed at GEMOC (Australia) and at LEI (Mexico). All values determined by laser ablation
(e) Deviation between values analyzed at GEMOC (Australia) and at LEI (Mexico)
(f) Ratio between values analyzed at GEMOC (Australia) and at LEI (Mexico). Ratios similar to 0 indicate good reproducibility and ratios near to ± 1 indicate non-good reproducibility.

The obtained data was processed using the IoliteTM 2.5 software (Paton et al., 2011) and chromium values obtained by electron microprobe were used as internal standard for chromite. The NIST 610 silicate glass (National Institute Standards and Technology; Norman et al., 1996) was used for instrument calibration, the basaltic glass GOR132-G (Jochum et al., 2006) and the in-house secondary standard chromite G15-28 (Mercedita, Cuba) were analyzed as unknowns during each analytical run to check the accuracy and precision of the analyses. The results obtained during the analyses of the of these two standards display very good reproducibility for all elements (-1-33.4 %) (Table C). Additionally, the variations of Zn, Ti and Sc values (-27.7%, 26.6% and 33.4%) (Table C) could be related to its natural origin. All laser ablation data including element concentration, 1 σ errors and detection limits are presented in Appendix 4.

Whole-rock Platinum-group elements

Chromitite samples were analyzed for whole-rock platinum-group elements (PGE) at Genalysis Ltd (Perth, Western Australia) using nickel sulfide fire assay collection with ICP-MS finish following the method described by Chan and Finch (2001). For the analytical procedure, 25 g of sample was fused at 1200°C with a flux containing borax, soda ash, silica, nickel oxide, and sulfur. The nickel sulfide button was dissolved with hydrochloric acid at ~100 °C. The undissolved PGE sulfides and gold were collected on a cellulose nitrate membrane filter and digested with aqua regia in sealed borosilicate test tubes. The solution was diluted with 10% v/v nitric acid and thoroughly mixed. The final solution was analyzed using a Perkin-Elmer Sciex ELAN 6000 ICP-MS. Six calibrating standard solutions were used as standards and samples were spiked with two internal standards for drift monitoring. A certified reference material (South African Reference Material SARM-7) and in-house standards were included in every analysis batch. The measured PGE isotopes were ⁹⁹Ru, ¹⁰¹Ru, ¹⁰²Ru, ¹⁰³Rh, ¹⁰⁵Pd, ¹⁰⁶Pd, ¹⁰⁸Pd, ¹⁸⁹Os, ¹⁹³Ir, ¹⁹⁵Pt, and ¹⁹⁶Pt. The results were corrected for interferences produced by Ni and Cu argides. Detection limits are 1 ppb for Rh and 2 ppb for all other PGE.

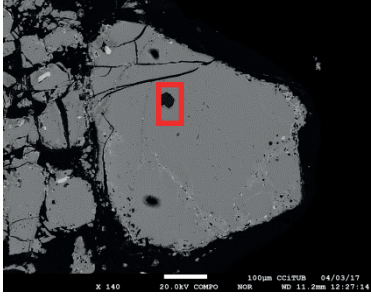
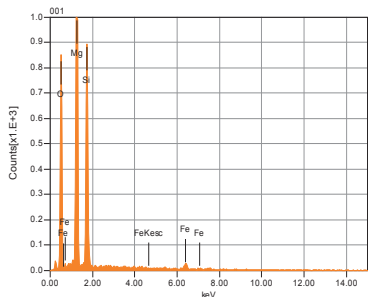
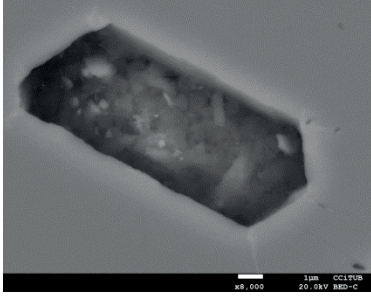
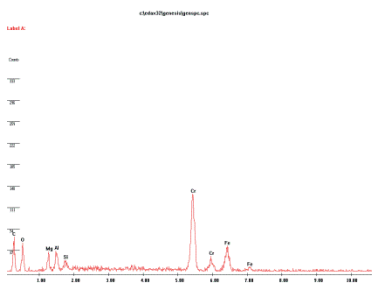
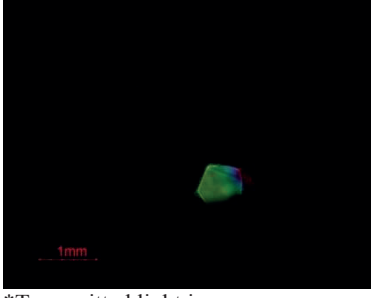
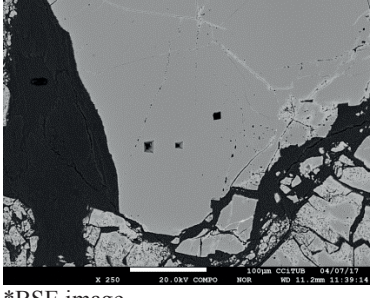
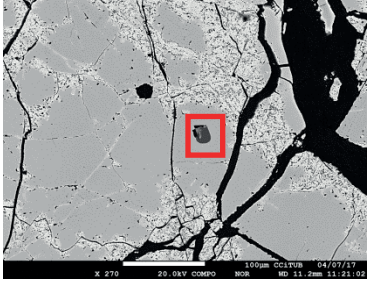
References

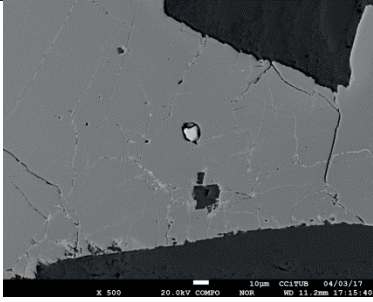

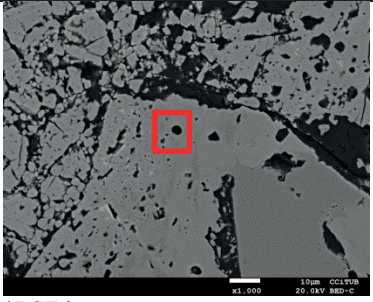
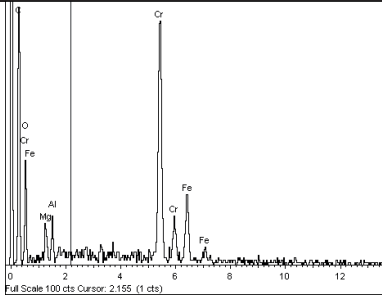
Carmichael, I.S.E., 1967. The mineralogy and petrology of the volcanic rocks from the Leucite Hills, Wyoming. *Contributions to Mineralogy and Petrology* 15, 24–66.

- Chan, T.K., Finch, I.J., 2001. Determination of platinum-group elements and gold by inductively coupled plasma mass spectrometry. In: Australian Platinum Conference, Perth, Western Australia
- Jochum, K.P., Stoll, B., Herwig, K., Willbold, M., Hofmann, A.W., Amini, M., Aarburg, S., Abouchami, W., Hellebrand, E., Mocek, B., Raczek, I., Stracke, A., Alard, O., Bouman, C., Becker, S., Dücking, M., Brätz, H., Klemm, R., de Bruin, D., Canil, D., Cornell, D., de Hoog, C.J., Dalpé, C., Danyushevsky, L.V., Eisenhauer, A., Gao, Y., Snow, J.E., Groschopf, N., Günther, D., Latkoczy, C., Guillong, M., Hauri, E.H., Höfer, H.E., Lahaye, Y., Horz, K., Jacob, D.E., Kasemann, S.A., Kent, A.J.R., Ludwig, T., Zack, T., Mason, P.R.D., Meixner, A., Rosner, M., Misawa, K., Nash, B.P., Pfänder, J., Premo, W.R., Sun, W.D., Tiepolo, M., Vannucci, R., Vennemann, T., Wayne, D., and Woodhead, J.D., 2006, MPI-DING reference glasses for in situ microanalysis: New reference values for element concentrations and isotope ratios: *Geochemistry, Geophysics, Geosystems*, 7 (2), Q02008.
- Norman, M.D., Pearson, N.J., Sharma, A., Griffin, W.L., 1996. Quantitative analysis of trace elements in geological materials by laser ablation ICPMS: instrumental operating conditions and calibration values of NIST glasses. *Geostand. News*. 20 (2), 247-261.
- Paton, C., Hellstrom, J., Paul, B., Woodhead, J., Hergt, J., 2011. Iolite: Freeware for the visualisation and processing of mass spectrometric data. *J. Anal. At. Spectrom.* 26 (12), 2508-2518.
- Pouchou, J.L., Pichoir, F., 1991. Quantitative analysis of homogeneous or stratified microvolumes applying the model "PAP". In: *Electron Probe Quantitation*. Heinrich, K.F.J., Newbury, D.E. (eds.). Springer US, DOI: 10.1007/978-1-4899-2617-3_4

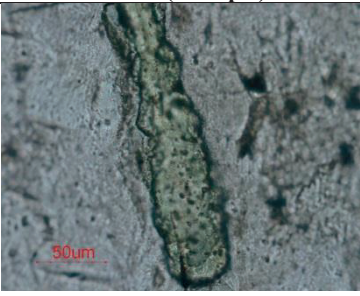
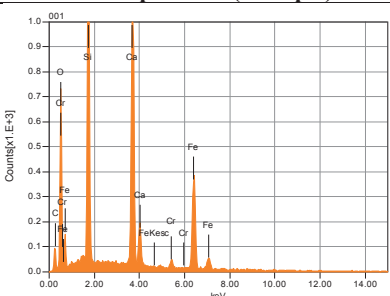
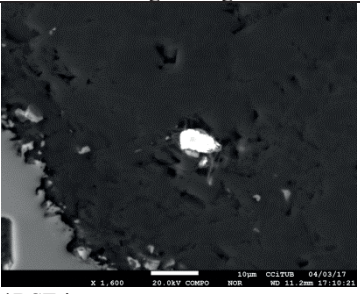
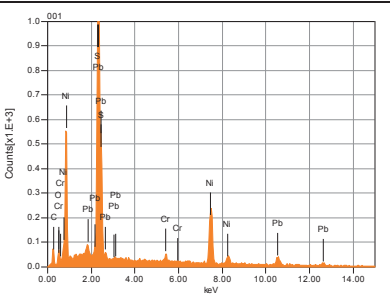
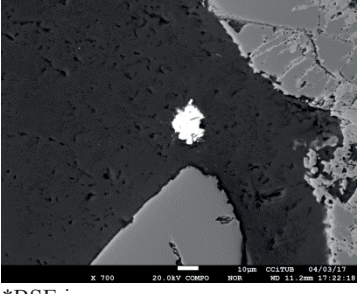
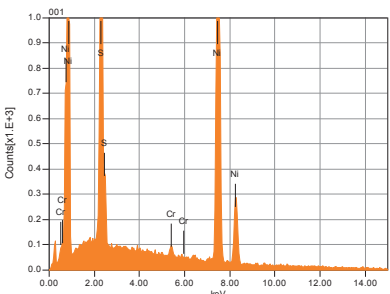
Appendix 2. List and examples of accessory minerals within the Bou Azzer chromitites.

Inclusions within chromite

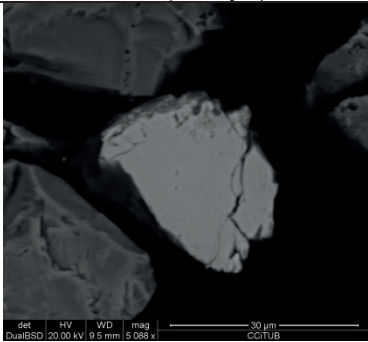
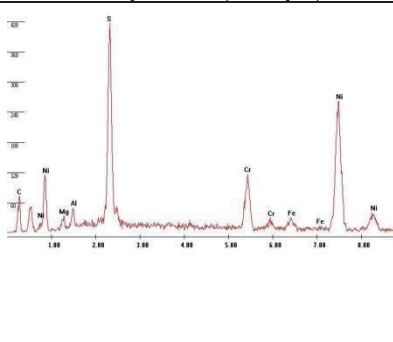
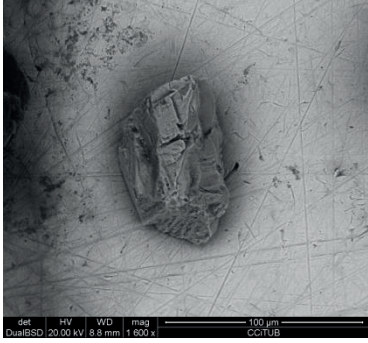
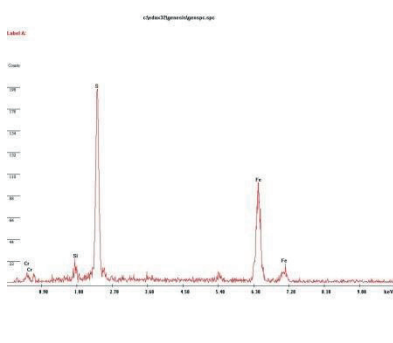
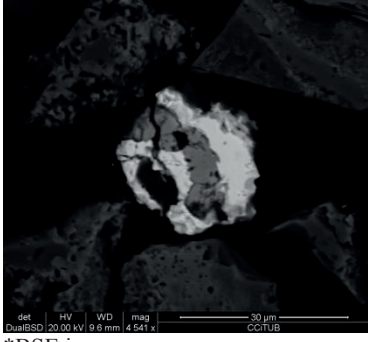
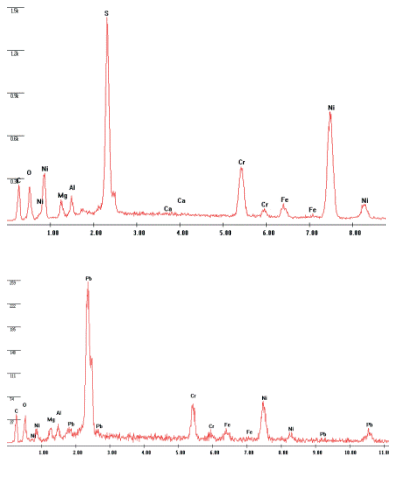
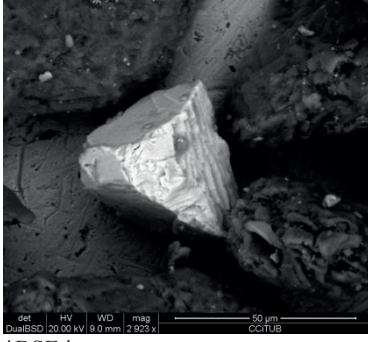
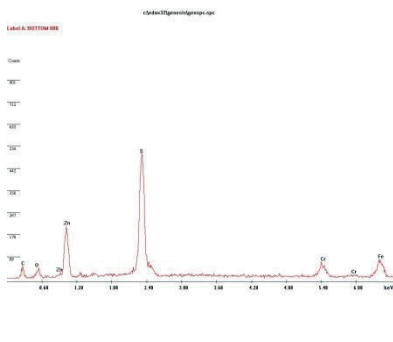
Mineral	Photo (example)	EDS spectrum (example)	Characteristics
Serpentine	 <p>*BSE image</p>		<i>Deposits:</i> Inguijem Filon 60 Ait Ahmane Monophase <i>Size:</i> 30 μm <i>Abundance:</i> +++
Clinochlore	 <p>*BSE image</p>		<i>Deposits:</i> Inguijem Filon 60 Ait Ahmane Monophase <i>Size:</i> 10 μm <i>Abundance:</i> +
Olivine	 <p>*Transmitted light image</p>		<i>Deposits:</i> Ait Ahmane Monophase <i>Size:</i> 60 μm <i>Abundance:</i> +
Negative cubic crystals	 <p>*BSE image</p>		<i>Deposits:</i> Inguijem Monophase <i>Size:</i> 10 μm <i>Abundance:</i> +
Clinopyroxene Clinochlore	 <p>*BSE image</p>		<i>Deposits:</i> Inguijem Polyphase <i>Size:</i> 15 μm <i>Abundance:</i> +

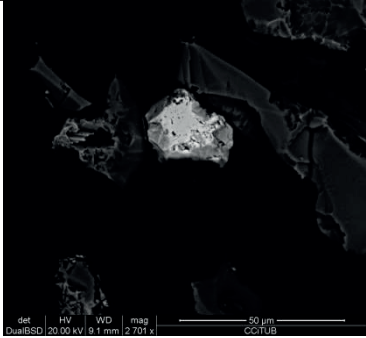
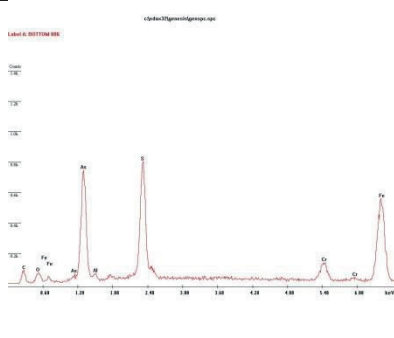

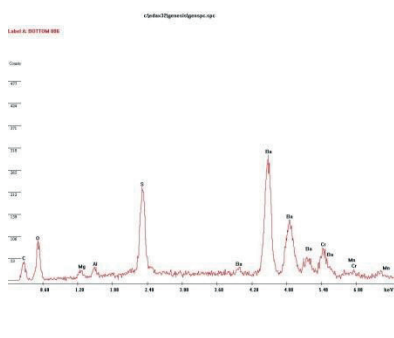
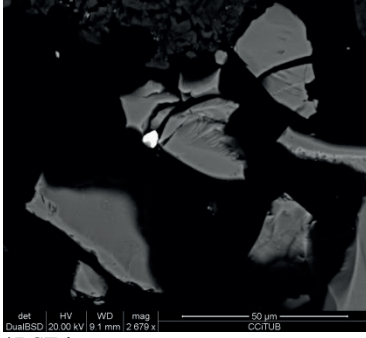
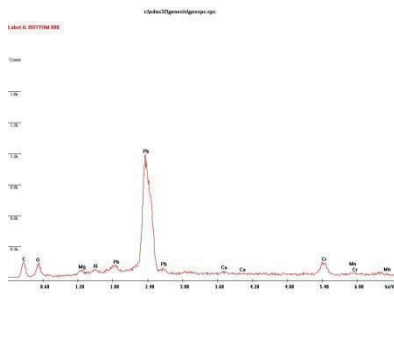
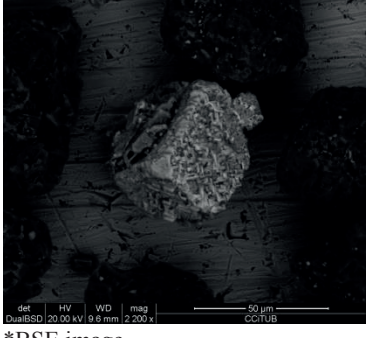
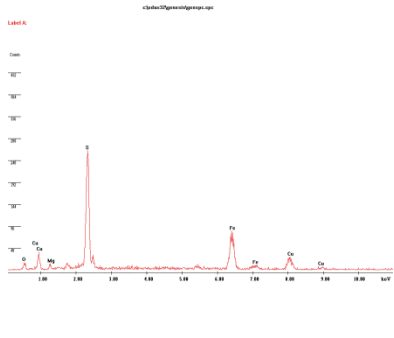
Mineral	Photo (example)	EDS spectrum (example)	Characteristics
Pyrite	 *BSE image		Deposits: Inguijem Monophase Size: 10 µm Abundance: +
Calcite	 *BSE image		Deposits: Inguijem Monophase Size: 3 µm Abundance: ++

Inclusions within the silicate matrix

Mineral	Photo (example)	EDS spectrum (example)	Characteristics
Andradite	 *Transmitted light image		Deposits: Ait Ahmane Monophase Size: <250 µm length Abundance: ++
PbNiS	 *BSE image		Deposits: Inguijem Monophase Size: 8 µm Abundance: +
Millerite	 *BSE image		Deposits: Inguijem Monophase Size: 10 µm Abundance: ++

Minerals recovered in the concentrates

Mineral	Photo (example)	EDS spectrum (example)	Characteristics
Millerite	 <p>*BSE image</p>		<i>Deposits:</i> Inguijem Monophase Size: 20-50 µm Abundance: +++
Pyrite	 <p>*BSE image</p>		<i>Deposits:</i> Inguijem Monophase Size: 60 µm Abundance: ++
Millerite Pb	 <p>*BSE image</p>		<i>Deposits:</i> Inguijem Polyphase Size: 25 µm Abundance: +
Sphalerite	 <p>*BSE image</p>		<i>Deposits:</i> Inguijem Monophase Size: 10 µm Abundance: +

Mineral	Photo (example)	EDS spectrum (example)	Characteristics
Arsenopyrite	 <p>*BSE image</p>		<i>Deposits:</i> Inguijem Monophase <i>Size:</i> 25 µm <i>Abundance:</i> +
Barite	 <p>*BSE image</p>		<i>Deposits:</i> Inguijem Monophase <i>Size:</i> 20 µm <i>Abundance:</i> +
Galena	 <p>*BSE image</p>		<i>Deposits:</i> Inguijem Monophase <i>Size:</i> 10 µm <i>Abundance:</i> +
Chalcopyrite	 <p>*BSE image</p>		<i>Deposits:</i> Inguijem Monophase <i>Size:</i> 40 µm <i>Abundance:</i> +

Appendix 3. EMPA analyses of chromite, altered chromite and hematite from the Bou Azzer chromitites. Abbreviations: chr - chromite, a-chr - altered chromite, hem - hematite, b.d.l. – below detection limit.

Deposit Sample	Filon 60																				
	BA16-11																				
Texture	Massive																				
Analysis	BA16-11 01-1	BA16-11 01-2	BA16-11 01-3	BA16-11 01-4	BA16-11 01-5	BA16-11 03-1	BA16-11 03-2	BA16-11 03-3	BA16-11 03-4	BA16-11 03-5	BA16-11 04-1	BA16-11 04-2	BA16-11 04-3	BA16-11 04-4	BA16-11 04-5	BA16-11 04-6	BA16-11 01-a1	BA16-11 01-a2	BA16-11 01-a3	BA16-11 05 al	
Mineral	chr	chr	chr	chr	chr	chr	chr	chr	chr	chr	chr	chr	chr	chr	chr	chr	chr	chr	a-chr	a-chr	a-chr
SiO ₂	0.02	0.02	0.02	0.04	b.d.l.	0.02	0.02	0.02	0.03	b.d.l.	0.06	0.05	0.05	0.03	0.14	0.03	0.01	0.16	0.06	b.d.l.	
TiO ₂	0.04	0.05	0.09	0.08	0.06	0.11	0.04	0.07	0.07	0.05	0.08	0.04	0.05	0.03	0.07	0.02	b.d.l.	0.15	0.08	0.08	
V ₂ O ₅	0.09	0.11	0.09	0.12	0.10	0.08	0.08	0.09	0.14	0.13	0.12	0.10	0.13	0.10	0.12	0.11	0.12	0.10	0.11	0.09	
Al ₂ O ₃	8.95	8.90	8.64	8.47	8.52	8.76	8.60	8.40	8.57	8.53	8.50	8.54	8.53	8.63	9.67	8.63	8.42	8.66	7.24	8.21	
Cr ₂ O ₃	61.10	61.30	61.29	60.60	61.10	60.68	60.86	61.47	60.76	61.22	61.39	61.58	61.63	61.54	60.41	61.59	61.41	59.34	61.24	61.15	
FeO _T	15.25	14.86	15.44	16.09	15.43	15.22	15.40	15.24	15.51	15.41	14.90	14.71	14.65	14.53	14.43	14.68	14.76	19.49	14.93	14.99	
MnO	13.08	13.38	12.90	12.83	13.03	13.22	13.19	13.08	12.81	13.10	13.11	12.94	13.08	13.15	13.38	13.25	13.39	9.30	13.48	12.98	
CaO	0.04	0.05	0.04	0.04	0.04	0.04	0.04	0.04	0.06	0.01	0.06	0.03	0.04	0.05	0.03	0.05	0.04	0.03	0.08	b.d.l.	
NiO	0.06	0.09	0.09	0.12	0.10	0.10	0.09	0.08	0.09	0.09	0.05	0.06	0.05	0.04	0.06	0.07	0.07	0.07	0.06	0.10	
ZnO	0.07	0.06	0.10	0.04	0.08	0.04	0.06	0.04	0.06	0.04	0.10	0.05	0.09	0.08	0.03	0.08	0.08	0.04	0.05	0.08	
Total	99.02	99.14	99.05	98.83	98.82	98.61	98.74	98.90	98.50	98.88	98.80	98.42	98.65	98.58	98.70	98.84	98.41	95.52	97.50	97.83	
APFU (4 O)																					
Cr	1.582	1.583	1.591	1.577	1.588	1.576	1.580	1.597	1.586	1.589	1.596	1.608	1.605	1.602	1.562	1.598	1.599	1.647	1.614	1.606	
Ti	0.001	0.001	0.002	0.002	0.001	0.003	0.001	0.002	0.002	0.001	0.002	0.001	0.001	0.001	0.002	0.000	0.000	0.001	0.002	0.002	
V	0.001	0.002	0.001	0.002	0.002	0.001	0.001	0.001	0.002	0.002	0.002	0.002	0.002	0.002	0.002	0.002	0.002	0.002	0.002	0.001	
Al	0.346	0.343	0.334	0.329	0.330	0.339	0.333	0.325	0.334	0.330	0.330	0.333	0.331	0.335	0.373	0.334	0.327	0.284	0.285	0.322	
Fe ³⁺	0.067	0.069	0.068	0.086	0.076	0.077	0.082	0.071	0.072	0.074	0.066	0.054	0.057	0.058	0.057	0.063	0.070	0.063	0.093	0.065	
Fe ²⁺	0.350	0.337	0.356	0.357	0.348	0.341	0.341	0.347	0.356	0.349	0.343	0.353	0.346	0.342	0.338	0.339	0.336	0.509	0.323	0.352	
Mn	0.009	0.009	0.010	0.011	0.010	0.010	0.010	0.010	0.011	0.008	0.012	0.009	0.011	0.011	0.010	0.009	0.003	0.002	0.005	0.004	
Mg	0.638	0.651	0.631	0.630	0.638	0.647	0.646	0.641	0.630	0.641	0.643	0.637	0.642	0.645	0.652	0.648	0.657	0.487	0.670	0.643	
Co	0.001	0.001	0.001	0.001	0.001	0.001	0.001	0.001	0.002	0.000	0.002	0.001	0.001	0.001	0.001	0.001	0.001	0.001	0.002	-	
Ni	0.002	0.002	0.002	0.003	0.003	0.003	0.002	0.002	0.002	0.002	0.001	0.002	0.001	0.001	0.001	0.002	0.002	0.002	0.002	0.003	
Zn	0.002	0.001	0.002	0.001	0.002	0.001	0.002	0.001	0.001	0.001	0.002	0.001	0.002	0.002	0.001	0.002	0.002	0.001	0.001	0.002	
Cr#	0.82	0.82	0.83	0.83	0.83	0.82	0.83	0.83	0.83	0.83	0.83	0.83	0.83	0.83	0.81	0.83	0.83	0.85	0.85	0.83	
Mg#	0.65	0.66	0.64	0.64	0.65	0.65	0.65	0.65	0.64	0.65	0.65	0.64	0.65	0.65	0.66	0.66	0.66	0.49	0.67	0.65	
Fe ³⁺ #	0.03	0.03	0.03	0.04	0.04	0.04	0.04	0.04	0.04	0.04	0.03	0.03	0.03	0.03	0.03	0.03	0.04	0.03	0.05	0.03	

Deposit	Filon 60																				
Sample	BA16-11.2								BA16-16												
Texture	Massive								Semi-massive												
Analysis	BA16-11.2_04- chr-03	BA16-11.2_05- chr-02	BA16-11.2_05- chr-04	BA16-11.2_05- a- chr-05	BA16-11.2_05- chr-06	BA16-11.2_05- a- chr-08	BA16-11.2_05- a- chr-09	BA16-11.2_05- chr-11	BA16-11.2_05- a- chr-13	BA16-11.2_05- a- chr-14	BA16-16_01- chr-01	BA16-16_01- chr-02	BA16-16_01- chr-03	BA16-16_01- chr-04	BA16-16_01- chr-05	BA16-16_01- chr-06	BA16-16_01- chr-07	BA16-16_01- chr-09	BA16-16_01- chr-11	BA16-16_02- chr-01	
Mineral	chr	chr	chr	a- chr	chr	a- chr	a- chr	chr	a- chr	a- chr	chr	chr	chr	a- chr	a- chr	a- chr	chr	a- chr	a- chr	chr	
SiO ₂	b.d.l.	0.02	0.02	0.12	0.01	0.89	0.08	b.d.l.	0.11	0.29	b.d.l.	0.01	0.02	0.03	b.d.l.	0.02	0.02	0.02	0.02	0.23	b.d.l.
TiO ₂	0.06	0.04	0.06	0.03	0.04	0.04	0.06	0.06	0.08	0.05	0.10	0.09	0.11	0.03	0.08	0.07	0.11	0.07	0.07	0.00	0.07
V ₂ O ₅	0.10	0.10	0.10	0.10	0.11	0.05	0.10	0.12	0.09	0.11	0.07	0.11	0.06	0.06	0.08	0.11	0.08	0.05	0.04	0.04	0.06
Al ₂ O ₃	8.07	7.78	8.50	3.74	8.63	2.21	2.69	8.32	3.97	4.85	9.23	9.09	9.16	0.45	0.22	0.23	9.28	0.20	1.15	1.15	8.84
Fe ₂ O ₃	62.61	62.98	62.74	61.50	62.97	60.46	61.36	62.61	61.28	59.27	58.42	58.78	58.78	39.83	34.52	31.44	58.54	33.54	53.65	53.65	59.27
FeO _T	15.73	15.43	15.07	20.51	14.43	24.94	25.70	15.21	23.89	24.37	19.73	19.84	20.50	49.70	55.52	58.39	20.12	55.43	34.23	34.23	20.09
MnO	0.28	0.29	0.33	0.49	0.29	0.29	0.39	0.28	0.42	0.33	0.46	0.43	0.44	0.42	0.50	0.46	0.46	0.47	0.77	0.77	0.42
MgO	12.21	12.31	12.39	8.20	12.62	6.05	4.15	12.25	4.75	4.92	9.88	9.91	9.41	2.84	3.43	3.68	9.78	3.46	6.12	6.12	9.44
CoO	0.05	0.03	0.07	0.08	0.03	0.05	0.08	0.05	0.07	0.06	0.09	0.09	0.11	0.12	0.10	0.09	0.08	0.11	0.08	0.10	0.09
NiO	0.05	0.08	0.03	0.09	0.05	0.12	0.09	0.06	0.08	0.15	0.04	0.08	0.01	0.51	0.68	0.72	0.02	0.68	0.10	0.10	0.06
ZnO	0.09	0.08	0.04	0.08	0.06	0.00	0.03	0.05	0.07	0.06	0.15	0.15	0.15	0.09	0.05	0.08	0.13	0.05	0.08	0.10	0.13
Total	99.25	99.14	99.35	94.95	99.24	95.10	94.73	99.01	94.80	94.45	98.17	98.56	98.74	94.09	95.20	95.28	98.61	94.06	96.46	96.46	98.47
APFU (4O)																					
Cr	1.634	1.647	1.632	1.755	1.636	1.776	1.820	1.636	1.798	1.738	1.556	1.561	1.564	1.199	1.019	0.924	1.554	1.002	1.544	1.544	1.583
Ti	0.001	0.001	0.001	0.001	0.001	0.001	0.002	0.002	0.002	0.001	0.003	0.002	0.003	0.001	0.002	0.002	0.003	0.002	0.000	0.000	0.002
V	0.002	0.002	0.002	0.002	0.002	0.001	0.002	0.002	0.002	0.002	0.001	0.002	0.001	0.001	0.002	0.002	0.001	0.001	0.001	0.001	0.001
Al	0.314	0.303	0.330	0.159	0.334	0.097	0.119	0.324	0.174	0.212	0.367	0.360	0.363	0.020	0.010	0.010	0.367	0.009	0.049	0.049	0.001
Fe ³⁺	0.045	0.045	0.032	0.081	0.024	0.123	0.054	0.033	0.021	0.043	0.069	0.071	0.065	0.777	0.963	1.058	0.070	0.984	0.405	0.405	0.352
Fe ²⁺	0.389	0.382	0.382	0.539	0.373	0.653	0.753	0.388	0.721	0.712	0.487	0.487	0.512	0.805	0.772	0.759	0.495	0.768	0.637	0.637	0.508
Mn	0.008	0.008	0.009	0.015	0.008	0.009	0.012	0.008	0.013	0.010	0.013	0.012	0.013	0.014	0.016	0.014	0.013	0.015	0.024	0.024	0.012
Mg	0.601	0.607	0.607	0.441	0.618	0.335	0.232	0.603	0.263	0.272	0.496	0.496	0.472	0.161	0.191	0.204	0.490	0.195	0.332	0.332	0.475
Co	0.001	0.001	0.002	0.002	0.001	0.001	0.002	0.001	0.002	0.002	0.002	0.002	0.003	0.004	0.003	0.003	0.002	0.003	0.002	0.002	0.002
Ni	0.001	0.002	0.001	0.003	0.001	0.004	0.003	0.001	0.002	0.004	0.001	0.002	0.000	0.016	0.021	0.021	0.001	0.021	0.001	0.001	0.002
Zn	0.002	0.002	0.001	0.002	0.001	0.000	0.001	0.001	0.002	0.004	0.004	0.004	0.004	0.003	0.002	0.002	0.002	0.003	0.001	0.002	0.003
Cr#	0.84	0.84	0.83	0.92	0.83	0.95	0.94	0.83	0.91	0.89	0.81	0.81	0.81	0.98	0.99	0.99	0.81	0.99	0.97	0.97	0.82
Mg#	0.61	0.61	0.61	0.45	0.62	0.34	0.24	0.61	0.27	0.28	0.50	0.50	0.48	0.17	0.20	0.21	0.50	0.20	0.34	0.34	0.48
Fe ³⁺ #	0.02	0.02	0.02	0.04	0.01	0.06	0.03	0.02	0.01	0.02	0.03	0.04	0.03	0.39	0.48	0.53	0.04	0.49	0.20	0.20	0.03

Deposit	Filon 60																Ait Ahmane			
Sample	BA16-16																BA16-17A2			
Texture	Semi-massive																Massive			
Analysis	BA16-16.02-a- chr-03	BA16-16.02-a- chr-04	BA16-16.02-a- chr-05	BA16-16.02-a- chr-06	BA16-16.02-a- chr-07	BA16-16.02-a- chr-09	BA16-16.02-a- chr-10	BA16-16.02-a- chr-11	BA16-16.03- chr-01	BA16-16.03- chr-02	BA16-16.03- chr-05	BA16-16.03- chr-06	BA16-16.03-a- chr-07	BA16-16.03-a- chr-08	BA16-16.03-a- chr-09	BA16-16.03- chr-10	BA16-16.03- chr-11	BA16-17A2- 01-1	BA16-17A2-01- 2	BA16-17A2-01- 3
Mineral	a- chr	chr	a- chr	chr	a- chr	chr	chr	a- chr	chr	chr	chr	chr	a- chr	a- chr	a- chr	chr	chr	chr	chr	chr
SiO ₂	0.02	0.02	0.03	b.d.l.	0.09	0.02	0.02	0.72	0.04	0.02	0.02	0.02	0.02	0.02	0.04	b.d.l.	0.04	b.d.l.	0.04	0.01
TiO ₂	0.08	0.08	0.11	0.06	0.09	0.10	0.07	0.11	0.09	0.11	0.13	0.12	0.11	0.05	0.07	0.14	0.13	0.08	0.09	0.11
V ₂ O ₅	0.09	0.11	0.11	0.09	0.04	0.07	0.02	0.12	0.05	0.09	0.09	0.09	0.09	0.05	0.07	0.09	0.09	0.16	0.10	0.23
Al ₂ O ₃	0.23	8.94	0.39	8.44	0.21	8.80	9.58	8.28	9.39	9.76	9.83	9.39	9.83	0.63	0.63	9.96	9.87	20.84	19.69	19.76
Cr ₂ O ₃	28.04	58.93	32.87	59.05	24.25	59.06	57.98	38.59	58.01	58.29	57.56	58.51	36.37	49.85	38.60	56.94	57.35	47.33	46.60	47.23
FeO _t	62.19	20.04	56.42	20.41	64.75	20.00	20.16	48.74	19.72	20.74	20.15	20.32	53.04	39.14	50.12	20.71	20.52	14.23	15.31	13.79
MnO	0.71	0.42	0.48	0.48	0.33	0.43	0.46	2.40	0.45	0.46	0.47	0.44	0.76	1.73	0.87	0.41	0.41	0.23	0.30	0.85
MgO	2.44	9.63	4.06	9.47	3.24	9.66	9.78	3.65	9.72	9.58	9.91	9.90	4.16	4.54	4.43	9.63	9.71	16.31	16.05	17.05
CoO	0.14	0.06	0.12	0.09	0.11	0.10	0.09	0.33	0.10	0.09	0.08	0.08	0.15	0.12	0.11	0.12	0.14	0.05	0.04	0.07
NiO	0.82	0.02	0.69	b.d.l.	1.03	0.03	0.05	0.46	0.06	0.00	0.04	0.03	0.57	0.18	0.49	0.03	0.04	0.21	0.19	0.17
ZnO	0.04	0.14	0.09	0.13	0.05	0.14	0.11	0.14	0.16	0.13	0.17	0.11	0.05	0.22	0.03	0.16	0.16	0.06	0.08	0.06
Total	94.80	98.41	95.36	98.23	94.19	98.42	98.32	95.54	97.79	99.28	98.44	99.00	95.63	96.55	95.49	98.19	98.47	99.50	98.50	99.34
APFU (4 O)																				
Cr	0.835	1.572	0.963	1.582	0.721	1.576	1.541	1.144	1.552	1.537	1.526	1.546	1.064	1.450	1.128	1.514	1.522	1.136	1.135	1.134
Ti	0.002	0.002	0.003	0.001	0.003	0.003	0.002	0.003	0.002	0.003	0.003	0.003	0.003	0.001	0.003	0.004	0.003	0.002	0.002	0.003
V	0.002	0.002	0.002	0.001	0.001	0.001	0.000	0.002	0.001	0.001	0.001	0.001	0.002	0.001	0.001	0.001	0.001	0.001	0.001	0.001
Al	0.010	0.356	0.017	0.337	0.009	0.350	0.380	0.012	0.375	0.384	0.389	0.370	0.014	0.025	0.028	0.395	0.391	0.746	0.715	0.708
Fe ²⁺	1.146	0.064	1.010	0.075	1.263	0.066	0.074	0.832	0.067	0.070	0.076	0.075	0.913	0.520	0.836	0.080	0.078	0.110	0.144	0.146
Fe ³⁺	0.814	0.501	0.739	0.504	0.775	0.498	0.493	0.697	0.491	0.509	0.489	0.493	0.728	0.684	0.714	0.502	0.498	0.252	0.251	0.204
Mn	0.023	0.012	0.015	0.014	0.010	0.012	0.013	0.076	0.013	0.013	0.013	0.012	0.024	0.054	0.027	0.012	0.012	0.006	0.008	0.022
Mg	0.137	0.484	0.224	0.478	0.182	0.486	0.490	0.204	0.490	0.476	0.495	0.493	0.229	0.249	0.244	0.483	0.486	0.738	0.737	0.772
Co	0.004	0.002	0.004	0.003	0.003	0.003	0.002	0.010	0.003	0.004	0.002	0.002	0.004	0.004	0.003	0.003	0.004	0.001	0.001	0.002
Ni	0.025	0.001	0.021	-	0.031	0.001	0.001	0.014	0.002	0.000	0.001	0.001	0.017	0.005	0.015	0.001	0.001	0.005	0.005	0.004
Zn	0.001	0.004	0.003	0.003	0.001	0.003	0.003	0.004	0.004	0.003	0.004	0.003	0.001	0.006	0.001	0.004	0.004	0.001	0.002	0.001
Cr#	0.99	0.82	0.98	0.82	0.99	0.82	0.80	0.99	0.81	0.80	0.80	0.81	0.99	0.98	0.98	0.79	0.80	0.60	0.61	0.62
Mg#	0.14	0.49	0.23	0.49	0.19	0.49	0.50	0.23	0.50	0.48	0.50	0.50	0.24	0.27	0.25	0.49	0.49	0.75	0.75	0.79
Fe ³⁺ #	0.58	0.03	0.51	0.04	0.63	0.03	0.04	0.42	0.03	0.04	0.04	0.04	0.46	0.26	0.42	0.04	0.04	0.06	0.07	0.07

Deposit		Ait Ahmane																				
Sample		BA16-17A2																				
Texture		Massive																				
Analysis	BA16-17A2.01-a- chr-06	BA16-17A2.01- oxide-08	BA16-17A2.02- chr-01	BA16-17A2.02- a- chr-02	BA16-17A2.02- a- chr-001	BA16-17A2.02- a- chr-002	BA16-17A2.02- a- chr-003	BA16-17A2.02- a- chr-004	BA16-17A2.02- a- chr-004	BA16-17A2.02- a- chr-004	BA16-17A2.02- a- chr-005	BA16-17A2.02- a- chr-006	BA16-17A2.02- a- chr-007	BA16-17A2.02- a- chr-008	BA16-17A2.02- a- chr-009	BA16-17A2.02- a- chr-010	BA16-17A2.02- a- chr-011	BA16-17A2.02- a- chr-012	BA16-17A2.02- a- chr-013	BA16-17A2.02- a- chr-014	BA16-17A2.02- a- chr-015	BA16-17A2.03- chr-01
	a- chr	hem	chr	a- chr	a- chr	a- chr	a- chr	a- chr	a- chr	a- chr	a- chr	a- chr	a- chr	a- chr	a- chr	a- chr	a- chr	a- chr	a- chr	a- chr	a- chr	a- chr
SiO ₂	0.03	0.68	b.d.l.	b.d.l.	0.03	b.d.l.	b.d.l.	0.33	0.21	0.02	0.01	0.05	b.d.l.	0.18	1.07	0.02	0.06	0.06	0.06	0.06	0.03	0.01
TiO ₂	0.02	b.d.l.	0.05	0.06	0.07	0.09	0.07	0.07	0.07	0.03	0.11	0.07	0.10	0.12	0.08	0.03	0.08	0.08	0.08	0.08	0.08	0.10
V ₂ O ₅	0.11	0.03	0.15	0.15	0.15	0.15	0.15	0.20	0.16	0.17	0.15	0.20	0.18	0.20	0.12	0.17	0.15	0.18	0.18	0.18	0.18	0.10
Al ₂ O ₃	10.18	0.04	18.46	11.82	15.95	16.34	12.84	18.75	18.75	18.75	18.72	18.59	18.04	16.54	14.73	16.23	16.98	18.05	18.05	18.05	18.77	18.52
Cr ₂ O ₃	57.11	7.03	47.49	54.67	50.06	50.38	49.76	49.76	47.51	48.25	48.16	47.58	48.01	47.96	46.91	50.19	48.38	47.12	47.12	47.12	47.16	47.50
FeO _t	14.22	81.79	14.85	15.72	12.92	12.56	12.47	19.70	12.23	12.19	12.31	12.54	13.39	14.86	15.57	13.22	14.79	15.56	15.56	13.88	13.88	15.36
MnO	2.59	0.16	0.43	1.22	1.75	1.44	4.14	4.14	0.98	0.80	0.80	0.82	1.20	3.74	4.65	1.64	2.04	2.16	2.16	0.81	0.81	0.26
MgO	13.30	0.26	15.43	13.19	15.59	15.90	10.79	10.79	16.10	16.87	16.81	16.63	15.64	12.57	12.81	15.03	13.69	13.34	13.34	15.36	15.36	15.50
CoO	0.04	0.14	0.09	0.09	0.10	0.06	0.11	0.11	0.05	0.04	0.03	0.03	0.08	0.14	0.19	0.11	0.06	0.07	0.06	0.06	0.06	0.05
NiO	0.09	0.16	0.23	0.12	0.14	0.15	0.22	0.22	0.18	0.17	0.18	0.20	0.18	0.19	0.16	0.19	0.19	0.18	0.18	0.17	0.17	0.22
ZnO	0.06	b.d.l.	0.04	0.07	0.20	0.16	0.16	0.16	0.08	0.09	0.08	0.12	0.17	0.28	0.54	0.21	0.21	0.21	0.11	0.11	0.12	0.05
Total	97.75	90.29	97.20	97.12	96.95	97.25	98.28	98.28	96.33	97.38	97.37	96.79	97.01	96.75	96.82	97.05	96.62	96.92	96.92	96.59	96.59	97.71
APFU (4 O)																						
Cr	1.483		1.179	1.419	1.258	1.258	1.296	1.296	1.184	1.184	1.183	1.176	1.195	1.231	1.218	1.264	1.230	1.192	1.192	1.177	1.177	1.174
Ti	0.000		0.001	0.002	0.002	0.002	0.002	0.002	0.002	0.002	0.003	0.002	0.002	0.003	0.002	0.001	0.002	0.002	0.002	0.002	0.002	0.002
V	0.002		0.002	0.002	0.002	0.003	0.002	0.002	0.002	0.003	0.002	0.003	0.003	0.003	0.002	0.003	0.003	0.003	0.003	0.003	0.002	0.002
Al	0.394		0.684	0.458	0.598	0.608	0.499	0.499	0.697	0.686	0.685	0.685	0.670	0.633	0.571	0.609	0.644	0.681	0.681	0.699	0.682	0.682
Fe ³⁺	0.117		0.130	0.115	0.136	0.124	0.197	0.197	0.110	0.123	0.122	0.130	0.124	0.125	0.203	0.120	0.124	0.117	0.116	0.116	0.116	0.134
Fe ²⁺	0.273		0.260	0.317	0.207	0.208	0.346	0.346	0.213	0.193	0.198	0.198	0.228	0.278	0.224	0.232	0.280	0.300	0.300	0.250	0.250	0.267
Mn	0.072		0.011	0.034	0.047	0.039	0.115	0.115	0.026	0.021	0.021	0.022	0.032	0.103	0.129	0.044	0.056	0.059	0.059	0.022	0.022	0.007
Mg	0.651		0.722	0.645	0.738	0.748	0.530	0.530	0.757	0.780	0.778	0.775	0.734	0.608	0.627	0.713	0.656	0.636	0.636	0.723	0.723	0.722
Co	0.001		0.002	0.002	0.002	0.002	0.003	0.003	0.001	0.001	0.001	0.001	0.002	0.004	0.005	0.003	0.001	0.002	0.002	0.001	0.001	0.001
Ni	0.002		0.006	0.003	0.004	0.004	0.006	0.006	0.005	0.004	0.004	0.005	0.004	0.005	0.004	0.005	0.005	0.005	0.005	0.004	0.004	0.005
Zn	0.001		0.001	0.002	0.005	0.004	0.004	0.004	0.002	0.002	0.002	0.003	0.004	0.007	0.013	0.005	0.005	0.005	0.003	0.003	0.003	0.001
Cr#	0.79		0.63	0.76	0.68	0.67	0.72	0.72	0.63	0.63	0.63	0.63	0.64	0.66	0.68	0.67	0.66	0.64	0.64	0.63	0.63	0.63
Mg#	0.70		0.74	0.67	0.78	0.78	0.61	0.61	0.78	0.80	0.80	0.80	0.76	0.69	0.74	0.75	0.70	0.68	0.68	0.74	0.74	0.73
Fe ³⁺ #	0.06		0.07	0.06	0.07	0.06	0.10	0.10	0.06	0.06	0.06	0.07	0.06	0.06	0.10	0.06	0.06	0.06	0.06	0.06	0.06	0.07

Deposit		Ait Ahmane																				
BA16-17A2		BA16-17B1								BA16-17C1												
Sample		Semi-massive																				
Texture		Massive																				
Analysis		BA16-17A2_03-a- chr-02	BA16-17A2_03-a- chr-04	BA16-17A2_03-a- chr-05	BA16-17A2_03-a- chr-07	BA16-17B1_02-1- chr	BA16-17B1_02-2- chr	BA16-17B1_02-3- chr	BA16-17B1_02-4- chr	BA16-17B1_03-1- chr	BA16-17B1_03-2- chr	BA16-17B1_03-3- chr	BA16-17B1_03-4- chr	BA16-17B1_03-5- chr	BA16-17B1_04-1- chr	BA16-17B1_04-2- chr	BA16-17B1_04-3- chr	BA16-17B1_04-4- chr	BA16-17B1_04-5- chr	BA16-17C1_05-1- chr	BA16-17C1_05-2- chr	
Mineral	a- chr	b.d.l.	0.03	0.10	0.02	0.06	0.05	0.02	0.04	0.03	0.04	0.02	0.02	0.02	0.08	0.03	b.d.l.	0.02	0.06	0.01	0.01	0.07
SiO ₂		0.08	0.03	0.06	0.03	0.03	0.04	0.04	0.08	0.10	0.03	0.04	0.02	0.02	0.09	0.03	0.04	0.11	0.04	0.06	0.06	0.07
TiO ₂		0.13	0.19	0.13	0.16	0.16	0.14	0.18	0.15	0.14	0.18	0.14	0.14	0.15	0.11	0.15	0.17	0.14	0.14	0.16	0.16	0.14
V ₂ O ₅		9.78	11.61	10.00	12.86	17.61	17.81	18.36	18.14	18.45	18.60	18.66	18.66	18.23	18.87	18.83	18.27	18.89	18.72	16.23	16.26	16.26
Al ₂ O ₃		58.62	55.68	57.80	54.72	49.26	49.60	48.84	49.22	49.00	49.33	48.97	48.55	49.37	48.60	48.15	49.04	48.89	48.32	48.66	49.25	49.25
Cr ₂ O ₃		15.25	14.62	16.83	14.72	16.43	16.25	15.67	16.23	15.23	15.35	15.43	15.43	15.53	15.35	15.65	15.61	15.22	15.16	18.91	18.52	18.52
FeO _t		1.72	1.62	0.49	1.31	0.30	0.34	0.32	0.30	0.31	0.26	0.28	0.28	0.30	0.32	0.34	0.35	0.32	0.30	0.99	0.74	0.74
MnO		12.88	13.43	12.54	13.96	15.21	14.74	14.97	14.83	15.38	15.40	14.97	14.97	15.59	15.64	16.08	15.11	15.96	15.89	13.34	12.66	12.66
MgO		0.07	0.05	0.05	0.09	0.05	0.06	0.05	0.04	0.04	0.04	0.06	0.06	0.06	0.06	0.05	0.06	0.05	0.06	0.06	0.06	0.06
CoO		0.13	0.10	0.11	0.10	0.11	0.09	0.13	0.09	0.10	0.12	0.13	0.13	0.12	0.14	0.15	0.12	0.12	0.14	0.11	0.08	0.08
NiO		0.09	0.07	0.08	0.22	0.07	0.06	0.05	0.09	0.03	0.04	0.03	0.03	0.01	0.05	0.03	0.05	0.02	0.02	0.07	0.05	0.05
ZnO		98.75	97.50	98.09	98.19	99.28	99.18	98.57	99.20	98.81	99.39	99.14	98.35	99.42	99.30	99.48	98.85	99.74	98.86	98.61	97.90	97.90
Total																						
APFU (4 O)																						
Cr		1.517	1.440	1.507	1.394	1.208	1.221	1.204	1.209	1.202	1.203	1.196	1.197	1.204	1.183	1.166	1.205	1.183	1.179	1.221	1.251	1.251
Ti		0.002	0.002	0.002	0.001	0.001	0.001	0.001	0.002	0.002	0.001	0.003	0.002	0.001	0.002	0.001	0.002	0.001	0.001	0.002	0.002	0.002
V		0.002	0.003	0.002	0.003	0.002	0.002	0.001	0.002	0.002	0.003	0.001	0.002	0.002	0.002	0.002	0.003	0.002	0.002	0.002	0.002	0.002
Al		0.377	0.448	0.389	0.489	0.644	0.654	0.675	0.664	0.675	0.677	0.688	0.686	0.663	0.685	0.680	0.669	0.681	0.681	0.608	0.616	0.616
Fe ³⁺		0.097	0.101	0.097	0.110	0.141	0.118	0.116	0.119	0.115	0.113	0.107	0.108	0.127	0.124	0.147	0.117	0.126	0.133	0.163	0.125	0.125
Fe ²⁺		0.320	0.299	0.367	0.286	0.286	0.305	0.293	0.303	0.281	0.283	0.290	0.294	0.274	0.271	0.254	0.289	0.263	0.258	0.339	0.372	0.372
Mn		0.048	0.045	0.014	0.036	0.008	0.009	0.008	0.008	0.008	0.007	0.008	0.007	0.008	0.008	0.009	0.009	0.008	0.008	0.027	0.020	0.020
Mg		0.628	0.655	0.616	0.670	0.703	0.684	0.695	0.687	0.711	0.708	0.703	0.696	0.717	0.718	0.734	0.700	0.728	0.731	0.631	0.606	0.606
Co		0.002	0.001	0.001	0.002	0.001	0.001	0.001	0.001	0.001	0.001	-	0.001	0.001	0.001	0.001	0.001	0.001	0.001	0.001	0.001	0.001
Ni		0.003	0.003	0.003	0.003	0.003	0.002	0.003	0.002	0.003	0.003	0.002	0.003	0.003	0.003	0.004	0.003	0.003	0.003	0.003	0.003	0.002
Zn		0.002	0.002	0.002	0.005	0.002	0.001	0.001	0.002	0.001	0.001	0.001	0.001	0.000	0.001	0.001	0.001	0.001	0.000	0.001	0.002	0.001
Cr#		0.80	0.76	0.79	0.74	0.65	0.65	0.64	0.65	0.64	0.64	0.63	0.64	0.64	0.63	0.63	0.64	0.63	0.63	0.67	0.67	0.67
Mg#		0.66	0.69	0.63	0.70	0.71	0.69	0.72	0.69	0.72	0.71	0.71	0.70	0.72	0.73	0.74	0.71	0.73	0.74	0.65	0.62	0.62
Fe ³⁺ #		0.05	0.05	0.05	0.06	0.07	0.06	0.06	0.06	0.06	0.06	0.05	0.05	0.06	0.06	0.07	0.06	0.06	0.07	0.08	0.08	0.08

Deposit		Ait Ahmane																		
Sample		BA16-17C1																		
Texture		Semi- massive																		
Analysis	BA16-17C1_05-3	BA16-17C1_05-4	BA16-17C1_05-5	BA16-17C1_07-1	BA16-17C1_07-2	BA16-17C1_07-3	BA16-17C1_07-4	BA16-17C1_07-5	BA16-17C1_07-6	BA16-17C1_07-7	BA16-17C1_07-8	BA16-17C1_07-9	BA16-17C1_07-10	BA16-17C1_01-a1	BA16-17C1_01-a5	BA16-17C1_01-a6	BA16-17C1_04-a1	BA16-17C1_04-a2	BA16-17C1_04-a3	BA16-17C1_04-a5
Mineral	chr	chr	chr	chr	chr	chr	chr	chr	chr	chr	chr	chr	chr	chr	chr	hem	chr	a-chr	hem	a-chr
SiO ₂	0.02	b.d.l.	b.d.l.	0.02	0.04	b.d.l.	0.03	0.08	0.03	0.04	0.01	0.01	0.04	0.03	0.05	b.d.l.	0.04	0.04	0.09	0.02
TiO ₂	0.04	0.05	0.02	0.05	0.07	0.08	0.07	0.06	0.10	0.07	0.06	0.10	0.07	0.06	b.d.l.	0.08	0.02	b.d.l.	0.09	
V ₂ O ₅	0.14	0.18	0.17	0.13	0.16	0.13	0.16	0.16	0.15	0.17	0.16	0.15	0.17	0.14	0.03	0.16	0.09	b.d.l.	0.09	
Al ₂ O ₃	16.52	15.93	16.00	16.76	16.29	16.25	16.06	16.37	16.31	16.41	15.83	16.41	16.41	16.49	0.01	16.18	19.28	0.01	16.13	
Cr ₂ O ₃	48.99	49.12	48.75	48.69	48.40	48.58	48.68	48.34	48.24	48.40	48.40	48.24	48.40	48.56	1.48	49.19	46.45	2.20	48.43	
FeO ^t	17.92	19.12	18.70	19.08	19.16	19.61	19.72	19.19	19.57	19.60	19.47	19.60	19.57	18.54	84.69	18.91	14.64	83.14	18.81	
MnO	1.53	0.81	1.41	0.36	0.41	0.91	0.67	0.60	0.54	0.52	0.35	0.52	0.35	0.96	0.19	0.18	3.11	0.15	1.10	
MgO	13.05	12.51	12.13	13.04	13.05	13.18	13.27	13.29	13.60	13.03	12.98	13.03	13.03	13.29	0.18	13.47	15.61	0.34	13.44	
CoO	0.03	0.07	0.06	0.04	0.10	0.04	0.07	0.04	0.07	0.08	0.10	0.07	0.08	0.14	0.16	0.05	0.11	0.11	0.06	
NiO	0.10	0.08	0.10	0.12	0.11	0.11	0.14	0.12	0.12	0.12	0.14	0.12	0.12	0.16	0.16	0.13	0.17	0.24	0.12	
ZnO	0.12	0.07	0.08	0.06	0.09	0.08	0.06	0.09	0.07	0.04	0.03	0.07	0.04	0.07	b.d.l.	0.05	0.29	0.02	0.04	
Total	98.46	97.91	97.45	98.41	98.79	98.98	98.95	98.32	98.80	98.49	97.53	98.32	98.80	98.30	86.93	98.39	99.81	86.30	98.37	
APFU (4 O)																				
Cr	1.233	1.249	1.248	1.224	1.219	1.216	1.220	1.217	1.206	1.218	1.231	1.222	1.222	1.222		1.237	1.123		1.218	
Ti	0.001	0.001	0.001	0.001	0.001	0.001	0.001	0.001	0.001	0.002	0.001	0.001	0.001	0.001	0.001	0.001	0.001	0.001	0.002	
V	0.002	0.002	0.003	0.002	0.002	0.002	0.003	0.002	0.002	0.003	0.003	0.002	0.002	0.002	0.002	0.002	0.001	0.001	0.002	
Al	0.620	0.604	0.611	0.628	0.625	0.607	0.600	0.615	0.608	0.616	0.601	0.619	0.616	0.601	0.619	0.607	0.695	0.605	0.605	
Fe ³⁺	0.141	0.140	0.134	0.140	0.151	0.168	0.171	0.161	0.176	0.157	0.160	0.157	0.157	0.160	0.153	0.148	0.178	0.169	0.169	
Fe ²⁺	0.336	0.375	0.372	0.368	0.356	0.351	0.352	0.350	0.342	0.365	0.364	0.341	0.341	0.365	0.341	0.355	0.196	0.331	0.331	
Mn	0.041	0.022	0.039	0.010	0.009	0.024	0.018	0.016	0.015	0.014	0.009	0.026	0.026	0.009	0.026	0.005	0.081	0.030	0.030	
Mg	0.619	0.600	0.585	0.620	0.629	0.622	0.627	0.631	0.641	0.618	0.623	0.630	0.630	0.623	0.630	0.638	0.711	0.637	0.637	
Co	0.001	0.002	0.002	0.001	0.002	0.001	0.002	0.001	0.002	0.002	0.003	0.002	0.002	0.003	0.002	0.001	0.003	0.002	0.002	
Ni	0.003	0.002	0.003	0.003	0.003	0.003	0.003	0.003	0.003	0.003	0.004	0.003	0.003	0.003	0.003	0.003	0.004	0.004	0.003	
Zn	0.003	0.002	0.002	0.001	0.002	0.002	0.001	0.002	0.002	0.001	0.001	0.002	0.001	0.002	0.002	0.001	0.007	0.007	0.001	
Cr#	0.67	0.67	0.67	0.66	0.66	0.67	0.67	0.66	0.66	0.66	0.67	0.66	0.66	0.66	0.66	0.67	0.62	0.62	0.67	
Mg#	0.65	0.62	0.61	0.63	0.64	0.64	0.64	0.64	0.65	0.63	0.63	0.65	0.65	0.63	0.65	0.64	0.78	0.78	0.66	
Fe ³⁺ #	0.07	0.07	0.07	0.07	0.08	0.08	0.09	0.08	0.09	0.08	0.08	0.08	0.09	0.08	0.08	0.07	0.09	0.09	0.08	

Deposit	Ingujimet																				
	15-FH-113-I								15-FH-113-V												
Sample	Massive																				
Texture	Massive																				
Analysis	15-FH-113-I_03-4	15-FH-113-I_03-5	15-FH-113-I_03-6	15-FH-113-I_03-7	15-FH-113-I_03-9	15-FH-113-I_05-a1	15-FH-113-I_05-a2	15-FH-113-I_05-a4	15-FH-113-I_05-a5	15-FH-113-I_05-a7	15-FH-113-V_01_chr-01	15-FH-113-V_01_chr-02	15-FH-113-V_01_chr-03	15-FH-113-V_01_chr-04	15-FH-113-V_01_chr-05	15-FH-113-V_01_chr-06	15-FH-113-V_01_chr-07	15-FH-113-V_01_chr-08	15-FH-113-V_01_chr-10	15-FH-113-V_01_chr-11	
Mineral	a-chr	a-chr	chr	a-chr	chr	a-chr	a-chr	a-chr	a-chr	a-chr	chr	a-chr	a-chr	a-chr	chr	a-chr	chr	a-chr	a-chr	a-chr	
SiO ₂	0.16	0.05	0.03	0.08	0.04	b.d.l.	b.d.l.	0.04	0.03	0.14	b.d.l.	0.04	b.d.l.	0.11	0.03	0.63	b.d.l.	0.04	0.01	0.01	
TiO ₂	0.03	0.06	0.05	0.11	0.05	0.01	b.d.l.	0.05	0.08	0.06	0.06	0.05	0.07	0.09	0.06	0.20	b.d.l.	0.02	0.01	0.03	
V ₂ O ₅	0.17	0.19	0.15	0.26	0.15	0.04	0.15	0.14	0.13	0.17	0.17	0.16	0.17	0.13	0.17	0.20	0.08	0.12	0.09	0.16	
Al ₂ O ₃	6.36	14.14	20.97	6.12	20.33	3.27	19.54	19.68	8.63	6.57	21.51	12.38	9.84	6.27	19.30	9.35	19.79	12.41	5.38	14.73	
Cr ₂ O ₃	57.38	54.49	49.18	58.27	49.77	67.92	51.93	52.34	51.69	61.07	50.30	56.43	51.39	60.83	51.89	55.58	52.77	59.20	65.90	57.56	
FeO _t	20.05	11.91	11.50	20.08	11.84	14.27	10.63	6.23	28.84	15.20	9.21	15.54	28.23	17.31	9.26	20.97	7.94	13.09	12.65	9.46	
MnO	0.18	0.07	0.04	0.30	0.04	0.22	0.09	0.08	0.44	0.58	0.22	0.38	0.36	0.48	0.20	0.47	0.25	0.27	0.82	0.34	
MgO	10.50	17.36	16.58	11.11	16.80	11.74	16.48	20.27	5.42	12.31	17.35	13.49	6.38	11.40	17.53	9.27	18.05	13.88	13.46	16.45	
CoO	0.08	0.07	0.04	0.06	0.04	0.05	0.04	0.03	0.08	0.04	0.02	0.05	0.05	0.08	0.03	0.04	b.d.l.	0.09	0.06	0.04	
NiO	0.12	0.19	0.12	0.18	0.14	0.00	0.09	0.11	0.40	0.01	0.11	0.05	0.31	0.08	0.12	0.10	0.08	0.08	0.18	0.08	
ZnO	0.02	b.d.l.	0.06	0.07	0.05	b.d.l.	b.d.l.	0.03	b.d.l.	0.09	0.01	0.06	0.02	0.06	0.04	0.05	0.06	0.04	0.13	0.09	
Total	95.04	98.53	98.71	96.63	99.25	97.61	98.96	99.01	95.85	96.24	98.95	98.62	96.83	96.85	98.63	96.72	99.21	99.25	98.69	98.95	
APFU (4 O)																					
Cr	1.587	1.346	1.187	1.581	1.197	1.845	1.259	1.237	1.456	1.649	1.203	1.441	1.415	1.645	1.254	1.514	1.263	1.501	1.734	1.424	
Ti	0.001	0.001	0.001	0.003	0.001	0.000	-	0.001	0.002	0.002	0.001	0.001	0.002	0.002	0.001	0.001	0.002	0.001	-	0.001	
V	0.003	0.003	0.002	0.004	0.002	0.001	-	0.002	0.004	0.003	0.002	0.002	0.003	0.002	0.003	0.003	0.003	0.002	0.001	0.002	
Al	0.262	0.521	0.755	0.248	0.729	0.132	0.706	0.694	0.362	0.265	0.767	0.471	0.404	0.253	0.696	0.380	0.706	0.469	0.211	0.543	
Fe ³⁺	0.143	0.125	0.052	0.156	0.067	0.020	0.030	0.063	0.169	0.078	0.021	0.080	0.171	0.093	0.042	0.096	0.021	0.025	0.052	0.026	
Fe ²⁺	0.444	0.186	0.242	0.420	0.234	0.390	0.444	0.093	0.690	0.356	0.212	0.339	0.651	0.403	0.194	0.509	0.180	0.326	0.300	0.222	
Mn	0.005	0.002	0.001	0.009	0.001	0.006	0.002	0.002	0.013	0.017	0.006	0.010	0.011	0.014	0.005	0.014	0.006	0.007	0.023	0.009	
Mg	0.548	0.808	0.754	0.568	0.762	0.601	0.753	0.903	0.288	0.627	0.782	0.649	0.331	0.581	0.799	0.476	0.814	0.663	0.668	0.767	
Co	0.002	0.002	0.001	0.002	0.001	0.002	0.001	0.001	0.002	0.001	0.001	0.001	0.001	0.002	0.001	0.001	-	0.002	0.002	0.001	
Ni	0.003	0.005	0.003	0.005	0.003	0.000	0.002	0.003	0.011	0.000	0.003	0.001	0.009	0.002	0.003	0.003	0.002	0.002	0.005	0.002	
Zn	0.001	-	0.001	0.002	0.001	0.002	-	0.001	-	0.002	0.000	0.001	0.001	0.001	0.001	0.001	0.001	0.001	0.001	0.003	
Cr#	0.86	0.72	0.61	0.86	0.62	0.93	0.64	0.64	0.80	0.86	0.61	0.75	0.78	0.87	0.64	0.80	0.64	0.76	0.89	0.72	
Mg#	0.55	0.81	0.76	0.57	0.76	0.61	0.76	0.91	0.29	0.64	0.79	0.66	0.34	0.59	0.80	0.48	0.82	0.67	0.69	0.78	
Fe ³⁺ #	0.07	0.06	0.03	0.08	0.03	0.01	0.02	0.03	0.08	0.04	0.01	0.04	0.09	0.05	0.02	0.05	0.01	0.01	0.03	0.01	

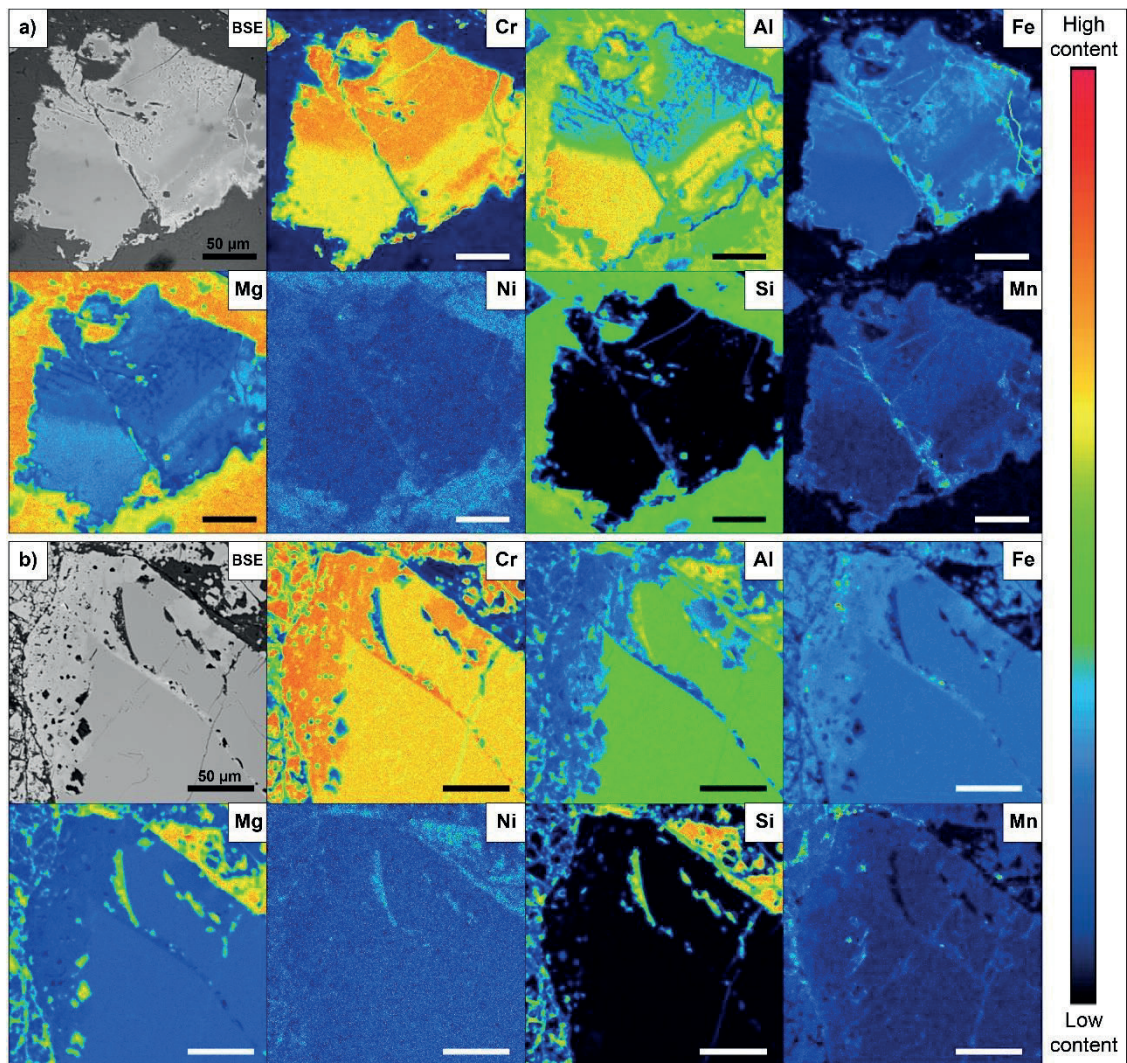
Deposit	Ingujiet														BA16-1		
Sample	15-FH-113-V														Massive		
Texture	Massive														BA16-1_04-1		
Analysis	15-FH-113-V_01_a-chr=12	15-FH-113-V_01_a-chr=13	15-FH-113-V_01_a-chr=14	15-FH-113-V_02_a-chr=04	15-FH-113-V_02_a-chr=07	15-FH-113-V_02_a-chr=08	15-FH-113-V_02_a-chr=10	15-FH-113-V_02_a-chr=12	15-FH-113-V_02_a-chr=13	15-FH-113-V_02_a-chr=15	15-FH-113-V_03_chr=-01	15-FH-113-V_03_chr=-02	15-FH-113-V_03_a-chr=03	15-FH-113-V_03_a-chr=05	15-FH-113-V_03_chr=-07	15-FH-113-V_03_a-chr=08	
Mineral	chr	a-chr	a-chr	a-chr	a-chr	a-chr	chr	chr	a-chr	a-chr	chr	chr	a-chr	a-chr	chr	a-chr	chr
SiO ₂	0.02	0.02	0.06	0.39	0.72	0.37	b.d.l.	0.01	0.86	0.86	0.03	b.d.l.	0.19	0.05	b.d.l.	b.d.l.	0.06
TiO ₂	0.03	0.04	0.07	0.06	0.04	0.01	0.06	0.05	0.03	0.07	0.11	0.02	0.06	0.03	0.05	b.d.l.	0.06
V ₂ O ₅	0.16	0.16	0.18	0.11	0.16	0.21	0.15	0.13	0.14	0.23	0.12	0.21	0.14	0.09	0.14	0.20	0.20
Al ₂ O ₃	21.19	13.47	6.36	8.84	6.93	5.93	21.20	15.13	7.67	8.66	21.08	19.86	6.99	4.97	19.09	11.99	14.82
Cr ₂ O ₃	50.12	57.89	52.59	61.49	57.14	56.32	48.85	55.42	46.97	56.00	50.61	62.07	62.07	64.69	53.01	53.86	53.96
FeO _t	11.67	14.67	29.53	12.27	22.68	25.88	12.12	12.81	31.34	19.48	9.12	12.22	18.31	15.55	11.79	19.35	15.94
MnO	0.20	0.26	1.39	0.58	0.86	1.80	0.25	0.29	0.33	0.66	0.20	0.18	0.41	0.87	0.20	0.27	0.27
MgO	15.96	13.12	6.10	14.79	8.25	6.05	15.62	14.48	9.96	12.67	16.60	15.05	10.32	11.89	15.05	11.25	13.63
CoO	0.08	0.06	0.08	0.07	0.08	0.09	0.03	0.05	0.11	0.04	0.04	0.05	0.04	0.03	0.05	0.06	0.05
NiO	0.14	0.12	0.33	0.08	0.14	0.17	0.15	0.08	0.02	0.16	0.12	0.10	0.08	0.07	0.11	0.22	0.15
ZnO	b.d.l.	0.04	0.05	0.10	0.08	0.22	0.02	0.06	0.04	0.05	0.08	0.05	0.10	0.29	0.08	0.05	0.09
Total	99.58	99.85	96.74	98.77	97.09	97.04	98.46	98.52	97.47	98.88	98.11	98.56	98.73	98.52	99.58	97.26	99.23
APFU (4 O)																	
Cr	1.205	1.460	1.475	1.583	1.581	1.586	1.188	1.391	1.269	1.466	1.228	1.246	1.660	1.727	1.293	1.415	1.355
Ti	0.001	0.001	0.002	0.001	0.001	0.000	0.001	0.001	0.001	0.002	0.002	0.000	0.001	0.001	0.001	-	0.001
V	0.002	0.002	0.003	0.002	0.003	0.004	0.002	0.002	0.002	0.004	0.002	0.003	0.002	0.001	0.002	0.003	0.003
Al	0.760	0.507	0.266	0.339	0.286	0.249	0.769	0.566	0.309	0.338	0.763	0.726	0.279	0.198	0.695	0.470	0.555
Fe ³⁺	0.029	0.026	0.249	0.072	0.125	0.157	0.036	0.036	0.415	0.185	0.001	0.020	0.053	0.071	0.005	0.109	0.080
Fe ²⁺	0.268	0.366	0.627	0.263	0.539	0.614	0.275	0.304	0.481	0.354	0.233	0.297	0.465	0.368	0.299	0.429	0.344
Mn	0.005	0.007	0.042	0.016	0.026	0.054	0.007	0.008	0.010	0.019	0.005	0.005	0.012	0.025	0.005	0.008	0.007
Mg	0.723	0.624	3.322	0.718	4.430	3.321	7.716	6.685	5.077	6.625	7.599	6.696	5.520	5.998	6.692	5.577	6.645
Co	0.002	0.002	0.002	0.002	0.002	0.002	0.001	0.001	0.003	0.001	0.001	0.001	0.001	0.001	0.001	0.001	0.001
Ni	0.003	0.003	0.010	0.002	0.004	0.005	0.004	0.002	0.001	0.004	0.003	0.002	0.002	0.002	0.003	0.006	0.004
Zn	-	0.001	0.001	0.002	0.002	0.006	0.000	0.001	0.001	0.001	0.001	0.001	0.003	0.007	0.002	0.001	0.002
Cr#	0.61	0.74	0.85	0.82	0.85	0.86	0.61	0.71	0.80	0.81	0.62	0.63	0.86	0.90	0.65	0.75	0.71
Mg#	0.73	0.63	0.34	0.73	0.44	0.34	0.72	0.69	0.51	0.64	0.76	0.70	0.53	0.62	0.70	0.56	0.65
Fe ³⁺ #	0.01	0.01	0.13	0.04	0.06	0.08	0.02	0.02	0.21	0.09	0.00	0.01	0.03	0.04	0.00	0.05	0.04

Deposit Sample	Ingujium																				
	BA16-1								BA16-4												
	Massive								Massive												
Texture	BA16-1 07-07 chr	BA16-1 06-a1 a-chr	BA16-1 06-a2 a-chr	BA16-1 06-a3 a-chr	BA16-1 06-a4 a-chr	BA16-1 06-a5 a-chr	BA16-1 06-a6 a-chr	BA16-1 06-a7 a-chr	BA16-4 01-1 chr	BA16-4 01-2 chr	BA16-4 01-3 chr	BA16-4 01-4 chr	BA16-4 01-5 chr	BA16-4 07-1 chr	BA16-4 07-2 chr	BA16-4 07-3 chr	BA16-4 07-4 chr	BA16-4 07-5 chr	BA16-4 09-1 chr	BA16-4 09-2 chr	
Mineral	0.03	0.04	0.03	0.09	0.03	0.06	b.d.l.	b.d.l.	b.d.l.	b.d.l.	0.05	b.d.l.	0.03	0.02	b.d.l.	0.04	0.02	b.d.l.	0.03	0.02	0.02
SiO ₂	0.12	0.05	0.08	0.08	0.08	0.10	0.05	0.09	0.08	0.07	0.07	0.04	0.06	0.10	b.d.l.	0.07	0.09	b.d.l.	0.09	0.09	0.05
TiO ₂	0.19	0.21	0.26	0.16	0.26	0.17	0.26	0.29	0.19	0.17	0.19	0.21	0.17	0.18	0.18	0.19	0.18	0.18	0.18	0.18	0.19
V ₂ O ₅	16.11	14.88	7.06	7.06	5.64	15.07	9.34	8.82	14.82	14.44	14.90	14.67	15.00	14.59	13.23	14.69	14.72	14.77	14.81	15.00	15.00
Al ₂ O ₃	52.39	53.27	58.89	58.70	61.62	52.81	57.63	56.94	53.97	54.91	54.49	54.52	54.26	54.59	56.68	54.31	54.64	54.47	53.30	53.12	53.12
Cr ₂ O ₃	15.99	15.82	19.56	19.31	19.05	16.00	18.04	19.07	14.39	14.45	14.11	14.19	14.60	13.97	13.95	14.03	14.32	14.36	16.20	16.33	16.33
FeO	0.28	0.09	0.08	0.34	0.46	0.10	0.13	0.19	0.14	0.16	0.12	0.11	0.18	0.15	0.12	0.12	0.15	0.10	0.17	0.25	0.25
MnO	14.28	13.53	10.84	10.61	9.39	13.28	11.52	11.43	14.22	13.67	14.18	14.18	13.97	14.05	13.65	14.32	13.93	14.34	12.85	12.55	12.55
MgO	0.02	0.04	0.09	0.06	0.04	0.08	0.05	0.09	0.07	0.06	0.06	0.01	0.07	0.05	0.07	0.03	0.04	0.07	0.07	0.06	0.06
CoO	0.16	0.09	0.11	0.03	0.07	0.05	0.07	0.10	0.12	0.12	0.14	0.14	0.10	0.10	0.08	0.09	0.09	0.12	0.16	0.12	0.12
NiO	0.08	0.05	b.d.l.	0.11	0.04	0.04	0.04	b.d.l.	b.d.l.	0.04	b.d.l.	0.03	0.07	0.03	b.d.l.	0.05	0.09	0.07	0.02	0.11	0.11
ZnO	99.65	98.09	97.12	96.56	96.68	97.75	97.12	97.03	98.00	98.10	98.31	98.10	98.50	97.83	97.97	97.93	98.17	98.58	97.88	97.79	97.79
Total																					
APFU (4.0)	1.298	1.352	1.588	1.595	1.699	1.345	1.531	1.518	1.364	1.395	1.374	1.378	1.367	1.385	1.449	1.374	1.383	1.369	1.362	1.360	1.360
Cr	0.003	0.002	0.004	0.002	0.002	0.002	0.001	0.002	0.002	0.002	0.002	0.001	0.001	0.002	-	0.002	-	0.002	0.002	0.001	0.001
Ti	0.003	0.003	0.005	0.003	0.004	0.003	0.004	0.005	0.003	0.003	0.003	0.003	0.003	0.003	0.003	0.003	0.003	0.003	0.003	0.003	0.003
V	0.595	0.563	0.284	0.286	0.232	0.573	0.370	0.351	0.559	0.547	0.560	0.553	0.564	0.552	0.504	0.562	0.556	0.554	0.564	0.573	0.573
Al	0.095	0.075	0.109	0.110	0.056	0.072	0.087	0.117	0.067	0.049	0.056	0.060	0.061	0.052	0.040	0.062	0.056	0.067	0.064	0.059	0.059
Fe ³⁺	0.324	0.350	0.449	0.445	0.499	0.359	0.420	0.420	0.318	0.339	0.321	0.320	0.329	0.323	0.337	0.314	0.328	0.315	0.374	0.384	0.384
Fe ²⁺	0.007	0.002	0.002	0.010	0.013	0.003	0.004	0.006	0.004	0.004	0.003	0.003	0.005	0.004	0.003	0.003	0.004	0.003	0.005	0.007	0.007
Mn	0.667	0.647	0.551	0.543	0.488	0.638	0.577	0.574	0.678	0.655	0.674	0.676	0.664	0.672	0.658	0.683	0.665	0.680	0.619	0.606	0.606
Mg	0.000	0.001	0.002	0.002	0.001	0.002	0.001	0.002	0.002	0.002	0.002	0.000	0.002	0.001	0.002	0.001	0.001	0.002	0.002	0.002	0.002
Co	0.004	0.002	0.003	0.001	0.002	0.001	0.002	0.003	0.003	0.003	0.004	0.003	0.002	0.003	0.002	0.002	0.002	0.003	0.004	0.003	0.003
Ni	0.002	0.001	-	0.003	0.001	0.001	0.001	-	-	0.001	-	0.001	0.002	0.001	-	0.001	0.002	0.002	0.000	0.003	0.003
Zn	0.69	0.71	0.85	0.85	0.88	0.70	0.81	0.81	0.71	0.72	0.71	0.71	0.71	0.72	0.74	0.71	0.71	0.71	0.71	0.70	0.70
Cr#	0.67	0.65	0.55	0.55	0.49	0.64	0.58	0.58	0.68	0.66	0.68	0.68	0.67	0.68	0.66	0.69	0.67	0.68	0.62	0.61	0.61
Mg#	0.05	0.04	0.06	0.06	0.03	0.04	0.04	0.06	0.03	0.02	0.03	0.03	0.03	0.03	0.02	0.03	0.03	0.03	0.03	0.03	0.03
Fe ³⁺ #																					

Deposit Sample	Inguilim																			
	BA16-4																			
Texture	Massive																			
	BA16-4_09-2	BA16-4_09-3	BA16-4_09-4	BA16-4_09-5	BA16-4_01-chr-01	BA16-4_01-chr-02	BA16-4_01-chr-03	BA16-4_01-chr-05	BA16-4_01-chr-06	BA16-4_01-chr-07	BA16-4_01-chr-08	BA16-4_01-chr-10	BA16-4_05-chr-01	BA16-4_05-chr-03	BA16-4_05-chr-05	BA16-4_05-chr-06	BA16-4_05-chr-08	BA16-4_05-chr-09	BA16-4_07-ox-03	BA16-4_07-ox-04
Mineral	chr	chr	chr	chr	chr	chr	a-chr	a-chr	a-chr	chr	a-chr	a-chr	chr	chr	a-chr	a-chr	chr	a-chr	hem	hem
SiO ₂	0.02	0.04	0.04	0.03	0.01	0.07	0.04	0.02	0.02	0.02	0.06	2.84	b.d.l.	b.d.l.	1.66	0.81	0.11	0.02	0.10	0.04
TiO ₂	0.05	0.06	0.04	0.03	0.06	0.02	0.00	0.06	0.06	0.06	0.01	0.01	0.06	0.06	0.02	0.05	0.07	0.07	0.03	0.00
V ₂ O ₅	0.19	0.14	0.18	0.15	0.18	0.06	0.06	0.18	0.18	0.18	0.07	0.07	0.15	0.16	0.10	0.19	0.16	0.12	0.03	0.02
Al ₂ O ₃	15.00	14.75	14.92	14.81	13.26	2.47	2.40	13.98	13.98	13.98	2.17	13.93	14.10	14.10	1.91	3.12	13.76	3.09	0.00	0.00
Cr ₂ O ₃	53.12	53.53	54.03	53.98	65.95	65.21	67.74	56.07	56.07	56.07	70.94	59.49	56.02	55.80	63.83	61.81	55.65	65.75	6.78	1.52
FeO	16.33	16.01	15.86	16.40	14.99	19.14	17.97	20.31	14.86	14.86	17.06	20.86	14.77	14.27	19.05	20.93	14.96	18.62	81.55	88.01
MnO	0.25	0.24	0.20	0.24	0.37	0.37	0.43	0.50	0.34	0.34	0.51	0.55	0.34	0.32	0.46	0.50	0.31	0.40	0.41	0.41
MgO	12.55	13.24	13.03	12.70	13.12	9.09	9.24	10.52	12.65	12.65	9.38	10.72	13.49	13.44	10.62	10.05	13.62	10.33	0.40	0.08
CoO	0.06	0.06	0.05	0.05	0.07	0.08	0.04	0.03	0.07	0.07	0.07	0.08	0.03	0.02	0.05	0.05	0.04	0.07	0.27	0.25
NiO	0.12	0.10	0.11	0.10	0.16	0.04	0.03	0.14	0.11	0.11	0.01	0.13	0.08	0.04	0.05	0.12	0.11	0.10	0.58	0.55
ZnO	0.11	0.03	0.04	0.06	0.07	0.09	0.06	0.06	0.10	0.10	0.06	0.09	0.05	0.06	0.13	0.05	0.02	b.d.l.	0.02	0.04
Total	97.79	98.19	98.49	98.56	97.48	97.58	98.00	96.70	98.44	98.44	98.59	97.02	98.92	98.28	97.89	97.67	98.81	98.56	90.90	90.92
APFU (4 O)																				
Cr	1.360	1.360	1.371	1.373	1.415	1.437	1.875	1.711	1.434	1.434	1.969	1.684	1.418	1.420	1.778	1.709	1.410	1.788		
Ti	0.001	0.001	0.001	0.001	0.001	0.001	0.000	0.002	0.001	0.001	0.000	0.000	0.001	0.001	0.001	0.001	0.002	0.002		
V	0.003	0.002	0.003	0.002	0.003	0.003	0.001	0.002	0.003	0.003	0.000	0.001	0.002	0.003	0.002	0.003	0.002	0.002		
Al	0.573	0.559	0.565	0.562	0.505	0.102	0.099	0.092	0.533	0.533	0.020	0.092	0.526	0.535	0.079	0.129	0.520	0.125		
Fe ³⁺	0.059	0.073	0.057	0.059	0.049	0.061	0.024	0.189	0.025	0.025	0.011	0.221	0.049	0.037	0.138	0.153	0.061	0.079		
Fe ²⁺	0.384	0.357	0.369	0.382	0.353	0.502	0.502	0.420	0.377	0.377	0.490	0.404	0.347	0.347	0.424	0.459	0.340	0.457		
Mn	0.007	0.006	0.005	0.007	0.008	0.010	0.013	0.015	0.009	0.009	0.015	0.017	0.009	0.009	0.014	0.015	0.008	0.012		
Mg	0.606	0.634	0.623	0.609	0.635	0.476	0.482	0.562	0.610	0.610	0.491	0.572	0.644	0.645	0.558	0.524	0.651	0.530		
Co	0.002	0.002	0.001	0.001	0.002	0.002	0.001	0.001	0.002	0.002	0.002	0.002	0.001	0.001	0.001	0.001	0.001	0.002		
Ni	0.003	0.003	0.003	0.003	0.004	0.001	0.001	0.004	0.003	0.003	0.000	0.004	0.002	0.001	0.002	0.003	0.003	0.003		
Zn	0.003	0.001	0.001	0.001	0.002	0.002	0.002	0.002	0.002	0.002	0.002	0.002	0.001	0.001	0.003	0.001	0.000	0.003		
Cr#	0.70	0.71	0.71	0.71	0.73	0.74	0.95	0.95	0.73	0.73	0.99	0.95	0.73	0.73	0.96	0.93	0.73	0.93		
Mg#	0.61	0.64	0.63	0.61	0.62	0.64	0.49	0.57	0.62	0.62	0.50	0.59	0.65	0.65	0.57	0.53	0.66	0.54		
Fe ³⁺ #	0.03	0.04	0.03	0.03	0.02	0.02	0.01	0.09	0.01	0.01	0.01	0.11	0.02	0.02	0.07	0.08	0.03	0.04		

Deposit Sample	Inguitem									
	BA16-4									
	Massive									
Texture										
Analysis	BA16-4_07-a-chr-06	BA16-4_07-chr-07	BA16-4_07-a-chr-08	BA16-4_07-a-chr-10	BA16-4_08-chr-01	BA16-4_08-a-chr-02	BA16-4_08-a-chr-03			
Mineral	a-chr	chr	a-chr	a-chr	chr	a-chr	a-chr			
SiO ₂	3.78	b.d.l.	2.73	0.53	0.03	2.91	2.61			
TiO ₂	0.05	0.06	0.02	0.06	0.04	0.03	0.04			
V ₂ O ₅	0.24	0.22	0.10	0.12	0.18	0.10	0.10			
Al ₂ O ₃	8.50	14.05	3.14	2.42	13.63	2.02	2.02			
Cr ₂ O ₃	49.48	55.46	60.65	64.46	55.45	57.52	62.01			
FeO†	18.65	14.72	17.84	18.41	15.68	21.96	20.25			
MnO	0.38	0.29	0.44	0.42	0.32	0.80	0.54			
MgO	14.02	13.17	11.75	9.68	12.61	10.72	11.54			
CoO	0.04	0.05	0.03	0.06	0.06	0.07	0.08			
NiO	0.15	0.10	0.08	0.02	0.09	0.10	0.05			
ZnO	0.11	0.01	0.13	0.09	0.05	0.17	0.11			
Total	95.40	98.14	96.91	96.27	98.13	96.40	99.19			
APFU(4O)										
Cr	1.358	1.416	1.698	1.815	1.423	1.639	1.708			
Ti	0.001	0.002	0.001	0.001	0.001	0.001	0.001			
V	0.004	0.003	0.002	0.002	0.003	0.002	0.001			
Al	0.348	0.535	0.131	0.102	0.522	0.086	0.077			
Fe ³⁺	0.283	0.039	0.167	0.076	0.047	0.270	0.210			
Fe ²⁺	0.259	0.358	0.362	0.472	0.379	0.392	0.380			
Mn	0.011	0.008	0.013	0.013	0.009	0.024	0.016			
Mg	0.726	0.634	0.620	0.514	0.610	0.576	0.599			
Co	0.001	0.001	0.001	0.002	0.001	0.002	0.002			
Ni	0.004	0.003	0.002	0.001	0.002	0.003	0.001			
Zn	0.003	0.000	0.003	0.002	0.001	0.005	0.003			
Cr#	0.80	0.73	0.93	0.95	0.73	0.95	0.96			
Mg#	0.74	0.64	0.63	0.52	0.62	0.59	0.61			
Fe ³⁺ #	0.14	0.02	0.08	0.04	0.02	0.14	0.11			

Appendix 4. X-ray maps of Bou Azzer chromite grains.



Appendix 5. Representative LA-ICP-MS analyses of chromite from the Bou Azzer chromitites.

Chromitite (Bou Azzer)	Sample	Texture	Chromite grain zone	Analysis #	C#	Y	2 σ	Mdl	Sc	2 σ	Mdl	Ti	2 σ	Mdl	Ni	2 σ	Mdl	Zn	2 σ	Mdl	Co	2 σ	Mdl	Mn	2 σ	Mdl	Yb	2 σ	Mdl	(Yb) _N	(Sc) _N	(Ga) _N	(Ti) _N	(Ni) _N	(Zn) _N	(Co) _N	(Mn) _N
Ingujijem	15-PH-113-1	Massive	Unaltered core	C2_1	0.61	940.20	9.80	1.24	3.60	2.00	5.69	38.40	1.40	0.60	219.00	9.30	8.55	1311.00	20.00	2.67	441.00	12.00	10.59	203.30	2.90	1.08	1069.10	9.60	3.43	1.264	0.679	0.731	0.163	0.742	0.948	1.232	1.214
Ingujijem	15-PH-113-1	Massive	Unaltered core	C2_2	0.61	924.00	11.00	1.04	2.10	2.20	15.06	38.60	1.50	0.00	209.00	13.00	31.63	1411.00	23.00	7.51	429.00	13.00	19.11	205.70	3.50	3.13	1084.00	13.00	3.50	1.242	0.396	0.735	0.156	0.799	0.923	1.247	1.230
Ingujijem	15-PH-113-1	Massive	Unaltered core	C2_3	0.61	961.00	6.30	0.49	3.34	0.72	2.21	42.21	0.87	0.00	217.70	5.70	7.16	1311.00	13.00	0.87	500.00	12.00	4.51	198.80	1.90	0.42	1110.20	6.70	1.07	1.292	0.630	0.804	0.162	0.742	1.075	1.205	1.260
Ingujijem	15-PH-113-1	Massive	Altered rim	C3_1	0.86	1208.00	14.00	1.00	4.62	0.97	4.38	28.15	0.78	0.33	272.00	10.00	9.84	1775.00	34.00	1.48	953.00	19.00	8.60	221.70	3.00	0.76	4183.00	63.00	1.99	1.624	0.872	0.536	0.203	1.005	2.049	1.344	4.748
Ingujijem	15-PH-113-1	Massive	Altered rim	C3_2	0.86	1197.10	8.50	0.39	4.31	0.63	3.72	31.27	0.78	0.00	307.80	6.80	8.37	2062.00	22.00	1.23	1093.00	29.00	3.64	221.80	2.10	0.23	4650.00	120.00	1.19	1.609	0.813	0.596	0.229	1.168	2.351	1.344	5.278
Ingujijem	15-PH-113-1	Massive	Altered rim	C3_3	0.86	1224.00	15.00	0.50	2.81	0.69	2.61	32.37	0.80	0.21	375.80	9.70	7.77	2357.00	35.00	0.94	916.00	33.00	3.01	244.00	3.80	0.50	4970.00	100.00	1.55	1.645	0.530	0.617	0.280	1.335	1.970	1.479	5.641
Ingujijem	15-PH-113-1	Massive	Unaltered core	C3_4	0.61	976.20	6.40	0.65	2.66	0.62	2.53	38.93	0.80	0.59	227.00	5.40	3.60	1322.00	11.00	1.23	491.00	12.00	3.89	196.70	1.90	0.45	1101.80	7.90	0.46	1.312	0.502	0.742	0.169	0.749	1.056	1.192	1.251
Ingujijem	15-PH-113-1	Massive	Unaltered core	C3_5	0.61	956.80	6.60	0.29	3.31	0.63	2.31	33.82	0.79	0.20	221.60	6.00	3.77	1425.00	12.00	0.91	493.00	13.00	3.63	192.30	2.00	0.63	1157.50	6.70	1.48	1.286	0.625	0.644	0.165	0.807	1.060	1.165	1.314
Ingujijem	15-PH-113-1	Massive	Unaltered core	C5_1	0.62	976.60	5.50	0.41	3.61	0.67	2.13	38.36	0.74	0.29	224.50	5.30	7.13	1332.00	12.00	0.00	516.00	13.00	4.23	198.90	1.70	0.27	1019.50	6.10	0.97	1.313	0.681	0.731	0.167	0.754	1.110	1.205	1.157
Ingujijem	15-PH-113-1	Massive	Unaltered core	C5_2	0.63	987.80	6.00	0.55	3.83	0.70	1.94	35.88	0.77	0.00	225.20	5.50	5.92	1164.00	11.00	1.14	522.00	14.00	3.44	200.70	1.90	0.56	1036.60	5.20	1.02	1.328	0.723	0.683	0.168	0.659	1.123	1.216	1.177
Ingujijem	15-PH-113-1	Massive	Unaltered core	C5_3	0.63	997.10	6.70	0.85	1.31	0.67	3.77	32.46	0.76	0.00	233.90	6.10	5.21	1207.00	11.00	1.36	667.00	19.00	5.89	203.50	2.20	0.36	1619.00	28.00	1.34	1.340	0.247	0.618	0.174	0.683	1.434	1.233	1.838
Ingujijem	15-PH-113-1	Massive	Altered rim	C5_4	0.86	1187.30	9.40	0.32	3.15	0.73	2.13	31.97	0.72	0.23	321.20	8.40	9.18	2451.00	21.00	2.40	1642.00	32.00	6.33	250.80	2.60	1.34	5276.00	53.00	0.77	1.596	0.594	0.609	0.239	1.388	3.531	1.520	5.989
Ingujijem	15-PH-113-1	Massive	Altered rim	C5_5	0.86	1341.00	13.00	0.45	2.57	0.70	4.04	39.55	0.91	0.23	421.70	9.70	4.62	3047.00	36.00	1.02	1104.00	15.00	2.28	228.00	2.40	0.50	4941.00	58.00	1.50	1.802	0.485	0.753	0.314	1.725	2.374	1.382	5.068
Ingujijem	15-PH-113-1	Massive	Altered rim	C5_6	0.86	1240.00	16.00	0.32	4.18	0.71	4.26	37.29	0.79	0.00	337.00	8.10	4.28	2254.00	32.00	1.03	1882.00	49.00	1.62	248.80	2.90	0.76	5869.00	86.00	1.08	1.667	0.789	0.710	0.251	1.276	1.4047	1.508	6.662
Ingujijem	15-PH-113-1	Massive	Unaltered core	C5_7	0.64	1022.90	7.00	0.57	1.45	0.71	3.20	36.40	0.98	0.23	236.90	6.80	9.97	1093.00	13.00	1.03	611.00	17.00	4.14	210.10	2.00	0.33	1143.00	10.00	0.77	1.375	0.274	0.693	0.176	0.619	1.314	1.273	1.297
Ingujijem	BA-16-1	Massive	Unaltered core	C4_1	0.71	1126.60	6.00	0.53	3.43	0.56	2.72	27.77	0.61	0.00	344.00	6.90	4.48	1109.00	11.00	0.91	1028.00	46.00	2.28	224.10	2.40	0.70	1814.00	29.00	0.68	1.514	0.647	0.529	0.256	0.628	2.211	1.358	2.059
Ingujijem	BA-16-1	Massive	Unaltered core	C4_2	0.71	1132.20	6.90	0.27	3.21	0.66	2.72	28.14	0.65	0.00	350.30	8.90	6.06	1060.00	12.00	0.00	917.00	26.00	2.34	232.30	2.50	0.41	1916.00	18.00	0.68	1.522	0.606	0.536	0.261	0.600	1.972	1.408	2.175
Ingujijem	BA-16-1	Massive	Unaltered core	C4_3	0.71	1133.40	6.30	0.85	3.81	0.70	3.71	28.09	0.63	0.00	337.20	6.80	5.76	989.00	11.00	0.96	598.00	17.00	3.62	221.10	2.10	0.64	1311.30	6.70	0.49	1.523	0.719	0.535	0.251	0.560	1.286	1.340	1.488
Ingujijem	BA-16-1	Massive	Unaltered core	C5_1	0.70	1134.90	7.40	0.96	3.27	0.65	2.08	27.22	0.54	0.00	344.80	7.30	8.58	1198.00	13.00	1.96	585.00	17.00	2.08	212.40	2.00	0.31	1284.80	6.50	0.70	1.525	0.617	0.518	0.257	0.678	1.258	1.287	1.458
Ingujijem	BA-16-1	Massive	Altered rim	C5_2	0.85	1408.00	12.00	0.54	4.22	0.72	3.01	22.98	0.62	0.00	403.00	7.90	4.93	1223.00	19.00	1.05	1598.00	31.00	1.37	268.00	2.20	0.51	2897.00	24.00	0.78	1.892	0.796	0.438	0.300	0.693	3.437	1.624	3.288
Ingujijem	BA-16-1	Massive	Unaltered core	C5_3	0.70	1137.20	7.40	0.65	3.68	0.61	2.81	27.87	0.60	0.23	332.00	6.80	9.72	1121.30	9.20	1.01	619.00	18.00	4.05	220.30	1.90	0.84	1281.90	6.60	0.61	1.528	0.694	0.531	0.247	0.635	1.331	1.335	1.455
Ingujijem	BA-16-1	Massive	Altered rim	C5_4	0.85	1381.00	12.00	0.30	2.78	0.63	4.68	24.91	0.66	0.22	430.60	8.40	8.15	919.00	9.70	0.99	1580.00	40.00	2.06	269.10	2.60	0.62	2886.00	39.00	0.71	1.856	0.525	0.474	0.321	0.520	3.398	1.631	3.276
Ingujijem	BA-16-1	Massive	Unaltered core	C6_1	0.70	1124.90	6.10	0.47	4.07	0.65	1.51	28.02	0.67	0.00	352.80	7.80	3.57	1064.00	9.70	0.00	798.00	28.00	3.53	226.30	2.00	0.78	1542.00	15.00	0.52	1.512	0.768	0.534	0.263	0.602	1.716	1.372	1.750
Ingujijem	BA-16-1	Massive	Altered rim	C6_2	0.85	1325.50	9.30	0.61	2.63	0.47	2.12	20.83	0.59	0.26	417.30	7.40	6.24	722.00	14.00	0.92	859.00	27.00	1.83	249.90	2.00	0.53	2461.00	35.00	0.33	1.782	0.496	0.397	0.311	0.409	1.847	1.515	2.793
Ingujijem	BA-16-1	Massive	Unaltered core	C6_3	0.71	1132.70	7.90	0.45	4.57	0.79	4.42	26.56	0.75	0.00	346.30	7.50	6.17	1210.00	11.00	1.94	711.00	27.00	3.57	216.40	1.90	0.74	1597.00	21.00	1.34	1.522	0.862	0.506	0.258	0.685	1.529	1.312	1.813
Ingujijem	BA-16-1	Massive	Altered rim	C6_4	0.88	1481.80	9.30	0.61	5.39	0.69	2.11	21.02	0.55	0.00	454.00	8.10	7.93	1145.00	26.00	1.06	1280.00	39.00	4.70	264.40	3.00	0.61	2897.00	68.00	0.97	1.992	1.017	0.400	0.338	0.648	2.753	1.602	3.288

Chromitite (Bou Azzer)	Sample	Texture	Chromite grain zone	Analysis #	Cr#	V	2 σ	Mdl	Sc	2 σ	Mdl	Ga	2 σ	Mdl	Ti	2 σ	Mdl	Ni	2 σ	Mdl	Zn	2 σ	Mdl	Co	2 σ	Mdl	Nb	2 σ	Mdl	(V)k	(S)k	(Ga)k	(Ti)k	(Nb)k	(Zn)k	(Co)k	(M)k
Ingujijem	BA-16-1	Massive	Altered rim	C6_5	0.88	1351.30	8.90	0.71	5.07	0.67	3.23	18.90	0.54	0.00	404.60	8.70	5.18	1210.00	14.00	0.00	1490.00	41.00	4.87	280.00	2.60	1.01	3908.00	36.00	0.52	1.816	0.957	0.360	0.301	0.685	3.204	1.697	4.456
Ingujijem	BA-16-1	Massive	Unaltered core	C6_6	0.71	1125.60	5.80	0.85	4.20	0.66	3.18	27.52	0.72	0.24	345.60	8.20	9.69	917.00	13.00	0.00	700.00	31.00	2.52	225.80	1.80	0.31	1332.60	9.70	0.61	1.513	0.792	0.524	0.257	0.519	1.505	1.368	1.513
Ingujijem	BA-16-1	Massive	Unaltered core	C7_1	0.68	1161.90	6.00	0.94	4.45	0.77	2.93	28.70	0.59	0.26	370.90	8.00	4.80	1280.00	10.00	1.17	539.00	15.00	2.25	207.90	2.20	0.63	1245.10	6.50	0.96	1.562	0.840	0.547	0.276	0.725	1.159	1.260	1.413
Ingujijem	BA-16-1	Massive	Unaltered core	C7_2	0.68	1155.10	6.80	0.79	4.34	0.64	1.92	29.33	0.61	0.00	353.40	7.70	4.72	1277.00	12.00	2.30	521.00	12.00	2.62	204.00	1.60	0.68	1206.30	7.20	0.90	1.553	0.819	0.559	0.263	0.723	1.120	1.236	1.369
Ingujijem	BA-16-1	Massive	Unaltered core	C7_3	0.68	1141.20	6.60	0.79	4.09	0.65	2.31	28.97	0.63	0.25	345.80	8.70	6.70	1261.00	12.00	2.41	539.00	16.00	1.56	208.40	1.60	0.50	1240.70	6.00	1.33	1.534	0.772	0.552	0.258	0.714	1.159	1.263	1.408
Filon60	BA-16-11	Massive	Unaltered core	C1_2	0.83	668.40	4.30	0.66	4.38	0.60	2.96	17.59	0.50	0.23	282.20	6.50	6.62	565.00	7.00	1.47	614.00	17.00	3.19	227.40	2.10	0.44	1677.60	8.90	0.95	0.898	0.826	0.335	0.210	0.320	1.320	1.378	1.904
Filon60	BA-16-11	Massive	Unaltered core	C1_2	0.83	680.40	4.50	0.88	4.11	0.61	4.20	17.83	0.48	0.00	283.40	6.30	8.60	592.80	8.30	0.00	555.00	16.00	2.78	226.60	1.70	0.30	1661.30	8.40	0.86	0.915	0.775	0.340	0.211	0.336	1.194	1.373	1.886
Filon60	BA-16-11	Massive	Unaltered core	C1_3	0.83	665.80	4.40	0.00	4.27	0.71	2.29	18.25	0.48	0.00	275.20	5.30	8.29	638.80	7.10	0.00	541.00	15.00	3.80	223.70	2.30	0.63	1683.10	7.70	0.48	0.895	0.806	0.348	0.205	0.362	1.163	1.356	1.910
Filon60	BA-16-11	Massive	Unaltered core	C3_1	0.83	667.30	4.60	0.65	4.30	0.65	1.35	19.79	0.51	0.23	283.10	6.20	8.45	797.90	8.30	2.15	407.00	11.00	3.90	213.70	2.30	0.67	1627.40	8.80	0.36	0.897	0.811	0.377	0.211	0.452	0.875	1.295	1.847
Filon60	BA-16-11	Massive	Unaltered core	C3_2	0.83	662.30	4.30	0.22	5.46	0.67	2.97	19.09	0.54	0.00	284.50	7.10	7.83	795.00	10.00	0.00	452.00	12.00	1.78	217.80	1.90	0.50	1656.40	9.50	0.37	0.890	1.030	0.364	0.212	0.450	0.972	1.320	1.880
Filon60	BA-16-11	Massive	Unaltered core	C3_3	0.83	664.10	3.90	0.46	4.08	0.61	1.62	18.31	0.56	0.00	283.40	6.90	2.98	691.50	7.00	1.03	518.00	14.00	1.25	222.30	2.10	0.30	1676.60	7.60	0.95	0.893	0.770	0.349	0.211	0.392	1.114	1.347	1.903
Air Ahmane	BA-16-17C1	Semimassive	Unaltered core	C1_1	0.67	909.70	5.20	0.35	1.88	0.68	3.22	24.34	0.60	0.26	259.40	7.30	9.39	903.90	9.20	0.00	690.00	20.00	2.21	307.70	2.50	0.34	2285.00	12.00	1.00	1.223	0.355	0.464	0.193	0.512	1.484	1.865	2.594
Air Ahmane	BA-16-17C1	Semimassive	Unaltered core	C1_2	0.67	920.50	6.00	0.51	3.57	0.65	3.57	25.69	0.66	0.00	257.30	7.30	5.14	882.10	8.70	1.48	713.00	21.00	2.32	315.40	2.50	0.49	3748.00	30.00	0.72	1.237	0.674	0.489	0.192	0.499	1.533	1.912	4.254
Air Ahmane	BA-16-17C1	Semimassive	Unaltered core	C4_1	0.67	971.70	5.90	0.57	3.23	0.63	2.35	25.81	0.63	0.00	258.80	7.10	5.26	923.30	9.60	0.00	761.00	22.00	3.94	327.00	3.30	0.43	3976.00	34.00	0.34	1.306	0.609	0.492	0.193	0.523	1.637	1.982	4.513
Air Ahmane	BA-16-17C1	Semimassive	Unaltered core	C4_1	0.67	933.10	5.70	0.55	2.16	0.78	2.71	24.73	0.62	0.00	272.40	7.00	7.45	904.20	9.50	1.09	651.00	18.00	1.44	303.30	2.60	0.32	1749.30	8.40	0.97	1.254	0.408	0.471	0.203	0.512	1.400	1.838	1.866
Air Ahmane	BA-16-17C1	Semimassive	Unaltered core	C5_1	0.66	940.70	5.80	0.75	3.54	0.66	3.11	24.23	0.79	0.23	238.80	6.80	7.95	821.30	9.10	0.00	671.00	23.00	2.00	309.20	3.10	0.68	3151.00	32.00	1.15	1.264	0.668	0.462	0.178	0.465	1.443	1.874	3.577
Air Ahmane	BA-16-17C1	Semimassive	Unaltered core	C5_2	0.66	949.30	7.20	0.34	3.20	0.67	2.33	25.75	0.57	0.00	259.50	6.50	5.62	802.00	11.00	0.00	675.00	19.00	2.34	314.30	2.60	0.31	4534.00	82.00	0.57	1.276	0.604	0.490	0.193	0.454	1.452	1.905	5.146
Air Ahmane	BA-16-17C1	Semimassive	Unaltered core	C5_2	0.66	947.30	6.40	0.53	1.66	0.62	2.81	24.92	0.65	0.23	262.10	6.90	5.08	889.00	10.00	1.36	661.00	18.00	1.38	308.60	2.90	0.44	2789.00	27.00	1.10	1.273	0.313	0.475	0.195	0.503	1.422	1.870	3.166
Air Ahmane	BA-16-17C1	Semimassive	Unaltered core	C7_1	0.66	916.20	5.00	0.84	0.86	0.67	2.45	22.44	0.61	0.00	265.40	6.90	7.81	875.80	9.30	1.04	664.00	19.00	2.73	305.40	2.50	0.43	1717.80	9.00	1.06	1.231	0.162	0.427	0.198	0.496	1.428	1.851	1.950
Air Ahmane	BA-16-17C1	Semimassive	Unaltered core	C7_2	0.66	944.70	5.60	0.63	2.66	0.70	2.65	26.06	0.76	0.00	247.00	7.40	4.46	783.70	8.20	1.00	936.00	13.00	1.85	346.80	3.50	0.45	5128.00	49.00	0.45	1.270	0.502	0.496	0.184	0.444	2.013	2.102	5.821

*Cr# from electron-microprobe
N= Normalized to chromite from MORB [Pagé and Barnes 2009; Econ. Geol. 104, 997-1018]
Mdl= Minimum detection limits (99% confidence).

Appendix 6. Whole rock PGE composition of studied chromitites and dunites from Bou Azzer. Abbreviations: Chr – chromite, Dun – dunite,

b.d.l. – below detection limit.

Samples	BA 16-1	BA 16-4	BA 16-11	BA 16-16	BA 16-17A	BA 16-17B	BA 16-17C	15-FH-113-III	BA 16-2	BA 16-5	BA 16-6	BA 16-12	BA 16-14
Rock type	Chr	Chr	Chr	Chr	Chr	Chr	Chr	Chr	Dun	Dun	Dun	Dun	Dun
Au (ppb)	13	5	2	b.d.l.	b.d.l.	b.d.l.	b.d.l.	4	b.d.l.	b.d.l.	b.d.l.	b.d.l.	b.d.l.
Os	48	37	19	26	16	15	18	79	3	b.d.l.	3	3	2
Ir	46	67	36	40	22	29	24	81	6	b.d.l.	1	4	5
Ru	90	133	114	60	56	82	71	105	10	2	2	8	8
Rh	9	14	14	7	7	10	5	12	2	b.d.l.	b.d.l.	1	2
Pt	9	11	5	4	8	5	3	22	6	1	5	10	10
Pd	3	2	2	2	7	6	3	14	2	b.d.l.	4	4	2
PGE Sum	205	264	190	139	116	147	124	313	29	3	15	30	29
Os/Pt	5.33	3.36	3.80	6.50	2.00	3.00	6.00	3.59	0.50	-	0.60	0.30	0.20
Os/Ir	1.04	0.55	0.53	0.65	0.73	0.52	0.75	0.98	0.50	-	3.00	0.75	0.40

*NORMALIZED TO CI

Samples	BA 16-1	BA 16-4	BA 16-11	BA 16-16	BA 16-17A	BA 16-17B	BA 16-17C	15-FH-113-III	BA 16-2	BA 16-5	BA 16-6	BA 16-12	BA 16-14
Au	0.086	0.033	0.013	-	-	-	-	-	-	-	-	-	-
Os	0.093	0.072	0.037	0.051	0.031	0.029	0.035	0.154	0.006	-	0.006	0.006	0.004
Ir	0.085	0.124	0.067	0.074	0.041	0.054	0.044	0.150	0.011	-	0.002	0.007	0.009
Ru	0.130	0.193	0.165	0.087	0.081	0.119	0.103	0.152	0.014	0.003	0.003	0.012	0.012
Rh	0.045	0.070	0.070	0.035	0.035	0.050	0.025	0.060	0.010	-	-	0.005	0.010
Pt	0.009	0.011	0.005	0.004	0.008	0.005	0.003	0.022	0.006	0.001	0.005	0.010	0.010
Pd	0.006	0.004	0.004	0.004	0.013	0.011	0.006	0.026	0.004	-	0.007	0.007	0.004
PPGEEn	0.059	0.084	0.079	0.043	0.056	0.066	0.033	0.107	0.020	0.001	0.012	0.022	0.023
IPGEEn	0.309	0.389	0.269	0.212	0.153	0.202	0.182	0.456	0.031	0.003	0.011	0.025	0.025
PPGEEn/IPGEEn	0.192	0.217	0.292	0.201	0.364	0.327	0.183	0.235	0.622	0.338	1.156	0.892	0.949

Appendix 7. Representative EMPA analyses of PGM in the Bou Azzer chromitites.

Alloys	Alloy_1					Alloy_2					Alloy_3					Alloy_4				
	#1	#2	#3	#4	#5	#1	#2	#3	#4	#5	#1	#2	#3	#4	#5	#1	#2	#3	#4	#5
Os	52.50	52.73	52.89	52.84	52.88	49.62	48.32	48.27	48.04	48.80	68.59	68.20	70.77	71.66	71.82	71.99	71.82	71.99	73.22	73.22
Ir	40.13	41.13	40.34	36.03	41.01	40.74	41.38	41.28	41.43	40.68	26.51	25.83	23.70	23.03	23.55	23.69	23.55	23.69	24.07	24.07
Ru	3.98	4.39	4.30	4.22	4.68	10.20	9.58	9.76	10.11	9.72	3.79	3.33	4.12	2.87	4.74	4.21	4.74	4.21	2.46	2.46
Pt	0.96	0.78	1.00	0.93	0.95	1.69	2.17	2.72	1.84	2.21	1.09	1.06	1.16	0.96	1.00	1.22	1.00	1.22	1.00	1.00
Pd	0.09	0.31	b.d.l.	b.d.l.	b.d.l.	b.d.l.	b.d.l.	0.44	0.39	0.05	b.d.l.	0.34	b.d.l.	0.15	0.48	0.27	b.d.l.	0.27	b.d.l.	b.d.l.
Rh	0.11	0.17	0.04	0.10	0.13	0.10	0.02	0.23	0.06	0.19	0.20	0.16	0.07	0.23	b.d.l.	0.05	b.d.l.	0.05	b.d.l.	b.d.l.
Fe	0.23	0.29	0.27	0.75	0.20	0.09	0.18	0.17	0.14	0.09	0.55	0.56	0.25	0.19	0.22	0.29	0.22	0.29	0.61	0.61
Cr	0.31	0.33	0.45	1.41	0.16	b.d.l.	b.d.l.	b.d.l.	b.d.l.	b.d.l.	1.50	1.27	0.30	0.54	0.25	0.20	0.25	0.20	0.50	0.50
Ni	0.02	0.11	0.05	1.24	0.06	0.05	0.03	0.04	0.02	b.d.l.	b.d.l.	0.02	0.02	b.d.l.	b.d.l.	b.d.l.	b.d.l.	b.d.l.	b.d.l.	b.d.l.
Cu	b.d.l.	b.d.l.	b.d.l.	b.d.l.	b.d.l.	b.d.l.	b.d.l.	b.d.l.	b.d.l.	b.d.l.	b.d.l.	b.d.l.	b.d.l.	b.d.l.	b.d.l.	b.d.l.	b.d.l.	b.d.l.	b.d.l.	b.d.l.
Co	b.d.l.	b.d.l.	b.d.l.	b.d.l.	b.d.l.	0.01	0.03	b.d.l.	b.d.l.	0.03	0.01	b.d.l.	b.d.l.	b.d.l.	b.d.l.	b.d.l.	b.d.l.	b.d.l.	0.01	0.01
S	b.d.l.	b.d.l.	b.d.l.	b.d.l.	b.d.l.	b.d.l.	b.d.l.	b.d.l.	b.d.l.	b.d.l.	b.d.l.	b.d.l.	b.d.l.	0.02	b.d.l.	0.02	b.d.l.	0.02	b.d.l.	b.d.l.
As	b.d.l.	b.d.l.	b.d.l.	b.d.l.	b.d.l.	b.d.l.	b.d.l.	b.d.l.	b.d.l.	b.d.l.	b.d.l.	b.d.l.	b.d.l.	b.d.l.	b.d.l.	b.d.l.	b.d.l.	b.d.l.	b.d.l.	b.d.l.
Total	98.34	100.24	99.34	97.51	100.06	102.51	101.71	102.90	102.02	101.76	102.25	100.77	100.39	99.65	102.05	101.95	102.05	101.95	101.87	101.87

Sulfides	Unaltered laurite					Altered laurite					
	#1	#2	#3	#4	#5	#6	#1	#2	#3	#4	#5
Os	6.62	6.60	3.30	5.21	6.48	5.44	1.82	3.36	2.35	3.76	2.08
Ir	3.05	3.03	2.72	2.72	2.95	2.72	1.53	2.21	1.44	2.82	1.89
Ru	51.85	51.81	55.84	54.20	52.85	53.10	65.64	60.68	63.74	57.86	62.81
Pt	b.d.l.	b.d.l.	b.d.l.	b.d.l.	b.d.l.	b.d.l.	b.d.l.	b.d.l.	b.d.l.	0.36	0.34
Pd	0.40	b.d.l.	0.08	0.15	b.d.l.	0.02	0.14	b.d.l.	0.24	0.22	0.27
Rh	0.51	0.65	0.62	0.54	0.51	0.54	0.61	1.02	0.60	0.46	1.42
Fe	0.03	b.d.l.	0.02	b.d.l.	b.d.l.	b.d.l.	0.08	0.13	0.14	0.12	0.07
Cr	b.d.l.	b.d.l.	b.d.l.	b.d.l.	b.d.l.	0.01	b.d.l.	0.02	0.02	0.04	0.05
Ni	b.d.l.	b.d.l.	b.d.l.	b.d.l.	b.d.l.	b.d.l.	0.50	0.64	0.74	0.68	0.75
Cu	b.d.l.	b.d.l.	b.d.l.	b.d.l.	b.d.l.	b.d.l.	b.d.l.	b.d.l.	b.d.l.	0.04	0.04
Co	b.d.l.	0.02	0.01	b.d.l.	b.d.l.	b.d.l.	0.02	b.d.l.	b.d.l.	0.08	0.04
S	37.67	37.83	38.30	38.81	37.96	38.65	29.48	30.14	29.82	33.48	32.26
As	b.d.l.	b.d.l.	b.d.l.	b.d.l.	b.d.l.	b.d.l.	b.d.l.	b.d.l.	b.d.l.	0.96	0.46
Total	100.12	99.94	100.90	101.63	100.75	100.47	99.82	98.20	99.08	100.89	102.48

Appendix 8. X-ray maps of Bou Azzer platinum group minerals. (a) Magmatic laurite crystal. (b) Altered laurite crystal. (c) Ir-Os alloy with a rim of secondary irarsite

